



National Technical University of Athens  
School of Applied Mathematical & Physical Sciences

---

Department of Physics  
Laboratory of Experimental High Energy Physics  
& Related Technology-Instrumentation

**Research and Development of the Detector Control  
& Data Acquisition Systems for the New Small  
Wheel Upgrade of the ATLAS experiment at CERN  
and Performance Evaluation of the Micromegas  
detector**

A dissertation presented by

**Polyneikis Tzanis**

to

The Department of Physics  
for the degree of  
Doctor of Philosophy  
in the subject of Physics

Athens, July 2024





---

# Research and Development of the Detector Control & Data Acquisition Systems for the New Small Wheel Upgrade of the ATLAS experiment at CERN and Performance Evaluation of the Micromegas detector

PhD Thesis

**Polyneikis Tzanis**

**Advisor:** Theodoros Alexopoulos  
Professor, N.T.U.A

Exam committee:

.....  
T. Alexopoulos  
Professor, N.T.U.A.,  
Greece

.....  
M. Kokkoris  
Professor, N.T.U.A.,  
Greece

.....  
T. Geralis  
Research Director, N.C.S.R.,  
Greece

.....  
S. Maltezos  
Emeritus Professor,  
N.T.U.A., Greece

.....  
M. Diakaki  
Assistant Professor,  
N.T.U.A., Greece

.....  
G. Stavropoulos  
Research Director, N.C.S.R.,  
Greece

.....  
G. Iakovidis  
Associate Scientist,  
B.N.L., USA

Athens, July 2024



.....

Διπλωματούχος Φυσικός Εφαρμογών, Σ.Ε.Μ.Φ.Ε., Ε.Μ.Π

© (2024) National Technical University of Athens. *All rights reserved.*

Funded by the Basic Research Program PEVE 2021 of the National Technical University of Athens.

Απαγορεύεται η αντιγραφή, αποθήκευση και διανομή της παρούσας εργασίας, εξ ολοκλήρου ή τμήματος αυτής, για εμπορικό σκοπό. Επιτρέπεται η ανατύπωση, αποθήκευση και διανομή για σκοπό μη κερδοσκοπικό, εκπαιδευτικής ή ερευνητικής φύσης, υπό την προϋπόθεση να αναφέρεται η πηγή προέλευσης και να διατηρείται το παρόν μήνυμα. Ερωτήματα που αφορούν τη χρήση της εργασίας για κερδοσκοπικό σκοπό πρέπει να απευθύνονται προς τον συγγραφέα.





ΕΘΝΙΚΟ ΜΕΤΣΟΒΙΟ ΠΟΛΥΤΕΧΝΕΙΟ  
ΣΧΟΛΗ ΕΦΑΡΜΟΣΜΕΝΩΝ ΜΑΘΗΜΑΤΙΚΩΝ ΚΑΙ  
ΦΥΣΙΚΩΝ ΕΠΙΣΤΗΜΩΝ

---

ΤΟΜΕΑΣ ΦΥΣΙΚΗΣ  
ΕΡΓΑΣΤΗΡΙΟ ΠΕΙΡΑΜΑΤΙΚΗΣ ΦΥΣΙΚΗΣ ΥΨΗΛΩΝ  
ΕΝΕΡΓΕΙΩΝ & ΣΥΝΑΦΟΥΣ ΟΡΓΑΝΟΛΟΓΙΑΣ

**Έρευνα και Ανάπτυξη των Συστημάτων Αυτόματου  
Ελέγχου & Λήψης Δεδομένων της Αναβάθμισης New  
Small Wheel του Πειράματος ATLAS στο CERN και  
Χαρακτηρισμός της Απόδοσης του Ανιχνευτή  
Micromegas**

Διδακτορική διατριβή του

**Πολυνείκη Τζανή**

Διπλωματούχου Φυσικού Εφαρμογών, Σ.Ε.Μ.Φ.Ε., Ε.Μ.Π  
& κατόχου Μεταπτυχιακού τίτλου Φυσικού Εφαρμογών, Σ.Ε.Μ.Φ.Ε., Ε.Μ.Π

**Επιβλέπων:** Θεόδωρος Αλεξόπουλος  
Καθηγητής Ε.Μ.Π.

Αθήνα, Ιούλιος 2024





ΕΘΝΙΚΟ ΜΕΤΣΟΒΙΟ ΠΟΛΥΤΕΧΝΕΙΟ  
ΣΧΟΛΗ ΕΦΑΡΜΟΣΜΕΝΩΝ ΜΑΘΗΜΑΤΙΚΩΝ ΚΑΙ  
ΦΥΣΙΚΩΝ ΕΠΙΣΤΗΜΩΝ

ΤΟΜΕΑΣ ΦΥΣΙΚΗΣ  
ΕΡΓΑΣΤΗΡΙΟ ΠΕΙΡΑΜΑΤΙΚΗΣ ΦΥΣΙΚΗΣ ΥΨΗΛΩΝ ΕΝΕΡΓΕΙΩΝ  
& ΣΥΝΑΦΟΥΣ ΟΡΓΑΝΟΛΟΓΙΑΣ

**Έρευνα και Ανάπτυξη των Συστημάτων Αυτόματου Ελέγχου &  
Λήψης Δεδομένων της Αναβάθμισης New Small Wheel του  
Πειράματος ATLAS στο CERN και Χαρακτηρισμός της  
Απόδοσης του Ανιχνευτή Micromegas**

Διδακτορική διατριβή του

**Πολυνείκη Τζανή**

Διπλωματούχου Φυσικού Εφαρμογών, Σ.Ε.Μ.Φ.Ε., Ε.Μ.Π  
& κατόχου Μεταπτυχιακού τίτλου Φυσικού Εφαρμογών, Σ.Ε.Μ.Φ.Ε., Ε.Μ.Π

**ΤΡΙΜΕΛΗΣ ΣΥΜΒΟΥΛΕΥΤΙΚΗ  
ΕΠΙΤΡΟΠΗ**

1. Θεόδωρος Αλεξόπουλος, Καθ. Ε.Μ.Π.
2. Μιχάλης Κόκορης, Καθ. Ε.Μ.Π.
3. Θεόδωρος Γέραλης, Διευθ. Ερευνών, ΕΚΕΦΕ Δημόκριτος

**ΕΠΤΑΜΕΛΗΣ ΣΥΜΒΟΥΛΕΥΤΙΚΗ ΕΠΙΤΡΟΠΗ**

1. Θεόδωρος Αλεξόπουλος, Καθ. Ε.Μ.Π.
2. Μιχάλης Κόκορης, Καθ. Ε.Μ.Π.
3. Θεόδωρος Γέραλης, Διευθ. Ερευνών, ΕΚΕΦΕ Δημόκριτος
4. Σταύρος Μαλτέζος, Ομ. Καθ. Ε.Μ.Π.
5. Μαρία Διακάκη, Επ. Καθ. Ε.Μ.Π.
6. Γεώργιος Σταυρόπουλος, Διευθ. Ερευνών, ΕΚΕΦΕ Δημόκριτος
7. Γεώργιος Ιακωβίδης, Ερευνητής Β', BNL, USA

Αθήνα, Ιούλιος 2024





---

# Περίληψη

---

Η παρούσα διδακτορική διατριβή αναφέρεται κυρίως στην έρευνα και ανάπτυξη του συστήματος ελέγχου του ανιχνευτή & συλλογής δεδομένων για την αναβάθμιση του πειράματος ATLAS στο CERN με τους δύο νέους "μικρούς τροχούς" (New Small Wheels, NSW) και την αξιολόγηση της απόδοσης του ανιχνευτή Micromegas. Η κύρια πρόκληση αυτής της διατριβής ήταν η κατανόηση και η επίλυση προβλημάτων ενός τόσο πολύπλοκου και μεγάλου συστήματος όπως το NSW. Η παρούσα διδακτορική διατριβή είχε βασικό ρόλο στην επιτυχή ολοκλήρωση, εγκατάσταση και λειτουργία των δύο τροχών του NSW στο πείραμα ATLAS.

Ο ανιχνευτής μιονίων του ATLAS, Small Wheel (SW), θα αντικατασταθεί από έναν νέο ανιχνευτή Small Wheel, προκειμένου να αντεπεξέλθει στις μελλοντικές αναβαθμίσεις του LHC υψηλής φωτεινότητας. Προκειμένου να αντιμετωπιστεί αποτελεσματικά η αυξημένη φωτεινότητα που θα παρέχει ο LHC φωτεινότητας (HL-LHC), θα πρέπει να αντικατασταθεί το SW του Φασματομέτρου Μιονίων του ATLAS. Το NSW θα πρέπει να λειτουργεί σε μια περιοχή υψηλής ακτινοβολίας υποβάθρου (έως και  $22 \text{ kHz/cm}^2$ ), ενώ παράλληλα θα ανακατασκευάζει τις τροχιές των μιονίων με μεγάλη ακρίβεια, καθώς και θα παρέχει πληροφορίες για το trigger του Level 1 (L1). Οι τεχνολογίες των ανιχνευτών που θα χρησιμοποιηθούν προέρχονται από την οικογένεια των ανιχνευτών αερίων, η πρώτη ονομάζεται small Thin Gap Chambers (sTGCs) και η δεύτερη προέρχεται από την κατηγορία των ανιχνευτών αερίων με micromesh και ονομάζεται Micromegas (Micromesh Gaseous Structure (MM)). Η νέα πειραματική διάταξη θα αποτελείται από 16 στρώματα ανίχνευσης συνολικά, ήτοι 8 στρώματα ανά τεχνολογία ανίχνευσης (οχτώ στρώματα sTGC και οχτώ στρώματα Micromegas). Οι ανιχνευτές sTGC έχουν σχεδιαστεί για να παρέχουν γρήγορη ενεργοποίηση και παρακολούθηση μιονίων υψηλής ακρίβειας υπό τις συνθήκες του HL-LHC. Από την άλλη πλευρά, οι ανιχνευτές Micromegas έχουν μικρή περιοχή μετατροπής της τάξεως των 5 mm και βήμα λωρίδας ανάγνωσης (readout strip pitch) της τάξεως των 0.45 mm με αποτέλεσμα εξαιρετική χωρική ανάλυση. Στο κεφάλαιο 1 & 2, θα γίνει μια σύντομη εισαγωγή στον Μεγάλο Επιταχυντή Αδρονίων (LHC), το πείραμα ATLAS και την αναβάθμιση του NSW. Θα παρουσιαστεί η αρχή λειτουργίας των δύο νέων ανιχνευτών, sTGC και Micromegas, καθώς και το αντικείμενο και η διάταξη του NSW. Επιπλέον, θα γίνει μια σύντομη εισαγωγή στην υποδομή του NSW και στη διαδικασία ελέγχου και εγκατάστασης που έλαβε χώρα μέχρι την εγκατάσταση του NSW στο ATLAS.

Ο βασικός λίθος του συστήματος DAQ του ATLAS θα είναι το FELIX, το οποίο είναι ένα σύστημα βασισμένο σε FPGA. Το FELIX θα είναι ουσιαστικά μια γέφυρα μεταξύ των ηλεκτρονικών στοιχείων του front-end όλων των υποσυστημάτων του ανιχνευτή ATLAS και των αντίστοιχων στοιχείων του back-end τους, τα οποία βασίζονται κυρίως σε λογισμικό. Το FELIX συνδέεται με τα ηλεκτρονικά του front-end του ATLAS μέσω οπτικών συνδέσεων ή συνδέσεων Giga-Bit Transceiver (GBT), κάθε μία από τις οποίες λειτουργεί με ταχύτητα 4.8 Gb/s. Για την περίπτωση NSW, το FELIX διασυνδέεται με τους κόμβους front-end μέσω 24 οπτικών συνδέσεων. Αυτές οι συνδέσεις μεταφέρουν το πλαίσιο GBT, το οποίο έχει εύρος 84 bit. Το GBT είναι ένα σύστημα μετάδοσης που περιλαμβάνει ASICs με ανοχή στην ακτινοβολία, τα οποία είναι ικανά να διαχειριστούν τις μεγάλες ποσότητες δεδομένων των πειραμάτων φυσικής υψηλής ενέργειας. Το GBT-SCA ASIC (Giga-Bit Transceiver - Slow Control Adapter) είναι ένα ολοκληρωμένο κύκλωμα κατασκευασμένο σε τεχνολογία CMOS 130 nm και είναι το

τμήμα του chipset GBT που έχει ως σκοπό να διανέμει σήματα ελέγχου και παρακολούθησης στα ηλεκτρονικά front-end που είναι ενσωματωμένα στους ανιχνευτές. Συνδέεται σε μια ειδική ηλεκτρική θύρα στα GBTx ASICs μέσω ενός διπλού κυκλώματος 80 Mbps πλεονάζουσας αμφίδρομης ζεύξης δεδομένων (e-links). Για τις ανάγκες της διαμόρφωσης (configuration) των διαφορετικών front-end ASIC σε διάφορα πειράματα, το SCA παρέχει έναν αριθμό ρυθμιζόμενων από τον χρήστη ηλεκτρικών θυρών διασύνδεσης, ικανών να εκτελούν ταυτόχρονες λειτουργίες μεταφοράς δεδομένων. Η θύρες διασύνδεσης είναι οι εξής: 1 SPI master, 16 ανεξάρτητοι I2C master, 1 JTAG master και 32 IO γενικής χρήσης σήματα με ξεχωριστή προγραμματιζόμενη κατεύθυνση και λειτουργικότητα παραγωγής διακοπών. Περιλαμβάνει επίσης 31 αναλογικές εισόδους πολυπλεγμένες (multiplexed) σε έναν ADC 12 bit που διαθέτει βαθμονόμηση offset και διόρθωση gain, καθώς και τέσσερις θύρες αναλογικής εξόδου που ελέγχονται από τέσσερις ανεξάρτητους DAC 8 bit. Το κεφάλαιο 3 αποτελείται από μια λεπτομερή περιγραφή των ηλεκτρονικών NSW και του συστήματος συλλογής δεδομένων (DAQ). Η περιγραφή περιλαμβάνει τα κύρια μέρη του NSW DAQ, όπως το FELIX, το GBTx και το GBT-SCA. Θα παρουσιαστεί λεπτομερώς το οικοσύστημα SCA το οποίο περιλαμβάνει το λογισμικό, το quasar framework και τον SCA OPC UA Server & Client. Τα διάφορα ηλεκτρονικά NSW θα περιγραφούν μαζί με τις εργασίες για τον ορισμό των συνδέσεων SCA. Για τις ανάγκες της λειτουργίας του SCA OPC UA Server, αναπτύχθηκε ένα εργαλείο προκειμένου να δημιουργηθούν τα απαιτούμενα αρχεία εισόδου τα οποία περιείχαν το αναπτυγμένο σχήμα ονοματοδοσίας NSW μέσα στις λίστες OKS. Για τις ανάγκες του κοινόχρηστου καναλιού εξόδου του VMM στο SCA, δημιουργήθηκε ένας νέος μηχανισμός προκειμένου να επιτευχθεί η επικοινωνία μεταξύ των back-ends DAQ και DCS. Η λειτουργία SCA θα παρουσιαστεί μαζί με το σχεδιασμό της αρχιτεκτονικής του περιβάλλοντος FELIX/OPC, καθώς και τις διάφορες δοκιμές επιδόσεων που πραγματοποιήθηκαν για την επικύρωση του νέου οικοσυστήματος FELIX/SCA. Τέλος, θα γίνει μια σύντομη εισαγωγή για το frontend VMM ASIC μαζί με τις δοκιμές επικύρωσης και τις δοκιμαστικές δέσμες ακτινοβολίας νετρονίων.

Λόγω της πολυπλοκότητας και της μακροχρόνιας λειτουργίας του, ο ATLAS απαιτεί την ανάπτυξη ενός εξελιγμένου συστήματος ελέγχου του ανιχνευτή (DCS). Η χρήση ενός τέτοιου συστήματος είναι απαραίτητη για να επιτρέψει στον ανιχνευτή να λειτουργεί με συνέπεια και ασφάλεια, καθώς και για να λειτουργεί ως απρόσκοπτη διεπαφή με όλους τους υπο-ανιχνευτές και την τεχνική υποδομή του πειράματος. Οι διάφοροι σταθμοί ελέγχου αναπτύσσονται μέσω της εφαρμογής WinCC Open Architecture, η οποία είναι ένα σύστημα εποπτικού ελέγχου και συλλογής δεδομένων (SCADA) και διεπαφής ανθρώπου-μηχανής (HMI) της Siemens. Στο κεφάλαιο 4 παρουσιάζεται μια σύντομη εισαγωγή στο ATLAS DCS, στην εφαρμογή SCADA WinCC-OA που χρησιμοποιείται για τη δημιουργία των διαφόρων σταθμών ελέγχου και στους OPC UA Servers που χρησιμοποιούνται για τη συνδεσιμότητα του υλικού. Για τις ανάγκες της ενσωμάτωσης των ανιχνευτών NSW, η απαίτηση ήταν ο σχεδιασμός και η υλοποίηση συστημάτων αργού ελέγχου για: (α) την πιστοποίηση υψηλής τάσης; (β) την πιστοποίηση διαδρομής αερίου των ανιχνευτών Micromegas; (γ) την ολοκλήρωση του Micromegas sector; (δ) τον περιβαλλοντικό σταθμό; (ε) την ηλεκτρονική παρακολούθηση τόσο των ηλεκτρονικών των Micromegas όσο και των ηλεκτρονικών των sTGC πριν από την εγκατάσταση στο NSW. Ένα μεγάλο μέρος του κεφαλαίου αποτελείται από την περιγραφή της αρχιτεκτονικής και των εννοιών σχεδιασμού του συστήματος ελέγχου παραγωγής NSW. Η αρχιτεκτονική και η σχεδιαστική υλοποίηση του DCS NSW πραγματοποιήθηκε προκειμένου να επιτευχθεί η παρακολούθηση και ο έλεγχος όλων των διαθέσιμων παραμέτρων του NSW. Η αρχιτεκτονική του NSW DCS και η ενσωμάτωσή του με το ATLAS DCS έχει ολοκληρωθεί και οι γραφικές διεπαφές χρήστη ακολουθούν την υπάρχουσα εμφάνιση και δομή εντολών του Muon DCS, ώστε να διευκολυνθούν οι λειτουργίες του χρήστη. Αν και το NSW απαιτεί την ανάπτυξη ενός προηγμένου DCS για την παρακολούθηση των ηλεκτρονικών με τη χρήση του SCA, το οποίο είναι εγκατεστημένο στις πλακέτες 8000 front-end του NSW. Το σύστημα αυτό μας δίνει τη δυνατότητα παρακολούθησης περισσότερων από 100 000 παραμέτρων, οι οποίες περιλαμβάνουν όλους τους αισθητήρες ισχύος/θερμοκρασίας, τη θερμοκρασία και τις πληροφορίες των τσιπ, οι οποίες είναι συνδεδεμένες με το SCA σε όλες τις πλακέτες front-end του NSW. Θα γίνει λεπτομερής παρουσίαση του έργου Electronics που αναπτύχθηκε για τις ανάγκες των ηλεκτρονικών του MMG & STG προκειμένου να επιτευχθεί η παρακολούθηση περισσότερων από 100 000 παραμέτρων. Τέλος, θα παρουσιαστεί το έργο Detector Safety System (DSS) για την ασφάλεια του NSW μαζί με άλλα έργα NSW και το έργο επισκόπησης του Supervisor Control Station (SCS). Κύρια πρόκληση αυτής της διατριβής ήταν η ανάπτυξη συστημάτων συλλογής δεδομένων, ελέγχου και παρακολούθησης για διάφορα υλικά, σύστημα τροφοδοσίας CAEN για εφαρμογές χαμηλής/υψηλής τάσης, ηλεκτρονικές πλακέτες/τσιπ, μικροελεγκτή Arduino, υπολογιστή μιας πλακέτας Raspberry-Pi, κιβώτιο(crate) VME/ATCA και για αισθητήρες πολλαπλών χρήσεων. Αυτές οι υλοποιήσεις μπορούν να έχουν διάφορες χρήσεις και μπορούν να χρησιμοποιηθούν σε οποιοδήποτε πλαίσιο, όπως στην πειραματική φυσική υψηλών ενεργειών ή στη βιομηχανία υψηλής τεχνολογίας,

λόγω της επεκτασιμότητας και της ευελιξίας τους, η οποία αποτελεί την ιδανική επιλογή για τη δημιουργία λύσεων, συμπεριλαμβανομένων κεντρικών σταθμών ελέγχου και γεωγραφικά ευρέως κατανεμημένων συστημάτων.

Ο ανιχνευτής αερίων Micromegas αποτελεί τον ακρογωνιαίο λίθο της αναβάθμισης του πειράματος ATLAS, η οποία θα έχει ως στόχο την ανακατασκευή της τροχιάς των σωματιδίων που διέρχονται από αυτόν κατά τη διάρκεια της σύγκρουσης των δεσμών στο σημείο της αλληλεπίδρασης (Interaction Point - IP). Θα αναλυθεί η αρχή λειτουργίας και η παραγωγή σήματος στον ανιχνευτή από τη διέλευση ενός φορτισμένου σωματιδίου και θα γίνει εκτενής αναφορά στην έρευνα για τη βελτίωση της τεχνολογίας του ανιχνευτή Micromegas μέχρι τον τύπο του ανιχνευτή που θα χρησιμοποιηθεί για το NSW. Η πρώτη μεγάλη μονάδα παραγωγής SM2, εξοπλισμένη με πρωτότυπες ηλεκτρονικές πλακέτες MMFE8 δοκιμάστηκε για πρώτη φορά. Ως εκ τούτου, η απόδοση του πρωτοτύπου έπρεπε να αξιολογηθεί κατά την ανάγνωση με το VMM3. Το αντικείμενο της δοκιμαστικής δέσμης ήταν: (α) Επαλήθευση της καλής απόδοσης του SM2; (β) επικύρωση της απόδοσης των ηλεκτρονικών; (γ) δοκιμή της τρίτης έκδοσης του VMM frontend ASIC σε συνθήκες δέσμης- (γ) εύρεση μιας καλής διαμόρφωσης των παραμέτρων του VMM; (δ) προσδιορισμός του βέλτιστου σημείου εργασίας υψηλής τάσης (ε) δοκιμή διαφορετικών μειγμάτων αερίων και προσδιορισμός της επίδρασης στον ανιχνευτή. Τα καλά αποτελέσματα που επιτεύχθηκαν με το τριμερές μείγμα από την άποψη της σταθερότητας HV χωρίς σωματιδιακό υπόβαθρο, προκάλεσαν μια σειρά μελετών στο GIF++ όπου είναι δυνατόν να επιτευχθεί ρυθμός αλληλεπίδρασης γάμμα υψηλότερος από αυτόν που αναμένεται στον HL-LHC στον ATLAS. Αμέσως μετά τη δοκιμαστική δέσμη H8, ο θάλαμος SM2 εκτέθηκε στη ροή φωτονίων γάμμα του GIF++ μέχρι ρυθμού αλληλεπίδρασης  $50 \text{ kHz/cm}^2$ , 2,5 φορές μεγαλύτερο από το αναμενόμενο υπόβαθρο του HL-LHC του ATLAS. Στόχος είναι η μέτρηση του ρεύματος που παράγεται στο στάδιο ενίσχυσης σε σχέση με την εφαρμοζόμενη υψηλή τάση και την προσπίπτουσα ροή. Ιδιαίτερη προσοχή δίδεται στα προβλήματα σταθερότητας του ρεύματος και στα φαινόμενα αιχμής που ενδέχεται να θέσουν σε κίνδυνο την απόδοση του ανιχνευτή κατά τη μακροχρόνια λειτουργία εντός του ανιχνευτή ATLAS. Πραγματοποιήθηκαν πλήρεις αναλύσεις με εφαρμογή διαφορετικής τιμής υψηλής τάσης προκειμένου να μελετηθεί η σταθερότητα σε υψηλό υπόβαθρο σε όλη την καμπύλη ενεργοποίησης και κοντά στο σημείο εκφόρτισης. Το μεγαλύτερο μέρος του κεφαλαίου 5 θα περιλαμβάνει αποτελέσματα και διαγράμματα που συγκεντρώθηκαν και αναλύθηκαν κατά τη διάρκεια των διαφόρων δοκιμαστικών ακτίνων H8&GIF++ προκειμένου να αξιολογηθεί η απόδοση του ανιχνευτή Micromegas.



---

# Abstract

---

This dissertation presents the research and development of the Detector Control and Data Acquisition Systems for the New Small Wheel (NSW) upgrade within the ATLAS experiment at CERN, alongside a comprehensive performance evaluation of the Micromegas detector. The NSW upgrade is pivotal for adapting the ATLAS detector to the challenges created by the increased luminosity of the future Large Hadron Collider (LHC) runs. This work navigates the complexities of integrating complex technologies into a high-radiation environment, demonstrating a critical contribution to the successful deployment and operation of the NSW project. The upgrade involves the replacement of the existing ATLAS Small Wheel Muon detector with a new, advanced system capable of operating in high background radiation levels-up to  $22 \text{ kHz/cm}^2$ , while maintaining high precision in muon track reconstruction and Level-1 trigger information. The NSW consists of two innovative gaseous detector technologies: small-strip Thin Gap Chambers (sTGCs) for rapid trigger response and high-precision tracking, and Micromegas (MM) detectors, which are micro-pattern gas detectors offering excellent spatial resolution due to their small conversion region and fine strip pitch. This thesis highlights the design, the operational principles and the integration of these technologies across 16 detection layers, detailing the challenges and solutions in configuring such a complex system. A significant focus is placed on the ATLAS Data Acquisition (DAQ) system, particularly the FELIX system- an FPGA based interface facilitating communication between the detector's front-end electronics and back-end software components. The intricacies of the GBT protocol, the GBT-SCA ASIC's role in signal processing, and the development of a robust control and monitoring network through the SCA ecosystem are discussed in detail. This includes the creation of novel tools and mechanisms for enhancing data integrity and system reliability. Moreover, the thesis delves into the Detector Control System (DCS), emphasizing its critical role in ensuring the detector's consistent and safe operation. The development and implementation of control systems for various operational aspects, such as high voltage and gas leak validation for Micromegas detectors, are examined. This segment highlights the bespoke architecture of the NSW DCS and its integration to the broader ATLAS DCS framework, showcasing the advanced electronics monitoring capabilities developed for overseeing more than 100 000 parameters. The experimental section presents a thorough analysis of the Micromegas detector's performance, including the operational gaseous detector principles, signal generation and the impact of various operational parameters. Results from extensive testbeam campaigns at H8 and GIF++ facilities offer insights into the detector's response under high interaction rates, illustrating the successful adaptation of the technology for high-luminosity environments. This research not only contributes to the ATLAS experiment's readiness for future LHC runs, but also advances the field of particle physics instrumentation. By addressing the challenges of high-luminosity data acquisition and control in one of the most demanding experimental environments, this work sets a precedent for future detector technologies and their implementation in large-scale scientific research. Through meticulous design, testing and validation, the thesis underscores the pivotal role of innovative detector and control technologies in pushing the boundaries of particle physics research, offering valuable lessons for the development of future experiments in high energy physics and beyond.



---

# Preface

---

Purpose of this dissertation is mainly the Research and Development of the Detector Control & Data Acquisition Systems for the New Small Wheel (NSW) Upgrade of the ATLAS experiment at CERN and the Performance Evaluation of the Micromegas detectors. This thesis was carried out within the ATLAS Muon Collaboration at CERN. The author's contributions are going to be presented in this section.

- **Chapter 1:** The chapter provides a detailed introduction to the Large Hadron Collider (LHC) and the ATLAS experiment, highlighting the LHC as the world's largest and most powerful particle accelerator located at CERN. It delves into the LHC's primary aim of exploring physics beyond the Standard Model through high-energy proton collisions within a 27 km ring, utilizing a complex network of accelerators. The ATLAS experiment is outlined as a key component in this scientific endeavor, designed to study various physics phenomena including the discovery of the Higgs particle. The text details the ATLAS experiment's major systems: the Magnet System, the Inner Detector, the Calorimeters, the Muon Spectrometer and the Trigger & Data Acquisition System (TDAQ), each playing a critical role in particle detection and data processing. The LHC's accelerator complex and its sequence of particle acceleration, culminating in collisions at four main experiments (ATLAS, CMS, ALICE, LHCb), are discussed, with emphasis on the purpose and design of each experiment. The chapter also describes the LHC's performance and its pivotal discovery of the Higgs particle in 2012, following its first run. Specific attention is given to the ATLAS experiment's subsystems, including the Magnet System, which comprises the Central Solenoid, the Barrel Toroid, and the End-Cap Toroids, crucial for bending charged particle tracks for momentum measurement. The Inner Detector, equipped with various technologies like the Pixel Detector and SemiConductor Tracker, is tasked with analyzing particle trajectories. The Calorimeters, responsible for absorbing and measuring particle energy, and the Muon Spectrometer, designed for muon identification and measurement, are explained in detail. The chapter also covers the TDAQ system, essential for data collection and processing, reducing initial collision data rates to manageable levels for analysis. The text concludes by emphasizing the ATLAS experiment's role in broadening our understanding of fundamental physics, pushing beyond the limits of the Standard Model through its advanced detection and data acquisition systems.
- **Chapter 2:** The chapter begins by setting the context of the NSW upgrade, outlining its objectives to improve the detection efficiency, resolution, and data processing speeds. It emphasizes the critical need for this upgrade in response to the increasing demands of LHC's high-luminosity experiments, which require more refined and robust detectors to cope with higher particle interaction rates. The integration process of the Micromegas and sTGC detectors is examined in detail, showcasing the complex techniques and technologies employed. For the Micromegas detectors, the chapter describes the innovative alignment strategies that ensure their precise positioning, crucial for the accurate measurement of particle trajectories. This section also explores the challenges faced during the integration process, including

the strict requirements for detector sensitivity and the solutions proposed to address these challenges. Similarly, the integration of the sTGC detectors is covered comprehensively, highlighting their role in providing fast trigger capabilities and spatial resolution. The chapter discusses the collaborative efforts involved in the sTGC integration, from design and fabrication to testing and final assembly, illustrating the collaborative nature of modern particle physics projects. Furthermore, the chapter analyzes the logistical and technical challenges encountered during the NSW upgrade, such as the transportation and installation of the detectors in the constrained environments of CERN's underground facilities. It details the innovative methods developed to overcome these obstacles, ensuring the project's successful completion within the scheduled timeframe. In summary, the chapter on the NSW Upgrade Project not only provides an in-depth look at the technical and procedural aspects of the upgrade, but also reflects the broader implications of this work for the future of particle physics research. It underscores the NSW upgrade's role in extending the LHC's research capabilities, facilitating the exploration of fundamental questions about the universe's structure and the fundamental forces that govern it.

- **Chapter 3:** This chapter starts with an in-depth exploration of the NSW's electronics architecture, emphasizing its critical role in enhancing the data acquisition capabilities, essential for advanced experimental physics research. It details the functionalities and the integration of major components such as the FrontEnd LInk eXchange (FELIX), which serves as the backbone for data flow management, alongside GBTx and GigaBit Transceiver Slow Control Adapter (GBT-SCA), which are pivotal in ensuring robust data transmission and signal conditioning. The discourse further advances into the Slow Control Adapter (SCA) Ecosystem, a cornerstone in the DAQ's operational framework. This section meticulously outlines the software strategies adopted, showcasing the quasar framework's adaptability and efficiency in handling data acquisition tasks. It provides an insightful overview of the SCA OPC UA Server & Client, illustrating how these components synergize to offer a reliable and scalable data communication infrastructure. Moreover, the chapter casts light on the diverse electronics used within NSW, presenting a detailed account of their functionalities, integration challenges, and the innovative solutions proposed to overcome them. It also delves into the meticulous work involved in defining the SCA connections, highlighting the technical intricacies and the collaborative efforts required to ensure seamless data flow and system interoperability. Actually, this chapter not only serves as a comprehensive guide to the NSW's electronics and DAQ system, but also exemplifies the cutting-edge technologies and methodologies being employed in the field of experimental physics. A brief introduction is made for the frontend VMM ASIC along with the validation tests and the neutron irradiation testbeams. Through detailed descriptions, technical insights, and schematic presentations, readers are afforded a clear understanding of the complexities and achievements in developing a state-of-the-art data acquisition system.
- **Chapter 4:** This chapter provides an in-depth exploration of the Detector Control System (DCS) employed in the ATLAS experiment, underlining its indispensable role in ensuring the detector's optimal functionality over extended periods. It starts with an overview of the DCS's complexity, highlighting its function as an essential interface for sub-detectors and the overall technical infrastructure. The text underscores the system's capability to manage operational state transitions, to monitor performance parameters continuously and respond to system abnormalities through alerts that trigger automatic or manual corrective actions. A significant part of the chapter is dedicated to detailing the SCADA (Supervisory Control and Data Acquisition) system's application within the DCS framework, illustrating how it facilitates industrial control and telemetry to maintain the detector's integrity and safety. The discussion extends to the specific design and architecture of the ATLAS DCS, including the operational mechanisms behind control stations, OPC UA Servers for hardware connectivity, and the comprehensive architecture of the NSW Production Control System. This section analyses the technical and logistical considerations behind monitoring over 100 000 parameters, emphasizing the Electronic project developed for MMG & STG electronics. Furthermore, the chapter elaborates on the DSS project for NSW safety, among other NSW projects, and provides an overview of the SCS (Supervisor Control System), highlighting the meticulous design and implementation strategies that ensure the seamless operation and safety of the ATLAS detector. Through detailed descriptions of the control systems, the hardware infrastructure and the project allocations, the chapter offers valuable insights into the innovating engi-



---

neering and management practices that underpin the successful operation of one of the most complex scientific instruments in the world.

- **Chapter 5:** The chapter includes a brief description of the Micromegas operation parameters and the mechanisms which characterize the micromesh gaseous detectors. It also elucidates on the quadruplet's efficiency in both external and self-tracking modes under various gas mixture conditions, providing a clear understanding of its performance dynamics. These insights are paramount, as they contribute to optimizing the detector's functionality, ensuring that it meets the strict requirements of precision and reliability demanded by the cutting-edge research conducted at the ATLAS experiment. Beyond the technical achievements, this evaluation carries significant implications for the field of particle physics. It not only validates the Micromegas detector as a formidable tool for muon detection tracking, but also sets a benchmark for future technological advancements within the ATLAS project and beyond. In addition, the position reconstruction techniques are described. Finally, the H8 & GIF++ testbeam runs and the analysis studies for the characterization of the Micromegas performance are described in detail. The lessons learned from addressing the challenges of detector calibration, the HV stability and the efficiency optimization offer a valuable blueprint for enhancing the performance of similar particle detectors used for other high-energy physics experiments. Furthermore, this chapter underscores the necessity of continuous innovation and rigorous testing in the advancement of particle detection technologies. It highlights potential avenues for future research, including the exploration of advanced computational techniques and the integration of machine learning algorithms for data analysis, which could revolutionize the way we approach experimental physics.



---

# Acknowledgments

---

It's now the time to thank all the people who supported me during this PhD and life journey.

First of all, I would like to express my deepest gratitude to my advisor, **Theodoros Alexopoulos**, who believed in me since 2016 and gave me the opportunity to join the NTUA EHEP team/school at CERN. His mentorship, guidance and trust allowed me to be part of various projects related to the New Small Wheel Upgrade project at the ATLAS experiment, where I gained invaluable skills and knowledge through countless hours at test beams and integration sites. I am deeply grateful to **Stavros Maltezos** for his help, and passion for experimental physics, especially for the countless hours we spent designing the gas tightness station.

I would also like to thank **George Iakovidis** for his trust, support, and collaboration over the years, which opened the door to the fascinating world of readout electronics. Additionally, I extend my thanks to **Vinnie Polychronakos** for his support provided through the Brookhaven National Laboratory.

My gratitude also goes to **Theodoros Gerasis** for his continuous support, valuable suggestions, and for giving me the chance to intern at NCSR Demokritos, where I discovered the Micromegas detector. I appreciate **Michael Kokkoris** for his enthusiasm for Nuclear Physics, our productive collaboration, and for being a part of my exam committee. I am also thankful to **George Stavropoulos** and **Maria Diakaki** for their help and for agreeing to be part of my exam committee.

I would like to pay a special tribute to **Stephanie Zimmermann** for her unwavering support and belief in my ability to manage the challenging New Small Wheel DCS coordination. Her loss was devastating, but her spirit continues to inspire us, and I am certain she would be proud of our success with the NSW project.

I am grateful to **Philipp Fleischmann** for his continuous support and assistance to be part of the Muon ATLAS team. I also thank **Paolo Iengo** and **Mario Antonelli** for their help and support on the NSW project, and **Zhen Yan** for the fruitful discussions and assistance with the Muon DCS.

Special thanks to the Central DCS team of ATLAS, especially **Paris Moschovakos**, **Piotr Nikiel**, and **Stefan Schlenker**, for their strong collaboration and help with the SCA OPC UA project and the successful integration of the NSW DCS into the ATLAS DCS.

I am thankful to **Lorne Levinson** for his guidance on the NSW Data Acquisition and Trigger system, and to **Cenk Yildiz** for his help and guidance during my initial steps with the NSW DAQ software. I appreciate the strong collaboration and support from the NSW DAQ team: **Alex Tuna**, **Jared Sturdy**, and **Rongkun Wang** in enhancing the NSW configuration software. I also extend my thanks to **Enrico Pasqualucci** for his

collaboration on the Muon DAQ system.

A heartfelt thanks to the NSW DCS team: **Christos Paraskevopoulos, Stamatis Tzanos, Thorwald Klapdor-Kleingrothaus, Efsthathios Karentzos, Henso Abreu, Matei-Eugen Vasile, Dorel Pietreanu, and Yiannis Drivas** for the success of the NSW DCS project. In particular, I am deeply grateful to **Christos Paraskevopoulos** for his dedication, unwavering support, and strong collaboration during stressful times for the NSW DCS.

My sincere thanks to the Micromegas testbeam team, especially **Aimilianos Koulouris** and **Chara Kitsaki**, for their guidance on the analysis code and their strong collaboration. I am also grateful to **Ralf Hertenberger** for explaining the Micromegas properties, and to **Valerio D'Amico** and **Patrick Scholer** for their help and feedback during various testbeams.

I would like to extend my gratitude to the Micromegas and sTGC integration team: **Kostas Ntekas, Gerardo Vasquez, Aimilianos Koulouris, Luigi Longo, Athina Kourkoumeli, Giada Mancini, Liang Guan, and Olga Zormpa**, for their help and strong collaboration during challenging periods.

Special thanks to the BB5 team: **Spyros Kompogiannis, Takis Damianoglou, Alan Peyaud, Ivan Gnesi, Marios Natsios, Ilias Alexopoulos, Stamatis Tzanos, Anthony Badea, Ikaros Frangkos, Foteini Kolitsi, Giannis Mesolongitis, Daniel Bitz, Emanuele Romano, Stelian Buda and Giannis Maniatis** for the playful collaboration.

I would also like to thank the current and past members of the NTUA EHEP team: **Christos Bakalis, Yiannis Drivas, Nikos Kanellos, Panagiotis Gkoutoumis, Stefanos Leontsinis, Dimitros Matakias and Georgios Koutelieris**.

Lastly, but most importantly, I wish to express my profound gratitude and love to **my family, parents, sister, and friends** for their unwavering love and support throughout this journey. A special thanks to **my Efi** for her continuous support, love, strength, and trust during the ups and downs of my PhD journey. I am truly grateful for everything!

---

# Contents

---

<b>Περίληψη</b>	<b>3</b>
<b>Abstract</b>	<b>7</b>
<b>Preface</b>	<b>9</b>
<b>Acknowledgments</b>	<b>13</b>
<b>0 Σύνοψη στα Ελληνικά</b>	<b>19</b>
<b>1 Introduction to the Large Hadron Collider and the ATLAS Experiment</b>	<b>43</b>
1.1 The Large Hadron Collider . . . . .	44
1.2 Accelerator Complex and Experiments . . . . .	44
1.3 LHC Performance . . . . .	46
1.4 ATLAS Experiment . . . . .	46
1.4.1 Magnet System . . . . .	47
1.4.2 Inner Detector . . . . .	48
1.4.3 Calorimeters . . . . .	48
1.4.4 Muon Spectrometer . . . . .	50
1.5 High Luminosity LHC (HL-LHC) . . . . .	53
<b>2 New Small Wheel Upgrade Project</b>	<b>55</b>
2.1 New Small Wheel Upgrade . . . . .	56
2.1.1 End-cap Muon Trigger . . . . .	57
2.1.2 Tracking Performance & Efficiency . . . . .	57
2.2 The concept of the New Small Wheel Upgrade . . . . .	57
2.3 Layout of the New Small Wheel . . . . .	59
2.4 Services and Infrastructure . . . . .	61
2.5 Integration . . . . .	63
2.5.1 Micromegas - BB5 . . . . .	63
2.5.2 sTGC - B180 . . . . .	65
2.5.3 B191 . . . . .	65
2.5.4 P1 . . . . .	67
2.6 Contributions . . . . .	67

<b>3</b>	<b>Electronics and Data Acquisition System</b>	<b>69</b>
3.1	Overview . . . . .	70
3.2	Electronics Boards . . . . .	73
3.3	VMM . . . . .	78
3.3.1	Validation Studies . . . . .	81
3.3.2	Neutron Irradiation Testbeam . . . . .	83
3.4	Front-End LInk eXchange - FELIX . . . . .	88
3.5	GBTX . . . . .	89
3.6	GBT-SCA . . . . .	91
3.7	Detector Resource Names . . . . .	93
3.7.1	FELIX Resource Identifier . . . . .	93
3.7.2	NSW Naming Scheme . . . . .	95
3.7.3	OKS Overview . . . . .	96
3.7.4	OKS Implementation in NSW . . . . .	96
3.8	SCA Ecosystem . . . . .	97
3.8.1	Software . . . . .	98
3.8.2	Quasar Framework . . . . .	99
3.8.3	OPC UA Server . . . . .	100
3.8.4	OPC UA Clients . . . . .	100
3.9	SCA Connections . . . . .	101
3.9.1	SCA OPC UA XML . . . . .	102
3.10	XML Generator . . . . .	104
3.11	GPIO Bit-Banger . . . . .	105
3.12	FreeVariable . . . . .	106
3.13	SCA Operation . . . . .	107
3.13.1	FELIX/OPC Granularity . . . . .	108
3.13.2	Performance Tests . . . . .	109
3.13.3	Monitoring . . . . .	111
3.13.4	Configuration . . . . .	111
3.13.5	Calibration . . . . .	116
3.14	Contributions . . . . .	120
<b>4</b>	<b>Detector Control System</b>	<b>123</b>
4.1	ATLAS DCS . . . . .	124
4.1.1	Building Blocks . . . . .	124
4.1.2	Control Hierarchy . . . . .	126
4.1.3	FSM . . . . .	126
4.1.4	Panels . . . . .	128
4.1.5	Alarm Screen . . . . .	129
4.2	WinCC Open Architecture . . . . .	129
4.2.1	Architecture . . . . .	130
4.2.2	Basic tools of WinCC-OA . . . . .	132
4.2.3	Joint Controls Project Framework (JCOP) . . . . .	135
4.2.4	OPC UA Servers . . . . .	137
4.3	Integration Control Systems . . . . .	140
4.3.1	Gas Tightness Station . . . . .	140
4.3.2	High Voltage Station . . . . .	155
4.3.3	ArdEnvironment Station . . . . .	166
4.3.4	Electronics Station . . . . .	173
4.3.5	Cosmics Station . . . . .	175

4.4	NSW Production Control System . . . . .	181
4.4.1	System & Architecture Design . . . . .	181
4.4.2	Hardware & Projects . . . . .	183
4.4.3	Projects Allocation . . . . .	184
4.4.4	Gitlab Repository Structure . . . . .	186
4.4.5	OPC UA Servers . . . . .	186
4.4.6	Electronics . . . . .	186
4.4.7	VME . . . . .	203
4.4.8	DSS . . . . .	205
4.4.9	Other Projects . . . . .	207
4.4.10	Supervisor Control Station . . . . .	211
4.5	Contributions . . . . .	214
<b>5</b>	<b>Micromegas Detector Performance Evaluation</b>	<b>217</b>
5.1	Interaction of charged particles with matter . . . . .	218
5.2	Excitation and ionization in gases . . . . .	220
5.3	Transmission of produced ions and electrons in the gas . . . . .	221
5.3.1	Ion Movement . . . . .	221
5.3.2	Electron Motion . . . . .	222
5.3.3	Townsend and Signal Generation . . . . .	224
5.4	Gas detectors . . . . .	226
5.5	Micromesh Gaseous Structure . . . . .	227
5.5.1	Structure and operating principle of the Micromegas detector . . . . .	227
5.5.2	Bulk Micromegas . . . . .	228
5.5.3	Resistive Micromegas . . . . .	229
5.6	Micromegas detectors for the NSW Upgrade of ATLAS . . . . .	230
5.6.1	Readout board & High Voltage Sections . . . . .	231
5.7	Position Reconstruction . . . . .	232
5.7.1	Charge Centroid method . . . . .	233
5.7.2	$\mu$ TPC method . . . . .	233
5.7.3	Charge Centroid and $\mu$ TPC method combination . . . . .	233
5.8	Testbeams . . . . .	234
5.8.1	SPS H8 . . . . .	235
5.8.2	GIF++-HV Performance . . . . .	253
5.8.3	GIF++-Electronics Performance . . . . .	256
5.9	Conclusions . . . . .	265
5.10	Contributions . . . . .	265
	<b>Conclusions</b>	<b>267</b>
<b>A</b>	<b>Acronyms</b>	<b>269</b>
<b>B</b>	<b>NSW boards SCA Connections</b>	<b>273</b>
<b>C</b>	<b>SCA OPC UA Codes</b>	<b>277</b>
	<b>List of Figures</b>	<b>295</b>
	<b>List of Tables</b>	<b>297</b>
	<b>Bibliography</b>	<b>304</b>





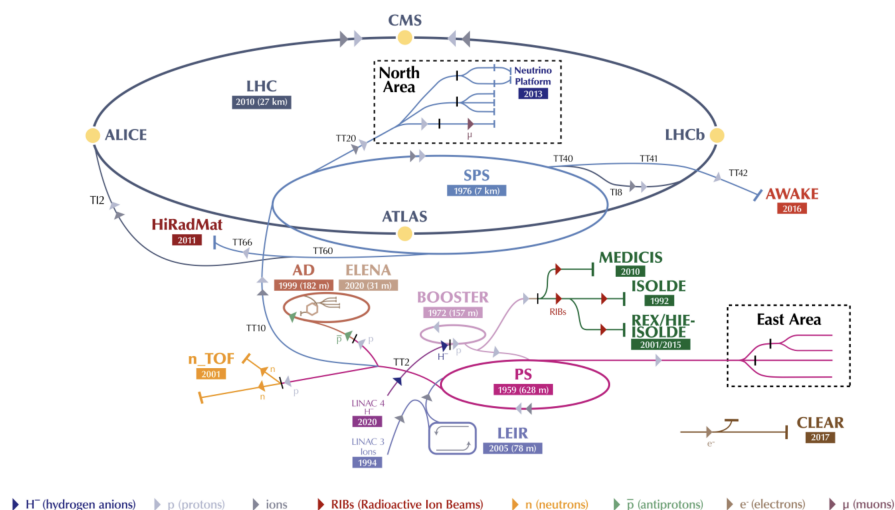
## Σύνοψη στα Ελληνικά

Στο παρόν Κεφάλαιο, θα παρατεθεί μία σύνοψη της διατριβής, στην Ελληνική γλώσσα.

### Εισαγωγή στον Μεγάλο Αδρονικό Επιταχυντή(LHC) και στο πείραμα ATLAS

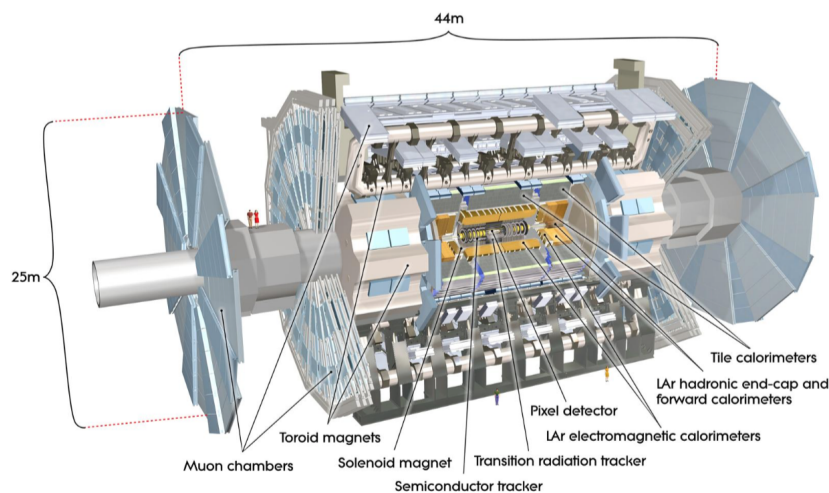
Ο Μεγάλος Επιταχυντής Αδρονίων (Large Hadron Collider, LHC) , είναι ο μεγαλύτερος και ισχυρότερος επιταχυντής σωματιδίων στον κόσμο. Ξεκίνησε τη λειτουργία του τον Σεπτέμβριο του 2008 και αποτελεί την πιο πρόσφατη προσθήκη στο σύμπλεγμα επιταχυντών του CERN. Αυτή η πειραματική εγκατάσταση βρίσκεται περίπου 100 μέτρα κάτω από την επιφάνεια της Γης, κοντά στα σύνορα Ελβετίας και Γαλλίας. Ο LHC είναι ένας υπεραγώγιμος επιταχυντής πρωτονίων επιταχύνονται πολύ κοντά στην ταχύτητα του φωτός και τελικά συγκρούονται, παράγοντας εξωτικά σωματίδια. Είναι εγκατεστημένος σε μία σήραγγα με περίμετρο 27 km, που κατασκευάστηκε στο χρονικό διάστημα από το 1984 έως το 1989 για τις ανάγκες του προηγούμενου επιταχυντή LEP, ο οποίος έκλεισε το 2000. Ο LHC μέσω των πειραμάτων σε αυτόν στοχεύει να αποκαλύψει φυσικά φαινόμενα πέρα από το Καθιερωμένο Πρότυπο, με ενέργειες κέντρου μάζας πάνω από 14 TeV για συγκρούσεις πρωτονίων-πρωτονίων.

Πριν τα σωματίδια φτάσουν στο δακτύλιο του LHC, περνούν από μία σειρά επιταχυντών, οι οποίοι αυξάνουν την ενέργειά τους προοδευτικά. Η διαδικασία αυτή ξεκινάει με μια φιάλη υδρογόνου που τροφοδοτεί τον θάλαμο πηγής ενός γραμμικού επιταχυντή (LINAC) με άτομα υδρογόνου. Ένα ηλεκτρικό πεδίο απογυμνώνει τα ηλεκτρόνια των ατόμων, αφήνοντας πίσω τους πυρήνες του υδρογόνου (πρωτόνια) που επιταχύνονται στη συνέχεια. Ο LINAC 2 επιταχύνει τα πρωτόνια σε ενέργεια 50 MeV, τα οποία στη συνέχεια εισέρχονται στον Proton Synchrotron Booster (PSB), αυξάνοντας την ενέργειά τους σε 1.4 GeV. Από εκεί, τα πρωτόνια μεταφέρονται στο Proton Synchrotron (PS), όπου επιταχύνονται σε 25 GeV. Το τελευταίο στάδιο πριν τον LHC είναι το Synchrotron Super Proton (SPS), που επιταχύνει τα πρωτόνια σε 450 GeV, προτού οι δέσμες εισαχθούν στον δακτύλιο του LHC, όπου επιταχύνονται σε 7 TeV. Ο δακτύλιος του LHC τροφοδοτείται με δύο αντιθέτου κατεύθυνσης δέσμες πρωτονίων που συγκρούονται σε τέσσερις πειραματικές περιοχές που αντιστοιχούν στα πειράματα ATLAS, CMS, ALICE, και LHCb. Η γραφική αναπαράσταση της πλήρους διάταξης επιταχυντή-εγχυτήρα παρουσιάζεται στο Σχήμα 1. Ο ανιχνευτής ATLAS (A Toroidal Apparatus) είναι ένας ανιχνευτής γενικής χρήσης, σχεδιασμένος να καλύψει τις ανάγκες πολλών πειραμάτων του LHC, όπως την μελέτη του ανακαλυφθέντος σωματιδίου Higgs, για αναζήτηση της υπερσυμμετρίας, την αναζήτηση σκοτεινής ύλης και την ύπαρξη επιπλέον διαστάσεων. Το γενικό σχήμα του



Σχήμα 1: Σχηματική αναπαράσταση επιταχυντών-εγχυτήρων του LHC. Φαίνεται παραπάνω ο εγχυτήρας και οι προ-επιταχυντές που τροφοδοτούν τον 27 km δακτύλιο με δέσμες σωματιδίων. Οι δέσμες συγκρούονται σε τέσσερις πειραματικές περιοχές εισαγωγής που αντιστοιχούν στα υπόγεια πειράματα (ATLAS, CMS, ALICE, LHCb).

είναι κυλινδρικό, με μήκος 45 m, διάμετρο 25 m, και βάρος 7000 T, και είναι μέχρι σήμερα ο μεγαλύτερος ανιχνευτής σε όγκο που έχει κατασκευαστεί. Η γραφική αναπαράσταση του ATLAS φαίνεται στο Σχήμα 2.



Σχήμα 2: Γραφική αναπαράσταση του πειράματος ATLAS. Τα διαφορετικά μέρη του πειράματος σημειώνονται πάνω στο σχήμα.

Οι δέσμες των σωματιδίων περνούν από τον άξονα κυλινδρικής συμμετρίας του ανιχνευτή και συγκρούονται στο κέντρο του, παράγοντας νέα σωματίδια. Τα διάφορα υποσυστήματα του ATLAS, τοποθετημένα σε στρώματα, καταγράφουν την τροχιά, την ορμή και την ενέργεια των παραγόμενων σωματιδίων. Ένας ισχυρός υπεραγώγιμος μαγνήτης κάμπει τις τροχιές των φορτισμένων σωματιδίων, επιτρέποντας τη μέτρηση της ορμής τους, ενώ τα δεδομένα συλλέγονται από τα ηλεκτρονικά συστήματα του ανιχνευτή.

Τα κύρια υποσυστήματα του ATLAS είναι τα εξής:

- Το σύστημα μαγνητών (Magnet System)
- Ο εσωτερικός ανιχνευτής τροχιών (Inner Detector)
- Τα καλορίμετρα (Calorimeters)

- Το φασματόμετρο μιονίων (Muon Spectrometer)
- Το σύστημα σκανδαλισμού και συλλογής δεδομένων (TDAQ)

Το φασματόμετρο μιονίων του ATLAS αποτελείται από δύο υποανιχνευτικά συστήματα για μετρήσεις ακριβείας: , Monitored Drift Tubes (MDT) και Cathode Strip Chambers (CSC). Και επιπλέον δύο τεχνολογίες σκανδαλισμού: Resistive Plate Chambers (RPC) και Thin Gap Chambers (TGC).

## Αναβάθμιση Νέου Μικρού Τροχού

Με την αύξηση της φωτεινότητας του LHC, ήταν αναγκαία η αναβάθμιση του υπάρχοντος Small Wheel (SW) του πειράματος ATLAS με νέους ανιχνευτές, οι οποίοι θα είναι ικανοί να διαχειρίζονται τον αυξημένο ρυθμό σωματιδίων. Η αναβάθμιση αυτή, γνωστή ως New Small Wheel (NSW), περιλαμβάνει δύο νέους τύπους ανιχνευτών, τους sTGC (small-strip Thin Gap Chambers) και Micromegas, οι οποίοι, σε συνδυασμό με ένα σύγχρονο σύστημα ηλεκτρονικών, θα μπορούν να επεξεργάζονται τον μεγάλο αριθμό σωματιδίων. Η αναβάθμιση αυτή επιτυγχάνεται μέσω των επιδόσεων του του NSW, καθώς και το τεχνολογικά και σχεδιαστικά προηγμένο VMM chip τύπου ASIC, το οποίο αποτελεί τον θεμέλιο λίθο για τη συλλογήτην ανάγνωση και επεξεργασία των δεδομένων από τους ανιχνευτές. Το NSW αποτελεί ένα σύνολο από ανιχνευτές παρακολούθησης τροχιών ακριβείας και ανιχνευτών σκανδαλισμού, ικανοί να λειτουργούν σε υψηλούς ρυθμούς ροής σωματιδίων, με εξαιρετική χωρική και χρονική ανάλυση σε πραγματικό χρόνο. Σε υψηλή φωτεινότητα, δύο παράγοντες είναι ιδιαίτερα σημαντικοί:

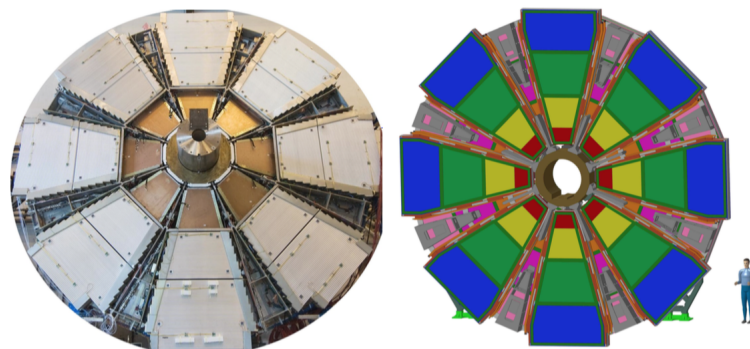
- Σκανδαλισμός μιονίων του end-cap (End-cap Muon Trigger)
- Αποτελεσματικότητα και απόδοση ανίχνευσης τροχιών (Tracking Performance & Efficiency)

Το σχέδιο του NSW ανταποκρίνεται στις προδιαγραφές για πολύ καλή γωνιακή διακριτική ικανότητα τροχιάς, της τάξης του 1 mrad στο Level-1 trigger. Τα σήματα υποβάθρου στο περιβάλλον υψηλής πυκνότητας τροχιών του NSW μπορούν να καταστέλλονται χρησιμοποιώντας αυτήν τη γωνιακή διακριτική ικανότητα. Για την Phase-II αναβάθμιση του συστήματος Level-1 triggering σε ακόμα υψηλότερη φωτεινότητα, ο χρόνος αντίδρασης θα μειωθεί ώστε να επιτρέψει πιο επιλεκτικούς σκανδαλισμούς από τα καλοριμέτρα και το νέο σύστημα σκανδαλισμού ανίχνευσης, καθώς και από το μιονικό σύστημα.

Το αναβαθμισμένο σύστημα ανίχνευσης του New Small Wheel βασίζεται σε τεχνολογίες από την οικογένεια των ανιχνευτών αερίου, συγκεκριμένα στους sTGC και Micromegas. Η νέα πειραματική διάταξη θα αποτελείται από 16 επίπεδα ανίχνευσης, διαμορφωμένα σε δύο στρώσεις των τεσσάρων επιπέδων ανά τεχνολογία (τέσσερα επίπεδα sTGC και τέσσερα επίπεδα Micromegas), καλύπτοντας πλήρως το NSW σε ανιχνευτική περιοχή της τάξεως των 1200 m<sup>2</sup> η κάθε μία. Η διάταξη θα ακολουθεί τις διαστάσεις του υπάρχοντος SW, με κατάτμηση σε 16 τμήματα ανά τροχό (wheel) για να ταιριάζει με τα υπάρχοντα Big Wheel και το μιονικό σταθμό του end-cap (Σχήμα 3). Η διάταξη του NSW περιλαμβάνει οχτώ επίπεδα ανίχνευσης της κάθε τεχνολογίας, χωρισμένα από ένα πλαίσιο της τάξεως των 50 mm. Το εσωτερικό μέρος αποτελείται από ανιχνευτές Micromegas, ενώ το εξωτερικό από sTGCs, σχηματίζοντας περιοχή της τάξεως των 400 mm. Κάθε τμήμα αποτελείται από δύο wedges. Οι ανιχνευτές sTGC θα είναι ακτινικά χωρισμένοι σε τρία modules, ενώ οι Micromegas σε δύο.

Οι ανιχνευτές sTGC έχουν αναπτυχθεί κυρίως για τον σκανδαλισμό, λόγω της ικανότητάς τους να πυροδοτούν καταγραφές χωρίς να απαιτούν αναγνώριση σωματιδίων. Οι ανιχνευτικές τεχνολογίες διατάσσονται με τρόπο που να μεγιστοποιεί την απόσταση μεταξύ των δύο στρωμάτων sTGC, επιτρέποντας βελτίωση της διακριτικής ικανότητας για την online ανακατασκευή της τροχιάς, βάσει της γωνίας που παρέχεται από το πρώτο στρώμα των ανιχνευτών. Οι ανιχνευτές Micromegas, με την εξαιρετική τους ακρίβεια στην καταγραφή της τροχιάς λόγω του μικρού κενού (5, mm) και του μικρού βήματος λωρίδων (strip pitch 0.5 mm), χρησιμοποιούνται για ανακατασκευή της τροχιάς.

Οι sTGC μπορούν να συμβάλλουν στην offline ακρίβεια εντοπισμού τροχιών με διακριτική ικανότητα περίπου 150 μm, ενώ οι Micromegas έχουν τη δυνατότητα συνέργειας υποβοηθώντας τους sTGC για ακριβέστερη ανακατασκευή της τροχιάς των σωματιδίων και θα λειτουργούν επίσης ως μηχανισμός σκανδαλισμού.



Σχήμα 3: Αριστερά: Το τωρινό Small Wheel στην επιφάνεια της γης πριν την εγκατάστασή του στο ATLAS. Δεξιά: Απεικόνιση της διάταξης του New Small Wheel.

## Ηλεκτρονικά και Σύστημα Λήψης Δεδομένων του Νέου Μικρού Τροχού

Το σύστημα λήψης δεδομένων και σκανδαλισμού (TDAQ) του NSW είναι ένα εξελιγμένο σύστημα που περιλαμβάνει περίπου 8000 ηλεκτρονικές μονάδες. Για την υποστήριξη αυτών των μονάδων έχουν σχεδιαστεί προσαρμοσμένα ολοκληρωμένα κυκλώματα ASIC (Application-Specific Integrated Circuits) ανθεκτικά στην ακτινοβολία, τα οποία παίζουν καθοριστικό ρόλο στην καταγραφή και την μετάδοση των σημάτων στο σύστημα ανάγνωσης του back-end.

Στο πλαίσιο των ηλεκτρονικών NSW που διέπουν τα μονοπάτια σκανδαλισμού (Trigger) και συλλογής δεδομένων (DAQ) και για τους δύο ανιχνευτές, προκύπτει μια ολοκληρωμένη κατηγοριοποίηση σε ηλεκτρονικά τοποθετημένα εντός και εκτός σπηλαίου του ATLAS, όπως απεικονίζεται στο Σχήμα 4. Τα ηλεκτρονικά πάνω στον ανιχνευτή, που βρίσκονται εντός του σπηλαίου του ATLAS, όπου υπάρχουν ακτινοβολία και μαγνητικά πεδία, περιλαμβάνουν ειδικά κατασκευασμένες πλακέτες που χρησιμοποιούν κυρίως ASICs ανθεκτικά στην ακτινοβολία.

Αντίθετα, τα ηλεκτρονικά εκτός του σπηλαίου του ATLAS, τα οποία περιλαμβάνουν στοιχεία όπως το Front End Link eXchange (FELIX), τον επεξεργαστή σκανδαλισμού, τη λογική του τομέα (Sector Logic) και υπηρεσίες που φιλοξενούνται σε εμπορικούς υπολογιστές διακομιστές όπως τα Read Out Drivers (ROD), το σύστημα αυτομάτου ελέγχου (Detector Control System -DCS), την παρακολούθηση συμβάντων (Event Display), τη διαμόρφωση (Configuration), την παρακολούθηση σκανδαλισμού και τη βαθμονόμηση (Calibration), θα τοποθετηθούν εκτός του σπηλαίου σε μια περιοχή που ορίζεται ως service cavern (USA15). Αυτός ο χωρικός διαχωρισμός, του συστήματος NSW με τη στρατηγική τοποθέτηση των εξαρτημάτων με βάση τις ειδικές λειτουργικές απαιτήσεις τους, εξασφαλίζει τη βέλτιστη λειτουργία ολόκληρου.

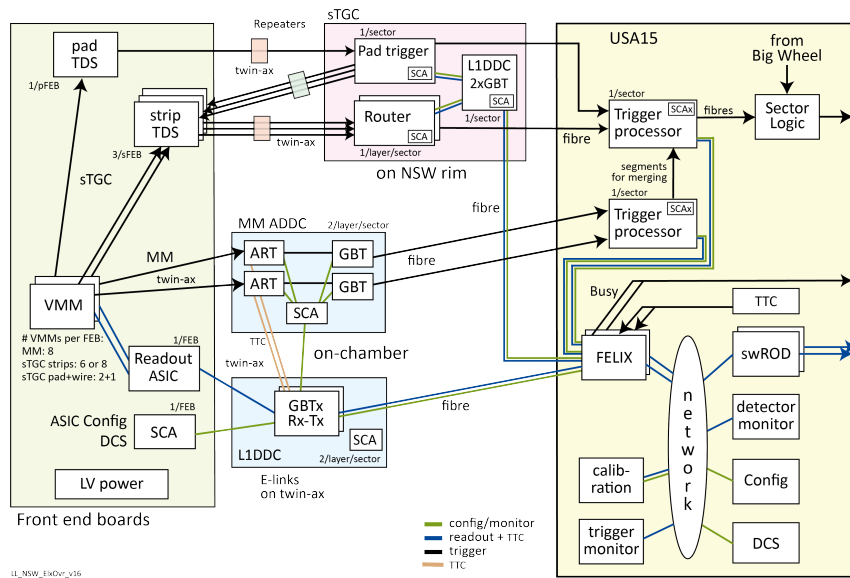
## Μονάδα ανάγνωσης VMM

Το κύριο front-end ASIC είναι το 64-κάνναλο VMM, ένα κοινό front-end ASIC τόσο για τις τεχνολογίες ανιχνευτών Micromegas όσο και για τις τεχνολογίες sTGC, το οποίο παρέχει μετρήσεις πλάτους και χρονισμού και άμεση έξοδο πρωτογενών στοιχείων σκανδαλισμού, καθώς και ρυθμιστικό επίπεδο σκανδαλισμού Level-0.

## Δοκιμαστικές δέσμες νετρονίων για έρεση SEU

Η δοκιμαστική δέσμη ακτινοβολίας νετρονίων διεξήχθη στο Εθνικό Κέντρο Επιστημονικών Ερευνών "Δημόκριτος" (ΕΚΕΦΕ) τον Μάιο του 2017 και τον Ιούνιο του 2018. Οι στόχοι της δοκιμαστικής δέσμης ακτινοβολίας νετρονίων στο Δημόκριτο περιλάμβαναν:

- Εκτέλεση δοκιμών Single Event Upsets (SEU) για τα VMM3, VMM3a, ROC και ART ASIC.
- Αξιολόγηση της λειτουργικότητας των πλακετών L1DDC, ADDC και Pad Trigger σε περιβάλλον νετρονίων.



Σχήμα 4: Το σχήμα επισκόπησης των ηλεκτρονικών NSW για τα ηλεκτρονικά εντός και εκτός σπηλαιού του ATLAS και τη συνδεσιμότητά τους. Στους ανιχνευτές (αριστερό πλαίσιο) υπάρχουν οι πλακέτες front-end, υπεύθυνες για την ανάγνωση των 2.1 εκατομμυρίων καναλιών του NSW, καθώς και οι πλακέτες ανάγνωσης και σκανδαλισμού. Εκτός των ανιχνευτών (αριστερό πλαίσιο) υπάρχουν οι επεξεργαστές σκανδαλισμού και τα ηλεκτρονικά που θα παραδώσουν τα δεδομένα στα συστήματα σκανδαλισμού και συλλογής δεδομένων του ATLAS.

- Διεξαγωγή δοκιμών SEU στον καθαριστή Jitter (Jitter Clenear), στον επαναλήπτη (repeater) και στα ολοκληρωμένα κυκλώματα 1-4 fan-out.

Παρόλο που η παρούσα μελέτη θα επικεντρωθεί κυρίως στις δοκιμές και τα αποτελέσματα του VMM3 & VMM3a, ο πρωταρχικός στόχος ήταν η κατανόηση της συμπεριφοράς των μονάδων ανάγνωσης του VMM3 & VMM3a σε ακτινοβολία νετρονίων, με μεγέθη συγκρίσιμα με αυτά που αναμένονται στο Run 3 του πειράματος ATLAS. Αυτό επιτεύχθηκε με τη συστηματική εγγραφή και ανάγνωση των καταχωρητών διαμόρφωσης του VMM3 για τη διερεύνηση της εμφάνισης των SEUs. Η διάταξη του NCSR, μαζί με την πλακέτα Mini1 που είναι εξοπλισμένη με το VMM3/VMM3a, απεικονίζεται στο Σχήμα 6.

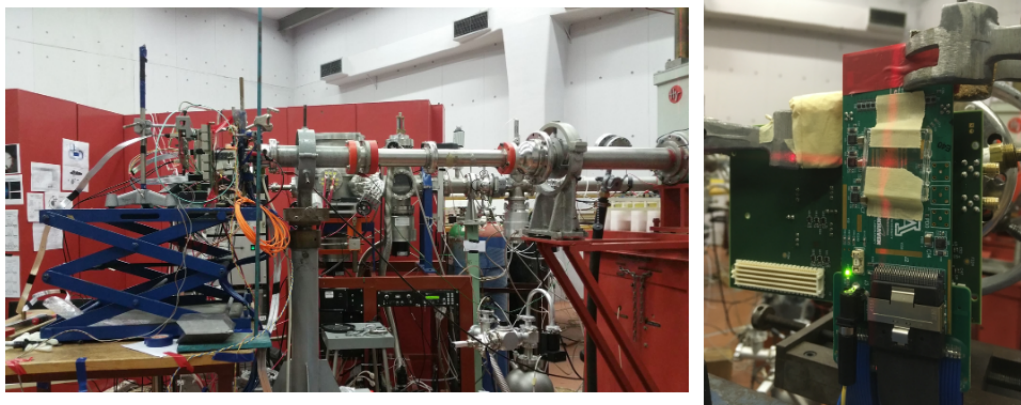
Η δοκιμαστική δέσμη διήρκεσε πέντε ημέρες και κάθε ημέρα περιελάμβανε μετατόπιση των θέσεων των πλακετών/ASIC για την απόκτηση των αντίστοιχων δεδομένων ροής νετρονίων. Σε αυτή την ολοκληρωμένη μελέτη, το VMM3&VMM3a, ενσωματωμένο στην πλακέτα Mini-1, υποβλήθηκε σε αυστηρές δοκιμές κάτω από μια επακριβώς καθορισμένη δέσμη νετρονίων 20, 22 και 24 MeV σε διάφορες θέσεις και ρυθμούς ροής. Καθ' όλη τη διάρκεια των πειραματικών συνεδριών, οι διαμορφώσεις της σειριακής περιφερειακής διεπαφής (SPI) διαβάζονταν συνεχώς κάθε 12 δευτερόλεπτα, εξασφαλίζοντας σταθερή και συνεπή απόδοση. Αξίζει να σημειωθεί ότι, ακόμη και μετά την έκθεση του συστήματος σε αθροιστική ροή νετρονίων περίπου  $\sim 3.54 \times 10^{11} \text{ n/cm}^2$  επί 71,6 ώρες, δεν παρατηρήθηκαν SEUs. Αυτό το αξιοσημείωτο αποτέλεσμα υπογραμμίζει την ευρωστία και την ανθεκτικότητα της διάταξης VMM3&VMM3a, επικυρώνοντας την καταλληλότητά τους για περιβάλλοντα υψηλής ακτινοβολίας.

## Μονάδα αργού ελέγχου GBT-SCA

Το GBT-SCA ASIC (Giga-Bit Transceiver - Slow Control Adapter) είναι ένα ολοκληρωμένο κύκλωμα που έχει σχεδιαστεί με τη χρήση εμπορικής τεχνολογίας CMOS 130 nm. Διαδραματίζει κρίσιμο ρόλο ως μέρος της μονάδας GBT, αφιερωμένο στη διανομή των σημάτων ελέγχου και παρακολούθησης στα ηλεκτρονικά front-end που είναι τοποθετημένα στους ανιχνευτές. Το GBT-SCA δημιουργεί σύνδεση με τα GBTX ASICs μέσω μιας διπλής πλεονάζουσας αμφίδρομης σύνδεσης δεδομένων 80 Mbps, γνωστής ως e-links. Το GBT-SCA αναπτύχθηκε για να εξυπηρετεί τις διαφορετικές απαιτήσεις των front-end ASIC σε διάφορα πειράματα και προσφέρει

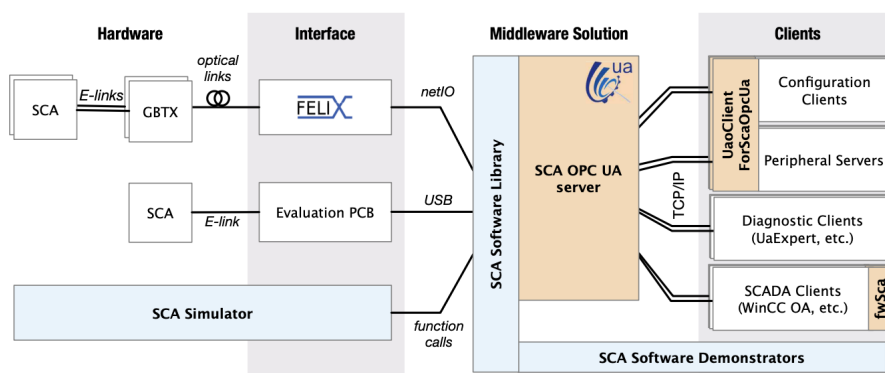






Σχήμα 6: Η διάταξη της δοκιμαστικής δέσμης ακτινοβολίας νετρονίων μαζί με την πλακέτα Mini1 εξοπλισμένη με το VMM3/VMM3a.

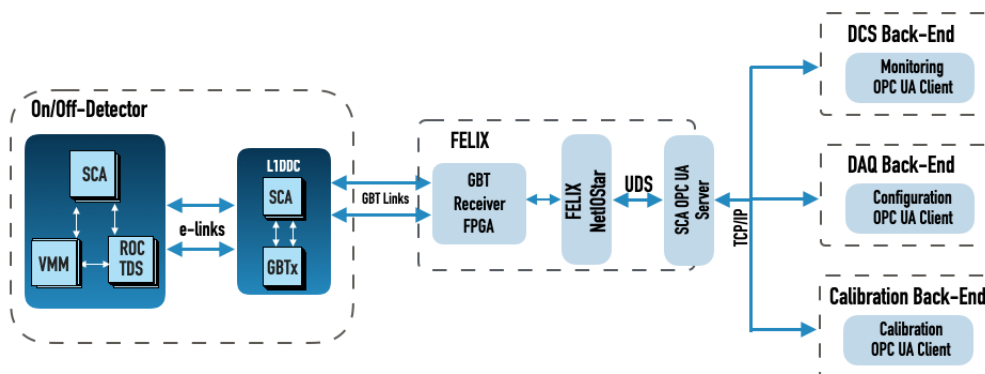
- **fwSca:** Αυτή η ενότητα παίζει καθοριστικό ρόλο στην αυτοματοποίηση της ενσωμάτωσης των δεδομένων του διακομιστή σε συστήματα SCADA.



Σχήμα 7: Προεπισκόπηση της δομικής σύστασης του GBT-SCA Software.

Στο πλαίσιο της αναβάθμισης του NSW, αυτές οι διαφορετικές διεπαφές του GBT-SCA εξυπηρετούν διαφορετικούς σκοπούς για διάφορες μονάδες. Δεδομένου ότι η αναβάθμιση του NSW περιλαμβάνει εννέα ξεχωριστές πλακέτες (MMFE8, sFEB, pFEB, ADDC, L1DDC-MMG, L1DDC-STG, Rim L1DDC, Pad Trigger και Router), δημιουργήθηκαν συνολικά εννέα μοναδικά πρότυπα λογισμικού SCA. Αυτά τα πρότυπα χρησιμεύουν ως αναφορές XML στο πρωταρχικό αρχείο SCA OPC UA Server. Η επόμενη κρίσιμη φάση της διαδικασίας περιλαμβάνει την αυτοματοποίηση της δημιουργίας αρχείων XML για τον NSW SCA OPC UA Server. Για να διευκολυνθεί αυτό, δημιουργήθηκε το εργαλείο **NswXmlGenerator**, το οποίο δίνει τη δυνατότητα στους χρήστες να παράγουν τα απαιτούμενα αρχεία XML. Το εργαλείο αναπτύχθηκε ως ένα απλό API Python και επιτρέπει στους χρήστες να παράγουν αρχεία XML του SCA OPC UA Server παρέχοντας εισόδους όπως ανιχνευτής, πλευρά και τομέας. Το NSW αποτελεί ένα πλήρως αυτόνομο σύστημα ανιχνευτών σκανδαλισμού και παρακολούθησης, εξοπλισμένο με μια εξελιγμένη ηλεκτρονική διάταξη, έτοιμο να αντιμετωπίσει τις προκλήσεις της υψηλής φωτεινότητας στον LHC. Αποτελείται από πάνω από 60.000 front-end ASICs και μερικές δεκάδες FPGAs, απαιτώντας αποτελεσματική και ταχεία διαμόρφωση πριν από κάθε πειραματική εκτέλεση, λόγω της συχνής ανάγκης διαμόρφωσης του VMM. Μια άλλη πρόκληση στα ηλεκτρονικά front-end του NSW, ιδίως με το VMM, ήταν ο περιορισμός της ύπαρξης μόνο ενός καναλιού εξόδου οθόνης ανά VMM. Η έξοδος οθόνης κάθε VMM συνδέεται στην ίδια θύρα αναλογικής εισόδου SCA, εξυπηρετώντας τους σκοπούς της παρακολούθησης και της βαθμονόμησης. Η πρόκληση με το κοινό κανάλι ADC SCA ήταν ότι το σύστημα ελέγχου ανιχνευτή (DCS) δεν γνώριζε την κατάσταση διαμόρφωσης(configuration) του VMM. Μετά από συζητήσεις με την κεντρική ομάδα του ATLAS DCS,

υλοποιήθηκε ένα νέο χαρακτηριστικό στον SCA OPC UA Server, γνωστό ως "FreeVariable". Η FreeVariable είναι μια μεταβλητή OPC-UA που μπορεί να προστεθεί οπουδήποτε στο χώρο διευθύνσεων. Δεν διέπεται από τον σχεδιασμό του διακομιστή και ο διακομιστής δεν μπορεί να επικοινωνήσει απευθείας με αυτή τη μεταβλητή. Μια ελεύθερη μεταβλητή μπορεί πάντα να εγγραφεί από οποιονδήποτε πελάτη OPC-UA. Σύμφωνα με το σχήμα 4, μπορούμε να απλοποιήσουμε τη λειτουργία SCA στο ακόλουθο σχήμα 8. Το σύστημα



Σχήμα 8: Απλουστευμένο σχηματικό διάγραμμα της λειτουργίας SCA της NSW Electronics.

μπορεί να χωριστεί σε τρία κύρια μέρη:

- **Ηλεκτρονικά:** Το SCA που είναι ενσωματωμένο στις ηλεκτρονικές πλακέτες συνδέεται απευθείας με διάφορα ASIC, όπως VMM, ROC και TDC. Στη συνέχεια, η πλακέτα συνδέεται μέσω ενός καλωδίου twinax με το L1DDC, το οποίο φιλοξενεί επίσης ένα SCA συνδεδεμένο απευθείας με το ASIC GBTX. Οι συνδέσεις μεταξύ του L1DDC και των άλλων πλακετών περιγράφονται από τους ηλεκτρονικούς συνδέσμους.
- **FELIX:** Αντιπροσωπεύει τον πραγματικό κεντρικό υπολογιστή FELIX. Το L1DDC συνδέεται απευθείας με το FELIX, συγκεκριμένα με το GBT Receiver FPGA μέσω μιας οπτικής ίνας που είναι γνωστή ως GBT Link. Στο εσωτερικό του FELIX, το λογισμικό netio/netio-star υλοποιεί την επικοινωνία χαμηλού επιπέδου μεταξύ των SCAs και του FPGA του FELIX. Ο SCA OPC UA Server, αρχικοποιημένος με τα παραγόμενα αρχεία XML που περιγράφουν τις διάφορες συνδέσεις SCA, εκθέτει όλες τις συνδέσεις SCA ως αντικείμενα OPC UA στο χώρο διευθύνσεων του SCA OPC UA Server.
- **Back-ends:** Περιλαμβάνει το back-end του DCS, της διαμόρφωσης και της βαθμονόμησης, το οποίο μπορεί να επικοινωνεί μέσω δικτύου με όλα τα SCA. Κάθε back-end λειτουργεί ως ξεχωριστός OPC UA Client, ικανός να εγγραφεί στον κοινό SCA OPC UA Server για τον έλεγχο και την παρακολούθηση των διαφόρων συνδέσεων SCA.

Συνοπτικά, όταν όλα τα ηλεκτρονικά του NSW, οι διαθέσιμοι παράμετροι είναι:

- **DCS:** Παρακολούθηση περισσότερων από 100.000 παραμέτρων.
- **Configuration:** Διαμόρφωση πάνω από 2 εκατομμυρίων καταχωρητών (registers).
- **Calibration:** Βαθμονόμηση πάνω από 100.000 παραμέτρων.

Για τους διακομιστές SCA OPC UA Servers, επιλέχθηκε να υιοθετηθεί μια προσέγγιση κατανομής τομέα ανιχνευτή. Ανάλογα, κάθε τομέας ανιχνευτή(detector sector) συνδέεται με έναν ειδικό διακομιστή SCA OPC UA. Συνολικά, υπάρχουν 32 τέτοιοι διακομιστές, καθένας εκ των οποίων λειτουργεί σε ένα διακριτό μηχανήμα FELIX και επικοινωνεί με τους αντίστοιχους SCA του τομέα. Η αρχικοποίηση των SCA OPC UA Servers, συμπεριλαμβανομένων και των διεργασιών felix-star, γίνεται κατά την εκκίνηση του κεντρικού μηχανήματος FELIX και διαχειρίζεται από τις αντίστοιχες εφαρμογές supervisord. Αυτή η δομή κατανομής εξυπηρετητών SCA OPC UA επιλέχθηκε για λόγους απόδοσης και συντηρησιμότητας, με την υποστήριξη εκτενών δοκιμών απόδοσης που πραγματοποιήθηκαν επί σειρά ετών από ειδικούς του FELIX και των εξυπηρετητών SCA OPC UA.

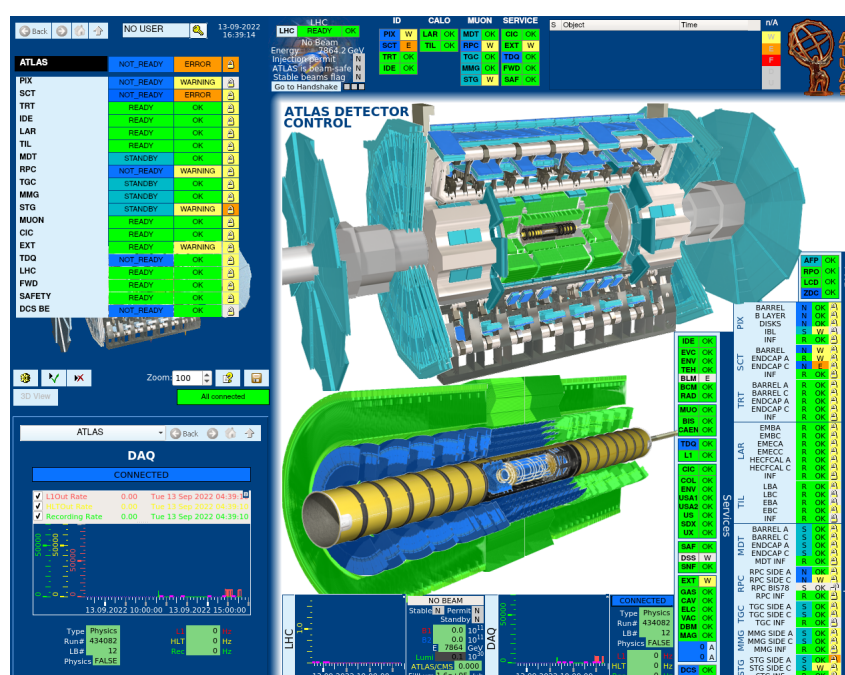


Η ευελιξία του SCA OPC UA Server είναι εμφανής στην ικανότητά του να προσαρμόζεται σε ρυθμίσεις διαφορετικών μεγεθών και τύπων. Ένα χαρακτηριστικό παράδειγμα αποτελεί η επιτυχής ανάπτυξή του στο έργο αναβάθμισης του NSW για το ATLAS. Σε αυτό το φιλόδοξο έργο, συνολικά 6976 SCA κατανέμονται στρατηγικά σε διάφορους τύπους ηλεκτρονικών front-end. Αυτό το δίκτυο SCAs διαχειρίζεται αποτελεσματικά από 30 κεντρικούς υπολογιστές FELIX, ο καθένας με 18 συνδέσεις οπτικών ινών, και τον αντίστοιχο αριθμό διακομιστών SCA OPC UA.

Το back-end παρακολούθησης αποτελεί αναπόσπαστο μέρος του DCS και του έργου SCADA WinCC-OA. Αυτό το σύστημα παρακολούθησης έχει αναπτυχθεί και θα αναλυθεί διεξοδικά στο επόμενο κεφάλαιο. Είναι σχεδιασμένο για να καλύπτει όλες τις απαιτήσεις για την παρακολούθηση του εκτεταμένου φάσματος παραμέτρων, που συνολικά ξεπερνούν τις 100.000, στο σύστημα NSW. Αυτή η υποδομή παρακολούθησης είναι ζωτικής σημασίας για την εποπτεία και τη διαχείριση της εγκατάστασης NSW, εξασφαλίζοντας στιβαρή και αποτελεσματική λειτουργία.

## Σύστημα Αυτομάτου Ελέγχου

Το ATLAS DCS σχεδιάστηκε και υλοποιήθηκε στα πλαίσια του κοινού έργου με τίτλο Joint Controls Project (JCOP) μίας συνεργασίας της ομάδας ελέγχου του CERN και των ομάδων DCS των πειραμάτων του LHC. Το JCOP συνδυάζει κοινά πρότυπα για την χρήση του DCS hardware βασιζόμενο στο SCADA σύστημα της Siemens, WinCC Open Architecture, γνωστό και ως PVSS με την παλαιότερη ονομασία του, όπου χρησιμεύει ως βάση για όλες τις εφαρμογές DCS. Το κύριο γραφικό περιβάλλον χρήστη του ATLAS DCS με όλα τα υποσυστήματα ενοποιημένα σε μία ιεραρχική δομή FSM αποτυπώνεται στο παρακάτω Σχήμα 9.



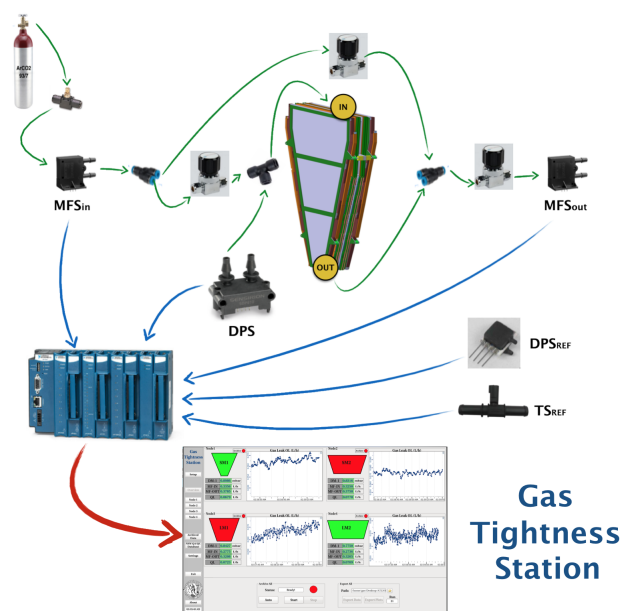
Σχήμα 9: Το κύριο γραφικό περιβάλλον χρήστη του ATLAS DCS με όλα τα υποσυστήματα ενοποιημένα σε μία ιεραρχική δομή FSM.

## Σταθμός μέτρησης διαρροής αερίου

Η μαζική παραγωγή μονάδων Micromegas για την αναβάθμιση NSW στο φασματόμετρο μιονίων ATLAS απαιτεί ένα ισχυρό σύστημα για ανεξάρτητη διασφάλιση ποιότητας και ποιοτικό έλεγχο (QA/QC). Μεταξύ των κρίσιμων πτυχών του ελέγχου, η διασφάλιση της στεγανότητας του θαλάμου (gas tightness) είναι μία βασική απαίτηση για την ομαλή λειτουργία και τη βέλτιστη απόδοση των ανιχνευτών Micromegas. Αυτοί οι ανιχνευτές αερίων λειτουργούν

με βάση τον ιονισμό του αερίου όταν ένα φορτισμένο σωματίδιο διέρχεται από τον ανιχνευτή, με αποτέλεσμα τη συλλογή ηλεκτρονίων στην περιοχή ενίσχυσης και την επακόλουθη διαμόρφωση παλμών στα ηλεκτρονικά στοιχεία ανάγνωσης. Η διατήρηση της στεγανότητας του αερίου είναι ζωτικής σημασίας, καθώς οποιαδήποτε διαρροή αερίου θέτει σε κίνδυνο την ικανότητα του ανιχνευτή να διαδίδει ηλεκτρόνια στην περιοχή ενίσχυσης. Η παρουσία αέρα, λόγω του οξυγόνου οξυγόνου, στο εσωτερικό του ανιχνευτή μπορεί να δεσμεύσει ηλεκτρόνια μειώνοντας σημαντικά την απολαβή του ανιχνευτή.

Για την εκτίμηση της διαρροής αερίου χρησιμοποιούνται δύο μέθοδοι: η μέθοδος της πτώσης πίεσης (PDR) και η μέθοδος της απώλειας ροής (FRL). Λόγω της αλγοριθμικής μορφής των πειραματικών μεθόδων ελέγχου διαρροής, ένα αυτοματοποιημένο σύστημα ελέγχου καθίσταται απαραίτητο. Το σύστημα αυτό πρέπει να διευκολύνει την επεξεργασία, τον έλεγχο και την καταγραφή των δεδομένων που συλλέγονται από τους αισθητήρες της πειραματικής διάταξης. Για να αντιμετωπιστεί αυτή η ανάγκη, σχεδιάστηκε ένα αυτόματο σύστημα ελέγχου διαρροής αερίου, όπως φαίνεται στο Σχήμα 10, με τη χρήση του λογισμικού WinCC-OA. Παρέχει τη δυνατότητα μέτρησης της διαρροής αερίου των ανιχνευτών Micromegas, εξασφαλίζοντας μια απλοποιημένη και αξιόπιστη διαδικασία για τη διασφάλιση και τον έλεγχο της ποιότητας στη μαζική παραγωγή αυτών των κρίσιμων εξαρτημάτων για το πείραμα ATLAS.

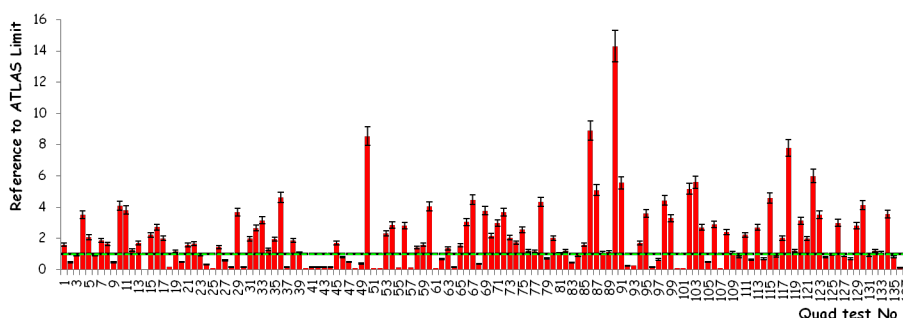


Σχήμα 10: Η τελική έκδοση του συστήματος ελέγχου διαρροής αερίου MM QP στο BB5.

Ως αναπόσπαστο μέρος των μέτρων ελέγχου ποιότητας που εφαρμόστηκαν κατά την ενσωμάτωση των μονάδων Micromegas (MM Τετραπλέτων) στο εργαστήριο BB5 του CERN, πραγματοποιήθηκε σχολαστική αξιολόγηση σε συνολικά 136 Τετραπλέτες. Το επίκεντρο της αξιολόγησης επικεντρώθηκε στην απόδοση της στεγανότητάς τους σε αέρια, χρησιμοποιώντας αέρια που προήλθε από ειδική ψιάλη. Η βασική παράμετρος υπό εξέταση ήταν ο ρυθμός διαρροής (QL), εκφρασμένος σε mL/h, ο οποίος κανονικοποιήθηκε σε στατική πίεση 3 mbar και στη συνέχεια μετατράπηκε για μείγμα αερίου  $\text{Ar}+7\%\text{CO}_2$  σύμφωνα με την καθιερωμένη βιβλιογραφία. Κάθε συνεδρία δοκιμής διήρκεσε 45 έως 60 λεπτά, ανάλογα με τη σύγκλιση του διαφορικού σήματος στη μέθοδο απώλειας ροής (FRL).

Μερικές επιλεγμένες Τετραπλέτες παρουσίασαν αυξημένα επίπεδα εσωτερικής διαρροής, γεγονός που επέβαλε την επιστροφή τους στα εργοτάξια για στοχευμένες επισκευές. Το όριο αποδοχής για το ποσοστό διαρροής, κρίσιμο κριτήριο σε αυτές τις αξιολογήσεις, καθορίστηκε ως κλάσμα του όγκου του υπό εξέταση ανιχνευτή ανά μονάδα χρόνου.

Ο μέσος ρυθμός διαρροής προσδιορίστηκε σε 58,3 mL/h (1,96 φορές το όριο αποδοχής, A.L.), με μέση τετραγωνική ρίζα (rms) 69,9 mL/h (2,04 φορές το A.L.). Η οπτική αναπαράσταση των αποτελεσμάτων στο Σχήμα 11 δείχνει ότι η πλειονότητα των Τετραπλέτων παρουσίασε τιμές ρυθμού διαρροής εντός του επιτρεπόμενου εύρους.



Σχήμα 11: Το ιστόγραμμα των συνολικών αποτελεσμάτων του ποσοστού διαρροής, σε σχέση με το όριο ATLAS (πράσινη οριζόντια διακεκομμένη γραμμή), από 136 Τετραπλέτων Micromegas κατά την επικύρωση της στεγανότητας τους από τον Ιανουάριο 2019.

## Σταθμός μέτρησης υψηλής τάσης

Η αρχή λειτουργίας των ανιχνευτών Micromegas βασίζεται στον ιονισμό του αερίου όταν αυτό διαπερνάται από σωματίδια μιονίων. Μετά τον ιονισμό, θετική υψηλή τάση εφαρμόζεται στην κάθοδο για τη συλλογή των παραγόμενων ηλεκτρονίων. Για να εξασφαλιστεί η βέλτιστη απόδοση του ανιχνευτή Micromegas, είναι επιτακτική ανάγκη να επικυρωθεί τόσο η στεγανότητα του αερίου όσο και η λειτουργία υψηλής τάσης (High Voltage-HV). Όπως αναφέρθηκε προηγουμένως, η μέτρηση της στεγανότητας αερίου εκτελείται μέσω του λογισμικού στεγανότητας αερίου στο BB5. Για να συμπληρωθεί αυτό, πρέπει να αναπτυχθεί μία πειραματική διάταξη και το αντίστοιχο λογισμικό για την ταυτόχρονη επικύρωση της υψηλής τάσης. Η γενική ιδέα περιλαμβάνει την παρακολούθηση της τάσης και του ρεύματος που εφαρμόζεται σε διάφορα τμήματα υψηλής τάσης του ανιχνευτή Micromegas μέσω του κεντρικής μονάδας CAEN και των πλακετών HV.

Για την πιστοποίηση από πλευράς υψηλής τάσης των μονάδων Micromegas, αναπτύχθηκαν δύο διαφορετικές διατάξεις σε διαφορετικές τοποθεσίες. Οι διατάξεις αυτές είναι οι ακόλουθες:

- **BB5 setup:** Αυτή η εγκατάσταση έχει σχεδιαστεί για την επικύρωση των μονάδων μετά την παραλαβή τους από διάφορα εργοτάξια.
- **Εγκατάσταση ακτινοβολίας γάμμα (GIF++):** Αυτή η εγκατάσταση είναι προσαρμοσμένη για την επικύρωση των μονάδων σε περιβάλλον υψηλής ακτινοβολίας, η οποία διεξάγεται πριν από την εγκατάστασή τους στο σπήλαιο ATLAS.

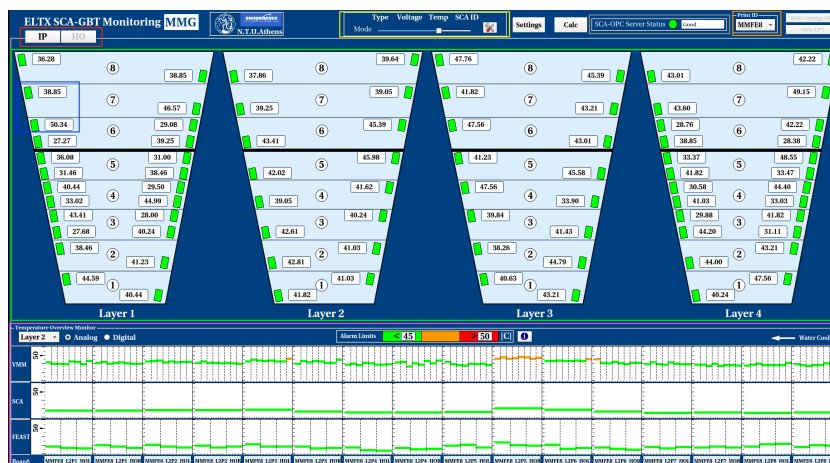
Η πειραματική διάταξη στο BB5 έχει διαμορφωθεί με τέσσερις παράλληλους κόμβους ή δοκιμαστικούς σταθμούς, επιτρέποντας την ταυτόχρονη εκτέλεση των διαδικασιών επικύρωσης των ανιχνευτών Micromegas με αέριο και υψηλή τάση. Μια οπτική αναπαράσταση της πειραματικής διάταξης παρουσιάζεται στο Σχήμα 12.

## Σταθμός ηλεκτρονικών

Ο σταθμός διαθέτει έναν απλοποιημένο και συμπαγή σχεδιασμό, με ένα μοναδικό παράθυρο, όπως απεικονίζεται στο Σχήμα 13. Μέσα σε αυτό το φιλικό προς το χρήστη περιβάλλον εργασίας, οι χρήστες μπορούν να πλοηγηθούν απρόσκοπτα μεταξύ των διαφόρων στρωμάτων του τομέα, παρέχοντας ολοκληρωμένη παρακολούθηση των τιμών των αισθητήρων θερμοκρασίας και τάσης. Αυτό το λογισμικό διαδραματίζει κρίσιμο ρόλο στη διασφάλιση της λειτουργικότητας των τομέων NSW πριν από την ενσωμάτωσή τους στο πείραμα ATLAS.



Σχήμα 12: Η πειραματική διάταξη επικύρωσης υψηλής τάσης του Micromegas στο BB5.



Σχήμα 13: Ο σταθμός SCA DCS για την παρακολούθηση των ηλεκτρονικών του Micromegas.

## Σταθμός κοσμικής ακτινοβολίας

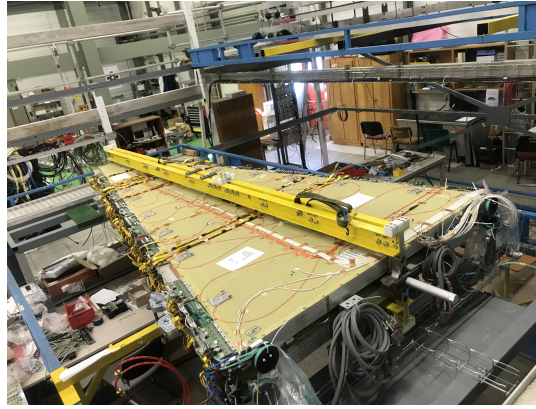
Αυτή η υποενότητα περιγράφει λεπτομερώς την πειραματική διάταξη και το λογισμικό που αναπτύχθηκε για την επικύρωση των τομέων Micromegas με χρήση κοσμικής ακτινοβολίας πριν από την εγκατάστασή τους στους Νέους Μικρούς Τροχούς του πειράματος ATLAS. Η κοσμική επικύρωση αποτελεί την τελική φάση της διαδικασίας επικύρωσης του ανιχνευτή Micromegas, που περιλαμβάνει διαδικασίες επικύρωσης αερίων, υψηλής τάσης (HV) και ηλεκτρονικών.

Η κοσμική επικύρωση αποσκοπεί στη διασφάλιση της συνολικής λειτουργικότητας του ανιχνευτή Micromegas υπό ρεαλιστικές συνθήκες λειτουργίας. Αυτό το στάδιο επικύρωσης περιλαμβάνει την ενσωμάτωση της επικύρωσης αερίου, HV και ηλεκτρονικών, παρέχοντας μια συνολική αξιολόγηση της απόδοσης του ανιχνευτή. Η πειραματική διάταξη και το λογισμικό παίζουν κρίσιμο ρόλο στην ενορχήστρωση και παρακολούθηση αυτών των διαδικασιών επικύρωσης, εξασφαλίζοντας την επιτυχή ενσωμάτωση και λειτουργία των τομέων Micromegas στο πείραμα ATLAS. Η εγκατάσταση του Cosmics Station είναι ένα κρίσιμο στάδιο στην προετοιμασία του τομέα Micromegas για την ενσωμάτωση στο σπήλαιο ATLAS. Αυτό περιλαμβάνει την παροχή στον τομέα όλων των βασικών υπηρεσιών, συμπεριλαμβανομένων της υψηλής τάσης, του αερίου, της ψύξης, της ευθυγράμμισης και των ηλεκτρονικών, πριν από την τελική εγκατάστασή του. Η πολυπλοκότητα αυτού του συστήματος είναι εμφανής, καθώς απαιτεί σημαντική προσοχή και φροντίδα από μια ομάδα εμπειρογνομόνων επί αρκετές εβδομάδες για την πλήρη διαμόρφωση κάθε τομέα Micromegas. Μια απεικόνιση ενός πραγματικού τομέα Micromegas στο πλαίσιο της εγκατάστασης του Cosmics Stand στο BB5 CERN παρουσιάζεται στο Σχήμα 14.

## Σύστημα ελέγχου ηλεκτρονικών

Το NSW είναι ένα εξελιγμένο ανιχνευτικό τμήμα του πειράματος ATLAS, που απαιτεί την εφαρμογή ενός εξίσου εξελιγμένου DCS. Ο σκοπός αυτού του συστήματος είναι υψίστης σημασίας, εξασφαλίζοντας τη συνεπή και α-





Σχήμα 14: Ένας πραγματικός τομέας Micromegas στην εγκατάσταση Cosmics Stand στο BB5 CERN.

σφαλή λειτουργία του ανιχνευτή, ενώ παράλληλα διασυνδέεται απρόσκοπτα με όλους τους υπο-ανιχνευτές και την ευρύτερη τεχνική υποδομή του πειράματος. Το DCS NSW λειτουργεί ως κεντρικό νευρικό σύστημα, διαχειριζόμενο τις μεταβάσεις μεταξύ των καταστάσεων λειτουργίας του ανιχνευτή και παρέχοντας συνεχή παρακολούθηση και αρχειοθέτηση κρίσιμων λειτουργικών παραμέτρων. Η εγγενής πολυπλοκότητα και οι παρατεταμένες περιόδους λειτουργίας του NSW υπογραμμίζουν την αναγκαιότητα ενός ισχυρού DCS. Ταυτόχρονα, το NSW DCS παρακολουθεί συνεχώς και αρχειοθετεί βασικές παραμέτρους, παρέχοντας ένα ολοκληρωμένο αρχείο του ιστορικού λειτουργίας του συστήματος.

Το NSW DCS ενσωματώνει ένα ισχυρό σύστημα συναγερμού που αντιδρά άμεσα σε τυχόν ανωμαλίες που ανιχνεύονται στα υποσυστήματα του ανιχνευτή. Σε περίπτωση απόκλισης από τις κανονικές συνθήκες λειτουργίας, το σύστημα ενεργοποιεί σήματα ή συναγερμούς (alarms) που ειδοποιούν τους χειριστές. Αυτές οι ειδοποιήσεις χρησιμεύουν ως έγκαιρες προειδοποιήσεις, επιτρέποντας την ταχεία παρέμβαση για την αποκατάσταση των προβλημάτων. Το σύστημα έχει σχεδιαστεί για να προσαρμόζεται σε αυτόματες διαδικασίες, όποτε αυτό είναι δυνατό, ή να διευκολύνει τις χειροκίνητες ενέργειες για την επαναφορά του ανιχνευτή, εξασφαλίζοντας την ορθή λειτουργία του.

Η αίθουσα ελέγχου για το πείραμα ATLAS, που απεικονίζεται στο Σχήμα 15, είναι ένας κεντρικός κόμβος όπου ειδικευμένοι χειριστές εργάζονται όλο το εικοσιτετράωρο, 24 ώρες την ημέρα και επτά ημέρες την εβδομάδα. Αυτό το αφοσιωμένο προσωπικό παίζει καθοριστικό ρόλο στην προετοιμασία του ανιχνευτή ATLAS για την απόκτηση δεδομένων, εξασφαλίζοντας την ετοιμότητά του να συλλάβει πολύτιμα πειραματικά δεδομένα. Η αίθουσα ελέγχου λειτουργεί ως νευραλγικό κέντρο, επιβλέποντας τις περίπλοκες λειτουργίες του πειράματος ATLAS και ανταποκρινόμενη σε τυχόν συναγερμούς ή συμβάντα που ανιχνεύονται από το NSW DCS.



Σχήμα 15: Η αίθουσα ελέγχου του πειράματος ATLAS. Διάφοροι μετατοπιστές οι οποίοι λειτουργούν τον ανιχνευτή ATLAS επί 24 ώρες την ημέρα και επτά ημέρες την εβδομάδα προκειμένου να τον προετοιμάσουν για την απόκτηση δεδομένων.

## Σύστημα Ελέγχου του Νέου Μικρού Τροχού

Ο σχεδιασμός του NSW DCS έχει υλοποιηθεί έτσι ώστε να ενσωματώνεται απρόσκοπτα στο ευρύτερο ATLAS DCS, παρέχοντας συνεχή παρακολούθηση και μια ισχυρή διασύνδεση για όλες τις μονάδες υλικού(hardware) του NSW. Δεδομένου ότι οι Micromegas και οι sTGC χρησιμεύουν ως ανιχνευτές μιονίων εντός του NSW, περιλαμβάνονται στο σύστημα Muon DCS, όπου ο CSC θα καταργηθεί σταδιακά, οδηγώντας στην αντίστοιχη κατάργηση των λειτουργιών του DCS. Για τις ειδικές απαιτήσεις του NSW, δύο νέοι υπο-ανιχνευτές θα ενσωματωθούν στο δέντρο FSM του Muon DCS, MMG για Micromegas και STG για sTGC.

Το NSW αποτελείται από τα ακόλουθα τμήματα υλικού(hardware):

- **Υψηλή Τάση (HV):** Αυτή η μονάδα είναι υπεύθυνη για την παροχή υψηλής τάσης στον ανιχνευτή, η οποία είναι ζωτικής σημασίας για τη λειτουργία και τη λειτουργικότητα του ανιχνευτή μιονίων.
- **Χαμηλή Τάση (LV):** Αυτή η μονάδα παρέχει χαμηλή τάση στα ηλεκτρονικά, εξασφαλίζοντας την ορθή λειτουργία τους.
- **MDT-DCS-Module (MDM):** Αυτή η μονάδα φιλοξενεί αισθητήρες θερμοκρασίας και μαγνητικού πεδίου, συμβάλλοντας στην παρακολούθηση και τον έλεγχο.
- **Ηλεκτρονικά (ELTX):** Περιλαμβάνει τα ηλεκτρονικά που είναι υπεύθυνα για την απόκτηση δεδομένων, την ενεργοποίηση και τη μεταφορά δεδομένων εντός του NSW.
- **Αέριο:** Διαχειρίζεται τα στοιχεία αερίου του ανιχνευτή, ζωτικής σημασίας για την κανονική λειτουργία των ανιχνευτών.
- **Ψύξη:** Το μπλοκ υλικού Cooling παρέχει την απαραίτητη υποδομή για την ψύξη των ηλεκτρονικών, αποτρέποντας την υπερθέρμανση.
- **VME:** Το VME χρησιμεύει ως περιβάλλον υλικού που φιλοξενεί τα αρθρωτά ηλεκτρονικά (modular electronics), εξασφαλίζοντας την αποδοτική λειτουργία τους.
- **ATCA:** Χρησιμοποιεί την αρχιτεκτονική ATCA για τη φιλοξενία αρθρωτών ηλεκτρονικών, παρέχοντας προηγμένες υπολογιστικές δυνατότητες.
- **Σύστημα ασφαλείας ανιχνευτή (DSS):** Το DSS είναι η διεπαφή υλικού που είναι υπεύθυνη για τη διασφάλιση της ασφάλειας του συστήματος ανιχνευτή, ενεργοποιώντας πρωτόκολλα ασφαλείας σε περίπτωση ανωμαλιών.
- **Σύστημα κλειδώματος δέσμης (BIS):** Η διεπαφή BIS παρέχει παραμέτρους κλειδώματος δέσμης, ζωτικής σημασίας για την ασφαλή εκτέλεση φυσικής και τη λειτουργία του LHC.

## Σύστημα Ελέγχου των Ηλεκτρονικών

Το αυτόματο σύστημα ελέγχου των ηλεκτρονικών είναι επιφορτισμένο με την παρακολούθηση όλων των παραμέτρων που είναι συνδεδεμένες στο SCA όλων των ηλεκτρονικών του NSW. Η σχηματική αναπαράσταση της λειτουργίας του SCA απεικονίζεται στο Σχήμα 8. Ο SCA OPC UA Server, με τη βοήθεια του FELIX, εγκαθιστά επικοινωνία με τον SCA και τις σχετικές συνδέσεις του. Καθώς ο SCA OPC UA Server είναι προσβάσιμος στο δίκτυο, το DCS Back-End, το οποίο στο πλαίσιο μας αντιπροσωπεύεται από το έργο WinCC-OA, μπορεί να ενεργήσει ως πελάτης OPC UA. Αυτό του επιτρέπει να εγγραφεί στο διακομιστή και να διαβάσει όλες τις τιμές που σχετίζονται με το SCA.

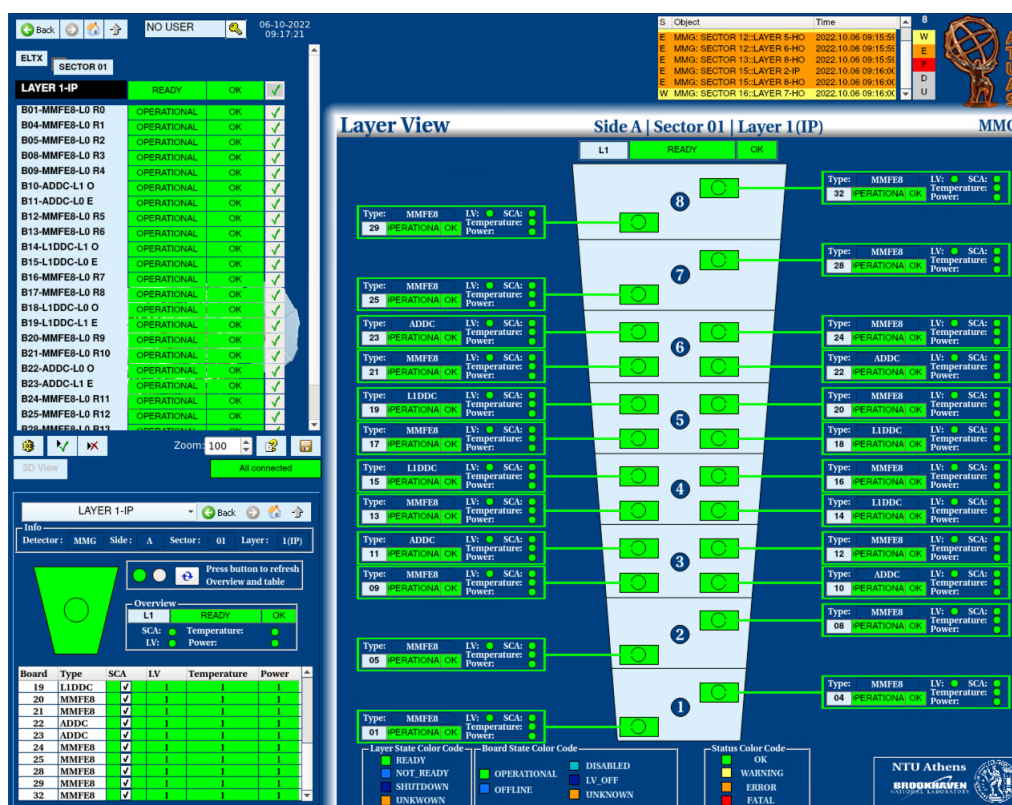
Ο πρωταρχικός στόχος του Electronics DCS είναι να παρέχει στους χρήστες τη δυνατότητα ασφαλούς παρακολούθησης των τιμών 7488 ηλεκτρονικών πλακετών, που περιλαμβάνουν πάνω από 100 000 παραμέτρους.

Το Electronics DCS αποτελείται από μηχανές πεπερασμένων καταστάσεων (FSM), όπου κάθε FSM κόμβος έχει μοναδικό όνομα με βάση το όνομα του υποσυστήματος και τη λειτουργικότητά του, σύμφωνα με τις συμβάσεις

του ATLAS DCS. Η κατάσταση κάθε FSM καθορίζεται από ένα αντίστοιχο εσωτερικό σημείο δεδομένων. Ο τύπος του αντικειμένου FSM, ο οποίος καθορίζει τη θεμελιώδη λειτουργικότητα του κόμβου και των στοιχείων του, εξαρτάται από τον λειτουργικό σκοπό και τη θέση του στοιχείου στην ιεραρχία της αρχιτεκτονικής DCS.

Κάθε FSM λειτουργεί με αυστηρή ιεραρχική δομή, δημιουργώντας σχέσεις γονέα-παιδιού. Σε αυτή τη δομή, οι εντολές ρέουν από τους γονείς στα παιδιά και οι ενημερώσεις κατάστασης ρέουν από τα παιδιά στους γονείς. Αυτή η ιεραρχική προσέγγιση διασφαλίζει την αποτελεσματικότητα στην εντολή ενεργειών σε πολλαπλούς κόμβους, καθώς ένας κόμβος υψηλότερου επιπέδου μπορεί να δώσει εντολή στα παιδιά του και η κατάσταση του υψηλότερου κόμβου συνοψίζει την κατάσταση όλων των κόμβων στην ιεραρχία του. Όλοι οι κόμβοι βρίσκονται αρχικά σε μια προκαθορισμένη κατάσταση και δέχονται μόνο προκαθορισμένες εντολές, όπως καθορίζεται από τον τύπο FSM στον οποίο ανήκουν.

Προχωρώντας προς τα πάνω στην ιεραρχία ELTX FSM, η επαφή χρήστη Layer View εμφανίζει βασικές πληροφορίες σχετικά με το επίπεδο του αντίστοιχου τομέα, όπως απεικονίζεται στο Σχήμα 16. Αυτός ο πίνακας παρέχει μια ολοκληρωμένη προβολή όλων των ηλεκτρονικών μονάδων που είναι εγκατεστημένες στο αντίστοιχο επίπεδο του ανιχνευτή, επιτρέποντας στους χρήστες να αξιολογήσουν την κατάσταση.



Σχήμα 16: Ο πίνακας λειτουργίας για την προβολή επιπέδου FSM.

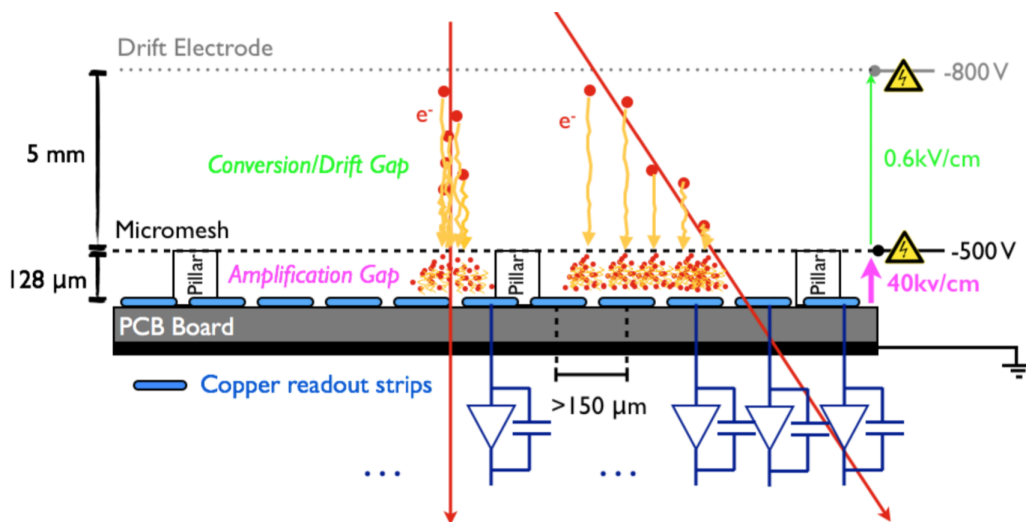
## Χαρακτηρισμός Απόδοσης του Ανιχνευτή Micromegas

Ο ανιχνευτής αερίου Micromegas αποτελεί βασικό ανιχνευτή στην αναβάθμιση του New Small Wheel του πειράματος ATLAS και έχει ως κύριο στόχο την ανακατασκευή των τροχιών των σωματιδίων κατά τις συγκρούσεις στο σημείο αλληλεπίδρασης. Η λειτουργία των ανιχνευτών στην Πειραματική Φυσική Υψηλών Ενεργειών βασίζεται στην αλληλεπίδραση της ακτινοβολίας και των σωματιδίων με το υλικό του ανιχνευτή, με μηχανισμούς που διέπονται από ηλεκτρομαγνητικές δυνάμεις. Καθώς τα φορτισμένα σωματίδια αλληλεπιδρούν με τα ηλεκτρόνια της ύλης, προξενούν διέγερση ή ιονισμό, χάνοντας ενέργεια ή ακόμη μπορούν και να σταματήσουν στον ανιχνευτή.. Οι ανιχνευτές αερίου βασίζονται στην αρχή του ιονισμού, όπου το εισερχόμενο σωματίδιο απελευθερώνει ζεύγη ηλεκτρονίων-ιόντων. Αυτά πολλαπλασιάζονται με εφαρμογή ηλεκτρικού πεδίου, δημιουργώντας μετρήσιμο σήμα.

Ο τυπικός ανιχνευτής Micromegas περιλαμβάνει:

- Επίπεδο ανόδου (drift electrode).
- Διάκενο αερίου λίγων χιλιοστών ως περιοχή μετατροπής και ολίσθησης (conversion gap).
- Μεταλλικό πλέγμα (mesh) σε απόσταση  $100\ \mu\text{m}$  από το ηλεκτρόδιο ανάγνωσης (readout cathode), δημιουργώντας την περιοχή ενίσχυσης (amplification gap).
- Κυλινδρικές κολώνες (pillars) για τη στήριξη του πλέγματος.

Στα ηλεκτρόδια του ανιχνευτή εφαρμόζονται κατάλληλες ηλεκτρικές τάσεις, παρέχοντας υψηλά ηλεκτρικά πεδία στην περιοχή ενίσχυσης και ασθενέστερα πεδία στην περιοχή μετατροπής. Αυτό είναι κρίσιμο για την αποτελεσματική λειτουργία του ανιχνευτή, επιτυγχάνοντας λόγο κέρδους έως  $10^4$ . Το ηλεκτρικό πεδίο ρυθμίζεται ώστε να κυμαίνεται από μερικές εκατοντάδες  $\text{V/cm}$  στην περιοχή μετατροπής και  $40 - 50\ \text{V/cm}$  στην περιοχή ενίσχυσης. Η άνοδος είναι διαιρεμένη σε λωρίδες (strips).



Σχήμα 17: Γραφική απεικόνιση μίας τυποποιημένης διατομής ενός ανιχνευτή Micromegas που απεικονίζει τα διάφορα μέρη της εσωτερικής δομής του ανιχνευτή και την αρχή λειτουργίας του.

Καθώς το φορτισμένο σωματίδιο περνάει από το ηλεκτρόδιο καθόδου (drift), εισέρχεται στην περιοχή ολίσθησης μερικών χιλιοστών πάνω από το πλέγμα (mesh). Εκεί, αλληλεπιδρά με το αέριο του ανιχνευτή, προκαλώντας ιονισμό και διέγερση, με αποτέλεσμα τη δημιουργία ηλεκτρονίων και ιόντων. Τα ηλεκτρόνια, υπό την επίδραση ασθενούς ηλεκτρικού πεδίου, κινούνται προς το πλέγμα, ενώ τα ιόντα προς την κάθοδο. Όταν τα ηλεκτρόνια περνούν από το πλέγμα, οδηγούνται στην περιοχή ενίσχυσης όπου το ισχυρό ηλεκτρικό πεδίο προκαλεί χιονοστιβάδα ηλεκτρονίων που συλλέγονται από τις ανοδικές λωρίδες (readout strips), ενώ τα ιόντα κινούνται πιο αργά προς το πλέγμα.

Με ένα ηλεκτρικό πεδίο στην περιοχή ενίσχυσης 50-100 φορές ισχυρότερο από αυτό της περιοχής ολίσθησης, το πλέγμα επιτρέπει τη διέλευση πάνω από το 95% των ηλεκτρονίων. Η χιονοστιβάδα ηλεκτρονίων διαρκεί περίπου  $1\ \text{ns}$ , δημιουργώντας έναν γρήγορο παλμό στις λωρίδες ανάγνωσης. Τα ιόντα που παράγονται στην περιοχή ενίσχυσης κινούνται προς το πλέγμα με πολύ χαμηλότερη ταχύτητα σε σύγκριση με τα ηλεκτρόνια.

Ο Micromegas πρέπει να προσφέρει ανακατασκευή με ακρίβεια καλύτερη από  $100\ \mu\text{m}$  κατά μήκος του πλήρους εύρους των γωνιών τροχιάς μιονίων. Οι μέθοδοι ανακατασκευής θέσης περιλαμβάνουν την τεχνική του κεντροειδούς φορτίου και την μικρο-χρονική θαλάμη προβολής (μTPC). Όταν το σωματίδιο είναι κάθετο στο επίπεδο ανάγνωσης, χρησιμοποιείται η τεχνική του κεντροειδούς φορτίου (charge centroid) για ακριβή ανακατασκευή θέσης. Για σωματίδια υπό γωνία, εφαρμόζεται η μέθοδος μTPC.



## Πειράματα χαρακτηρισμού Micromegas με δοκιμαστική δέσμη

Η δοκιμαστική δέσμη πραγματοποιήθηκε στη γραμμή δέσμης H8 της εγκατάστασης Super Proton Synchrotron (SPS) στο CERN τον Ιούλιο του 2018, όπως φαίνεται στο Σχήμα 18. Η γραμμή δέσμης H8 διαθέτει σωματίδια που αποτελούνται από 180 GeV/c πιόνια ή μιονία, που χαρακτηρίζονται από ένα μέγεθος στόχου περίπου  $10 \times 10 \text{ cm}^2$ . Αυτό το σημαντικό γεγονός σηματοδότησε την εναρκτήρια αξιολόγηση της πρώτης μονάδας παραγωγής SM2, εξοπλισμένης με πρωτότυπες πλακέτες MMFE8, υπό πραγματικές συνθήκες δέσμης. Ταυτόχρονα, διεξήχθη η εναρκτήρια δοκιμή της τρίτης έκδοσης του VMM front-end ASIC, η οποία έμοιαζε πολύ με την τελική έκδοση παραγωγής του. Οι πρωταρχικοί στόχοι αυτής της δέσμης δοκιμών περιλάμβαναν ένα ευρύ φάσμα αξιολογήσεων και επικυρώσεων:

1. **Επαλήθευση απόδοσης του SM2:** Εξέταση της λειτουργικότητας της μονάδας SM2 υπό συνθήκες πραγματικής δέσμης.
2. **Επικύρωση ηλεκτρονικών:** Δοκιμές για την αξιολόγηση της απόδοσης των ηλεκτρονικών εξαρτημάτων, εξασφαλίζοντας την συμμόρφωσή τους με τα απαιτούμενα πρότυπα.
3. **Δοκιμή τρίτης έκδοσης VMM ASIC:** Αξιολόγηση της λειτουργίας του νέου ASIC VMM υπό πραγματικές συνθήκες δέσμης.
4. **Ρύθμιση παραμέτρων VMM:** Αναζήτηση της βέλτιστης διαμόρφωσης για την αποδοτική λήψη και ανάλυση δεδομένων.
5. **Προσδιορισμός τιμής υψηλής τάσης:** Καθορισμός της ιδανικής τιμής για μέγιστη απόδοση.
6. **Δοκιμές με μείγματα αερίων:** Αξιολόγηση της επίδρασης διαφόρων μειγμάτων αερίων στην απόδοση του ανιχνευτή.

Εκτός από τη διεξοδική αξιολόγηση του ανιχνευτή, το ολοκληρωμένο πεδίο εφαρμογής της δοκιμαστικής δέσμης περιελάμβανε τη σχολαστική ρύθμιση των κρίσιμων παραμέτρων και διαμορφώσεων που είναι απαραίτητες για τη διασφάλιση της απρόσκοπτης λειτουργίας του συστήματος. Αυτή η πολύπλευρη προσέγγιση στόχευε όχι μόνο στην πιστοποίηση του ανιχνευτή αλλά και στη βελτιστοποίηση της αλληλεπίδρασης των μεταβλητών που στηρίζουν τη λειτουργικότητα της τεχνολογίας.



Σχήμα 18: Η γραμμή δέσμης H8 του SPS στην περιοχή Preveessin North του CERN, στην οποία έχει εγκατασταθεί η πειραματική ρύθμιση δοκών δοκιμής Micromegas.

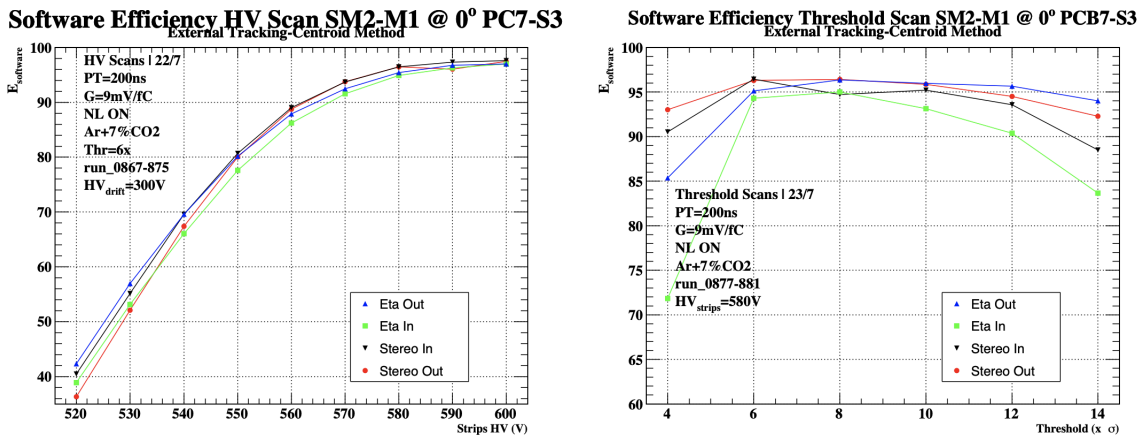
Η πειραματική ρύθμιση της δοκιμαστικής δέσμης περιλαμβάνει τρεις θαλάμους προβολής  $10 \times 10 \text{ cm}^2$  T<sub>Z</sub> Micromegas. Αυτοί οι θάλαμοι διαθέτουν λωρίδες πλάτους 150 μm με βήμα 250 μm και είναι εξοπλισμένοι

με πλακέτες MMFE8 που ενσωματώνουν προστινά άκρα VMM FPGA. Αυτοί οι θάλαμοι λειτουργούν ως σημεία αναφοράς για την ανακατασκευή εξωτερικών τροχιών. Ο θάλαμος SM2, με τέσσερις πλακέτες MMFE8 τοποθετημένες σε ένα στρώμα ανιχνευτή, είναι μόνο κατά το ήμισυ εξοπλισμένος με όργανα. Για το πείραμα χρησιμοποιούνται δύο σπινθηριστές ως σκανδαλιστές. Οι υπόλοιποι θάλαμοι περιλαμβάνουν πρωτότυπα Micromegas με διαφορετικά συστήματα ανάγνωσης (APV/SRS) και δεν συμβάλλουν στην ανακατασκευή τροχιών.

Η απόδοση ανίχνευσης είναι καίρια για την αξιολόγηση του ανιχνευτή και εκφράζεται ως ο λόγος των καταγεγραμμένων σημάτων προς τα αναμενόμενα φορτισμένα σωματίδια που διέρχονται. Στη διάρκεια των πειραμάτων, συλλέξαμε πολλές τροχιές ενώ ρυθμίζαμε συστηματικά την τάση σε κάθε στρώμα, επιτρέποντας σαρώσεις τάσης και την χαρτογράφηση της απόδοσης σε σχέση με την τάση ενίσχυσης. Αυτή η μεθοδολογία μας βοήθησε να εντοπίσουμε τις βέλτιστες συνθήκες λειτουργίας του ανιχνευτή, εξασφαλίζοντας ότι η πειραματική μας εγκατάσταση θα καταγράφει δεδομένα με αξιοπιστία και ακρίβεια. Αυτές οι μετρήσεις προσέφεραν μια ολοκληρωμένη κατανόηση της απόδοσης του ανιχνευτή και διευκόλυναν τη ακριβή βελτιστοποίηση της λειτουργίας του, ενισχύοντας την ακρίβεια των δεδομένων μας στην έρευνα σωματιδιακής φυσικής.

Για την αξιολόγηση των τριών κατηγοριών απόδοσης, χρησιμοποιήσαμε δύο διακριτές μεθόδους για την ανακατασκευή της τροχιάς: εξωτερική παρακολούθηση(External-Tracking) χρησιμοποιώντας τους θαλάμους τηλεσκοπίου και αυτο-παρακολούθηση(Self-Tracking) χρησιμοποιώντας πληροφορίες από τα άλλα τρία στρώματα του ανιχνευτή.

Ιδιαίτερο ενδιαφέρον είχε η εντατική μελέτη της αποτελεσματικότητας του λογισμικού(software efficiency). Για την πλήρη κατανόηση και βελτιστοποίηση αυτής της πτυχής, πραγματοποιήσαμε διάφορες μελέτες, συμπεριλαμβανομένων των σαρώσεων κατωφλίου(threshold) και υψηλής τάσης. Τα αποτελέσματα αυτών των μελετών απόδοσης λογισμικού απεικονίζονται στο Σχήμα 19. Αυτές οι έρευνες μας επέτρεψαν να βελτιστοποιήσουμε τις παραμέτρους του λογισμικού, όπως τα όρια και τις ρυθμίσεις τάσης, για να μεγιστοποιήσουμε την απόδοση του ανιχνευτή μας. Διεξάγοντας αυτές τις εις βάθος μελέτες, όχι μόνο βελτιστοποιήσαμε την απόδοση του θαλάμου, αλλά και εξασφαλίσαμε την αξιοπιστία της ανάλυσης των δεδομένων μας. Ένας άλλος σημαντικός στόχος των



Σχήμα 19: Αριστερά: Η απόδοση λογισμικού(software efficiency) είναι συνάρτηση τη υψηλής τάσης των λωρίδων ανάγνωσης (readout strips). Δεξιά: Η απόδοση λογισμικού είναι συνάρτηση του ορίου.

πειραμάτων δοκιμαστικής δέσμης ήταν η διεξοδική διερεύνηση των επιδράσεων διαφορετικών μιγμάτων αερίων στο φορτίο συστάδας(cluster charge), την πολλαπλότητα των συστάδων(cluster multiplicity) και την απόδοση λογισμικού εντός του θαλάμου SM2. Πραγματοποιήσαμε μια ολοκληρωμένη μελέτη που περιελάμβανε τρεις διακριτές συνθέσεις αργού και διοξειδίου του άνθρακα κατά τη φάση της δοκιμαστικής δέσμης. Ο πρωταρχικός στόχος ήταν να εξακριβωθεί εάν η τροποποίηση του μείγματος αερίων θα μπορούσε να αποφέρει βελτιώσεις στην απόδοση του θαλάμου. Με τη συστηματική διερεύνηση αυτών των διαφορετικών συνθέσεων αερίων, επιδιώξαμε να αποκαλύψουμε πιθανές βελτιώσεις στις ακόλουθες βασικές παραμέτρους:

- **Cluster Charge:** Αξιολογήσαμε σχολαστικά πώς το μείγμα αερίων επηρέασε την κατανομή φορτίου των συστάδων που σχηματίστηκαν εντός του θαλάμου. Οι παραλλαγές στη σύνθεση του αερίου θα μπορούσαν

να επηρεάσουν τα χαρακτηριστικά εναπόθεσης ενέργειας των σωματιδίων που διέρχονται από τον ανιχνευτή.

- **Cluster Multiplicity:** Οι έρευνές μας εξέτασαν επίσης την πολλαπλότητα των συστάδων, εξετάζοντας πώς διαφορετικά μείγματα αερίων επηρέασαν τον αριθμό των συστάδων που σχηματίστηκαν ως απόκριση στις αλληλεπιδράσεις των σωματιδίων. Αυτή η παράμετρος είναι ζωτικής σημασίας για την κατανόηση των δυνατοτήτων παρακολούθησης του ανιχνευτή.
- **Αποτελεσματικότητα λογισμικού:** Επιπλέον, μελετήσαμε την απόδοση λογισμικού του θαλάμου SM2 κάτω από διαφορετικές συνθήκες μίγματος αερίων. Αυτή η ανάλυση παρείχε πληροφορίες για το πώς οι αλλαγές στη σύνθεση του αερίου θα μπορούσαν να επηρεάσουν την ικανότητα του θαλάμου να ανακατασκευάζει με ακρίβεια τα ίχνη σωματιδίων.

Διεξήγαμε συστηματικές μελέτες και εξερευνήσαμε διάφορα μείγματα αερίων με στόχο τη βελτιστοποίηση της απόδοσης του θαλάμου SM2, την ενίσχυση των ικανοτήτων παρακολούθησης και τη βελτίωση της αποτελεσματικότητάς του για τη φυσική των σωματιδίων. Η έρευνά μας επικεντρώθηκε στον εντοπισμό πιθανών βελτιώσεων στην πειραματική μας διάταξη.

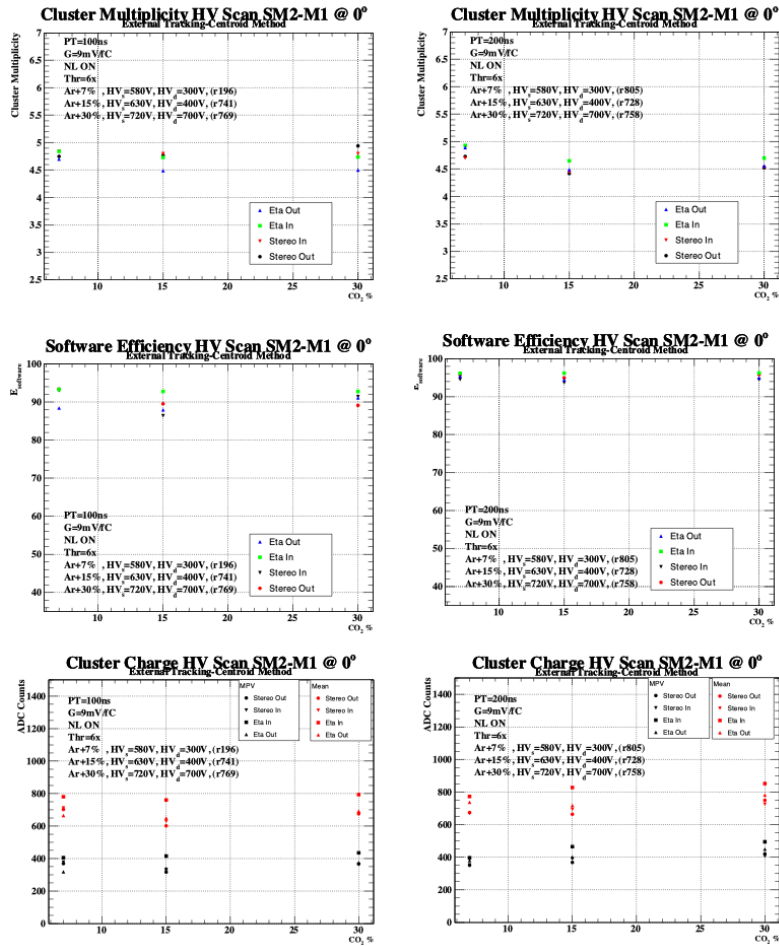
Για τα δύο νέα μείγματα αερίων, ακολουθήθηκε προσεκτική προσέγγιση στην επιλογή των τάσεων μετατόπισης και ενίσχυσης, με στόχο τη σταθερότητα της μετατόπισης των ηλεκτρονίων και τη συνοχή στην εγγάρσια διάχυση. Η επιλογή αυτή ήταν κρίσιμη για τη διατήρηση της απόδοσης του ανιχνευτή.

Στο Σχήμα 20, παρουσιάζουμε οπτικά τα αποτελέσματα για τα τρία διαφορετικά μείγματα αερίων, υπό τις ίδιες συνθήκες απολαβής και διαφορετικές ρυθμίσεις χρόνου αιχμής. Οι συγκρίσεις αυτές δείχνουν ότι τα μείγματα  $Ar + CO_2$  παρουσίασαν ελάχιστη διακύμανση και σταθερή χωρική ανάλυση, αποδεικνύοντας τη στιβαρότητα και τη συνέπεια του ανιχνευτή σε διαφορετικές συνθέσεις αερίων. Επικεντρωθήκαμε επίσης στο ποσοστό  $CO_2$ , το οποίο επηρεάζει τη σταθερότητα του πεδίου ενίσχυσης. Ένα υψηλότερο ποσοστό  $CO_2$  βελτιώνει τη καταστολή των σπινθήρων εντός του θαλάμου, αν και μειώνει τον αριθμό των πρωτογενών ιονισμών. Συνοψίζοντας, η προσεκτική επιλογή των μειγμάτων αερίων και η εστίαση στις παραμέτρους σταθερότητας και απόδοσης ήταν κρίσιμες για τη βελτιστοποίηση της απόδοσης και της αξιοπιστίας του θαλάμου SM2 στην έρευνα της φυσικής των σωματιδίων.

Πριν αναλύσουμε την απόδοση, αντιμετωπίσαμε το σημαντικό έργο της βαθμονόμησης πάνω από 2000 καναλιών VMM που αναπτύχθηκαν για την εγκατάσταση. Η βαθμονόμηση αυτή περιελάμβανε λεπτομερείς παραμέτρους όπως τα κατώφλια φόρτισης(charge threshold) και η μετατροπή των ADC μετρήσεων σε φυσικές μονάδες χρόνου και φόρτισης. Ειδική προσοχή δόθηκε στη βαθμονόμηση του χρόνου, εξετάζοντας δύο διαφορετικές μεθοδολογίες: μία βασισμένη σε δεδομένα και μία που περιλάμβανε την έγχυση δοκιμαστικών παλμών. Τα αποτελέσματα από τη βαθμονόμηση βασισμένη σε δεδομένα χρησιμοποιήθηκαν για τις μελέτες απόδοσης και ανάλυσης του συστήματος ανάγνωσης. Οι μελέτες επικεντρώθηκαν σε δύο κύριους στόχους. Ο πρώτος ήταν η επιβεβαίωση της λειτουργικότητας του τσιπ VMM σε έναν Micromegas πλήρους μεγέθους, δείχνοντας χωρική ανάλυση περίπου 100  $\mu m$  και απόδοση ανακατασκευής πάνω από 90%. Αυτά τα αποτελέσματα επιβεβαίωσαν την αποτελεσματικότητα της μονάδας VMM στην ανάγνωση του Micromegas.

Η εγκατάσταση GIF++ είναι ένα σημαντικό καταφύγιο που περιλαμβάνει μια πηγή  $^{137}Cs$  για ακτινοβολία γάμμα, προσφέροντας συνολική δραστηριότητα 14 TBq με εμφανή ενεργειακή αιχμή στα 667 KeV. Η εγκατάσταση αυτή επιτρέπει σταθερή παροχή ακτινοβολίας καθ' όλη τη διάρκεια του έτους. Διαθέτει δύο ανεξάρτητες ζώνες ακτινοβολίας που επιτρέπουν την ταυτόχρονη δοκιμή ανιχνευτών πλήρους μεγέθους και μικρότερων πρωτότυπων ανιχνευτών. Η εγκατάσταση διαδραματίζει κεντρικό ρόλο σε ερευνητικές δραστηριότητες, περιλαμβανομένης της αξιολόγησης της συμπεριφοράς θαλάμων Micromegas κάτω από παρατεταμένη ακτινοβολία και της εξερεύνησης νέων μειγμάτων αερίων. Επιπλέον, χρησιμεύει ως πόρος για δοκιμές συστημάτων DAQ και αλγορίθμων ανακατασκευής σε ρεαλιστικό περιβάλλον. Η γραμμή δέσμης CERN SPS H4 παρέχει μια δέσμη μιονίων με χαμηλή ένταση, που διασχίζει το bunker του GIF++, επιτρέποντας μετρήσεις MIP παρουσία ης πηγής  $^{137}Cs$ .

Με αυτές τις συνδυασμένες δυνατότητες, το GIF++ είναι κεντρικός κόμβος για ερευνητικές προσπάθειες στην τεχνολογία ανιχνευτών και στις μελέτες ακτινοβολίας.



Σχήμα 20: Εμφανίζονται η software efficiency, το cluster charge και το cluster multiplicity για κάθετες διαδρομές με το ίδιο κέρδος για τα τρία διαφορετικά μείγματα αερίων. Οι συγκρίσεις έγιναν χρησιμοποιώντας ένα κατώφλι υλικού  $6 \times \sigma$ , λογική γειτονικού ON και δύο διαφορετικές ρυθμίσεις χρόνου αιχμής (100 και 200 ns). Δεν υπάρχει μεγάλη διαφορά μεταξύ αυτών των τριών συνδυασμών  $Ar + CO_2$ .

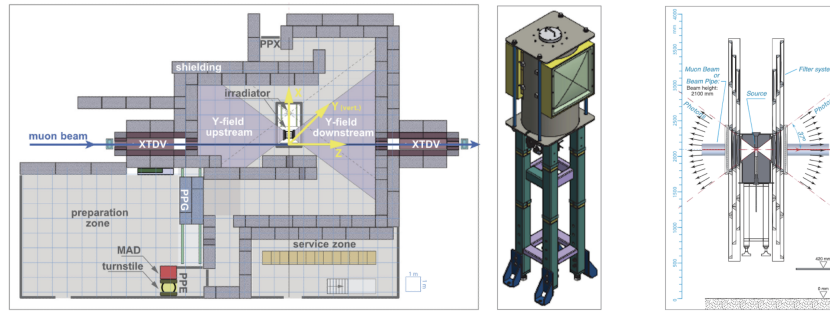
Για να εμβαθύνουμε στην κατανόηση των επιδόσεων ηλεκτρονικών συσκευών, δημιουργήθηκε μια προσεκτικά σχεδιασμένη πειραματική εγκατάσταση, με στόχο την εξέταση της απόκρισης διαφόρων μονάδων ανιχνευτή στην ακτινοβολία ακτίνων γάμμα. Επιπλέον, προσομοιάζονται οι συνθήκες που σχετίζονται με το πείραμα του Μεγάλου Επιταχυντή Αδρονίων Υψηλής Φωτεινότητας (HL-LHC).

Στην ενότητα αυτή παρουσιάζονται λεπτομερείς δοκιμές που πραγματοποιήθηκαν στο νέο CERN GIF++, χρησιμοποιώντας μια δέσμη μιονίων με συχνότητα 100 KHz και πηγή ακτινοβολίας  $^{137}\text{Cs}$ , η οποία ρυθμίστηκε σε ρυθμό έως και δεκαπλάσιο από τον αναμενόμενο ρυθμό στις συνθήκες του HL-LHC. Αυτές οι δοκιμές αποσκοπούν στην αξιολόγηση της απόδοσης των θαλάμων Micromegas και της ανάγνωσής τους.

Οι προηγούμενες μελέτες μας έχουν επικεντρωθεί σε κάθετες τροχιές σωματιδίων, με δοκιμές σε μικρούς και μεγάλους θαλάμους, διατηρώντας σταθερά επίπεδα ανάλυσης ανακατασκευής θέσης. Ωστόσο, στην πράξη, ο ανιχνευτής θα πρέπει κυρίως να ανακατασκευάζει σωματίδια που κινούνται σε κεκλιμένες τροχιές, προσθέτοντας πολυπλοκότητα. Μία από τις κύριες προκλήσεις για τον ανιχνευτή Micromegas είναι η χρονική απόκριση των στρωμάτων eta, απαραίτητη για την ακριβή ανακατασκευή των κεκλιμένων τροχιών σωματιδίων.

Στο πλαίσιο της πειραματικής μας εγκατάστασης, αξιολογήσαμε τη χρονική απόκριση του ανιχνευτή για τροχιές με κλίση  $30^\circ$  προς την επιφάνειά του, χρησιμοποιώντας συστάδες back-to-back των επιπέδων SM1 eta.

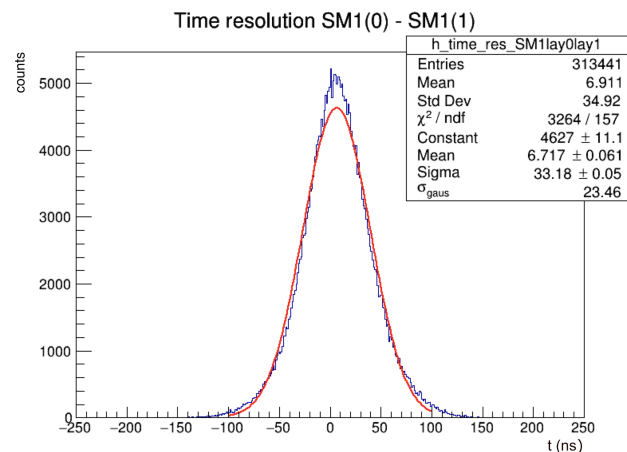
Εφαρμόσαμε βαθμονόμηση του χρόνου απόκρισης (TDO) ανά κανάλι και ευθυγράμμιση του γενικού πρωταρχικού χρόνου ( $t_0$ ) για την εξασφάλιση ακριβών μετρήσεων. Αναλύοντας τα χρονικά υπολείμματα μεταξύ των στρωμάτων, δημιουργήσαμε κατανομές χρόνου, τις οποίες προσαρμόσαμε με διπλή Γκαουσιανή κατανομή. Η



Σχήμα 21: Αριστερά: Κάτοψη της εγκατάστασης GIF++. Μέση: Σχηματικό σχέδιο του ακτινοβολητή GIF++ με γωνιακά διορθωτικά φίλτρα και ανεξάρτητα συστήματα φίλτρων και στις δύο πλευρές. Δεξιά: Και στις δύο πλευρές, ένα σύνολο ανεξάρτητα κινητών και τηλεχειριζόμενων φίλτρων εξασθένισης και πλασίων ρυθμιστών επιτρέπει τη μεταβολή της έντασης των εκπεμπόμενων φωτονίων.

ανάλυση χρόνου κανονικοποιήθηκε διαιρώντας τη τυπική απόκλιση της κατανομής με την τετραγωνική ρίζα του 2, προσφέροντας ακριβή μέτρηση της χρονικής ακρίβειας. Αυτή η ανάλυση ενίσχυσε την κατανόησή μας για τη χρονική απόδοση του ανιχνευτή σε συνθήκες κεκλιμένων τροχιών, κρίσιμη για τη βελτίωση της απόδοσης ανακατασκευής micro-TPC.

Για μια οπτική αναπαράσταση των ευρημάτων μας και την υπολογισμένη ανάλυση χρόνου, ανατρέξτε στο Σχήμα 22. Αυτό το σχήμα παρέχει μια οπτική περιήληψη της ανάλυσής μας, βοηθώντας στην ερμηνεία των αποτελεσμάτων μας και τη σημασία τους. Τώρα που έχουμε επιτύχει ακριβή ανάλυση χρονισμού, είμαστε καλά προετοιμασμένοι



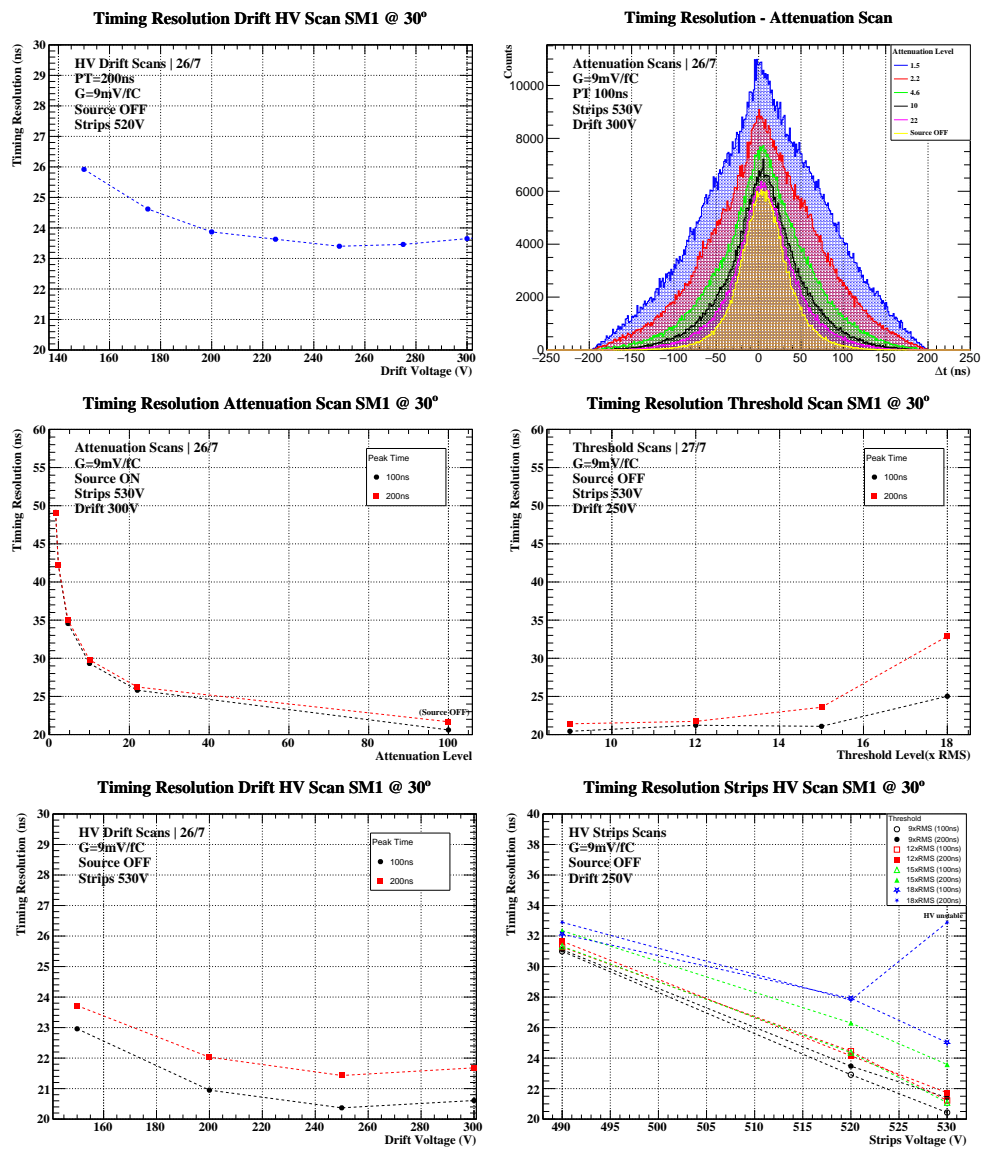
Σχήμα 22: Η χρονική ανάλυση του ανιχνευτή SM1 χρησιμοποιώντας το σύμπλεγμα back-to-back των πλησιέστερων λωρίδων ανάγνωσης. Η ανάλυση χρόνου είναι το σίγμα της διανομής κατά  $\sqrt{2}$ .

να ξεκινήσουμε μια ολοκληρωμένη εξερεύνηση διαφόρων μελετών, καθεμία βασισμένη σε διαφορετικά σενάρια περιπτώσεων, αποτυπώνονται στα επόμενα γραφήματα.

Κατά τη διάρκεια του προηγμένου πειράματος H8 στο CERN, η αξιολόγηση του SM2 Micromegas συνιστά σημαντικό βήμα στην κατανόηση του ανιχνευτή. Αυτή η δοκιμή ήταν απολύτως απαραίτητη για την αποτελεσματική πορεία της αναβάθμισης του NSW του πειράματος ATLAS στο CERN, αναδεικνύει τις επιδόσεις του Micromegas και αποκαλύπτει προκλήσεις για περαιτέρω βελτίωση. Η πλήρης ανάλυση της απόδοσης επιβεβαιώνει την αξιοπιστία της τεχνολογίας Micromegas, επιδεικνύοντας την καταλληλότητά της για ακριβή παρακολούθηση σε απαιτητικά περιβάλλοντα.

Η αυστηρή βαθμονόμηση πάνω από 2000 καναλιών VMM επέφερε σημαντικές βελτιώσεις στην πιστότητα του σήματος και την απόκριση του ανιχνευτή. Η βελτιστοποίηση των μιγμάτων αερίων αντιμετώπισε αστάθειες HV, μειώνοντας τις λειτουργικές ανωμαλίες και ενισχύοντας τη σταθερότητα του συστήματος. Η αξιολόγηση των μετρήσεων σε εξωτερικούς τρόπους και σε αυτο-παρακολούθηση παρείχε κρίσιμα δεδομένα για τις λειτουργικές





Σχήμα 23: Συνδυαστικά γραφήματα μελέτης της χρονικής απόκρισης του ανιχνευτή Micromegas.

παραμέτρους και τα όρια απόδοσης του ανιχνευτή. Η συνεχής βελτίωση των διαδικασιών βαθμονόμησης και των συνθέσεων του μείγματος αερίων, καθώς και η ενσωμάτωση προηγμένων υπολογιστικών μοντέλων και αλγορίθμων μηχανικής μάθησης για ανάλυση δεδομένων σε πραγματικό χρόνο, αποτελούν πεδία που προσφέρουν νέες δυνατότητες και αποδόσεις.







# Chapter 1

---

## Introduction to the Large Hadron Collider and the ATLAS Experiment

---

This chapter serves as an introduction to the Large Hadron Collider (LHC) and the ATLAS experiment. The LHC, operational since 2008, stands as the world's largest and most complex accelerator, located at CERN. Its primary objective is to delve into realms of physics beyond the confines of the Standard Model. Forming a complex network of accelerators and a 27 km ring, the LHC accelerates protons close to the speed of light, resulting in high-energy collisions. Within this colossal complex, the ATLAS experiment as a general-purpose detector, designed to undertake various particle physics studies. Its complex structure encompasses a Magnet System, an Inner Detector, Calorimeters, a Muon Spectrometer and an advanced Trigger and Data Acquisition System (TDAQ). The Magnet System, featuring a Central Solenoid, a Barrel Torroid and End-Cap Toroids, generates essential magnetic fields for bending charged particle orbits and determining their momentum. The Inner Detector, equipped with the Pixel Detector, the SemiConductor Tracker and the Transition Radiation Tracker, utilizes the concept of pseudorapidity to describe particle angles. Calorimeters play a crucial role in absorbing and measuring particle energy. In the ATLAS setup, these include the Liquid Argon (LAr) and the Tile barrel (Tile). The Muon Spectrometer utilizes advanced technologies such as Monitored Drift Tubes (MDT), Cathode Strip Chambers (CSC) which they will be replaced by the NSW, Resistive Plate Chambers (RPC) and Thin Gap Chambers (TGC) to identify and measure muons. The TDAQ encompasses three trigger levels (L1, L2, EF) to efficiently collect and process data. Through these trigger levels, the initial collision rate is systematically reduced to manageable levels for subsequent analysis. Mainly, this chapter provides an introductory overview of the intricate machinery and systems constituting the LHC and the ATLAS experiment. It underscores their collective efforts in pushing the boundaries of our understanding of fundamental physics, surpassing the confines of the established Standard Model.

## 1.1 The Large Hadron Collider

The LHC, cited as [1], stands as the world's most extensive and potent accelerator, was deployed in September 2008 as the latest enhancement to the CERN accelerator complex. Situated beneath the Earth's surface on the Swiss-French border, this groundbreaking experimental facility operates as a twin-pack superconducting accelerator and collider. Proton beams, accelerated to light speed, traverse the 26.7 km perimeter tunnel until their ultimate convergence for high-energy collisions. Figure 1.1 visually captures the intricate configuration of the LHC's superconducting magnets. Moreover, it is noteworthy that the LHC repurposes the tunnel initially constructed between 1984 and 1989 for the CERN LEP [2] accelerator, which ceased operations in 2000. The LHC's primary mission not only extends beyond particle collision, but it seeks to unravel the mysteries of physics beyond the Standard Model, achieving center-of-mass energies for proton-proton collisions, surpassing 14 TeV. This ambitious pursuit positions the LHC at the forefront of cutting-edge scientific exploration.

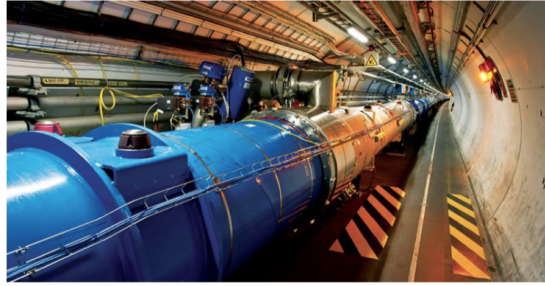


Figure 1.1: The LHC superconducting magnets in the 27 km LEP tunnel at CERN.

## 1.2 Accelerator Complex and Experiments

The journey of particles within the LHC starts with a orchestrated series of accelerators. These accelerators, akin to a finely tuned symphony, progressively elevate the particles to ever-greater energies. Initiated by a simple hydrogen bottle, the process unfolds as hydrogen atoms in the source chamber of a linear accelerator undergo electron stripping through an applied electric field. The liberated protons embark on their acceleration odyssey. Advancing to the Proton Synchrotron Booster (PSB), the proton energy surges to 1.4 GeV before traversing the Proton Synchrotron (PS), where it reaches an energy level of 25 GeV. The next stage in this acceleration process is continuing at the Super Proton Synchrotron (SPS), propelling protons to an energy zenith of 450 GeV. Subsequently, the LHC accelerates the particles to its nominal energy of 7 TeV. The injector and pre-accelerators are feeding the 27 km ring with clusters of particles, ending up to collisions within four distinct experimental input regions corresponding to the underground experiments (ATLAS [3], CMS [4], ALICE [5], LHCb [6]). Although, the accelerators constituting this chain were originally conceived for the LEP machine, subsequently undergoing enhancements to meet the exacting demands of the LHC. These upgrades involved augmenting Linac 4's power, implementing new RF systems in the PSB and the PS, elevating PSB's energy from 1 GeV to 1.4 GeV with two phases of PS filling, and installing high-resolution beam profile meters. Figure 1.2 provides a visual representation of the comprehensive accelerator-injector assembly, capturing the intricacies of this marvel of scientific engineering.

During the Run-1 phase of the LHC, its operational dynamics were mainly characterized by the division of proton bunches at intervals of 25 ns, resulting in an impressive frequency of approximately 1404 proton bunches per beam. The intricacies of the LHC's performance are encapsulated in the concept of instantaneous luminosity ( $\mathcal{L}$ ) for proton-proton ( $p-p$ ) collisions. This luminosity, a key metric, is intricately linked to the ratio ( $R$ ) of  $p-p$  processes and is mathematically expressed as  $\mathcal{L} = R/\sigma$ , where  $\sigma$  represents the active cross section of the  $p-p$  process. The absolute luminosity, a critical parameter, is contingent upon various beam characteristics and finds expression in Eq. (1.1) [7]. Here,  $f_r$  denotes the rotation frequency of the LHC, while  $n_b$  signifies the number of proton bunches colliding at the point of interaction. Furthermore,  $n_1$  and  $n_2$

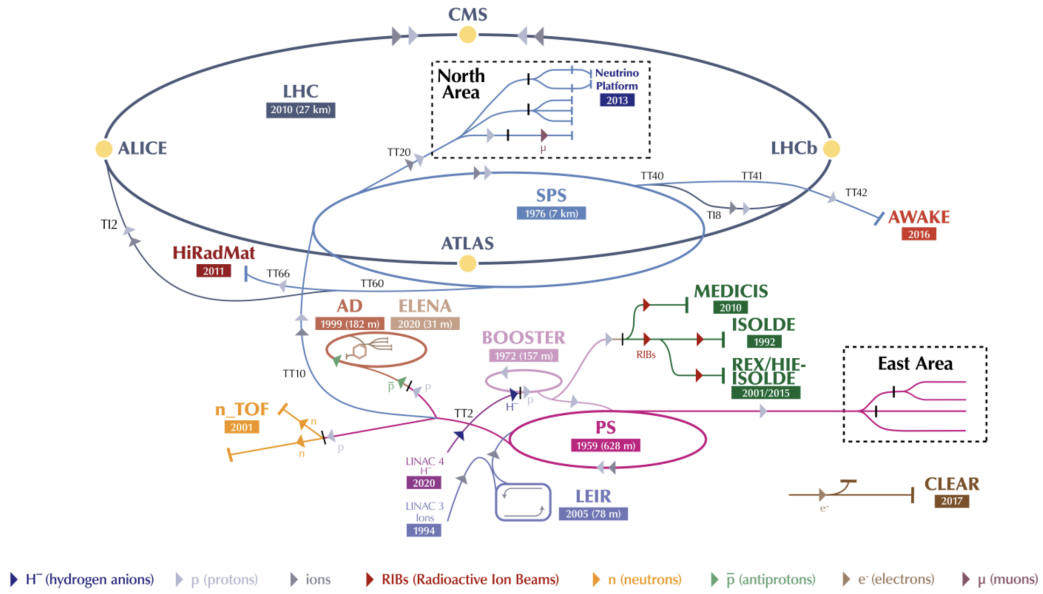


Figure 1.2: Schematic representation of the accelerators-injectors of LHC. Above is the injector and pre-accelerators that supply the 27 km ring with particle beams. The beams collide into four experimental input regions corresponding to the underground experiments (ATLAS, CMS, ALICE, LHCb).

represent the particle numbers in the two colliding proton bunches, while  $\sigma_x$  and  $\sigma_y$  delineate the horizontal and vertical profiles of the beam, respectively. Understanding the operational intricacies involves delving into the rotation frequency, the specific number of colliding particles and the particle counts within each packet. Additionally, the horizontal and vertical profiles contribute to the comprehensive understanding of the absolute luminosity, making it a multifaceted parameter essential for unraveling the intricacies of particle collisions within the LHC. The comprehensive formulation of this interplay is encapsulated in the elegant Eq. (1.1), providing a quantitative framework for the assessment of luminosity in the dynamic realm of high-energy particle physics.

$$\mathcal{L} = \frac{n_b f_r n_1 n_2}{2 \pi \sigma_x \sigma_y} \quad (1.1)$$

The luminosity of the LHC exhibits dynamic fluctuations during its operational course, primarily due to circular beam depletion and various emission processes. A significant contributor to the diminishing luminosity during LHC operations is the loss of the beam resulting from collisions. Additionally, beam losses arise from Touschek scattering and particle losses induced by slow particle emissions.

The LHC hosts four main experiments, each tailored for specific luminosity detection objectives. Notably, the ATLAS and CMS experiments focus on probing general luminosity at the order of  $\mathcal{L} = 10^{34} \text{ cm}^{-2}\text{s}^{-1}$ . The collider also accommodates two low-luminosity experiments: LHCb, dedicated to B-physics, designed for a luminance of  $\mathcal{L} = 10^{32} \text{ cm}^{-2}\text{s}^{-1}$ , and the TOTEM [8], which detects protons through elastic scattering at low angles with a luminosity of  $\mathcal{L} = 2 \times 10^{29} \text{ cm}^{-2}\text{s}^{-1}$ . In addition to proton-proton ( $p-p$ ) beams, the LHC operates with lead-lead (Pb-Pb) and proton-lead (p-Pb) beams. Finally, the ALICE experiment focuses on ion beams with a luminosity of  $\mathcal{L} = 10^{27} \text{ cm}^{-2}\text{s}^{-1}$ .

This intricate experimental setup highlights the LHC's versatility, used for diverse scientific investigations across a broad spectrum of luminosities and collision scenarios. As a result, the LHC significantly contributes to advance our understanding of fundamental particle physics.

## 1.3 LHC Performance

The year 2012 marked the end of a successful first run of LHC (Run-1) with  $\sqrt{s} = 7$  TeV proton collisions and increase to  $\sqrt{s} = 8$  TeV in 2012. The discovery of the Higgs particle was announced by the experiments ATLAS and CMS in the summer of 2012, where search was one of the primary goals for the first run of LHC. Subsequently, LHC was shut down for upgrades in 2013 and 2014 and  $p - p$  collisions returned in 2015 to greater collision energy  $\sqrt{s} = 13$  TeV.

## 1.4 ATLAS Experiment

The ATLAS detector [3] is a versatile instrument constructed to fulfill the diverse requirements of various LHC experiments, including the search for Higgs particles, the study of supersymmetry, addressing questions about dark matter and exploring any potential additional dimensions. With a cylindrical shape, a length of 45 m, a diameter of 25 m and a weight of 7000 t, it remains the largest volume detector ever constructed. Notably, its overall symmetry in length relative to the Interaction Point (IP) enhances its functionality.

The ATLAS experiment, depicted graphically in Figure 1.3, comprises a barrel region with cylindrical layers and two endcaps regions where detectors form discs to extend coverage. The cohesive design of these components is a result of meeting the general requirements for LHC detectors, ensuring effective performance in diverse scientific investigations.

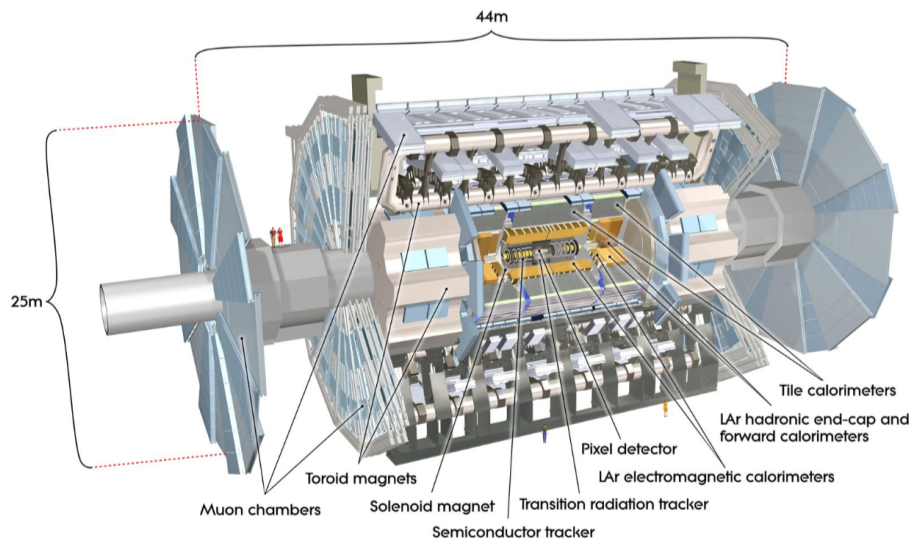


Figure 1.3: Graphical representation of the ATLAS experiment. The different parts of the experiment are marked on the figure.

The bunches of particles pass through the probe's cylindrical axis of symmetry and collide in the center, producing new particles. The different ATLAS's layers of subsystems record the trajectory, momentum and energy of the particles produced. A powerful magnet bends the orbits of the charged particles allowing them to measure their momentum, while the data is collected by the detector's electronic systems.

In order to clarify the details of the following ATLAS detection systems, it is good at this point to define the concept of pseudorapidity ( $\eta$ ). If the angle with respect to the beam axis equals  $\theta$ , then the pseudorapidity  $\eta$  [9] is defined as

$$\eta = -\ln \left[ \tan \left( \frac{\theta}{2} \right) \right] \quad (1.2)$$

A particle with a high value of  $\eta$  is likely to escape the detector, since it will move almost horizontally with the beam. As a result, the end-caps of the detector correspond to large values of  $\eta$ , while the barrel cylinder

corresponds to lower values of  $\eta$ .

The main ATLAS subsystems are:

- Magnet System
- Inner Detector
- Calorimeters
- Muon Spectrometer
- Trigger and Data Acquisition System (TDAQ)

### 1.4.1 Magnet System

The ATLAS detector comprises three types of superconducting magnet systems to provide the force required to bend the charged particle orbits and then to measure their momentum around the point of interaction (IP):

- The Central Solenoid [10] responsible for the magnetic field in the internal detector
- The air-core Barrel Torroid [11]
- The two air-cored End-Cap Toroids [12], which provide the necessary toroidal field for the muon spectrometer

The overall dimensions of the magnetic system are determined by the structure of the Barrel Torroid, where it extends to 26 m length and outer diameter of 20 m. The ATLAS superconducting magnetic system is cooled with liquid helium at 4.8 K, in energy terms the toroidal magnets are electrically connected in series and operate at a current of 20 kA, while the central solenoid operates at a lower rated operation of 7.6 kA. Photos of the three different parts of the magnetic system of the experiment ATLAS are shown below in Figure 1.4 .

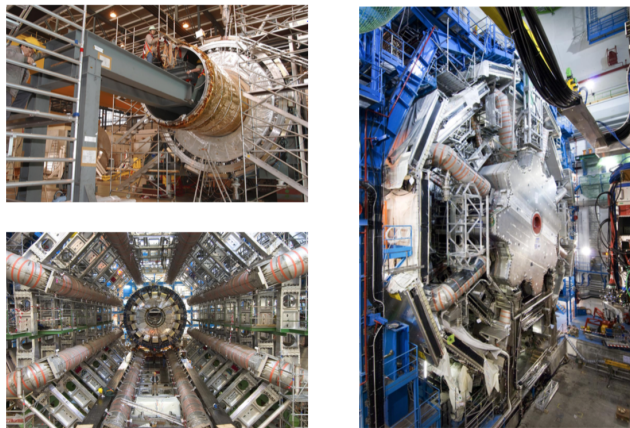


Figure 1.4: Photos of the three different parts of the experimental magnetic system of ATLAS. In the top left image, the cylindrical tubular magnet is inserted into the liquid argon caliper on the surface. In the Figure below, eight barrel coils inside ATLAS and to the right, one of the two end-cap toroidal magnets in their final position surrounded by barrel toroid coils.

The central superconducting solenoid is aligned with the beam axis and is designed to provide magnetic pitch at 2 T along the beam to measure the momentum in the Inner Detector, minimizing its emitted thickness, in front of the electromagnetic calorimeter located at the barrel. The inner and outer diameters are 2.46 m and 2.56 m accordingly and their length is 5.8 m. It is mounted on a cryostat which is shared with the calorimeter to minimize hardware usage and operates at 4.8 K.



The toroidal magnet system provides a magnetic field for measuring momentum in the muon spectrometer and has an average intensity value of about 0.5 T. The magnetic field, which is toroidal and perpendicular to that of the solenoid, is created by eight superconducting coils in the barre and by two rotors with eight coils each in endcaps.

The magnitude of the magnetic field varies according to pseudorapidity for the region of barrel with a maximum value of 3.9 T, while for endcaps the maximum value touches 4.1 T. A schematic representation of the magnetic system of ATLAS comprising the three parts mentioned above is shown in Figure 1.5 .

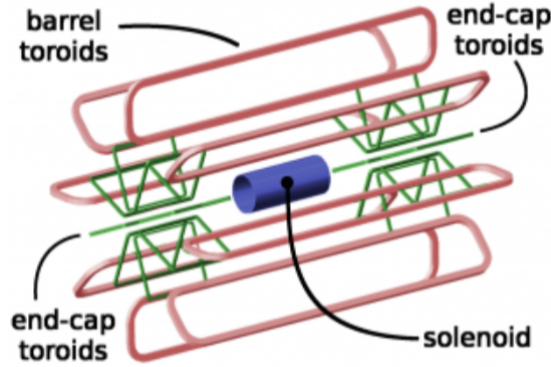


Figure 1.5: Schematic representation of the magnetic system of ATLAS. The central solenoid is installed within the liquid slow calorimeter (blue), surrounded by barrel (red) and end-cap toroid coils (green).

### 1.4.2 Inner Detector

The internal trajectory detector of ATLAS (ID) [13] [14], totaling 6.2 m, covers the pseudorapidity range of  $|\eta| \leq 2.5$  and analyzes the orbits of the particles that have escaped from the interaction point (IP). It is located inside a cylinder of length 7 m and radius 1.15 m and consists of three sub-detectors. On the inside, we find the Pixel Detector, then the SemiConductor Tracker and finally the Transition Radiation Tracker. The inner track detector combines the high-resolution detectors in the inner part with the detectors in its outer radius. All are included in the central solenoid, which provides a magnetic field of 2 T. Higher resolution is achieved around the peak region (vertex region) using semiconductor pixel detectors (Silicon Pixel Detectors). Typically, for each route, the semiconductor pixel detector contributes to three track points, while the silicon microfluidic detector contributes to four track points. On the outside of the inner detector is the Transition Radiation Tracker which provides information at 36 points per orbit and helps identify the experiment's electrons by detecting the photon transition radiation using its drift tubes. The schematic representation of the ATLAS internal trajectory detector is shown in Figure 1.6 .

The relative accuracy of the measurement is well combined so that no measurement overrides the momentum sharpness. In the barrel area, the Pixel Detector and the SemiConductor Tracker are mounted in concentric cylinders around the beam axis, while the end-caps of the probe are mounted in trays perpendicular to the axis of the beam. The sensors are mounted in a very strong magnetic field, created by a cylindrical superconducting coil, which curves the particle orbits. By measuring the parameters of the orbit, we can find the momentum, the direction, the energy and the point of origin of the particle.

### 1.4.3 Calorimeters

Around the inner track detector are the calorimeters[15], devices designed to fully absorb the energy of some type of particles crashing on them. Usually, calorimeters are either hadronic (detection of mesons) or electromagnetic (detection of electrons, positrons and photons). The calorimeters of the ATLAS experiment are

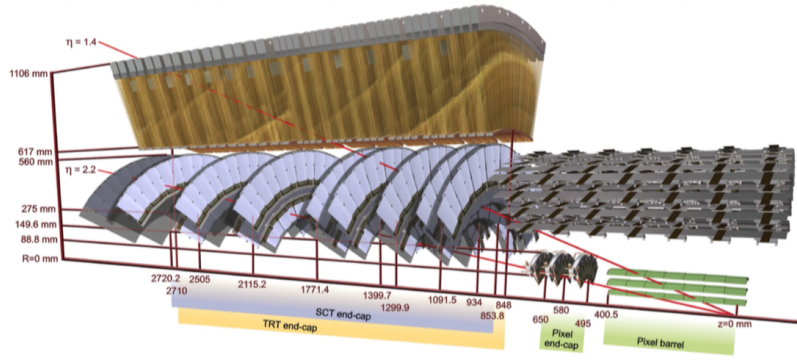


Figure 1.6: Schematic representation of the different subsystems of the ATLAS internal trajectory detector. On the inside there is the Pixel Detector, then the SemiConductor Tracker and finally the Transition Radiation Tracker.

responsible for accurately measuring the energy and position direction of electrons and photons or jets, also evaluating the lack of momentum  $p_T$  of each event. In addition, they are able to identify particles and contribute to the reconstruction of the muon track. Due to the high energy center of mass provided by LHC, the calorimeters used in the experiments should be able to meet demanding performance requirements over an unprecedented energy range extending from a few GeV up to the scale of TeV.

A graphical representation of ATLAS calorimeters is shown in Figure 1.7, where the various parts of the calorimeter are visible. The Electromagnetic Calorimeter (EM) covers the pseudorapidity region  $|\eta| < 3.2$ . It is a Liquid Argon detector (LAr) [16] with electrodes kapton in accordion shape and lead absorption plates over its full coverage, divided into barrel and end-caps. LAr is complemented by a hadronic calorimeter designed with the tile scintillator technique (Tile) [17], which covers the pseudorapidity region  $|\eta| < 1.7$  and the region even closer to the beam end-cap  $3.1 < |\eta| < 4.9$ , completing the experiment calorimeter system ATLAS.

The level of the electromagnetic calorimeter, which is located closest to the beam conductor, is capable of providing very accurate measurements of the position of the incoming particles and the deposited energy, based on their electromagnetic interaction with the material. The energy absorption materials of the electromagnetic calorimeter in the area of the barrel are lead and stainless steel with liquid argon as a sampling material. The hadronic calorimeter absorbs energy from the particles through strong interaction (mainly hadrons) and passes through the electromagnetic calorimeter which is less accurate both in their energy size and in their detection. The energy-absorbing material is steel, with spark-plated tiles accepting energy deposition.

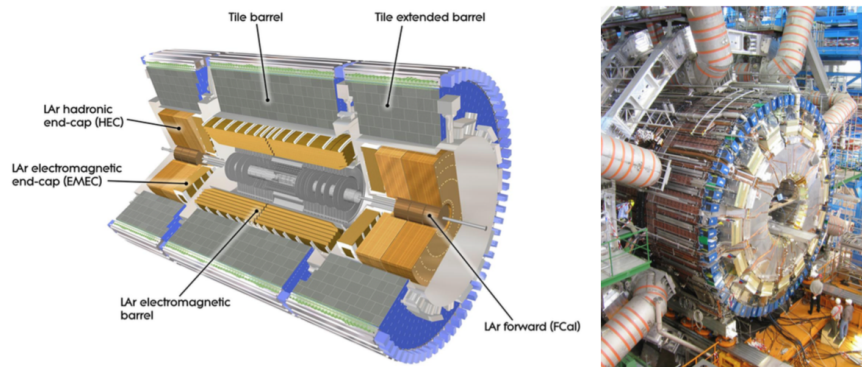


Figure 1.7: Left: Schematic representation of the cross section of ATLAS calorimeters. LAr and Tile are illustrated along with their segmentation in barrel and end-cap calorimeters. Right: Photograph of the barrel calorimeter mounted on the ATLAS detector. The rotating coils of the end-cap surrounding the calorimeter layout are also visible.

### 1.4.4 Muon Spectrometer

The role of the Muon Spectrometer (MS) [18] is to identify, measure and trigger on muons. It encompasses monomer spectrometer systems and systems incorporating state-of-the-art technologies for triggering and reconstruction of muon tracks (tracking). Figure 1.8 shows the layout of the ATLAS muon detection system.

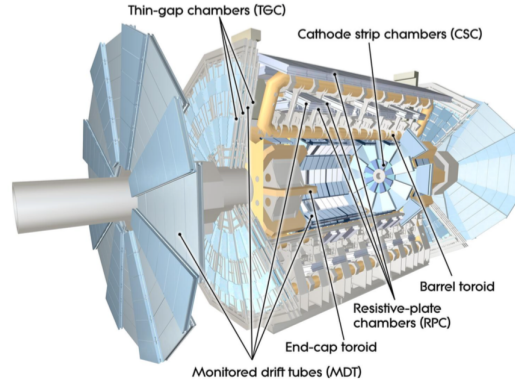


Figure 1.8: Schematic representation of the ATLAS muon spectrometer. The various technologies of the probe's masonry chambers are visible.

The muon spectrometer of ATLAS consists of two sub-detectors [18] for precision measurements:

- Monitored Drift Tubes (MDT)
- Cathode Strip Chambers (CSC) (replaced by NSW, will be described in the next chapter)

and two triggering technologies:

- Resistive Plate Chambers (RPC)
- Thin Gap Chambers (TGC)

### Monitored Drift Tubes (MDT)

Drift chambers are gas-filled enclosures containing electrodes that capture electrons from the gas ionizations of the gas mixture  $\text{Ar} + 7\%\text{CO}_2$ , carrying the electrical signal. They can accurately calculate the bending of particle orbits at the  $r - z$  plane of the toroidal magnet and provide measurements of the particle's momentum. In the ATLAS experiment, MDT covers the whole region of the high pseudorapidity of  $|\eta| < 2.7$ . The basic structure of an MDT is illustrated in Figure 1.9 (left). It consists of two multi-level drift chambers separated by a support frame. Each multi-layer comprises three levels of tubes with the exception of the internal structures of the muon spectrometer (small beam), where a floating tube frame is used in each multi-layer to improve pattern recognition in areas with a high background. A photo of an MDT is shown in Figure 1.9 (right) during the manufacturing process and their inspection process. The spatial resolution of an MDT tube, after the calibration process for the correction of the electric field, can be as high as  $80\ \mu\text{m}$ . By combining ionization electron measurements in each drift tube in each tube, a 6-point segment can be reconstructed by improving the spatial resolution to  $40\ \mu\text{m}$ .

### Cathode Strip Chambers (CSC)

The CSC are analog chambers where the descent is the readout strip and a symmetric cell within which the gap between the anode and the cathode is equal to the thickness of the anode pitch. The precision of its



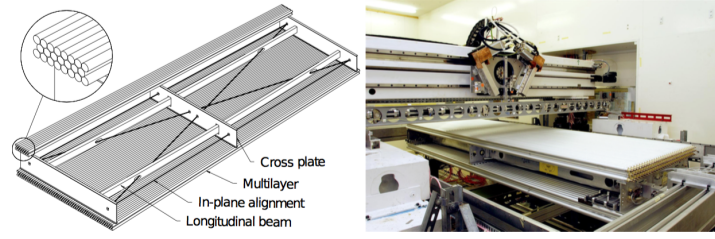


Figure 1.9: Left: Schematic representation of an MDT cell of the region barrel consisting of two multilevel three-level tubes each. Right: Photograph of an MDT chamber during its construction and inspection process.

coordinate position is measured by measuring the charge induced on the partial cathode strips by the electron avalanche formed on the anode wire. They essentially cover areas where particle flow is high and replace MDTs and at the same time combine high spatial and temporal accuracy at high rates. They are filled with a gas mixture  $\text{Ar} + 20\%\text{CO}_2$  and the wires have a voltage equal to 1800 V. Their spatial precision is  $60\text{ }\mu\text{m}$  for the coordinates of strips and 5 mm for the wires. In addition, they consist of four levels in each region end-cap and cover values pseudorapidity  $|\eta| < 2.7$ . The CSCs measure the set of events using an almost rectangular arrangement of ascending wires and cantilevers (strips). The cathode strips move radially from the beam and are used to measure the location of events, while the anode wires are used for the radial position. The signal generated on both strips and wires, can be used to determine the time of an event with similar resolution. Figure 1.10 illustrates the structure and function of a CSC, as well as its internal structure. As a particle passes through the gaseous medium of a CSC, it ionises it, resulting in electrons created to move to the anode wires.

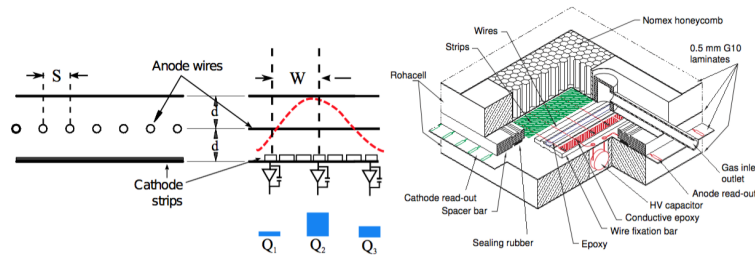


Figure 1.10: Left: Schematic representation of how a CSC detector operates. Right: The internal structure of a CSC.

## Resistive Plate Chambers (RPC)

In the barrel area of ATLAS, the RPC system is responsible for providing the trigger signals. The RPCs are parallel-plate gas detectors capable of providing particle time measurements with an accuracy of 1 ns wherever they meet the requirements of the ATLAS trigger system. Multi-component gas mixture is based on  $\text{C}_2\text{H}_2\text{F}_2 + 4.5\% + \text{C}_4\text{H}_{10} + 0.3\%\text{SF}_6$ . In addition, fast and coarse track measurement can be used to identify events from precision detectors related to the detection of muon tracks. There are three layers of these chambers in each end-cap of the detector and cover the area of pseudorapidity  $|\eta| < 1.05$ . The structure of RPCs is illustrated in Figure 1.11.

## Thin Gap Chambers (TGC)

Information on the trigger in the muon region end-cap is provided by the TGCs. In addition, they are able to provide a measurement of the azimuthal coordinate to complete the bending coordinate from the end-cap MDT. The middle end-cap area from the MDTs is complemented by seven levels of TGCs, which provide

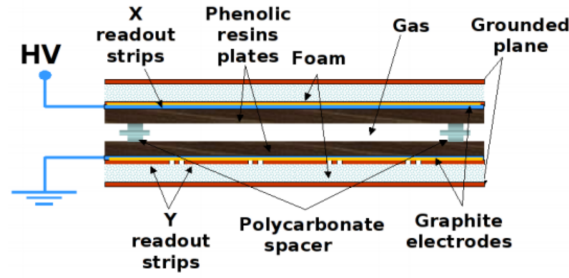


Figure 1.11: Internal structure of an RPC detector.

both measurements for triggering and azimuthal coordinate, while the two layers are from the inner muon end-cap Small Wheel measures the azimuthal coordinate. The TGCs are similar in technology to the multi-channel analogue chambers with anode wires MWPC enclosed by two levels of cathode and two levels of reading strips perpendicular to the wires. For momentum and azimuthal coordinate measurements, they operate with a high damping gas  $\text{CO}_2 + 45\% \text{n} - \text{C}_5\text{H}_{12}$  and a high electric field 3200 V. There are four layers of TGCs in each end-cap of the ATLAS detector and the internal structure of the detector is shown in Figure 1.12 .

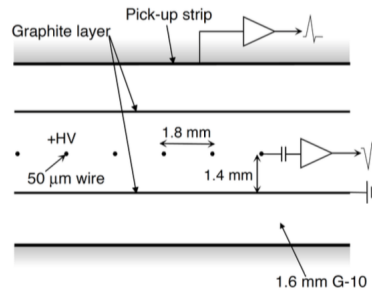


Figure 1.12: Internal structure of a TGC detector.

## Trigger and Data Acquisition System (TDAQ)

Reading the data collected from the interactions that occur during the experiment on ATLAS requires a DAQ [19]. The trigger system consists of three separate levels: Level-1 (L1), Level-2 (L2) and Event Filter (EF). Each level of trigger improves previous level decisions and constantly sets new dynamic selection criteria. On the other hand, the data collection system temporarily receives and saves data from these events from the special electronic detector reading systems at the selection rates permitted by L1. The first level of triggering, using the data from the muon chamber detectors and triggering systems, makes the first decision in less than  $2 \mu\text{s}$ . This procedure reduces the initial particle collision rate to 75 kHz. Afterwards, the data is ready to supply the Level-2 (L2) with data in the Region Of Interest (ROI). The triggering two layers is software-based and uses the data derived from L1 and in combination with the Inner Detector data optimizes the data selection. This process enhances data selection, resulting in an event rate of 3.5, kHz.

Once the data is ready from the L2 [20] layer, it reaches the final level of the Event Filter, which is based on software and has access to all the previous information. The rate is now reduced to 0.4 kHz and the data are ready for final analysis.

After the level of the Event Filter, the data are ready for analysis. The particle trajectory is reconstructed, and identification, as well as momentum measurement, are performed. With all this data, new particles and theories can be discovered, extending beyond the Standard Model. Figure 1.13 shows, in an event display, the trajectories by the particles resulting from the  $p - p$  interaction at the interaction point.

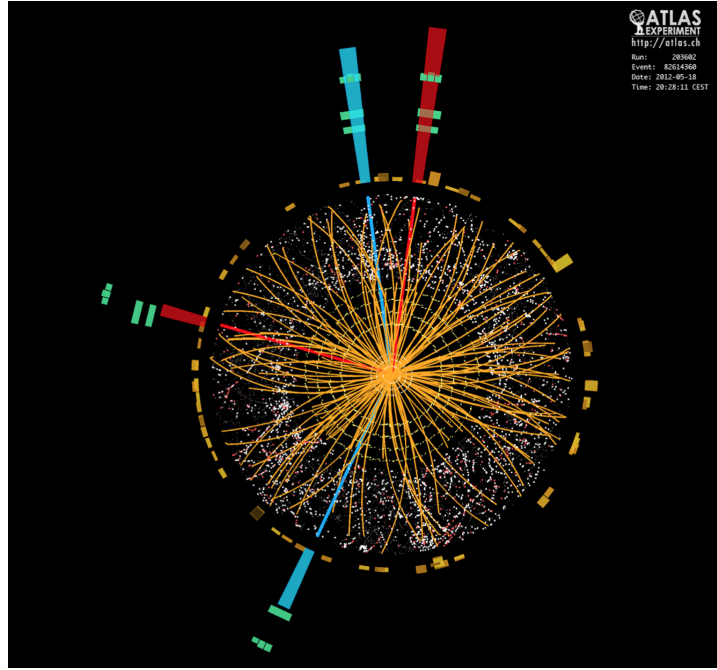


Figure 1.13: Detector event display showing a Higgs decay to four electrons recorded by ATLAS in 2012.

## 1.5 High Luminosity LHC (HL-LHC)

During Run-1 (2010-2012), LHC could distribute a total of  $\int \mathcal{L} dt = 28.26 \text{ fb}^{-1}$  at 14 TeV center mass energy from  $p - p$  collisions, leading to remarkable physical results from experiments such as the discovery of the Higgs boson [21].

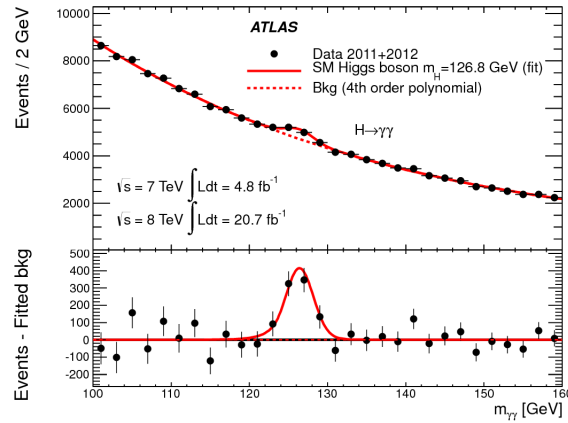


Figure 1.14: The discovery of the Higgs boson during Run-1 using experiment data from ATLAS [22].

The very successful first LHC run came to an end in December 2012, followed by a major shutdown of LHC (Long Shutdown 1 (LS1)). During the two year period of shutdown, the accelerators as well as the experiments went through a series of upgrades and maintenance activities to address the LHC program. During Run-2 launched in early 2015, LHC was scheduled to run at twice the mass center energy (14 TeV) and smaller bunch crossing (BC) of the order of 25 ns and will result in an increased luminosity equal to  $\mathcal{L} \approx 10^{34} \text{ cm}^{-2} \text{ s}^{-1}$ .

The current timetable of LHC, as shown in Figure 1.15, provides for two additional periods shutdown Long Shutdown 2 (LS2) (2019) and Long Shutdown 3 (LS3) (2024). The upgraded injector chain and LHC after LS2, will lead to a further increase in luminosity wherever it reaches  $\mathcal{L} = 2 \times 10^{34} \text{ cm}^{-2} \text{ s}^{-1}$ . The transition

from LHC to High-Lumi (HL-LHC) will take place during LS3, with more than  $3000 \text{ fb}^{-1}$  data being delivered during Run-3. The HL-LHC environment will be particularly demanding for experiments due to the predicted maximum luminosity in the order of  $\mathcal{L} = 7.5 \times 10^{34} \text{ cm}^{-2}\text{s}^{-1}$  for experiments ATLAS and CMS. In order to cope with the experiments with the predicted high particle rate, a series of upgrades have been proposed for the LHC experiments to maintain their operation during the HL-LHC period.

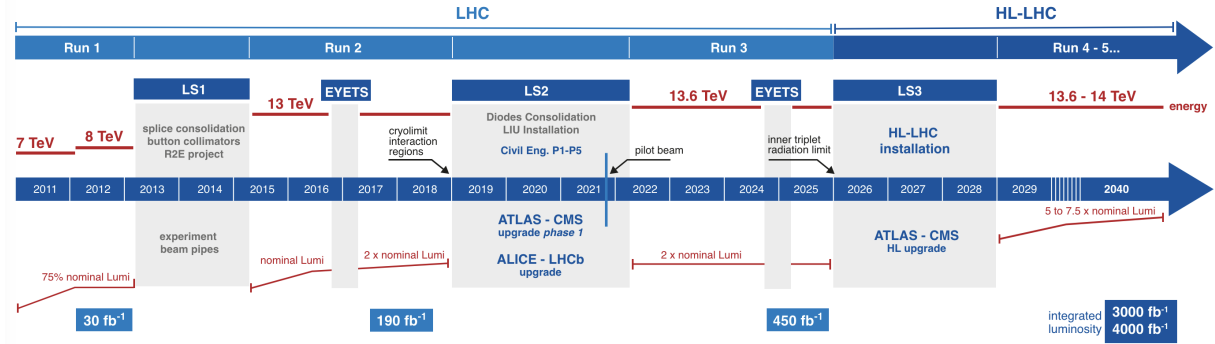


Figure 1.15: The timeline of the HL-LHC.

# Chapter 2

---

## New Small Wheel Upgrade Project

---

This chapter provides an in-depth examination of the New Small Wheel (NSW) project at CERN, a critical component of the LHC experiment. The integration process of Micromegas (MMG) and small-strip Thin Gap Chambers (sTGCs) detectors is outlined, detailing specific procedures in Building 899 (BB5) and Building 180. The Micromegas integration involves precise alignment and testing at various rotation stations, ensuring optimal functionality. Meanwhile, the sTGC integration, a complex undertaking spanning global production sites, showcases the coordination and challenges overcome. The chapter delves into the commissioning phases, emphasizing the thorough validation steps for sectors installed on the wheel. The process includes checks on Low Voltage connections, gas tightness and electronics functionality. The chapter unfolds the step-by-step progression from sector preparation to final validation, providing insights into the complexity of ensuring reliable detector performance. Furthermore, it introduces the ongoing P1 commissioning, illustrating its comprehensive nature and integration into the broader ATLAS Production systems. The extended duration of the P1 commissioning reflects a commitment to establish a secure and reliable operational state for the NSW within the ATLAS experiment. The chapter encapsulates the intricate journey from detector integration to commissioning, highlighting the dedication to precision and reliability in advancing particle physics research at the LHC.

## 2.1 New Small Wheel Upgrade

For the ATLAS experiment, such an increase in luminosity means an increase in the particle rate. The following Figure 2.1 depicts the maximum mean number per crossing of the beam over time for  $p - p$  events during 2010-2012.

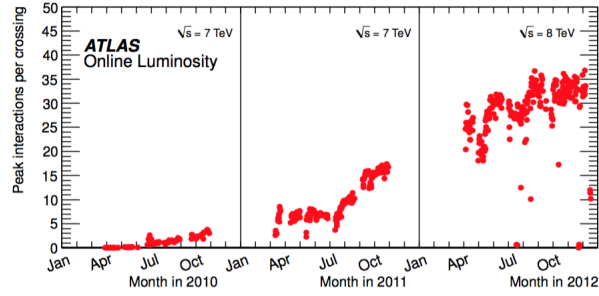


Figure 2.1: The maximum average number per beam crossing over time for  $p - p$  events during 2010-2012 [23].

In the period between LS1 and LS2, the number of inelastic scattering for each packet junction (bunch-crossing) was increased from 35 to 60-70 and thereafter LS3 this number will exceed 140. Most of the ATLAS muon systems have enough room to handle the high particle rates, but the "front" system of the muon spectrometer, called Small Wheel, is unable to handle this number based on the detectors currently installed (MDTs, TGCs), which are provided in pseudorapidity  $|\eta| = 2.7$ , with a particle rate of  $15 \text{ kHz/cm}^2$ . However, the end-cap area covers about 63 % of the ATLAS muon system, so it is necessary to upgrade this area to meet the needs of HL-LHC [24].

The Phase-1 [25] upgrade of the ATLAS muon spectrometer focuses on the endcaps region. The barrel system covers the region of pseudorapidity for  $|\eta| < 1.0$ , while the endcaps system covers  $1.0 < |\eta| < 2.7$  for muon detection and  $1.0 < |\eta| < 2.4$  for Level-1 trigger. The areas above are plotted in Figure 2.2, displaying a transverse cross-section of the ATLAS detector at the plane  $z - y$ . Thus, in high luminosity the following two points are of particular importance:

- The Muon triggering of end-cap
- The Detector Tracking Performance & Efficiency

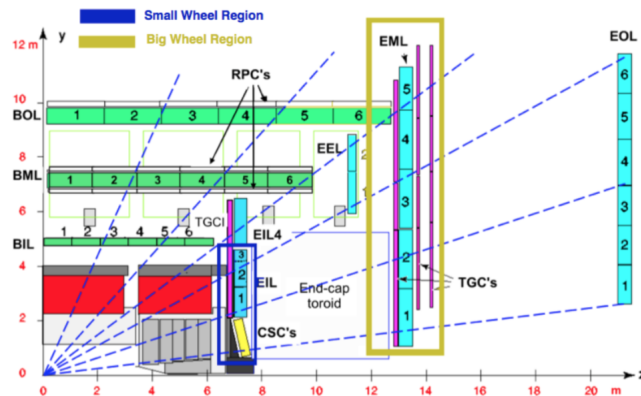


Figure 2.2: Cross-section of the ATLAS on the plane  $z - y$  [26].

### 2.1.1 End-cap Muon Trigger

The Level-1 muon triggering of the end-cap region is based on orbital imprints on the chambers TGC at the midsize station (Big Wheel), located behind the end-cap torroid magnet. The transverse momentum of the muons,  $p_T$ , is determined by the angle of the signal segment with respect to the direction pointing to the IP. Low-energy particles, such as protons, produced in the material located between the Small Wheel and the EM, producing false triggers as they pass through the chambers of the end-cap region at an angle similar to the really high transverse momentum  $p_T$  muons. These fake triggers constitute 90% of the total triggers, and thus the muon Level-1 trigger rate at the end-caps is projected to be eight to nine times higher in the region of the barrel. This situation is shown in Figure 2.3, showing that a large fraction of reconstructed muons do not match the candidate muons from the IP.

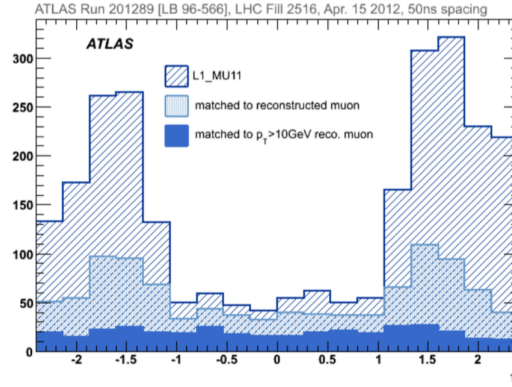


Figure 2.3: The pseudorapidity distribution of Level-1 trigger rate in three levels [26].

In Figure 2.3, the intermittent distribution of the muon trigger Level-1 with transverse momentum  $p_T > 10$  GeV (L1\_MU11) is plotted; with the light blue distribution depicts the subset of the candidate muons resulting from the offline reconstructed muons by combining the information from the inner probe track and the muon spectrometer with  $p_T > 3$  GeV. In addition, the blue distribution reflects the reconstructed muons with a threshold at the transverse momentum equal to  $p_T > 10$  GeV. This analysis conducted in 2012 showed us that 90% of the total trigger in the end-cap is due to fake triggers.

### 2.1.2 Tracking Performance & Efficiency

In the Small Wheel region, the luminosity will increase the particle rate to  $25 \text{ kHz/cm}^2$ , resulting in the present detection devices (MDTs, CSCs, TGCs) not be able to cope with such high particle flow rates. This can be seen from the dependency of the efficiency of a single MDT pipe on the rate of events. The efficiency shows a rapidly decreasing trend as opposed to increasing the event rate, already reaching the level of 70% for the event rate predicted for the high luminosity of LHC ( $\approx 300 \text{ kHz/tube}$ ). The above conclusion is drawn from Figure 2.4.

## 2.2 The concept of the New Small Wheel Upgrade

To solve the above two problems that limit the performance of ATLAS during the HL-LHC, ATLAS planned to replace the existing muon Small Wheels with the NSW during the LS2. The NSW is a set of precision orbital tracking and triggering detectors capable of working at high particle rates with excellent spatial and timing resolution in real time.

An explanation of particle trajectory estimation is illustrated in Figure 2.5. The existing Big Wheel trigger system accepts all three tracks (A, B, C). With the introduction of the new New Small Wheel [26] trigger system, the trigger logic of the end-cap region will only accept the track (A), where the desired track will be confirmed both from Big Wheel and New Small Wheel. Track (B) will be discarded because the NSW will not



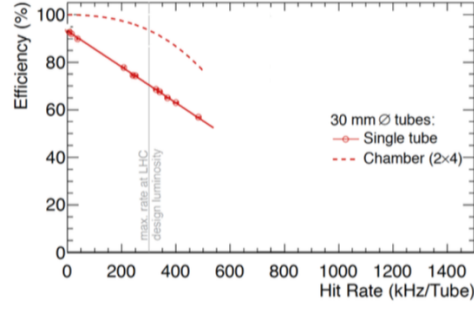


Figure 2.4: The efficiency of a single MDT tube and an MDT chamber,  $2 \times 4$  tube levels, as a function of events from beam experiment data to luminosity  $\mathcal{L} = 3 \times 10^{34} \text{ cm}^{-2}\text{s}^{-1}$  [26].

find any part coming from the interaction point that fits into the Big Wheel. The trajectory (C) will be rejected because the part of the trajectory from the NSW does not match the point of interaction (IP).

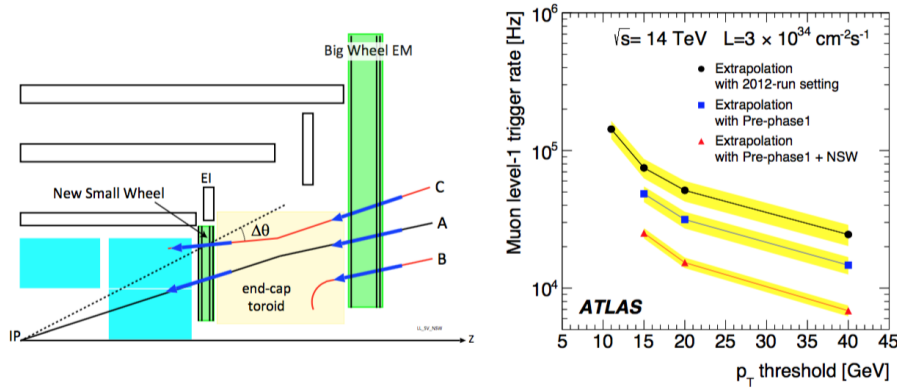


Figure 2.5: Left: Illustration of the expected improvement of the muon trigger system in the end-cap region by installing the NSW. Without the NSW, the trigger candidates are only formed based on the angle of the particle tracks passing through the TGC detectors mounted on the first of the two big wheels. If the angle is compatible with a particle coming from the IP, a trigger candidate is formed. Including the Level-1 trigger information of the NSW, the track reconstruction at trigger level is improved by rejecting tracks B and C which do not come from the IP, but are induced by background particles like neutrons or particles created by the interaction with the structural elements of ATLAS or the end-cap toroid magnet. Right: The estimation of the Level-1 trigger rate for  $p - p$  collisions in energy  $\sqrt{s} = 14 \text{ TeV}$  with instantaneous luminosity  $\mathcal{L} = 3 \times 10^{34} \text{ cm}^{-2}\text{s}^{-1}$  is plotted as a function of the threshold  $p_T$  for three different configurations.

After upgrading the triggering system by adding the NSW system, only the real muon track A, which will be confirmed by the BW at the same time, will be accepted by the NSW, reducing the false triggers based on the paths B and C. The simulations were done to fully understand the effect of the increase in luminosity on the overall rate of triggering. In Figure 2.5, the estimation of the Level-1 trigger rate for  $p - p$  collisions in energy  $\sqrt{s} = 14 \text{ TeV}$  with instantaneous luminosity  $\mathcal{L} = 3 \times 10^{34} \text{ cm}^{-2}\text{s}^{-1}$  is plotted as a function of the threshold  $p_T$  for three different configurations. The forecasts of the trigger rate, assuming the current configuration of the trigger system, are shown in black, while the blue curve illustrates the expected reduced trigger rate using data from the chambers EI4-TGC with Tile area  $1 < |\eta| < 1.3$ . Finally, the red curve represents the expected trigger rate given by the NSW which shows a significant decrease in the rate  $\approx 15 \text{ kHz}$  for a threshold of  $p_T = 20 \text{ GeV}$ .

The design of the NSW meets the specifications for a very good angular trajectory resolution of 1 mrad at Level-1 trigger. Background signals in the high density environment of the NSW can be suppressed using this



resolution. For the Phase-2 [27] upgrade of the Level-1 trigger system for even higher luminosity, the reaction time will be reduced to more selective triggering than calorimeters and new Level-1 trigger system as well as the muon system could be implemented. Phase-2 upgrade will dramatically improve the resolution of  $p_T$  of the muon trigger system Level-1, lowering the activation threshold and reducing the contribution from lower  $p_T$  muons to less than nominal threshold.

Actually, this will be achieved by using the data from the Precision Detector (Monitored Drift Tubes) as part of the muon trigger system at the endcaps and combining it with the angle of the corresponding activated segment provided from the NSW. In addition, following the principles of the current muon system, the NSW should consist of multiple levels of detection to improve the pattern recognition performance of track reconstruction, rejecting the multiple background events expected in the environment of the Small Wheel.

## 2.3 Layout of the New Small Wheel

The proposed New Small Wheel [26] detection system is designed to meet all the specifications presented in the previous subsection. The detection technologies used come from the family of gaseous detectors, the first being a wire chamber called small-strip Thin Gap Chambers (sTGCs) [28], and the second comes from the category of Micro-Pattern Gaseous Detectors (MPGDs) and is named Micromesh Gaseous Structure (MicroMeGas) [29]. The new experimental layout consists of 16 detection levels in two levels of four layers per detection technology (four levels of sTGC and four levels of Micromegas). The Micromegas and sTGC detectors fully cover the NSW in a  $1200 \text{ m}^2$  detection range. The NSW follows the dimensions of the existing SW and the same segmentation into 16 sections per wheel, are followed to match the existing Big Wheel and muon station end-cap. Figure 2.6 shows the current Small Wheel on the surface prior to its installation in ATLAS as well as an overview of the overall layout of the New Small Wheel.

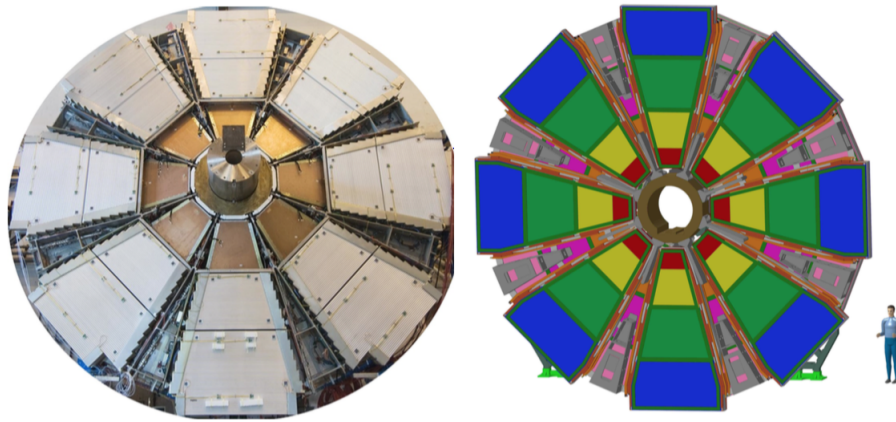


Figure 2.6: Left: The current Small Wheel on the surface before been installed in ATLAS. Right: Illustration of the New Small Wheel layout.

The sectors installed on the layer closer to the IP are slightly smaller than those closer to the HO side (they are about half the angle of the large sectors), lending them the name small sector while the other ones are called large sectors. Each sector is comprised by the four so-called wedges stacked parallel to the beamline, each hosting four layers of either Micromegas (inner two wedges) or sTGC detectors (outer two wedges). The inner part consists of micromegas detectors while the outer part consists of sTGCs detectors, forming a width of 400 mm. This leads to a total of 16 detection layers in each NSW sector. The wedges themselves are further segmented along the radial direction into the so-called quadruplets (also referred as modules or chambers). In the case of the Micromegas, each wedge consists of two quadruplets, where the one at smaller radius is referred as Module 1 (M1) and the one at large radius is called Module 2 (M2). The M1s are shown in brown and turquoise depending on the sector size. For the sTGCs, the wedges are segmented into three quadruplets.

The four detector layers in a wedge slightly differ in terms of geometry. For the sTGCs, the geometry of the pads is different to improve the capability to separate tracks for the trigger. For the Micromegas, the strips in the four outermost layers are perpendicular to the radial direction, allowing the precise measurement of the  $\eta$  (eta) coordinate of a track. Therefore, they are referred as  $\eta$ (eta) layers. To measure the track position parallel to the strips, the strips of the four inner Micromegas layers are tilted by  $\pm 1.5^\circ$  with respect to the ones in the eta layers. Those layers are called stereo layers. The layout of the NSW is provided with eight levels of each technology separated by a frame of 50 mm. Each section consists of two wedges (a set of modules of a single technology in the direction  $z$ , covering an entire sector, at the level  $r - \phi$ , oriented as shown in the schematic representation in Figure 2.7 (left). The sTGC detectors are divided into three modules, (a set of multiplets in the direction of  $r$  which is a single independent object), while the micromegas in two. An overall representation of a segment is shown in Figure 2.7 (right).

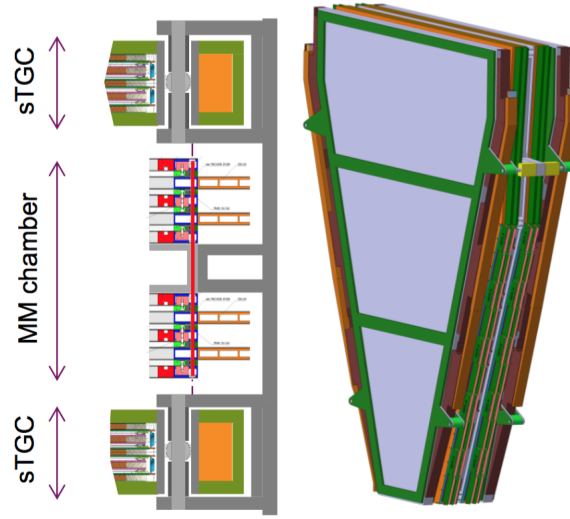


Figure 2.7: Left: Layout of the detectors inside a sector. Right: Illustration of a sector of the New Small Wheel.

Detection technologies are arranged in such a way (sTGC-MM-MM-sTGC) to maximize the distance between the two sTGC layers. As the online track is reconstructed, this distance (level arm) between the sTGC layers allows for improved resolution for the online track, given the angle provided by the first layer of detectors. On the other hand, MM detectors are used for track analysis due to their excellent track tracking accuracy, due to the small drift region (5 mm) and the small strip pitch (strip pitch of 0.425 mm for small modules and 0.450 mm for large modules), details on the Micromegas detector mounted on the NSW will be given in the chapter 5. In addition, the NSW is expected to run throughout the life of the ATLAS experiment, as a result of the high number of layers which ensure a proper detector performance and in case any of the layers fails to function properly. Finally, the two probe technologies used also complement each other in their main functions. The sTGC can contribute to offline tracking accuracy as they are able to measure a muon single hit resolution of approximately  $150 \mu\text{m}$ . The MM detectors assist sTGC to provide improved trigger signal.

### Detection technology of the sTGC

The NSW trigger system necessitates detectors capable of identifying and separating the pulses passing through them. Additionally, it mandates high time and angular resolution to facilitate online track segment reconstructions. In addition, these detectors are characterized by good discretion for offline track detection, using the best precision coordinates (from readout strips), compared to current TGC and detector's strip pitch equal to 3.2 mm, as a result of these detectors helping to accurately track the particle trajectory during the HL-LHC. The internal structure of the sTGC detectors is illustrated in Figure 2.8. The signal due to the drift of the

ionization particles and their multiplication by the avalanche effect is induced on the anode wires, the readouts strips and the pads.

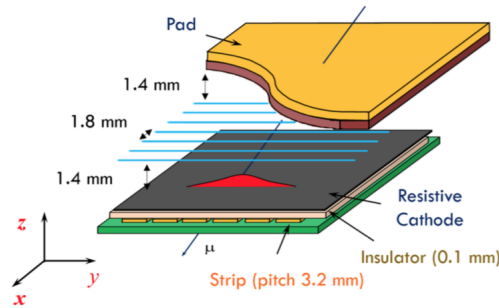


Figure 2.8: The principle of operation of the sTGC detector. In the middle of a 1.4 mm wide gas gap, wires are located on where a voltage of 2.8 kV is applied. The two electrodes are segmented into different patterns. The one uses a strip pattern to provide high spatial resolutions while the other is segmented into so-called pads, which provide a fast signal for the event selection.

### The Micromegas detector

The resistive-strip Micromegas used in the upgrade of New Small Wheel will be the main track detection mechanism, featuring excellent spatial resolution ( $\sigma < 100 \mu\text{m}$ ) despite the particle incidence angle, the high detection efficiency even at the highest background noise values and the good two-track separation to reject the delta electron angles accompanying the muons. The very thin segmentation of the MM readouts (readout-strips) together with sufficiently good time resolution, can also be exploited to complement the sTGC trigger system, adding to system stability and verification even as backups. A sketch of a Micromegas detector is given in Figure 2.9. The setup consists of a stainless steel mesh in a gas gap, splitting it into two parts. The upper gas gap, called drift gap, has a width of 5 mm. Here the muons interact with the gas, leading to the occurrence of the primary ionizations. Due to a voltage of 600 V/cm applied to the drift gap, the electrons drift towards the micromesh. The lower gas gap is only 128  $\mu\text{m}$  thick. A voltage of about 45 kV/cm is applied to the so-called amplification gap, leading to a multiplication of the primary electrons in an avalanche process. The anode located at the lower end of the amplification gap is segmented into strips with a pitch of 450  $\mu\text{m}$ . As protection against sparks in the amplification gap due to the high rate environment, a resistive layer is placed on top of the copper readout strips. The thin amplification gap allows the ions, that were created in the avalanche, to quickly drift to the grounded mesh where they are collected. This yields a small dead time, while the narrow strip pitch leads to an excellent spatial resolution in the order of 100  $\mu\text{m}$ . The Micromegas are operated with a gas mixture of  $\text{Ar} + 7\%\text{CO}_2$ , where Argon is the gas and the  $\text{CO}_2$  is the quenching gas.

## 2.4 Services and Infrastructure

The complex infrastructure of the NSW, as illustrated in Figure 2.10, plays a pivotal role in the functionality of the ATLAS. Including High Voltage power supplies, Low Voltage power supplies, Electronics boards, Gas/Cooling devices, ATCA & VME crates, temperature & BField sensors, Detector Safety Systems (DSS), and LHC Beam infrastructure, the NSW is a complex system.

Among the notable features of the NSW are the incorporation of state-of-the-art detector technologies, custom ASICs and electronic boards. These advancements contribute to the overall efficiency and precision of the system. The implementation of a novel readout system, based on the Front End Link eXchange (FELIX), showcases a commitment to adopting innovative solutions for data acquisition and processing.

Impressively, the NSW boasts a staggering 2.5 million readout channels, reflecting the scale and complexity of data management within the system. The establishment of a Common Configuration, Calibration and DCS

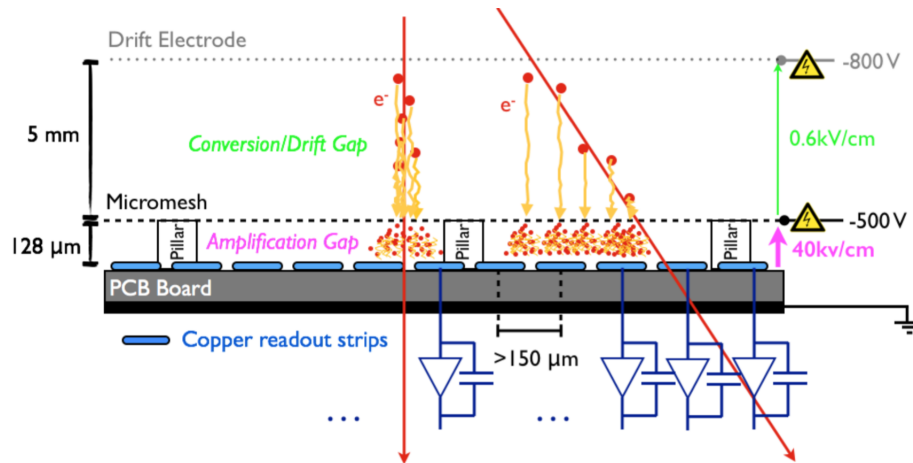


Figure 2.9: The principle of the resistive-strip Micromegas. The stainless steel micromesh separates the gas gap of a Micromegas into two regions of different field strengths, the drift and the amplification field. In the drift region, the charged particle crossing the detector ionizes the gas molecules along its track, and due to the drift field applied between the cathode and the mesh the electrons drift towards the mesh. The amplification field between the readout electrodes and the mesh is much stronger. Therefore, the electrons entering this region undergo multiplication. Finally, the electrons created in the avalanche induce charge by the strip-like segmented readout electrodes.

path enhances the coherence and uniformity of operations, ensuring seamless integration across different components.

A significant aspect of the NSW's infrastructure evolution is the introduction of a new Power supply system, reinforcing the reliability and stability of power distribution. Leveraging existing ATLAS & CERN infrastructure, it further emphasizes the collaborative nature of this scientific endeavor, utilizing proven frameworks to enhance overall efficiency.

Actually, the NSW represents a remarkable advancement in detector technologies and infrastructure within the LHC framework. Its complex design and incorporation is a critical component. The assembly of the detector modules for the NSW followed a process, initialized at the NSW institutes. The constructed modules were shipped to CERN, where the integration phase took place. This integration occurred at specific locations, with B899 (BB5) dedicated to Micromegas (MMG) and B180 for the sTGC. The final integration into the complete NSW sectors at B191, where each sector corresponds to 1/16th of the wheel geometry.

Ensuring the reliability and precision of the NSW, rigorous testing protocols were implemented at every stage of the assembly. These tests validated the functionality and performance of the detector modules, ensuring that each component met the strict standards set for the experiment.

Once the sectors were fully assembled, they were strategically mounted on the NSW structure on the surface. Subsequently, the entire wheels, now consisting of integrated and tested sectors, were transported to the ATLAS experimental cavern. The installation within the cavern marked the culmination of the intricate assembly process, positioning the NSW for its crucial role in advancing the scientific objectives of the ATLAS experiment.

This comprehensive approach to construction, integration and testing underscores the commitment to precision and reliability in the development of the NSW. The successful installation within the ATLAS experimental cavern paves the way for the NSW to contribute significantly to the scientific endeavors and discoveries at the LHC.



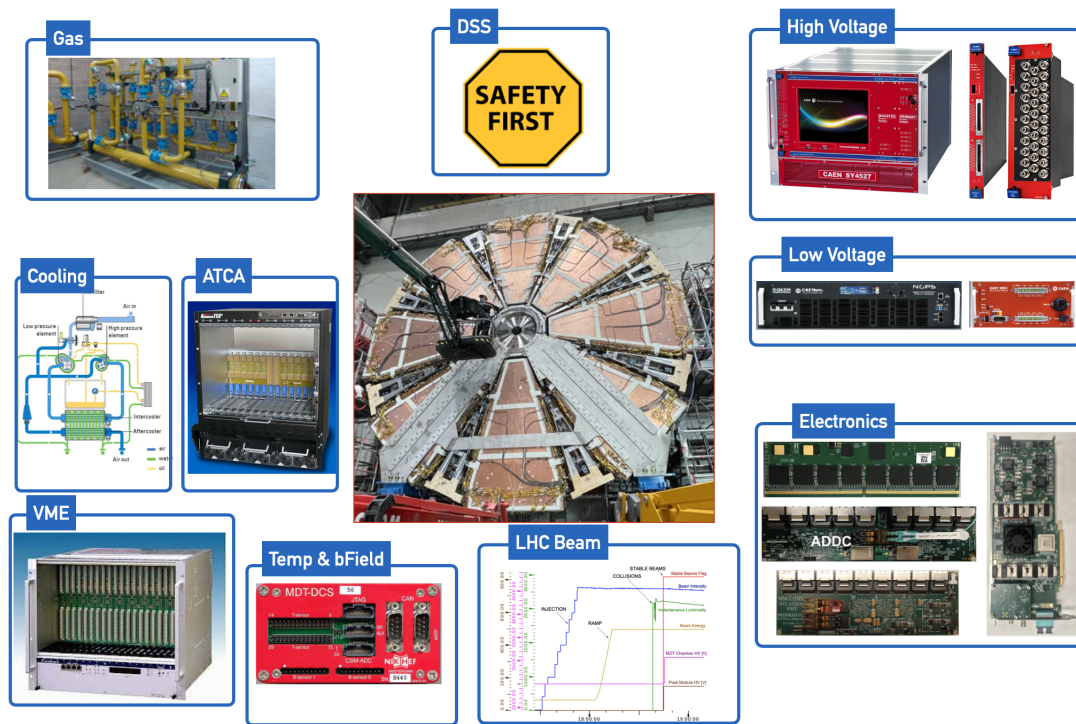


Figure 2.10: A brief overview of the NSW hardware.

## 2.5 Integration

### 2.5.1 Micromegas - BB5

The workflow in B899 (BB5) involved several specialized groups, each assigned to specific tasks [30]. Upon the arrival of the modules in BB5, the reception team conducted acceptance tests to ensure the modules remain unchanged or undamaged during shipping. These tests included assessments of gas leaks and high voltage stability in each high voltage section. Selected chambers underwent further analysis at GIF++, where their behavior under a substantial particle flow was studied, focusing on voltages and currents stability tests.

Simultaneously, the preparation of the spacer frame, including essential services like cooling and gas interconnections, HV cables, LV cables and optic fibers, took place. The integration progressed as two type-1 modules and two type-2 modules, along with the spacer frame, were combined into a double-wedge. Alignment checks were conducted after each integration step to ensure precision.

The completed double-wedge underwent testing in a rotation station, assessing electrical connections to identify any defects such as bad welds or short-circuits. It then moved to a second rotation station for the installation of full readout electronics. Following this, the double-wedge was ready for final validation and was transferred to the cosmic ray stand.

Building BB5 at CERN housed a dedicated cosmic ray stand for this purpose. Four scintillators, organized in two up and down pairs of varying dimensions, serve as triggers. Placing the double-wedge under the two scintillator pairs, with the IP wedge facing the floor, the expected final rate is approximately 105 Hz.

For a more detailed overview of the workflow and tasks, refer to Figure 2.11. This comprehensive process ensures the robust integration and validation of detector modules within the NSW, maintaining the high standards required for optimal performance in the ATLAS experiment.

The alignment of the the installation of the Front-End Boards (FEBs) poses a considerable challenge due to the intricate alignment required for connectors on the MMFE8 boards [31]. With a channel pitch of  $200\text{ }\mu\text{m}$  between channels and the need to align them precisely with the readout strips of the anode, this task demands expertise. Complications were caused due to the limited space, densely packed with services. To streamline the process, three stations were set up, enabling work on three Micromegas sectors concurrently in a "sliding

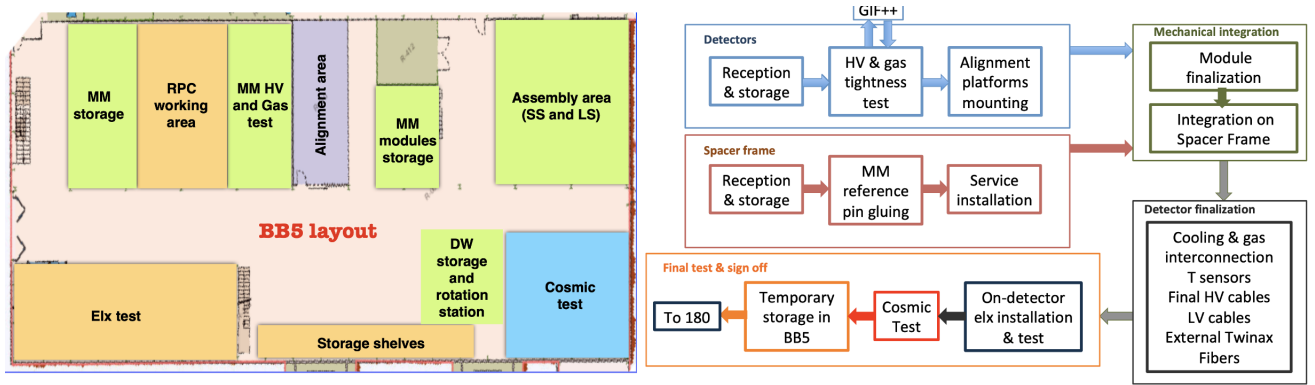


Figure 2.11: Left: The layout of the BB5 building which use for the Micromegas Integration. Right: The Micromegas Integration workflow, from late in production, when it was fully optimized. Each colour reflects the work of a distinct team.

mode” and facilitating the installation and commissioning of the FEBs.

The actual mounting, alignment and connection of the FEBs occurred in Rotation Station 3, as depicted in Figure 2.12. Meanwhile, the Rotation Station 2 housed a complete readout system. At this stage, the configuration of the Slow Control Adapters (SCA)[32] was carried out for all boards. SCAs serve three key functions: monitoring operational parameters like temperature and power consumption, configuring the ASICs of the boards, and calibrating the VMM chips [33] of the MMFE8 boards [34]. This step ensures the establishment of communication with the FEBs. The alignment of MMFE8 boards was facilitated by custom-built test boards, equipped with 512 LEDs—one for each strip of the detector that a MMFE8 board reads. These LEDs acted as visual aids for achieving the optimal position of the MMFE8.

Once the alignment was confirmed and communication with all FEBs was established, the sector was moved to the cosmic stand. The initial step involved identifying noisy or dead channels of each VMM. VMMs were set to internal mode and a mapping of noisy channels was performed. MMFE8s with more than 5% of noisy channels (due to the misalignment of the MMFE8 board and the readout strips of the readout PCB) are systematically replaced, ensuring the overall integrity and functionality of the system.



Figure 2.12: The cosmic ray stand along with the rotation stations at BB5 during the integration of the Micromegas electronics and wedge preparation.

The subsequent stage in the cosmic stand involved validating the trigger path. The electronics integration and validation process culminated in a test using cosmic rays. Scintillators act as triggers, prompting the activation

of High Voltage sections in the detector, and final HV settings were defined, marking the conclusive HV validation.

The sector's total efficiency was determined through the cosmic run and an initial study on the detector characteristics was conducted with the acquired data. Subsequently, the sector returned to Rotation Station 2 for a final inspection. This involved verifying alignment corridors, envelope, labeling and the overall arrangement of all components. A sign-off document was generated, serving as a certificate accompanying the sector throughout its operational life. The signed-off sectors were then stored in a transport basket, prepared for shipment to integrate with the sTGC and ultimately for installation on the NSW.

### 2.5.2 sTGC - B180

The integration of sTGC wedges at CERN[35] was an extraordinary undertaking, involving the testing and mechanical assembly of 192 individual chambers into 64 wedges. Beyond the intricate assembly process, the installation of over 2000 electronics boards and the subsequent validation of the proper functioning of more than 360 000 detector channels added to the complexity.

The sTGC integration process involved receiving individual quadruplet detectors from production sites across the globe, including Canada, Chile, China, Israel and Russia. These detectors were assembled into wedges, followed by the installation of electronics and comprehensive validation of the entire electronics and detector system. Each step in the integration process, while some had to be sequenced, was executed by separate teams working concurrently on different wedges at various stages of completion. Managing and coordinating this highly intricate parallel schedule posed a significant challenge, necessitating exceptional coordination among the leaders of each team.

### 2.5.3 B191

The (double) wedges arrived at B191 after being validated from BB5 and B180 (Micromegas and sTGC integration sites at CERN). The assembly of the wedges into sectors and the placement on the wheel was done in B191 by NSW and ATLAS engineers. The NSW service team would take over for routing finalization, since most services were installed and routed on the wheels in advance. The initial aim of the setup was to allow parallel operation of two (out of 16) sectors on a single wheel. This was later augmented to allow further parallelization of certain operations. This allowed multiple teams to operate on different sectors, thus achieving an efficient scheme of staggered commissioning of the sectors. The surface commissioning operations are described in this subsection, starting with the reception of the detector modules from the integration sites, outlining the test procedures and results, and ending with the signing-off of the wheels. The 3D view of B191 and the high-level connectivity scheme for commissioning in B191 is shown in Figure 2.13.

The Commissioning process, as detailed in [36], encompassed comprehensive validation steps for the sectors installed on the wheel, taking a full two days after service installation. The procedure involved preparing the MM Double Wedges (DWs) for integration into a complete NSW sector alongside the two sTGC wedges. Various preparatory steps were executed to ensure the sector's readiness for installation, including checks on fiber integrity, T-sensors, cables, gas pipes and grounding.

Upon readiness, each sector was installed on the wheel, with initial connections to services. The validation process then proceeded with checks on Low Voltage connections and polarity for all cables extending from the detector to the power supply. Subsequently, testing covered the cooling system and gas tightness of the MM detectors. The final steps involved High Voltage (HV) validation and comprehensive electronics testing, including specific data collection to assess the functionalities of the Data Acquisition (DAQ) and trigger systems. This testing aimed to ensure the electronics' robustness in anticipation of the Phase-1 and Phase-2 upgrade requirements. The entire process of the sector commissioning can be divided into the following steps:

- Preparation of the sector and visual inspections
- Sector assembly

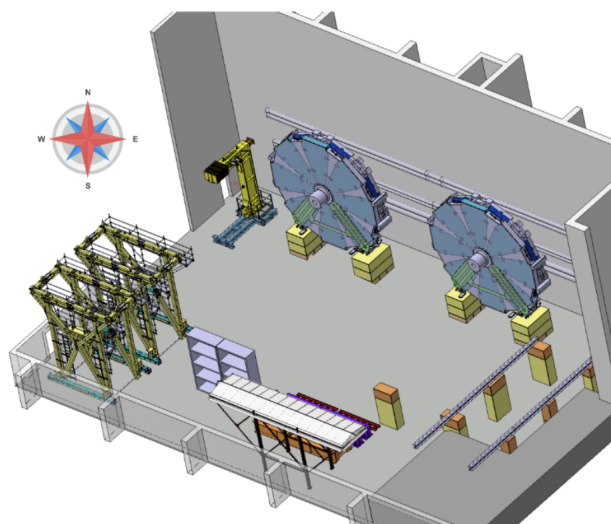


Figure 6: Perspective 3D view of b191.

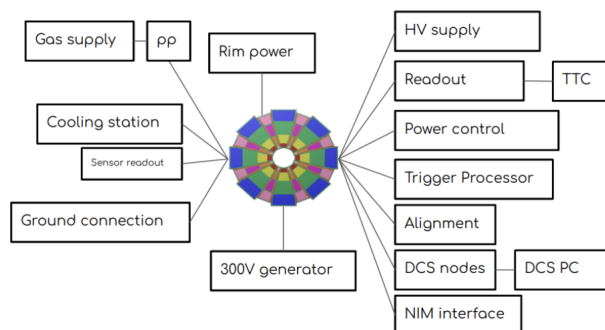


Figure 2.13: Top: 3D view of the B191 commissioning area. Bottom: High-level connectivity scheme of the commissioning procedure.

- Installation on the wheel
- Connectivity test for all services
- Validation of all the systems (gas, HV, LV, Electronics and Trigger)

In the following lines, a summary of the different general steps followed for sector commissioning are presented. The preparation of the sector includes the pre-installation validation on the balcony, with ground tests, visual checks of the gas impedances, fibers and additional grounding connections. LV extension cables are also mounted on the sectors at this stage. In parallel, before the installation takes place, the HV splitter boxes are mounted on the JD, LV cables connected and checked for polarity inversions, and T-sensors and HV channels are checked to ensure their connectivity.

Then, after the sector installation, all the services are tested and connected: LV, HV, fibers and T-sensors cables. Cooling pipes are connected and water flow is regulated, gas leak test is performed together with impedance measurement, grounding is ensured, LV cables are checked for polarity and T-sensors monitoring is connected. Then the sector validation proceeds through the HV validation, DAQ and trigger tests to ensure hardware and electronics functionality. Few sectors were also undergoing data taking with cosmics.

At the conclusion of the NSW commissioning, all sectors underwent thorough testing and successful validation, culminating in the installation of both NSWs in the ATLAS cavern for the LHC Run 3.



### 2.5.4 P1

The P1 commissioning, as illustrated in Figure 2.14 and detailed in [37], encompasses all validation steps conducted at B191. However, it utilized production tools to ensure the safe operation of the NSW within the ATLAS experiment. This commissioning process also included the integration of the Detector Control System (DCS) and DAQ into the broader ATLAS Production systems. As of the latest information, the NSW P1 commissioning is an ongoing process expected to extend over several months to ensure a secure and reliable operational state.



Figure 2.14: Left: The NSW during the transportation from the B191 commissioning site to the P1. Right: The NSW during the installation at the ATLAS cavern.

## 2.6 Contributions

A large part of the New Small Wheel upgrade of the ATLAS detector consisted of the integration as well as commissioning of the detectors, electronics and services. The candidate:

- Actively participated in the integration of the Micromegas detectors in the BB5 building and the sTGC detectors in the 180 building at CERN.
- Actively participated in the integration and commissioning of the detectors, electronics and services in the 191 building and P1 ATLAS cavern at CERN.
- Developed tools and systems for the optimization and implementation of various quality control systems.



# Chapter 3

---

## Electronics and Data Acquisition System

---

The chapter provides an description of the NSW electronics and the DAQ [\[34\]](#). It delves into the core components of the NSW DAQ, featuring detailed discussions on pivotal elements such as FELIX, GBTx (Gigabit Transceiver) and the GBT-SCA (GBT Slow Control Adapter). A focal point of the chapter is the thorough presentation of the SCA Ecosystem, encompassing Software, the quasar framework and the SCA OPC UA Server & Client. The diverse array of NSW electronics is described, accompanied by a comprehensive overview of the efforts invested in defining the SCA connections. A crucial tool was developed for the operation of the SCA OPC UA Server, facilitating the creation of necessary input files embedded with the devised NSW naming scheme within the OKS lists. In response to the specific requirements of the VMM monitor output shared channel on the SCA, an innovative mechanism was developed to establish seamless communication between the DAQ and DCS back-ends. The chapter focuses into the operation of the SCA, shedding light on the architecture design of the FELIX/OPC granularity. Additionally, various performance tests were conducted to validate the efficacy of the new FELIX/SCA ecosystem. The chapter continues with an introduction to the frontend VMM Application-Specific Integrated Circuit (ASIC), offering insights into the validation tests and the neutron irradiation testbeams. This comprehensive exploration serves as a guide to understanding the complexity of the NSW electronics and the robust DAQ architecture supporting the ATLAS experiment at CERN.

### 3.1 Overview

The NSW readout and trigger architecture [38], constitutes a sophisticated system employing around 8000 front-end boards. To support these boards, a suite of custom ASICs has been designed. These ASICs play a crucial role in propelling trigger and tracking primitives to the back-end trigger processor and readout system. In the context of the NSW electronics governing the TDAQ paths for both detectors, a comprehensive categorization into on-detector and off-detector electronics emerges, as illustrated in Figure 3.1. The on-detector electronics, situated within the cavern where radiation and magnetic fields are present, encompass specially crafted boards predominantly utilizing radiation-tolerant ASICs. Communication among these boards is established through the utilization of mini Serial Attached Small Computer System Interface (SCSI) cables. Additionally, the off-detector electronics, comprising elements such as FELIX [39], trigger processor, and services hosted on commercial server computers like Read Out Drivers (ROD), DCS [40], event monitoring, configuration, trigger monitor, and calibration, will find placement outside the cavern in an area designated as USA15. This spatial segregation ensures the optimal functioning of the entire NSW system by strategically situating the components based on their specific operational requirements. The main front-end ASIC is the

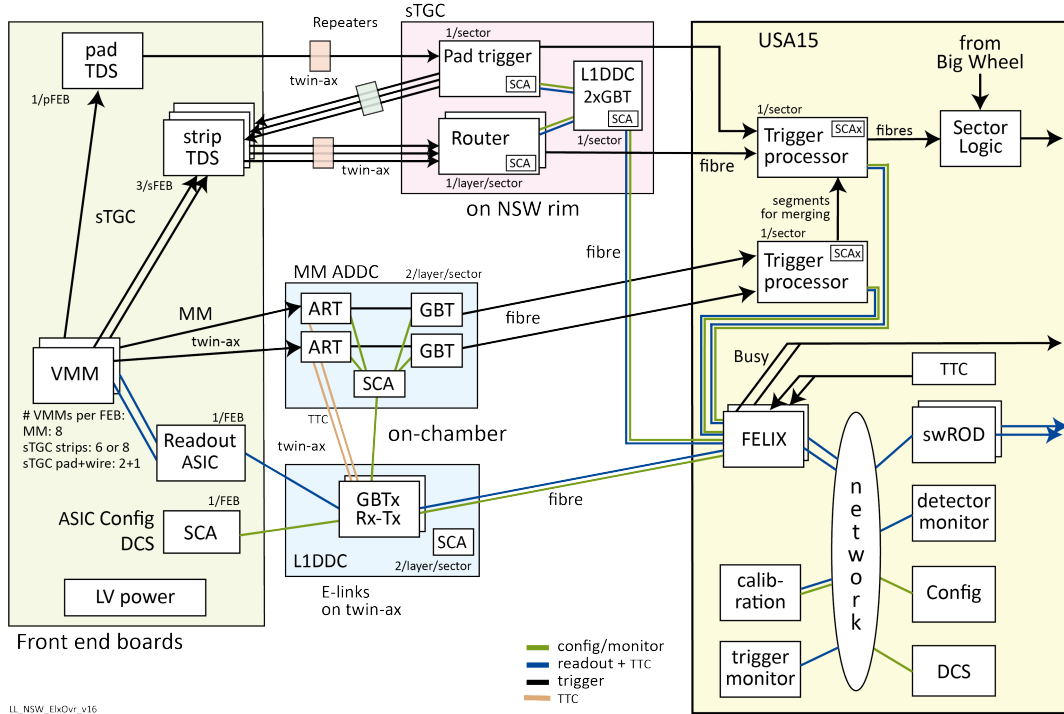


Figure 3.1: The NSW electronics overview scheme of on-detector and off-detector electronics and their connectivity. On the detectors (left box) there are the front-end boards, responsible for reading out the 2.1M channels of NSW, as well as the readout driver and trigger boards. Off the detectors (right box) there are the trigger processors and the aggregator electronics that will deliver the data to the ATLAS trigger and data acquisition systems.

64-channel VMM[33], a common front-end ASIC for both the MM and sTGC detector technologies, which provides amplitude and timing measurements and direct output of trigger primitives as well as Level-0 trigger buffering. The Readout Controller (ROC)[41] ASIC aggregates, processes, and formats the data sent by the VMMs and transmits them via multiple serial electrical E-links to the CERN GBTx [32] ASIC, a high-speed serializer/deserializer that runs at 4.8 Gbps. Data are collected by the L1DDC (Level-1 Data Driver Card)[42] from up to eight front-end boards. The MM ART (Address in Real Time)[43] ASIC performs a priority-based hit selection for triggering where the data are transmitted to the trigger processor through the ADDC (ART Data Driver Card)[43] board. The sTGC Trigger Data Serializer (TDS)[44] ASIC transmits digitized charges and binary hits to the trigger processor via the Router and the Pad Trigger boards. The sTGC trigger system

makes use of coincidences of detector Pads to identify regions where a muon candidate was detected. To reduce the amount of data sent to the off-detector trigger processors, only sTGC[28] strip information coming from the regions selected by the pad trigger logic are transmitted off the detector. The TDS and Router[45] electronics handle the serialization and subsequent routing of active trigger data signals from the front-end of the sTGC detectors to track-finding processors. The rim-L1DDC boards placed on the rim of the wheels will be used to provide high quality clocks, configuration, and other data to the Pad trigger and router boards. Finally, the CERN GBT-SCA[32] ASIC is used for configuration and monitoring. The data-flow architecture is based on a high-throughput approach that routes the custom GBTx links to and from a standard network.

In the context of the NSW system, the exchange of data, trigger signals, and configuration information with the on-detector electronics is facilitated by an advanced network infrastructure built upon optical fibers, as illustrated in Figure 3.1. The selection of an optical fiber architecture stems from its remarkable efficiency in transporting large volumes of data with minimal latency, particularly in radiation-intensive environments generated by the collisions at the LHC within the ATLAS cavern. The process begins with the aggregation of data originated from the detectors into the L1DDC cards. Subsequently, these L1DDC cards employ the GBTx ASIC to channel and aggregate the data into the optical fibers. At the termination point of these fiber cables, situated in the USA15 of the ATLAS cavern, a dedicated cluster of servers takes on the responsibility of managing the GBTx traffic. A system, known as FELIX, has been developed to streamline and optimize the flow of optical fiber traffic. FELIX ensures seamless communication between the on-detector electronics and the off-detector servers, thereby playing a pivotal role in the overall functionality and efficiency of the NSW system.

The overall architecture of the NSW electronics[34] is shown in Figure 3.1. There are five data and signal paths:

- Synchronization, trigger, test pulse and reset signals and the LHC bunch-crossing clock
- Digitized readout data from the detector including monitoring and calibration
- Configuration parameters and status indicators
- Busy path
- Digitized data from the detector for the trigger path

The integration of the radiation-hard GBTx ASIC into the NSW electronics architecture has a profound impact, particularly on the connectivity between the collision cavern and the radiation-protected room, USA15. This influence is most evident in the intricate design of the first three paths, which are time-multiplexed over fibers to and from a GBTx ASIC. This ASIC interfaces with distinct electrical "E-links" through twin-ax cables, also known as MiniSAS cables, leading to electronics boards strategically positioned on the detector. The aggregation of slow serial links into the 4.8 Gb/s fiber is orchestrated by the GBTx ASICs installed on the L1DDC. This approach ensures efficient and reliable data transmission between the on-detector electronics and the off-detector servers in USA15. Fibers play a pivotal role in connecting electronic boards within the NSW wheel itself, spanning the collision cavern and the radiation-protected room. All fibers employed are of the multi-mode OM3 type, allowing for transmission speeds of up to 10 Gb/s, and possess radiation-tolerant characteristics. The array of fibers ranges from LC pairs to bundles of 36 and 144 fibers, accommodating the diverse communication requirements of the NSW electronics. Upon arrival in USA15, a comprehensive network of fibers is established, comprising 2304 trigger fibers and 4608 readout fibers, inclusive of spare fibers. The MTP-36 cables, varying in length based on their angular position on the wheel, connect Small and Large boxes, ensuring a robust and flexible communication infrastructure. Notably, the readout trunk cables are intentionally extended to reach various locations within USA15, as the specific positioning of the Phase-2 FELIX servers was initially uncertain. This strategic design choice anticipates potential server relocation and underscores the adaptability and foresight embedded in the NSW electronics architecture.

### Synchronization, trigger, test pulse, reset signals and the LHC bunch-crossing clock

The signaling pathway commences with the ALTI Timing, Trigger & Control (TTC) module [34]. This module initiates the process by dispatching a serial stream containing crucial control signals through optical fan-outs and dedicated fibers to each FELIX Field-Programmable Gate Array (FPGA). These control signals can be synchronized with the LHC Bunch Crossing (BC) clock, introducing a specified offset in BCs from the commencement of the LHC orbit. Upon receipt of the control signals, FELIX undertakes the task of decoding, recovering, and jitter-cleaning the BC clock. The decoded control signals, including Level-1 Trigger Accept (L1A), Event Counter Reset (ECR), Bunch Crossing Counter Reset (BCR), Test-Pulse (TP), Soft-Reset (SR), Orbit Count Reset (OCR), and the BC clock itself, are then dispatched to the Readout Controller (ROC) on the front-end boards. Additionally, these signals are relayed to the Rim boards and the Micromegas trigger boards via the GBTx ASIC embedded within the L1DDC boards. The BC clock, recovered by the GBTx ASIC, is distributed to all ASICs. Simultaneously, the Trigger Processor, employing firmware that emulates the GBTx, receives identical signals. It's worth noting that the higher speed reference clocks of all serial links are harmonized multiples of the recovered BC clock. The Readout Controller on each front-end board is forwarding, the requisite control signals, the bunch crossing clock and configurable delays to the various ASICs on the board. An inherent characteristic is its fixed latency, consistently reproducible across power cycles, ensuring reliable and predictable communication from the ALTI Timing, Trigger & Control module to the front-end ASICs. This stability is crucial for the accurate and synchronized operation of the NSW electronics system.

### Digitized readout data from the detector including monitoring and calibration

The pathway for digitizing detector data [34] commences with the 64-channel VMM front-end ASIC. Signals from strips, pads, and wires undergo processing by digitizing their peak voltage after shaping. Simultaneously, the time of the peak relative to the Bunch Crossing (BC) clock edge is digitized, or at the threshold upon configuration. The resulting charge and time information are buffered until requested by the Read Out Controller (ROC) for specific bunch crossings indicated by the Level-1 Trigger Accept (L1A) signal. Unchosen data is retained until it exceeds the time range of interest.

The Read Out Controller consolidates data from up to eight VMMs, directing the chosen information, as dictated by the L1A signal, to a GBTx ASIC on the Level-1 Data Driven Readout (L1DDC) card through one or more copper twin-ax serial readout "E-links". The GBTx, in turn, aggregates several of these readout E-links, each operating at speeds of up to 320 Mb/s, onto a 4.8 Gb/s optical link. Subsequently, the Front-End Link eXchange (FELIX) takes on the role of aggregating multiple optical links and directing the data from readout E-links to the "software Read Out Driver" (swROD) or data handler [46].

The swROD processes numerous readout E-links and ultimately transmits the front-end data in a standardized ATLAS format to the High Level Trigger (HLT). Moreover, the swROD generates a data stream for histograms, facilitating real-time monitoring of the detector and data flow. Beyond the primary Level-1 Accept (L1A) event flow, calibration triggers can divert front-end data along this path. This diversion can either lead to a swROD for offline calibration or a separate swROD dedicated to calibration processing, which does not connect to the HLT but focuses solely on calibration tasks.

In addition to event data, the Trigger Processors contribute by sending monitoring data for non-triggered bunch crossings to a swROD, where local processing of this information takes place.

### Configuration parameters and status indicators

The configuration of operational parameters for all components within the NSW electronics [34] is facilitated through the SCA ASIC present on each board or its FPGA firmware emulator, known as SCAX (as depicted in Figure 3.1). Acting as a crucial interface, an OPC UA server establishes communication with both the SCA and SCAX. The connection between them is established through the FELIX and GBTx E-links. This setup allows the OPC UA server, serving as the software interface to the SCA and SCAX, to access various configuration and



status registers present within these components. Configuration and status reporting processes, functioning as OPC UA clients, utilize this established path to retrieve information and configure settings as needed. This unified path is also shared by the DCS OPC UA client, which monitors conditions such as voltages and temperatures of boards and ASICs. These conditions are sampled and reported by the SCA, providing a comprehensive and centralized approach to monitoring and configuring the NSW electronics components.

### Busy path

In the event that a FELIX FPGA approaches the limit of its buffer space, a BUSY signal can be asserted [34]. This BUSY signal is transmitted on a dedicated electrical line. The logical "OR" operation is applied to all such BUSY signals, collectively forming a request that is communicated to the Central Trigger. Upon receipt of this request, the Central Trigger halts the generation of Level-1 Accept triggers, effectively preventing the front ends from generating additional data. This pause allows the FELIX FPGA or server to recover from the buffer overflow condition. The BUSY signal can also be asserted when FELIX temporarily suspends the transmission of events in response to the Software Read Out Driver (swROD) sending an Ethernet XOFF signal. This mechanism provides a means to manage the data flow and maintain system stability during potential buffer congestion scenarios. Additionally, the NSW Read Out Controller possesses the capability to send BUSY requests to FELIX. However, it's important to note that this feature is not typically enabled in the normal operation of the detector. It serves as a contingency measure, allowing for controlled intervention when necessary to ensure the proper functioning and resilience of the NSW electronics system.

### Digitized data from the detector for the trigger path

The initial point of the trigger paths is identified by detecting hits from various sources within the NSW system. These hits originate from the VMM "direct" 6-bit charge data outputs for sTGC strips, the VMM Time-over-Threshold (ToT) outputs for sTGC pads, and the VMM ART output for the Micromegas detector. All the trigger primitives generated from these hits are then directed to the Trigger Processor through ART, Router and the Pad Trigger. In the case of the sTGC and Micromegas detectors, their respective Trigger Processors independently identify track segments based on the hits within their detectors. For the sTGC, hits are defined as the centroids of charges induced on strips, while for the Micromegas, hits are characterized by the channel number of the first hit in the bunch crossing per front-end VMM ASIC. These identified hits define the extraction of track segments, each pointing toward the IP. Specifically, on every bunch crossing, the sTGC Trigger Processor unifies the sTGC and Micromegas segments and forwards them to the Sector Logic.

## 3.2 Electronics Boards

The total number of the NSW electronics boards[34] are shown in the following table and will be described extensively in the following subsections:

### Micromegas Front-end board – MMFE8

The electronic board designated for the Micromegas detector, known as MMFE8 (Micromegas Front-End Electronics 8), acts as the interface between the detector and the trigger (ADDC) and data acquisition (L1DDC) electronics. This board is specifically designed to collect the signals from the readout channels within the Micromegas detector.

Given the high number of readout channels on the Micromegas detector, approximately 2.1 million, a total of 4096 MMFE8 boards are required. Each MMFE8 board efficiently handles 512 channels, contributing to the comprehensive readout coverage of the Micromegas detector. The board comprises eight VMM ASICs, one ROC ASIC, one SCA ASIC, and three FEAST ASICs. Each VMM ASIC is equipped with 64 channels,

Board	#
MMFE8	4096
sFEB	768
pFEB	768
ADDC	512
L1DDC-MMG	512
L1DDC-STG	512
Rim L1DDC	32
Pad Trigger	32
Router	256
Serial Repeaters	880
LVDS Repeaters	140
<b>Summary =</b>	<b>7996</b>

Table 3.1: NSW Electronics boards.

corresponding to individual strips on the detector. Consequently, each MMFE8 board reads signals from 512 readout-strips of the Micromegas detector.

Two FEAST ASICs supply power to the analog sections of the eight VMMs (one FEAST per four VMMs). Another FEAST ASIC provides 1.2 V to the digital supplies of all the VMMs, the ROC, and the SCA ASIC. The input voltage of 11 V is supplied through the Low Voltage Distributor Board (LVDB). The power consumption of the MMFE8 board has been measured to be approximately 16 W.

External access protection against sparks is integrated into these boards to ensure the safety of the equipment and facilitate entry to the eight VMMs. The connection between the Micromegas detector and the VMM channels is established using two ZEBRA elastomeric connectors.

The MMFE8 boards interface with both ADDC and L1DDC boards through MiniSAS connectors and twinax cables. The connector to the ADDC carries the eight ART signals. The connection to the L1DDC includes the TTC signals and the bunch crossing clock to the MMFE8. Additionally, four data lines are directed to the GBTx (one per small ROC, sROC). The SCA E-link is also transmitted through the same connector, ensuring clarity about which ROC and VMMs are configured or reset by the SCA. The on-board ROC ensures dedicated trigger, clock, and reset connections to each VMM, enhancing the precision and efficiency of the overall Micromegas detector readout process. A schematic representation of the MMFE8 board is illustrated in Figure 3.2.

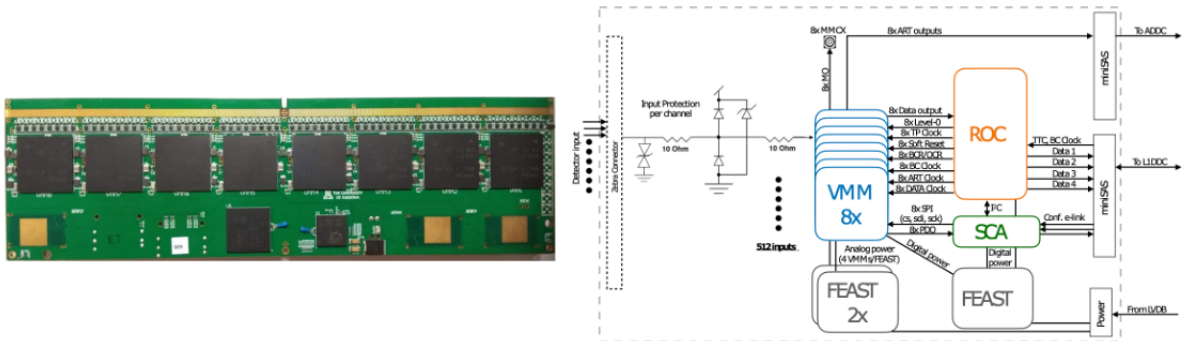


Figure 3.2: Left: Photograph of the production NSW MMFE8 board. Designed in the University of Arizona, the board features eight VMMs (top row), one ROC (bottom center), and one SCA (on the righthand side of the ROC). Right: The MMFE8 block diagram showing the ESD protection, the VMM front end ASIC's, the Readout Controller ASIC, the Slow Control Adapter ASIC, the FEAST DC-to-DC converter ASIC's, and the MiniSAS twin-ax connectors for the different interfaces. [34]



### sTGC Front-end boards – sFEB and pFEB

The strip and pad Front-end boards serve as crucial interfaces to the detector strips, pads, and wire groups within the NSW system. Their primary function is to provide the charges from the detector elements to the readout path upon receiving a Level-1 trigger and to the trigger path on every bunch crossing. Specifically, each sTGC gas gap within an sTGC quadruplet is connected to a pair of boards: the pad-FEB (pFEB) and the strip-FEB (sFEB). These boards have the capability to operate independently from other layers, enhancing the modularity and flexibility of the overall system.

Within an sTGC gas gap, there are approximately 30 wire groups, up to 112 pads, and up to 400 strips. The pFEB is responsible for the readout of both pads and wires, whereas an sFEB is dedicated to the readout of the entire strip plane. For the pFEB, analog signals from sTGC pads are routed through a high-density connector and a dedicated analog input network. These signals are then sensed by two 64-channel VMM3a ASICs, which represent the production version of the NSW Front-End ASIC. In the trigger path, these two VMMs have their direct output connected to a 104-channel pad-TDS (Time-over-Threshold Digitizing Sampler). In this process, ToT pulses are sampled with the 40 MHz bunch clock. The pad-TDS channel count in the trigger path is effectively limited by the transceiver bandwidth, allowing the transmission of 120 bits per 25 ns bunch crossing. Out of these, 12 bits are allocated for the Bunch Crossing ID (BCID), with an additional 4 bits for the data packet. This configuration is sufficient to provide the required trigger coverage for the NSW, even with a pseudorapidity of 2.4.

The output from the pad-TDS is then routed to a Serial AT Attachment (SATA) connector, which is connected to the Pad Trigger Board via a SATA breakout cable. On the other hand, the sTGC wire groups are connected to a third VMM without utilizing its direct output, as no trigger function is required in this context.

The sFEB board is designed as a dense 14-layer circuit board, incorporating six or eight VMMs, one ROC ASIC, two strip-TDS modules, one SCA ASIC, and six FEAST ASICs. On the other hand, the pFEB board is a dense 12-layer circuit board, consisting of three VMMs, one ROC ASIC, one pad-TDS module, one SCA ASIC, and three FEAST ASICs. This intricate setup ensures the efficient and precise handling of signals from the detector elements, facilitating the necessary readout and triggering functions within the NSW electronics system.

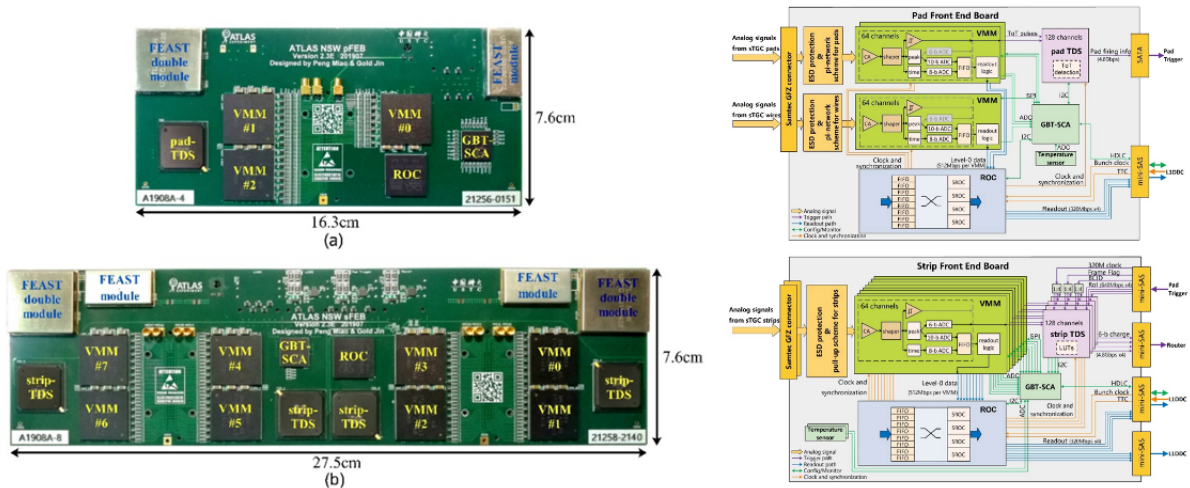


Figure 3.3: Left: The fully assembled production version of sTGC pFEB and sFEB. Right: The functional block diagram of the sTGC sFEB and pFEB and the connectivity on board. [47]

### Level-1 Data Driver Card - L1DDC

The L1DDC [34] plays a crucial role in the DAQ system for both the MMG and sTGC detectors. This intermediate board serves to aggregate and transmit data from up to eight FEB boards to the backend electronics,

which comprises commercial electronics integrated with FPGAs.

The L1DDC is designed to consolidate three distinct paths—Timing and Trigger, Data Acquisition, and Slow Control information—into one or more bidirectional optical links, each operating at a rate of 4.8 Gbps. This amalgamation is achieved through the utilization of a custom Application Specific Integrated Circuit (ASIC) chipset developed at CERN. The chipset includes several key components, namely a high-speed serializer/deserializer GBTx, a SCA, a GigaBit TransImpedance amplifier (GBTIA), and a GigaBit Laser Driver (GBLD). The GBTIA and GBLD collectively form the Versatile optical Transceiver (VTRx), and two GBLDs constitute the Versatile Twin Transmitter (VTTx) module. Additionally, the CERN custom FEAST DC-DC converter is employed for power distribution within the L1DDC.

The L1DDC exists in three variants, each featuring the same basic functionality but differing in mechanics and channel counts. Two of these variants are integrated into the sTGC electronics, while the third is designated for the Micromegas detector. This modular approach allows for adaptability to the specific requirements and configurations of each detector subsystem within the overall NSW electronics architecture.

- **MM-L1DDC (Micromegas L1DDC):**

- Interfaces with eight FEB boards and one ADDC board.
- Implements three GBTx ASICs: one bi-directional link (VTRx) plus two transmit-only links (VTTx) to accommodate the extra bandwidth needed for Phase-2.
- On-board SCA ASIC for configuration of the three GBTx ASICs, monitoring board temperature and voltage levels, and providing configuration and TTC distribution to the ADDC board.
- Utilizes a total of 41 E-links. There is one MM-L1DDC for each edge of each Micromegas layer.
- Total power consumption is approximately 7 W.

- **sTGC-L1DDC (Small Thin Gap Chamber L1DDC):**

- Interfaces with three FE boards using twin-ax cables.
- Features two GBTx ASICs for two independent bi-directional links (VTRx). One link is used for pad+wire FEBs, and the second strip GBTx provides the extra bandwidth needed for Phase-2.
- Utilizes a total of 21 E-links. There is one L1DDC on each edge of each sTGC layer.
- Overall power consumption of the sTGC-L1DDC is approximately 6 W.

- **Rim-L1DDC (Rim Level-1 Data Driver Card):**

- Supports the Pad Trigger and eight Router cards in the sTGC trigger chain electronics.
- Located in a dedicated crate called "the Rim crate," situated in the rim of the NSW structure.
- Consists of two independent boards (primary and auxiliary) sharing the same PCB.
- Each board includes one GBTx, one VTRx, and nine MiniSAS connectors, providing redundancy to the system.
- On-board SCAs can switch off/on the Pad Trigger and Router boards by controlling the enable/disable signal of the Front End ASIC Test (FEASTs).
- A dedicated clock is provided through an additional fiber to address GBTx's E-link clock jitter. This low-jitter 160 MHz clock is distributed to the Router and Pad Trigger boards via low-jitter fanouts.
- The power consumption of the board is approximately 8 W.

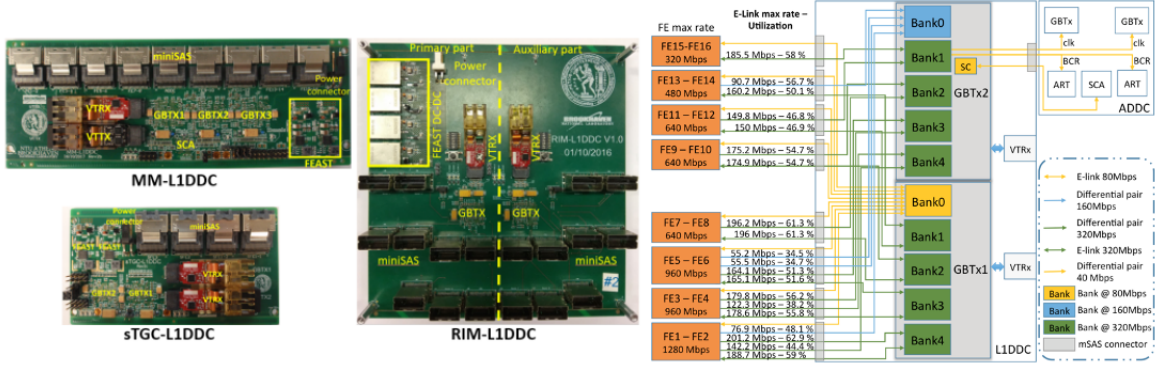


Figure 3.4: Left: The MM-L1DDC, the sTGC-L1DDC, and the RIM-L1DDC board. MiniSAS connectors, power connector, FEAST DC-DC converters, VTRX, and VTTX are visible. GBTxS, SCA, and fan-out buffers are placed on the bottom layer of the board. Right: MM e-Link connectivity. For most FEs, additional differential pairs will be used to collect the Level-1 data. These pairs will be multiplexed in different banks and may use different e-Link speeds. Eight GBTx banks will run at 320 Mbps, one at 160 Mbps, and one at 80 Mbps, which will be used for the configuration of the VMM and ROC ASICs.

### Micromegas trigger data serializer - ADDC

The ADDC [34] serves a crucial role in the context of Micromegas detectors, specifically in processing the ART data. This card is designed to receive ART signals, the earliest data above the threshold per VMM from eight MMFE8 boards. This signal corresponds to a 5-bit geographical address at the strip for each event. Communication between the ADDC and the L1DDC is established, allowing the transmission of configuration data from the control center and providing essential timing signals. The data collected by two GBTx ASICs is then transmitted in two stages via an optical fiber link to the back-end electronics, notably to the USA15, serving as the trigger host.

The ADDC incorporates two ART ASICs, two GBTx ASICs, one GBT-SCA ASIC, one VTTx optical transmitter, and two Front End ASIC Test (FEAST) ASICs. Each GBTx ASIC transmits the data to the trigger processor through a dedicated transmission line in the VTTx. The on-board GBT-SCA ASIC is responsible for the configuration and control of the ART and GBTx ASICs.

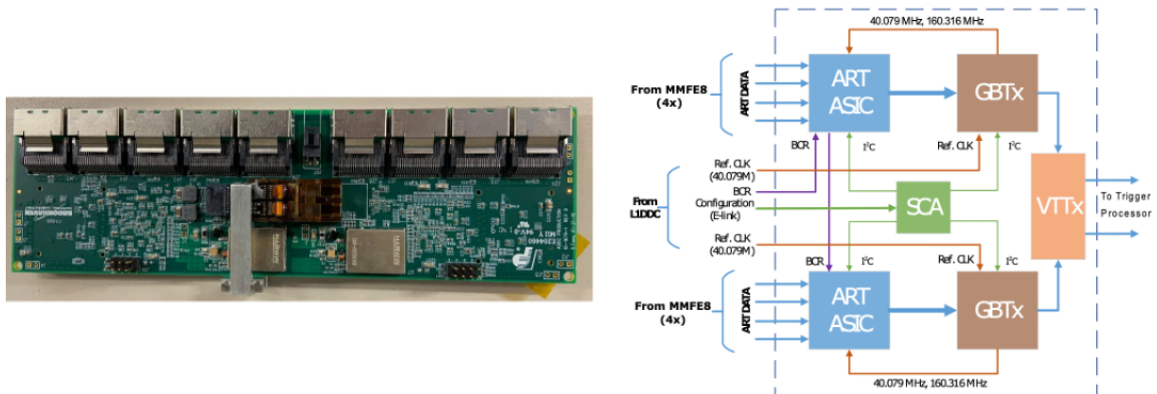


Figure 3.5: Left: The top side of a fully assembled ADDC production board. Right: The ADDC block diagram. Each ADDC receives 64 inputs of ART data using two ART ASIC's. Output to the Trigger Processor is via two GBTx ASIC's. [34]

## Pad Trigger

The sTGC Pad Trigger[34] is a trigger board that finds tracks passing through a pointing tower of logical sTGC pads. Its purpose is to send out only the charge data from those bands of strips that pass through the pad tower coincidences. Up to four towers can be found. It receives the binary pad hits from 24 Front-end boards, three per layer, in a sector. The band of 17 strips in each layer that pass through each tower is identified by a Band-id. The Band-ids of triggered towers are sent to the relevant strip-TDS's which then send the charges of each strip in the band to the Trigger Processor via the Router. One Pad Trigger per sector resides in the Rim Crate for that sector. Its context and block diagram are shown in Figure 3.6. For redundancy, the Pad Trigger is connected to both of the redundant Rim-L1DDC's. The SCA on the Pad Trigger is connected to both. This allows the SCA to choose which Rim-L1DDC provides the 160 MHz reference clock for the Pad Trigger's gigabit transceivers.

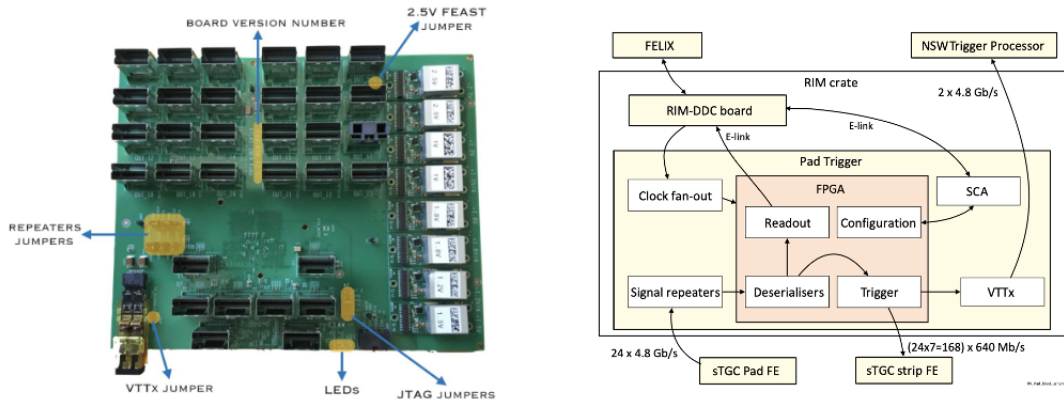


Figure 3.6: Left: The top side of a fully assembled Pad Trigger production board. Right: The Pad Trigger context and block diagram. [34]

## Router

The sTGC Router[34] serves as a packet switch for routing sTGC strip charges held by the strip-TDS to the sTGC Trigger Processor. It was implemented in a Xilinx FPGA, the XC7A200TFFG1156 from the Artix-7 family. There is one Router per layer for each sTGC sector. A scheme was developed to maintain low and fixed-latency packet multiplexing through the Router. The Router is unaware of the ATLAS run state and does not send any data in response to a Level-1 trigger. The on-board SCA ASIC is used to control the Router. The sector-id is set in the FPGA via the SCA GPIO. The twin-ax cables from the inner and middle radii front-end boards were made the same length. The cable from the outer Front-end board is shorter by one or two clock periods. In order to align all the inputs, the Router therefore inserts a delay, either one (two) 160 MHz clocks, for signals from the outer front-end boards of the large (small) sectors. The Router FPGA can be configured from on-board Flash memory or by FELIX via the JTAG port of the SCA.

## 3.3 VMM

The VMM [48] [33] front-end readout ASIC, designed by Brookhaven National Laboratory (BNL), have been used to address the evolving requirements of the New Small Wheel within the ATLAS experiment at CERN. The ASIC is designed using the 130 nm Global Foundries 8RF-DM process and houses an impressive five million transistors, all realized through CMOS technology.

Each of the 64 channels in the VMM is intricately connected to a read-out strip, featuring a comprehensive electronic subsystem. This subsystem encompasses a load amplifier (charge amplifier), a configuration amplifier shaping amplifier, a clarifier discriminator with lower threshold and peak detection, and a Timing to



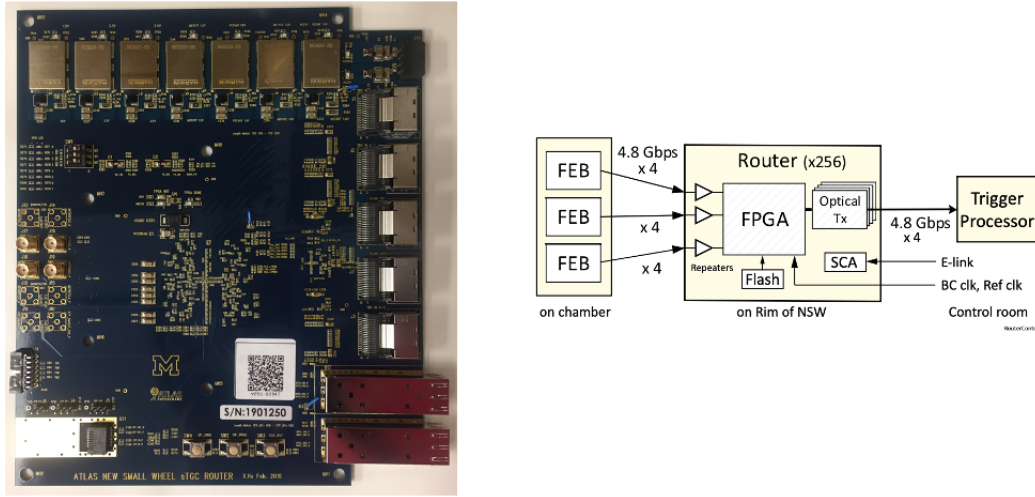


Figure 3.7: Left: The top side of a fully assembled Router production board. Right: Context diagram of the Router for a layer showing the four electrical inputs from each of the three Front-end boards in one layer of a sector and the four fibre outputs. [34]

Amplitude Converter (TAC). The analog signals generated by these subsystems undergo digitization through three Analog-to-Digital Converters (ADC) with outputs of 6, 8, and 10 bits. The resultant digital data is stored in a First-In-First-Out (FIFO) buffer, facilitating the subsequent transmission of data to the ROC ASIC of the MMFE8 or sFEB or pFEB.

Looking ahead, the VMM3 iteration is poised to be manufactured using Ball Grid Array (BGA) technology, featuring 400 balls with a pitch of 1 mm. The device's overall dimensions are tailored to match the pitch of the Micromegas detectors, resulting in a compact size of  $21 \times 21 \text{ mm}^2$ . The package size, or die size, comes in at  $15.00 \times 8.38 \text{ mm}^2$ . These dimensions are visually depicted in Figure 3.8 for further clarity. The innovative design and advanced features of the VMM series position it as a key component in the ATLAS experiment's pursuit of enhanced data acquisition and readout capabilities. Inside the VMM [49] when a pulse enters, the

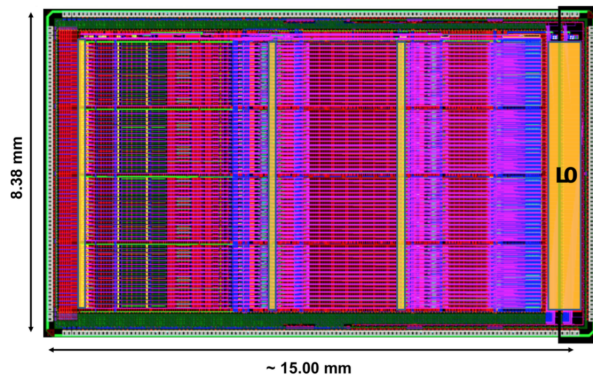


Figure 3.8: VMM3 die layout. [33]

preamplifier converts it into an analog voltage pulse, and then the shaper forms the final form of the input voltage. The shaper filter is 3rd degree designed in retrospective delay feedback (delayed dissipative feedback (DDF)), and can be set to 4 load end times (peaking time), 25, 50, 100, 200 ns. In addition, it is possible to increase the gain to 0.5, 1, 3, 4.5, 6, 12, 16 mV/fC. The modulated signal then enters the discriminator, where when a pulse exceeds the threshold (threshold) set, the pulse peak detection method is activated. Adjacent to the shapers in the VMM architecture [49], essential components such as sub-hysteresis discriminators with neighbor-enabling logic and individual threshold trimming, the peak detector, and the time detector play a crucial role in the signal processing pipeline. The adjustment of the threshold is a nuanced process involving a



by an 8-bit ADC. This component extracts timing information from the output of the TAC. The 8-bit resolution ensures a fine-grained representation of time, enabling precise event timing and synchronization. This temporal data holds significance in reconstructing the chronological sequence of events within the detector.

2. **Energy Measurement (10-bit ADC):** For quantifying the energy deposited by ionizing particles in the detector medium, a dedicated 10-bit ADC system comes into play. This ADC receives signals containing critical information about the maximum height of the pulse from the peak detector. The higher bit resolution (10 bits) of this ADC ensures accurate and detailed measurements of the pulse's energy content. This level of precision is particularly valuable for applications that demand a nuanced understanding of the energy deposition patterns.
3. **Direct Output (6-bit ADC):** Another part of the signal processing pipeline is the 6-bit ADC responsible for digitizing signals originating from the peak detector. While offering a slightly lower level of accuracy compared to the 10-bit ADC, the 6-bit ADC provides a reasonable compromise, making it suitable for scenarios where a balance between precision and data size is desired. This component is chosen for applications that prioritize efficiency while maintaining a satisfactory level of accuracy.

The selection of the appropriate ADC system is contingent upon the specific needs and preferences of the user. This modular approach allows for customization, catering to diverse applications with varying priorities. Whether prioritizing high precision in energy measurements, fine temporal resolution, or a balanced compromise between the two, the VMM's adaptable ADC systems ensure versatility in addressing the unique requirements of Micromegas detectors and beyond.

### 3.3.1 Validation Studies

#### MMFE1 Board

The MMFE1 board, a component in the experimental setup, integrates a single VMM alongside an Artix®7 FPGA manufactured by Xilinx®[49][50]. This board plays a crucial role in multiple configurations explored within this dissertation, serving as the cornerstone for the VMM Front End readout firmware in both digital and analog readout schemes, as well as contributing to the VMM Readout System [51].

In Figure 3.10, the MMFE1 board is depicted, showcasing its key features. Communication with the software host is facilitated through the FPGA and a commercial network Ethernet Physical Interface (PHY) operating at speeds of 10, 100 or 1000 Mb/s. The power distribution circuit employs stepdown regulators, accommodating input voltages ranging from 3.4 to 42 V, with an output ripple minimized to less than 10 mV peaktopeak. To ensure stability, the four power rails of the VMM ( $V_{ddp}$ ,  $V_{dd}$ ,  $V_{ddad}$ , and  $V_{ddd}$ ) are independently powered by distinct Low DropOut (LDO) regulators, effectively mitigating any potential ripple effects.

The board features three LEMO connectors providing access to the monitoring, peakdetector, and time-detector outputs (MO, PDO, TDO, respectively) of the onboard VMM. Additionally, the MMFE1 board possesses the capability to output the ART signal and receive an external trigger signal.

The FPGA on the MMFE1 board is accessible through a standard JTAG connector for programming and monitoring purposes. The configuration file is stored in a flash memory accessible via the Serial Peripheral Interface (SPI) protocol. An additional memory (EEPROM) is employed to store the Media Access Control (MAC) and network addresses, with configurability for each. The EEPROM is accessed by the FPGA through the I2C protocol, enabling dynamic reconfiguration of its network address—an essential feature for system scalability. The board further incorporates a  $\mu$ HDMI connector, providing access to external signals such as reference clock, trigger, and reset. For external interfacing with other boards, such as the L1DDC developed for the NSW upgrade, a miniSAS1 connector is provided.

To protect the VMM, the input protection mechanism employs steering diodes in a railtorail configuration along with series resistors. Several frontend boards based on a similar architecture have been fabricated to

interface with diverse types of detectors. Notably, the MMFE1 board was specifically fabricated to validate the functionality of the VMM ASIC on  $10 \times 10 \text{ cm}^2$  Micromegas prototype chambers.

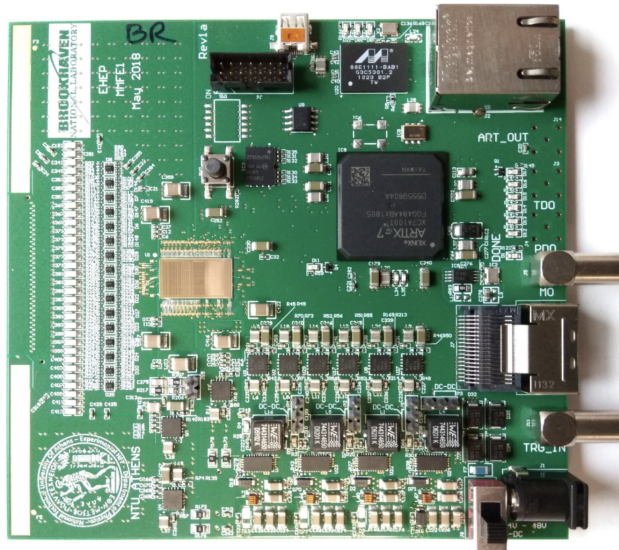


Figure 3.10: The overview of the MMFE1 board.

### VERSO Software

User control of the VRS FrontEnd FPGA boards is facilitated by a software tool known as 'VERSO'—an acronym for VMM Ethernet Readout Software [51]. Developed entirely in C++ and utilizing the Qt framework for the Graphical User Interface (GUI), VERSO plays a pivotal role in orchestrating configuration processes and managing DAQ. The GUI of VERSO is depicted in Figure 3.11.

VERSO employs a custom-made protocol within the UDP standard to execute its functions. It has two primary responsibilities: configuration processes and data acquisition. The tool also incorporates automated functionalities for calibration of the frontend electronics and data-taking with a fixed number of triggers.

The DAQ functionality of VERSO is designed to handle the readout of multiple frontend boards. The event building process relies on a trigger counter transmitted with each data fragment upon the reception of a trigger signal at the frontend. An 'event' is thus defined as the collection of data fragments with the same trigger number. The trigger signal can either be an internal signal configured by VERSO and generated by the firmware or an external signal.

Due to the asynchronous nature of the UDP protocol, events based on the same trigger number are not guaranteed to be captured by VERSO within the same UDP packet. To address this, VERSO adopts a single-producer/single-consumer threading model. In this model, one thread is responsible for reading the data fragment from the frontend(s), and a second processing thread handles the processing of data fragments associated with each unique trigger number received. The data fragments received by the reading thread are indexed by their trigger numbers and buffered in a queue for eventual processing by the second thread. The queue is implemented as a lock-free concurrent queue, ensuring efficient readout even at maximal data-taking rates observed during test-beam scenarios.

The processing of an event involves decoding the raw data fragments transmitted by the frontend(s) and constructing high-level data structures representing each event. These structures are continuously stored on disk in the .ROOT data format throughout a given data-taking period, ready for offline data analysis. The robust design of VERSO ensures efficient and reliable control and data acquisition from the VRS FrontEnd FPGA boards.



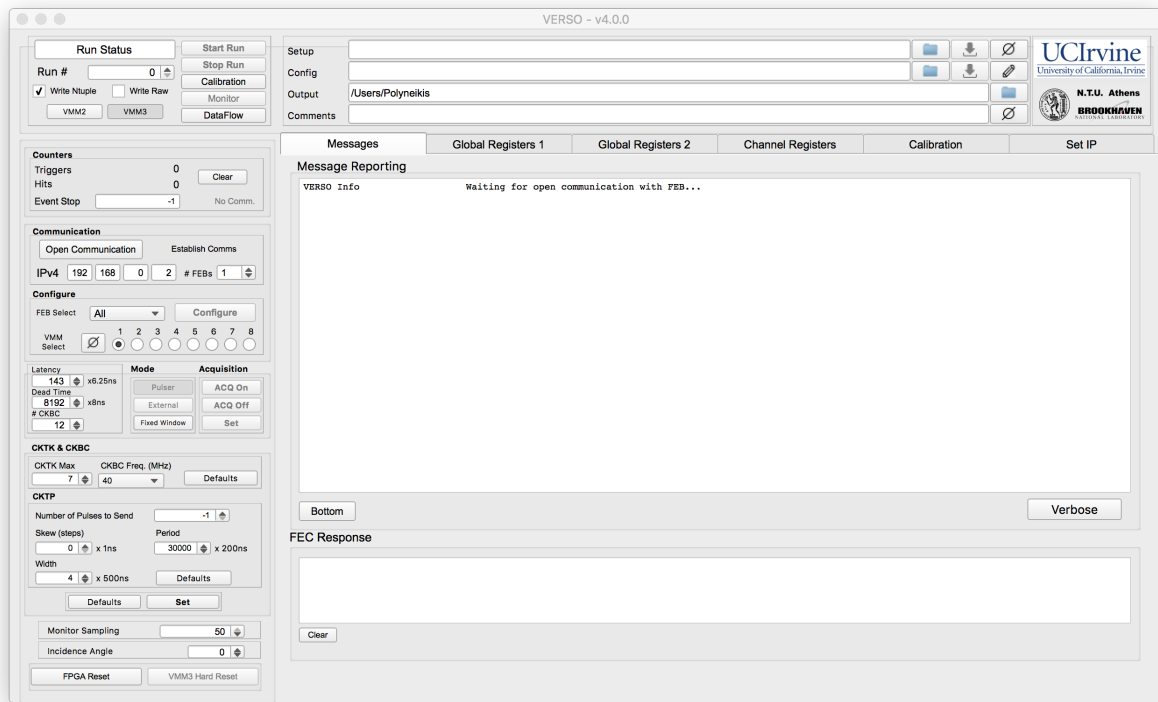


Figure 3.11: The overview of the VERSO software. [51]

## Studies

During studies of the VMM3 ASIC[50], several issues were identified, shedding light on potential areas for improvement and optimization. The studies revealed the following concerns:

- **Missing Codes:** Figure 3.12(a) illustrates the absence of readings in both the 10-bit and 8-bit ADCs.
- **Channel Threshold Range Equalization Problem:** Figure 3.12(b) showcases the dynamic range of trimmers for each channel, revealing challenges in defining a unique value for all channels due to equalization issues in the threshold range.
- **High Baseline in Higher Gains:** Some channels exhibited a high baseline, especially at higher gains (e.g., Gain of 9 mV/fC and 12 mV/fC), as depicted in Figure 3.12(c).
- **Positive Channel Issue:** It was discovered that the VMM was not able to efficiently read positive pulses when configured at positive polarity.

These findings underscore the importance of addressing these issues to enhance the performance and reliability of the VMM3 ASIC in various applications.

### 3.3.2 Neutron Irradiation Testbeam

The Neutron Irradiation Testbeam was conducted at the National Centre for Scientific Research Demokritos (NCSR)[52] from May 2017 to June 2018.

The objectives of the neutron irradiation testbeam at Demokritos included:

- Performing Single Event Upsets (SEU) tests for VMM3, VMM3a, ROC, and ART ASICs.
- Verifying the Router board for Multi-Bit Upsets (MBU).
- Assessing the functionality of L1DDC, ADDC, and Pad Trigger boards in the neutron environment.

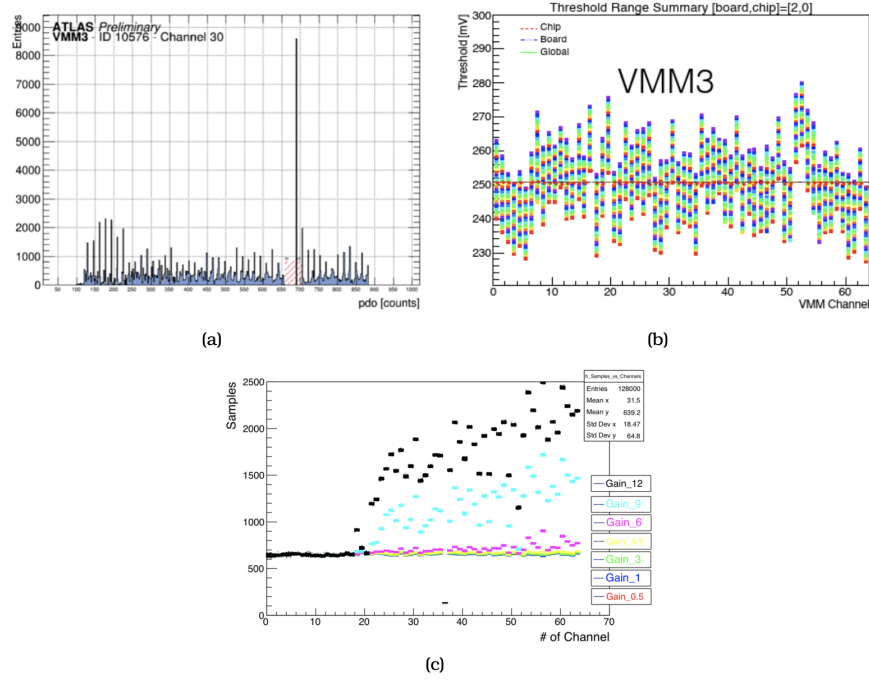


Figure 3.12: (a) Missing codes in the VMM's ADCs, (b) Dynamic range of trimmers illustrating the channel threshold equalization problem, (c) High baseline issue observed in some channels at higher gains.

- Conducting SEU tests on the Jitter cleaner, repeater, and the 1-4 fan-out ICs.

Although this study will primarily focus on the VMM3 & VMM3a tests and results, the primary aim was to understand the behavior of the VMM3 & VMM3a read-out chips under neutron radiation, with quantities comparable to those expected at Run 3 of the ATLAS experiment. This was achieved by systematically writing and reading the VMM3's configuration registers to investigate the occurrence of SEUs. The NCSR setup, along with the Mini1 board equipped with the VMM3/VMM3a, is illustrated in Figure 3.13.

### Neutron Facility Setup

The neutron irradiation tests were conducted at the 5.5 MV HV TN-11 TANDEM accelerator of NCSR "Demokritos"[52] in Athens, Greece. Mono-energetic neutrons were generated through the  $^3\text{H}(d,n)^4\text{He}$  reaction, where a deuteron beam of approximately 4 – 5.5 MeV interacted with a thin solid tritiated titanium target deposited on a copper backing. To protect against wear, a 10  $\mu\text{m}$  molybdenum foil was placed in front of the tritiated target. The target was cooled by utilizing lateral heat conduction from the aluminum beam dump/target housing to the surrounding pressured cold air channel. Under these experimental conditions, the  $^3\text{H}(d,n)^4\text{He}$  reaction produced neutrons in the energy range of 19 – 22 MeV, simulating the expected neutron energies in the ATLAS cavern. Neutron fluences reached approximately  $3 \times 10^6$  neutrons/cm<sup>2</sup>s.

### Monte Carlo estimations

The neutron flux was initially estimated using the NeuSDesc program, developed at the JRC Institute for Reference Materials and Measurements in Belgium. The estimation involved providing specific inputs related to the target's characteristics, deuteron energy, and distances between the two VMMs. NeuSDesc utilizes Monte Carlo simulations from the SRIM-2013 program, considering factors such as energy loss, energy spread, and angular straggling of deuterons in the target. It calculates average neutron energies, fluences, and resolutions. One notable advantage of NeuSDesc is its capability to include detailed calculations for stopping power, en-

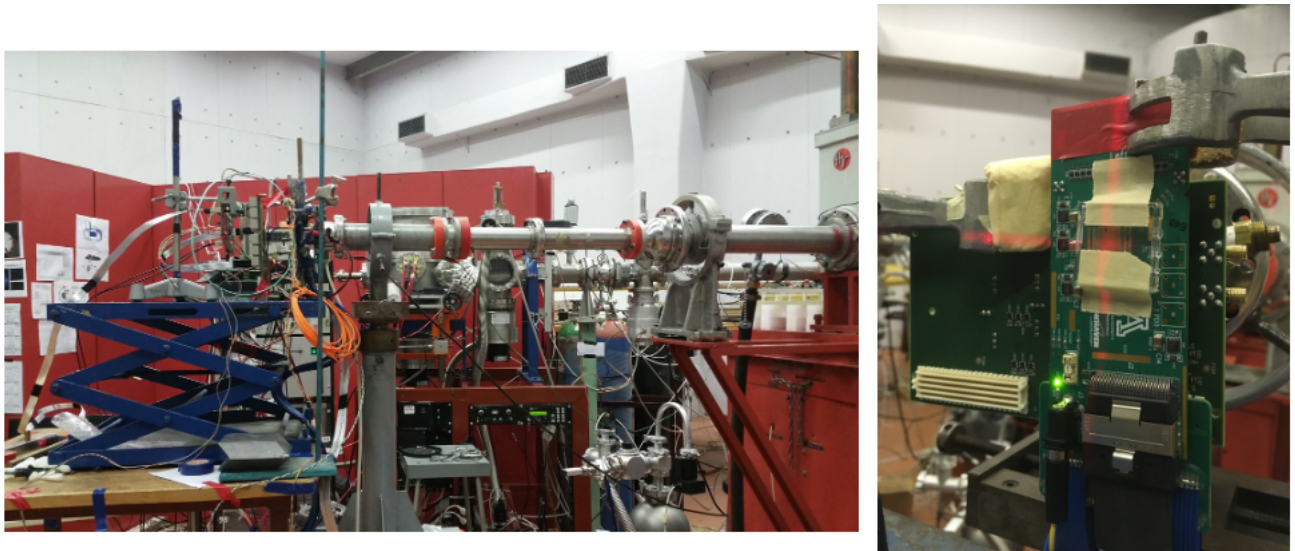


Figure 3.13: The Neutron Irradiation Testbeam setup along with the Mini1 board equipped with the VMM3/VMM3a.

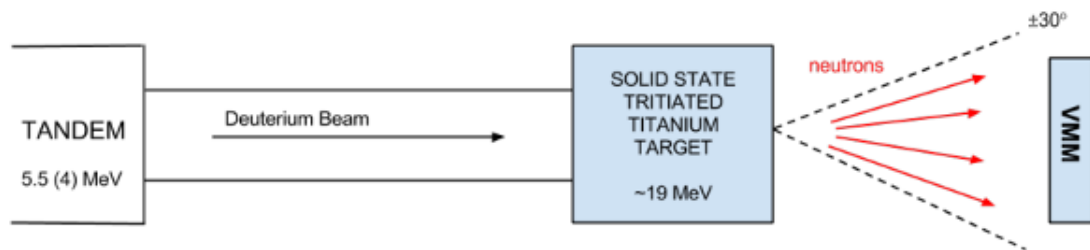


Figure 3.14: Schematic of the neutron irradiation setup used for irradiation testing.

ergy, and lateral straggling of impinging deuterons. The calculated mean flux for the VMM concerning the deuteron energy is illustrated in Figure 3.15.

### Mini1 - VMM board

For both testbeam periods, the VMM3&VMM3a were installed on a Mini1 board. The VMM incorporates adjustable functionalities accessible through 1072 global and channel configuration register bits, including selectable gain, threshold, integration time, etc. These registers can be configured using a GUI environment, such as LabVIEW, which communicates with a FPGA evaluation board (digitizer). The digitizer, equipped with an Altera FPGA, is employed to access the VMM ASIC. The firmware is developed to perform read and write operations on the configuration registers, as well as proper data read-out.

The LabVIEW platform serves as the user interface for all functionalities related to the VMM's operation. Additionally, it is adapted to incorporate an automated section dedicated to the neutron irradiation tests. During these tests, the VMM's global and channel registers are sequentially filled, and the information is then sent to the digitizer and read out through the FPGA after a two-minute interval. All relevant data is stored in a text file for subsequent inspection and is simultaneously available in real-time through a dedicated LabVIEW panel. This panel provides information such as the bits filled and read during each operation, the total number of SEUs, as well as details about the energy and current of the beam.

In case of an SEU occurrence, where one of the 1072 bits of the registers is altered, the LabVIEW interface enables the user to monitor the time, address, and transition of the upset ( $1 \rightarrow 0$  or  $0 \rightarrow 1$  transition). This information is both displayed in real-time on the LabVIEW panel and saved in a dedicated text file.

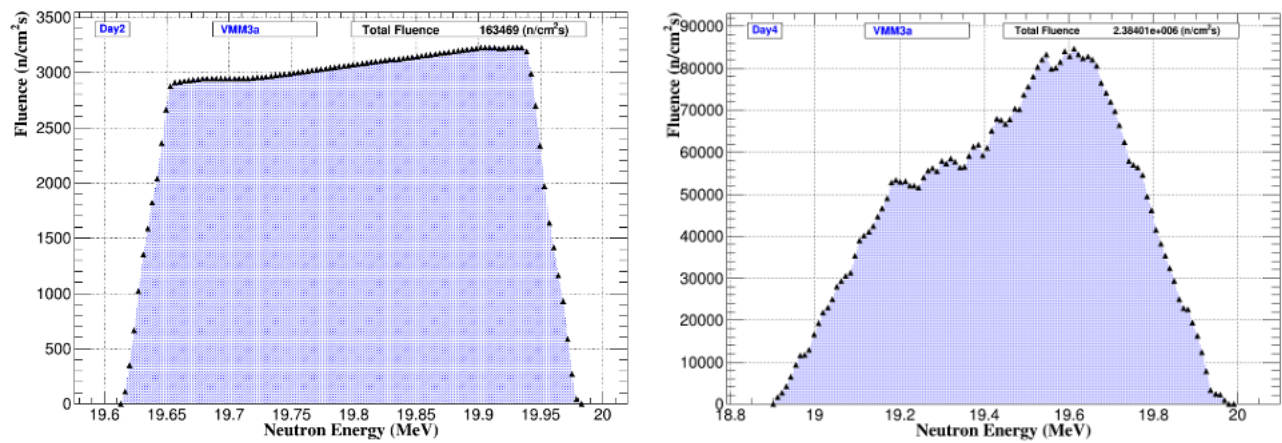


Figure 3.15: The calculated mean flux for the VMM with respect to the deuteron energy

### Experimental Setup - May 2017

The experimental setup for the May 2017 irradiation test included the following electronics boards/ASICs:

- Mini1 board equipped with VMM3
- Repeater board
- 2 Router boards
- Jitter Cleaner ASIC
- ART ASIC
- ADDC board
- Rim-L1DDC board

The testbeam spanned 5 days, and each day involved shifting the positions of the boards/ASICs to acquire corresponding neutron flux data.

During the first two days, the VMM3 was positioned at distances of 14.8 mm from the target, and the deuteron energy was set at 20.1 MeV with a current of 0.7  $\mu\text{A}$ . On the third day, the current was increased to 1.1  $\mu\text{A}$ , and the VMM3 distance increased to 22 mm. On the fourth and final day, the VMM3 distance was further reduced to 12 mm, and the current was decreased to 1.0  $\mu\text{A}$ . Figure 3.16 illustrates the neutron fluence as a function of the board/ASIC distance for Day 1, along with the experimental setup for Day 1.

### Experimental Setup - June 2018

The experimental setup for the June 2018 irradiation test included the following electronics boards/ASICs:

- Mini1 board equipped with VMM3a
- FanoutRim ASIC
- Fanout ASIC
- ROC ASIC
- Pad Trigger board

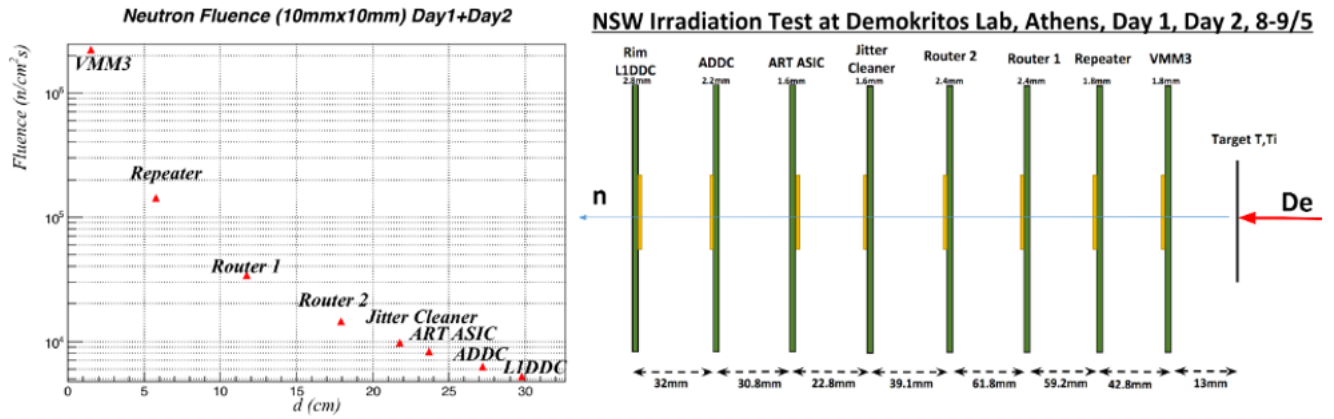


Figure 3.16: An example of the neutron fluence as a function of the board/ASIC distance and also the experimental setup for one particular testbeam day.

The testbeam spanned four days in total, with daily adjustments to the positions of the boards/ASICs to acquire corresponding neutron flux data.

An overview of the VMM3a Neutron Irradiation test is presented in Figure 3.17. The Figure illustrates the total neutron flux as a function of the testbeam day. Additionally, the parameters for each daily run, including energy, current, flux, and duration, are displayed.

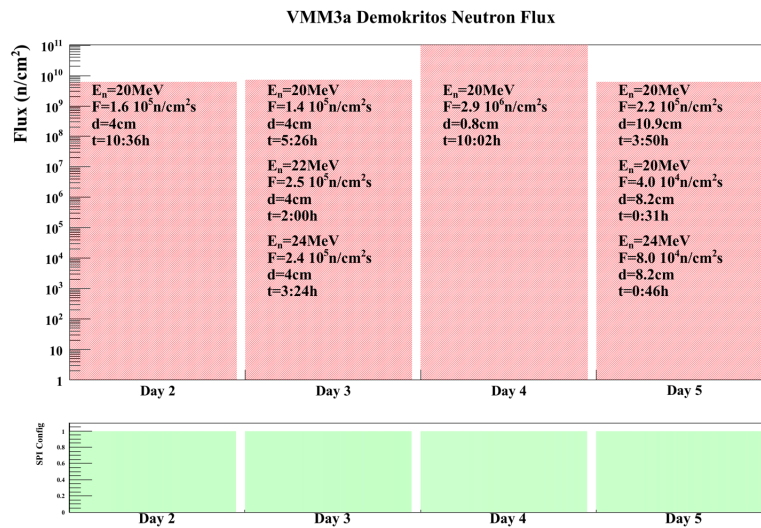


Figure 3.17: An overview representation of the VMM3a Neutron Irradiation test. The total neutron flux is shown as a function of the testbeam day. In addition, the daily run's parameters (energy, current, flux, and duration) are shown.

In Figure 3.18, the Day 2 neutron fluence is presented as a function of the board/ASIC distance, along with the experimental setup for the same day.

Additionally, neutron fluxes were measured and verified by analyzing an activated  $^{115}\text{Id} + ^{197}\text{Au}$  foil that was exposed for 12 hours during a run. The neutron rate was monitored using a  $BF_3$  neutron counter, as illustrated in Figure 3.19. The neutron rates remained constant over time during long runs.

## Results

In this comprehensive study, the VMM3&VMM3a, integrated into the Mini-1 board, underwent rigorous testing under a precisely defined 20, 22, 24 MeV neutron beam at various positions and fluence rates.





links individually between Front-end electronics and software processes on the network. It also distributes the TTC signals, including the LHC Bunch Crossing clock, to all the NSW electronics. FELIX provides a common platform for some ATLAS Phase-1 subsystems and will do so for all ATLAS subsystems in Phase-2. For Phase-1, there are 60 FELIX FPGA boards in 30 servers. Phase-2 requires 40 additional boards (based on 24 input links per FPGA). Although the Phase-2 fibres reach USA15, the Phase-2 FELIX boards and servers will not be installed until Phase-2.

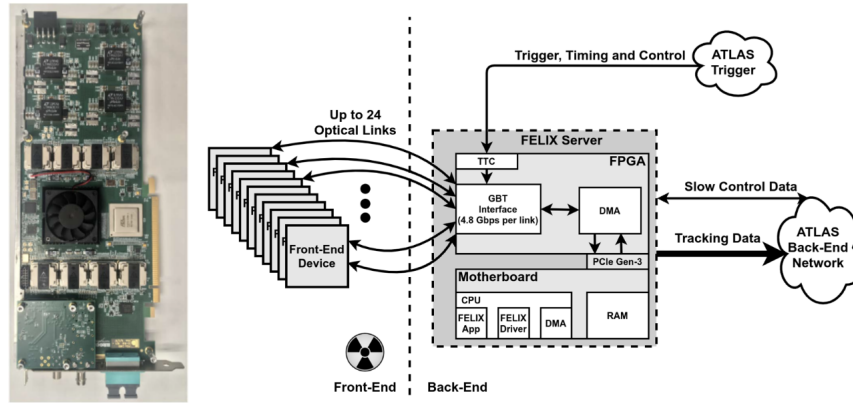


Figure 3.20: Left: The FELIX BNL712 FPGA board, which the NSW will use for its needs. It features a Xilinx® Kintex Ultrascale XCKU115 FPGA, a PCIe connector to interface with the CPU and the back-end network, and an optical coupler supporting up to 24 links. A dedicated mezzanine board receives the reference clock and the trigger information from the ATLAS TTC system. Right: FELIX and its relationship with other parts of the DAQ system.

### 3.5 GBTX

The GBTX is a radiation tolerant chip that can be used to implement multipurpose high speed (3.2–4.48 Gb/s user bandwidth) bidirectional optical links for high energy physics experiments. Logically the link provides three ”distinct” data paths for TTC, DAQ and Slow Control (SC) information. In practice, the three logical paths do not need to be physically separated and are merged on a single optical link as indicated in Figure 3.21. The aim of such architecture is to allow a single bidirectional link to be used simultaneously for data readout, trigger data, timing control distribution, and experiment slow control and monitoring. This link establishes a point-to-point, optical, bidirectional (two fibres), constant latency connection that can function with very high reliability in the harsh radiation environment typical of high energy physics experiments at LHC. The

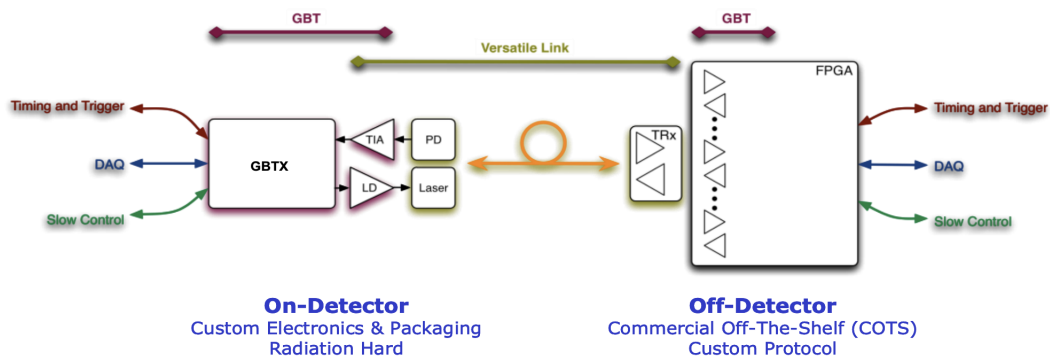


Figure 3.21: Link architecture with the GBT chip set and the Versatile Link optocomponents. [53]

development of the proposed link is conceptually divided into two distinct but complementary parts: the GBT

link chips and the Versatile link opto components. The versatile link selects and qualifies appropriate fibres and opto-electronic components for use in radiation. The GBT develops and qualifies the required radiation hard ASICs. Embedded in the experiments, the receivers and transmitters are implemented by the GBT chipset and the Versatile Link optoelectronic components. This architecture clearly distinguishes between the counting room and front-end electronics because of the very different radiation environments. The on-detector front-end electronics works in a hostile radiation environment requiring custom made components. The counting room components operate in a radiation free environment and can be implemented by COTS components. The use of COTS components in the counting house allows this part of the link to take full advantage of the latest commercial technologies and components enabling efficient data concentration and data processing from many front-end sources to be implemented in very compact and cost efficient trigger and DAQ interface systems. The GBTX ASIC is part of the GBT chipset composed of the following chips: a GBTIA, a GBLD, a GBT-SCA and the GBTX link ASIC that implements all the needed functions of the data and timing transceiver. The GBTX is a highly flexible link interface chip with a large number of programmable options to enable its efficient use in a large variety of front-end applications:

- Can be configured to be a bidirectional transceiver, a unidirectional transmitter or a unidirectional receiver.
- Different front-end interface modes and options.
- Extensive features for precise timing control.
- Extensive Control and monitoring features.
- Very high level of error correction from SEU's and transmission errors.

The general architecture of the GBTX ASIC and its main external connections are displayed in Figure 3.22. In its generic configuration the GBTX connects to the GBLD laser driver ASIC and to the GBTIA transimpedance amplifier ASIC. The Clock and Data Recovery (CDR) circuit receives high speed serial data from the GBTIA. It recovers and generates an appropriate high speed clock to correctly sample the incoming data stream. The serial data is then de-serialized (that is converted in parallel form) and then DECodeD, with appropriate error corrections, and finally DeSCRambled (DSCR). This will sometimes be referred to as the 'downlink'. In the transmitter part the data to be transmitted is SCRambled (SCR), to obtain DC balance, and then encoded with a Forward Error Correction (FEC) code before being serialized and sent to the GBLD laser driver. This will sometimes be referred to as the 'uplink'. The configuration of the GBLD can be performed via a simplified "I2C-Light" connection from the GBTX. A clock manager circuit takes care of generating and manage the different high speed and low speed clocks needed in the different parts of the GBTX. A programmable Phase Shifter is available to generate 8 external user clocks with programmable frequency and phase. An external clock or an on-package crystal oscillator is used during start-up as a locking aid for the CDR circuit and as a clock reference for the ASIC watchdog circuit. General control and monitoring logic takes care of controlling the different parts of the chip according to the operation mode selected and the ASIC configuration information. Initial configuration information is taken from the on chip e-Fuses that can then be modified via the optical link itself or via an I2C slave interface. A JTAG interface is available for boundary scan. Connections to the front-end modules or ASICs are made through sets of local Electrical Links (E-Links). Depending on the data rate and transmission media used, E-Links allow connections that can extend up to a few meters. E-Links use Low Voltage Differential Signaling, with signal amplitudes that are programmable to suit different requirements in terms of transmission distances, bit rate and power consumption. The E-Links are driven by a series of ePorts on the GBTX and are associated with E-link ports in the front-end modules. The number of active E-Links and their data rate are programmable (see chapter 3 for further details). Parallel front-end interfaces with different bit widths are valid sub-sets of the flexible E-Links.



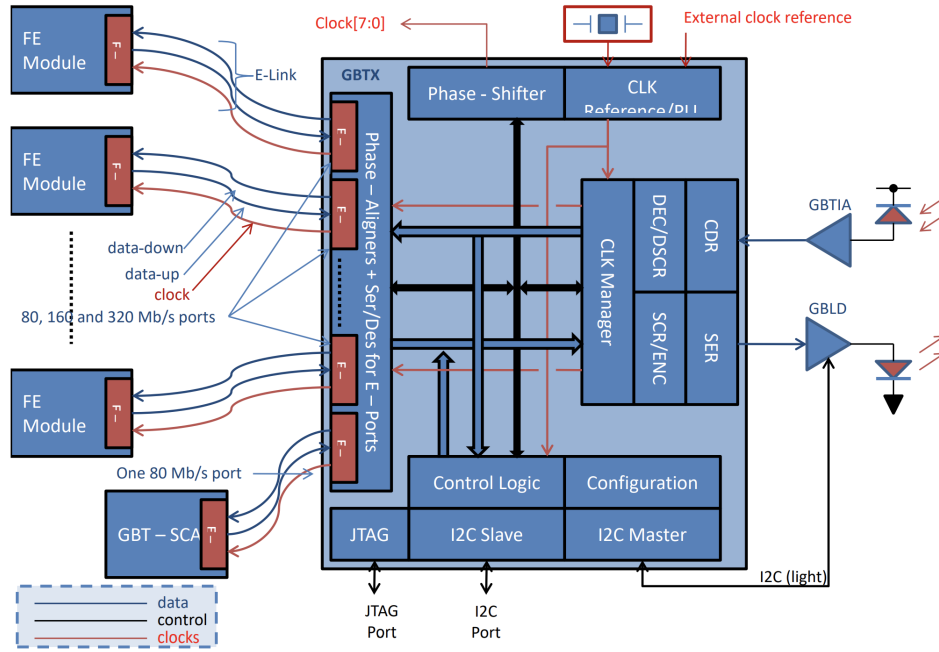


Figure 3.22: GBTX architecture and interfaces. [50]

### 3.6 GBT-SCA

The GBT-SCA ASIC [32] is an integrated circuit designed using a commercial 130 nm CMOS technology. It plays a crucial role as part of the GBT chipset, dedicated to the distribution of control and monitoring signals to the front-end electronics integrated into the detectors. The GBT-SCA establishes connection with the GBTX ASICs through an 80 Mbps dual-redundant bidirectional data-link, known as the e-links.

Developed to accommodate diverse front-end ASIC requirements across various experiments, the GBT-SCA offers a range of user-configurable electrical interface ports. These ports facilitate concurrent data transfer operations, ensuring adaptability and versatility to meet the specific needs of different front-end ASICs in various experimental setups.

The SCA ASIC integrates the following interface channels:

- **16 I2C Master Serial Bus Channels:** The I2C channels offer individually programmable data transfer rates from 100 KHz to 1 MHz. They support 7-bit and 10-bit addresses, single-byte and multi-byte I2C bus transactions, and various transaction types (Read, Write, and Read/Modify/Write). Transactions are initiated by user commands and executed by the channel's state machines. Each channel can be disabled individually to conserve power during inactivity.
- **1 SPI Serial Bus Master Channel:** The SPI channel functions as a full-duplex synchronous serial bus master with a single transaction length of up to 128 bits. It supports transfer rates up to 20 MHz, implements standard SPI bus operating modes (00, 01, 10, and 11), and features 8 independent slave-select lines. The SPI channel is protocol-agnostic, and user-specific protocols are implemented in FPGA circuitry at the control room electronics. Power-down capability is available to conserve power.
- **1 JTAG Serial Bus Master Channel:** The JTAG channel supports bus transactions of up to 128 bits, with longer transactions possible through segmentation. It includes an asynchronous reset line with configurable pulse width. Similar to the SPI channel, the JTAG channel operates at frequencies from 156 KHz to 20 MHz, and the actual JTAG bus cycles are generated by FPGA circuitry at the control room electronics. Power-down functionality is also provided.
- **1 Parallel Interface Adapter (PIA) Channel:** The PIA channel features 32 General Purpose digital

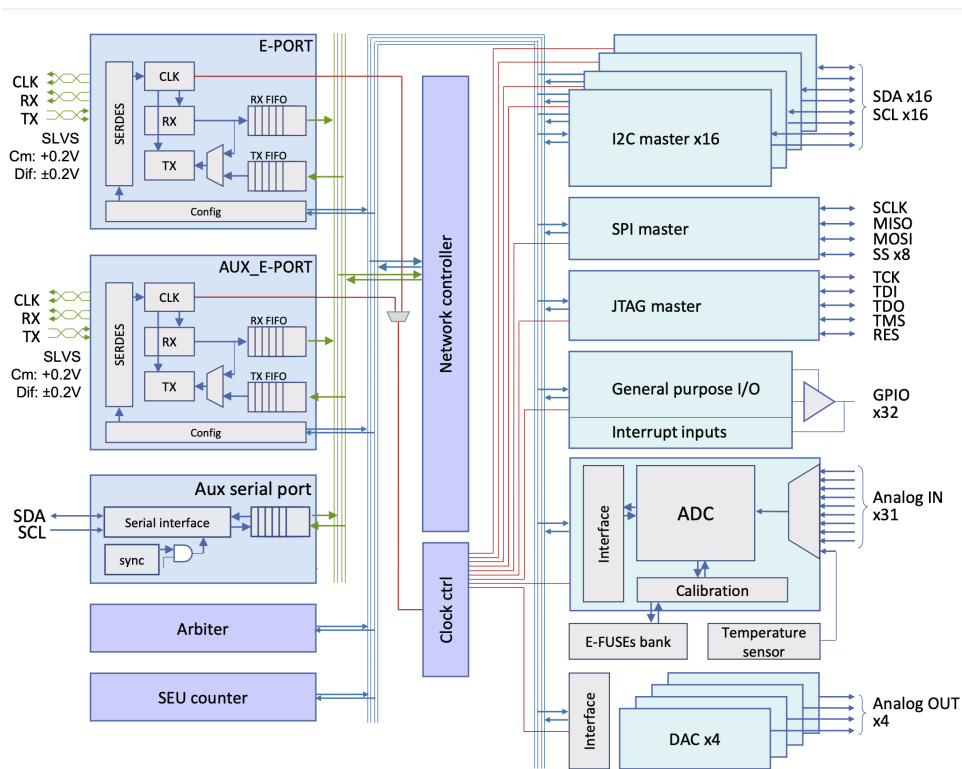


Figure 3.23: The GBT-SCA block diagram. [50]

IO lines, each individually programmable as input, output, or in tri-state mode. Input signals are sampled and registered at the rising or falling edges of the system clock or an external strobe signal. Any configured input line can generate an interrupt request to the control room electronics. The electrical levels on all digital IO lines are 0 V to 1.5 V.

- **31 ADC Channel:** The ADC channel incorporates 31 multiplexed analog inputs. It consists of a 32-input analog multiplexer connected to a 12-bit ADC. One input is internally connected to the embedded temperature sensor, and the remaining 31 inputs are available to the user. The ADC features a switchable 10  $\mu$ A current source, and its single-slope Wilkinson architecture ensures compatibility with slow-varying parameters. The analog input range is 0 V to 1.0 V, with a maximum conversion rate of 3.5 kHz and a maximum quantization error of 1 LSB. The ADC includes automatic offset cancellation and gain correction circuitry. The gain calibration coefficient, stored on the on-chip e-fuse bank, can be overridden by the user.
- **4 DAC Channels:** Four independent DAC channels with 8-bit resolution capable of generating voltage signals in the range of 0 V to 1.0 V.

The e-link port on the SCA ASIC implements a packet-oriented full-duplex transmission protocol based on the HDLC standard (ISO/IEC 13239:2002). The structure of the HDLC data packet is shown in Figure 3.24 and consists of the following components:

- **Frame Delimiter (SOF):** A frame delimiter character composed of six consecutive '1s.' The HDLC protocol employs the "bit-stuffing" technique to ensure the uniqueness of the frame delimiter character. A '0' is inserted in any sequence of five consecutive '1s' at the transmitter side, and this trailing '0' is stripped off at the receiver side.
- **Address Field:** An 8-bit address field.

- **Control Field:** An 8-bit control field containing frame sequence numbers of the currently transmitted frame and the last correctly received frame. It implements an acknowledgment handshake mechanism between the SCA and the control room electronics. The control field is also used to convey three supervisory level commands:
  - **CONNECT Command:** Instructs the SCA e-port to activate and receive data, deactivating the alternate redundant e-port simultaneously.
  - **RESET Command:** Resets the SCA e-port, its internal FIFOs, and state machines.
  - **TEST Command:** Sets the SCA e-port in loopback mode to facilitate link verification and debugging operations in the field application.
- **Data Payload Field:** A variable-length data payload field.
- **Frame Check Sequence (FCS) Field:** A 16-bit frame checksum field calculated over the address, control, and information field using the CCITT standard 16-bit CRC (Cyclic Redundancy Check).

All transmitted HDLC frames require the reception of HDLC response frames with positive acknowledgment. Bits within the frame are transmitted from the least significant bit first.

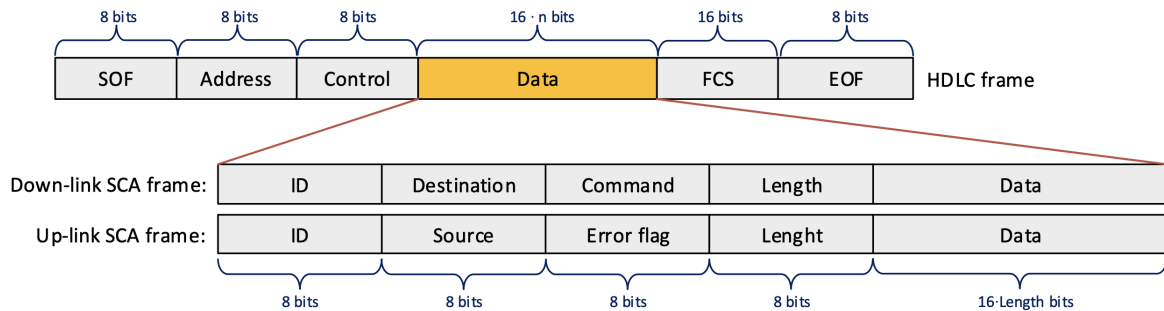


Figure 3.24: The structure of the HDLC data packet which the e-link port on the SCA ASIC implements a packet oriented full duplex transmission protocol.

## 3.7 Detector Resource Names

### 3.7.1 FELIX Resource Identifier

In this section, we explore the proposed architecture of the **FelixID** [54], shedding light on its structure, size, and the rationale behind each component. The **FelixID** itself is envisioned as a 64-bit-wide field, intricately divided into sub-fields, each dedicated to a specific system component, whether physical or logical. The allocation of bits to each sub-field is determined by the anticipated number of instances of that component within a singular instance of the parent field.

The development of the proposed **FELIX Identifiers** is anchored in several fundamental requirements and overarching objectives:

#### 1. Transparency in Internal Routing and Cabling:

- The internal routing and cabling of the **FELIX** system must seamlessly integrate with sub-detector traffic. Changes to the internal cabling should necessitate no additional bookkeeping or processing modifications on the part of the sub-detector.

#### 2. Global Uniqueness:

- FELIX Identifiers must be globally unique across the entire ATLAS system, ensuring that each identifier serves as a distinct and unambiguous label.

### 3. Query Interface for Link Services:

- Every FELIX system should offer an interface enabling clients to query and ascertain the specific links serviced by it. This information is denoted by FELIX Identifiers, contributing to an efficient and transparent communication infrastructure.

### 4. Flexibility for Evolution:

- Identifiers should exhibit flexibility to accommodate the dynamic evolution of sub-detector cabling and front-end electronics throughout their operational lifespan. This adaptability ensures resilience to changes and upgrades within the system.

By adhering to these guiding principles, the development of FELIX Identifiers aims to create a robust and scalable identification system that meets the intricate demands of the ATLAS project.

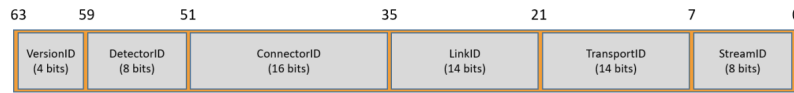


Figure 3.25: Structure of a complete FELIX Identifier (FID), with all sub-components indicated in logical order.

The FID comprises several distinct sub-components, each playing a crucial role in delineating and organizing the identifier space:

- **VersionID:** Reserved for the upper 4 bits of the **FelixID**, the **VersionID** is dedicated to denoting the revision. This allocation ensures the FID's capability to adapt to unexpected requirement changes gracefully.
- **DetectorID:** A unique identifier assigned to each sub-detector. This sub-component facilitates the differentiation and identification of individual sub-detectors within the FELIX system.
- **ConnectorID:** Serving as a counter, the **ConnectorID** signifies the specific trunk fiber under consideration. This counter aids in tracking and distinguishing between different trunk fibers within the system.
- **LinkID:** Assigned to differentiate between the various links delivered by each bundle, the **LinkID** sub-component plays a pivotal role in managing and organizing the multitude of links within the FELIX infrastructure.
- **TransportID:** This component demarcates the different E-links within the GBT link. The **TransportID** serves as a key identifier for the individual E-links, contributing to the efficient routing and handling of data within the GBT link.
- **StreamID:** Reserved for denoting a specific stream, the **StreamID** sub-component aids in the categorization and organization of data streams. It allows for a systematic approach to handling and processing data streams within the FELIX system.

The segmentation of the FELIX Identifier into these distinct sub-components ensures a structured and efficient organization of the identifier space, enabling seamless communication and identification within the ATLAS project.

	63..60	59..52	51..36		35..22		21..8		7..0	
<b>Field</b>	Version	DetectorID	ConnectorID		LinkID		TransportID		StreamID	
<b>Width</b>	4	8	16		14		14		8	
<b>Sub-field</b>			Trunk-ID (1.8)	MTP24 ID (1..12)	V	LinkID	E-link	Dir	Protocol	
<b>Sub-width</b>			8	8	1	13	6	1	7	

Figure 3.26: The format of the 64-bit FID for NSW.

## NSW FID

The format of the 64-bit FID for NSW is:

The **TrunkID** and **MTP24-ID** fields within the **ConnectorID** are specific to the NSW subsystem. These fields hold information tailored to the NSW configuration.

The **E-link** field corresponds to the low bit of the E-link in the 80-bit GBT word, divided by 2. For instance, for  $EC = 112/2 = 56$  and  $IC = 114/2 = 57$ . This aligns with the conventions used in the **-I** option of the **fupload** and **felink** commands, with the exception of the factor of 2. The rationale behind this design choice is to avoid defining a connection path using an E-link definition that includes the E-link width. This is crucial because the same GBTx E-link input pin may be configurable for different speeds/widths. The speed/width and other attributes of the E-link are exclusively defined by **elinkconfig** and should not be duplicated in multiple places.

For example, the E-link whose data starts at bit 0 (denoted as **-I 0**) can be configured as a 2, 4, or 8-bit E-link without necessitating any alterations to physical connections. Additionally, **V=1** signifies virtual E-links, **Dir=1** denotes To-FrontEnd links, **Protocol=0** corresponds to GBTx links, and **StreamID=0** represents a specific StreamID.

### 3.7.2 NSW Naming Scheme

Proposed here is a geographical or logical naming scheme for NSW data sources and destinations. In this subsection, the data sources and destinations are referred to as "Detector Resource Names" [54]. Detector Resources, such as sROC's on FEB's, SCA's on FEB's, and other boards, map to E-links. Detector Resource Names allow subscribing to E-links by names that reflect their functional position in the NSW detector. This is facilitated by using a FID and two databases, as described below:

- A mapping between Detector Resource Names to the fiber bundle (an MTP-24) from underground identified by a visible label, the fiber number in the bundle, and the E-link on that fiber. The detector group populates and maintains this database.
- A mapping between the FID (MTP-24 fiber bundle) and a particular FELIX server, FELIX FPGA board, and the optical connector on the FPGA board to which the fiber bundle is connected. TDAQ populates and maintains this database.

For NSW, the names of the possible locations and attributes are shown in the table below. To the right of each are shown its possible values.

Detector Resource names are a string of location and attribute values, separated by "/"s. For example: "MM-A/V0/L1A/strip/S4/L3/R11/E3" refers to L1A data from Micromegas, Version 0, Endcap A, strips, Sector 4, Layer 3, Radial position 11, sROC 3. All the numbers start from 0, preserving coherency with numerical representation. In other words, sector numbers, for instance, are in the interval 0-15, corresponding to sectors 1-16 in the usual ATLAS "Enumeration by the human eye". So, sector 4 in the example corresponds to sector 5 in that enumeration.

The Detector Resource Name string should be used to identify OPC-UA SCA endpoints in the OPC-UA SCA XML configuration file, i.e., the value of the **OpcNodeId** field. In preparation of the configuration file, the

# bits	attribute	abbrev	Possible values							
8	DetectorID		MM-A: 0x6b	MM-C: 0x6c	sTGC-A: 0x6d	sTGC-C: 0x6e				
3	version	V	0x0							
1	reserved									
3	data-type		L1A: 0	Monitor: 1	to-SCA: 2	from-SCA: 3	TTC: 4	L1Ainfo: 5	Ext: 6	Exc: 7
3	resource-type	T	Pad FEB: 0	Strip FEB: 1	Trig Proc: 2	Pad Trig: 3	L1DDC: 4	ADDC: 5	Router: 6	Rim-L1DDC: 7
4	sector	S	0..15							
3	layer	L	0..7							
4	radius	R	sTGC: 0..2	MM: 0..15	Rim-L1DDC: A/P		MM L1DDC: E/O		sTGC L1DDC: P/S	
3	E-link	E	sROC0..3	Rim-L1DDC SCA: 0/1 (prim/aux)						

32

Figure 3.27: Description of the possible locations and attributes for the NSW Detector Resource Name.

Detector Resource Name will be translated to an FID and stored in the XML configuration file. This means that the value of the `OpcServerIp` field is not hard-coded in the file but rather the OPC-UA client should use the FID to look up the OPC server's IP address and connect to the standard OPC server port.

### 3.7.3 OKS Overview

The Object Kernel Support (OKS)[55] is a robust library designed to facilitate a straightforward, active, and persistent in-memory object manager. Tailored for applications that necessitate the creation of persistent structured information with rapid access, OKS provides a flexible framework that does not require the complexity of a full-fledged database system. This library finds its applications as the backbone of configuration databases and real-time object managers in Data Acquisition and Detector Control Systems, particularly in areas such as setup, diagnostics, and general configuration description.

OKS operates based on a comprehensive object model that encompasses support for various key features, including objects, classes, associations, methods, inheritance, polymorphism, object identifiers, composite objects, integrity constraints, schema evolution, data migration, and active notification. Class definitions and instances are stored in portable XML files, fostering portability and ease of management. OKS further enriches its capabilities by providing query facilities, complete with indices support.

The library exposes a powerful C++ API (Application Program Interface) and includes Motif-based GUI applications for designing class schemas and manipulating objects with utmost convenience.

### 3.7.4 OKS Implementation in NSW

In the context of the NSW project, OKS is instrumental in managing crucial information related to Detector Resource Names and FIDs. These details are stored in dedicated OKS files, exclusively earmarked for the NSW. Accessible through the ATLAS Technical Network (ATCN) via the ATLAS Gateway (atlasgw), these files are consistently available through the corresponding ATLAS Control room desk, in this case, the Muon Desk.

The OKS files are organized under the relevant TDAQ release version, specifically located at:

```
/atlas/oks/tdaq-09-04-00/muons/segments/NSW/ELinks/
```

Each XML file is structured per sector and per detector technology, adopting a naming convention such as:



NSW-ELinks-sTGC-C-S2.data.xml

Within each XML file, detailed information pertaining to each board is documented. For the Signal Conditioning and Acquisition (SCA) path, each board's SCA is delineated into two paths: the receiver (from-SCA or RX) and the transceiver (to-SCA or TX). Each SCA RX/TX is represented by an XML object class known as `SwRodInputLink`, encompassing attributes such as:

- **FelixId:** This unique FELIX ID, described in a preceding section, is a *u64* hex value containing FELIX connectivity information.
- **DetectorResourceId:** This attribute denotes the unique ID corresponding to the specific board's object, represented as a *u32* hex value.
- **DetectorResourceName:** A unique string value that signifies the resource name for the particular board's object.

A concrete example of an SCA object for the L1DDC board is provided in Appendix C. By combining the RX and TX `FelixId` values, one can construct the complete FELIX address of the `sTGC-A/V0/SCA/L1DDC/S0/L0/P` object.

If you have more text you'd like to improve or expand, feel free to provide it!

## 3.8 SCA Ecosystem

The software package[56] plays a critical role in providing a level of abstraction and a versatile interface to handle all communication channels within the SCA. This software leverages the inherent hardware parallelism among independent channels. To ensure reliability, the software undertakes essential bookkeeping for synchronous communication and transaction tracking.

One of the paramount requirements is achieving optimal performance and minimal latency. This necessitates incorporating features like request grouping to execute time-consuming operations, such as FPGA programming, which involves transferring substantial data over the Joint Test Action Group (JTAG). Given the extensive use of SCAs in detector systems, scalability is a crucial design consideration. Simultaneously, tasks related to monitoring and control demand exceptionally high availability, approaching 100%, emphasizing the need for robustness.

The software must exhibit adaptability to diverse communication scenarios within the SCA framework. This includes support for a simulated chip, as well as communication interfaces for prototype board interactions during development and testing phases. In the context of the final production system, the SCA software establishes a crucial interface with the optical link receiver system, FELIX, through a dedicated communication link known as `netIO`. This comprehensive approach ensures that the SCA software is not only performance-driven but also flexible and resilient, catering to the multifaceted demands of large-scale detector systems. The SCA Ecosystem, illustrated in Figure 3.28, is composed of the following key components:

- **SCA Software[57]:** This encompasses the SCA Software API designed for communication with the SCA through various back-end interfaces.
- **SCA OPC UA Server [58]:** Serving as the middleware of choice, it facilitates the exchange of data with the front-end systems.
- **SCA Simulator:** This middleware option is employed for data exchange with the front-end systems, providing a simulation environment.
- **UaoClientForScaOpcUa [59]:** A library enabling clients to establish communication with the SCA server.
- **fwSca [60]:** This module plays a crucial role in automating the integration of server data into SCADA systems.



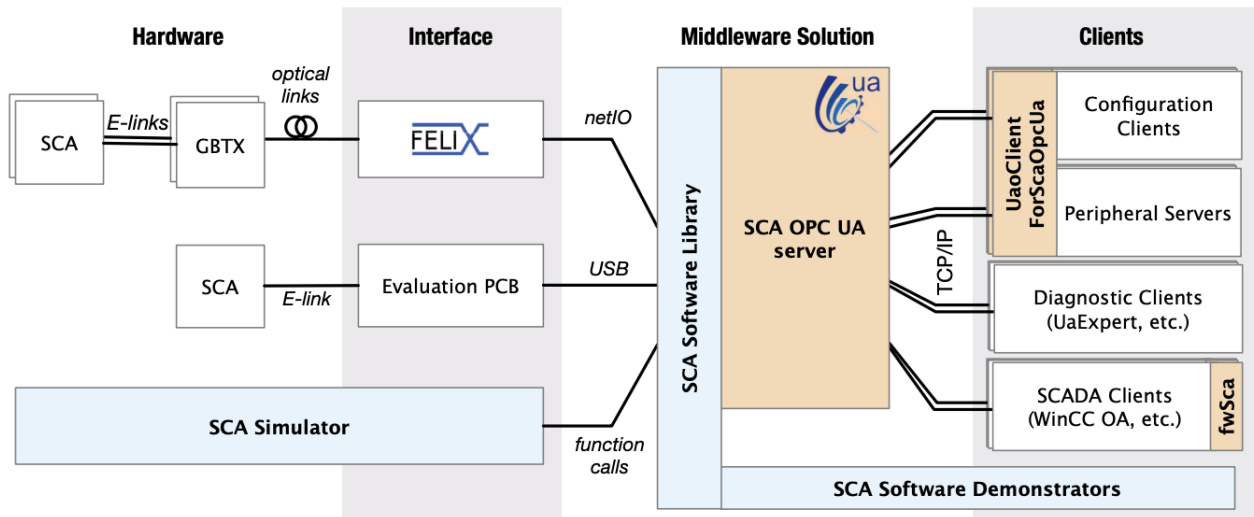


Figure 3.28: Overview of the SCA Ecosystem.

### 3.8.1 Software

The SCA Software package encompasses a core library organized into modules that implement the requisite functionality across various layers. This library has been developed with the intent of providing flexibility and easy adaptability to a myriad of systems, facilitated by its polymorphic HDLC back-end. The software architecture of this library is elucidated in the block diagram presented in Figure 3.29.

Furthermore, within the SCA Software package, Demonstrators play a pivotal role. These tools directly leverage the library and serve a dual purpose: testing the functionality and conducting low-level diagnostics. As an integral component of the package, an SCA Simulator has been developed. This simulator possesses the capability to generate SCA traffic, replicating realistic SCA behavior. This functionality proves invaluable, allowing for seamless development and testing procedures in the absence of physical hardware. The HDLC

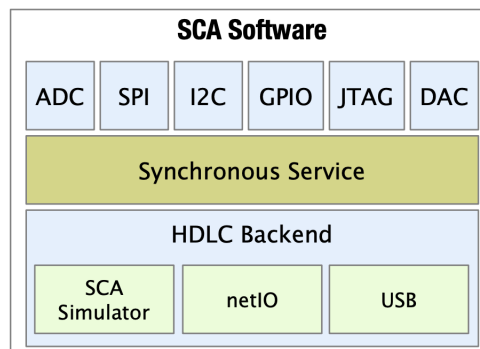


Figure 3.29: The SCA Software Library stack.

back-end within the SCA Software package serves as a versatile software abstraction of the backend infrastructure. Designed with polymorphism in mind, it accommodates diverse existing back-end implementations, originally crafted for netIO (specifically tailored for FELIX-based systems), ScaSimulator, and the SCA evaluation board via USB. This HDLC back-end operates independently of the actual SCA data provider, providing a unified and polymorphic interface for sending requests and subscribing to replies.

This abstraction layer streamlines the handling of payload and establishes a standardized addressing scheme across various back-ends. The synchronous service component is pivotal, managing transaction tracking, time-out handling, and crucially, synchronization for multiple threads accessing the same SCA. It ensures full

concurrency among SCA channels.

The SCA communication interfaces library, another integral part of the SCA Software package, serves as a high-level abstraction library. It facilitates the control of user interface ports and the configuration of the ASIC. Users can execute complex operations, such as SPI/I2C configuration of an ASIC or programming a Xilinx FPGA via JTAG, through simple API calls.

Additionally, the SCA Software package incorporates standalone low-level tools known as Demonstrators. These tools leverage the SCA API to perform independent operations, like I2C write/read or ADC monitoring. Demonstrators serve multiple purposes, acting as debugging and diagnostic tools while also providing illustrative examples of SCA API usage, such as SPI configuration for a specific ASIC.

### 3.8.2 Quasar Framework

The Quasar (Quick OPC-UA Server Generation Framework)[61] stands as a robust OPC-UA server generation framework within the software landscape. This project encompasses a comprehensive software ecosystem designed to offer OPC-UA support for distributed control systems. Leveraging Quasar, developers can model, generate, and optimize OPC-UA servers, streamlining the development, deployment, and maintenance phases. The framework extends its utility by enabling the generation and publication of OPC-UA client libraries for end-users, fostering client-server chaining for enhanced flexibility.

Quasar has been employed to construct OPC-UA servers across diverse computing platforms, ranging from conventional server machines to compact credit-card computers and even system-on-chip solutions. The servers generated by Quasar exhibit versatility as they can seamlessly integrate into other software projects written in higher-level programming languages such as Python. This integration facilitates efficient OPC-UA information exchange within a control system.

One of Quasar's notable strengths is its compatibility with various OPC-UA stack implementations, making it an adaptable solution for both free and open-source contexts and commercial applications. In the context of distributed control systems, where seamless data transfer between system components is imperative, Quasar serves as an essential middleware solution. Its capabilities make it particularly well-suited for integration into control systems based on the WinCC-OA SCADA platform, offering quick and efficient OPC-UA server integration.

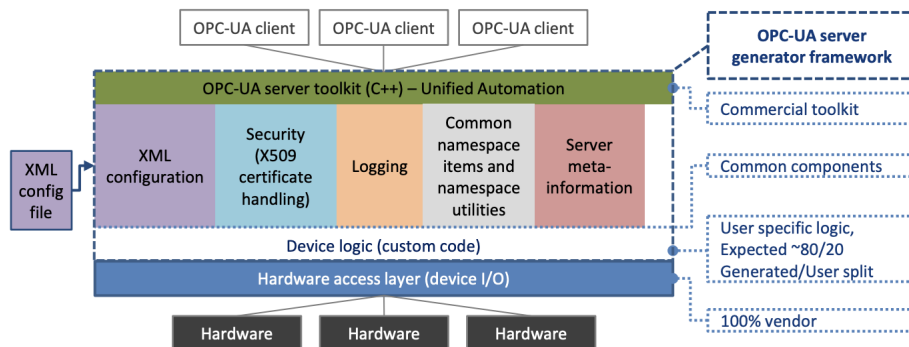


Figure 3.30: Overview of the quasar generic server framework components.

The DCS exemplifies a distributed control system, intricately organized as a hierarchical mesh of diverse components. The middleware chosen to navigate this complexity must be versatile, portable, and high-performing. For the ATLAS DCS, the OPC Unified Architecture (UA) has emerged as the standard middleware for device integration. This selection is primarily attributed to UA's object-oriented design and platform independence, which aligns well with the system's diverse data models.

To streamline development and minimize maintenance costs, a unified approach is adopted in creating UA servers for various device types within the ATLAS DCS. Identifying common functionality across identical

software parts, such as server startup code and logging implementation, has contributed to more efficient development practices. A pivotal realization is that considering the data model as a parameter of a generalized UA server can significantly reduce development efforts. This data model, enriched with additional information, is termed a "design." With a sufficiently rich design format capable of describing complex subsystems, a substantial portion of a UA server implementation can be automatically generated. Handwritten custom code, referred to as "device logic," becomes essential for providing high-level business logic and handling specific subsystem types, like hardware access libraries or protocol implementations.

The layered structure of quasar is illustrated in Figure 3.30, providing context for the different layers. Access to controllable devices or systems occurs through their specific access layer, often supplied with the respective device. The device logic layer serves as the interface with the higher-level layers of quasar, comprising various modules that address different functional aspects. The address space module, situated on the UA end of the server, exposes data to UA clients and is implemented using a commercial UA SDK. A configuration module facilitates address space and device instantiation, leveraging XML as the configuration format backed by XML schema definitions. A generator (xsd-cxx) translates XML schemas into C++, producing actual instances from configuration files. An additional subsystem named 'calculated items,' operating within the address space, allows for the creation of new variables derived from existing ones using mathematical functions.

Quasar also includes optional modules like component-based logging, certificate handling, server metadata, and embedded Python processing, enhancing its versatility and functionality.

### 3.8.3 OPC UA Server

The implementation of the SCA OPC UA server leverages the quasar framework, a powerful tool for the efficient creation of OPC UA servers that streamlines the development process. The SCA OPC UA server maximizes the capabilities provided by quasar, including features like calculated variables, various types of variables, methods, and advanced threading mechanisms. The server architecture is designed to categorize SCA channels into device classes, each corresponding to specific hardware functions such as I2C or ADC interfaces.

In addition to the device classes, a Global Statistician module has been developed to aggregate and measure general statistics across the entire setup, exposing these metrics to clients. Furthermore, an SCA Supervisor software module is implemented to monitor the system's state and provide supervisory functionalities, including automatic recovery from communication losses with SCAs, SCA ID validation, and other administrative tasks.

The structure of all quasar classes employed in the server is outlined in the quasar design diagram depicted in Figure 3.31. To accommodate applications from different domains that need access to the same SCA system for distinct purposes, the general SCA OPC UA server functions as a centralized hub for data flow and synchronization. Simultaneously, specialized applications are decentralized (as illustrated in Figure 4.12), ensuring manageable maintenance, dividing responsibilities among different communities, facilitating staging for higher-level wrapper applications, and enabling interoperability between diverse clients. To facilitate the operation of the SCA OPC UA Server, users are required to provide an XML file that comprehensively describes all potential SCA connections utilizing the object types outlined in Figure 3.31. The construction of these SCA OPC UA XML files will be elaborated upon in the subsequent section.

### 3.8.4 OPC UA Clients

To facilitate the implementation of the concept, a dedicated C++ library, `UaoClientForOpcUaSca`, has been generated using the quasar framework. This library serves the purpose of constructing specialized OPC UA clients on demand. By leveraging the information derived from the design of the SCA OPC UA server, this library provides a comprehensive interface to establish seamless communication with the server.

Applications within ATLAS benefit from this library, particularly in the form of Trigger/DAQ OPC UA clients employed for configuration purposes. Additionally, peripheral servers make use of this library to execute

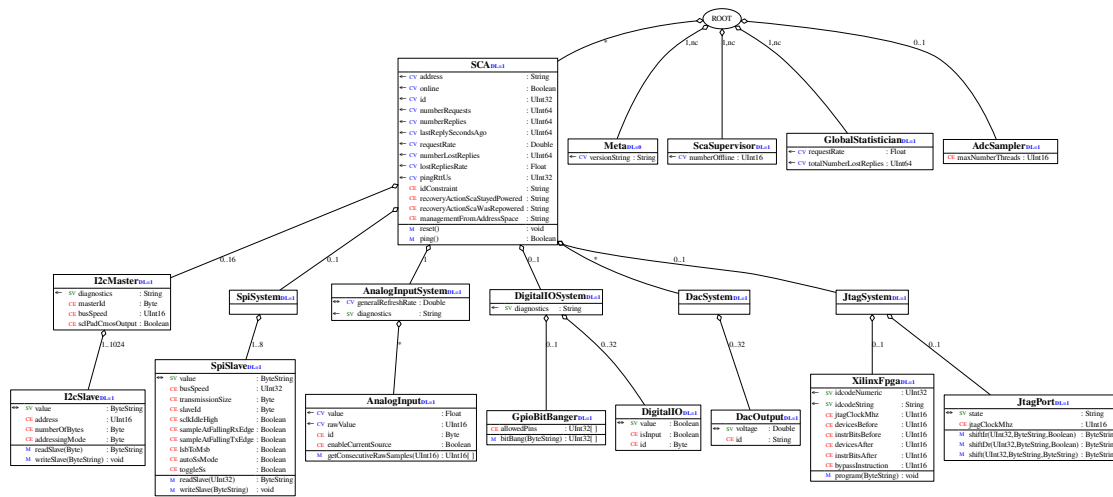


Figure 3.31: The quasar design diagram of SCA OPC UA server.

higher-level operations specific to sub-detectors. The overall architecture of the OPC UA SCA server, along with an illustrative example of an SCA OPC UA client utilizing this library, is presented in Figure 3.32.

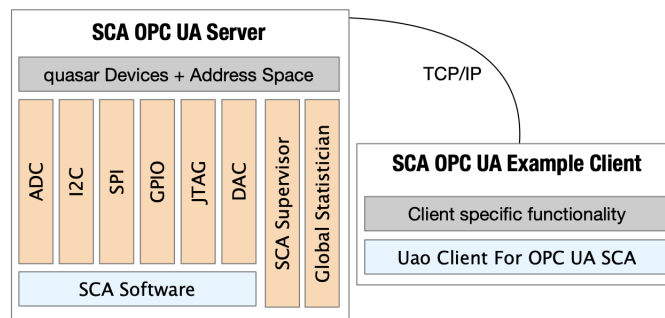


Figure 3.32: The SCA OPC UA stack.

The server provides flexibility by accommodating the use of general-purpose test clients for diagnostic purposes, exemplified by tools like UaExpert. Furthermore, the prevalent mode of interaction with an OPC UA server within the DCS is through SCADA WinCC-OA based systems. These systems employ OPC UA clients to establish connections with servers, fetching data and presenting it through a user interface. Typically, this interface is deployed in a counting room where system monitoring is overseen by a designated shifter. For WinCC-OA, the OPC UA connectivity is facilitated through a dedicated module, fwSca. This module is constructed using code generated by quasar tooling and is an integral part of the SCA software suite. It expedites integration by generating all the essential configuration on the WinCC-OA side, leveraging prior information about the SCA OPC UA information schema.

### 3.9 SCA Connections

The primary function of the SCA is to distribute control and monitoring signals to the front-end electronics integrated into the detectors. As outlined in the preceding section, the SCA encompasses the following electrical interface ports:

- ADC
- GPIO

- I2C
- JTAG
- DAC

In the context of the NSW project, these diverse interfaces serve distinct purposes for various chips. The subsequent subsection will delve into the specific SCA configurations for each board, elucidating the contentions[54] associated with each. The schematics for the NSW boards can be found in Appendix B.

### 3.9.1 SCA OPC UA XML

For the operation of the SCA OPC UA Server, the user needs to feed the server with the corresponding XML file which describes the SCA object(s). As is shown in Figure 3.31, the XML must contain the board's active SCA connections:

- AnalogInputSystem with the corresponding AnalogInput objects
- DigitalIOSystem with the corresponding DigitalIO objects
- SpiSystem with the corresponding SpiSlave objects
- I2cMaster with the corresponding I2cSlave objects
- JtagSystem with the corresponding XilinxFpga objects

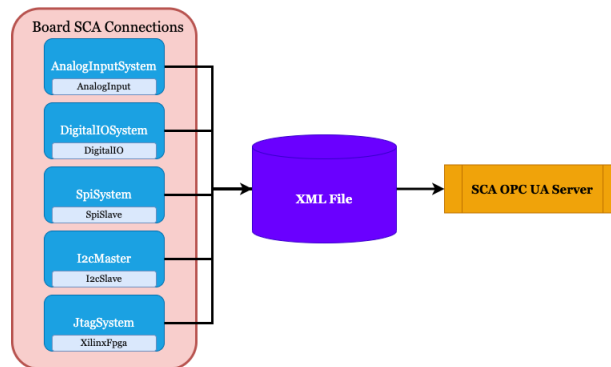


Figure 3.33: SCA connections of the Router board.

Thus, in the following subsections the procedure in order to construct and generate the SCA OPC UA Server XML files will be described in details.

#### SCA Template

Given that the NSW project comprises nine distinct boards (MMFE8, SFEB, PFEB, ADDC, L1DDC-MMG, L1DDC-STG, Rim L1DDC, Pad Trigger, and Router), a total of nine unique SCA templates were designed. These templates serve as XML references in the primary SCA OPC UA Server file. The dedicated directory housing these SCA templates resides under the MUO DCS directory, precisely at:

```
/det/dcs/Production/ATLAS_DCS_MU0/muoNswEltxScaOpcConfigTemplates/SCA_*.xml
```

For example, the SCA template of the L1DDC-MMG is shown in Appendix C.

The AnalogInputSystem block provides a detailed description of the SCA connections associated with AnalogInput functionalities. The parameter "generalRefreshRate" (OpcUa\_Double) signifies

the refresh rate in Hz. All channels within this particular SCA undergo refreshing at this specified rate. A value of zero indicates that ADC refreshing is disabled for this specific SCA. The "id" (OpcUa\_Byte) within AnalogInput represents the analog channel number, ranging from 0 to 31 inclusive. Notably, channel 31 is hardware-mapped to an internal temperature sensor. The "name" in AnalogInput denotes the user-inputted name of the corresponding parameter. Additionally, "enableCurrentSource" (OpcUa\_Boolean) in AnalogInput defines whether to enable the current source during ADC conversion.

CalculatedVariable, as a "synthetic" variable derived from other "real" variables in the address space, can be declared under any object in the configuration file. The "name" of CalculatedVariable is the last part of the address, while the "value" represents the analytical formula for calculating the variable. It's noteworthy that "applyGenericFormula" in CalculatedVariable allows the use of predefined formulas defined in other template XML files.

Next, I2cMaster serves as the parent class for I2C slaves. The "masterId" (OpcUa\_Byte) within I2cMaster designates the I2C master channel of the SCA (I2Cx), ranging from 0 to 15. "busSpeed" (OpcUa\_UInt16) represents the programmable data transfer rate of the I2C bus, with possible values including 100, 200, 400 and 1000 kHz. "sclPadCmosOutput" (OpcUa\_Boolean) in I2cMaster defines the SCL mode of operation. For the false case, the SCL pad operates as open-drain, where SCL value equal to 0 forces the SCL line to DGND, and SCL value equal to 1 places the SCL line in high impedance.

Moving on to I2cSlave, "addressingMode" (OpcUa\_Byte) denotes either 7 for 7-bit addressing mode (default) or 10 for 10-bit addressing mode. "address" (OpcUa\_Byte) is the I2C slave address, allowing values between 0-127 for 7-bit addressing mode. "numberOfBytes" (OpcUa\_Byte) in I2cSlave signifies the option for single-byte or multi-byte I2C read/write bus operations. The "numberOfBytes" is also indicative of the I2C slave address.

Since the SCA template have been constructed, it can be referenced in the final SCA OPC UA XML file as:

```
<!ENTITY SCA_PFEB SYSTEM "/det/dcs/Production/ATLAS_DCS_MU0/muoNswEltxScaOpcConfigTemplates/SCA_L1DDC.xml">
```

### SCA XML Object

The main part of the SCA OPC UA Servers consists of the SCA objects, as shown in Appendix C. The SCA object is characterized by the following attributes:

- **address:** The address of the given SCA follows the ScaSoftware convention. The generic form is `netio-next://fid/felixIdTx/felixIdRx` to connect using FIDs to Felix-star using FIDs `felixIdTx` for the FromHost direction and `felixIdRx` for the ToHost direction (both treated in hex, e.g., 0x16d1801001800000). It also supports:

`simple-netio://direct/felixhost/port1/port2/mlink` to directly connect to Felix-core on host `felixhost`, FromHost port `port1` (often 12340), ToHost port `port2` (often 12345 or 12350), and Elink (treated in hex, e.g., "3F").

- **name:** The name is provided by the NSW following the Detector Resource Name, which has been described in the previous subsections and is archived inside the OKS lists.
- **idConstraint:** Any value other than "dont\_care" will enforce a check against the connected SCA ID. The connected SCA will not be accepted (and its initialization will be periodically retried) until the values match.
- **recoveryActionScaStayedPowered:** Specifies what to do after communication to the given SCA is recovered, and it seems that the SCA itself stayed powered (i.e., it hasn't lost its settings).

- **recoveryActionScaWasRepowered:** Specifies what to do after communication to the given SCA is recovered, and it seems that the SCA itself lost power (i.e., it lost its settings).
- **managementFromAddressSpace:** Defines how to treat calls to the reset method in the SCA's address-space.
- **&SCA\_XXXX:** Refers to the referenced SCA template.

## 3.10 XML Generator

The subsequent pivotal phase in the process involves the automation of the generation of XML files for the NSW SCA OPC UA Server. To facilitate this, the **NswXmlGenerator** tool [62] was created, empowering users to produce the required XML files. Developed as a straightforward Python API, the tool allows users to generate SCA OPC UA Server XML files by providing inputs such as detector, side, and sector.

The primary files associated with the **NswXmlGenerator** tool are as follows:

1. **generateXML.py:** This is the main Python executable responsible for generating the SCA OPC UA Server XML. It coordinates all the different steps of the procedure to produce the final XML file.
2. **setEnv.sh:** This script sets the corresponding TDAQ release environment for both GPN and ATCN networks.
3. **setup.yml:** It contains information about various directories such as OKS, SCA Templates, felixSector JSON, and the XML path.
4. **felixSectorMapping.json:** A JSON-formatted file containing information about the FELIX/OPC host and port for all sectors of the MMG and STG detectors.
5. **src:** A folder containing various tools used by the main script. It includes general tools as well as OKS and XML-specific tools.
6. **tools:** A folder with various standalone tools designed for performing standalone actions or debugging various parameters.

Figure 3.34 shows the diagram of the **NswXmlGenerator** tool.

The analytical steps of the **NswXmlGenerator** tool are as follows:

1. **User Execution:**
  - The user executes the **generateXML.py** script, providing input arguments for the detector, side, and sector.
2. **Input Processing:**
  - The **generateXML.py** script collects user input, parses JSON and YAML files to retrieve required directories, and obtains the FELIX/OPC host and port mapping.
3. **SCA RX/TX Pair Collection:**
  - The tool gathers all SCA RX/TX pairs corresponding to the provided detector, side, and sector.



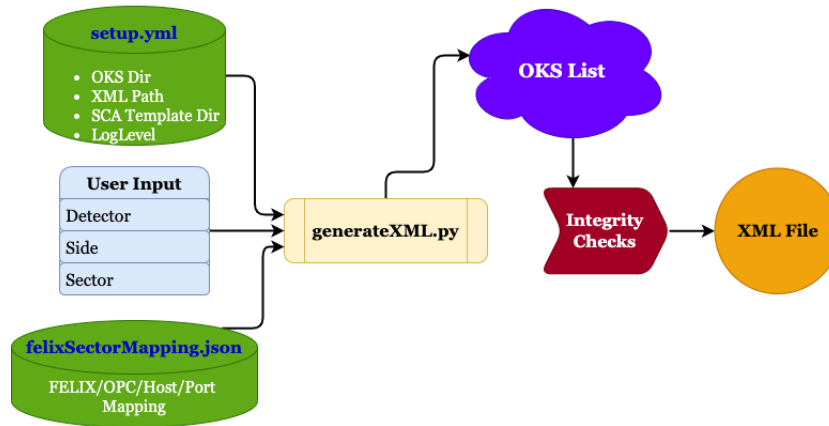


Figure 3.34: Block diagram of the NswXmlGenerator tool which is producing the SCA OPC UA Server XML files for the NSW .

#### 4. SCA Checks:

- Various checks are performed on the list of RX/TX SCAs, including duplication checks, consistency checks ensuring fromSCA and toSCA refer to the same object, verification that fromSCA and toSCA have the same number of parts divided by the separator '/', and a check for a specific number of board types per sector.

#### 5. Organizing SCA List:

- The tool organizes the SCA list with L1DDC sorting to display which boards are connected to the specific L1DDC.

#### 6. XML File Generation:

- The final SCA OPC UA XML file is produced by constructing various XML blocks. These blocks include the SCA reference template directories, the Git hash commit ID of the OKS lists, the log level, the ADC samples, and the list of SCA objects.

The final SCA OPC UA Server XML file name (as shown in Appendix C) contains the FELIX host and the port which the corresponding detector side sector SCA server is running:

ScaOpcUaServer\_pc-tdq-flx-nsw-mm-00\_48020\_MMG\_A1.xml

## 3.11 GPIO Bit-Banger

A significant challenge encountered with the frontend electronics of the NSW was the inability to read back the ROC's registers via the SCA's I2C. Despite the successful configuration of the ROC's registers via the SCA's I2C, a solution needed to be devised using low-level software tools. The resolution came from the Central DCS, primarily led by Paris Moschovakos, who leveraged the corresponding GPIO interface connected to the SCL and SDA lines of the ROC chip. Essentially, by employing a batch of grouped requests, a simulated I2C communication could be established, leading to successful reading of the ROC registers.

The newly designed tool, called **GPIO BitBanger**[58], is a crucial component of the **SCA OPC UA server**, enabling certain time-critical digital interfacing using GPIO. This module validates commands, considering the allowed pins declared in the server's configuration file. Upon invocation

(through method call), it prepares a batch based on the requested pins, values, and directions, forwarding it to the SCA while awaiting replies. The maximum number of requests in a batch is currently limited to 254 due to constraints imposed by `ScaSoftware`. The time-critical aspects of `GpioBitBanger` result from sending all SCA requests as a batch, expecting them to be treated as a block on their route via `netIO`, `felixcore`, DMA, up to the `FLX` card. It is important to note that while this feature is anticipated to work with any chosen SCA connectivity method (i.e., HDLC backend), its time-critical properties are expected to be available only with `netIO` HDLC backend and only from certain versions of `felixcore` and with specific versions of `FLX` firmware. The first step involves declaring a `BitBanger` module in the server's configuration XML file. The only required attribute is a name. The `GpioBitBanger` element must be declared as a child element of `DigitalIOSystem`. Following this, the pins that the `BitBanger` is allowed to use need to be declared.

```
<GpioBitBanger name="bitBanger">
  <allowedPins>
    <value>17</value>
    <value>18</value>
    <value>19</value>
    <value>20</value>
  </allowedPins>
</GpioBitBanger>
```

With the `BitBanger` now set up in the server, upon server start-up, we should observe the `BitBanger` providing information about the allowed pins, as illustrated below.

```
2019-11-19 10:40.01.189187 [DGpioBitBanger.cpp:77, INF, BitBanger] BitBanger: initializing!
2019-11-19 10:40.01.189225 [DGpioBitBanger.cpp:88, INF, BitBanger] BitBanger: Allowed GPIO pin 17
2019-11-19 10:40.01.189246 [DGpioBitBanger.cpp:88, INF, BitBanger] BitBanger: Allowed GPIO pin 18
2019-11-19 10:40.01.189271 [DGpioBitBanger.cpp:88, INF, BitBanger] BitBanger: Allowed GPIO pin 19
2019-11-19 10:40.01.189290 [DGpioBitBanger.cpp:88, INF, BitBanger] BitBanger: Allowed GPIO pin 20
```

The `BitBanger` interface is supported by the `UaoClientForOpcUaSca`. To leverage the `BitBanger` in the client, one should utilize the `IoBatch` library, which streamlines the usage of the `BitBanger`. Through `IoBatch`, all the fundamental operations required for bit banging can be executed:

```
void addSetPins( std::map<uint32_t, bool> pinValue, uint32_t delay = 0 );
void addGetPins( uint32_t delay = 0 );
void addSetPinsDirections( std::map<uint32_t, direction> pinDirection,
                           uint32_t delay = 0 );

std::vector<OpcUa_UInt32> dispatch();
```

Upon dispatching, the server will gather all the replies corresponding to the `addGetPins` requests, if any, and return them to the client. These replies contain the contents of the SCA GPIO data register, which is a 32-bit mask of all IO values. The `IoBatch` API offers additional functionality, such as sorting out the relevant pins from the collected replies. For example, to print out the values read for pin #1:

```
std::vector<bool> pinValues = repliesToPinBits( interestingReplies, 1 );

std::for_each(
    pinValues.begin(),
    pinValues.end(),
    []( const bool & pinValue )
    { std::cout << "Pin Value: 0b" << pinValue; }
);
```

## 3.12 FreeVariable

Another challenge in the NSW front-end electronics, particularly with the VMM, was the limitation of having only one monitor output channel per VMM. The monitor output of each VMM is connected

to the same SCA analog input port, serving the purposes of monitoring and calibration. To capture the corresponding monitor output, the user must configure the VMM with the following registers:

- Pulser DAC: sm = 1 & scmx=0 & sbmx=1 & sbfp=1
- Threshold DAC: sm = 2 & scmx=0 & sbmx=1 & sbfp=1
- Bandgap reference: sm = 3 & scmx=0 & sbmx=1 & sbfp=1
- Temperature sensor: sm = 4 & scmx=0 & sbmx=1 & sbfp=1

The challenge with the common SCA ADC channel was that the Detector Control System (DCS) would be unaware of the configuration status of the VMM. Following discussions with the Central DCS, a new feature was introduced in the SCA OPC UA Server known as "FreeVariable." The FreeVariable is an OPC-UA variable that can be added anywhere in the address space. It is not governed by the server Design, and the server cannot directly communicate with this variable. A free variable can always be written to by any OPC-UA clients. The required attributes for a free variable are the name and the type (Boolean, Byte, SByte, UInt16, Int16, UInt32, Int32, UInt64, Int64, Float, Double, String).

Thus, a new field in each front-end board VMM SCA's XML template was introduced:

```
<SpiSlave autoSsMode="true" busSpeed="20000000" lsbToMsb="false" name="vmm0"
sampleAtFallingRxEdge="true" sampleAtFallingTxEdge="false"
sclkIdleHigh="false" slaveId="0" toggleSs="true" transmissionSize="96">
<FreeVariable name="configurationStatus" type="Boolean" initialValue="false" />
</SpiSlave>
```

### 3.13 SCA Operation

Following Figure 3.1, we can simplify the SCA operation in the following Figure 3.35 . The system

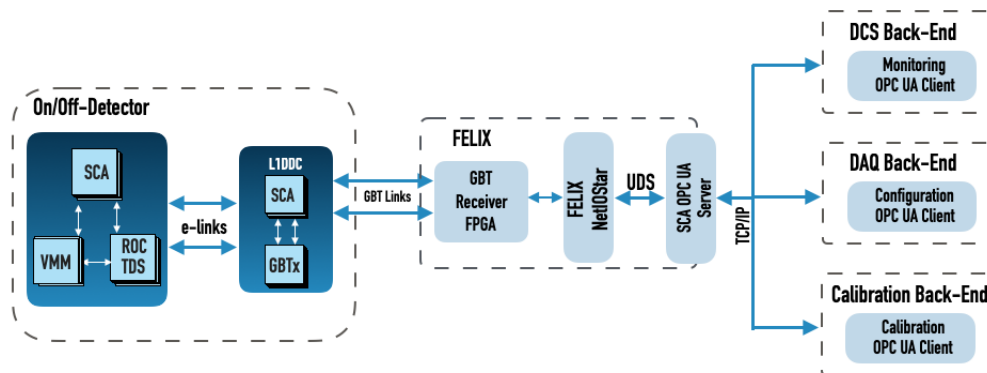


Figure 3.35: Simplified schematic of the NSW Electronics SCA operation.

can be divided into three main parts:

1. **On/Off Detector:** Illustrates the on/off electronics. The SCA embedded on the electronics boards is directly connected to various ASICs such as VMM, ROC, and TDS. Subsequently, the board is connected via a twinax cable to the L1DDC, which also hosts an SCA directly connected to the GBTx ASIC. The connections between the L1DDC and the other boards are described by the e-links.
2. **FELIX:** Represents the actual FELIX host. The L1DDC is directly connected to the FELIX, specifically to the GBT Receiver FPGA via a fiber known as the GBT Link. Inside the FELIX,

the netio/netio-star software stack establishes low-level communication between the SCAs and the FELIX FPGA. The SCA OPC UA Server, initialized with the produced XML files describing various SCA connections, exposes all SCA connections as OPC UA objects in the SCA OPC UA Server address space.

3. **Back-ends:** Comprises the DCS, configuration, and calibration back-end, which can communicate via the network with all the SCAs. Each back-end acts as a distinct OPC UA Client, capable of subscribing to the common SCA OPC UA Server to control and monitor the various SCA connections.

In summary, when all NSW DCS connections are available, we have the following parameters:

- **DCS:** Monitoring of over 100 000 parameters
- **Configuration:** Configuration of over 2 million registers
- **Calibration:** Calibration of over 10 000 parameters

The utilization of the various back-ends will be described in the next subsections.

### 3.13.1 FELIX/OPC Granularity

In the NSW project, the allocation of 7488 electronics boards is distributed across 28 FELIX machines. Specifically, 12 of these machines are designated for Micromegas, while the remaining 16 are assigned to sTGC. Figure 3.36 provides an illustrative example of the MTP connections for NSW Side A and outlines the allocation of SCA OPC UA Servers.

Micromegas					sTGC				
sector		MTP	OPC	FELIX server		MTP	OPC	FELIX server	
1	L	A	OPC server	FELIX server pc-tdq-flx-nsw-mm-00	L	A	OPC server	FELIX server pc-tdq-flx-nsw-stgc-00	
		E			S	E, F	OPC server		
2	S	B	OPC server	FELIX server pc-tdq-flx-nsw-mm-01	S	B	OPC server	FELIX server pc-tdq-flx-nsw-stgc-01	
					L	A	OPC server		
3	L	A	OPC server	FELIX server pc-tdq-flx-nsw-mm-02	S	E, F	OPC server	FELIX server pc-tdq-flx-nsw-stgc-02	
		E			L	A	OPC server		
4	S	B	OPC server	FELIX server pc-tdq-flx-nsw-mm-03	S	B	OPC server	FELIX server pc-tdq-flx-nsw-stgc-03	
					L	A	OPC server		
5	L	A	OPC server	FELIX server pc-tdq-flx-nsw-mm-04	S	E, F	OPC server	FELIX server pc-tdq-flx-nsw-stgc-04	
		E			L	A	OPC server		
6	S	B	OPC server	FELIX server pc-tdq-flx-nsw-mm-05	S	B	OPC server	FELIX server pc-tdq-flx-nsw-stgc-05	
					L	A	OPC server		
7	L	A	OPC server	FELIX server pc-tdq-flx-nsw-mm-06	S	E, F	OPC server	FELIX server pc-tdq-flx-nsw-stgc-06	
		E			L	A	OPC server		
8	S	B	OPC server	FELIX server pc-tdq-flx-nsw-mm-07	S	B	OPC server	FELIX server pc-tdq-flx-nsw-stgc-07	
					L	A	OPC server		
9	L	A	OPC server	FELIX server pc-tdq-flx-nsw-mm-08	S	E, F	OPC server	FELIX server pc-tdq-flx-nsw-stgc-08	
		E			L	A	OPC server		
10	S	B	OPC server	FELIX server pc-tdq-flx-nsw-mm-09	S	B	OPC server	FELIX server pc-tdq-flx-nsw-stgc-09	
					L	A	OPC server		
11	L	A	OPC server	FELIX server pc-tdq-flx-nsw-mm-10	S	E, F	OPC server	FELIX server pc-tdq-flx-nsw-stgc-10	
		E			L	A	OPC server		
12	S	B	OPC server	FELIX server pc-tdq-flx-nsw-mm-11	S	B	OPC server	FELIX server pc-tdq-flx-nsw-stgc-11	
					L	A	OPC server		
13	L	A	OPC server	FELIX server pc-tdq-flx-nsw-mm-12	S	E, F	OPC server	FELIX server pc-tdq-flx-nsw-stgc-12	
		E			L	A	OPC server		
14	S	B	OPC server	FELIX server pc-tdq-flx-nsw-mm-13	S	B	OPC server	FELIX server pc-tdq-flx-nsw-stgc-13	
					L	A	OPC server		
15	L	A	OPC server	FELIX server pc-tdq-flx-nsw-mm-14	S	E, F	OPC server	FELIX server pc-tdq-flx-nsw-stgc-14	
		E			L	A	OPC server		
16	S	B	OPC server	FELIX server pc-tdq-flx-nsw-mm-15	S	B	OPC server	FELIX server pc-tdq-flx-nsw-stgc-15	
					L	A	OPC server		

Figure 3.36: The FELIX/OPC mapping granularity of the NSW Side A.

For the SCA OPC UA Servers, a decision was made to adopt a detector sector granularity approach. Consequently, each detector sector is associated with a dedicated SCA OPC UA Server. In total, there are 32 SCA OPC UA Servers, each running within a dedicated FELIX machine, interfacing with the corresponding sector SCAs. The initialization of SCA OPC UA Servers, along with the

felix-star processes, occurs during the boot of the FELIX host and is managed by corresponding supervisor applications.

This sector-specific allocation of SCA OPC UA Servers has been chosen for reasons of performance and maintainability, supported by extensive performance testing conducted over several years by FELIX and SCA OPC UA Server experts.

A simplified representation of the FELIX/OPC mapping is provided in Figure 3.37. Using this table, users can retrieve information on which FELIX host and port the SCA OPC UA Server for a specific sector is running.

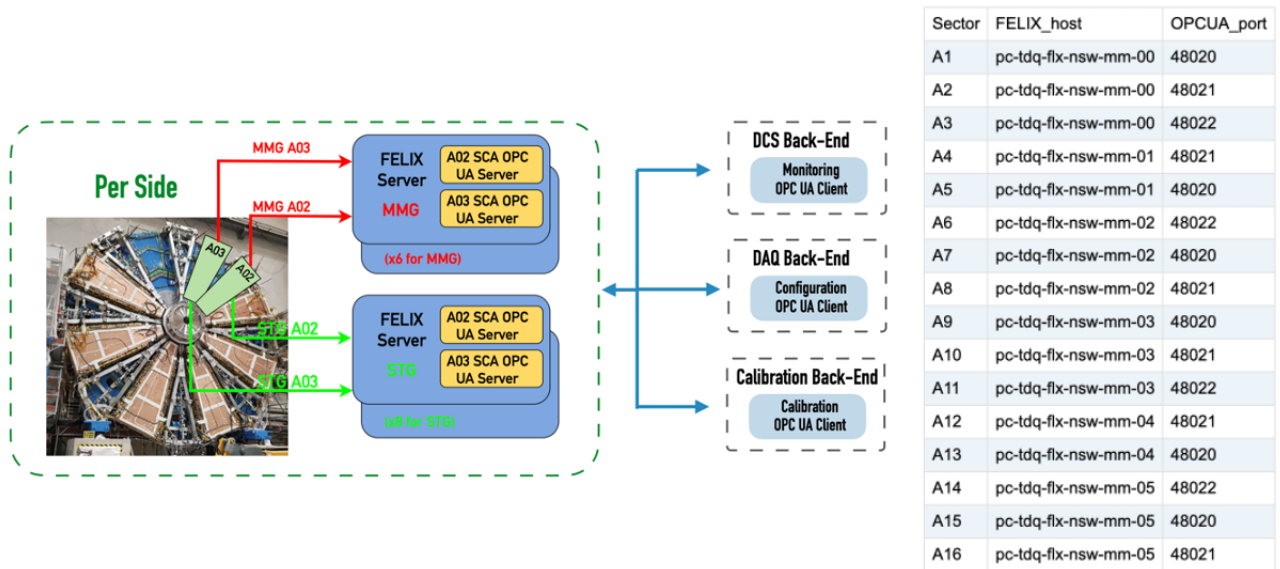


Figure 3.37: Simplified illustration of the FELIX/OPC mapping.

### 3.13.2 Performance Tests

#### Multiple concurrent component usage

Extensive tests were carried out to validate the performance of the SCA OPC UA Server and the associated hardware, particularly under the scenario of multiple concurrent component usage. A test program, implemented in Bash and utilizing the Uao client in C++, was deployed to expose and quantify potential issues.

The primary objectives of the test were to saturate the SCA by performing the following operations:

- Calling the "getConsecutiveSamples" method with N=10 k
- Reading GPIO
- Calling JTAG programming
- Reading a random register via SPI

This testing tool played a crucial role during each iteration of new FELIX firmware and software releases, as well as updates to the OPC software. Its usage ensured a comprehensive evaluation of the system's robustness and performance under diverse operational conditions. The systematic application of these tests has contributed to the refinement and optimization of the SCA OPC UA Server, fostering its reliability in real-world scenarios.

### Micromegas Sector

The versatility of the SCA OPC UA Server is evident in its ability to cater to setups of varying sizes and types, with a notable example being its deployment in the NSW upgrade project for ATLAS. In this ambitious project, a total of 6976 SCAs are strategically distributed across different types of front-end electronic boards. This extensive network of SCAs is efficiently managed by 30 FELIX hosts, each equipped with 18 optical fiber connections, and a corresponding number of SCA OPC UA servers.

During the early stages of integration, the SCA OPC UA server underwent rigorous testing against a full sector slice of the NSW micromegas sub-system. This slice encompassed 8 detector layers, each fully equipped with its front-end electronics, and served a total of 160 SCAs. Remarkably, a single server successfully handled this comprehensive scenario, showcasing its adaptability and robust performance.

The SCAs in the NSW project are categorized into three types, each featuring distinct functionality and interfaces. The testing setup utilized a FELIX host powered by an Intel(R) Xeon(R) CPU E5-1650 v4 @3.6 GHz. Within this host machine, the SCA OPC UA server seamlessly coexisted with FELIX software.

In a constant-throughput scenario, a WinCC-OA SCADA application monitored the analog inputs from a separate host. Simultaneously, three OPC UA clients were connected, providing essential diagnostic capabilities. Transitioning to a burst traffic scenario, the server efficiently handled the load imposed by an additional 128 configuration clients. These testing scenarios reflect the SCA OPC UA Server's resilience and efficiency in real-world applications, particularly in large-scale projects such as the NSW upgrade for ATLAS. In scenarios where no configuration activities are actively pursued,

Board Name	MMFE8	ADDC	L1DDC
Functionality	readout	trigger aggregator	data aggregator
SCA Numbers	128	16	16
ADC Inputs	15	10	9
Calculated variables	15	10	9
I <sup>2</sup> C Master	2	6	2
I <sup>2</sup> C Slave	44+60	6	2
SPI Slave	8	-	-
GPIO	19	18	-

Figure 3.38: SCA channel usage in the ATLAS NSW micromegas full sector slice. The setup was used to evaluate the performance of the server.

the SCA OPC UA Server continually serves the purpose of providing essential monitoring data from the detector electronics. These monitoring data primarily involve analog inputs and represent the baseline activity of the server. In a specific testing setup, the global request rate was measured to be approximately 7800 requests per second for 2192 ADC inputs. Each analog input read involves two SCA requests, resulting in an effective refresh rate of around 2 Hz per analog input. The CPU usage of the server averaged at approximately 25%, and the utilized share of available physical memory remained stable at 340 MB, showing consistency and independence from usage fluctuations.

The most demanding aspect, in terms of open sessions and process complexity, arises during the configuration of the front-end boards. Emulating the cold start of the NSW micromegas detector, a comprehensive sector configuration was executed alongside the constant-throughput monitoring traffic. Throughout this process, up to 58 concurrent sessions were established from various OPC

UA clients. The configuration clients engaged in programming the front-end electronics by interleaving operations between GPIO, I2C, and SPI, accumulating approximately 2700 requests for each SCA. The global request rate surged to around 35000 requests per second, and the instantaneous CPU usage peaked at 218% (hyper-threading). Notably, the total time required to initialize all front-ends was measured to be 10 seconds. This real-world testing scenario underscores the server's capability to handle high loads and complex configurations efficiently.

### 3.13.3 Monitoring

The monitoring back-end is integral to the DCS and the SCADA WinCC-OA project. This monitoring system has been developed and will be comprehensively detailed in the subsequent chapter under the "Electronics" section. It is specifically designed to fulfill all the requirements for monitoring the extensive array of parameters, totaling over 100 000 in the NSW system. This monitoring infrastructure is crucial for overseeing and managing the diverse aspects of the NSW setup, ensuring robust and efficient performance.

### 3.13.4 Configuration

The NSW stands as a fully autonomous trigger and tracking detector system, equipped with a electronics setup, poised to tackle the challenges posed by increased instantaneous luminosity at the High Luminosity LHC. Comprising over 60 000 front-end ASICs and a few dozen FPGAs, the NSW system requires efficient and rapid configuration before each experimental run. This frequent configuration necessity, occurring multiple times a day, particularly pertains to the VMM, the primary ASIC responsible for front-end signal pre-processing across 64 channels.

The configuration process involves handling a few kilobytes of data, encompassing channel-specific thresholds, as well as global registers defining parameters such as gain and time-to-amplitude conversion. To execute this configuration, the SCA's SPI master comes into play, establishing communication with the eight SPI slaves within the VMMs. Additionally, the SCA's GPIO interface functions as an essential enable signal. A parallel scheme utilizes the SCA's I2C interface for configuring the TDS chip, responsible for timing and triggering, and the ROC chip, serving as a data buffer and FIFO.

To streamline and organize the configuration of various elements within the NSW electronics, a collaborative effort has led to the development of the NSWConfiguration software. This software, implemented in both C++ and Python, serves as the official tool for configuration within the NSW DAQ software. The entry point for NSWConfiguration is the `NSWConfiguration` class, where the configuration objects' structure is represented using `boost::property_tree` or `ptree`.

The NSWConfiguration package boasts the capability to parse input JSON files, incorporating correction mechanisms for comments and handling poorly formatted JSON. This parsing process results in an in-memory representation of the per-chip register configuration, facilitating the subsequent steps in the configuration workflow.

For the configuration of the NSW electronics using the `NSWConfiguration` software, the config JSON file must include three common configurations that are applicable to all front ends. These common configurations are:

1. `vmm_common_config`: This configuration pertains to common settings for the VMM ASICs. It encompasses parameters such as thresholds, gain, and other characteristics relevant to the VMM functionality.
2. `roc_common_config`: The `roc_common_config` focuses on common configurations for the ROC ASICs. This includes settings related to data buffering and acting as a FIFO (First-In-First-Out) mechanism.



3. **tds\_common\_config**: This configuration category, **tds\_common\_config**, is associated with common settings for the TDS chip. The TDS chip is utilized for timing and triggering purposes within the NSW electronics.

Each of these common configurations must provide essential information such as the OPC server IP address and the OPC node ID associated with the specific front-end element. The structure of these common configurations ensures consistency and coherence in the configuration process across all front ends within the NSW system.

```
"MM-A/V0/SCA/Strip/S0/L0/R0":{
    "OpcServerIp": "pc-tdq-flx-nsw-mm-00:48020",
    "OpcNodeId": "MM-A/V0/SCA/Strip/S0/L0/R0"
},
```

The NSWConfiguration software comprises several components, and the main idea revolves around the following key elements:

- **ConfigReader**: This component reads the configuration database and returns property tree (ptree) objects. It serves as the entry point for reading a configuration database and dumping its contents into ptree objects. The ConfigReader class is exposed to the user and is designed not to depend on any other component.
- **ConfigReaderApi**: ConfigReaderApi is the base class for any reader API. It defines the interface for various reader APIs and provides a set of methods that should be implemented.
- **Frontend Specific Configuration Classes**: These classes take ptree objects, manipulate them if necessary, and create the bit configurations that can be sent to frontends. Depending on the frontend type, specific methods, such as readFEB(), combine common and frontend-specific configurations to generate the final ptree for the frontend. Configuration classes, like FEBConfig, act as containers for configuration registers and are initialized by a ptree returned from ConfigReader::read(std::string element).
- **ConfigSender**: This component communicates with frontends using the OpcClient and frontend-specific configuration classes. It is the main class exposed to the user and hides the implementation details of OpcClient.
- **UaoClientForOpcUaSca**: These classes are used to read/write from SCAs using OpcUa. Generated by the OpcUa team, this module is added to the software as a git submodule. Periodically, one may need to checkout a new version, especially if a new frontend element is added.
- **OpcClient**: OpcClient utilizes classes and methods from UaoClientForOpcUaSca to perform read/write operations on frontends. It selectively uses relevant classes from UaoClientForOpcUaSca.

In the following subsections, detailed descriptions will be provided for the tools and implementations contributed to the NSWConfiguration.

### SCA Online Status, ID and address

The functions in order to read the SCA online status, the SCA ID and the SCA address have been implemented (as shown in Appendix C).

Furthermore, a dedicated executable application has been developed to empower users with a seamless tool within the NSWConfiguration framework, facilitating swift retrieval of essential information. Aptly named "app/read\_sca\_info.cpp," this application serves the purpose of parsing user-input JSON files and promptly delivering key details such as the SCA online status, address, and ID for all boards specified within the JSON file. The widespread utilization of this application at integration and commissioning sites for the Micromegas & sTGC detectors attests to its effectiveness and user-friendly design. Its implementation stands as a testament to the commitment to providing practical solutions within the NSWConfiguration suite.

### MMFE8 PCB Location

Addressing one of the paramount challenges within the NSW electronics, the quest for accurate mapping—essential for determining the precise geographical location of each front-end board—unfolded as a critical pursuit. In the expansive landscape of the NSW project, boasting 7488 electronic boards and over 1 million physical connections encompassing cables, twinax, and fibers, obtaining comprehensive geographical information emerged as indispensable. This information proved instrumental in diagnosing actual hardware mapping discrepancies effectively.

The breakthrough solution materialized during the Micromegas detector's design phase, wherein PCB information was ingeniously incorporated into the physical PCB strips. These strips, intricately linked to the MMFE8, facilitated data retrieval through the SCA GPIO interface. This enabled validation of critical parameters such as Eta/Stereo orientation, Large/Small classification, PCB number, and left/right positioning. Specifically, eight dedicated readout strips were designated to ascertain the geographical location of the MMFE8 board. The ingenious integration of PCB design schematic, coupled with a Lookup Table (LUT) for position identification, is vividly depicted in Figure 3.39. This innovative approach not only provides a visual representation of the PCB design but also underscores the significance of utilizing LUTs for accurate position determination in the hardware landscape.

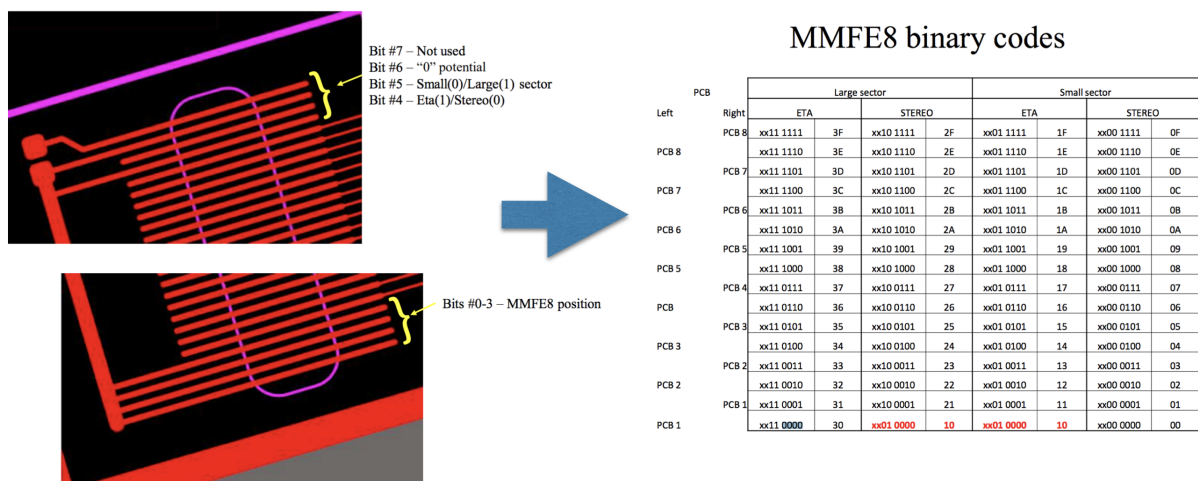


Figure 3.39: Left: The Micromegas PCB design schematic. Right: The MMFE8 binary code LUT.

An actual example of the MMFE8 location and the strips binary identification is shown on Figure 3.40. The board is placed on Large Sector, PCB 2, Left side and Layer 1 (Eta). Someone can easily read the strips identification and get the binary "11000010" and verify that it is placed on the correct position according to 3.39.

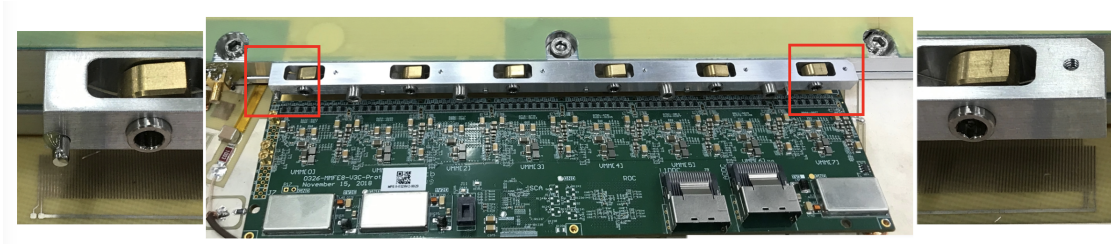


Figure 3.40: The MMFE8 placed on Large Sector, PCB 2, Left side and Layer 1 (Eta).

Since the PCB strips are directly connected to the MMFE8's SCA, we had to add the extra GPIO part on the MMFE8 SCA template as:

```
<DigitalIO id="0" isInput="true" name="mmfe8Id0"/>
<DigitalIO id="1" isInput="true" name="mmfe8Id1"/>
<DigitalIO id="2" isInput="true" name="mmfe8Id2"/>
<DigitalIO id="3" isInput="true" name="mmfe8Id3"/>
```

Moving forward, a pivotal stride involves the integration of a tool within NSWConfiguration, offering users the capability to effortlessly extract the geographical location details of any MMFE8 boards. This quest materialized through the development of an application named "read\_mmfe8\_pcb\_location.cpp," situated within the /app directory of NSWConfiguration. Operating with a common JSON file as its input, the application systematically traverses all MMFE8 instances—either within the predefined set or as specified by the user through the -n argument.

The core functionality lies in the application's ability to correlate MMFE8 locations utilizing the current SCA name (e.g., MMFE8\_L1P1\_IPL) or an impending Logical ID. This correlation is achieved by cross-referencing the SCA GPIO data connected to the PCB binary code—an established code already deciphered by the Lookup Table (LUT). The strategic alignment of these components ensures a seamless and efficient process of extracting valuable information about the geographical location of MMFE8 boards. The integration of this tool stands as a testament to the commitment to user convenience and the optimization of hardware mapping processes within the NSW electronics landscape. However, the outcomes for Micromegas sector A16 proved to be rather disheartening, with only five out of the 128 MMFE8s being accurately read. The depicted results, while indicative of a limited success rate, underscore the ongoing challenges and intricacies associated with pinpointing the precise geographical locations of MMFE8 boards within the sector. As the pursuit of optimal hardware mapping and accurate geographical information remains a continuous effort, these findings serve as a catalyst for further refinement and enhancement of the tools and methodologies employed in the NSW electronics landscape. The commitment to addressing challenges head-on and iterating upon solutions is paramount in the pursuit of a robust and reliable configuration framework. Following extensive hours of debugging and code scrutiny, a critical revelation came to light: the mapping of VMMs was inverted between the MMFE8 board design and the corresponding PCB strips. Specifically, VMM0 occupied the slot designated for VMM7, leading to a sequence misalignment in the GPIOs. This revelation brought forth two significant challenges:

- **Loss of 1 Bit:** A bit, connected to GND and unmonitored via GPIO, was rendered inaccessible, resulting in a perpetual loss.
- **4-Bit MMFE8 PCB Location Loss:** An additional bit of the 4-bit MMFE8 PCB location was forfeited due to this mapping inversion.

Consequently, the tool's assessment underscored the inherent challenge of reliably extracting the geographical location of MMFE8s. This newfound insight emphasizes the critical importance of exercising utmost caution during the integration and commissioning of boards. The need for attention

to detail becomes paramount to circumvent potential discrepancies arising from mapping intricacies, ensuring a seamless and accurate configuration process.

### ROC Registers Readout

The implementation of the NSWConfiguration was significantly enhanced with the introduction of a crucial feature: the capability to read ROC registers through the Bit-Banger tool. This tool, encapsulated within the "roc\_register\_readout" application, operates within the NSWConfiguration framework. It empowers users to effortlessly read ROC registers for selected MMFE8s defined in the provided JSON file. The tool orchestrates a read I2C transaction, sampling the register values, transmitting them, and subsequently clearing the transaction. To validate the robustness of the program, a comprehensive set of ROC registers was systematically read, encompassing the following parameters:

- Address 1: Elink Speed
- Address 2: SROC0 VMM connections
- Address 3: SROC1 VMM connections
- Address 4: SROC2 VMM connections
- Address 5: SROC3 VMM connections

### VMM Capture Status

The internal architecture of the VMM Capture channel is illustrated in Figure 3.41. The process begins with the deserialization of the VMM3 serial data stream (serial data i), transforming it into 10-bit wide words (enc\_data bus validated by the data\_valid\_des signal). The Comma Align module plays a crucial role in aligning the 8b10b stream correctly, resulting in 8b10b symbols (10-bit enc aligned data bus validated by the aligned and data valid align signals). These symbols are then decoded and forwarded to the Assembler module through the 8-bit dec\_data bus and the associated comma signal, both validated by the dec data valid signal.

The Assembler module performs protocol and data integrity checks, pushing the valid L0 packets into the FIFO through the 33-bit wide assemble data bus validated by the fifo wr signal. If the FIFO has only one available address (indicated by FIFO almost full), the current packet is truncated. The logic of the VMM Capture module is synchronized with internal RO clock signals. Additionally, the VMM Capture FIFO transfers input data into the BC clock domain. The writing of the L0 data can be disabled using the fake VMM failure signal (from Config). The parity check can be configured as even or odd using the even parity signal (from Config).

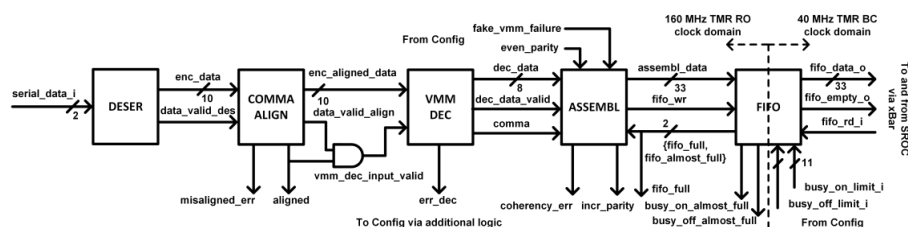


Figure 3.41: The internal architecture of a VMM Capture channel showing the evolution of the main data buses that link its components.

Following the successful read of the ROC registers via the tool described in the previous subsection, the next step was the deployment of the VMM capture status ROC registers. For that reason a

new tool was implemented under /app of the NSWConfiguration in order to give the ability to the users to read the 8 VMM capture status ROC registers of selected or all the MMFE8s of the provided JSON file. For the ROC registers upon a read I2C transaction, their value is sampled, transmitted and then cleared but this is not the case for the VMM Capture's aligned bit that indicates the current state of alignment.

The tool was used massively during the integration of the Micromegas & sTGC electronics in order to spot any problem during the data taking procedure and especially at the Micromegas BB5 cosmics stand. Also, the tool used as a base for the various checks which take place before the NSW data taking.

### FreeVariable

Now that the FreeVariable has been implemented and the "configurationStatus" of each VMM is accessible as an OPC-UA object in the OPC UA address space via the SCA OPC UA Server, the next step involves implementing the logic within the NSWConfiguration (as shown in Appendix C). The function is an integral part of the primary ConfigSender application within the NSWConfiguration framework, invoked during each configuration process of the NSW electronics. In its initial phase, the function retrieves the relevant VMM registers as defined in the corresponding API. Subsequently, the program conducts a verification check to ensure the accuracy of the retrieved VMM registers. Upon successful validation, the VMM's configurationStatus is then updated as follows:

- 1: When  $scmx==0$  &  $sbm x==1$  &  $sbf p==1$  &  $sm==4$  &  $reset!=3$
- 0: For all the other possible combinations

Therefore, with the implementation of FreeVariable, the DCS back-end client gains real-time insights into the configuration status of each VMM. This includes crucial information such as whether a VMM is operating in temperature monitoring mode, allowing the DCS back-end to take appropriate actions based on this dynamic status. A comprehensive overview of the DCS back-end implementation will be provided in the subsequent chapter, specifically within the "Electronics" section.

### 3.13.5 Calibration

The calibration procedures for the NSW can be categorized into three types, as illustrated in Figure 3.42:

- **Phase Alignments:** This crucial operation involves shifting the clock phase in relation to the data to ensure accurate decoding.
- **SCA-Based Calibration:** In this calibration type, L1A data is not utilized. Instead, it leverages the ADC implemented in the SCA to sample the Monitor Output (MO) of the VMM.
- **Data-driven calibration:** Through this type of calibration, several parameters can be extracted which can be applied on the data taken. The sequence of this calibration type involves the full data-taking with L1A data.

#### Phase alignments

The primary clock source in the NSW electronics is the Bunch Crossing (BC) clock, distributed by the ATLAS Trigger and TTC system [34]. Various clocks required for the operation of the NSW electronics are derived from this BC clock. Given that data generated on one board may not be synchronized with the clock needed for decoding on another board, a clock-data alignment process becomes essential.

The alignment is necessary for several components within the NSW electronics:

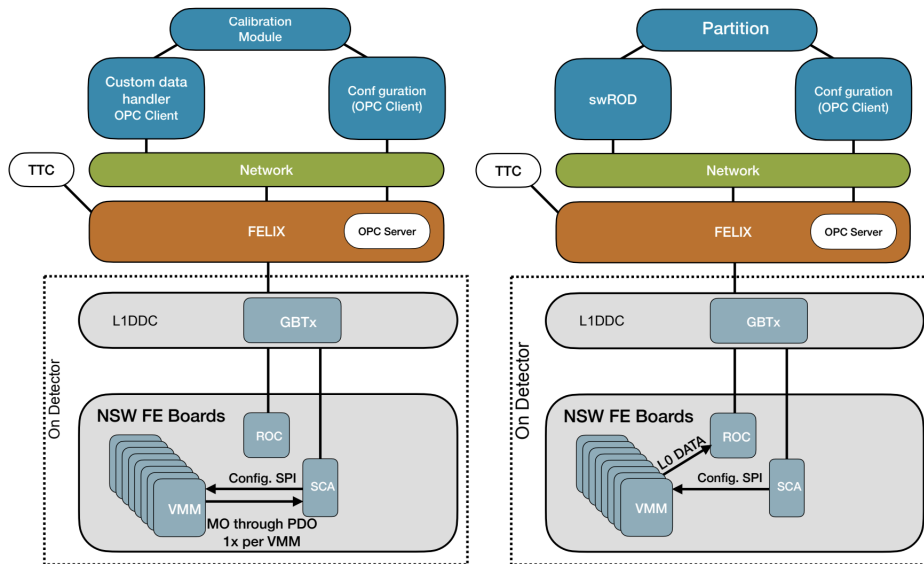


Figure 3.42: Left: The schematic representation of the NSW electronics setup illustrates the pathways involved in the SCA-based calibration process. Commands are transmitted through the OPC client-server and FELIX to the on-detector electronics. The SCA ADC is then instructed to sample the analog output of the VMM. Subsequently, the acquired data is transmitted back to the custom data handler software. Right: The schematic representation illustrates the data-taking path in the calibration procedure. The partition configures the system via the OPC client-server through FELIX. The TTC system is configured to produce a sequence of test pulses along with L1A and L0A signals. The data captured during this process is then handled by the swROD. This comprehensive setup ensures effective calibration and data acquisition for the NSW system. [34]

- **ROC TTC Reception:** The ROC ASIC receives and distributes the TTC stream. As the stream lacks clear start and end markers, the BC clock undergoes a shift to ensure correct decoding of the serial stream bits.
- **VMM-ROC Data Line:** The VMM transmits data to the ROC using a 160 MHz clock. When not actively transmitting data, the VMM sends K28.5 idle characters. Although the ROC provides the data clock to the VMM, the received signal is shifted concerning the transmitted clock. To compensate for this, the ROC generates an internal copy of the clock that can be appropriately shifted, ensuring correct data decoding. Detected errors during decoding are flagged in a status register, allowing for subsequent readout.
- **VMM-TDS Serial Stream:** The VMM transmits charge information serially (6 bits after a flag) to the TDS using a 160 MHz clock provided by the TDS. Similar to the VMM-ROC scenario, the TDS maintains an internal copy of the provided clock, adjusted to correctly decode the received data.
- **VMM-ART Serial Stream:** In this case, the ART receives the 6-bit address after a flag, with the clock to generate the data provided by the ROC ASIC. Despite this, the ART ASIC generates its clock. Leveraging a Phase Aligner, the data can be decoded by synchronizing with the generated clock.
- **GBTx:** To deserialize the input data stream from, for example, the ROC ASIC, the GBTx clock requires phase adjustment. To ensure accurate sampling of e-link data, GBTx features phase aligner circuits, one per e-group with eight adjustable channels. The phase aligner op-



erates in three modes: static, automatic phase tracking, and initial training with learned static phase selection [32].

These alignment procedures ensure the proper functioning of the NSW electronics, enabling synchronized and error-free communication among various components.

### SCA-based Calibration

This type of calibration, known as SCA-based calibration, does not involve the L1A data [34]. Instead, it utilizes the ADC implemented in the SCA to sample the MO of the VMM. The MO is physically routed on a connector on the front-end boards. The VMM is configured to copy the MO to the Peak Distribution Output (PDO), which is then routed through a voltage divider to the SCA's ADC multiplexer.

The voltage divider is necessary since the MO output has a range up to 1.2 V, while the ADC of the SCA has a 1 V range. The measured parameters obtained through this calibration are crucial for the optimal configuration of the NSW electronics to acquire data efficiently.

The schematic in Figure 3.42 illustrates the involved components in this calibration procedure. The configuration software transmits commands through the OPC client to the OPC server. Through FELIX, these commands reach the front-end ASICs. Subsequently, the SCA is instructed to sample the ADC line, and the data are made available through the OPC server to a custom data handler.

This calibration procedure enables the following types of measurements:

- **Baseline Measurement and ENC Estimation:** The Slow Control Adapter's ADC employs a single-slope Wilkinson architecture. The slow ramp is ideal for slowly varying parameters but underestimates fast ones. To correct this, a correction factor is applied to establish the real noise level on the detector.
- **Measurement of Pulser and Threshold DAC Conversion:** This measurement allows for the conversion from DAC counts to millivolts. It helps apply the correct threshold to the electronics, enabling the calculation of input charge.
- **Channel Trimmers:** This measurement enables the setting of individual 5-bit trimmers of VMM channels. The goal is to equalize the amount of charge from baseline to the discrimination level across channels.

External measurements via the SCA can be made for each VMM channel's analog output when no signals are present at the channel input. These measurements provide insights into the channel baseline (ambient level when no signal is present) and fluctuations about the baseline, offering a measurement of inherent channel noise. Knowledge of both the absolute baseline and noise levels allows for optimal threshold setting for the VMMs. Setting the threshold just above the baseline is essential, defining the effective zero-level of an observable signal. In practice, the VMM threshold is set a few times the magnitude of the measured noise above the baseline (typically six to nine times the noise standard deviations). The SCA samples each channel's baseline, and the noise level is obtained from the width of the distribution of these measurements.

### Data-driven calibration

Through the process of this calibration type, as outlined by [34], a multitude of parameters can be extracted, enriching the dataset with refined insights applicable to subsequent data analysis. The intricate sequence of this calibration involves comprehensive data-taking synchronized with L1A data. The data generation is orchestrated through the internal VMM pulser, driven by a dedicated TTC bit, ensuring synchronous operation across the entire system.



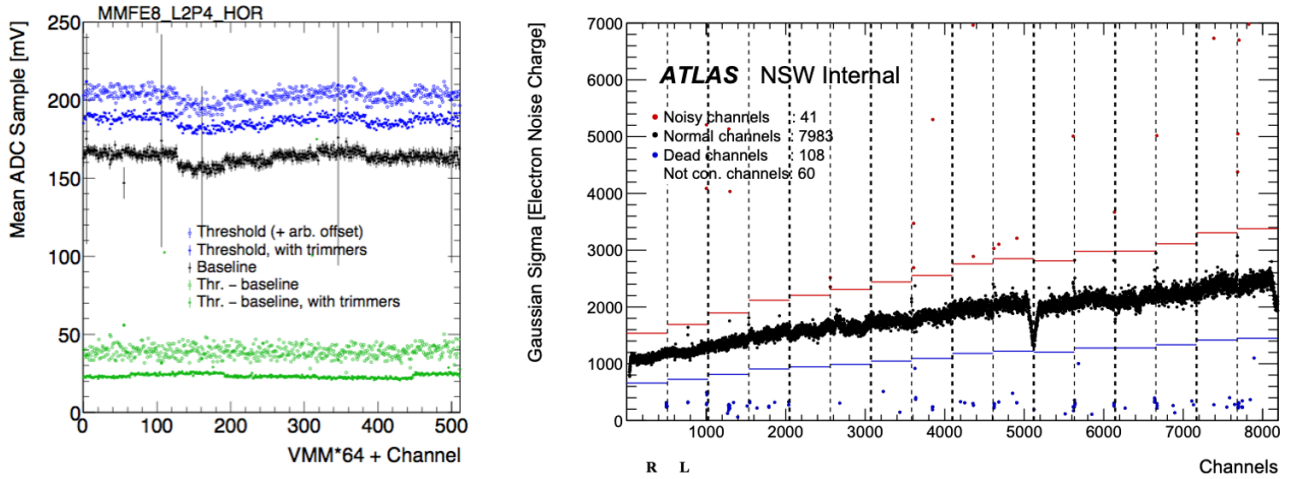


Figure 3.43: Left: A typical plot produced during the SCA-based VMM calibration procedure. Right: Baseline rms per strip for one layer of the Micromegas Small Sector C08. The layer used for the plot is of the stereo type (with the strips orthogonal to the longitudinal axis of the double wedge). The baseline rms values are indicative of the detector noise and depend on the input capacitance to each electronic channel. As expected, the rms value is increasing as a function of the strip number and the corresponding strip length. The dotted lines define the MMFE8 boards (16 in total), while bold dotted lines define the PCBs (eight in total) of the layer. The noisy channels are defined as all the channels above the red limits (1.4 times the board median), the dead channels are defined as all channels below the blue limits (0.6 times the board median), while the channels between these limits are defined as normal. Also, in each sector type, there are some standard unconnected channels that are omitted in this plot. Furthermore, the effect of the decreasing length of the strips at the beginning and at the end of the modules in the stereo layers can be observed in these areas.

For the seamless execution of this sequence, a dedicated partition is generated, encompassing the configuration procedure facilitated by the OPC client-server. The pivotal role played by the TTC system in this calibration is noteworthy, as it orchestrates the production of specific time sequences of signals. These signals are instrumental in driving the VMM pulser, generating essential L1A and L0A signals that facilitate the subsequent data readback process. The captured data are channelled through an instance of the swROD, strategically decoupled from the ATLAS High-Level Trigger for streamlined calibration.

This comprehensive calibration procedure unfolds various possibilities and avenues for in-depth analysis, including:

- **VMM gain calibration:** This involves injecting varying amounts of charge into the VMM and storing the resulting PDO. The gain of the electronics can be precisely established through this process, offering valuable insights that can be leveraged to correct charge measurements. Additionally, the calibration procedure presents an opportunity to measure time-walk phenomena using the TDO data.
- **TAC calibration:** The VMM records, as TDO, a voltage level representing the amplitude of the TAC. This calibration process initiates either at the peak or threshold and concludes at the falling edge of the CKBC. The injected charge, guided by a specific time sequence through the TTC, ensures synchronization with the system and the CKBC. To account for any skew in time units introduced by the ROC ASIC, a series of steps are performed during this procedure. The resulting TAC ramp measurements are invaluable, serving as a crucial reference to translate ADC counts into meaningful time units.

### 3.14 Contributions

The electronic unit VMM was developed within the framework of the NSW upgrade and processes the primary signals generated by the detectors during the muon detection, which include Micromegas and sTGC. The doctoral candidate:

- Participated in the characterization of the unit by performing tests and collecting data from hundreds of units. Specifically, using prototype boards that integrate VMM and FPGA capable of connecting to detection chambers and acquiring measurements from them, and that can also be used without detection media, they checked the proper functioning of the VMM unit and calibrated its different parameters.
- The results obtained contributed to the improvement of the existing unit as well as the creation of a new electronic unit.
- Actively participated in 2 test beam periods at the Demokritos National Center for Scientific Research, aimed at investigating the functionality of the unit under neutron beam irradiation conditions and specifically the occurrence of SEU (Single Event Upset).

The data acquisition system of the NSW consists of many components, most of which are electronic units responsible for transferring/extracting/receiving data from the detector to the storage systems of the ATLAS experiment. The doctoral candidate:

- Actively participated in the electronic system test weeks (integration weeks).
- Developed tools for the parameterization of electronic system parameters and additionally conducted studies for the parallel calibration of the electronic units acquiring the detection signals using the VMM unit.
- Parts of the detection system were exposed to cosmic rays in the BB5 building to verify their proper functioning before installation in ATLAS. Within this project, the candidate developed a variety of tools that supported the data extraction system of the detectors.
- Supported the FELIX system, which manages data coming from the detector's electronics via optical fiber interfaces. Specifically, they developed tools for configuring the system's parameters and tested new versions with the support of the Central DAQ team of ATLAS.
- Supported the GBT-SCA system responsible for the parameterization and monitoring of various units and parameters of the electronic boards. Additionally, they served as a mediator between NSW and the Central DCS team of ATLAS for the development and optimization of the SCA Ecosystem.
- Developed tools for the recognition of the geographical location of electronic boards (MMFE8) in the Micromegas chamber.
- Developed central tools for the acquisition and control of data and parameters of all electronic boards in the context of communication through GBT-SCA and FELIX via the SCA OPC UA Server.
- Played a key role in defining the architecture of the data acquisition system for all electronics and integrating them into the central data acquisition system of ATLAS.

In addition, the doctoral candidate contributed to the following published papers:

- **“Electronics Performance of the ATLAS New Small Wheel Micromegas Wedges at CERN”**  
DOI: [10.1088/1748-0221/15/07/C07002](https://doi.org/10.1088/1748-0221/15/07/C07002)
- **“Development of the Configuration, Calibration and Monitoring System of the New Small Wheel Electronics for the ATLAS experiment”**  
DOI: [10.22323/1.397.0170](https://doi.org/10.22323/1.397.0170)
- **“The New Small Wheel electronics”**  
DOI: [10.1088/1748-0221/18/05/P05012](https://doi.org/10.1088/1748-0221/18/05/P05012)



# Chapter 4

---

## Detector Control System

---

Due to its complexity and long-term operation, the ATLAS detector requires the development of a sophisticated detector control system or otherwise DCS. The use of such a system is necessary to allow the detector to function consistently and safely as well as to function as a seamless interface to all sub-detectors and the technical infrastructure of the experiment. The central system handles the transition between the probe's possible operating states while ensuring continuous monitoring and archiving of the system's operating parameters. Any abnormality in any subsystem of the detector triggers a signal or alert (alarm), which alerts the user and either adapts to automatic processes or allows manual actions to reset the system to function properly. In fact, it is a SCADA (Supervisory Control and Data Acquisition) system that describes a class of industrial automatic control and telemetry systems. The chapter includes a brief introduction to the ATLAS DCS, the SCADA application which is used in order to create the various control stations and the OPC UA Servers which are used for the hardware connectivity. A detailed description of the control stations, which were developed for the needs of the the NSW integration and commissioning, will be presented. A big part of the chapter consists of the description of the architecture and design concepts of the the NSW Production Control System. The hardware infrastructure, the projects allocation and the OPC UA Servers connectivity will be presented. A detailed presentation will be given for the Electronics project which were developed for the needs of the MMG &STG electronics in order to achieve the monitoring of more than 100 000 parameters. Lastly, the DSS project for the NSW safety will be presented along with other NSW projects and the SCS overview project.

## 4.1 ATLAS DCS

The ATLAS DCS (Detector Control System), as outlined in the references [40] and [63], was developed within the collaborative framework of the Joint COntrols Project (JCOP). This innovative project is a joint effort between the CERN and DCS groups of LHC experiments, establishing unified standards for the deployment of DCS hardware. The foundation of this endeavor is the SCADA system Siemens, WinCC Open Architecture [64], also recognized by its previous name PVSS. This system serves as the cornerstone for all DCS applications within JCOP.

Illustrated in Figure 4.1, the architecture of the DCS [65] [29] can be dissected into two primary components: the Front-End (FE) equipment and the Back-End (BE) system. The FE encompasses DCS equipment, including custom made electronic systems and associated services such as high-voltage power supplies and cooling circuits. On the other hand, the BE system leverages the WinCC-OA software, seamlessly integrating front-end control systems into the JCOP framework. This integration facilitates the installation of standard hardware devices and the implementation of uniform control applications.

Communication between the two ends of the DCS primarily transpires through the industrial protocol bus CAN, with the OPC communication standard serving as a crucial software protocol. The BE system operates hierarchically across three levels: Local Control Stations (LCS), Sub-detector Control Stations (SCS), and Central Control Stations (Global Control Stations (GCS)). In its entirety, the BE comprises over a hundred computer stations interconnected within a distributed system. WinCC-OA manages communication between subsystems via a local area network.

A distributed Finite State Machine (FSM) serves as the comprehensive hierarchy of the BE system. This FSM integrates more than 10 million data elements into a singular tree structure, ensuring the proper operation and efficient handling of errors at each operational layer. The cornerstone of this system is the datapoint (DP) structure, functioning as the global variable network. Each element within this structure possesses a unique name and configurability. Special DPs facilitate the extraction of data from hardware components, updated through the OPC client-server communication interface [66].

The collaborative efforts within the JCOP framework, coupled with the advanced architecture of the ATLAS DCS, underscore the commitment to excellence in the realm of detector control systems for cutting-edge scientific endeavors.

### 4.1.1 Building Blocks

#### Front-End

The DCS FE equipment had to meet common requirements such as low cost, low power consumption, and high I/O channel density. For equipment interconnection, the CAN industrial field-bus and the CANopen protocol is used wherever possible and appropriate. Electronics in the detector cavern had to allow for remote firmware upgrades, be insensitive to magnetic fields, and be tolerant to radiation exposure expected during the experiment lifetime.

- **ELMB:** A low-cost custom-built I/O concentrator, the Embedded Local Monitoring Board (ELMB) was developed as a common solution for interfacing custom designs to the DCS. The ELMB board ( $50 \times 67 \text{ mm}^2$ ) features a 8-bit 4 MHz micro-controller with 64 analog, 32 digital channels and a CAN bus interface. The board is tolerant to strong magnetic fields and radiation hard for integrated doses up to 50 Gy. Furthermore, the ELMB can be embedded within custom designs and has a modular, remotely extendable firmware with a general purpose CANopen I/O application. More than 10 000 ELMBs are in use within all LHC experiments and over 5000 alone within ATLAS.

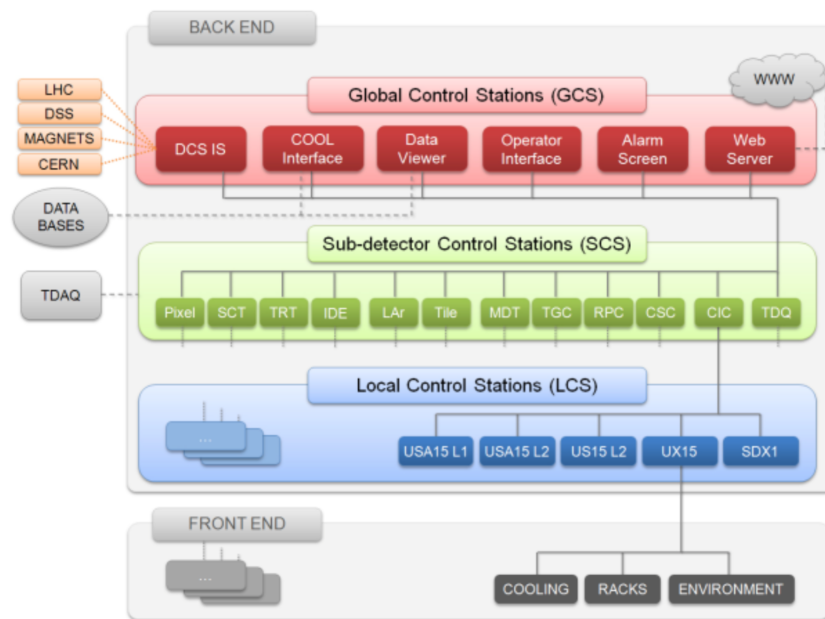


Figure 4.1: Graphical representation of the DCS architecture of the experiment ATLAS divided into three levels: GCS, SCS and LCS.

- **Standardized Commercial Equipment:** The industrial standard Versa Module Europa (VME) is used to house electronics. For all crates, monitoring is implemented for temperature and general status information as well as power and reset control. The detector components are powered by different types of industrial power supplies featuring control of voltages/currents, over-voltage/current protection, and thermal supervision.

### Back-End

- **DCS Control Station PC:** The hardware platform for the BE system are industrial, rack-mounted server machines. Two different standard machine types, one for applications requiring good I/O capability, a second for processing-intensive applications with I/O via Ethernet connectivity. Both models feature redundant, hotswappable power supplies and disk shadowing.
- **PVSS:** The SCADA package PVSS (re-branded to SIMATIC WinCC-OA) is the main framework for the BE applications. Four main concepts of PVSS make it suitable for a large scale control system implementation. (1) Generic types of control process templates may be used depending upon the type of the required application avoiding unnecessary overhead. (2) Each PVSS application uses a local database for the storage of control parameters providing synchronized access for all connected processes. Data processing is performed with an event-based approach and data is made persistent by archiving selected DCS parameters to an external Oracle database. (3) Different control systems can be connected via LAN to form a Distributed System allowing for highly scalable remote data access and event notification. (4) A generic Application Programming Interface (API) allows to further extend the functionality of control applications.
- **Front-end interface software:** For interfacing the front-end devices with PVSS, the industry standard OPC was chosen. Commercial equipment manufacturers as well as developers of custom devices provide the OPC servers for which PVSS provides an OPC client. For the ELMB CAN bus readout and control, a dedicated CANopen OPC server has been developed.



Device types for which OPC could not be used due to maintenance or platform constraints (OPC is limited to MS Windows™), custom readout applications were interfaced to PVSS using the CERN standard middle-ware DIM PLCs are interfaced to PVSS via Mod-Bus.

- The Finite State Machine Toolkit: The JCOP FSM provides a generic, platform-independent, and object oriented implementation of a state machine toolkit for a highly distributed environment, interfaced to a PVSS control application. The attributes of an FSM object instance are made persistent within the associated PVSS application database. This allows for archiving of the FSM states and transitions, and integration of the FSM functionality into PVSS user interfaces.

### 4.1.2 Control Hierarchy

The complete DCS BE is mapped onto a hierarchy of FSM elements using the FSM toolkit. State changes are propagated upwards and commands downwards in the hierarchy, allowing the operation of the complete detector by a single FSM object at the top level. A fixed state model (see Figure 4.2) has been applied, reflecting detector conditions for which physics data taking is optimal (READY) or compromised (NOT READY), or the detector has been turned off (SHUTDOWN). A special STANDBY state is reserved for detectors with intermittent stage for unstable beam conditions. The state UNKNOWN is used when the actual condition cannot be verified. TRANSITION signals a transient state, e.g. ongoing voltage ramps. The actual state of these logical objects is determined by the states of the associated lower level objects (children) via state rules. The lower level objects may follow a more sub-system-specific state model for which guidelines exist. For each critical parameter,



Figure 4.2: State & status model of the ATLAS DCS high level objects.

alarms can be configured and are classified into one of the severity Warning, Error, or Fatal. To avoid the accumulation of a large number of alarms on the user interface, a masking functionality has been added to hide past occurrences e.g. after a follow-up has been initiated. Each FSM object in the lowest hierarchy level has an attribute called Status which assumes the highest severity of alarms active for the respective device. The Status is then propagated up in the FSM hierarchy and thus allows for error recognition within the top layers of the detector tree and permits to identify problematic devices by following the propagation path downwards. The DCS is operated from two primary, remotely accessible user interfaces – the FSM Screen for operation of the detector Finite State Machine hierarchy and the Alarm Screen for alarm recognition and acknowledgment. Static status monitoring is provided by web pages on a dedicated web server allowing to quickly visualize all high level FSM user interface panels world-wide and without additional load of BE control stations.

### 4.1.3 FSM

Each FSM node within the ATLAS DCS is assigned a unique name, derived from the subsystem name and its designated functionality, aligning with the established conventions of ATLAS DCS. The

specification of the state of each node is determined by a corresponding internal DP. The type of FSM object, showcasing the fundamental functionality of the node and its components, is contingent upon the functional purpose and position of the element within the hierarchical architecture of the DCS.

The primary graphical user interface of ATLAS DCS, encapsulating all subsystems in a comprehensive hierarchical FSM structure, is displayed in Figure 4.3. This FSM adheres to a stringent hierarchical framework, establishing parent-child relationships. In this construct, commands traverse from parents to children, while feedback and statuses flow from children to parents. This hierarchical approach ensures exceptional efficiency when issuing commands that belong to all children; a command directed at a higher node inherently summarizes the status of all nodes within any generation.

Each node within this framework is initialized in a predefined state and exclusively accepts predefined commands in accordance with the FSM type to which it belongs. This systematic approach not only streamlines command transmission but also enhances the overall coherence of the DCS, contributing to a robust and reliable control system for the intricate components of the ATLAS experiment. The fusion of unique naming conventions, precise hierarchical structuring, and predefined states manifests a complex control architecture that is fundamental to the success and precision of the ATLAS DCS.

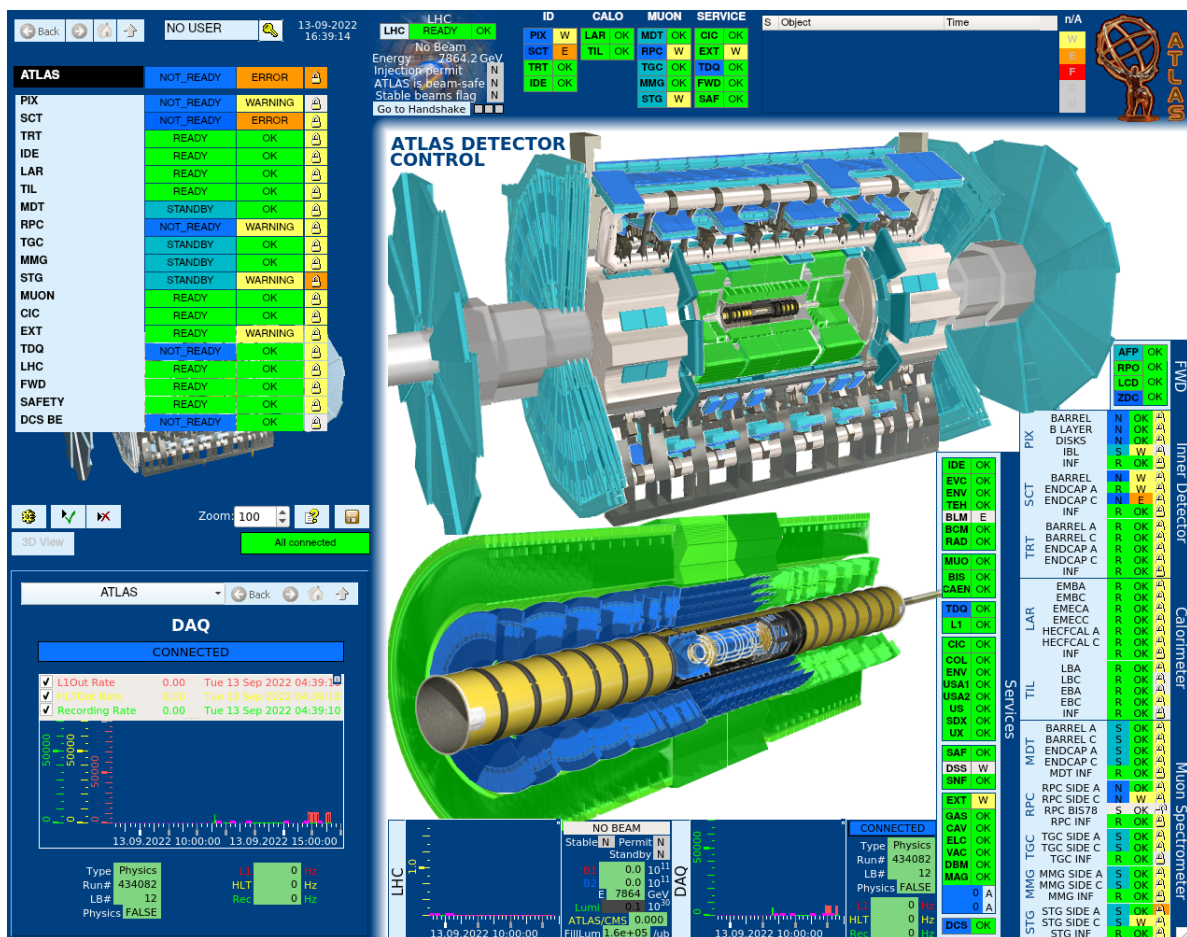


Figure 4.3: The main user interface of ATLAS DCS with all subsystems integrated into a hierarchical structure FSM.

### 4.1.4 Panels

The fundamental principle guiding the design of the ultimate Operator Interface (OI) for the ATLAS DCS is the consolidation of all relevant information into a single, easily navigable window. The intention is to enhance human-machine performance by eliminating the need to scout information across multiple windows within the process control system.

To achieve seamless navigation through the diverse levels of the FSM hierarchy, a comprehensive user interface has been developed. This interface comprises a singular frame, divided into five constituent parts, as illustrated in Figure 4.4. This design ensures that all DCS information is readily available in parallel, fostering a holistic and efficient user experience.

The operator screens are composed of two distinct segments: the FSM screen and the Alarm screen, each boasting a resolution of  $1280 \times 1024$ . The FSM screen is embodied by a WinCC-OA panel with fixed dimensions spanning the entirety of the screen. Within this panel, numerous modules are incorporated, presenting the behavior of the system and enabling control at various levels of the DCS hierarchy.

The FSM Module takes center stage, displaying the STATE and STATUS of a FSM node along with its offspring, encapsulating all FSM functionality within a limited space. In instances where numerous FSM children exist, a scroll bar dynamically appears, facilitating smooth navigation through the expansive hierarchy. This strategic design choice ensures that the wealth of DCS data is efficiently accommodated within a single display, fostering a user-friendly and comprehensive overview of the intricate control system governing the ATLAS experiment.

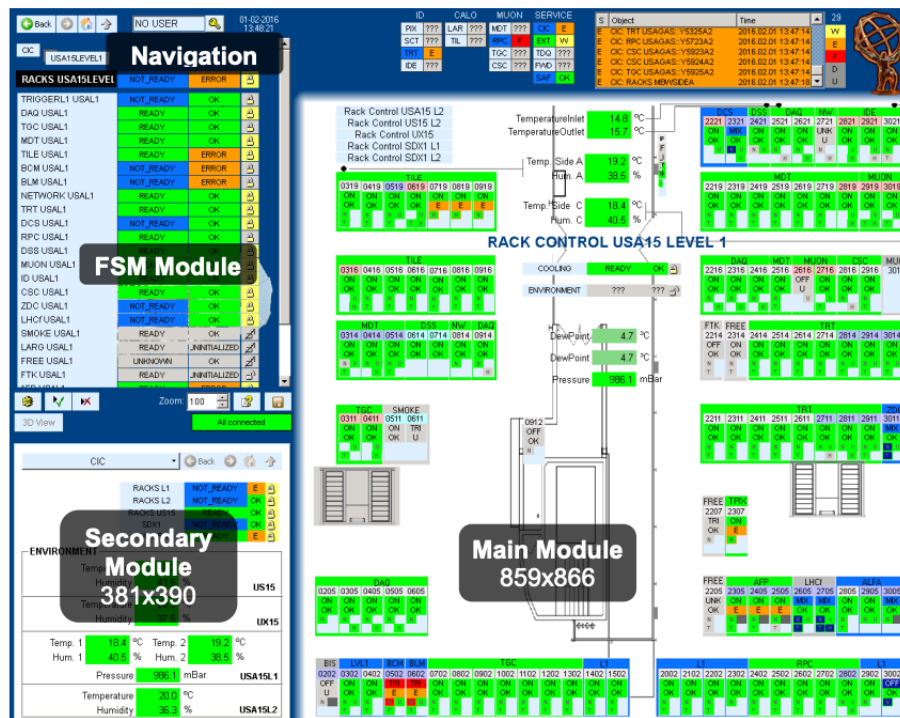


Figure 4.4: FSM operator screen components.

The FSM operator screen consists of the following modules:

- **Main Module:** Its dimensions are  $859 \times 866$ . This is the main panel for the selected FSM node, this can be a SCS, a HV (High Voltage) system, etc. Two dollar parameters are passed from the FSM Module to the Main Panel ( $\$node$  and  $\$obj$ ).
- **Secondary Module:** Its dimensions are  $381 \times 390$ . The purpose of this is to keep a main view of a certain sub-detector while studying more in detail a problem that triggers deeper in the

hierarchy. Thus, it is needed to create an additional panel with a summary of the information presented for each main panel. Two dollar parameters are passed from the Main Panel to the Secondary Panel (\$node and \$obj). Optionally, the secondary module is used to display a 3-dimensional view of the detector DCS objects.

In both Main and Secondary module, the developer has full FSM functionality (i.e. one can send FSM commands, change the partitioning mode, etc.). This also means that within a certain workspace (i.e. a HV system) information related to any other workspace (i.e. cooling) could be displayed. Using the navigation functionality the operator can jump from one workspace to another using any of both, main and secondary modules.

### 4.1.5 Alarm Screen

The Alarm Screen, exemplified in Figure 4.5, serves as a real-time display presenting a dynamic list of active alarms within the designated ATLAS DCS system. These alarms are triggered in response to malfunctions in one or multiple hardware or software components, with severity categorizations ranging from WARNING to ERROR and FATAL. Importantly, the occurrence of an alarm is immediately reflected in the status of the corresponding FSM node.

This alarm scheme is crucial for swift detection by shifters and facilitates the efficient response of experts to potential issues that may arise during routine operation. Alarms are classified based on severity, enabling prioritized attention to critical events. The Alarm Screen user interface is designed with features that permit filtering based on various attributes, such as the corresponding system, description, severity, and time. Additionally, it provides the capability to query the alarm history of a specific system, encompassing all the aforementioned features.

This tool proves to be indispensable for the safe and efficient operation of the ATLAS detector. It not only empowers shifters with real-time awareness of potential issues but also offers a comprehensive history and filtering options that enable experts to conduct in-depth analyses and investigations. The Alarm Screen stands as a pivotal component in the variety of tools ensuring the robustness and reliability of the ATLAS DCS, emphasizing its significance in maintaining the high-performance standards of this complex scientific experiment.

## 4.2 WinCC Open Architecture

WinCC-OA stands out as a versatile software package designed primarily for the supervision and control of technical installations, employing a comprehensive graphical interface to visualize and simulate diverse modules. The software plays a pivotal role in implementing and managing intricate processes, offering an interactive communication environment that interfaces with hardware. This interaction enables real-time monitoring, seamless command transmission, efficient alarm handling, and the storage of operational history.

The selection of WinCC-OA by the JCOP committee was a strategic decision driven by its widespread adoption and proven efficacy in constructing automated control systems within the development and experimental domains at CERN. The tool's established track record and familiarity among developers and experimenters within the CERN community underscored its suitability for the ambitious requirements of the JCOP.

By leveraging the capabilities of WinCC-OA, the ATLAS DCS benefits from a robust platform that not only streamlines the visualization and control of technical installations but also facilitates seamless integration with the wider framework of the JCOP. This strategic alignment with a widely used and trusted tool exemplifies the commitment to efficiency, reliability, and interoperability within the landscape of CERN's experimental endeavors.



- \* Sends/receives data from drivers.
  - \* Transfers data to Database Managers for storage.
  - \* Distributes data to relevant Managers.
  - \* Maintains the process image in memory (current values of all data).
  - \* Manages system alerts and alarms.
- **Drivers:**
    - **Responsibility:** Implements communication protocols with hardware.
    - **Functions:**
      - \* Provides connections to external devices using templates like OPC, ModBus, etc.
      - \* Allows instant editing and modification during operation.
      - \* Streamlines data flow, performs value conversion, and communicates with drivers.
      - \* Provides an application programming interface (API) for creating new interfaces.
  - **Database Manager (DBM):**
    - **Responsibility:** Links WinCC-OA to the database.
    - **Functions:**
      - \* Records latest system values and alerts.
      - \* Stores historical data.
      - \* Accesses the database using SQL language.
      - \* Supports optimized versions of RAIMA and Oracle.
  - **User Interface Managers (UIM):**
    - **Responsibility:** Visualizes messages from the Event Manager.
    - **Functions:**
      - \* Retrieves or sends hardware data to/from the database.
      - \* Runs in a deployable state (PARA) for configuring DPTs/DPs.
      - \* Uses GEDI for the graphic editor to design panels.
      - \* Includes libraries, allows adding plugins and panels, and provides a script editor for code writing.
  - **Control Manager (CTRL):**
    - **Responsibility:** Allows development of algorithms for graphic design, decision making, command generation, and data processing.
    - **Programming Language:** CTRL (based on ANSI-C syntax with modifications).
    - **Features:**
      - \* Algorithm development with a vast library of functions.
      - \* Unique syntax features like absence of pointers and special processing strings.
  - **API Managers:**
    - **Responsibility:** Enables users to build a library of algorithms in CTRL and integrate them into the system.



- **Archive Managers:**

- **Functions:** Allow users to archive data for later retrieval and examination. Configuration options are available for selecting which data to store.

- **ASCII Managers:**

- **Functions:** Facilitates exporting/importing project configurations (DPTs/DPs) to/from an ASCII file. Users can selectively export items, making integration into existing projects more user-friendly.

In WinCC-OA a system is an application containing a Event Manager, a Data Manager as well as a number of other managers, user interfaces and other things that run only when they are called. This allows the system to be easily adapted to each user's needs and managers to open or close without having to restart the entire software. This specific structure and communication through a common protocol TCP/IP enables distributed systems to be created on a single computer network by sharing the burden on multiple computers and separating functions by creating a distributed system.

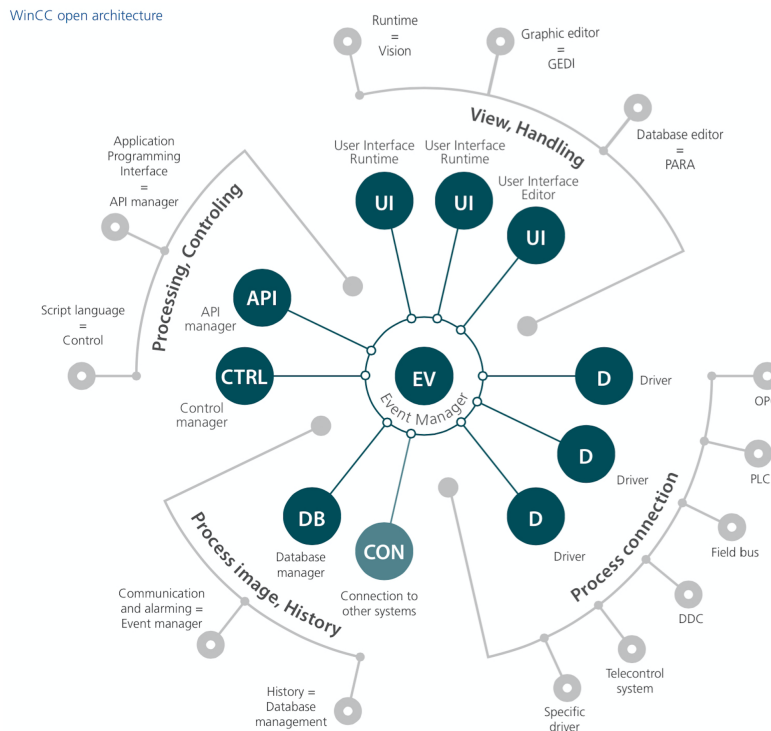


Figure 4.6: The architecture of a typical WinCC-OA system and the set of managers it consists of.

## 4.2.2 Basic tools of WinCC-OA

### Database

Data processing and communication among managers within WinCC-OA adheres to an object-oriented paradigm, where the cornerstone of the system is formed by datapoints. At the apex of this hierarchical structure are Datapoint Types (DPT), serving a role analogous to classes in a radial terminology. These DPTs correspond to either a mechanical system or an integrated assembly of their sub-units. Objects within the system possess Datapoints (DP) that reference a collection of properties or devices within the control system.



The repository of all Datapoint information resides in Datapoint Elements (DPE), with each DPE representing a specific value or state. Through Datapoint Attributes (DPA), valuable information can be extracted to either modify a state or alter various variables. This modular and hierarchical approach allows for a highly flexible and customizable structure, empowering users to define, modify, and create their own configurations through the intuitive PARA Database Editor of WinCC-OA.

Moreover, users have the privilege of specifying diverse settings for notifications or establishing connectivity with various devices or archives. This is achieved by seamlessly incorporating configuration files (configs) into the respective DPEs. The adaptability and extensibility of this structure underscore the user-centric design philosophy, allowing for the seamless integration of tailored configurations and facilitating a dynamic and responsive control environment.

To visualize this intricate structure, Figure 4.7 provides a glimpse of the PARA tool, offering an insightful depiction of its interface. Additionally, it includes an example showcasing the structured hierarchy of a Datapoint Type (DPT), highlighting the practical implementation and organization of this versatile and powerful data processing system. The FieldPoint is DPT, which consists of four

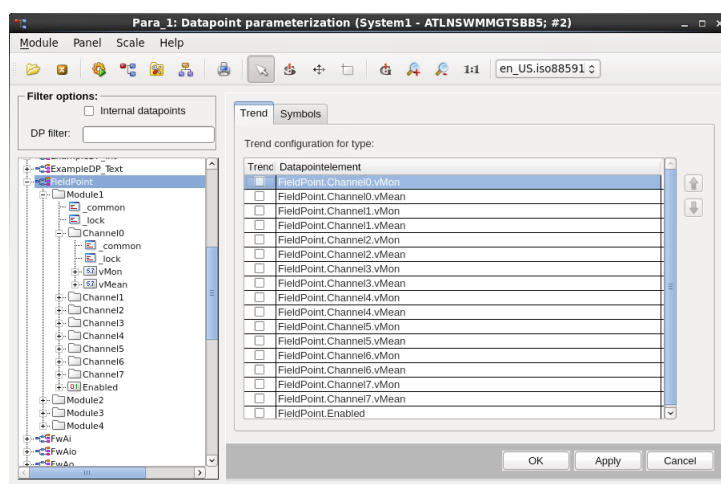


Figure 4.7: The PARA Database Editor of WinCC-OA and an example of a DPT's structure.

Structure Elements (Modules). Each of the Modules consists of eight Structure Elements (Channels), which then include each of the two Datapoint Elements type float, as well as a DPE where type boolean. In addition, each DPE may contain some configuration files (configs).

### Graphical Editor Environment

WinCC-OA empowers users to develop personalized panels using a specialized User Interface Manager known as GEDI (Graphical EDItor). Within GEDI, users can construct custom user interfaces, referred to as panels. The versatile object-oriented framework of WinCC-OA allows users to incorporate various elements, including buttons, tables, text fields, lists, and more, into their panels. These objects can be manipulated through scripts, offering developers the flexibility to define processes such as initialization, button click actions, closure behavior, and more, according to their specific requirements.

While the software provides fundamental commands through dialogs, creating intricate processes demands the development of scripts. In this way, developers can implement complex algorithms tailored to their unique needs. Figure 4.8 provides a visual representation of the Graphical Editor of WinCC-OA, showcasing the various toolbars, panels, and the Property Editor. The Property Editor is particularly noteworthy as it serves as the interface where developers align the functions of different objects with Datapoint Elements, establishing a crucial link between the user interface and the underlying data processing structure.

This user-centric approach not only facilitates the creation of aesthetically pleasing and functional panels but also ensures a seamless integration with the underlying Datapoint hierarchy. GEDI, with its scriptable functionalities, emerges as a powerful tool for developers to design intuitive and efficient interfaces that align with the specific needs of their control systems.

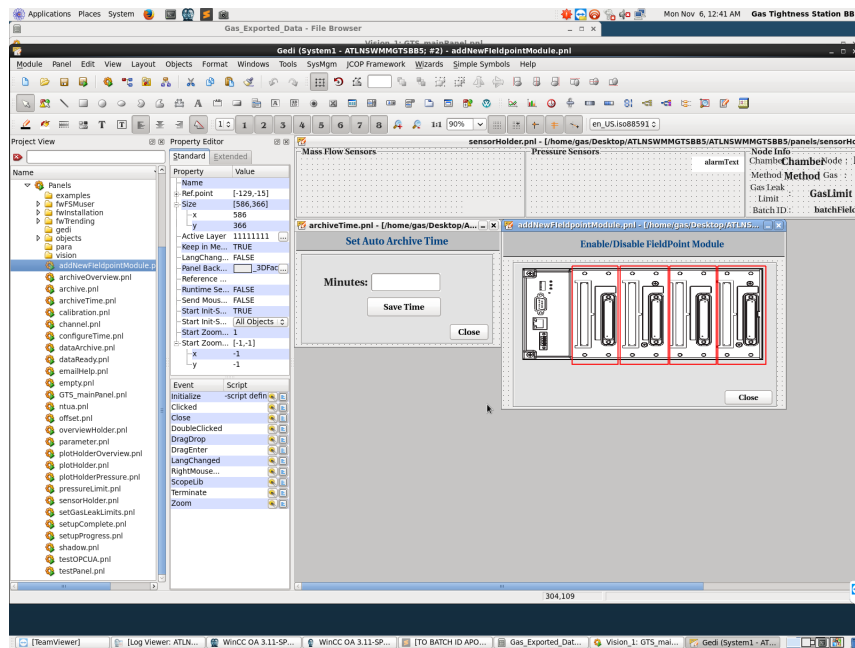


Figure 4.8: Graphical Editor Environment tool of WinCC-OA.

## Programming in Control

As highlighted previously, programmers have the autonomy to design and implement their own algorithms, dictating the behavior of objects within their panels and enabling dynamic manipulation of graphical elements alongside technical processing. WinCC-OA boasts an extensive library of methods and functions designed to streamline data management, graphics rendering, and external communications. This versatility empowers developers to tailor their applications with precision. The programming language at the core of this customization is Control, a language built upon the foundations of C but introducing certain variations. Notably, Control introduces new variable types and supports dynamic size tables. This strategic enhancement allows for efficient and flexible programming, providing developers with the tools necessary to create intricate and responsive control systems. The amalgamation of Control with WinCC-OA's comprehensive library equips developers with a robust environment to express their creativity and address the unique requirements of their projects.

## Hardware Connectivity

The linkage between the Event Manager and hardware components within WinCC-OA is facilitated through drivers. Consequently, WinCC-OA incorporates a diverse array of drivers, each tailored to specific communication protocols. These protocols encompass a variety of industry standards, ensuring compatibility with a wide range of hardware. Some notable drivers include:

- **OPC:** Facilitates communication with devices supporting the OPC (OLE for Process Control) standard, fostering interoperability in process control systems.
- **ProfiBus:** Enables seamless communication with devices utilizing the ProfiBus protocol, a widely used fieldbus standard in industrial automation.

- **CanBus:** Supports communication over the CanBus protocol, commonly employed in automotive and industrial applications for reliable data exchange.
- **DIM:** Establishes communication with devices compatible with the DIM protocol, enhancing the connectivity options within the WinCC-OA framework.

These drivers play a pivotal role in ensuring the interoperability and connectivity of WinCC-OA with a diverse range of hardware components. By supporting various communication protocols, WinCC-OA provides a versatile and adaptable platform for integrating with different devices, contributing to the system's flexibility and broad applicability in diverse industrial settings.

### Archiving

The WinCC-OA system employs an automated archiving mechanism for the database, ensuring that the various values stored in DPEs are systematically archived. This archival process serves a crucial purpose, allowing users to retrieve historical data from different user interfaces. The archived data becomes accessible for display, editing, and any other user-specific requirements.

This feature enhances the system's capability to provide a comprehensive historical record, enabling users to analyze and visualize past states, trends, and events. Whether for troubleshooting, trend analysis, or performance evaluation, the archived data in the database offers a valuable resource for users to interact with and derive insights from, contributing to the overall efficiency and effectiveness of the WinCC-OA system.

### Alarm generation and handling

The Alert Screen in WinCC-OA serves as a powerful tool for users to investigate and manage alarms generated within the system. Users can gain insights into the various alarms, examining the reasons behind their triggering and the specific locations where they originated. This information is stored in a dedicated database, allowing users to selectively display and analyze alarms through the alert presentation.

The Alert Screen not only provides a real-time overview of active alarms but also offers a historical perspective by retrieving and presenting stored alarm data. This selective display capability enhances the user's ability to focus on specific alarms, facilitating a more efficient investigation process. Users can leverage this feature to identify patterns, troubleshoot issues, and ensure the smooth operation of the WinCC-OA system.

By centralizing alarm information and providing a user-friendly interface for investigation, the Alert Screen contributes to the system's overall robustness and empowers users to maintain a proactive approach to system monitoring and management.

## 4.2.3 Joint COntrols Project Framework (JCOP)

The incentive to create the JCOP Framework package was to facilitate the development of the control system in CERN experiments. It consists of a set of instructions, parts and tools designed to facilitate the user in the implementation of automatic control applications. The Framework instructions define a convention-based name for Datapoints, the functions and files of WinCC-OA, and also cover the look and feel of the control system's graphical interfaces. Therefore, JCOP provides the user with an easy-to-use interface for composing their system and offering common features across a range of time and labor saving systems. As shown in Figure 4.9, JCOP framework occupies the first level of the hierarchy associated with hardware.

Some of the key tools of the JCOP Framework are:

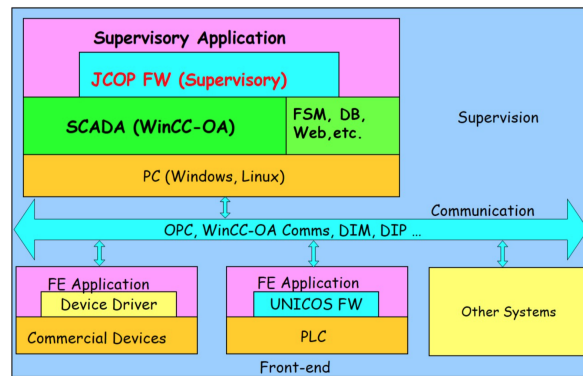


Figure 4.9: The system architecture and the location of JCOPFW in the core of DCS.

- **Installation Component:** Necessary for the installation of the various components, the removal or renewal of the existing components and the supervision of the operation of the various components. Installation of this component is required to install the various components.
- **Core Component:** It provides the basic functions of various components such as configuration, hierarchy, hardware connectivity and alerts.
- **Access Control Component:** Necessary tool for controlling and accessing users.
- **CAEN Power Supplies Component:** Allows WinCC-OA to connect to CAEN high-voltage power supplies via an OPC server and their supply channels.
- **Configuration Database:** Required for storing and retrieving control system data in an Oracle external database to automate the handling of configuration data required at runtime.
- **Trending Tool:** It allows the graphical representation of DPEs value differences by generating graphs.

Figure 4.10 depicts a panel for managing components. The partial approach followed by the Framework promotes standardization within control applications and allows code reuse, significantly reducing development and maintenance efforts.

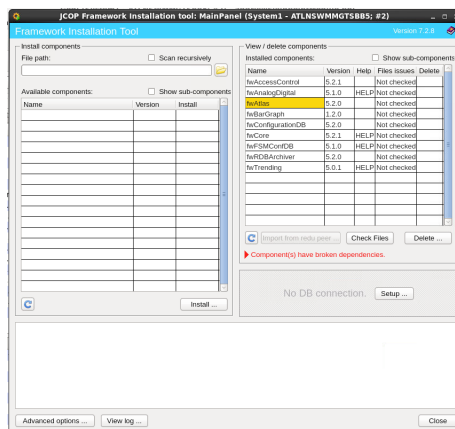


Figure 4.10: The panel to install components of the JCOPFW.

### Finite State Machine (FSM)

Ensuring the secure operation of the ATLAS detector control system, managed by a small shift crew, necessitates well-defined transitions between operational states and the swift identification and response to potential error conditions. The operational framework of the ATLAS detector relies on a FSM, seamlessly integrated with the JCOP toolkit and the PVSS alarm screen. Employing an FSM to represent all probe controls is imperative for maintaining uniform control over a diverse array of Front-End (FE) probe systems. The proposed system behavior model entails a finite number of states, transitions between these states, and associated actions. This model is crucial for orchestrating the operation of subsystem detectors within the LHC. The adopted mechanism involves structuring the subsystem detectors in a parent/child hierarchical arrangement, comprising three distinct types of nodes:

- Device Units
- Logical Units
- Control Units

This hierarchical FSM structure, with parent and child nodes, offers a systematic and comprehensive approach to modeling and managing the complex interactions within the ATLAS detector control system. It ensures not only the safety of operations but also enables the quick identification and response to potential error conditions, aligning with the stringent requirements of high-energy physics experiments.

The concluding segment of the FSM hierarchy on the back-end side is represented by the LCSs. This layer plays a pivotal role in providing low-level control and monitoring services for the SCSs. The LCSs execute commands received from the SCSs and, concurrently, have the capability to autonomously trigger predefined actions when necessary. Each LCS is specifically assigned to manage a particular system within the sub-detector, such as High Voltage (HV), Low Voltage (LV), Racks, gas, cooling, and more.

At the lowest level of the hierarchy are the Device Units (DU), serving as the interface layer between the FSM and the hardware. These DUs define the granularity of the system, establishing a boundary that restricts access beyond this point through the FSM. Essentially, everything below these boundaries is not accessible through the FSM.

The hierarchical structure of the FSM is succinctly summarized in Figure 4.11, providing an illustrative example of the FSM hierarchy. This visual representation elucidates the organized and layered approach adopted in managing the control and monitoring aspects within the ATLAS detector control system. Each layer in this hierarchy contributes to the overall efficiency and reliability of the system, ensuring seamless integration and effective control of the myriad subsystems and components.

#### 4.2.4 OPC UA Servers

In the ATLAS DCS, one of the widely employed communication protocols for establishing connectivity between various devices and WinCC-OA is the OPC UA Server.

The OPC Server serves as the cornerstone of OPC communication, acting as software that implements the OPC standard and provides standardized interfaces to the external environment. Internally, it incorporates the proprietary communication protocol specific to the manufacturer's control system. OPC Servers are developed and offered by different entities. The fundamental concept of OPC revolves around hardware manufacturers providing an OPC Server for their systems, enabling standardized access. Manufacturers can deliver the OPC Server as stand-alone software or embed it directly into the device or machine controller.

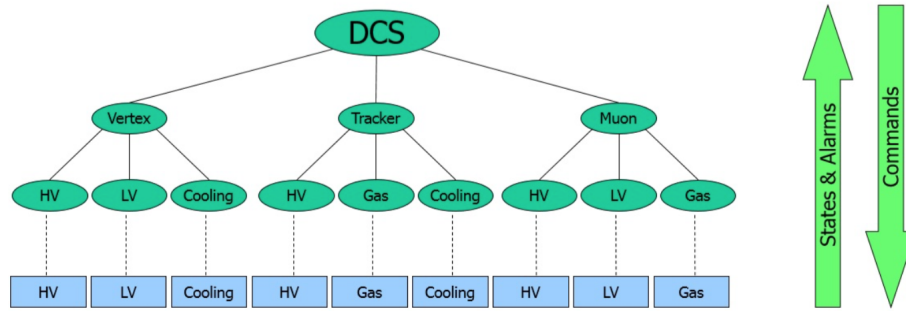


Figure 4.11: Modeling control system using FSM.

The OPC Client serves as the logical counterpart to the OPC Server. It establishes a connection to the OPC Server and retrieves the data made available by the Server. As OPC Servers adhere to the predefined interfaces of the OPC standard, any OPC Client can access any OPC Server, facilitating seamless data exchange between the client and server. Common applications for OPC Clients include systems that depend on exchanging data with industrial processes, such as visualization and SCADA systems (like WinCC-OA) or Manufacturing Execution Systems (MES).

The OPC Router, equipped with its OPC UA Client Plug-in, functions as both a client and a gateway, as depicted in Figure 4.12. This configuration allows the OPC Router to connect to OPC Servers, retrieve data, and serve as an intermediary for data exchange between different systems. This versatile setup enhances the interoperability and flexibility of the ATLAS DCS by enabling standardized communication between diverse devices and WinCC-OA through the OPC UA protocol.

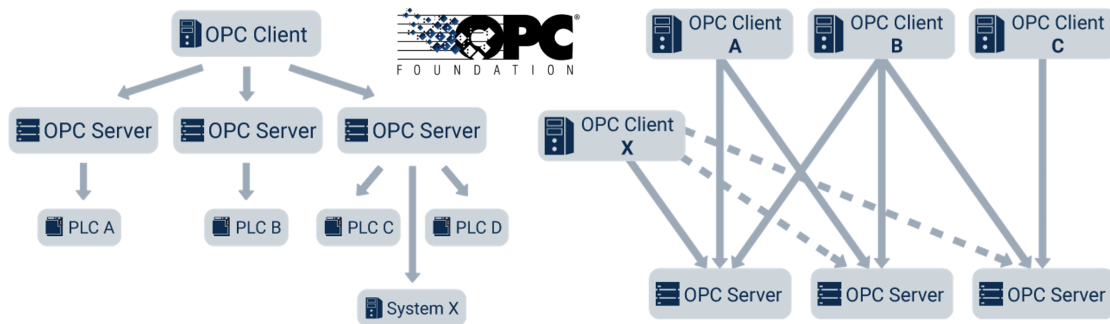


Figure 4.12: The OPC Router with its OPC UA Client Plug-in is also a client with a gateway function.

The current standard in the OPC specification is OPC UA, succeeding the older OPC Classic standard. While many installations still utilize Classic OPC Servers, OPC UA represents a significant advancement. The original OPC Classic standard effectively addressed the challenge of achieving data exchange in automation, providing a solution that transcended manufacturer dependencies and defined essential interfaces. However, a notable drawback of OPC Classic was its lack of platform independence. Built on Microsoft technologies COM and DCOM, OPC Classic limited installations of OPC Servers and OPC Clients to Microsoft Windows operating systems and networks.

Recognizing the evolving landscape of technologies with the rise of platforms like Linux, web architectures, Cloud, IoT devices, and Cyber-Physical Systems (CPS), the OPC Foundation responded by introducing OPC UA. OPC UA prioritizes platform independence and interoperability. Technically, OPC UA is constructed on fundamental web technologies such as TCP/IP and http/SOAP. The OPC UA standard comprises individual specifications, each delineating a specific function and stipulating the server and client interfaces necessary to support that function.

Crucially, OPC servers and clients are not obligated to support all specifications. Depending on

the application, developers often implement only the necessary specifications. Consequently, when utilizing an OPC server and clients, careful consideration is required to determine the specifications essential for the given scenario and ensure that both the server and client appropriately implement them. OPC UA's emphasis on platform independence enhances its adaptability to diverse technological environments, making it a key enabler for modern and heterogeneous automation systems. OPC UA consists of these specifications:

- **Models:** Using models, OPC UA specifies basic rules for exposing data to any application or device that wants to consume it. OPC UA itself is an information-centric data model. It comprises a generic object model with an extensible type system with built-in models for data access. These built-in models specify functions such as alarms and events information, information about historic data, data access details, device descriptions, and to execute programs.
- **Data flow and connections:** OPC UA supports communication between components on five levels in industrial organizations: enterprise, management, operations, control, and field (vendor-specific devices). Devices expose their data through OPC UA, which enables the transport of this information over a network to a consuming application using standard web services. Data is transported using IP-based protocols and SOAP whereby low-end servers may use UA TCP. Using standard SOAP web services over HTTP allows non-OPC UA clients to request data published by an OPC UA server. Bridging and gateway software known as OPC UA wrappers enable the flow of data on vendor-specific hardware between OPC UA levels. OPC UA wrappers can also be used to migrate from OPC Classic to OPC UA, or when an OPC server supports UA but an OPC client does not.
- **Nodes:** A node is the basic unit of data in the OPC UA address space, which provides a standard way for OPC UA servers to represent objects to OPC UA clients. Nodes are pieces of information (for example, a unique temperature) and consist of attributes, the actual data value, and one or more references to other nodes, each in its own address space. A unique temperature will therefore take up multiple addresses in an address space. Nodes are referenced by a unique node ID: a namespace URI (unique resource identifier), a data type, and the identifier itself. Each node belongs to a specific namespace. The namespace URI is located in a separate namespace table on the OPC UA server. The namespace table stores separate URIs for information models used by individual organizations that have their own requirements for how data should look and behave. This allows OPC UA to extend its services without changing the underlying design of the standard. In OPC UA, nodes have multiple classes that enable the creation of variants on the basic node. There are eight core node classes in OPC UA, including objects (physical entities), methods (functions that store data when queried), and variables (actual data). Object node classes in OPC UA are the key to how it can create complex data and distinguish between similar but different entities, for example a temperature sensor for an air conditioner and a temperature sensor for a boiler.
- **Data Access:** The Data Access specification describes the classic exchange of current data. The OPC Classic Standard already specifies that the data exchange is data point-oriented. A value can be read and written for each data point. A data point value is described by the actual value, the time stamp at which the value was current and by the quality, which describes whether the value is valid or whether, for example, the connection to the controller was interrupted and the value is therefore not valid. This specification alone makes it possible to obtain and process data independently of the underlying system.
- **Historical Access:** Using the Historical Access specification, it is possible not only to read data with the current value, but also to query historical values. An OPC server that implements this specification must have an internal data memory in order to provide the values of



the data points for possible historical accesses. A client that reads historical data points via Historical Access also transfers the desired time span to the server in addition to the data point information.

- **Alarms and Conditions:** The Alarms and Conditions specification defines a standardized model for alarm messages and alarm logic as part of OPC UA. For OPC client applications this simplifies the task of generating alarms from data point values because the logic can be implemented by the OPC server and not by the manufacturer of the client software.
- **Service-oriented architecture (SOA):** OPC UA is based on the SOA client-server communication framework. In OPC UA, there are OPC UA servers and OPC UA clients. An OPC UA server provides an OPC UA client with applications and control systems, for example MES and SCADA, and with secure access to industrial automation data using OPC UA information models that specify the way data is organized, stored, and collected. The term OPC UA server refers to the OPC UA software standard on the machine, not the hardware itself, which could be a virtual server. An OPC UA client is a client that can support an OPC UA information model. OPC UA clients request data from and write data to components in a system via OPC UA servers. SOA systems like OPC UA integrate disparate applications over a network and connect devices on different network nodes.

## 4.3 Integration Control Systems

This section delves into the diverse experimental setups and control stations that were deployed and extensively utilized by hundreds of users for the integration and commissioning of the New Small Wheel detectors and electronics. The comprehensive design and implementation of the system are scrutinized, providing insights into the intricacies of its architecture. Finally, a detailed account of the communication with the sensors is presented, emphasizing the utilization of the OPC communication protocol.

The experimental setups and control stations served as pivotal components in the integration and commissioning processes, providing users with a robust framework for effective management and monitoring. The design considerations, coupled with the implementation strategies, are explored to elucidate the decision-making processes that contributed to the successful deployment of these critical components.

A key focus of this section is the communication infrastructure, particularly the adoption of the OPC protocol. The OPC protocol plays a central role in facilitating seamless communication with the sensors, ensuring a standardized and interoperable approach. The report delves into the nuances of this communication protocol, shedding light on its implementation intricacies and the benefits it brings to the overall efficiency and reliability of the system.

By presenting a detailed analysis of the experimental setups, control stations, and the communication protocols employed, this section provides valuable insights into the technological underpinnings of the integration and commissioning processes for the New Small Wheel detectors and electronics.

### 4.3.1 Gas Tightness Station

The mass production of Micromegas Modules (MM) for the NSW upgrade in the ATLAS muon spectrometer demands a robust system for independent Quality Assurance and Quality Control (QA/QC). Among the critical aspects of control, ensuring chamber leakage (gas tightness) is paramount for the smooth operation and optimal performance of Micromegas detectors. These gas detectors operate based on the ionization of gas when a charged particle traverses the detector, leading to

the collection of electrons in the amplification region and subsequent pulse shaping in the reading electronics.

Maintaining gas tightness is crucial, as any gas leakage compromises the detector's ability to propagate electrons in the amplification region. The presence of air, particularly oxygen, inside the detector can capture electrons resulting a quantitative drop of of the gas gain. As per the NSW specifications, the general criterion for the accepted gas leakage rate in various Micromegas Modules is defined as  $10^{-5} \times V$  per minute, where  $V$  represents the volume of each module. The leakage limits vary due to differences in module volumes.

For this system, the NTUA group has taken responsibility [67]. In particular, we have studied the independent methods for the sensitivity and instrumentation of the basic stage-1 which is the basis of the Gas Sealing Control Station (GSCS) at the BB5 laboratory at CERN. In particular, two independent control methods (essentially leakage rate measurements) have been adopted as a baseline: the classical 'pressure decay method' (PDR) and a proposed innovative and dedicated 'flow rate loss' (FRL) method. It should be noted that the GSCS device should measure the actual gas leakage rate (volume loss per unit time, typically in  $stl/h$ ) under a pressure difference inside and outside the detectors of 3 mbar (as conventionally defined). For these pressure differential levels the gas leakage rate is proportional (to a good approximation for small pressure differences) to the square root of the pressure difference. Therefore, there is a pressure dependence, which requires a determination of the measuring pressure. The classical PDR method, under these circumstances, needed to be extended in terms of its working principle. When the detector volume is isolated to start recording the pressure drop, two phenomena occur simultaneously: a) pressure drop due to gas mass loss (according to the end gas law) and b) change in leakage rate due to change in through-channel pressure loss of viscosity (in general). Consequently, a pressure-dependent leakage rate occurs. However, this function is unknown. This problem is essentially unsolvable, with model uncertainty, since the leakage channel is of unknown geometric shape (unknown length and cross-sectional shape along its length) and possibly coexists with others during measurement, which means that the superposition of individual leakage rates must be taken into account. The only possible solution is an approximate optimal solution based on so-called 'leak models'. These are essentially three leakage mechanism assumptions, laminar flow, turbulent flow and a combination of the two. During the data analysis (pressure as a function of time with an initial value of 3 mbar) the best fit of the data is sought by testing the three models using the minimum  $\chi^2/ndf$  criterion. The results obtained from the three models, as has been shown theoretically, may differ from each other by a factor of two. In fact, a possibility of upgrading stage-2 by applying noise suppression through the specially designed Modern Dual Amplifier technique (Dual Phase - Double Synchronous Chopping Lock-in Amplifier in the proposed FRL method) has been foreseen.

To address this need, an automatic gas leakage control system has been designed using WinCC-OA software. This system offers a user-friendly interface for automation, enhancing efficiency and optimizing measurements. It provides the capability to measure gas leakage in Micromegas Modules, ensuring a streamlined and reliable process for quality assurance and control in the mass production of these critical components for the ATLAS experiment. Subsequent sections will delve into a detailed analysis of this automated control system, shedding light on its functionalities and contributions to the overall QA/QC process.

### Theoretical Setup

For the gas leakage control of Micromegas Modules (MM QPs), an experimental setup is proposed, illustrated in Figure 4.13. This setup is designed for the simultaneous measurement of four MM QPs using the FRL method as baseline and the PDR alternative method.

The proposed method, FRL, boasts advantages outlined, simplicity, speed, and direct measurement of gas leakage, emphasizing to its capability to accurate even in variable volumes, as the MM Quadru-

plets. The critical factor in this method is the internal pressure of the chamber under investigation. In contrast, the PDR method necessitates recording both temperature and atmospheric pressure throughout the measurement to accurately determine the final result. An essential advantage of the FRL method over PDR is its speed. In less than one hour, sufficient conclusions can be drawn regarding the chamber's leakage. In contrast, the PDR method takes several hours to reach a conclusion, during which the final result may be influenced by changes in both temperature and atmospheric pressure. These changes could lead to potential underestimation or overestimation of the gas leakage during the extended measurement period.

The proposed experimental setup offers efficiency and expediency in assessing gas leakage, making it a valuable tool for quality control in the production of Micromegas Modules for the ATLAS experiment. The subsequent sections will provide a detailed analysis of this experimental setup, elucidating its components, functionalities, and the role of the WinCC-OA software in automating and optimizing the gas leakage control process.

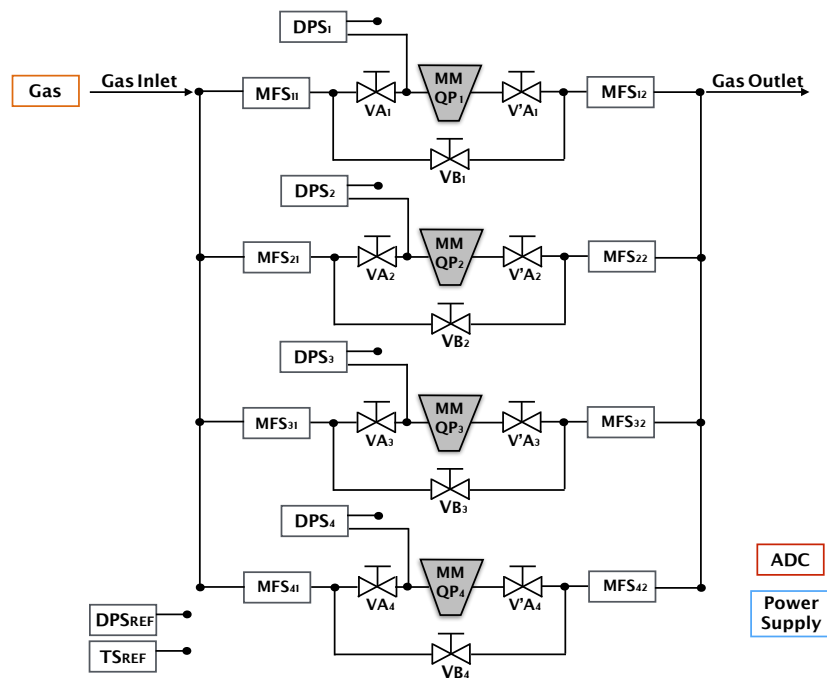


Figure 4.13: The experimental gauge for measuring gas leakage four Micromegas QPs in the laboratory BB5 of CERN.

The experimental device for measuring the gas leakage of 4-QPs consists of four nodes. The layout is an overlay of a node and for simplicity and description can be represented in the layout of Figure 4.14 in the form of a node where  $1 \leq n \leq 4$ . The setup consists of the following items:

- Gas bottle (air or mixture  $\text{Ar} + 7\%\text{CO}_2$ )
- 3 high tightness valves,  $V_{An}$ ,  $V'_{An}$  and  $V_{Bn}$
- 2 mass flow sensors,  $\text{MFS}_{n1}$  and  $\text{MFS}_{n2}$
- 2 differential pressure sensors,  $\text{DPS}_n$ ,  $\text{DPS}_{\text{ref}}$
- 1 temperature sensor,  $\text{TS}_{\text{ref}}$
- 1 Analog-to-Digital Converter (ADC)

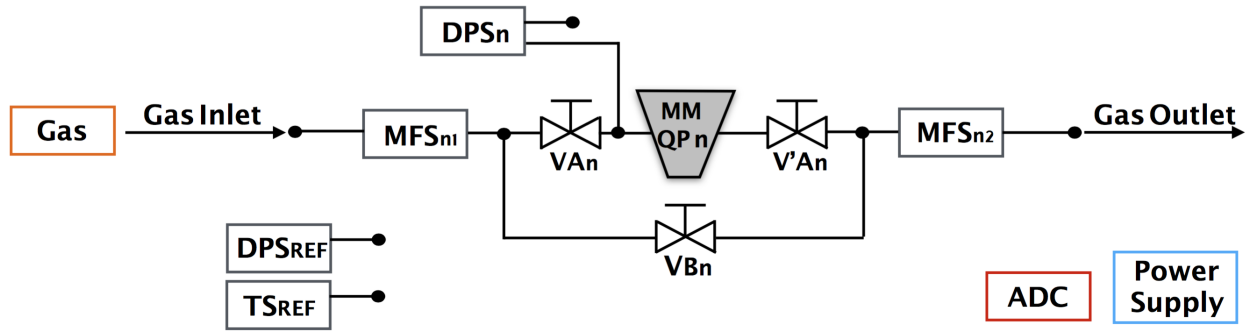


Figure 4.14: The simplified form of the experimental gas leakage measuring device 4 MM QPs in the BB5 laboratory of CERN.

- 1 power Supply
- Micromegas quadruplet

This system can support the measurement of the gas leakage of the detectors MM QP using both methods FRL and PDR with the support of the appropriate sensors respectively. As the gas flows through the device, the various sensors will produce an analog output voltage  $V_{out}$  which will be converted by the appropriate coefficient into a mass flow  $Q$  or the differential pressure  $P$ , this analog the voltage  $V_{out}$  will be recorded via a ADC connected to a computer. In the following subsections we will analyze the measurement process with the two methods and how to utilize the device.

### FRL method

In the flow loss method FRL [68], the gas leakage rate from the detector MM QP is expressed by the difference in flow loss between the inlet and outlet chamber gas pressure equals 3 mbar from the following relation:

$$Q_L = \frac{1}{b} (\Delta V_0^A - \Delta V_0^B) \quad (4.1)$$

where  $b$  is the conversion factor of the analogue output signal of the probe to mass flow,  $\Delta V_0^A$  is the differential analog signal of class A and  $\Delta V_0^B$  is the class B differential analog signal. Branch A is the gauge of the gas leakage of the chamber while Branch B is the gauge of ter/offset of the two sensors. The method of measuring the proportional voltage of branches A and B will then be analyzed.

The primary step before measuring the ter of the sensors is to check the flow pressure equal to 3 mbar using the differential pressure sensor  $DPS_n$ .

The sensors ter are measured by bypassing the chamber MM QP n and passing the gas only through the two mass flow sensors,  $MFS_{n1}$  and  $MFS_{n2}$ , by closing the valves  $V_{An}$ ,  $V'_{An}$ , and opening the valve  $V_{Bn}$ . As illustrated in Figure 4.15, this procedure allows the gas to pass through the sensors and bypass the chamber MM QP n. By stabilizing the flow, the differential signal  $\Delta V_0^B$  is recorded.

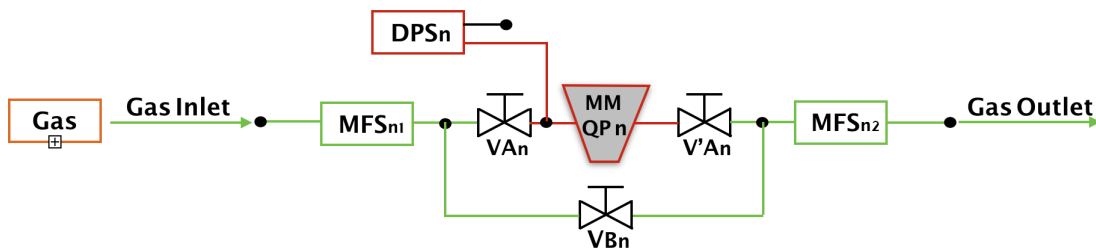


Figure 4.15: The measurement of the tare branch of the device sensors.

The leakage of the chamber MM QP n is measured by bypassing Class B and passing the gas only through the two mass flow sensors,  $MFS_{n1}$  and  $MFS_{n2}$ , and the chamber by opening the valves  $V_{An}$ ,  $V'_{An}$ , and closing the valve  $V_{Bn}$ . As illustrated in Figure 4.16, this procedure allows the gas to pass through the sensors and the chamber MM QP n. By stabilizing the flow, the differential signal  $\Delta V_0^A$  is recorded.

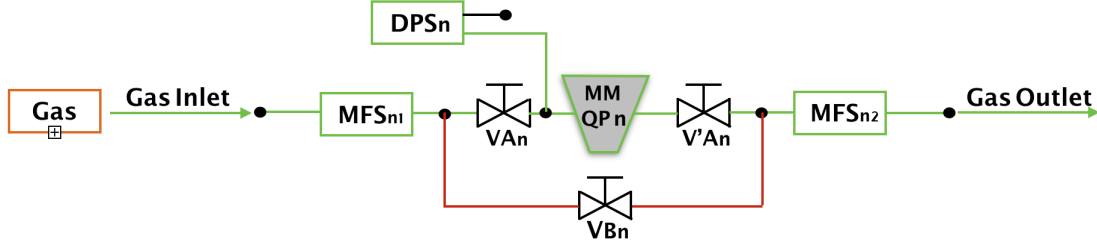


Figure 4.16: The leakage measurement of MM QP n of the device.

### PDR method

Measuring the leakage rate using the PDR method first requires the chamber MM QP n to be supplied with a pressure gas such as 5 mbar, by activating the valves  $V_{An}$ ,  $V'_{An}$  and valve closure  $V_{Bn}$  that does not affect our layout, as illustrated in Figure 4.17. It then takes time for the so-called flashing of the detector and its complete filling with gas. The achievement of flushing is reflected in the stabilization of the output flow signal by the sensor  $MFS_{n2}$ . From the moment of stabilization, the next step is

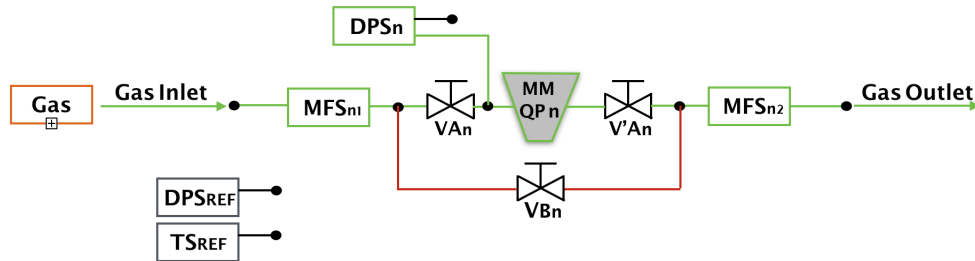


Figure 4.17: Filling of MM QP n with a specified pressure gas.

to isolate the chamber MM QP n by closing the valves  $V_{An}$ ,  $V'_{An}$  and recording the pressure drop through the sensor  $DPS_n$  as well as atmospheric pressure through the sensor  $DPS_{ref}$  and ambient temperature  $TS_{ref}$ , as illustrated in Figure 4.18.

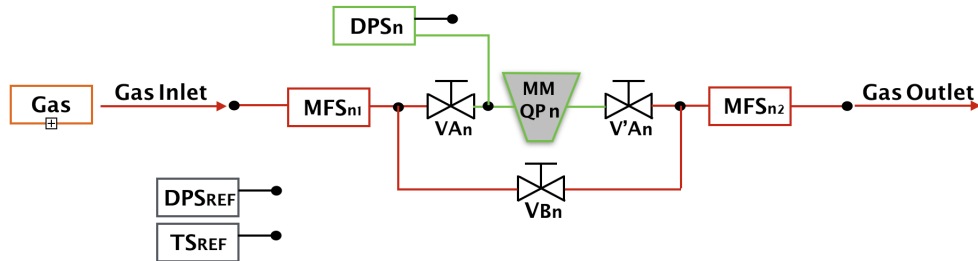


Figure 4.18: Isolation of MM QP n to measure pressure drop.

### Experimental Setup

The design of the Gas Tightness Station has reached completion, marking a significant milestone in establishing an experimental gauge for assessing gas leakage in the BB5 laboratory at CERN. The final layout of the measurements is depicted in Figure 4.19, illustrating the flow of gas through the gas mixture bottle  $\text{Ar} + 7\%\text{CO}_2$  regulated by a flow regulator. The gas then enters four branches (nodes), each equipped with an input flow sensor  $\text{MFS}_{in}$ .

Within each node, the gas is further divided into leakage and bypass branches, both controlled by high-tightness valves. Upon entering the leakage branch, the gas passes through a pressure sensor before reaching the Micromegas Quadruplet (MM QP), where it exits and is measured by the outlet flow sensor  $\text{MFS}_{out}$ . Concurrently, atmospheric pressure and temperature values are recorded by sensors  $\text{DPS}_{ref}$  and  $\text{TS}_{ref}$ , respectively. All sensors generate analog voltage signals that are transmitted to FieldPoint, where the data is digitized.

Finally, the digitized data is transferred to the computer via Ethernet. Using the OPC communication protocol, the Gas Tightness Station checks, records, and analyzes the data. This automated system streamlines the process of gas leakage assessment, providing efficiency and accuracy in the quality control of Micromegas Modules for the ATLAS experiment. Subsequent sections will delve into the detailed analysis of the Gas Tightness Station, elucidating its components, functionalities, and the role of WinCC-OA software in automating and optimizing the gas leakage control process.

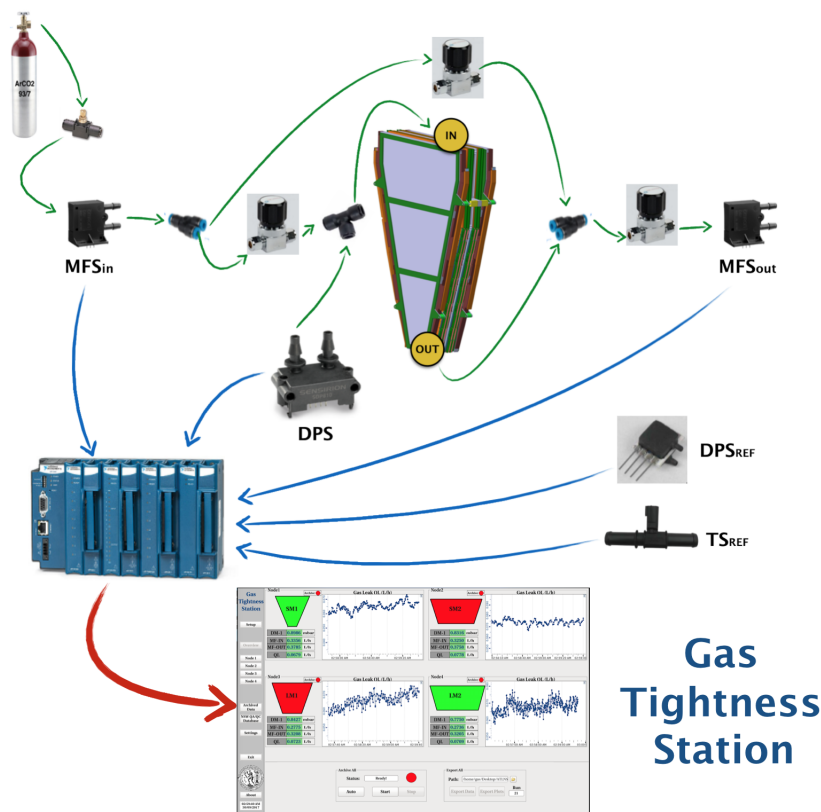


Figure 4.19: The final version of the MM QP gas leakage control system in BB5. The setup consists of input and output mass flow sensors,  $\text{MFS}_{IN}$  and  $\text{MFS}_{OUT}$ , atmospheric pressure and temperature values are recorded by sensors  $\text{DPS}_{ref}$  and  $\text{TS}_{ref}$ . All sensors generate analog voltage signals that are transmitted to FieldPoint where the data are digitized and are transmitted to the Gas Tightness Station for monitor and control.

As mentioned in this chapter, the input and output mass flow sensors,  $\text{MFS}_{IN}$  and  $\text{MFS}_{OUT}$ , show some variation of some mV for this it is necessary to measure the offset/tare of the sensor pairs of

each node. To perform the measurement of the offset of the sensors we adjust the valves so that the gas bypasses the chamber MM QP as shown in Figure 4.15. The offset can be measured via the GTS, in particular the Mass Flow Sensors Offset button in the Tab Settings area and in the Mass Flow Sensor Offset as shown in Figure 4.20. Selecting this button gives the user a new window

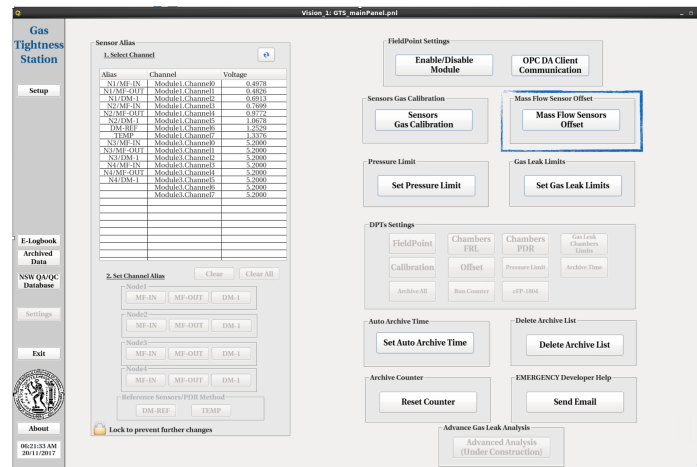


Figure 4.20: Measurement of offset of the input and output mass flow sensors,  $MFS_{IN}$  and  $MFS_{OUT}$  of the experimental device.

as shown in Figure 4.21. Through it, the user in real time can control the proportional voltage of the input and output flow sensors for each node and their difference through the DV frame. In the available boxes on the right, the user specifies offset in units of mV for each node. It should be noted that the voltages reported for the sensors for each node are the statistical average of 60 measurements per second. The determination of offset can be performed for the first time when measuring the experimental device. However, it should be noted that if the test MM QP has a very low leakage therefore some tens of mV voltage differential signal, the offset should be set equal to 0 and study the behavior of offset in order to be removed after the result of the leak. Once the offset setting for each node is set, the user presses the Save Offsets button to save their settings. It should be emphasized again that if the user wants to measure or restart the system there is no need to reset the offset because the values are stored permanently until the user is reset.

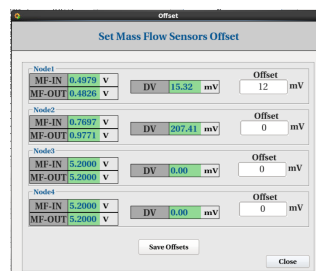


Figure 4.21: Measurement of offset of the input and output mass flow sensors,  $MFS_{IN}$  and  $MFS_{OUT}$  of the experimental device.

One of the most important steps is to calibrate all the sensors of the experimental device. That is, the transformation of the proportional output order of the flow, pressure and temperature sensors must be determined for each node separately and for each type of gas to be used as air and mixture  $Ar + 7\%CO_2$ . The calibration of the sensors will be done by the specifications set by the manufacturers as well as by artificial leakage using a medical needle as depicted in Figure 4.22. Without the proper calibration of the sensors, the produced flow or pressure values will be incorrect as a result of the



MM QP leakage effect.

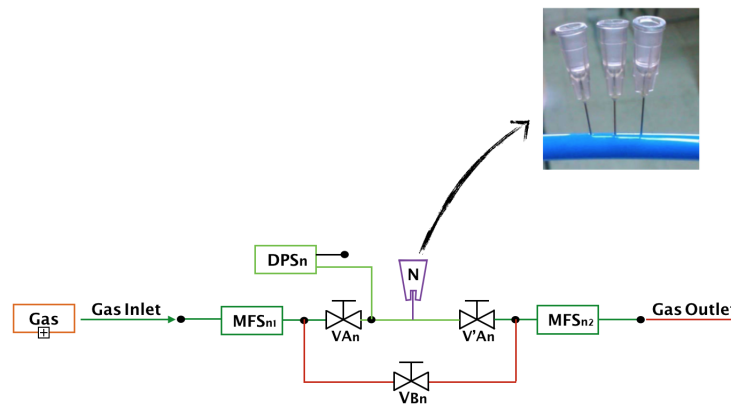


Figure 4.22: Experimental device for mass flow sensor calibration using hypodermic medical needles.

### Gas leak measurement with FRL method

By completing the steps mentioned in the previous sections, the user is now able to measure the gas leak using the FRL method. The first step is to adjust the valves so that the gas enters the leakage branch and yes it passes through the detector MM QP for each node as shown in Figure 4.16. The next step is to set up the experimental layout through the GTS panel. The user prepares the system through the Tab Setup where he/she is given the choice between FRL and PDR method. Pressing the FRL method makes it possible to select the gas to be used for the measurement, the options given are for air, argon and Ar + 7%CO<sub>2</sub> as shown in Figure 4.23 .

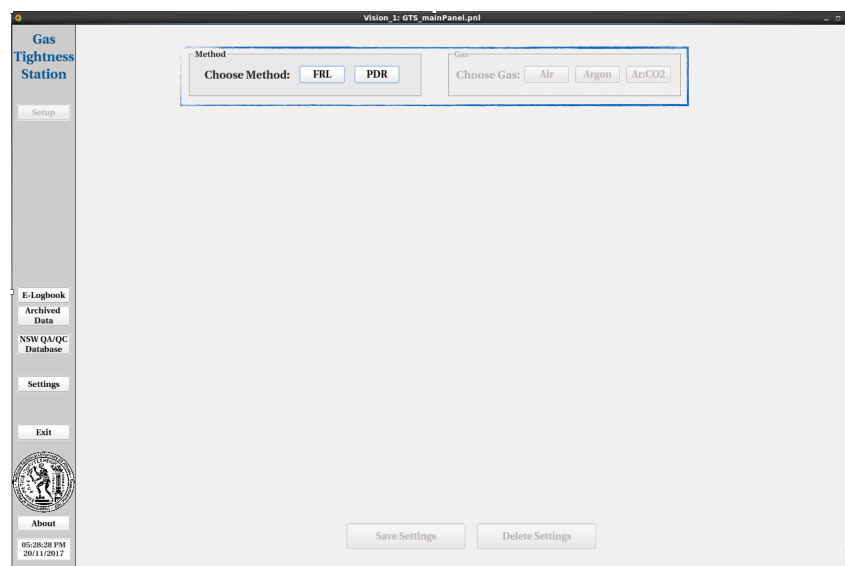


Figure 4.23: Choice of method and gas to be used to measure leakage of MM QP.

By selecting the gas, the user FRL is made visible to the user comprising four sub-frames each for a node of the experimental layout, which include the information of each node respectively.

The configuration of a node method FRL is divided into the following frames:

- **Blue frame:** Enable the corresponding node.
- **Red frame:** Select the type of MM QP found in the corresponding node and enter the 14-digit code MTF Batch ID that is the identifier of the detector.
- **Green frame:** Includes information on mass flow sensors MFS and pressure DPS for channels with FieldPoint. Sensor panels are automatically completed by activating each node once the mapping described in previous subsection has been completed.
- **Yellow frame:** Returns the value of offset/tare of the two sensors MFS of the corresponding node, a value that was set by the procedure described in previous section.

Figure 4.24: Configure the settings for each node to measure gas leakage using the FRL method.

After completing the nodes setting for the available detectors MM QP under review, the user is ready to press the Save Settings button to start the final setting of the automatic control system for the number of nodes selected, as shown in Figure 4.24. It should be noted that the fact that GTS enables the measurement of one to four node simultaneously and depends on the user activating nodes. The Delete Settings button deletes the settings from a pre-set setting to restart the creation of a new experimental layout.

Upon completion of the nodes setup, the user will notice that the Overview and Node 1-Node 4 buttons on the right side of the gray bar (depending on the number of nodes selected). Through these buttons the user can have a general overview of the experimental layout with simultaneous control of the 4 4-Node Mode he has selected (Overview button) as well as detailed control of each node (1-Node Mode) and hence each MM QP separately (Node X button, where  $X = 1-4$ ), as shown in Figure 4.25. The functions of the two types of buttons will be discussed in greater detail in the following subsections. The user by pressing one of the Node X buttons enters the 1-Node control, that is, the control and recording of the data of all the sensors of a Node. At the moment the button is pressed, a new user interface appears, as shown in Figure 4.26, which contains all the information for each node and is divided into four information boxes:

- Checking the values of node sensors and checking leakage directly through alarm.

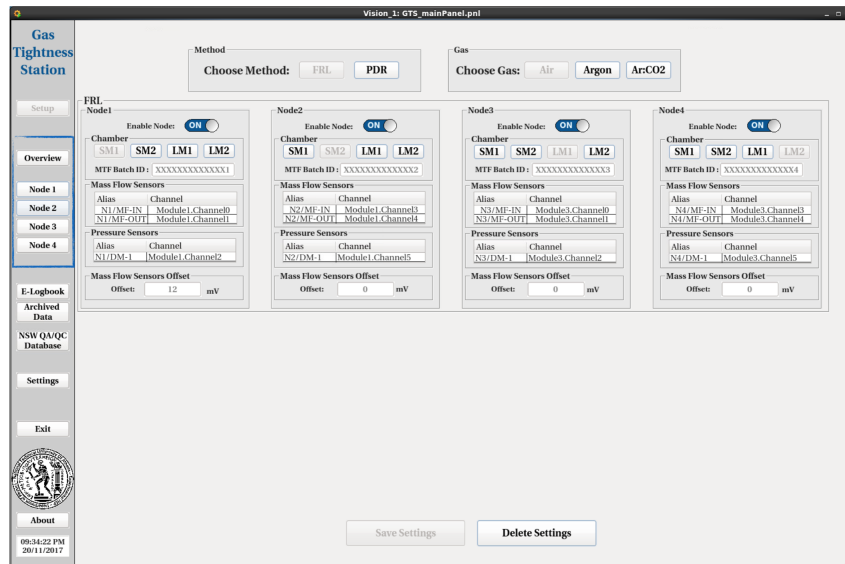


Figure 4.25: The control options of nodes, 1-Node Mode and 4-Node Overview Mode.

- Information on the leak limit, BatchID of MM QP and the method and gas of the measurement.
- Graphical representation of sensor behavior and leakage over time.
- Recording and storing sensor values in data or graph formats.

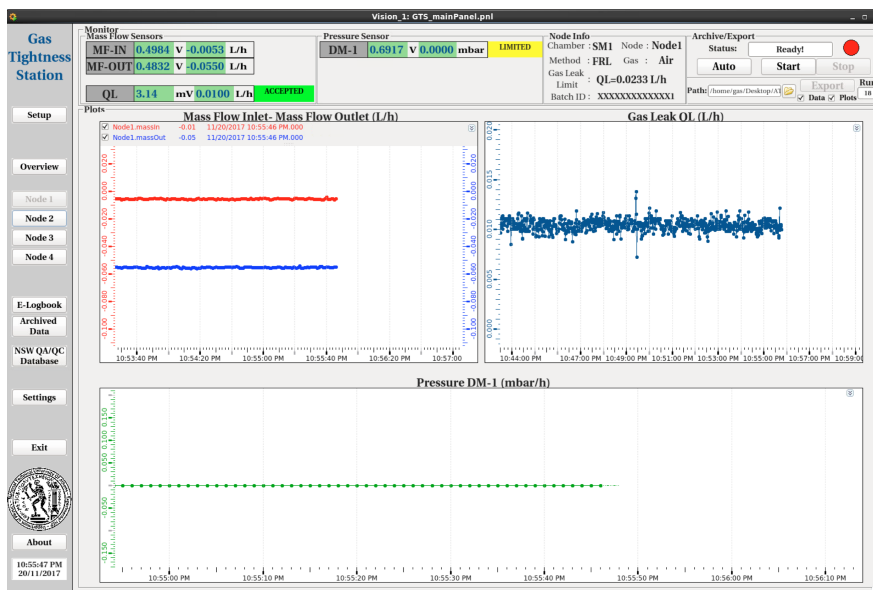


Figure 4.26: Check the sensors and MM QP of each node with 1-Node Mode.

## Monitor

Through the Monitor box, as shown in Figure 4.27, the user can monitor in real time the value of the mass flow sensor (MFS) in and out of units  $V$  and  $L/h$ , as well as the leakage  $Q_L$  of MM QP in the same units where the leakage is actually the difference between the sensor MF-OUT and MF-IN. The user has the ability to monitor in real time the value of the pressure sensor DM in  $V$  and  $mbar$  units. In addition, alarm enables the user to be notified whether the detector is over or within the leakage

threshold as well as the pressure inside the detector set in accordance with the procedure described in previous sections. All sensor values listed are the average of 60 measurements per second recorded by FieldPoint.

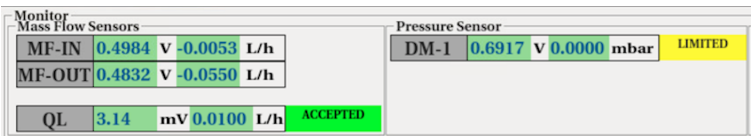


Figure 4.27: Checking the values of the sensors and the MM QP of each node with 1-Node Mode in the FRL method.

Plots

It enables the user to monitor the behavior of the various sensors over time through the plots frame, in particular it can monitor the inlet and outlet mass flow sensor, the gas leakage of the detector as well as the pressure inside the node, as shown in Figure 4.28 .

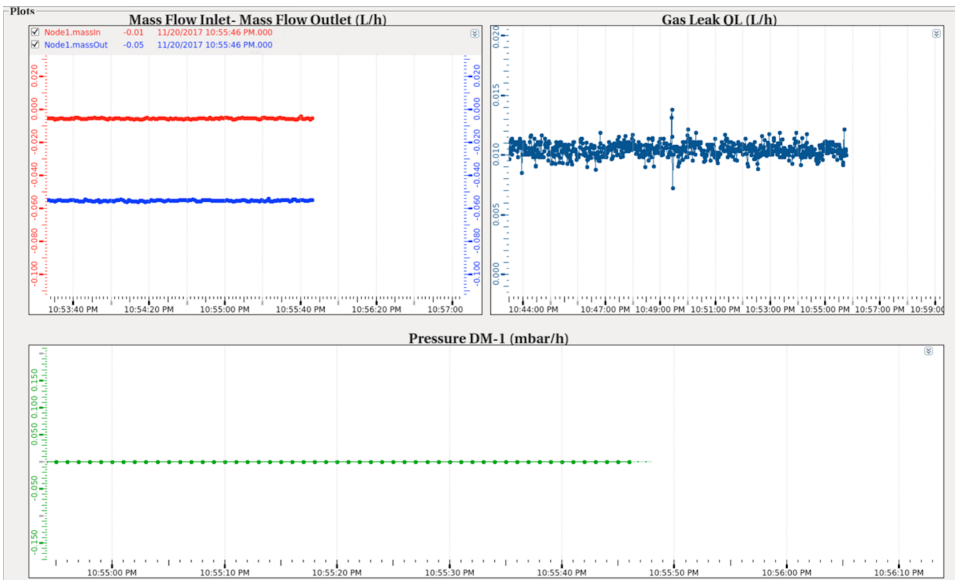
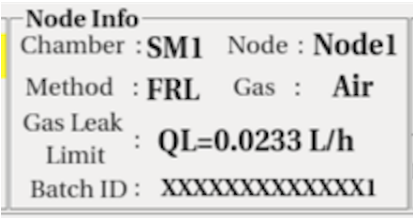


Figure 4.28: Check the sensors and MM QP of each node with 1-Node Mode in the FRL method.

Node Info



This box provides the user with information about the type, leakage limits and MTF Batch ID of the detector MM QP as well as what node is present and what gas or method is used to measure the gas leak, as illustrated in the Figure 4.28 .

Archive/Export

Through this frame, the user is able to store and export node’s sensor data. As the user initiates the data logging process using the Start button, the Status box changes to Archiving mode while the circle shows the status of the logging system or not. With the Stop button, the user stops recording the data and the Export button becomes available to export the data. After the specified time in Auto or when

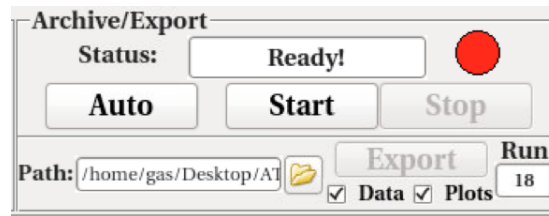


Figure 4.29: Frame for storing and extracting experimental data sensor data.

the user presses Stop, the data logging stops and the Export button becomes available to the user. In the Path box via the folder icon it can specify the location on the computer where the data will be exported. GTS enables exporting data to data or plots either to two. When the user selects the export format data, an ASCII file is exported named run\_X.dat, where X is the number of measurement (Run) in the path specified. The ASCII file that is created has a specific structure and consists of a line that contains the information of node, the type of the detector, the method, the gas, the offset of the sensors as well as the Batch ID of the detector. It then includes a column of measurement time, the input and output mass flow sensor columns  $L/h$ , the gas leak in units  $L/h$ , and the pressure in units  $mbar$ . The second option for the user is to export the data in graphs for easier investigation

*run_15.dat					
Node: Node1   Chamber: SM1   Method : FRL   Gas : Air   Offset : 0.039L/h   BatchID : SMSMSMSMSMSMSH					
Time	MF-IN(L/h)	MF-OUT(L/h)	QL(L/h)	Pressure(mbar)	
11/10/2017 10:21:38	4.93776	3.28720	1.68992	0.00000	
11/10/2017 10:21:39	4.93802	3.28720	1.69017	0.00000	
11/10/2017 10:21:40	4.93802	3.28642	1.69096	0.00000	
11/10/2017 10:21:41	4.95077	3.28798	1.70215	0.00000	
11/10/2017 10:21:42	4.94557	3.28746	1.69746	0.00000	
11/10/2017 10:21:43	4.93854	3.28590	1.69200	0.00000	
11/10/2017 10:21:44	4.93854	3.28737	1.69053	0.00000	
11/10/2017 10:21:45	4.93854	3.28746	1.69044	0.00000	

Figure 4.30: The structure of the export file ASCII with the sensor data and node data measured by the FRL method.

of the results. The graphs were created using the ROOT Data Analysis Framework [69] of CERN where an algorithm can be run in the background via the shell script and generate the graphs from the data of the detectors. The export file is a png image named run\_X\_plot.png, where X is the number of the measurement (Run), and stored in the path specified by the user. An example of the generated graph file is given below in Figure 4.31. The graph of the inlet and outlet mass flow sensors, the inlet and outlet flow distribution histograms, the pressure graph and finally the gas leak are produced. In addition, all histograms give the measurement information (Entries), that is, how many seconds the measurement took and the mean of the measurements along with the standard deviation RMS in  $L/h$ . Finally, a table is provided that provides the measurement information, such as the type and Batch ID of MM QP, the gas used, the method, the date, the final leak of the detector as well and the measuring pressure. The user by selecting the Overview button on the left side of GTS has the ability to overview the experimental layout in a common graphical environment. This new environment, as shown in Figure 4.32, enables the control of gas leakage in all nodes activated by the user. The user can control inlet/outlet flows, pressure and gas leakage simultaneously for all MM MPs available. In addition, a graphical representation of the gas leak is provided to control the leakage over time. The different colors of the detectors shown represent the alert (alarm) whether the detector is within or six of the leakage limits set. Additionally, there is Archiving indicating where the record is node when data is recorded through 1-Node Mode. In the 4-Node Mode control, the user has the ability to archive the sensor's data of all MM QPs simultaneously by pressing the Start or Auto button, where the duration of the auto test is common with that one for the 1-Node Mode. By pressing the Stop button, user has the ability to finish the data acquisition. When, the data acquisition procedure is completed, the Export Data and Export Plots buttons are becoming available, and the

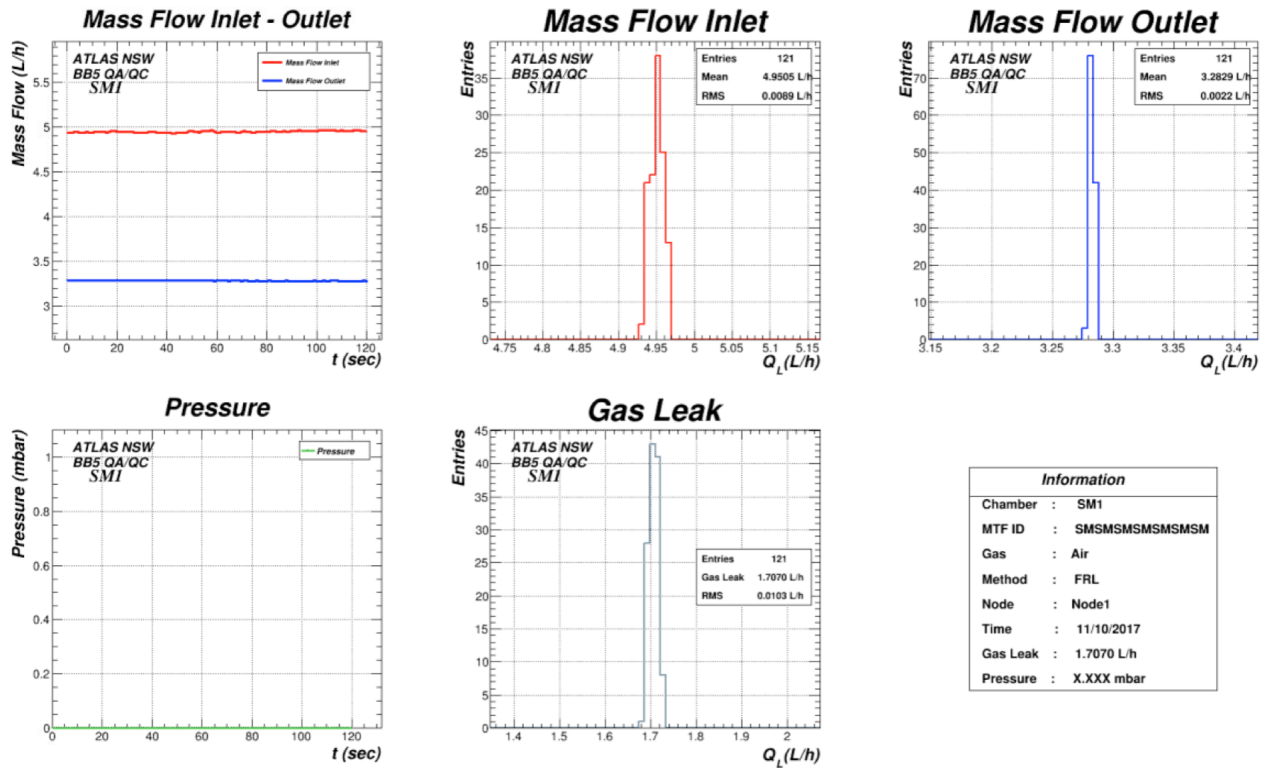


Figure 4.31: The exported plots using the ROOT Data Analysis Framework [69].

user can export the data and plots accordingly. The structure of the ASCII file and the data plot which are produced has exactly the same form with that one that described in the 1-Node Mode, with the difference that the final data contains the 1-Node Mode file for every node, as shown in Figure 4.30, and also different plot files are produced for the different nodes with the same structure of 1-Node Mode, as shown in Figure 4.31 .

### Advanced Analysis

As mentioned above, the gas leakage rate is equal to the difference of the mass flow sensor (MFS) differential signal with the offset of these sensors. In the case of a very small gas leak of some  $mV$ , it is necessary to study the behavior of the sensors offset by recording the data in the branch offset. In the event of a minor leak, GTS provides detailed leak analysis using the Advanced Analysis button of Tab Settings. To perform the measurement, the user must collect two different sets of measurements with the value offset of the corresponding node equal to 0, one set will consist of the data of the two sensors for the offset of the sensors and a set of measurements by measuring the leakage of MM QP according to the procedure Selecting the two files will provide a detailed analysis of the leak and the end result will consist of a bar chart containing the offset and leak distributions along with the characteristics of the two partitions and the final leakage of the resulting from the difference between these two distributions, as shown in Figure 4.33 .

### NSW QA/QC Database

In addition to storing the measurement data in the local disk of the computer, it is necessary to secure the measurement results in a central Database. For the purpose of validating the results of the QA/QC measurements, i.e. measuring the leakage of detectors MM QP, the central Logistics Database was built by the University of Freiburg ATLAS \_MUON \_NSW \_MM \_LOG. Includes ID (ID) and handling of all NSW equipment such as components and lots regardless of whether





Figure 4.32: Check the sensors and MM QP of each node with 4-Node Mode in the FRL method.

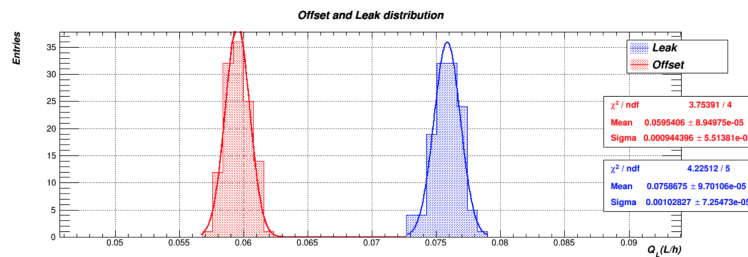


Figure 4.33: Use advanced analysis to determine the gas leakage of MM QP by additionally calculating the offset distribution of mass flow sensors in the FRL method.

it is Micromegas, sTGC or electronic equipment as well as the history of various values that have been saved. Below the central Logistics Database ATLAS\_MUON\_NSW\_MM\_LOG are 3 sub databases containing detailed information about Micromegas, sTGC, Electronics and are ATLAS\_MUON\_NSW\_MM\_QAQC, ATLAS\_MUON\_NSW\_STGC\_QAQC and ATLAS\_MUON\_NSW\_ELEC\_QAQC, respectively. The databases include the saved settings as well as the type of measurements, as illustrated in Figure 4.34 below. In addition, Figure 4.35 depicts the structure of Database Logistics (left) and the structure of MM QA/QC (right). The databases consist of several tables, for example MM QA QC consists of central CENTRALMEAS where it contains the list of metrics with result information, exact time and shifter, MEASCOMMENTS which includes the user's comments on the measurement they made, MEASDOCUMENTS which contains the metrics data files where the user can finally add MEASDOCLINK containing the metering link to the files the user added.

## Results

As an integral facet of the quality control measures employed during the integration of MM QPs in Lab BB5 at CERN, an assessment was conducted on a total of 136 Quads [67]. The focus of the evaluation centered on their gas tightness performance, utilizing air sourced from a dedicated bottle. The key parameter under scrutiny was the leak rate (QL), expressed in  $mL/h$ , which was





### 4.3.2 High Voltage Station

As outlined in previous chapters, the New Small Wheel will incorporate Micromegas detectors as a fundamental component. The operational principle of Micromegas detectors relies on the ionization of gas when traversed by muon particles. Following ionization, a positive high voltage is applied to the cathode to collect the generated electrons. These electrons constitute the signal or "pulse," produced as they traverse the readout strips connected to the electronics boards. Therefore, to ensure optimal performance of the Micromegas detector, it is imperative to validate both gas tightness and high voltage operation, aiming for a flawless 100% performance rate.

As previously discussed, the gas tightness measurement is executed through the Gas Tightness Software at BB5. To complement this, an experimental setup and corresponding software need to be developed for the concurrent validation of high voltage. The overarching concept involves monitoring the voltage and current applied to different high voltage sections of the Micromegas detector through the CAEN mainframe and HV boards. An illustrative example of these devices is presented in Figure 4.37.



Figure 4.37: The CAEN mainframe SY4527 and CAEN HV boards A7038 with 32 channels which are commonly used for the Micromegas HV validation.

A Micromegas detector is segmented into distinct HV sections, and the validation procedure focuses on each of these individual HV sections. The numbering of these HV sections is specific to the type of chamber. For the Micromegas detectors slated for integration into the New Small Wheel, there are two distinct types:

- **Type 1:** These are the SM1/LM1 modules which include 5 PCBs or 40 readout strips and 4 drift channels.
- **Type 2:** These are the SM2/LM2 modules which include 3 PCBs or 24 readout strips and 4 drift channels.

The two types of Micromegas detectors are visually represented in Figure 4.38. In the figure, one can discern the varying number of PCBs per detector type. Additionally, the HV sections are highlighted in yellow. As an illustrative example, the L1L1 section is identified as the HV section at PCB 1, Layer 1, and the Left side of a Micromegas detector of Type 1. This sectional breakdown provides a clear delineation of the distinct HV regions within each detector type. Thus, the HV validation consists of the validation of all HV sections per module and the experimental setups which developed will be described in the next section.

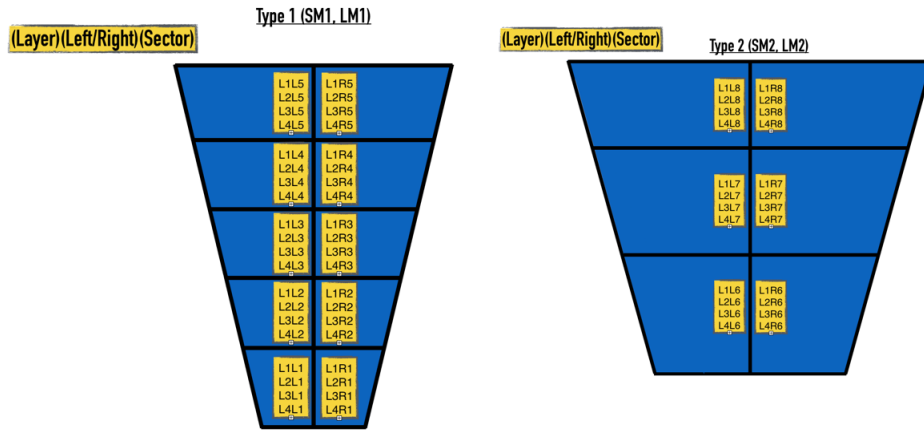


Figure 4.38: The Micromegas high voltage PCB sections mapping.

### Experimental Setup

For the high voltage validation of the Micromegas (MM) modules, two distinct setups have been developed in different locations to test the high voltage under various conditions. These setups are as follows:

- **BB5 setup:** This setup is designed for the validation of the modules after their reception from different construction sites.
- **Gamma Irradiation Facility (GIF++) setup:** This setup is tailored for the validation of the modules under high radiation environments, conducted prior to their installation in the hazardous ATLAS cavern.

Certainly, the upcoming subsections will provide a comprehensive description of the distinct setups, outlining their specific configurations and functionalities.

### BB5

The experimental setup at BB5 is configured with four parallel nodes or test stands, enabling the simultaneous execution of gas and high voltage validation procedures for the Micromegas detectors. A visual representation of the experimental setup is presented in Figure 4.39.



Figure 4.39: The Micromegas high voltage validation experimental setup at BB5.

The image above provides a visual representation of the BB5 experimental setup, featuring four parallel nodes, each equipped with independent HV and gas channels capable of simultaneous operation. The HV validation process at BB5 is organized into three distinctive sub-stations, enhancing the efficiency and precision of the validation procedures:

- **HV Station:** This sub-station comprises two CAEN SY4527 Mainframes, each supplied with 7 A7038STP CAEN boards, resulting in a total of 224 HV channels. The well-structured HV Station serves as a crucial component for the high voltage validation process.
- **Gas Station:** Each node is equipped with a dedicated Gas Station, featuring a mass flow, humidity, and pressure sensor interconnected with an Arduino and a Raspberry Pi for comprehensive gas monitoring during the validation procedures.
- **Environmental Station:** The BB5 setup includes an Environmental Station designed to monitor external factors such as pressure, humidity, and temperature. This station is equipped with sensors connected to an Arduino, contributing to the comprehensive environmental monitoring aspect of the validation process.

In the subsequent sections, we will delve into the detailed functionalities and specifications of each sub-station, providing a thorough understanding of their roles in the BB5 experimental setup.

An overview schematic of the Micromegas high voltage validation experimental setup at BB5 is shown below in Figure 4.40.

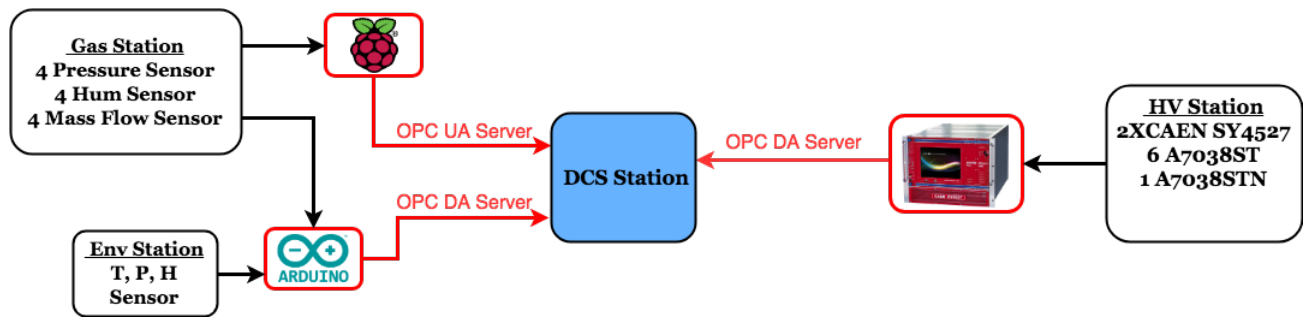


Figure 4.40: The overview schematic of the Micromegas high voltage validation experimental setup at BB5.

## GIF++

The experimental setup at the GIF++ irradiation area is designed with the flexibility to concurrently perform high voltage validation on multiple Micromegas detectors under elevated irradiation conditions, as illustrated in Figure 4.39. Situated within the GIF++ irradiation area is a 14 TBq Cs<sup>137</sup> source emitting 662 keV photons. Notably, this source generates a gamma field that is 30 times more intense than that at GIF, enabling the accumulation of doses equivalent to the anticipated conditions at the HL-LHC in a relatively short timeframe.

The GIF++ irradiation bunker spans 100 m<sup>2</sup> and encompasses two independent irradiation zones. This design allows for the testing of detectors at their full size, reaching several square meters, as well as the evaluation of a diverse array of smaller prototype detectors and electronic components. The photon flux in each irradiation zone is controlled through a set of Lead filters, offering tunability to suit specific testing requirements.

The comprehensive infrastructure of the GIF++ irradiation area includes electronic racks, gas systems, radiation and environmental monitoring systems, and a spacious preparation area. This infrastructure is strategically designed to facilitate the efficient installation of detectors, ensuring a streamlined and time-effective process. The availability of such resources positions GIF++ as a robust and versatile environment for conducting high voltage validation under challenging irradiation conditions.

The GIF++ experimental setup is ingeniously organized into three parallel nodes, with each node

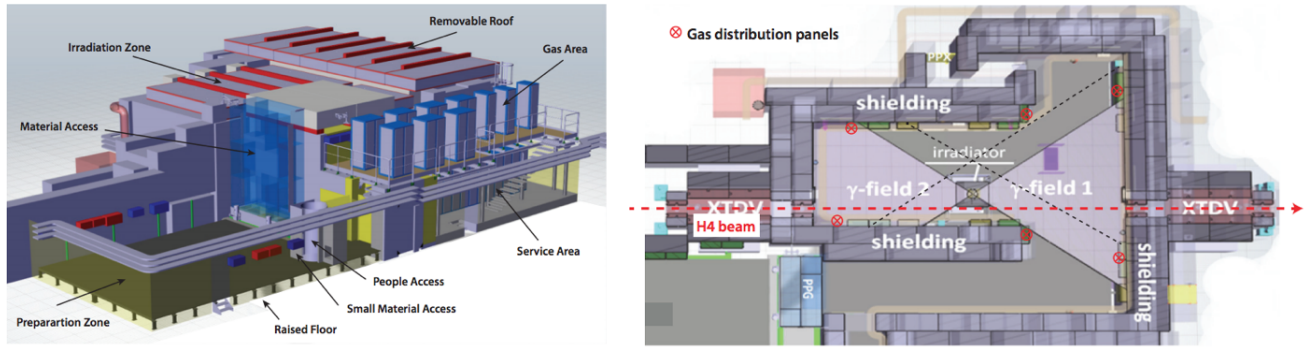


Figure 4.41: The Micromegas high voltage validation experimental setup at GIF++ irradiation setup.

housing independent high voltage (HV) and gas channels capable of simultaneous operation. This design enhances efficiency and allows for concurrent testing. The GIF++ setup incorporates three distinct sub-stations dedicated to HV validation:

- **HV Station:** This station is equipped with a CAEN SY4527 Mainframe, comprising two A1821P CAEN boards, seven A7030STP CAEN boards, one A1821N CAEN board and one A7038STP CAEN board to accommodate a comprehensive array of HV channels.
- **Gas Station:** Each station in this category is furnished with a suite of sensors, including mass flow, humidity, and pressure sensors, all seamlessly connected to an Arduino. This setup ensures monitoring and control of gas parameters.
- **GIF++ Station:** The external GIF++ station is equipped with sensors for temperature, pressure, humidity, and irradiator, establishing a robust connection via the DIP protocol. This external station plays a pivotal role in providing critical environmental and irradiation data for comprehensive testing.

Together, these sub-stations create a cohesive and versatile environment for HV validation at the GIF++ irradiation area, allowing for the concurrent assessment of multiple Micromegas detectors under the challenging conditions of heightened radiation exposure.

An overview schematic of the Micromegas high voltage validation experimental setup at BB5 is shown below in Figure 4.42 .

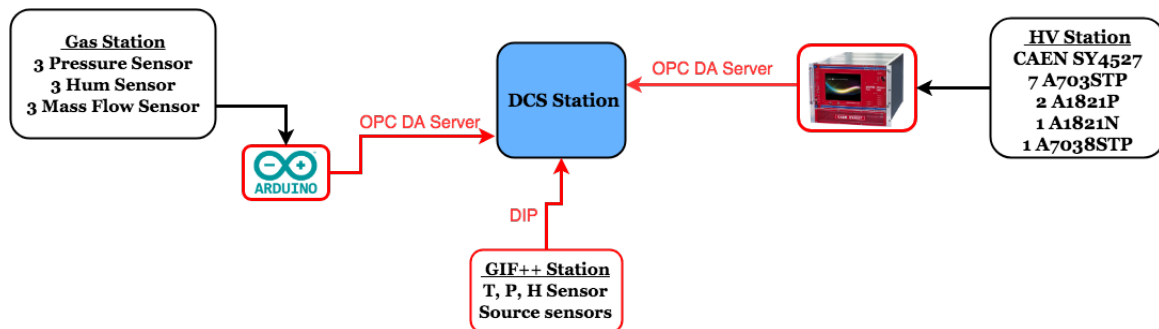


Figure 4.42: The overview schematic of the Micromegas high voltage validation experimental setup at BB5.

### Control Station

The HV Station DCS has been developed to monitor and control the high voltage (HV) sections of the Micromegas modules, facilitating comprehensive validation of their HV status. The software



boasts various user-friendly functionalities, each contributing to the effective management of HV validation.

### HV Mapping Setup

The initial phase for operating the HV involves the HV mapping configuration, also known as the matching process between the Micromegas HV sections and the CAEN HV channels. This critical procedure is seamlessly executed through the "Setup" tab of the HV DCS, as illustrated in Figure 4.43 .

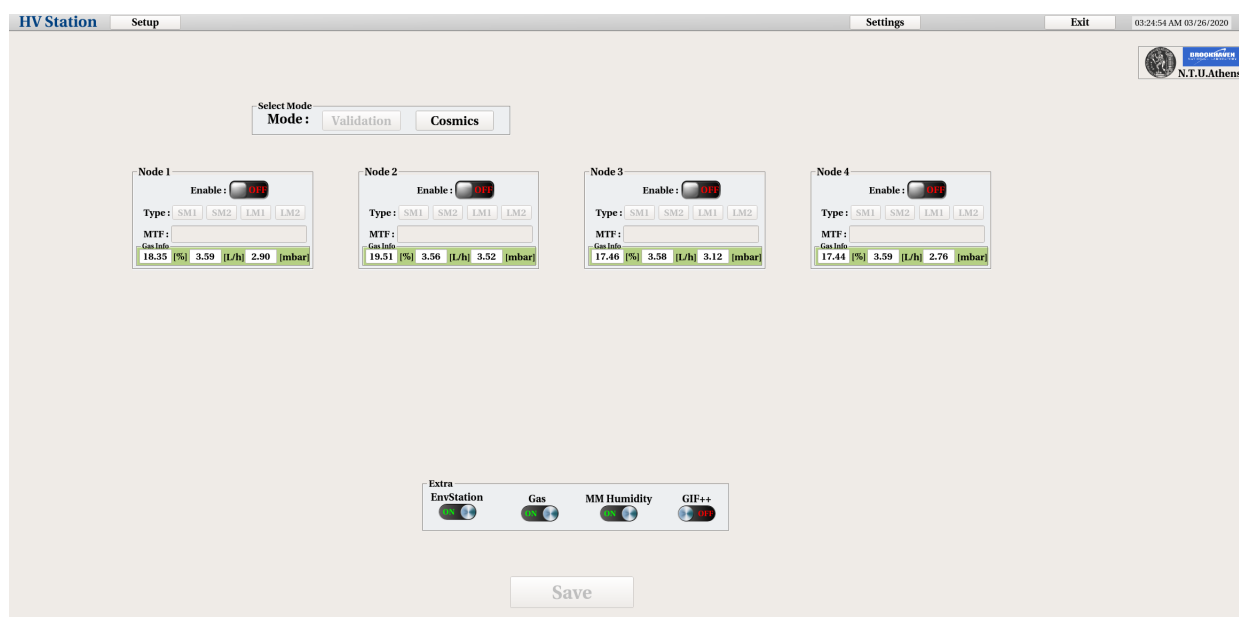


Figure 4.43: The "Setup" tab of the HV DCS where user can set the HV Mapping.

User via the button "Settings" is opening the Settings panel and via the "HV Setup" is opening the "HV Mapping setup" as shown in the Figure 4.44 . Within this "Setup" panel (Figure 4.43), users

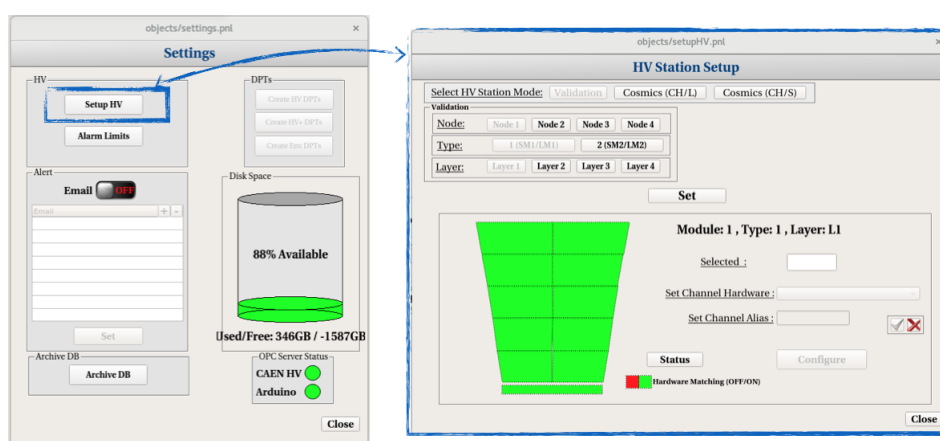


Figure 4.44: The panel for the HV Mapping setup via the "Settings" panel.

can choose the mode ("Validation" in our case, while the "Cosmics" mode will be detailed in the next section), the node or MM module (four parallel test stands/nodes), the module type ("Type 1" for SM1/LM1 or "Type 2" for SM2/LM2), and the layer of the MM module. Upon pressing "Set," a secondary window appears at the bottom, presenting a graphical widget of the selected Node, Type,

and Layer, with different HV sections highlighted. The green/red color indicates whether there are HV channel settings for the corresponding HV section.

To perform the HV mapping setup, the user needs to select one section (Figure 4.45), and the selection will be displayed near the "Selected Sector" text field. In the "Set Channel Hardware" text field, users must input the CAEN board and channel by choosing from the channel list that will appear. After selecting the HV channel, users must click the "green Tick" button and then the "Configure" button to save the settings for that specific HV section. This procedure needs to be repeated for all HV settings, ensuring each HV section is correctly mapped to the corresponding HV channel.

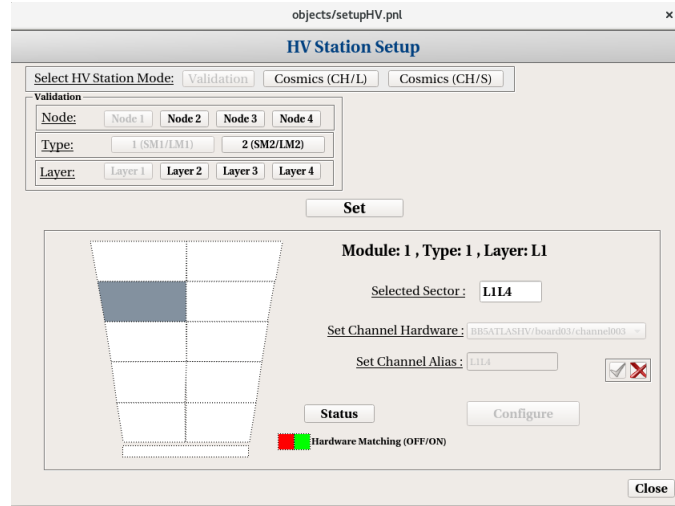


Figure 4.45: User sets the HV board and channel of the selected HV section.

When user has complete the HV mapping of the nodes that he/she will use he can press "Close" button and return to the first "Setup" tab as shown in Figure 4.43 .

### Node Setup

The subsequent step involves the node setup, an essential phase in configuring the high voltage (HV) validation process. In the initial "Setup" tab, depicted in 4.46, users are prompted to select the desired "Mode" ("Validation" for our case, with the "Cosmics" mode to be detailed in the following section). Four windows corresponding to the modules under testing are presented, and users can enable the relevant node, designate the type of chamber (SM1/SM2/LM1/LM2), input the 14-string MTF Batch ID of the module, and select additional features in the "Extra" frame.

Furthermore, users can monitor the pressure, mass flow, and humidity values of the gas line associated with each node, ensuring optimal conditions for the subsequent HV validation process. This comprehensive node setup ensures a streamlined and efficient configuration tailored to the specific requirements of each testing module. The "Extra" frame includes all the extra sensors of the experimental setup and these are:

- **EnvStation:** Environmental sensors for monitoring the temperature, pressure and humidity of the environment
- **Gas:** Mass flow and pressure sensors of the node gas lines
- **MM Humidity:** Humidity sensors of the node gas lines
- **GIF++:** Various sensors provided by GIF++ infrastructure via DIP protocol



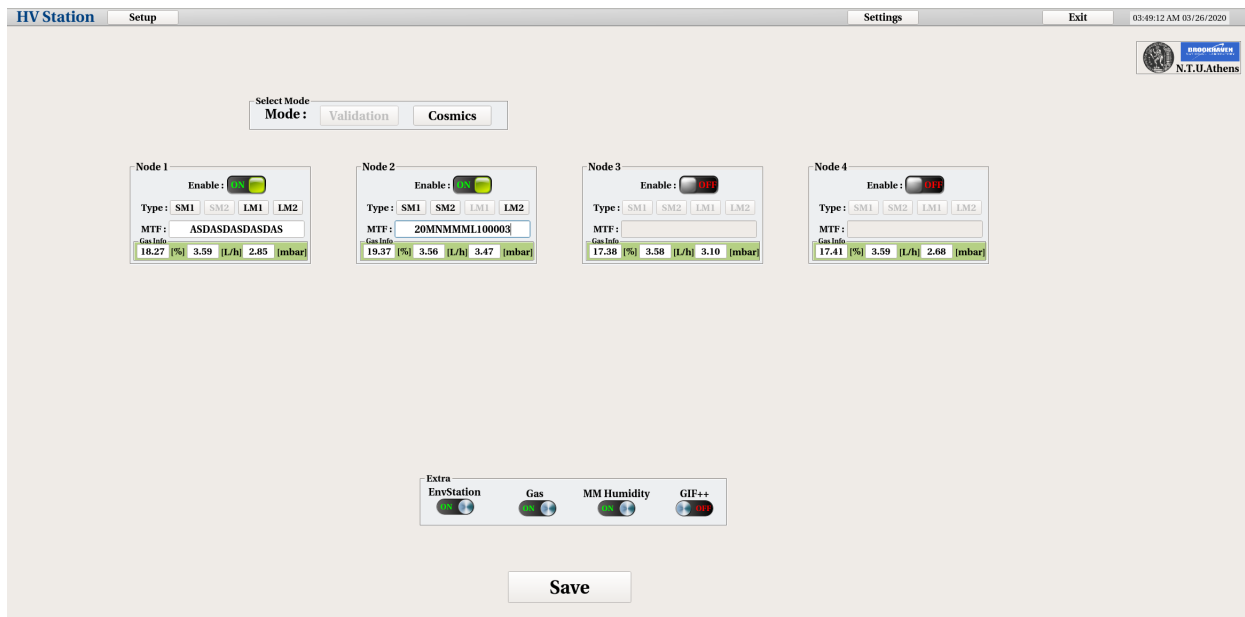


Figure 4.46: User sets the HV board and channel of the selected HV section.

When user inputs the information of the node's corresponding module under testing and also the extra feature that he want to monitor, he should press the "Save" button in order to save the node settings, as shown in 4.46 .

And that's it, users can continue with the Micromegas HV validation.

## Operation

As outlined in the preceding section, once the user presses the "Save" button within the "Setup" tab, the software automatically saves the configured settings for each node. This action triggers the initialization of the enabled nodes, and the corresponding user-enabled nodes are then displayed in the top bar of the HV DCS interface. The top bar, illustrated in Figure 4.47 below, showcases these nodes as buttons, providing users with quick and convenient access to the individualized settings and configurations of each node. This user-friendly feature enhances the overall efficiency and accessibility of the high voltage (HV) validation process.

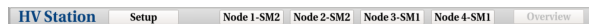


Figure 4.47: When user is pressing the "Save" button, the HV DCS is saving the node settings and the user enabled Nodes are appearing.

As depicted in Figure 4.47, the appearance of "Node X-Type" buttons signifies the user-defined settings for each node. Each button corresponds to a specific module connected to the respective node. Pressing a "Node" button allows the user to navigate through the settings and configurations of the associated module. Additionally, an "Overview" button is present, providing the capability to monitor and control all nodes simultaneously. The subsequent sections will delve into the detailed analysis of monitoring and controlling individual nodes. This comprehensive functionality enhances the user's ability to efficiently manage and navigate through the high voltage (HV) validation process.

## Monitor

Upon pressing the "Node X-Type" button, users are directed to the main control and monitoring window of the HV DCS software, as depicted in Figure 4.48. This window provides a wealth of information and functionalities that warrant detailed explanation and exploration. Each component

and feature within this window plays a crucial role in facilitating effective control and monitoring during the high voltage (HV) validation process. Let's delve into a comprehensive overview of the various elements present in this monitoring interface.

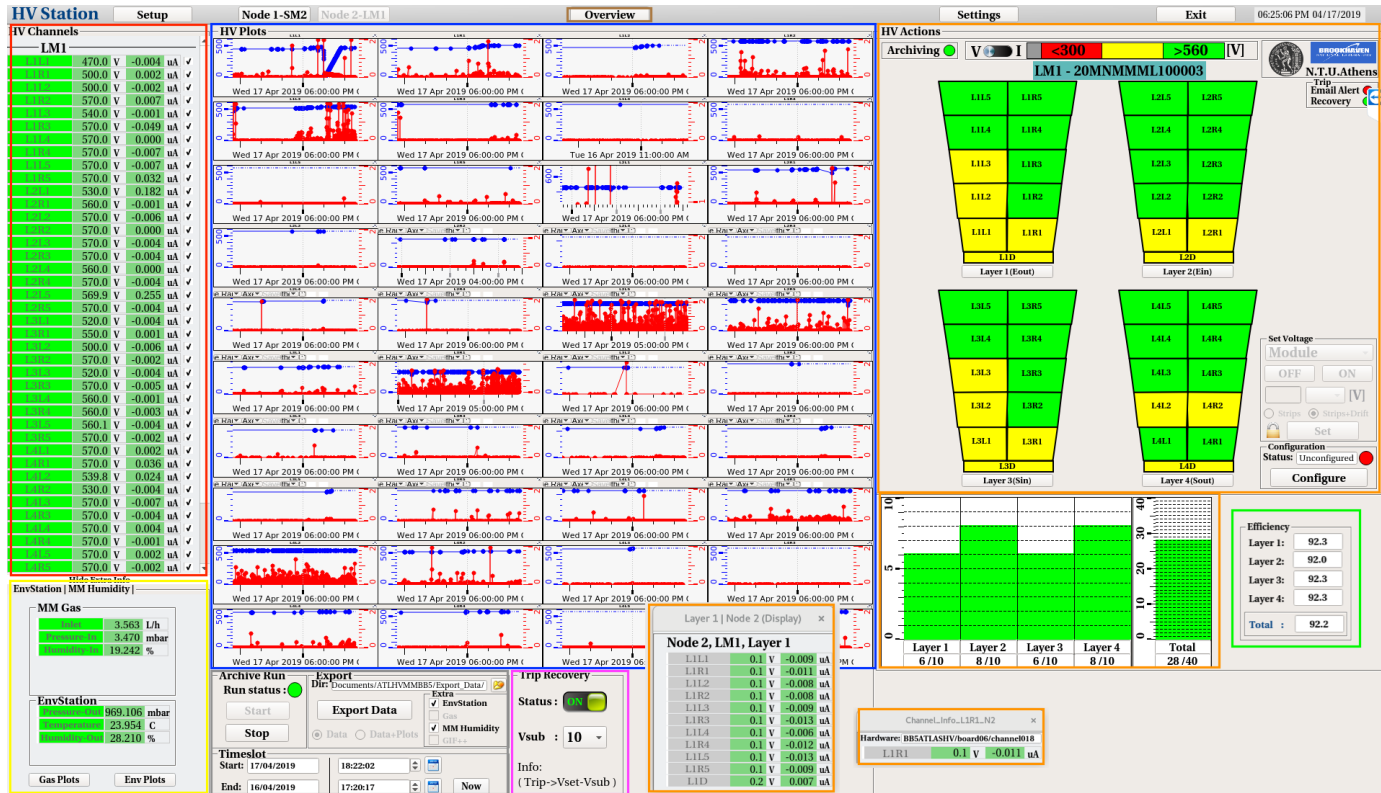


Figure 4.48: The main panel of HV DCS software for control and monitoring.

Let's start analyzing the main panel Figure 4.48, it is divided in different purpose windows:

- HV Channels:** User can monitor the all the individual HV sections, he/she can monitor the voltage value and the current value. The green color indication of the HV section label displays the current status of the channel. The different states of the channel are: "Green" for ON channel, "Grey" for OFF channel and "Red-Grey" blinking for Tripped channel. There is also an option, where user can right-click over the HV section label and a pop-up window will open with the corresponding HV section graph of the voltage/current versus time. User also can check the checkbox option in order to open the graph of the voltage/current versus time in the "HV Plots" window.
- HV Plots:** This is the regions where the checkboxed HV sections of the "HV Channels" window graphs of the voltage/current versus time are displayed.
- Extra Info:** This is the region where user can monitor the sensors that are defined in the "Extra" frame of the "Setup" tab. For example, user can monitor under the "MM Gas" frame, the mass flow, pressure and the humidity of the corresponding node. Also, under the "EnvStation" frame, user can monitor the pressure, environment and humidity value of the environment. Via the "Env Plots" and "Gas" Plots, user can open the corresponding plots. For the GIF++ mode, inside this "Extra Info" window, the various GIF++'s sensors are displayed.
- HV Alarm:** In this region, user can have a visually representation of the module under testing. The user has the option to select between two modes, voltage or current representation using the "switch" button. The limits are user-defined and user can set them up through the

”Settings” button and the ”Alarm Limits” button, procedure that will be described in the next sub-sections. Near the ”switch” button, user can find the voltage or current limits and the color representation for this limits. Also, users have the ability to monitor the Layer’s HV sections by left-clicking on the ”Layer X” button and the individual HV section by left-clicking in the corresponding HV section in the graphical representation. In the bottom part, users can monitor the status of the HV sections that are in the user defined ”green (OK)” area per Layer and per full Module. By using the histogram, histogram can have a quick idea of the HV status of the module.

- **HV Efficiency:** User has the ability to monitor the HV efficiency per Layer and per Module in total, in order to estimate and validate quickly the HV status of the Micromegas module under testing. The HV efficiency is based on an experimental curve that collected during the testbeam of a SM2 Micromegas module during summer of 2018 at H8 area of North area at CERN. The experimental curve is

$$\epsilon_{layer}(V) = \frac{\sum_{n=1}^n \frac{x_0}{1+e^{-x_1(V-x_2)}}}{n} \quad (4.2)$$

where  $n$  the number of the HV sections,  $V$  is the HV Section voltage and  $x_0 = 96.7336$ ,  $x_1 = 0.0626969$ ,  $x_2 = 521.418$

- **Archive/Export:** In this region, user can archive and export the all the data which are selected, will be described under details in the next sub-sections.
- **Auto-Trip recovery mechanism:** Users can enable the auto-trip recovery mechanism and set the  $V_{sub}$  value. By enabling this, it means that when a HV section will trip and is powering off, the auto mechanism is powering on it and it sets the  $V_{set}$  of this value into  $V_{set} - V_{sub}$ .
- **Overview mode:** In order to insert this mode, users must press the ”Overview” button and then he is navigating in the Overview mode display where he/she can monitor all the modes in parallel as shown in Figure 4.49. In this mode, users can easily validate the module by monitoring the HV sections alarm-color limits, the histograms which show the sections are in the good region and the gas info per node.

## Control

User has several options to control the Micromegas’s HV sections. In principal, via the HV DCS software user has the ability to control the following parameters of the CAEN boards hardware:

- **onOff:** This is the power on/off setting of the HV channel
- **vSet:** This is the voltage setting of the HV channel
- **i0:** This is the first current limit that the HV channel cannot exceed
- **i1:** This is the second current limit that the HV channel cannot exceed
- **tripTime:** This is the time limit which if a HV channel’s current value is over  $i0/i1$ , it trips
- **vMax:** This is the max voltage setting that user can insert for safety reasons in order to not exceed it
- **rUp:** This is the voltage ramping up step of the HV channel, for example 10 V/s

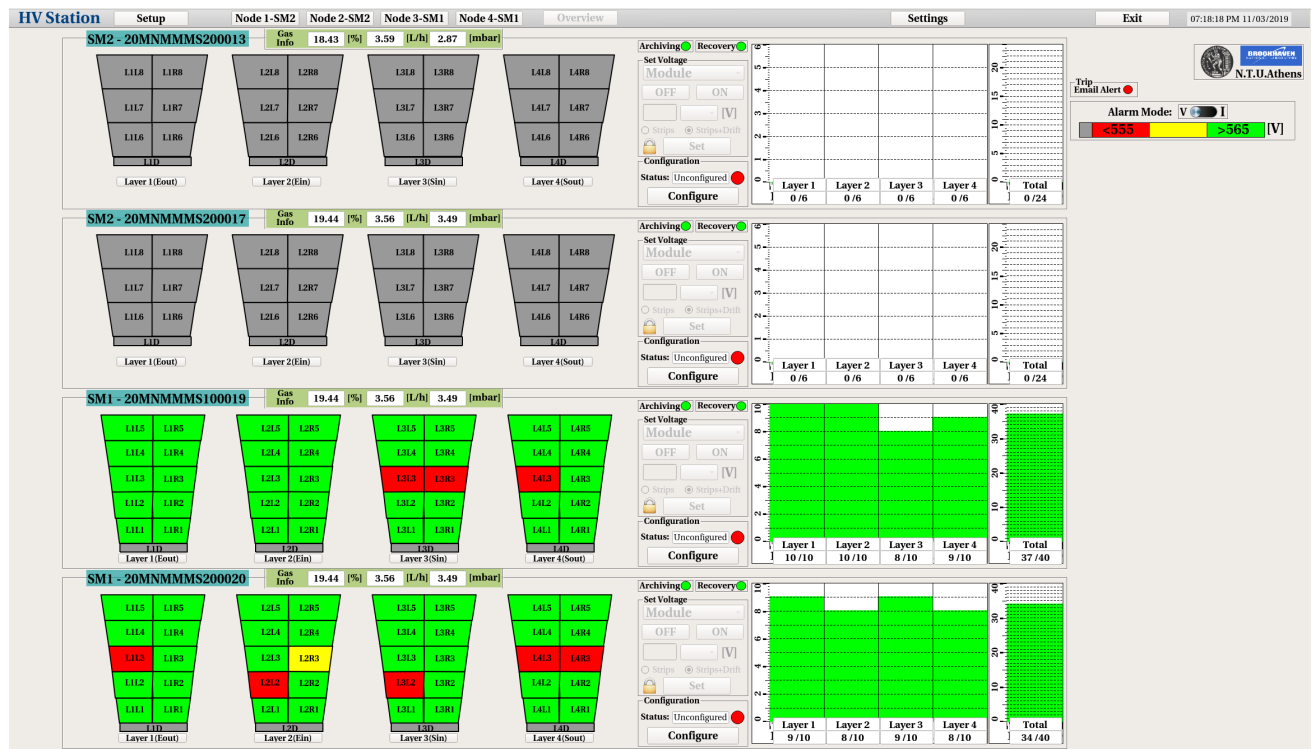


Figure 4.49: The overview panel of HV DCS software for control and monitoring all the nodes in parallel.

- **rDown:** This is the voltage ramping down step of the HV channel, for example 10 V/s

In the following Figure 4.50, the different ways of HV controlling is shown and described. User has multiple ways to control the HV sections, from module up to individual channel control, and the ways are the following as shown also in Figure 4.50 :

- **Node Control:** User has the ability to control all the HV sections of the Micromegas module by pressing the "Configure". He/she has the ability to select all or individual channel and controls all the settings.
- **Layer Control:** Users has the ability to control all the HV sections of the Micromegas layer by pressing the "Layer X" button.
- **Channel Control:** Users has the ability to control one individual HV section of the Micromegas module pressing a section object, "L1L2" for example.
- **Quick Control:** Users has the ability to control the Module or Layer, strips or drift channel in a quick compact way.
- **Overview Control:** Via the "Overview" panel users have the ability to access all the control function. He/She can control the the Module, Layer and individual channels by accessing the Node, Layer, Channel and Quick Control "functions", as shown in Figure 4.51.

### Archive/Export

The monitor and control of the HV channels is the first step of the HV validation. The second step is the archiving, exporting and analyzing the data. The HV DCS software has the ability for unstoppable archiving of all the data. In other words, all the HV channel, gas, environment, and

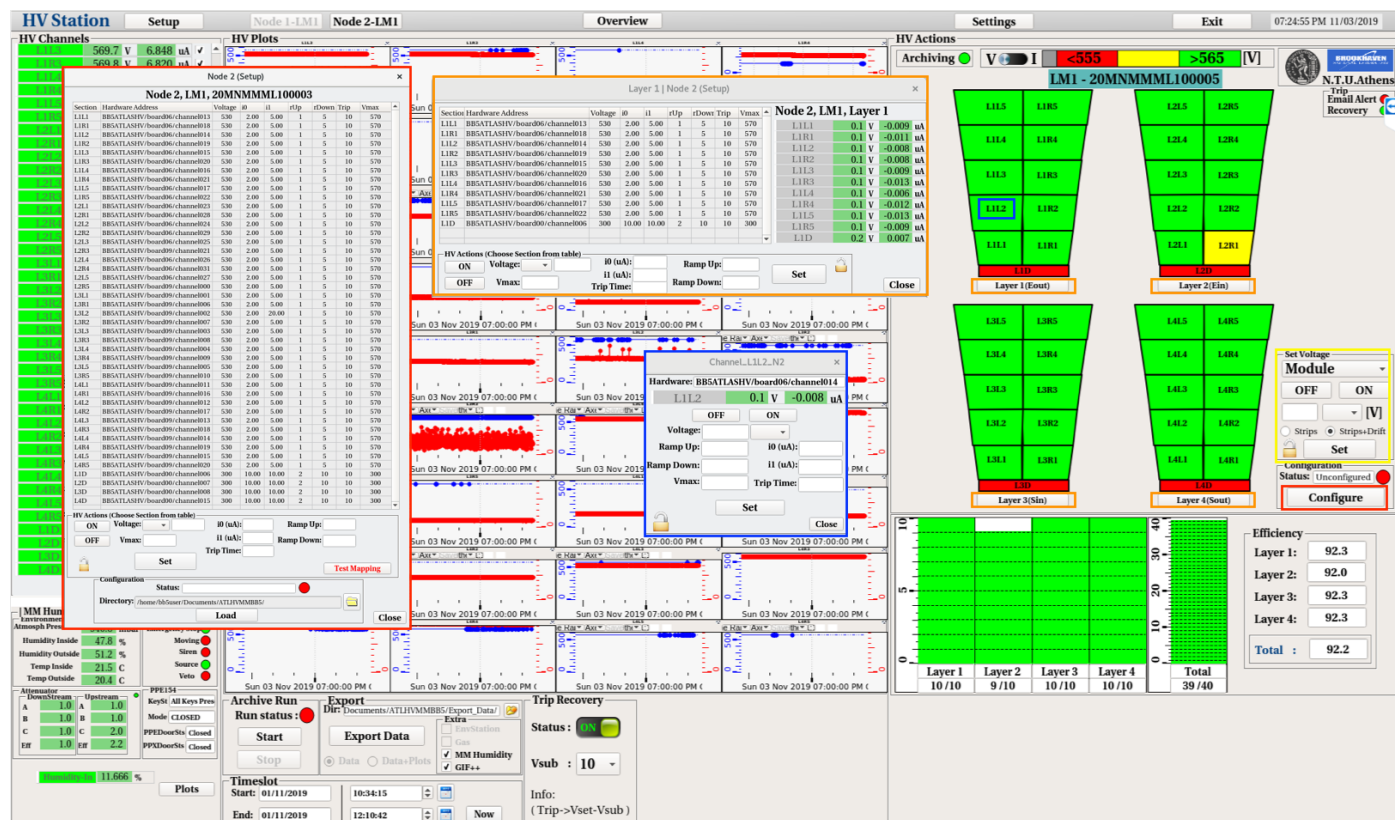


Figure 4.50: The HV control options of HV DCS software.

GIF++ parameters are archived during the operation of the Micromegas module. As shown in Figure 4.52, user has the ability to start and stop a Run by clicking the corresponding button. By doing this, the time-slot between the start and the end of the run is autofilled and thus, user can press the "Export" button. By pressing the "Export" button, user is exporting the HV and the "Extra" data which are selected to a user-defined directory specified under the "Dir" text-field. Also, user has the ability to manually select the "Start" and "End" time of the data that he wants to export manually by filling the corresponding fields under the "Timeslot" frame.

## Archive DB

Via the "Settings" button and the "Archive DB" button as shown in Figure 4.44, user has the ability to access the history of the HV measurements which he took using the "Start/Stop Run" mechanism which described in the previous subsection. As you can see in the Figure 4.53, user has the ability to search by the type of the chamber or the MTF Batch ID, select the corresponding data time-slot that he/she prefers and export all the HV data plus the "Extra" data that he/she has already took during this run.

## Alarm Limits

Via the "Settings" button and the "Alarm Limits" button as shown in Figure 4.44, user can set the voltage and current limits as shown in Figure 4.54, which are used for the "HV Alarm" as described in previous section.

## Features

The HV DCS software gives the ability for email notification for HV channel Trip, CAEN hardware and Arduino lost communication. If something of the above cases is happened, user is notified via





Figure 4.51: The Overview HV control options of HV DCS software.

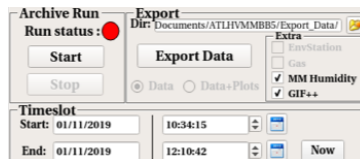


Figure 4.52: The archive/export options of the HV DCS software.

an email in order to investigate the problem more. The user can subscribe to this email notification list by enabling the "Email" switch, adding his/her email under the list and presses the "Set" button via the "Settings" panel as shown in the below Figure 4.55.

Also, user has the ability to monitor the hard disk space of the computer and also the CAEN and Arduino hardware connectivity status via the "Settings" panel as shown in the below Figure 4.55.

### 4.3.3 ArdEnvironment Station

This section provides detailed insights into the ArdEnvironment Station, a pivotal component installed across various critical setups, including the Gas Tightness Station, HV Validation Station, Cosmics Test Stand at BB5, the NSW commissioning setup at B191, and the Vertical Slice (VS) laboratory at 188. The ArdEnvironment Station serves as a multifunctional system designed to monitor and control environmental conditions crucial for the optimal performance and safety of diverse experimental setups. Its integration within each of the mentioned stations ensures consistent data acquisition and management across different testing environments.

#### Setup Wiring

The ArdEnvironment Station is a comprehensive system comprised of an Arduino Mega 2560 Board, Wiznet W5500 Ethernet board, and the Adafruit BME 280 sensor designed for measuring pressure,

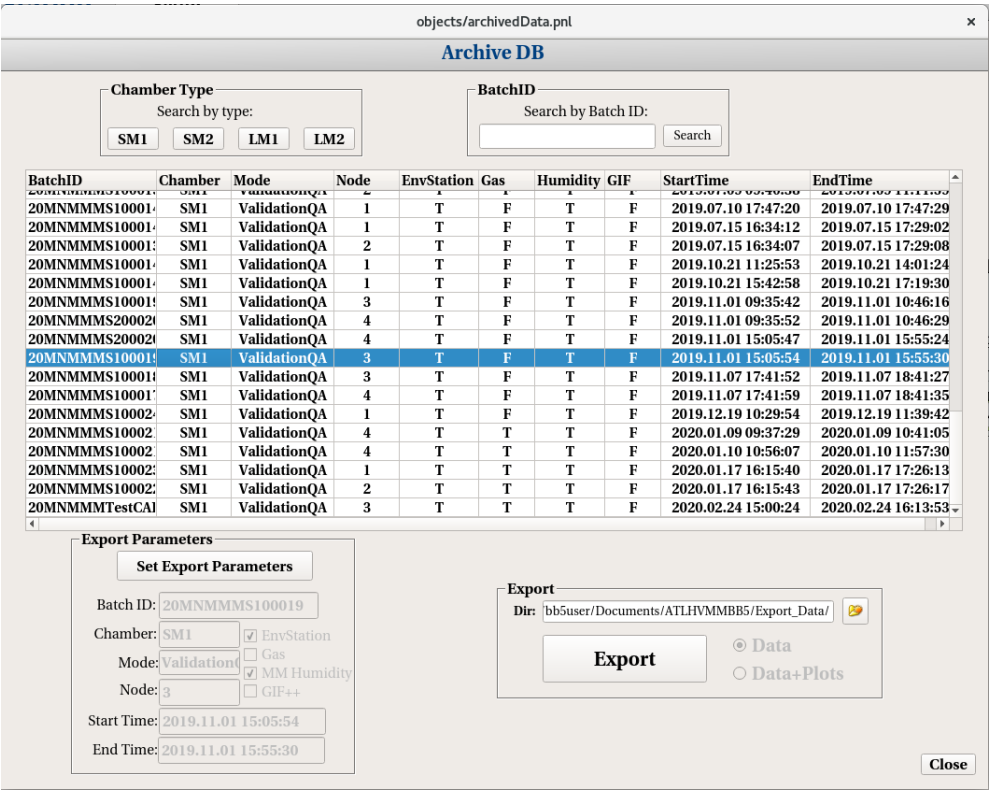


Figure 4.53: The Run Archive DB of the HV DCS software.

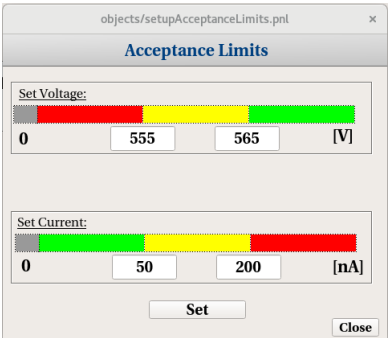


Figure 4.54: The Alarm Limit Settings of the HV DCS software.

temperature, and humidity. The diagram below illustrates the setup, featuring the Arduino-Wiznet configuration, the BME280 sensor, and labeled wiring connections between the Arduino and the sensor. Following the wiring connection, users can ensure the correct linkage by powering on the Arduino and verifying the flashing blue LED indicator. If the blue LED fails to flash, the user should inspect the wiring connections. Pressing the white button for Arduino Soft Reset, located on the top right side of the red Wiznet board, is a corrective measure. After performing the reset, users should recheck the blue LED to confirm proper functioning, as illustrated below.

### OPC DA Server Operation

If blue LED flushes, user can connect the Arduino to a computer via an ethernet cable. The IP of the Arduino is 10.0.0.10, so for the right connection with the computer user must set computer's static ip under the same subnet (10.0.0.X). Also, user can test the connection with Arduino by executing the following command via terminal and checking the output:



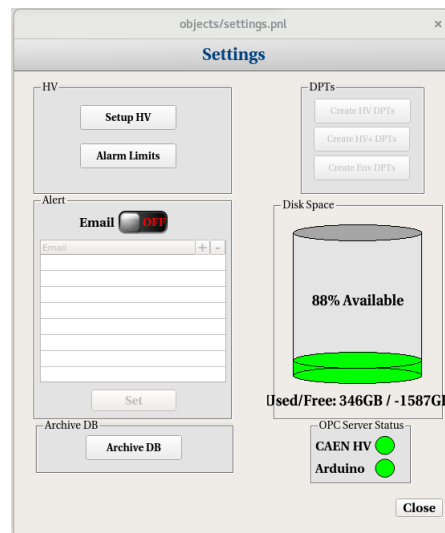


Figure 4.55: The Settings panel of the HV DCS software.

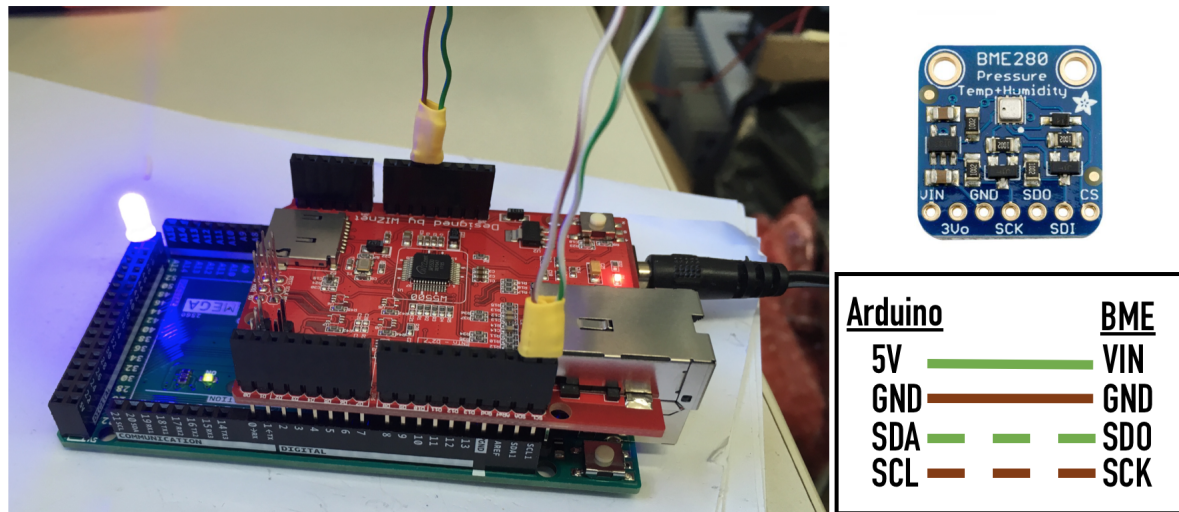


Figure 4.56: Left: The ArdEnvironment setup consists of the Arduino Mega 2560 and the Wiznet 5500 Ethernet Shield, Top Right: The BME280 sensor for pressure, humidity and temperature measurements, Bottom Right: The wire connection between Arduino and BME280 sensor.

```
> ping 10.0.0.10
```

If ping is successful, the steps which user must follow to establish the Arduino OPC DA Server operation are:

1. Open "OPC Server for Arduino/Genuino" program as administrator under Windows
2. Press "Arduino Ethernet" Tab and insert 10.0.0.10 in "Arduino IP" field and 80 in "Port" field
3. Press "Save Configuration" button and close the window by tapping "X" icon
4. Run "register.bat" file as administrator
5. Open "OPC Server for Arduino/Genuino" program as administrator under Windows

After the completion of these steps, the OPC DA server forwards the sensor's values to WinCC-OA software. Also, it is important to be mentioned that "OPC Server for Arduino/Genuino" program is initialized in minimized mode under the Notification area of Windows down right.

### OPC UA Server Development

To enhance the maintainability and versatility of the ArdEnvironment Station, a new in-house OPC UA server has been developed from scratch. The initial implementation is designed for an Arduino equipped with a BME280 sensor (Pressure, Temperature, Humidity), utilizing I2C for communication and analog ports for monitoring various input sensors.

The first stage of development involved modifying the Arduino firmware to establish communication with the BME280 sensors, both digital and analog embedded ports. The firmware was configured to export parameter values through the Arduino's serial port, with a refresh rate of 1000 ms and a baud rate of 9600 bps.

Subsequently, the OPC UA Server, named PyOpcUaServer, was created as a Python executable script. This server operates as a wrapper for the sensor data, utilizing serial port communication. The primary purpose of the PyOpcUaServer is to aggregate data from various sensors and provide accessibility through a TCP endpoint port. This functionality enables WinCC-OA to function as an OPC UA client, subscribing to the PyOpcUaServer and efficiently collecting sensor data. The key features of the PyOpcUaServer are outlined below:

- **Development:** Implemented in Python and built upon the FreeOpcUa API, ensuring flexibility and compatibility.
- **Deployment:** Facilitates plug-and-play deployment, simplifying the integration of the server into different environments.
- **Sensor Compatibility:** Supports a wide range of sensors, including analog, I2C, and digital, making it versatile for diverse sensor setups.
- **Scalability:** Designed to scale with the number of parameters, allowing seamless integration with systems of varying complexities.
- **Platform Independence:** Ensures Linux distribution independence, promoting compatibility across different operating systems.
- **Multi-Client Access:** Accessible on a single endpoint by multiple OPC UA clients, enhancing flexibility and usability.

Additionally, the project is openly accessible through a GitLab repository, serving as a valuable resource for the development of other OPC UA server solutions. The GitLab CI/CD pipeline has been established to conduct static analysis, evaluate code quality, and run tests on the PyOpcUaServer executable. This CI/CD process is automatically triggered after each new Git commit, providing a systematic approach to ensuring the reliability and effectiveness of the server.

### ArdEnvironment Station

The ArdEnvironment Station is shown on Figure 4.58. The main panel consists of three plots and values which displays the pressure, temperature and humidity values respectively as shown below.

The user has the capability to simultaneously archive pressure, temperature, and humidity values by clicking the "Start" button located in the "Archive" area. The default sampling time is configured to generate one mean value per minute, but users retain the flexibility to adjust sampling time settings by selecting the "Settings" icon within the "Archive" section.

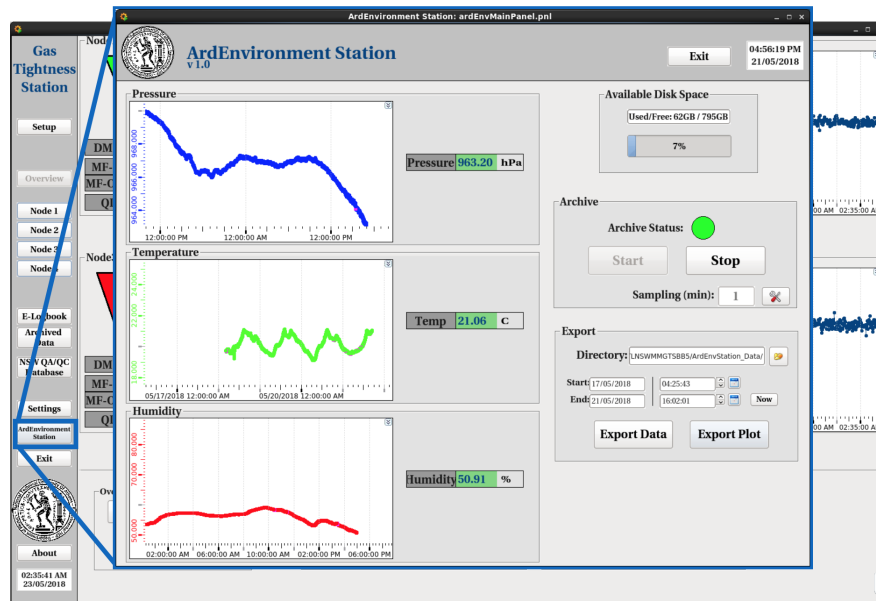


Figure 4.57: ArdEnvironment Station main panel, user can monitor and archive/export the pressure, temperature and humidity.

Under the "Export" area, users can export the archived data for a specific user-defined time slot by indicating the start and end date/time. The software provides the option to export the data either as a data file named "ArdEnvStation\_Start\_TO\_End.dat" or as a plots file named "ArdEnvStation\_Plots\_Start\_TO\_End.png." The output is stored in the default output directory within the project folder "ArdEnvStation\_Data" or in a directory of the user's choice by clicking the "Folder" icon. Examples of the exported data and plots are illustrated below. It's essential to note that the archive must always be turned on (indicated by a green indicator). If the indicator is not green, the users need to press the "Start" button to initiate archiving.

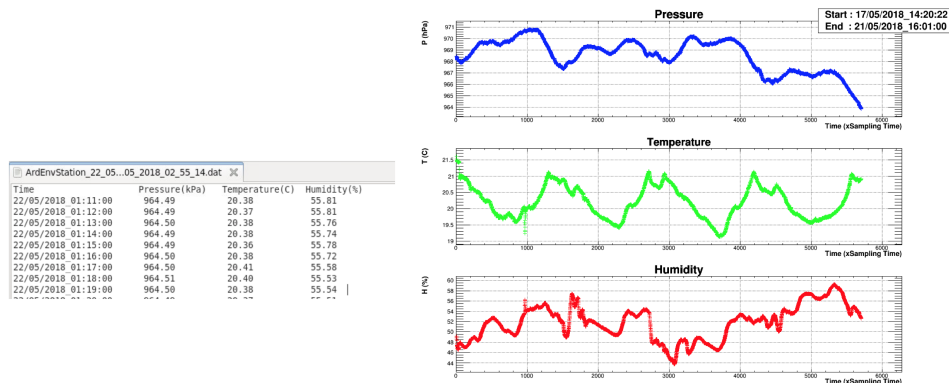


Figure 4.58: Form of exported data and plots using ArdEnvironment Station.

### Vertical Slice Setup

For the specific demands of the Vertical Slice (VS) lab, an advanced ArdEnvironment Station has been developed to streamline the monitoring of crucial environmental parameters within the lab. Additionally, it is designed to oversee the intricate network of cooling lines that play a pivotal role in providing optimal cooling to the Micromegas/sTGC electronics setup, exemplified in Figure 4.59. This enhanced station demonstrates a commitment to precision and efficiency, ensuring seamless operations within the laboratory environment.



Figure 4.59: The NSW electronics setup at the Vertical Slice laboratory.

The VS setup is composed of three cooling lines dedicated to the NSW electronics, monitored through TMP36 Analog temperature sensors. The connection schematic between Arduino and these sensors is illustrated in Figure 4.60. In this setup, the BME280 is intricately linked to the SDA/SCL I2C master of the Arduino, while the three TMP36 analog sensors establish direct connections to the A1-3 analog interfaces of the Arduino. This configuration ensures a comprehensive monitoring system for the temperature parameters critical to the efficient functioning of the NSW electronics within the laboratory environment.

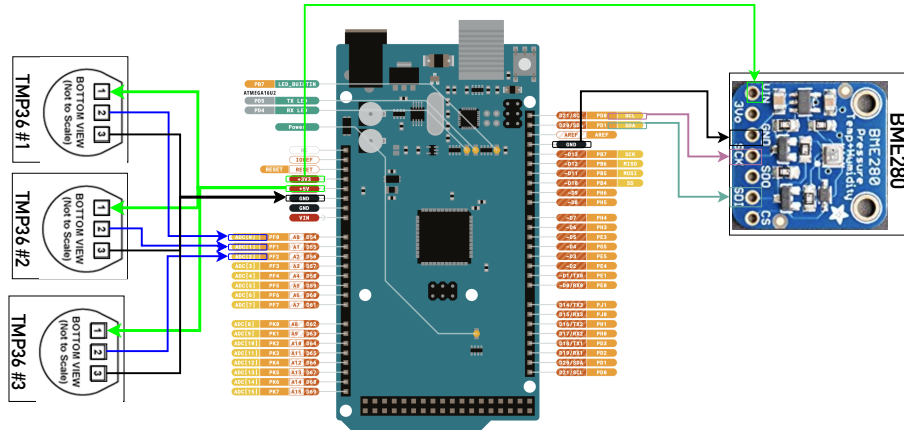


Figure 4.60: The VS Arduino sensor connection schematic. The setup consists of one BME280 environmental sensor and 3 TMP36 analog sensors which are connected to the I2C and analog Arduino's interfaces accordingly.

The improved ArdEnvironment Station, as shown in Figure 4.61, includes the monitoring of one BME280 environmental sensor(atmospheric pressure, temperature, humidity) and three TMP36 analog temperature sensors. Although, it includes also the monitoring of the dewpoint temperature which can be described by

$$T_{dewpoint} = T_{env} - \frac{100 - RH}{5} \quad (4.3)$$



Another important feature for the safe and unattended operation of the NSW electronics, is the new alarm handling notification system which sends email and SMS when the following conditions are true:

- Cooling temperature sensor will be over the ERROR limit( WARNING:  $30^{\circ}\text{C} < T < 35^{\circ}\text{C}$ , ERROR:  $T > 35^{\circ}\text{C}$ )
- Dewpoint measurement will be over the WARNING limit in order to prevent the liquefaction of the cooling lines( WARNING:  $T_{\text{dewpoint}} - T_{\text{input},i} < 2^{\circ}\text{C}$ )

The updated ArdEnvironment Station is showing in Figure 4.61 :

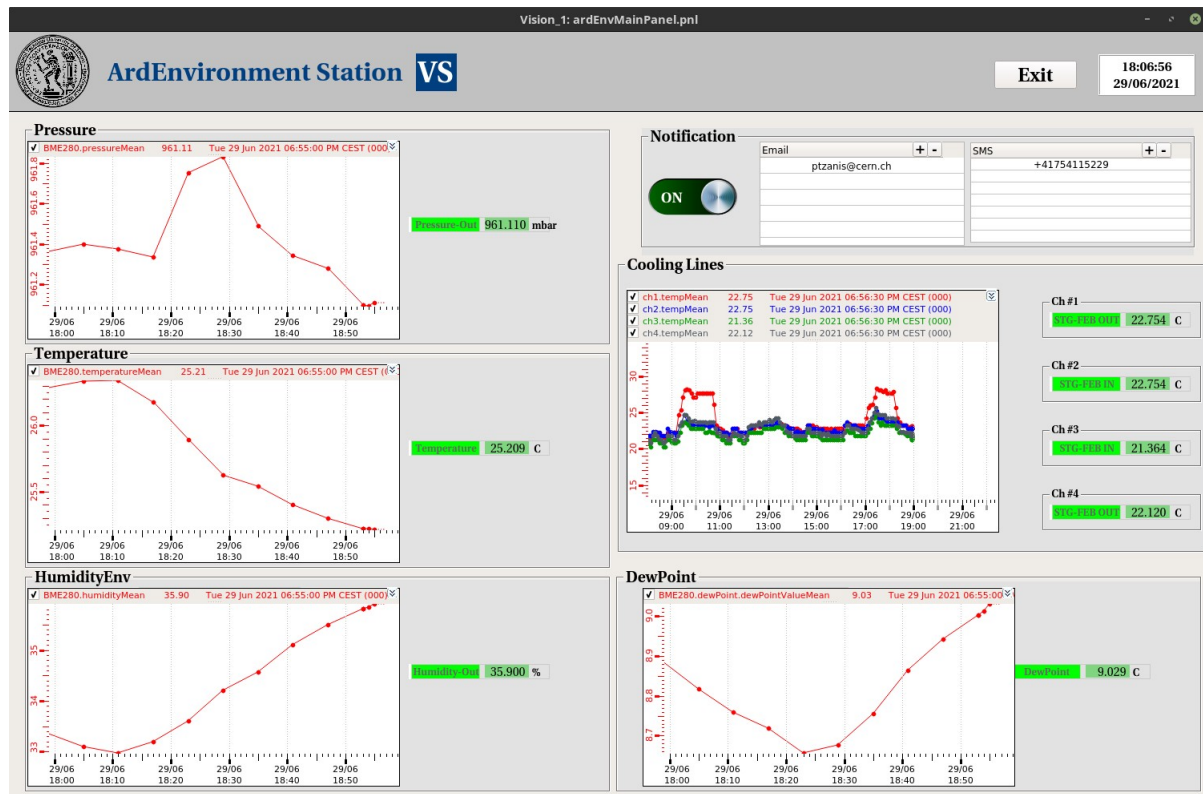


Figure 4.61: Updated ArdEnvironment Station main panel. Users have now the ability to monitor the dewpoint and the VS electronics setup's cooling lines temperatures. In addition, he/she can enable/disable the automatic alarm handling notification system and can manually input the SMS/e-mails which he/she wants to get notification when the alarm conditions are satisfied.

In summary, the ArdEnvironment Station boasts a rich set of features tailored for comprehensive environmental monitoring and management. Key functionalities include:

- **Environmental Monitoring:**
  - Continuous monitoring and archival of environmental parameters, including temperature, humidity, and atmospheric pressure.
  - Precise recording of the dewpoint temperature, providing critical insights into ambient conditions.
- **Cooling Lines Monitoring:**
  - Real-time monitoring and archival of temperatures in input cooling lines, ensuring a thorough understanding of the thermal dynamics.

- **Alarm Handling System:**

- Flexible configuration to enable or disable an automatic alarm handling notification system.
- Customization options for users to input specific SMS or email preferences for receiving timely notifications when alarm conditions are met.

This robust set of features empowers users with in-depth data on environmental and thermal conditions, contributing to informed decision-making and effective management of experimental setups. The ArdEnvironment Station's adaptability and user-friendly interfaces make it a valuable asset for a wide range of laboratory applications, ensuring optimal performance and reliability in diverse environments.

### 4.3.4 Electronics Station

This subsection details the software developed for the electronics validation of the NSW sectors before their installation in the ATLAS experiment. The sector validation occurs at multiple CERN buildings, including BB5, B180, and B191.

The Electronics Station boasts a streamlined and compact design, featuring a singular window, as depicted in Figure 4.62. Within this user-friendly interface, operators can seamlessly navigate between different layers of the sector, providing comprehensive monitoring of temperature and power sensor values. This software serves a crucial role in ensuring the robustness and functionality of the NSW sectors before their integration into the ATLAS experiment.

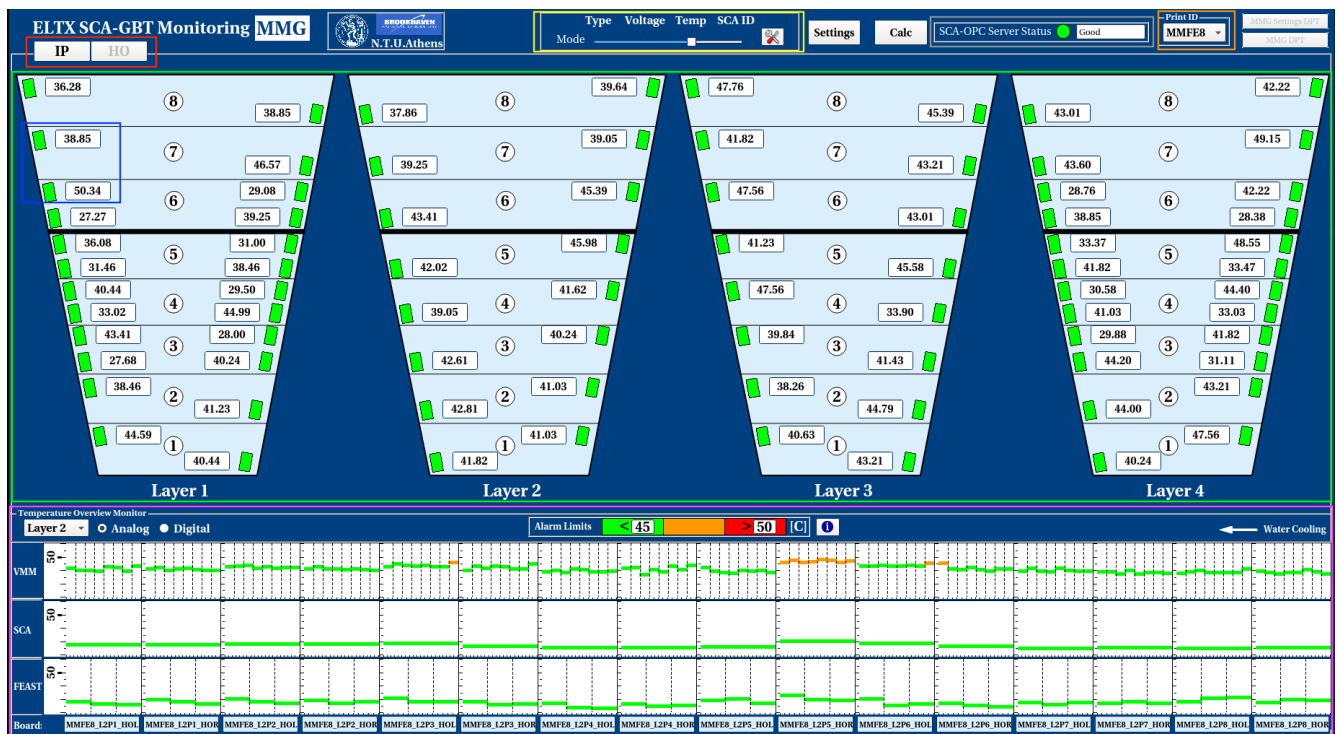


Figure 4.62: The main SCA DCS panel for Micromegas electronics monitoring.

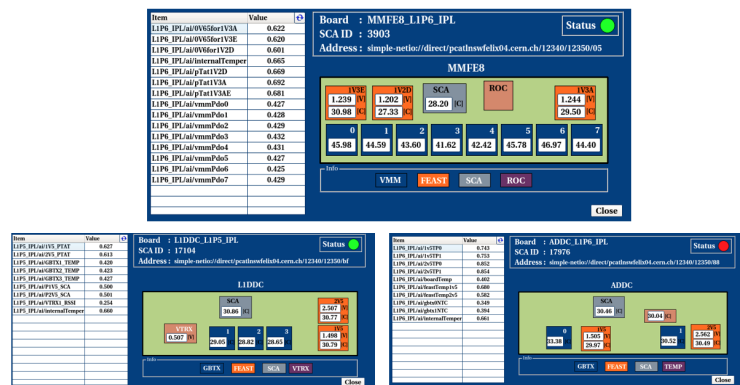
The Electronics Station offers a range of features designed to streamline the monitoring and validation process for the New Small Wheel sectors. These include:

- **Wedge Side Selection:** Users can seamlessly switch between the IP and HO wedges of the sector, providing flexibility in monitoring specific components.

- **Quick Display:** Users have the ability to monitor the SCA connectivity status and a specific board parameter. A left-click opens a pop-up plot of the parameter, while a right-click initiates full board monitoring.
- **Layer Display:** The system enables users to monitor the SCA connectivity status and parameters for all boards across different layers of the sector, facilitating comprehensive oversight.
- **Mode View Selection:** Users can easily switch between different monitoring modes, including board type, voltage, temperature, and SCA ID value. The "Settings" button allows users to customize parameters for quick display based on the board type.
- **SCA OPC UA Status:** The system provides a clear display of the SCA OPC UA connection status via the main panel, ensuring users are informed about the communication status.
- **SCA ID Print:** Users can export the SCA ID list per board, conveniently saving it in the /Desktop area of their computer for reference.
- **Temperature Overview Monitor:** Users can visualize all parameters for all boards within the sector, seamlessly switching between layers and different board types (Analog - MMFE8, Digital - ADDC, L1DDC). The system employs color-coded alarms for quick identification of values outside predefined limits, allowing users to adjust limits as needed within the interface.

These features collectively contribute to an efficient and user-friendly platform for validating and monitoring the electronics of the New Small Wheel sectors.

The user via the "Quick Display" which described in the previous section, has the ability to monitor all the parameters of the board by right-clicking on the board. A window per board is opening, so users have the ability to monitor in details all the parameters as shown in Figure 4.63.





### 4.3.5 Cosmics Station

This subsection details the experimental setup and software developed for the cosmics validation of the Micromegas sectors before their installation into the New Small Wheels of the ATLAS experiment. Cosmics validation represents the concluding phase of the Micromegas detector's validation procedure, incorporating gas, high voltage (HV), and electronics validation processes.

The cosmics validation aims to ensure the comprehensive functionality of the Micromegas detector under realistic operating conditions. This validation step involves the integration of gas, HV, and electronics validation, providing a holistic assessment of the detector's performance. The experimental setup and software play crucial roles in orchestrating and monitoring these validation processes, ensuring the successful integration and operation of the Micromegas sectors within the ATLAS experiment.

#### Setup

The Cosmics Station setup is a crucial stage in preparing the Micromegas sector for integration into the ATLAS cavern. This involves providing the sector with all the essential services, including high voltage (HV), gas, cooling, alignment, and electronics, before its final installation. The complexity of this system is evident, requiring significant attention and care from a team of experts over several weeks for each Micromegas sector to be fully configured. An illustration of a real Micromegas sector within the Cosmics Stand setup at BB5 CERN is presented in Figure 4.64.

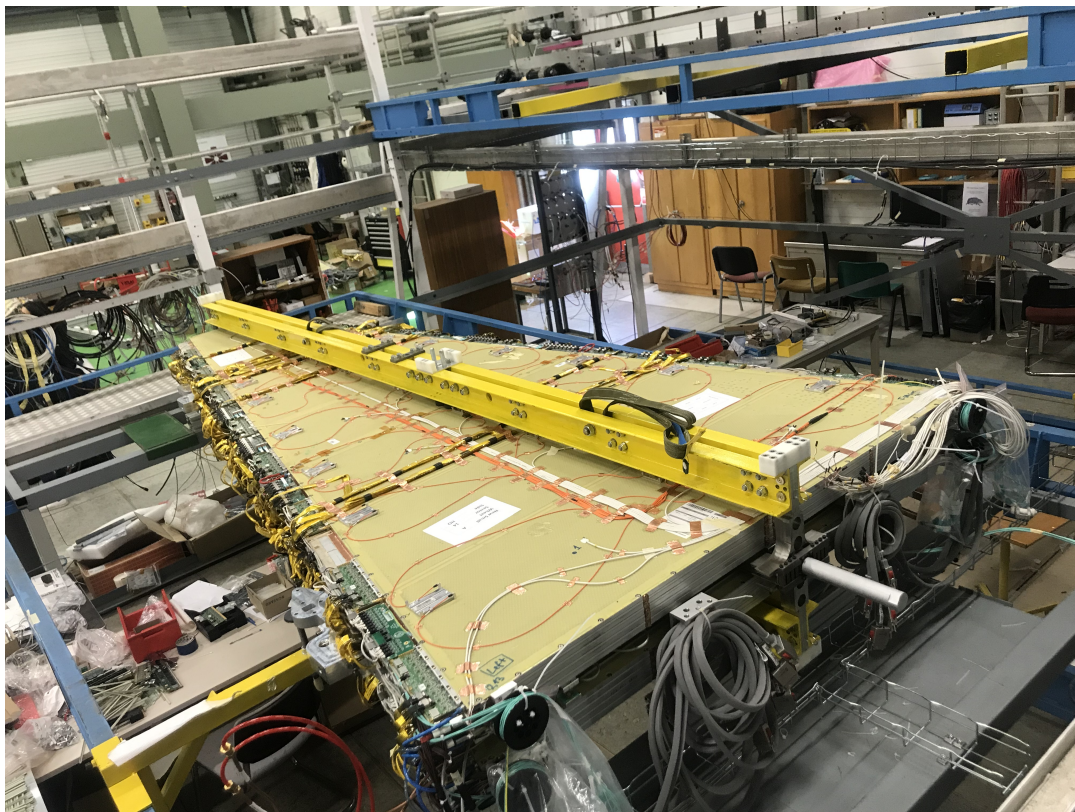


Figure 4.64: A real Micromegas sector at the Cosmics Stand setup at BB5 CERN.

Due to the intricate nature of the Micromegas sector, the Cosmics Stand Station is a comprehensive combination of various sub-stations, each serving a specific purpose:

- **HV Station:** Responsible for the monitoring and control of the HV channels.
- **LV Station:** Focused on controlling the low voltage (LV) of the electronics boards installed on the sector.

- **SCA Station:** Dedicated to monitoring the temperature and power levels of the electronics boards.
- **MDM Station:** Tasked with monitoring the temperature sensors installed on the surface of the sector.
- **Gas Station:** Handles the monitoring of the gas sensors of the sector.
- **Env Station:** Manages the monitoring of environmental conditions during the cosmic runs.
- **Safety Station:** Deals with safety mechanisms in case of incidents.

An overview schematic is shown in the below Figure 4.65 .

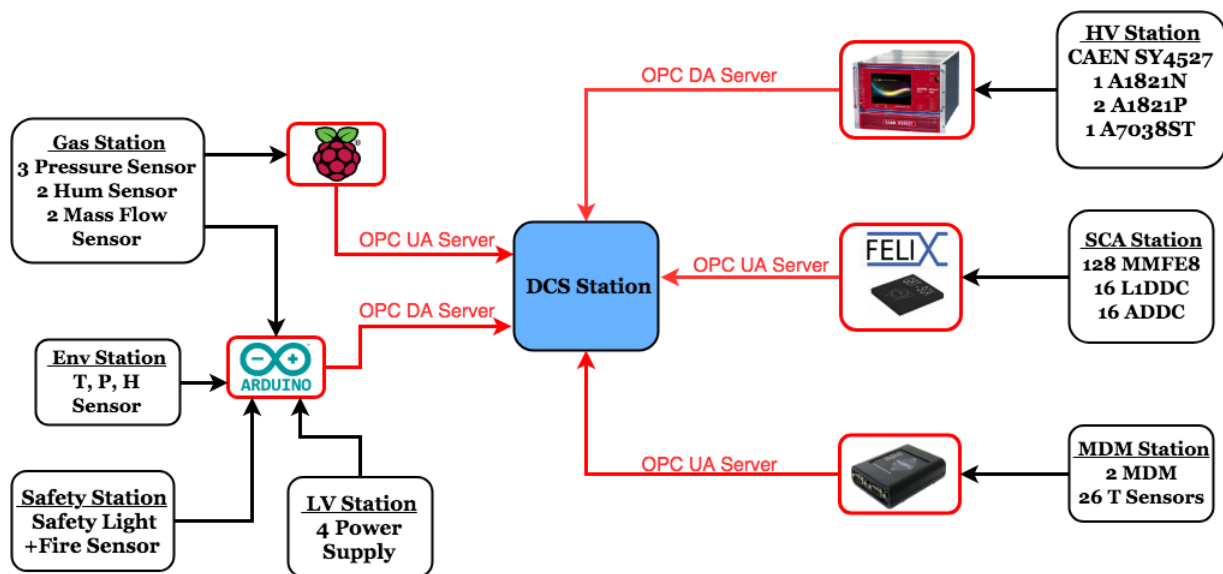


Figure 4.65: The overview schematic of the Cosmics Stand DCS Station

## HV Station

When a user presses the "Sector X" button, he/she is inserting to the main control/monitor window of the HV DCS software as shown in Figure 4.66, and as you can see there is a lot of information that should be described in details. Let's start analyzing the main panel Figure 4.66, it is divided in different purpose windows:

- **HV Channels:** Users can monitor all individual HV sections, he/she can monitor the voltage value and the current value. The green color indication of the HV section label displays the current status of the channel. The different states of the channel are: "Green" for ON channel, "Grey" for OFF channel and "Red-Grey" blinking for Tripped channel. There is also an option, where users can right-click over the HV section label and a pop-up window will open with the corresponding HV section graph of the voltage/current versus time. Users can also check the checkbox option in order to open the graph of the voltage/current versus time in the "HV Plots" window.
- **HV Plots:** This is the regions where the checkboxed HV sections of the "HV Channels" window graphs of the voltage/current versus time are displayed.

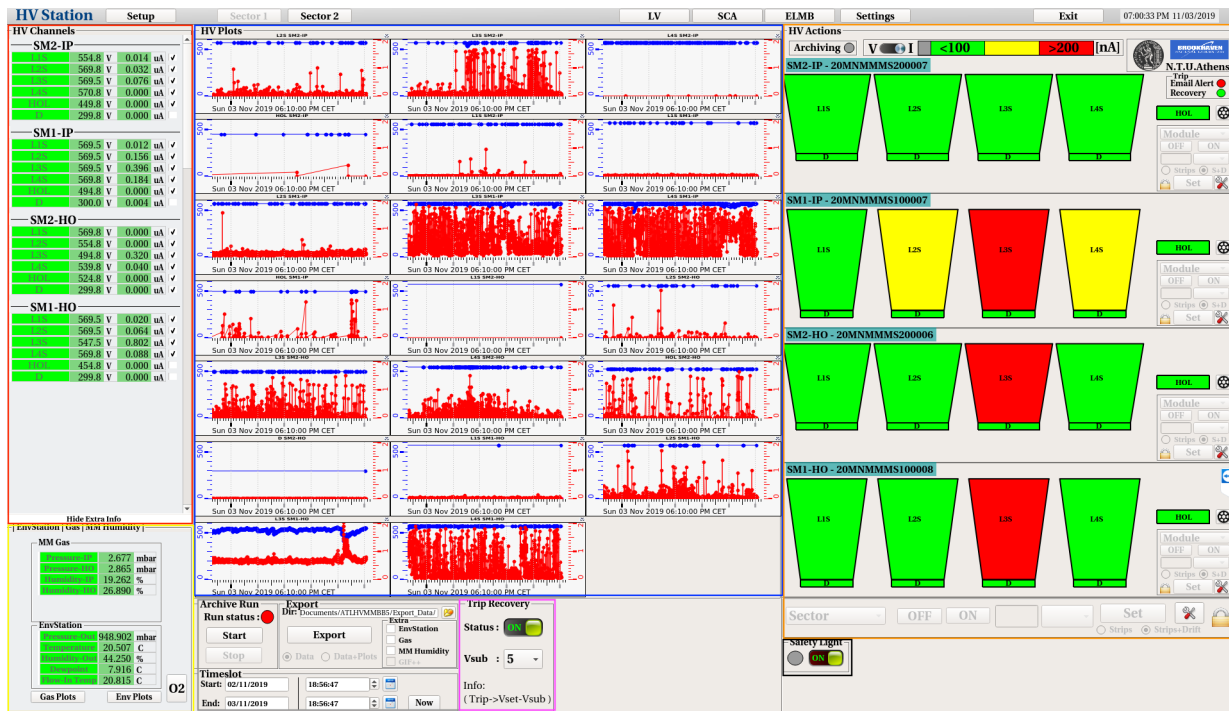


Figure 4.66: The main panel of HV DCS software for control and monitoring.

- Extra Info:** This is the region where user can monitor the sensors that are defined in the "Extra" frame of the "Setup" tab. For example, user can monitor under the "MM Gas" frame, the mass flow, pressure and the humidity of the IP and HO wedge. Also, under the "EnvStation" frame, user can monitor the pressure, environment and humidity value of the environment. Via the "Env Plots" and "Gas" Plots, user can open the corresponding plots.
- HV Alarm:** In this region, users can have a visual representation of the module under testing. The user has the option to select between two modes, voltage or current representation using the "switch" button. The limits are user-defined and user can set them up through the "Settings" button and the "Alarm Limits" button, procedure that will be described in the next sub-sections. Near the "switch" button, user can find the voltage or current limits and the color representation for this limits. Also, user has the ability to monitor the Layer's HV sections by left-clicking on the "Layer X" button and the individual HV section by left-clicking in the corresponding HV section in the graphical representation. In the bottom part, user can monitor the status of the HV sections that are in the user defined "green (OK)" area per Layer and per full Module. By using the histogram, histogram can have a quick idea of the HV status of the module.
- Archive/Export:** In this region, user can archive and export all data which are selected and will be described under details in the next sub-sections.
- Auto-Trip recovery mechanism:** Users can enable the auto-trip recovery mechanism and set the  $V_{sub}$  value. By enabling this, it means that when a HV section will trip and is powering off, the auto mechanism is powering on it and it sets the  $V_{set}$  of this value into  $V_{set} - V_{sub}$ .
- Safety Light:** User has the ability to power on-off the HV safety light indication in order to inform lab users that HV is enabled.

## Control

User has several options to control the Micromegas's HV sections. In principal, via the HV DCS software user has the ability to control the following parameters of the CAEN boards hardware:

- **onOff:** This is the power on/off setting of the HV channel
- **vSet:** This is the voltage setting of the HV channel
- **i0:** This is the first current limit that the HV channel cannot exceed
- **i1:** This is the second current limit that the HV channel cannot exceed
- **tripTime:** This is the time limit which if a HV channel's current value is over  $i0/i1$ , it trips
- **vMax:** This is the max voltage setting that user can insert for safety reasons in order to not exceed it
- **rUp:** This is the voltage ramping up step of the HV channel, for example 10 V/s
- **rDown:** This is the voltage ramping down step of the HV channel, for example 10 V/s

User has multiple ways to control the HV sections, from module up to individual sector control, and the ways are the following:

- **Sector Control:** User has the ability to control all the HV sections of the Micromegas sector by pressing the "Configure". He/she has the ability to select all or individual channels and control all the settings.
- **Layer Control:** Users has the ability to control one individual HV layer of the Micromegas sector pressing a section object, "L1S" for example.
- **Quick Control:** Users has the ability to control the Module or Layer, strips or drift channel in a quick compact way.

## Archive/Export

The monitor and control of the HV channels is the first step of the HV validation. The second step is the archiving, exporting and analyzing the data. The HV DCS software has the ability for unstoppable archiving of all the data. In other words, all the HV channel, gas, environment, and GIF++ parameters are archived during the operation of the Micromegas module. User has the ability to start and stop a Run by clicking the corresponding button. By doing this, the time-slot between the start and the end of the run is auto-filled and thus, user can press the "Export" button. By pressing the "Export" button, user is exporting the HV and the "Extra" data which are selected to a user-defined directory specified under the "Dir" text-field. Also, user has the ability to manually select the "Start" and "End" time of the data that he wants to export manually by filling the corresponding fields under the "Timeslot" frame.

## LV Station

Via the LV button through the Cosmics DCS panel as shown in Figure 4.66, user has the ability to access the LV Station as shown in Figure 4.67. User has the ability to power on/off the Analog(MMFE8) and Digital(L1DDC,ADDC) boards via a trigger relay which is interconnected to power supplies and an Arduino.



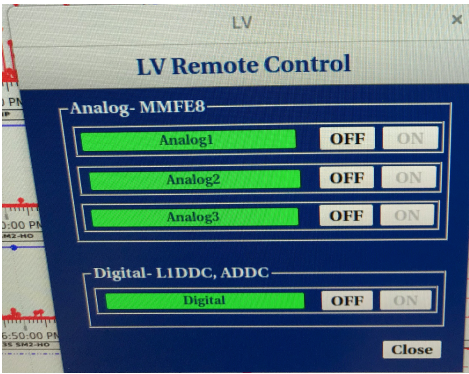


Figure 4.67: The LV Station of the Cosmics Test Stand Station.

SCA Station

By clicking the "SCA" button within the HV DCS panel, depicted in Figure 4.66, users can access the SCA Station, as illustrated in Figure 4.68. This allows them to monitor the temperature and power levels of all the electronics boards, utilizing the monitoring options detailed in the previous section.

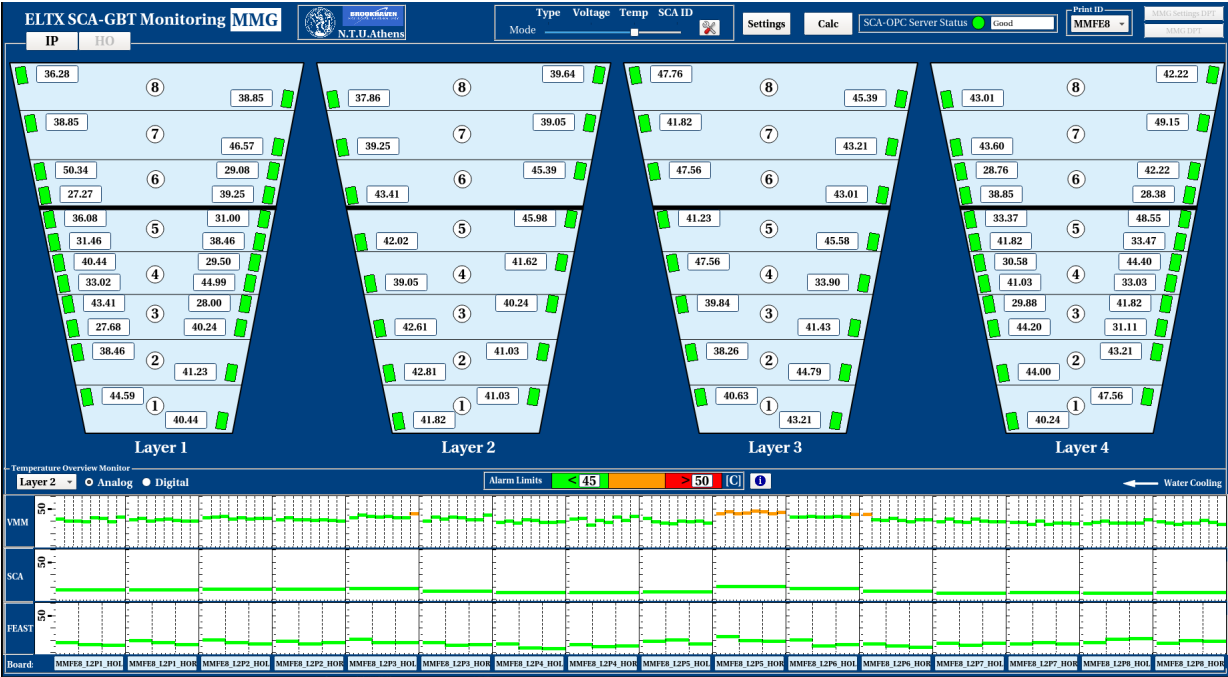


Figure 4.68: The SCA Station of the Cosmics Test Stand Station.

MDM Station

By clicking the "ELMB" button within the HV DCS panel, as depicted in Figure 4.66, users can access the MDM Station, shown in Figure 4.69. This station allows users to monitor the temperature sensors installed on the surface of the sector. The MDM Station has been designed by my colleague and friend, Christos Paraskevopoulos.

Gas Station

By selecting the "Gas plots" button within the HV DCS panel, as illustrated in Figure 4.51, users can access the Gas Station, depicted in Figure 4.70. In this station, users can monitor the pressure and

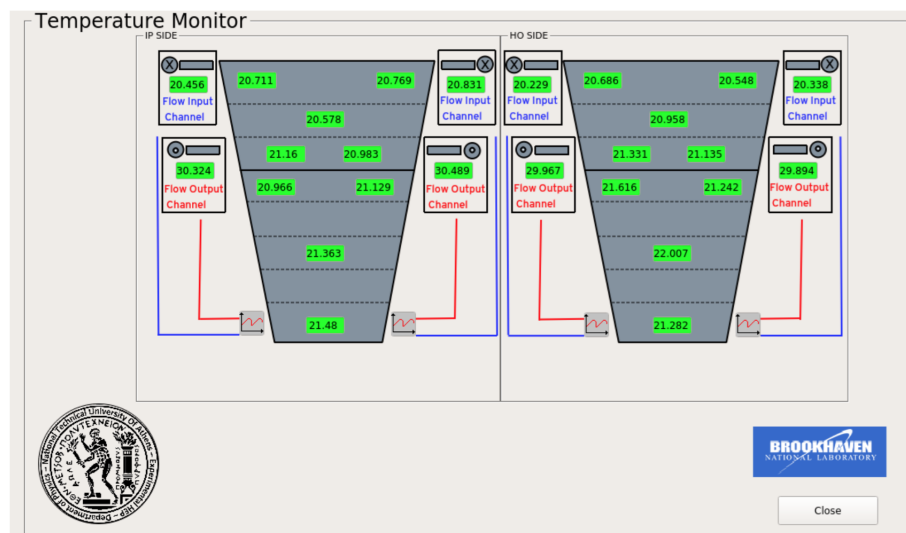


Figure 4.69: The MDM Station of the Cosmics Test Stand Station.

humidity sensors installed in the gas lines of the Micromegas sector. The pressure sensor system has been designed by my colleague and friend, Stamatis Tzanos.



Figure 4.70: The Gas Station of the Cosmics Test Stand Station.

### Env Station

By selecting the "Env plots" button within the HV DCS panel, as depicted in Figure 4.66, users can access the Env Station, illustrated in Figure 4.71. In this station, users can monitor the environmental parameters, including pressure, humidity, and the dewpoint levels of the laboratory. The monitoring options are described in detail in the previous section.

### Safety Station

The Safety Station is a crucial component equipped with automated scripts that run continuously to proactively prevent incidents related to various aspects, including electronics, gas, and cooling systems. The system is designed to promptly respond to potential issues, ensuring a safe operating environment. The active alarms, operational 24/7, are as follows:



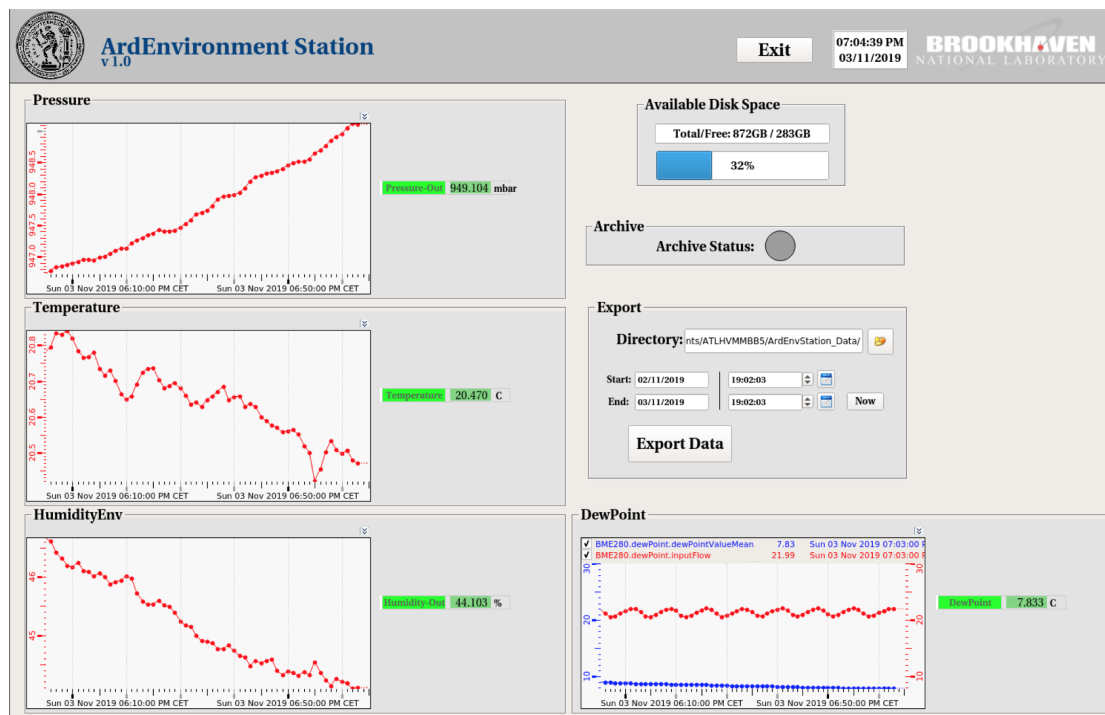


Figure 4.71: The Env Station of the Cosmics Test Stand Station.

- **Temperature Overlimit (LV Shutdown):** If the input/output flow temperature surpasses 30 C, the LV is automatically powered off. Simultaneously, SMS and email notifications are triggered, alerting safety personnel and enabling swift response.
- **High Temperature Warning:** When the input/output flow temperature exceeds 27 C, automated SMS and email notifications are promptly dispatched to safety personnel, ensuring timely awareness of the elevated temperature conditions.
- **Pressure Alert:** In case the sector's pressure exceeds 6 mbar, the Safety Station triggers automated SMS and email notifications. This immediate alerting mechanism helps in addressing pressure-related issues promptly.
- **Temperature-Dewpoint Differential Alert:** If the temperature difference between the input flow and dewpoint falls below 2 C, the Safety Station initiates automated SMS and email notifications. This ensures a proactive response to conditions that might lead to potential concerns.

This comprehensive safety setup plays a crucial role in maintaining a secure and stable operational environment for the Micromegas sector during cosmics validation.

## 4.4 NSW Production Control System

A detailed description will be given for the New Small Wheel Detector Control System which designed and developed for the smooth operation of the detector inside the ATLAS experiment.

### 4.4.1 System & Architecture Design

The NSW is a advanced component of the ATLAS experiment, demanding the implementation of an equally complex DCS. The purpose of this system is paramount, ensuring the consistent and

safe functioning of the detector, while seamlessly interfacing with all sub-detectors and the broader technical infrastructure of the experiment. The NSW DCS serves as the central nervous system, managing transitions between the detector's operating states and providing continuous monitoring and archival of crucial operational parameters.

The inherent complexity and extended operational periods of the NSW underscore the necessity for a robust DCS. This system becomes indispensable, not only for maintaining the detector's functionality but also for serving as a bridge to facilitate communication with various sub-detectors and the broader technical framework of the experiment. It acts as the linchpin in orchestrating the detector's intricate dance of functionalities.

The central system is designed to vigilantly handle transitions between different operational states of the probe. This adaptability is crucial for accommodating the diverse requirements of experimental conditions, seamlessly switching between modes, and ensuring optimal performance. Simultaneously, the NSW DCS continuously monitors and archives essential parameters, providing a comprehensive record of the system's operational history.

The NSW DCS incorporates a robust alarm system that reacts promptly to any abnormalities detected in the detector's subsystems. In the event of a deviation from normal operating conditions, the system triggers signals or alerts (alarms) that notify operators. These alerts serve as early warnings, allowing for swift intervention to rectify issues. The system is designed to adapt to automatic processes whenever possible or facilitate manual actions to reset the detector, ensuring its proper functioning.

The control room for the ATLAS experiment is a central hub where skilled shifters operate around the clock, 24 hours a day and seven days a week. These dedicated personnel play a crucial role in preparing the ATLAS detector for data acquisition, ensuring its readiness to capture valuable experimental data. The control room serves as the nerve center, overseeing the intricate operations of the ATLAS experiment and responding to any alerts or events detected by the NSW DCS.

In essence, the NSW DCS stands as a testament to the engineering required to manage a complex and long-running experiments like the ATLAS. It acts as the vigilant guardian, overseeing the detector's health, adapting to changing conditions, and enabling the sustained success of the ATLAS experiment. The NSW DCS design is conceived to seamlessly integrate within the broader ATLAS DCS, providing continuous monitoring and a robust interface for all NSW hardware components. Given that Micromegas (MMG) and small-strip Thin Gap Chambers (sTGC) serve as muon detectors within the NSW, they are included in the Muon DCS system. The Muon DCS encompasses several sub-detectors, such as Monitored Drift Tubes (MDT), Resistive Plate Chambers (RPC), Thin Gap Chambers (TGC), and Cathode Strip Chambers (CSC).

Notably, due to the NSW Upgrade project, the CSC will be phased out, leading to the corresponding removal of its DCS functionalities. For the specific requirements of the NSW, two new sub-detectors will be incorporated under the Muon FSM tree, as illustrated in Figure 4.72 :

- MMG for Micromegas
- STG for sTGC

Within the Muon DCS, a typical configuration involves a total of three FSM nodes, as depicted in Figure 4.73. Following this established pattern, the MMG&STG sub-system adheres to the following structure:

- **Side A:** Comprising projects dedicated to servicing the hardware and associated services on Side A.
- **Side C:** Encompassing projects dedicated to servicing the hardware and associated services on Side C.

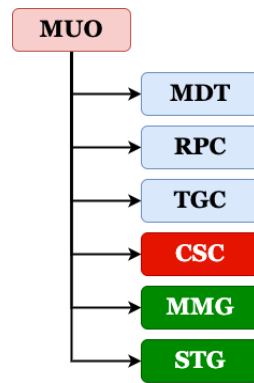


Figure 4.72: The structure of the MUO FSM DCS. Due to the NSW Upgrade, the CSC will be removed and MMG&STG DCS will be added as new sub-detectors.

- **Infrastructure (INF):** Involving projects catering to common hardware, services, and infrastructure requirements.

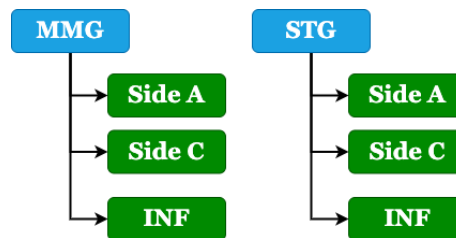


Figure 4.73: The FSM node structure of the MMG&STG following the Muon DCS schema.

#### 4.4.2 Hardware & Projects

Since the NSW is a significant project, its various hardware components must be organized into categories for a smooth architectural design. The NSW consists of the following hardware blocks:

- **HV:** This hardware block is responsible for providing high voltage to the detector, which is crucial for the muon detector's operation and functionality.
- **LV:** The LV hardware block supplies low voltage to the electronics, ensuring their proper functioning.
- **MDT-DCS-Module (MDM):** This hardware interface hosts temperature and magnetic field (BField) sensors, contributing to monitoring and control.
- **Electronics (ELTX):** The ELTX block encompasses electronics responsible for data acquisition, triggering, and data transfer within the NSW.
- **Gas:** This hardware block manages the gas components of the detector, crucial for the normal operation of the detectors.
- **Cooling:** The Cooling hardware block provides the necessary infrastructure for cooling the electronics, preventing overheating.
- **VME:** VME serves as the hardware environment hosting modular electronics, ensuring their efficient operation.

- **Advanced Telecommunications Computing Architecture (ATCA):** This hardware block utilizes the ATCA architecture to host modular electronics, providing advanced computing capabilities.
- **Detector Safety System (DSS):** DSS is the hardware interface responsible for ensuring the safety of the detector system, triggering safety protocols in case of abnormalities.
- **Beam Interlock System (BIS):** The BIS interface provides beam interlock flags, crucial for safe physics runs and LHC operation.

In the following subsections, a comprehensive description of the various hardware blocks will be provided.

The next step in the architecture is to define the WinCC-OA projects where all the NSW hardware will be distributed. A schematic of the proposed plan can be seen in Figure 4.74 below:

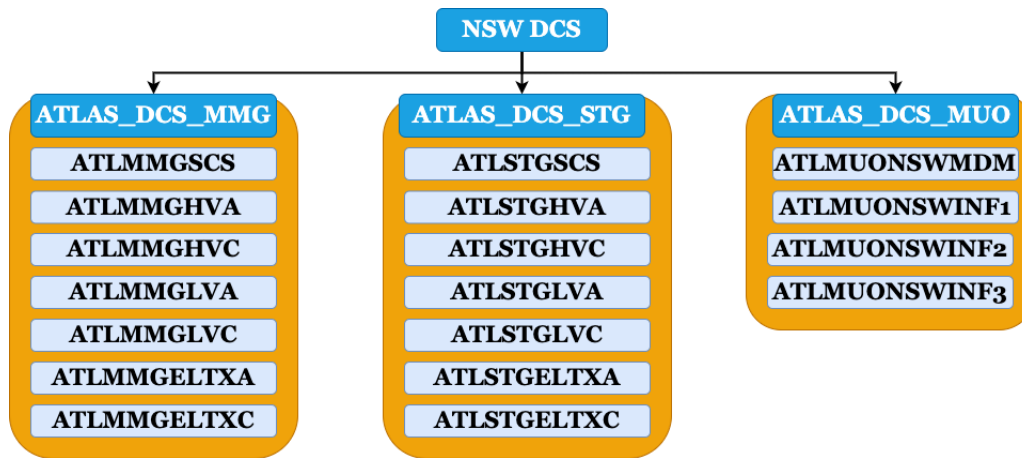


Figure 4.74: The proposed MMG&STG WinCC-OA projects allocation between the sub-detector.

The division of the various projects is based on the following criteria:

1. **Project type:** The Supervisor Control Station (SCS) project will serve as the overarching control station that encompasses all projects and functionalities.
2. **Detector:** Projects are categorized based on the detector they will serve (e.g., MMG, STG).
3. **Side of NSW:** Projects are organized according to the side of the NSW they will serve (e.g., A, C).
4. **Hardware:** Projects are classified based on the hardware they will serve (e.g., HV, LV, ELTX, MDM, and INF, which are used for the common infrastructure).

#### 4.4.3 Projects Allocation

The next crucial step involves defining and inventorying the computer that will host the WinCC-OA projects. After extensive consultation with the ATLAS Central DCS team, the selected server is the PowerEdge R440 Server 1U. The PowerEdge R440 offers value in a compact form factor, providing platform flexibility and maximizing performance with dual 2nd Generation Intel® Xeon® Scalable processors, up to 16 DIMMs, and scalable storage that allows for a mix of SSDs and NVMe PCIe SSDs. Embedded diagnostics and SupportAssist contribute to the R440's ability to deliver maximum uptime in a worry-free environment. For the NSW, the decision was made to purchase a total of 12 servers, with 10 intended for active use and two acquired as backups. Subsequently, the project

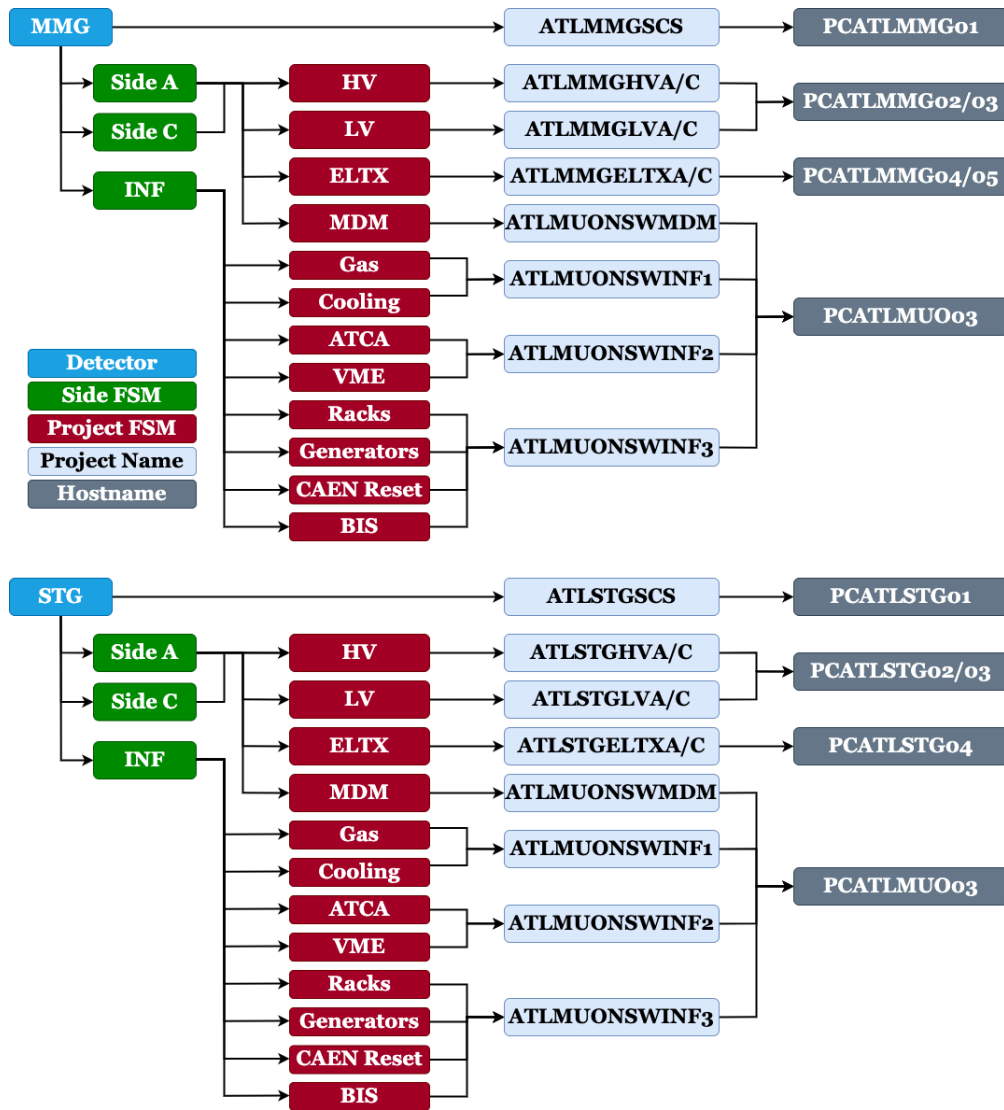


Figure 4.75: The WinCC-OA projects allocation between the various server machines.

allocation per hostname had to be defined, following the logic illustrated in Figure 4.75 below: The information derived from Figure 4.75 provides insights into the project, hostname, and the specific detector part running on a given server. Distinct color deviations signify the Side FSM, Project FSM, Project name, and hostname. The allocation of projects adhered to the following criteria:

- **Number of Monitored Parameters:** Projects were organized based on the quantity of monitored parameters, ensuring efficient management.
- **Arrangement by Side:** Projects were grouped by Side to enhance maintainability and organization.
- **Functional Grouping:** Projects sharing the same hostname were grouped based on functionality. For instance, all common infrastructure projects were placed under the pcatlmuo03 machine.

Consequently, a total of 18 WinCC-OA projects are distributed across 10 machines, establishing a scalar distributed system within the ATCN network of ATLAS. The 10 DCS machines are strategically located on the Y.26-16.A1 rack in the USA15 service area of ATLAS, connected to the ATCN network, with access exclusively granted via the ATLAS gateway.

#### 4.4.4 Gitlab Repository Structure

The NSW DCS projects are archived under the Central DCS GitLab repository [https://gitlab.cern.ch/atlas-dcs-subsystems/atlas\\_dcs\\_xyz](https://gitlab.cern.ch/atlas-dcs-subsystems/atlas_dcs_xyz), where `xyz` corresponds to `mmg`, `stg`, or `muo`. An essential prerequisite before initiating developments is the definition of the project structure. The GitLab repository has been organized to adhere to Central DCS requirements and adopt the common Muon naming convention. This involves the creation of dedicated folder directories for individual projects, incorporating naming conventions that clearly indicate the scope of both folders and files.

#### 4.4.5 OPC UA Servers

For communication with most NSW hardware, the well-known OPC UA Server and corresponding WinCC-OA OPC UA clients are employed. The following list enumerates the OPC UA Servers developed by the Central DCS and the BE-ICS in the quasar framework, serving the needs of NSW:

1. **SCA OPC UA Server:** Establishes communication between the FELIX and the SCA embedded across all NSW electronics.
2. **MDM CanOpen OPC UA Server:** Establishes communication between the MDM and the connected temperature and magnetic field (BField) sensors.
3. **CAEN OPC UA Server:** Facilitates communication for the CAEN and NGPS infrastructure used in the HV and LV projects.
4. **ATCA OPC UA Server:** Manages communication for the ATCA crates.
5. **VME OPC UA Server:** Handles communication for the VME crates.

The allocation of OPC UA Servers among the NSW DCS projects is illustrated in Figure 4.76. This diagram provides information on the rack and area position of the hardware, as well as the connections of OPC UA clients between various projects.

#### 4.4.6 Electronics

In this subsection, a comprehensive overview of the Electronics DCS project will be provided. This will include a detailed description of the project's components, functionalities, and the integration steps involved. Additionally, the various techniques employed in WinCC-OA for seamless integration will be thoroughly explored.

##### Introduction

The Electronics project is tasked with monitoring all parameters connected to the Slow Control Adapter (SCA) of all NSW electronics. The schematic of the SCA operation has been illustrated in Figure 3.35. The SCA OPC UA Server, facilitated by the FELIX, establishes communication with the SCA and its associated connections.

As the SCA OPC UA Server is accessible on the network, the DCS Back-End, represented by the WinCC-OA project in our context, can act as an OPC UA client. This allows it to subscribe to the server and read all the values associated with the SCA.

The primary goal of the Electronics DCS project is to provide users with the capability to safely monitor the values of 7488 electronics boards, encompassing over 100 000 parameters.

The DCS ELTX projects responsible for monitoring are as follows:



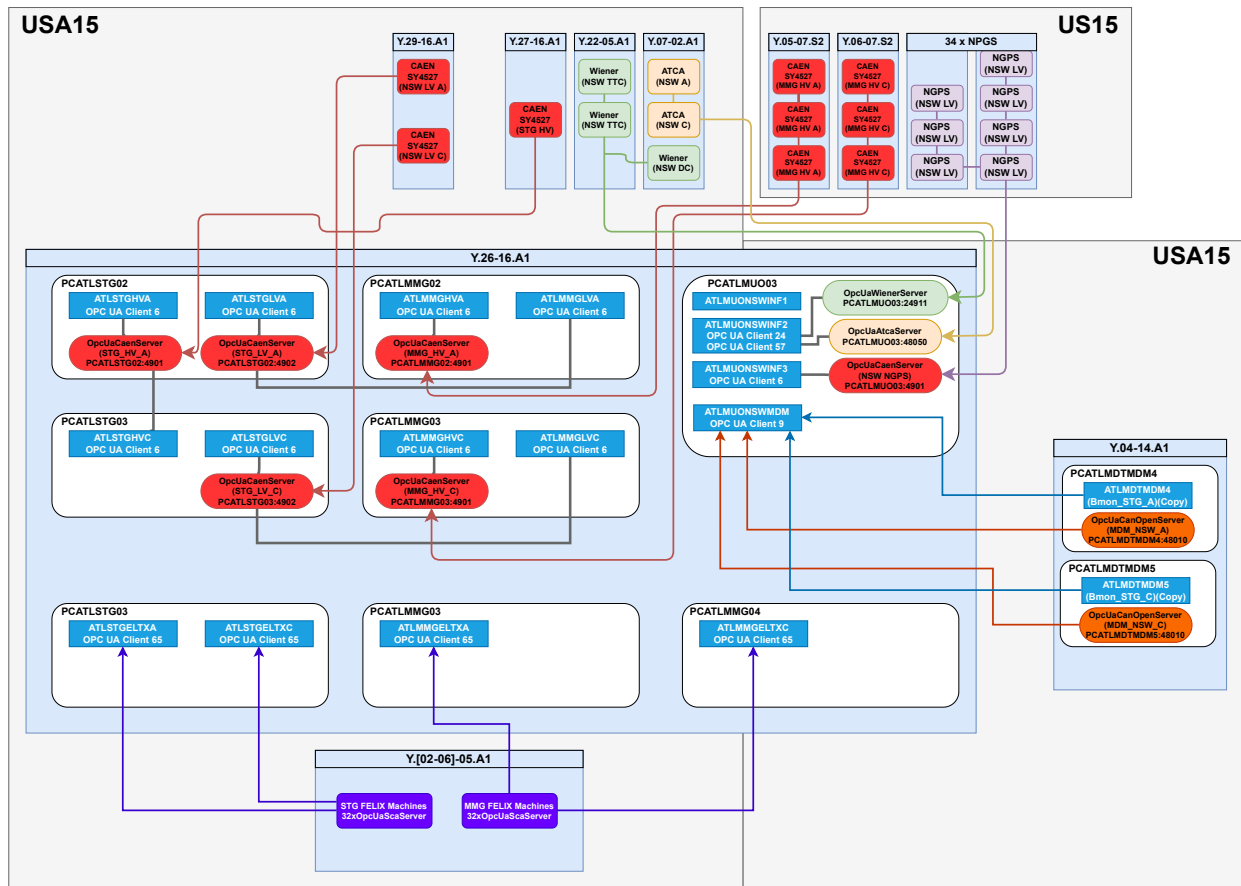


Figure 4.76: Overview of the OPC UA schematic.

1. **ATLMMGELTXA:** Monitors the parameters of MMG-A.
2. **ATLMMGELTXC:** Monitors the parameters of MMG-C.
3. **ATLSTGELTXA:** Monitors the parameters of STG-A.
4. **ATLSTGELTXC:** Monitors the parameters of STG-C.

### Framework Component - fwSca

The installation of the corresponding framework component is crucial for project deployment. To meet the requirements of the SCA ELTX project, the **fwSca** component has been developed. It can be installed using the JCOF Framework, particularly through the Installation Tool. The **fwSca** component comprises libraries and functions specific to SCA needs, particularly used to create the appropriate data points (DP). Upon installing **fwSca**, the following data point types (DPT) are generated through the `.postinstall` script:

1. **fwScaSCA:** Corresponds to one physical SCA chip.
  - (a) `.address` (string): The address of the given SCA in an ScaSoftware convention. (e.g., `netio-next://fid/0x10100000007f0000`)
  - (b) `.online` (bool): True if the SCA responds to periodic ping requests from the SCA Supervisor; otherwise, false.
  - (c) `.id` (uint): Stores the unique ID number of the SCA queried from the hardware during initialization.

- (d) `.lastReplySecondsAgo` (ulong): Number of seconds since the last reply from this SCA has been received.
  - (e) `.lostRepliesRate` (ulong): Rate of lost replies expressed in requests per second.
  - (f) `.numberLostReplies` (float): Total number of lost replies.
  - (g) `.numberReplies` (ulong): Number of SCA replies received from this SCA since initialization.
  - (h) `.numberRequests` (ulong): Number of SCA requests sent to this SCA since initialization.
  - (i) `.requestRate` (float): Request rate sent to this SCA expressed in requests per second.
2. `fwScaGlobalStatistician`: Corresponds to one global statistician per SCA OPC UA server.
    - (a) `.totalNumberLostReplies` (float): Total number of lost replies per SCA OPC UA Server.
    - (b) `.requestRate` (float): Request rate sent to this SCA expressed in requests per second.
  3. `fwScaScaSupervisor`: Corresponds to one supervisor per SCA OPC UA server.
    - (a) `.numberOffline` (unit): Stores the number of SCAs in deferred initialization ("not yet online") plus those initialized but currently offline.
  4. `fwScaMeta`: Needs to be created manually and corresponds to the server version per SCA OPC UA Server.
    - (a) `.versionString` (string): Contains versions of the server, SCA-SW, and relevant dependent libs (FELIX SW, etc.).

The final step involves creating the corresponding DPs by pressing the corresponding buttons in the 4.77 panel.

### OPC UA Client connection

The installation of the 'fwSca' component also includes an OPC UA Client with the number 65, which is visible on the Console of the corresponding project (referred to as 'startConsole'). The next crucial step involves creating the necessary connections and subscriptions. To achieve this, the 'fwAtlasOpcUa' JCOP framework component is essential and can be installed using the JCOP Installation Tool.

The 'fwAtlasOpcUa' component provides the following functions for creating connections and subscriptions:

- `fwAtlasOpcUa_createConnection(unsigned managerNumber, string connectionName, string endpointUrl);`
  - `managerNumber`: Driver number (e.g., 65)
  - `connectionName`: Connection name of the SCA OPC UA Server (e.g., 'SCA\_OPC\_UA\_MMG\_Sector\_A01')
  - `endpointUrl`: The endpoint URL of the SCA OPC UA Server, typically running inside the FELIX machines (e.g., "opc.tcp://pc-tdq-flx-nsw-mm-00:48020").
- `fwAtlasOpcUa_createSubscription(string connectionName, string subscriptionName);`

- `managerNumber`: Driver number (e.g., 65)
- `subscriptionName`: Subscription name of the SCA OPC UA Server (e.g., ‘SCA\_OPC\_UA\_MMG\_Sector\_A01\_subscription’)

By pressing the “Create Connection Subscription” button in the panel `ATLAS_DCS_MMG/panels/mmgEltx_tools/mmgEltx_fwSca_dpCreation.pnl`, as depicted in Figure 4.77, the corresponding 16 SCA OPC UA connections and subscriptions are created under the `_OPCUAServer` and `_OPCUASubscription` DPTs within each project.

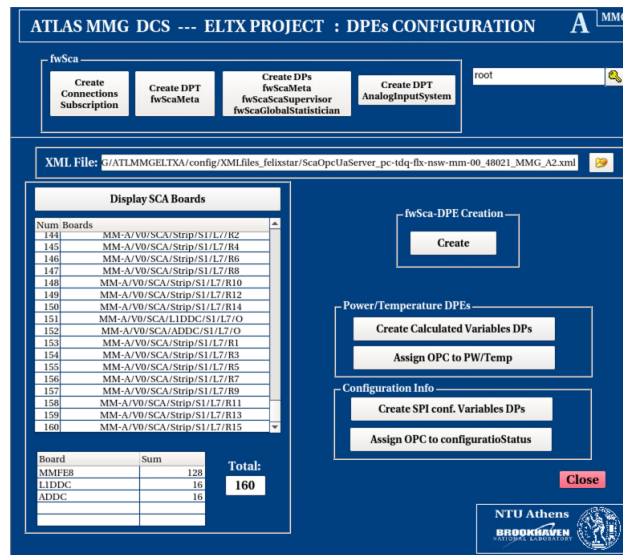


Figure 4.77: The panel “`mmgEltx_fwSca_dpCreation.pnl`” which creates the corresponding 16 SCA OPC UA connections and subscriptions under each project.

## Datapoints Creation

If the corresponding SCA OPC UA Server is connected, the Data Processing Element (DPE) `SCA_OPC_UA_MMG_Se` will be set to `TRUE`. This indicates that the SCA OPC UA items are available in the OPC UA address space, allowing for subscription. Consequently, all SCA datapoints can be created and subscribed to their respective SCA OPC UA items.

For the creation of datapoints, the same panel used for the SCA OPC UA Connection Subscription is employed, as illustrated in Figure 4.77. Users can open the corresponding XML file and press the “Display SCA boards” button to review its contents. Subsequently, pressing the “Create” button generates the `fwScaSCA` datapoints and connects them to the corresponding OPC UA objects.

It is noteworthy that the `fwSca` component does not handle the calculated parameters in the SCA OPC UA Server XML files, which contain actual temperature and power values for various SCA connections. The classic `fwScaAnalogInput` Data Processing Type (DPT) includes:

- `value (OpcUa_Float)`: Stores the most recent voltage of the given channel, expressed in volts. Will be `NULL` if conversion isn’t successful.
- `rawValue (OpcUa_UInt16)`: Stores the most recent conversion result of the given channel, expressed in ADC counts. Will be `NULL` if conversion isn’t successful.

To address this, a new DPT named `AnalogInputCalculatedVariables` is introduced, encompassing the following parameters:

- `.temperature (float)`: The corresponding temperature value after conversion.

- **.power (float):** The corresponding power value after conversion.

Users can press the designated button in Figure 4.77 to create and connect the corresponding data-points for the specific sector using the loaded XML file.

### Internal Mapping & Board Settings

One of the crucial steps in a DCS project is the internal mapping configuration, which involves mapping the physical SCA object to geographical objects. This process ensures that information about the location of an SCA object can be obtained.

To facilitate this mapping, the "MMG\_ELTX\_Board" Data Point Type (DPT) has been designed, as illustrated in Figure 4.78. The structure of this DPT includes the following components:

- **Sector Division:** This corresponds to the sector folder structure. In each of the four ELTX projects, there are 16 sectors, each identified by a specific name (e.g., MMG\_ELTX\_A01).
- **Layer Division:** This encompasses the layer folder structure. While MMG contains a total of eight layers, STG has an additional layer for Rim Electronics (e.g., Layer9).
- **Board Division:** This involves the board folder structure. For MMG, there are 24 or 16 boards depending on the layer. In the case of STG, there are eight boards for each layer, but for Rim Layer 9, there are a total of 11 boards.

Each of the Board consists the following DPT structure:

- **info:**
  - **.logicalName:** Includes the SCA name which is specified in the SCA OPC UA Serve XML file (e.g. /MM-A/SCA/L1DDC/S0/L0/E);
  - **.type:** Includes the board type (e.g MMFE8, L1DDC, ADDC, SFEB8, SFEB6, PFEB, Router, PadTrigger, RimL1DDC1, RimL1DDC2).
- **power:** It consists of the power folder structure.
  - **.channel:** Includes the LV channel from the corresponding LV project which provides the LV power to this specific SCA board.
- **state:** It consists of the state structure which is an internal datapoint which is used for summary information;
  - **.temperature:** Includes a sum up of all the temperature values of the corresponding SCA boards. It consists of 3 severity levels (1: OK, 2:WARNING, 3:ERROR) and it's functionality will be described in the next subsection;
  - **.power:** Includes a sum up of all the power values of the corresponding SCA boards. It consists of 3 severity levels (1: OK, 2:WARNING) and its functionality will be described in the next subsection.
- **.enabled:** Included the information if the corresponding SCA board is enabled or disabled. A description will be given in the next subsection.

In order to create the DPT and DPs of the project, users can do it by pressing the corresponding buttons under the panel "mmgEltx\_Fsm\_Dpe\_Creation.pnl".

Another crucial Data Point Type (DPT) is the one containing board settings for each board type. The Board Settings DPT, depicted in Figure 4.80, is structured as follows:

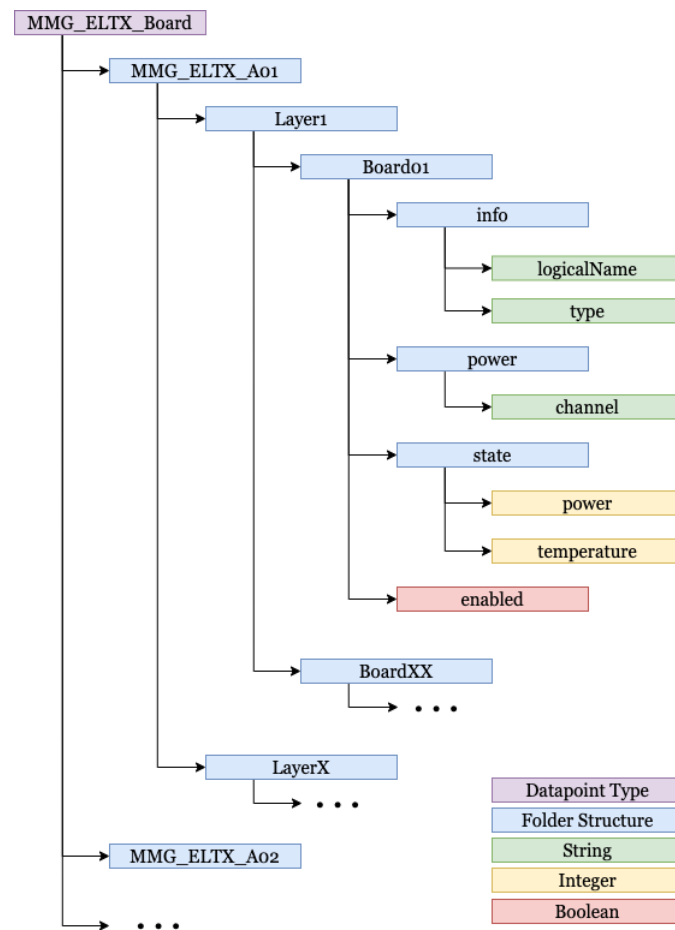


Figure 4.78: The structure of the internal mapping DPT.

- **Board\_Settings:** Consists of the settings folder structure, encompassing all detector board types (MMG: MMFE8, L1DDC, ADDC, and STG: SFEB8, SFEB6, PFEB, Router, PadTrigger, RimL1DDC1, RimL1DDC2).
- **Board(MMFE8):** Represents the board type folder structure.
- **parameter(vmmPdo):** Encompasses the board parameter folder structure.
  - **downLimit:** The default lower alert limit for the corresponding parameter.
  - **upLimit:** The default higher alert limit for the corresponding parameter.
  - **description:** The descriptive text used for description handling.

### Description Handling

The next crucial step in the project integration is description handling, which is employed to utilize more user-friendly names for the datapoints. In the ELTX projects, all datapoints and parameters have descriptions, and for each datapoint element, the following schema is employed:

- **Description:** It contains the geographical location according to the internal mapping and the parameter description specified under the Board\_Settings DPT (e.g., MMG ELTX A 01 L1 B11 SCA Temp).

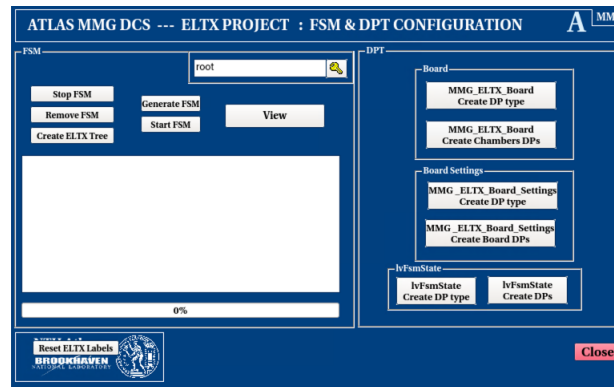


Figure 4.79: The panel which is used for the creation of the internal mapping and the board settings.

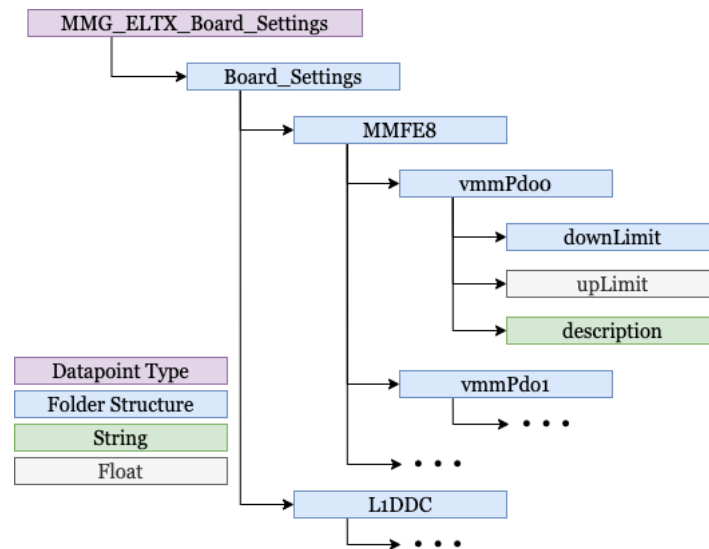


Figure 4.80: The structure of the board settings DPT.

- **Alias:** It contains the geographical location according to the DAQ convention, the board type, and the parameter description specified under the Board\_Settings DPT (e.g., MMG ELTX A ADDC S0 L0 SCA Temp).

To apply descriptions and aliases to all datapoints in the project, the user needs to press the corresponding button in the panel `mmgEltx_descriptionHandling.pnl`, as shown in Figure 4.81.

### Alarm Handling

One of the pivotal aspects of project development and operation is the handling of alarms. The alert handling of continuous values becomes crucial when the entire value range needs to be covered with specified intervals (limits). In WinCC-OA, the framework (FW) Alarm Screen is employed for this purpose, designed to facilitate detailed problem tracking and acknowledgment.

It is highly advisable to configure alert handling for each Data Point (DP) corresponding to a specific Data Unit (DU). This configuration involves different threshold limits, triggering corresponding alarm severity levels when the value falls within predefined conditions. WinCC-OA defines four levels of alarm severity:

- **OK:** Indicates that the system is functioning properly.
- **WARNING:** Represents a low-severity alert. The system can continue operating, and the issue should be addressed in the subsequent working hours.



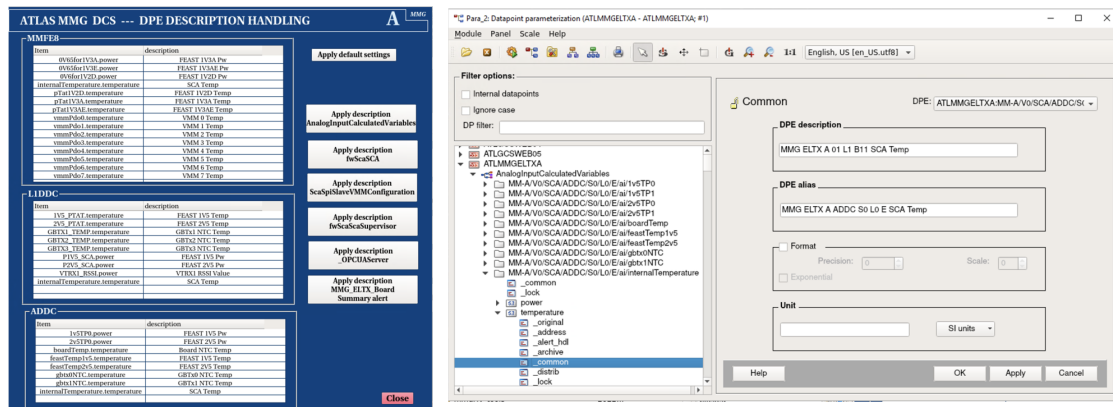


Figure 4.81: The panel is used for the description handling configuration for all project's datapoints.

- **ERROR:** Signifies a high-severity alert, indicating a serious error affecting the system's functionality. Immediate attention is required to rectify the issue.
- **FATAL:** Denotes a very high-severity alert, indicating that the system cannot continue to operate.

The alert handling configuration in WinCC-OA ensures that alarms are appropriately classified based on severity levels, allowing for effective monitoring, quick identification, and prompt resolution of issues.

The user has the capability to configure the alarm limits for all datapoints in the project using the panel "mmgEltx\_alert\_Configuration.pnl," illustrated in Figure 4.82. Within the ELTX project, the following alarms are defined:

- **SCA OPC UA Server State:** Alarm indicating the connection status.
- **SCA OPC UA Supervisor:** Alarm tracking the number of offline SCAs per server/sector.
- **SCA Sector Online:** Summary alert triggered when there are more than 10 offline SCAs per server/sector.
- **SCA Online Status:** Alarm for the SCA online status, indicating whether the SCA is online or offline.
- **RDB Manager:** Alarm associated with the database manager responsible for data archiving.
- **VMM Configuration Status:** Alarm related to the VMM configuration status.
- **Temperature and Power Values:** Specific alarms for temperature and power parameters, indicating if the values fall within normal ranges.

The configuration panel allows users to set up precise limits for each alarm, ensuring effective monitoring and timely response to deviations from expected values.

### Archive Configuration

Another critical aspect of ensuring the safe operation of the ELTX DCS is the archival of data, making it promptly available when new values are acquired. For the ELTX and, in general, the ATLAS DCS Production systems, data is archived in a Production Oracle DB. Given the long-term nature of the project, it is imperative to archive data at a nominal rate to prevent issues such as

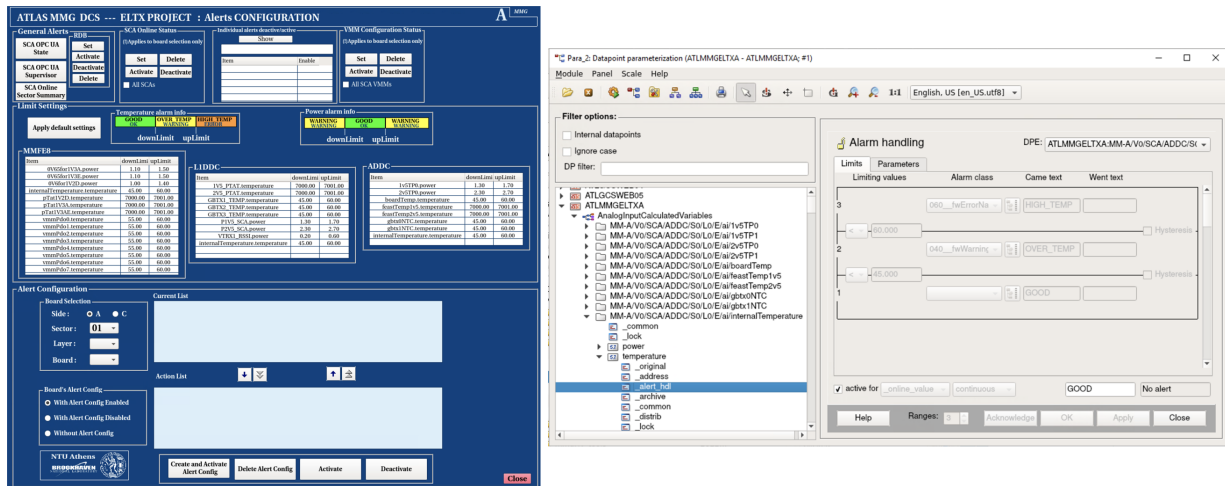


Figure 4.82: The panels is used for the alarm handling configuration for all project's datapoints.

disk space exhaustion or data loss. To address this requirement, the well-established WinCC-OA technique known as "smoothing" is employed.

Smoothing plays a pivotal role in minimizing communication loads and reducing the volume of data processed within a WinCC-OA system. This technique effectively mitigates the communication load between drivers, managers, and other components, while simultaneously optimizing the amount of data processed. By implementing smoothing, the ELTX DCS ensures efficient data archival practices over an extended period, safeguarding against potential storage challenges and ensuring the integrity of historical data.

In the archival process, smoothing values are archived only when they meet the specified smoothing criteria. The WinCC-OA Data Manager is responsible for smoothing the values, comparing each new system value with the last archived value before deciding whether to archive or apply smoothing. Various smoothing types are available for both driver and archive smoothing, each serving specific purposes and outlined below:

- **Value-dependent smoothing:** The value passes smoothing when it is defined as a percentage (defined % smaller or larger) than the last valid value.
- **Time-dependent smoothing:** Values occurring within a set tolerance time after the last value are discarded. After this time has elapsed, the next value change passes smoothing.
- **Value AND time-dependent smoothing:** Discards values arriving within the tolerance time AND within a specified tolerance range. The value passes smoothing after the time has elapsed or when the set value (limit) is exceeded within the tolerance time.
- **Value OR time-dependent smoothing:** Values within the set tolerance time OR within the set tolerance range after the tolerance time has elapsed are discarded. The value passes smoothing after the time has elapsed or when the set value (limit) is exceeded.
- **Old/new comparison:** Values pass smoothing only if the value itself or one of the status bits of the variables changes.
- **Old/new AND time-dependent:** Suppresses unchanged variable values within a tolerance time. After a value change, unchanged values do not pass smoothing during the tolerance time until the original value or one of the status bits changes. New values pass smoothing if the value changes within the tolerance time.

- **Old/new OR time-dependent:** Suppresses value changes or changes of status within the tolerance time. After the tolerance time, only the old/new comparison is valid. Value changes pass smoothing if the original value or a status bit changes.

Adhering to the outlined rules, the user can configure the archive handling of specific datapoints using the panel depicted in Figure 4.83. This interface enables the user to set, start, stop, or delete the archive handling for the following datapoints:

- **SCA Online Status:** Controls the archiving behavior related to the online status of the SCA.
- **Board Analog Variables:** Manages the archive handling for the analog variables associated with each board.
- **Board VMM Configuration:** Configures the archive handling for the VMM (Voltage Mode Module) configuration of each board.
- **SCA OPC UA Connection State:** Determines the archiving strategy for the connection state of the SCA OPC UA Server.
- **Number of Offline SCA per Server/Sector:** Controls the archiving behavior concerning the count of offline SCAs per server/sector.
- **FSM State:** Manages the archiving settings for the FSM state.

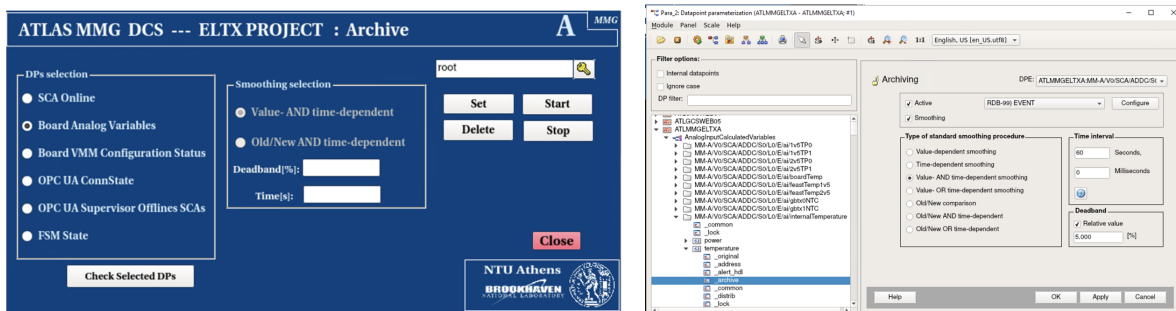


Figure 4.83: The panels is used for the archive handling configuration for all project's datapoints.

## Board states

As mentioned in the previous subsection, the internal mapping datapoint, depicted in Figure 4.78, includes temperature and power datapoints for each SCA board. These datapoints provide a consolidated calculation of all parameters for a board, enabling quick identification of potential power or temperature issues. The computation of these flags is facilitated by a control manager (number eight) operating in the background, known as `mmgEltx_calculateTemperaturePowerBoardStates.ctl`, illustrated in Figure 4.29.

In the process of calculating the state flag, instead of using the online value, the alert states per parameter (OK, WARNING, ERROR) are utilized. Specifically, the control manager collects all the alert states of the board's parameters during runtime and sets the state flag based on the most severe alert state.

The state flag schema is:

- `.temperature:`

1. OK
  2. WARNING
  3. ERROR
- .power:
    1. OK
    2. WARNING

### LV Connectivity

The subsequent step involves providing information about the LV channel that supplies power to each SCA board, as illustrated in Figure 4.78. The internal mapping datapoint encompasses details about the LV FSM node corresponding to the SCA board (e.g., `MMG_SIDE_A_LV|EIZ2A01_Digital_L1_L2`). Subsequently, a control manager (number 9) operates in the background and duplicates the LV channel FSM node of the SCA board from the respective LV project into an internal DPT called `lvFsmState`. This DPT comprises the following structure:

- **General:** The copy mechanism executed by the control manager checks the status (FSM and project are running) of the remote LV FSM and sets the `General.fsm.currentState` accordingly (e.g., `DEAD_NO_DISTCONN`, `DEAD_FSM_DOWN`).
- **LV channel:** The copy mechanism via the control manager duplicates the remote LV channel FSM's `fsm.currentState` to the equivalent local datapoint (e.g., `MMG_SIDE_A_LV|EIZ2A01_Digital_L1`).

### DDC - FreeVariable

As previously mentioned, the DCS, calibration, and configuration processes all utilize the common SCA OPC UA Server path for the SCA. However, the front-end boards equipped with the VMM use the same SCA ADC input channel for both monitoring and calibration purposes. During the Physics run, the VMM monitor output corresponds to the VMM temperature. In contrast, during the Calibration run, the VMM monitor output displays the baseline measurement, which is employed for board noise calibration measurements. Consequently, during the Calibration run, the VMM presents fictitious temperature values, necessitating the implementation of an interface plugin between DCS and DAQ to prevent the triggering of numerous alarms and warnings by the DCS.

The proposed solution involves utilizing the common SCA OPC UA Server and the FreeVariable status, primarily a user-defined OPC-UA item that can be controlled and monitored by both DCS and DAQ back-end applications. Consequently, during the Calibration run, the DCS monitors the configuration status for this specific VMM of the FEB, and the alarm corresponding to the FEB's VMM is disabled, as depicted in Figure 4.84 .

Users can effortlessly create and connect the VMM configuration Data Point Type (DPT) and Data Points (DPs) by simply pressing the corresponding buttons, as illustrated in Figure 4.77. Following this, a control manager (number 7) operates in the background, reading the configuration status for each Front-End Board (FEB) VMM from the local DPT "ScaSpiSlaveVMMConfiguration." The control manager then executes the following actions:

- **Configuration Status = 1:** When `scmx==0 & sbmx==1 & sbfp==1 & sm==4 & reset!=3`, the configuration status is set to 1. In this case, the control manager establishes the correct alert limits on the corresponding VMM.

- **Configuration Status = 0:** If the configuration status is 0, the control manager sets incorrect alert limits on the corresponding VMM. This action is taken to "mask" the incorrect VMM monitor output, which does not correspond to the VMM temperature.

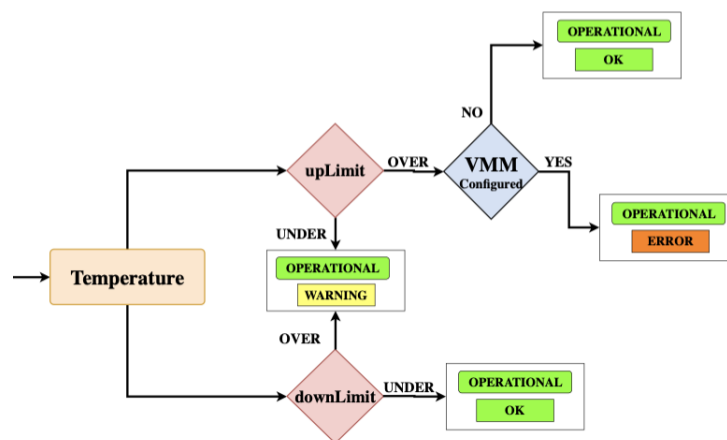


Figure 4.84: A flow chart of the logic for the status and state definition based on the VMM temperature and the configuration status.

### FSM Hierarchy & Units

Each node FSM is uniquely named based on the subsystem name and its functionality, adhering to the conventions of ATLAS DCS. The state of each FSM is specified by a corresponding internal Data Point (DP). The type of FSM object, which defines the fundamental functionality of the node and its components, depends on the functional purpose and position of the element in the DCS architecture hierarchy.

The FSM operates on a strict hierarchical structure, establishing parent-child relationships. In this structure, commands flow from parents to children, and status updates flow from children to parents. This hierarchical approach ensures efficiency in commanding actions on multiple nodes, as a higher-level node can command its children, and the status of the higher node summarizes the status of all nodes within its hierarchy.

All nodes are initially in a predefined state and only accept predefined commands as specified by the FSM type to which they belong.

For the ELTX projects, the FSM structure is as follows:

- **Side-Control Unit (CU):** There is one Side CU per actual side (e.g., A, C).
- **Sector-Control Unit (CU):** There are 16 Sector CU units per actual side (e.g., 1-16).
- **Layer-Logical Unit (LU):** For MMG, there are 8 Layer LU units (1-8), and for STG, there are 9 Layer LU units (1-9).
- **Board-Device Unit (DU):** For MMG, there are 16 or 21 Board DU units, and for STG, there are 8 or 11 Board DU units, depending on the layer they are placed.

The FSM hierarchy begins with the SCA board, which consists of a DU defining the FSM State & Status at the SCA board level, as illustrated in Figure 4.86. The Board DU has the following states:

- **OFFLINE:** When the board's SCA is disconnected or offline.
- **DISABLED:** When the alert configuration of the SCA board is disabled.

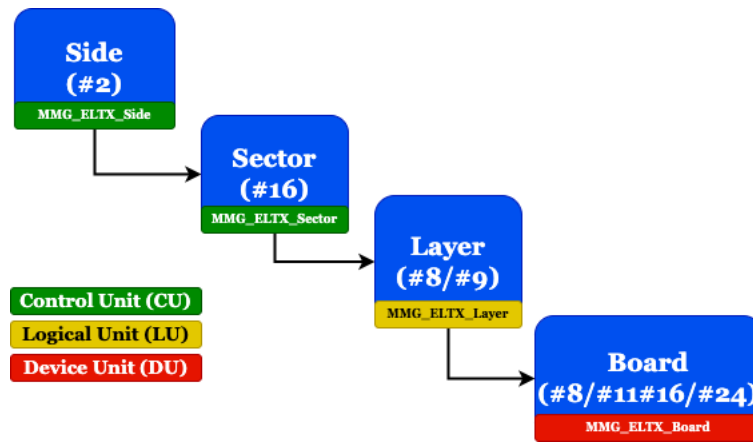


Figure 4.85: The FSM Hierarchy of the ELTX projects.

- **LV\_OFF:** When the LV channel of the SCA board is powered off.
- **UNKNOWN:** When the LV FSM or LV channel is in an unknown state, or the SCA OPC UA Server for the specific SCA board is not running.
- **OPERATIONAL:** When everything is okay, and none of the above states have occurred.

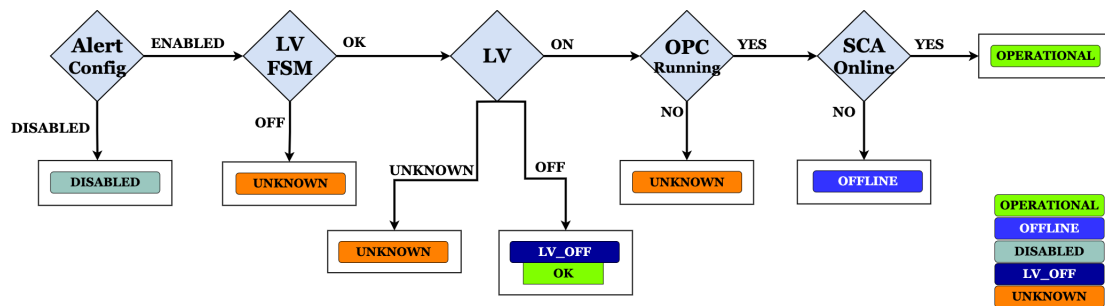


Figure 4.86: A flow chart of the logic Board SCA DU state calculation.

The Status of the Board DU is defined by the temperature and power alert limits using the command:

```
fwFsmAtlas_connectStatusWithDpeAlerts(domain, device, dpesForStatusCalculation)
```

The determination of alert states is based on temperature and power values, and the resulting severity status is calculated using the function described in Figure 4.87. Various severity levels (STATUS) guide the evaluation process:

- **FATAL:** This status is excluded from the overall status calculation and serves as a critical indicator that does not directly contribute to the general evaluation.
- **ERROR:** Occurs when the temperature values exceed the defined upLimit. Specifically, for VMM temperature values, an initialization check ensures that the VMM is configured in temperature mode through the common FreeVariable parameter.
- **WARNING:** Triggered when the temperature value falls between the upLimit and downLimit. For power values, a WARNING is registered when the value surpasses the upLimit or falls below the downLimit.
- **OK:** This status is assigned when both power and temperature parameters remain within acceptable ranges, causing no alarms or warnings.



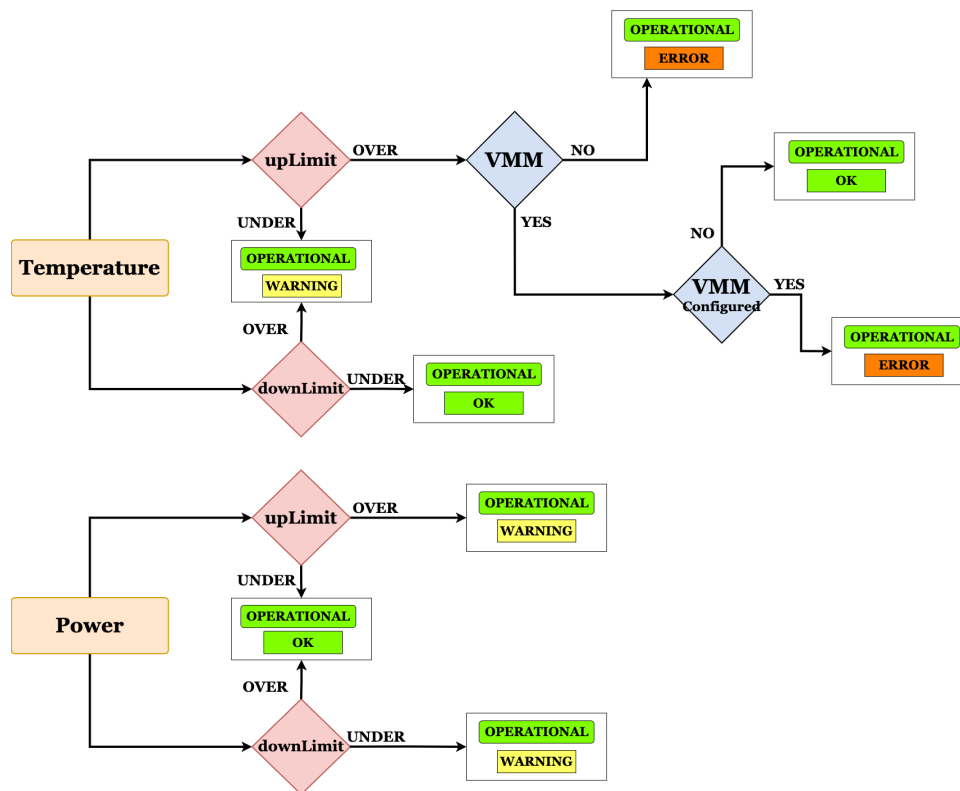


Figure 4.87: A flow chart of the logic Board SCA DU status calculation according to the temperature and power alert limits.

Additionally, the DU introduces two FSM actions that users can execute:

1. **REFRESH:** This action is employed to refresh the state and status of the SCA Board DU. It ensures that the latest information about the board is accurately reflected.
2. **DISABLE/ENABLE:** The DISABLE action is used to deactivate the SCA board, resulting in the unsetting of power and power alarm limits by assigning large values and unsetting the invalid bit. Conversely, the ENABLE action is employed to activate the SCA board, setting appropriate power and power alarm limits and enabling the valid bit.

Following the sequence, the FSM structure, as depicted in Figure 4.85, includes the following FSM units, each with its associated states:

- **Layer - LU):**

- **NOT\_READY:** When any Board DU is in LV\_OFF or OFFLINE state.
- **SHUTDOWN:** When all Board DUs are in LV\_OFF or DISABLED state.
- **UNKNOWN:** When any Board DU is in UNKNOWN or DEAD state.
- **READY:** When all Board DUs are in OPERATIONAL or DISABLED state.

- **Sector - Control Unit (CU):**

- **NOT\_READY:** When any Layer LU is in NOT\_READY or SHUTDOWN state.
- **SHUTDOWN:** When all Layer LUs are in SHUTDOWN state.
- **UNKNOWN:** When any Layer LU is in UNKNOWN or DEAD state.

- **READY:** When all Layer LUs are in READY state.
- **Side - Control Unit (CU):**
  - **NOT\_READY:** When any Sector CU is in NOT\_READY or SHUTDOWN state.
  - **SHUTDOWN:** When all Sector CUs are in SHUTDOWN state.
  - **UNKNOWN:** When any Sector CU is in UNKNOWN or DEAD state.
  - **READY:** When all Sector CUs are in READY state.

Moreover, all Control and Logical Units feature the FSM action "REFRESH," allowing users to refresh the corresponding FSM state and status.

## Panels

In this subsection, we will provide detailed descriptions of various operational panels, following the FSM hierarchy starting from the board and progressing through the layers, sectors, and side panels.

Starting from the bottom part of the ELTX FSM, we first encounter the board panel, which displays all the essential information of the SCA Board. The Board View panel encompasses the following features:

- **Board Info:** Contains the SCA's name and FELIX address, which are defined in the SCA OPC UA Server XML file.
- **OPC Info:** Provides information about the board's SCA OPC UA Server, including the connection endpoint info, connection status, and server state.
- **SCA Info:** Contains details about the board's SCA, such as the ID, connection status, and the time elapsed since the last reply in seconds.
- **Board View:** Displays all temperature and power parameters of the specific board. Users can easily check if the values are within the correct alert limits using the color-coded fields. Additionally, users can view the plot of the corresponding parameter by right-clicking on the field.
- **LV FSM Info:** Provides information about the LV channel that supplies power to the board. Specifically, it shows the LV channel, the LV FSM general state, and the LV FSM channel state.
- **Temperature & Power Plots:** Displays corresponding parameter values as a function of time.
- **Board Overview:** Shows summarized board states, including temperature, power, and LV states. For temperature & power states, it considers all corresponding power & temperature parameters.
- **Board State & Status Color Code:** Displays the FSM states and status using a color-coded scheme.

Moving up the ELTX FSM hierarchy, the Layer View panel displays essential information about the corresponding sector's layer. This panel provides a comprehensive view of all boards physically installed on the layer, allowing users to assess the layer's status and state through an intuitive color-coded scheme. For each board, the Layer View panel includes the following details:

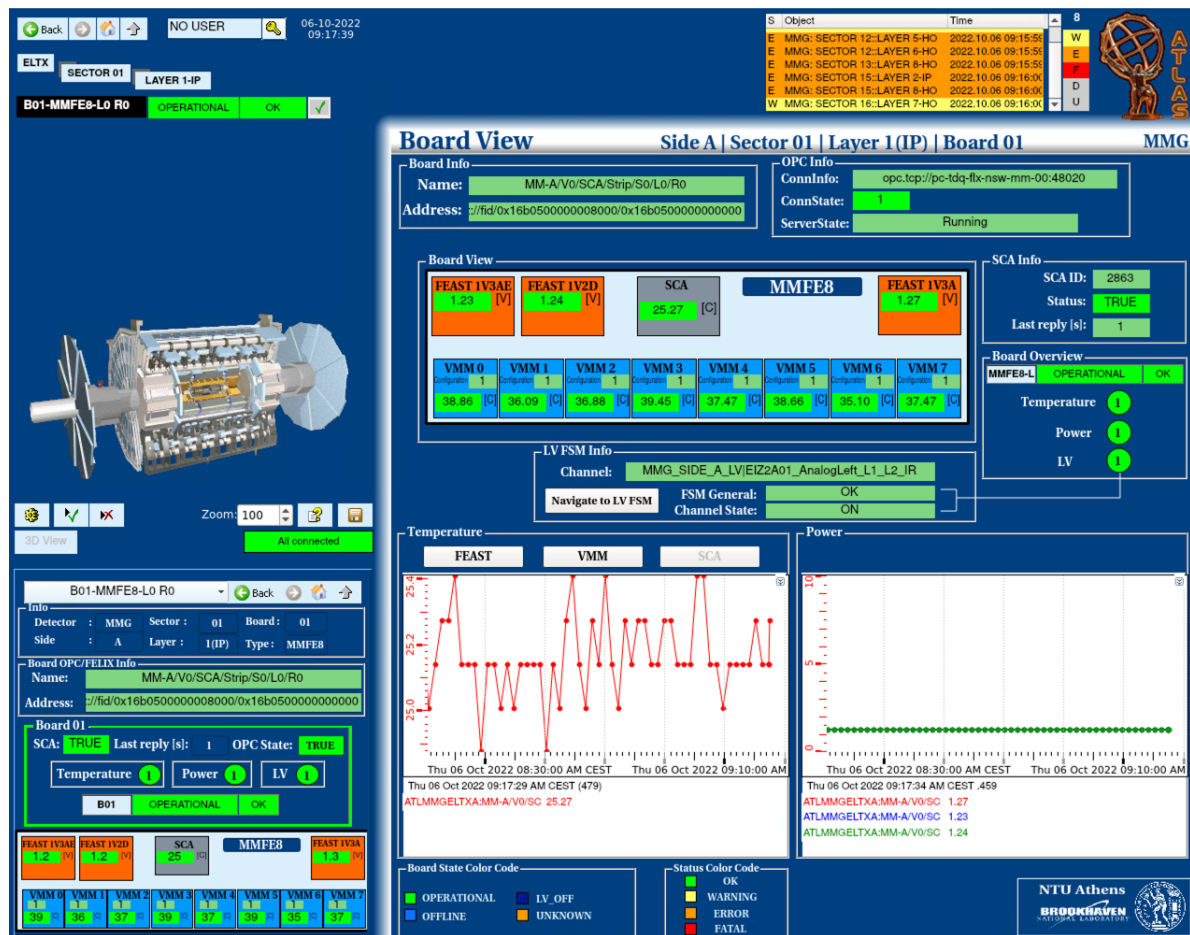


Figure 4.88: The operation panel for the FSM Board View.

- **Type:** Indicates the type of the board.
- **State & Status:** Displays the FSM state and status of the board.
- **LV Channel Status:** Provides the status of the LV channel associated with the board.
- **SCA Online Status:** Indicates whether the SCA associated with the board is online or offline.
- **Temperature & Power State:** Reflects the combined state of temperature and power parameters for the specific board.

Advancing up the FSM hierarchy, the Sector View panel provides users with an overview of all boards installed in the corresponding sector. This panel offers a range of features to facilitate comprehensive monitoring. Key components of the Sector View panel include:

- **Board View Selection:** Users can choose from various options, such as state/status, temperature, power, LV, SCA temperature, SCA status, and Type, for the boards' rectangle mode.
- **Board View Info:** Includes the color code corresponding to the selected board view option.
- **Layer View:** Displays the status and state of the layer, presenting all installed boards in their physical locations on the layer.
- **OPC Info:** Provides information about the board's SCA OPC UA Server, including the connection endpoint info, connection status, and server state.

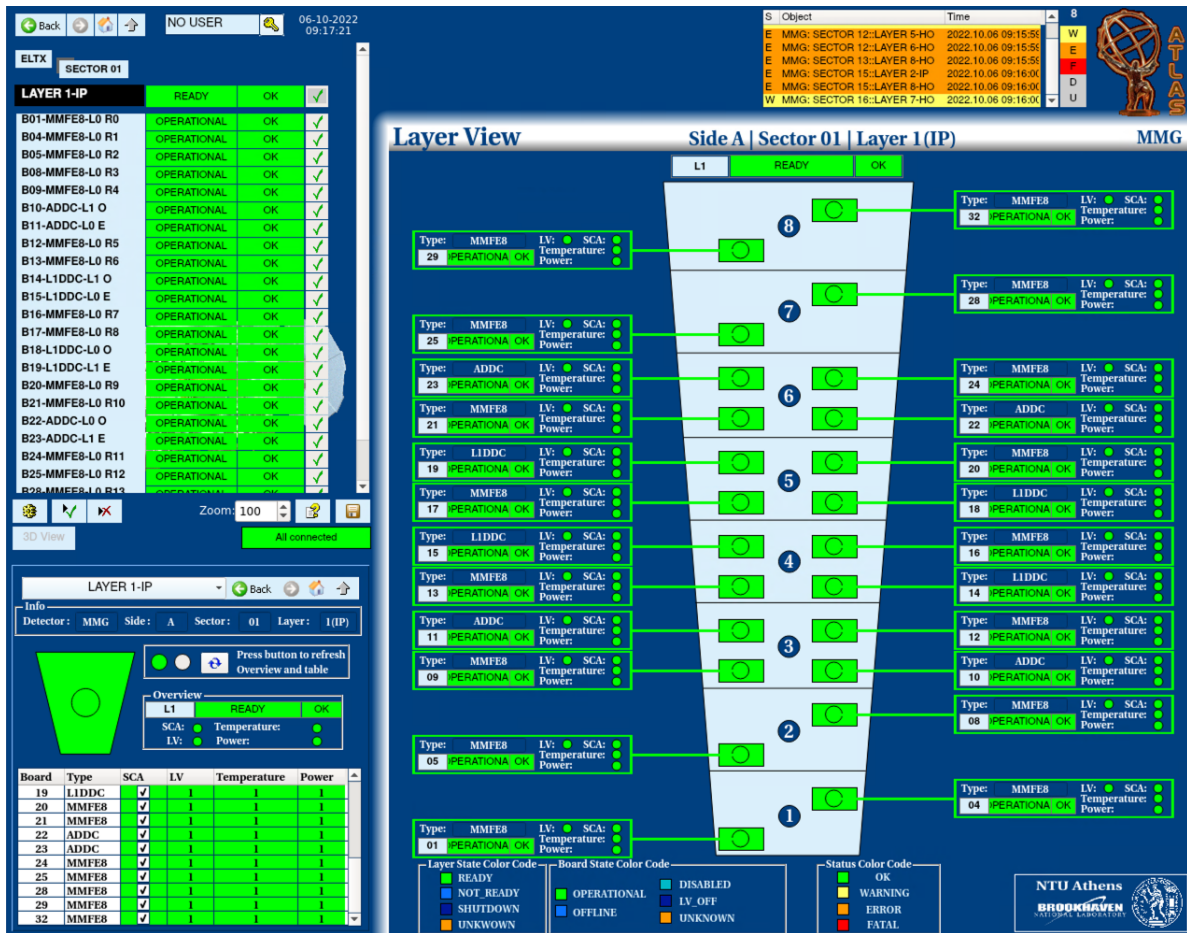


Figure 4.89: The operation panel for the FSM Layer View.

- **SCA Supervisor:** Indicates the number of offline SCAs per sector/server.
- **Connectivity Map:** Illustrates the L1DDC to MMFE8/ADDC actual connections.
- **Layer/Board State & Status Color Code:** Exhibits the FSM states and status color scheme.

At the pinnacle of the FSM hierarchy, the Side View panel encapsulates the holistic status and state of the entire ELTX system. This panel encompasses the following key features:

- **Wheel View:** Provides a comprehensive overview of the FSM state and status of all sectors within the side.
- **Sector View:** Offers detailed information on each sector, including the sector's state and status, SCA OPC UA Server status, the number of offline SCAs, LV status, and temperature & power states.
- **Layer View:** Displays the FSM state and status of all layers per sector.
- **Layer/Sector State & Status Color Code:** Exhibits the FSM States and Status color scheme.



Figure 4.90: The operation panel for the FSM Sector View.

#### 4.4.7 VME

For the monitoring of the three Wiener VME crates in the NSW project, a dedicated project was created. All necessary deployment steps were executed within the ATLMUONSWINF2 project on the pcatlmuo03 computer host.

The initial step of the project involves establishing hardware connectivity with the WinCC-OA project through the Wiener OPC UA Server developed by the BE-ICS department. The Wiener OPC UA Server runs on the pcatlmuo03 hostname and requires an XML input specifying the connected devices. The server's auto-discovery functionality is utilized to generate the XML file automatically, containing all essential hardware information.

With the Wiener OPC UA server operational, the next step is to subscribe WinCC-OA to it and establish connections for various datapoints. The JCOP component fwWiener is employed via the JCOP installation tool. Using the Device manager, three Wiener VME Crates are created:

1. PS-MUO-NSW-VME-01
2. PS-MUO-NSW-VME-02
3. PS-MUO-NSW-VME-03

The component generates all necessary datapoints and establishes connections with the OPC-UA objects. Key DPTs for the project include:

- **FwWienerCrate:** Encompasses general information and online parameters of the Wiener Crate.





Figure 4.91: The operation panel for the FSM Side View.

- **FwWienerChannel:** Contains online parameters for each channel of the Wiener Crate.

The subsequent step involves configuring various voltage, temperature, and fan speed limits for alert handling. The final setup processes include description configuration and archiving setup to archive all necessary datapoints. These steps are executed using the dedicated service panel called "muoNswWiener\_general.xml," illustrated in Figure 4.92.

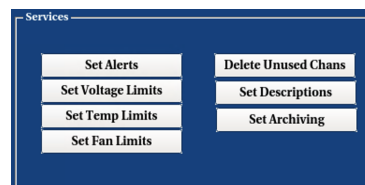


Figure 4.92: The service panel of the Wiener project in order to configure the alert limits and the description &amp; archive configuration.

The FSM hierarchy for the Wiener VME project is organized with the VME Crates CU as the top-level node. Below the control unit, there are three VME Crates, each functioning as DU, as depicted in Figure 4.93.

The FSM status for the Wiener VME DU is determined by individual temperature, power, and fan speed alert limits. The VME Wiener DU encompasses the following FSM states:

- **OFF:** Indicates the VME Crate power is turned off.



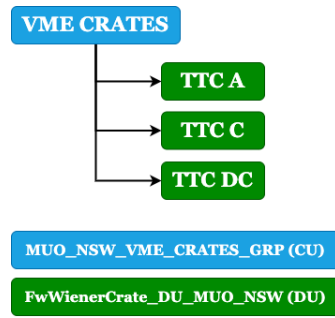


Figure 4.93: The Wiener VME FSM Hierarchy.

- **LOCKED:** Signifies that the user interlock is enabled.
- **UNKNOWN:** Occurs when there is no communication with the crate, the Wiener OPC UA server is not running, or the power status is invalid.
- **ON:** Represents the normal operating state when everything is functioning correctly.

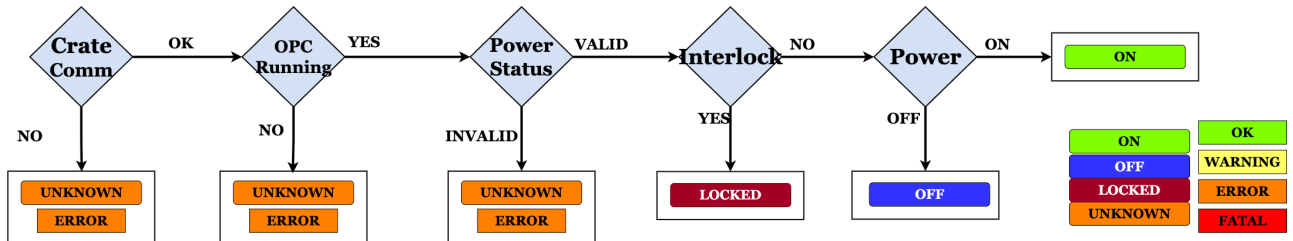


Figure 4.94: The Wiener VME DU initialisation and the calculation of the various states.

The last step in the Wiener VME project is the operation panel, designed for the monitoring of the three VME Crates, as depicted in Figure 4.95. This panel provides comprehensive monitoring of various VME crate parameters, along with the individual status flags for each channel. Additionally, users can view the hostname of the VME crate, its scope of use, and the rack in which it is located in the USA15 cavern of the ATLAS experiment.

#### 4.4.8 DSS

##### Introduction

The smooth operation of the experiment is under the supervision of the DCS, a distributed system comprising approximately 200 PCs. Detecting severe safety hazards, such as fire, smoke, or flammable gas, which could potentially endanger human lives, is the responsibility of the CERN Safety Alarm Monitoring (CSAM). Bridging the gap between these two systems, specifically focusing on the protection of equipment during abnormal and potentially dangerous operating conditions, is the Detector Safety System (DSS) [70], the subject of this paper.

The definition of the DSS was collaboratively established by the four LHC experiments within the JCOP, with implementation carried out by the CERN controls group IT/CO. The overarching strategy of the DSS is to place (parts of) the ATLAS experiment into a safe state when faced with abnormal and potentially dangerous situations. Shutdown procedures initiated by the DSS are designed to be non-harmful to the detector, requiring no further actions by an operator. However, human intervention is always necessary to analyze and rectify faults, ensuring equipment safety and restoring normal operation. The DSS does not automatically re-enable equipment; this decision is left to human

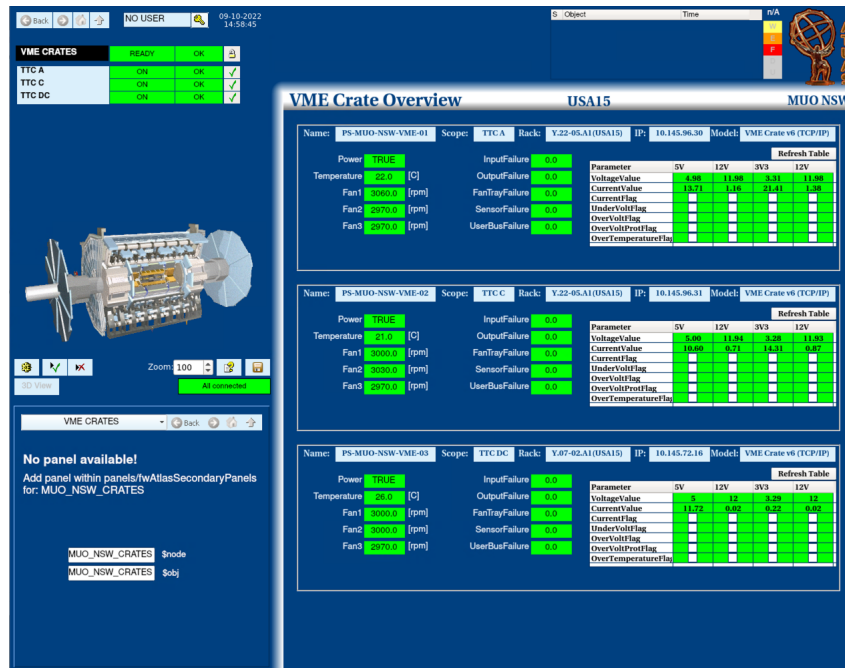


Figure 4.95: The operation panel for the monitoring of the 3 NSW Wiener VME crates.

operators. Importantly, the definition of DSS actions remains independent of the experiment's operational status, encompassing scenarios such as data taking, maintenance, etc., as equipment safety is paramount and not contingent on operational modes.

The DSS is logically composed of three main parts:

- **Sensors:** Responsible for detecting abnormal and potentially dangerous situations.
- **Alarms:** Generated by programmable logic using the sensor signals.
- **Actions:** Implemented to place equipment in a safe state in response to alarms.

The implementation of the Detector Safety System (DSS) is structured into two main components:

- **Front-End (FE):** This component is responsible for connecting to the sensors, establishing alarms, and triggering actuators in response to detected anomalies.
- **Back-End (BE):** The Back-End includes operator interfaces, facilitating the configuration of the FE. It also provides views of the DSS status and allows for the resetting of alarms and actions.

The BE communicates DSS alarms and actions information over Ethernet using the CERN proprietary Data Interchange Protocol (DIP) to the DCS. The DCS, in turn, distributes this information to all subdetector systems, enabling them to execute shutdown procedures. Additionally, the relevant DSS information is injected into the overall ATLAS status and alarm display managed by the DCS. This integration ensures that the DSS is seamlessly incorporated into the broader monitoring and control infrastructure. Importantly, the DSS operates independently, and no software information flows into the DSS from other systems, ensuring a high degree of autonomy.

### NSW DCS-DSS Case

For the specific requirements of the Detector Safety System (DSS) Alarms and Actions monitoring within the NSW project, dedicated expert tools were deployed within the Slow Control Systems (SCS)

projects for both the MMG and STG sub-detectors, namely ATLMMGSCS and ATLSTGSCS. To facilitate the configuration of the various components required for the DSS tool, expert panels were created for each sub-detector, illustrated in Figure 4.96.

The expert panel encompasses the following functionalities:

- **Creation of DSS Actions and Alarms Datapoints (DPs) in the Local Project:** This function is responsible for generating the necessary DSS Actions and Alarm DPs within the local project.
- **Setup of DSS Actions and Alarm DPs Description Handling:** The panel allows users to configure the description handling for DSS Actions and Alarm DPs, ensuring proper documentation.
- **Setup of DSS Actions and Alarm DPs Alert Handling:** Users can define and configure alert handling for DSS Actions and Alarm DPs, enabling appropriate responses to potential issues.
- **Creation of Internal Datapoint Functions:** The tool provides the functionality to create internal datapoint functions, which are utilized to monitor multiple datapoints simultaneously.

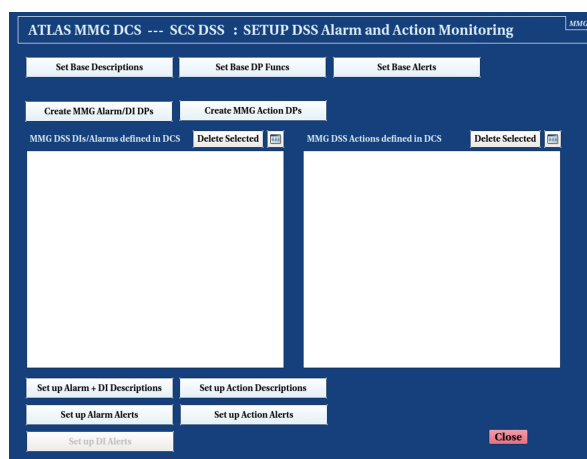


Figure 4.96: The expert panel which is used for the setup of the various DSS parts.

The update of the local DSS actions and alarms is handled by the control manager which runs the script "mmgDssWatchdog.ctl" which is responsible to copy the required information from the Central DCS project ATLGCSIS1. The shifter via the expert panels, as shown in Figure 4.97, can monitor the detector associated DSS Alarms and Actions.

In Figure 4.98, we can see a use case example of an event which took place during October 2022. During the event, a cooling leak event triggered the DSS alarms as shown on the Figure 4.98 and as a sequence the DSS Actions were triggered by shutting down the HV and LV of the detector in order to protect the system. Thus, the DSS for NSW worked as expected and no hardware problems occurred.

In addition the NSW DCS DSS project allows the expert to associate the various with DCS actions. The API is already implemented and ready to use by the NSW DCS developers in order to deploy solutions where DSS actions are not applicable.

#### 4.4.9 Other Projects

##### High and Low Voltage

High and Low voltages for MMG and STGC are supplied by the widely used CAEN system, developed for the LHC experiments. Communication with the control machines is achieved through

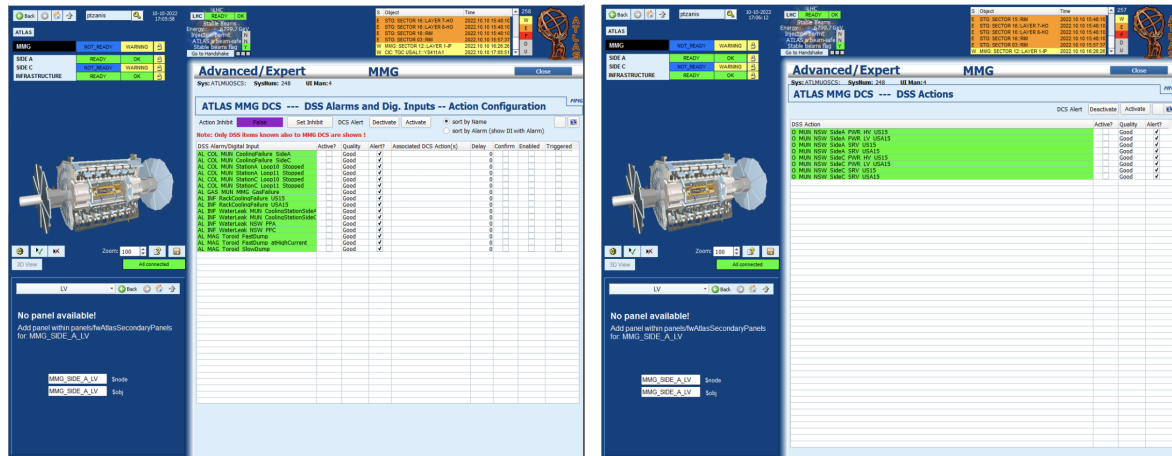


Figure 4.97: The expert panels where shifter can monitor the detector associated DSS Alarms and Actions.

OPC UA server-client connection. On Side A and C, NSW OPC UA servers are deployed on the host servers, while the OPC UA clients, running on the same machines, gather the address space of the individual channel parameters and transmit them to the projects.

The system architecture consists of mainframes housing the branch controllers, connected with the LV and HV crates. Both MMG and sTGC will use the same basic layout for the Low Voltage. The LV for the electronics boards, both on-chamber and on the rim, is regulated and distributed by means of DC/DC distributors, called Intermediate Conversion Stage (ICS) are placed on the rim. A total of 136 such devices are to be deployed.

The control and monitoring communication path is based on the CAEN EASY6000 system. Eleven CAEN mainframes of type SY4527 will control all LV and HV for NSW. Each HV branch controller is connected to a set of Embedded Assembly System (EASY) crates, which are connected as a daisy-chain. HV Crates and boards are supplied with external DC power of 48V generated by separate AC-DC converters, while the LV ICS crates are powered from primary generators with adjustable voltage output. The mainframes, generators, and branch controllers are located in ATLAS Underground Service areas, while EASY crates and boards are in the ATLAS cavern.

### MDM T-Sensors and BField

The environmental parameters monitoring comprises 64 MDT Device Modules (MDM) that will be attached to the wheels and will serve to monitor the detector surface temperatures. They will also be used for measuring the magnetic field when attached to sTGC chambers. The system will be included in the current muon temperature and magnetic field monitoring.

MDMs are Radiation and Magnetic tolerant, based on Embedded Local Monitor Board technology. Every NSW Sector will have 36 T-Sensors on the chamber and 16 for cooling channel monitoring. The CanOpen OPC UA Server is the interface between hardware and projects, handling the monitoring of wedges and cooling temperature sensors alarms. Each of the large sTGC sectors has four Bfield sensors that are connected through MDM and read out via the Controller Area Network (CAN) protocol.

### ATCA

CERN has utilized Versa Module Eurocards (VME) since the 1980s. However, with the technology aging, there are concerns about its suitability for future upgrades. If the current readout architecture is maintained, VMEs might not suffice for all future upgrades, especially for the anticipated needs

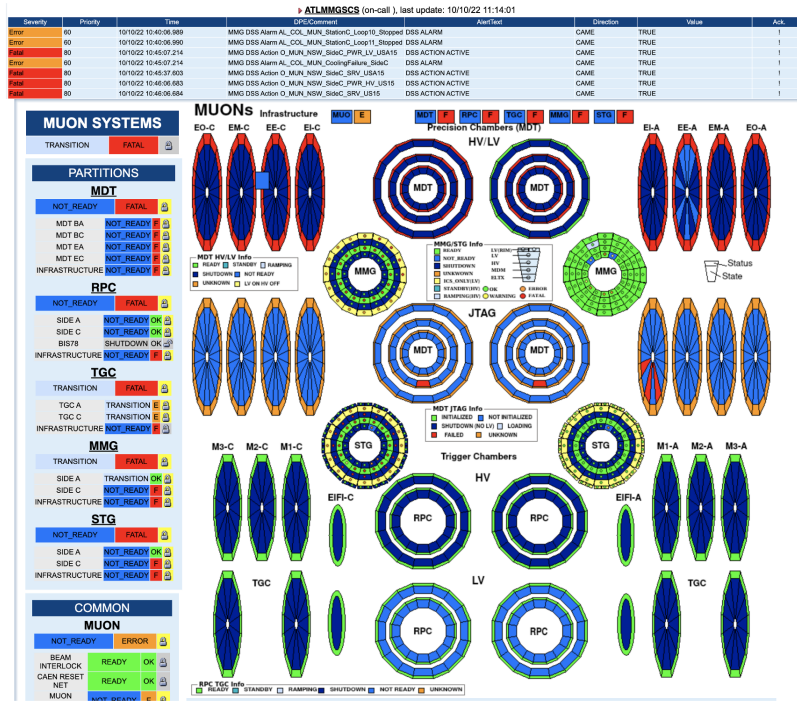


Figure 4.98: The expert panels where shifter can monitor the detector associated DSS Alarms and Actions.

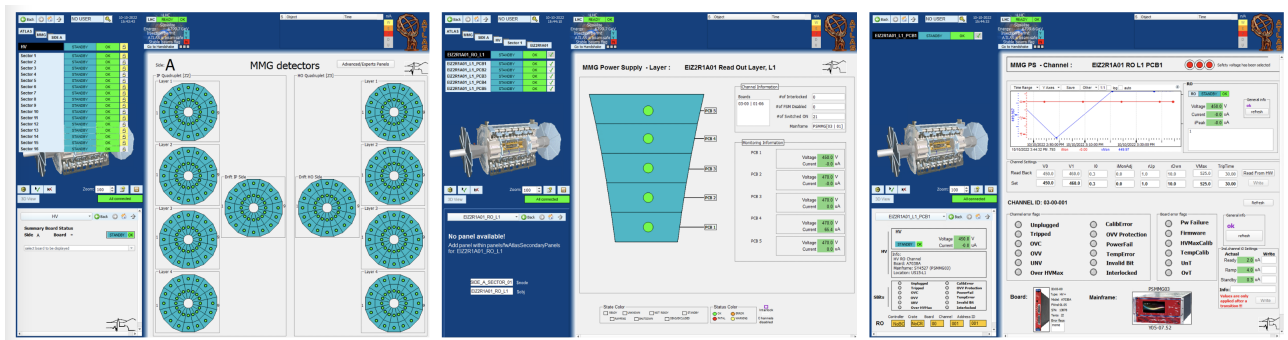


Figure 4.99: The DCS FSM and panels for the NSW High Voltage monitoring.

of Phase-2 operations beyond 2022. Consequently, a shift in the current readout architecture is likely, and one promising candidate is the Advanced Telecommunications Computing Architecture (ATCA).

ATCA systems offer high reliability, redundancy at all levels, exceptional data throughput, and a remote monitoring and control system. Various groups have already initiated development efforts for long-term upgrades in ATLAS using ATCA technology. ATCA Shelves, containing a Pigeon Point Shelf (PPS) Manager, have been a focal point in these developments.

The common shelf manager mezzanine card, such as PPS Manager, provides management components for management-aware open modular platforms like ATCA systems. These components include protocols like Remote Management Control Protocol (RMCP), Simple Network Management Protocols (SNMP), Intelligent Platform Management Interface (IPMI), and Hardware Platform Interface (HPI). In this work, the SNMP protocol has been chosen.

Several reasons support the choice of SNMP: its protocol simplicity, the built-in SNMP manager in WinCC-OA, the secure V3 option allowing authentication if needed, the defined MIB files in PPS Managers providing a standard for firmware developers, and the easy configuration of PPS Manager



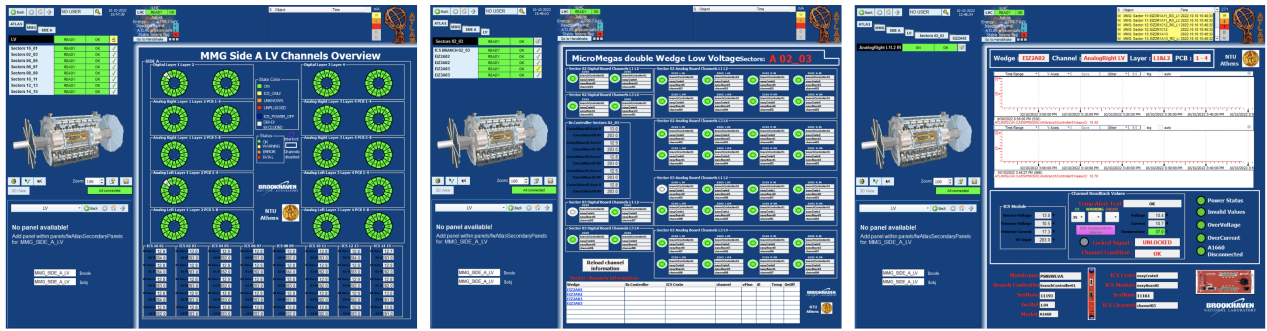


Figure 4.100: The DCS FSM and panels for the NSW Low Voltage monitoring.

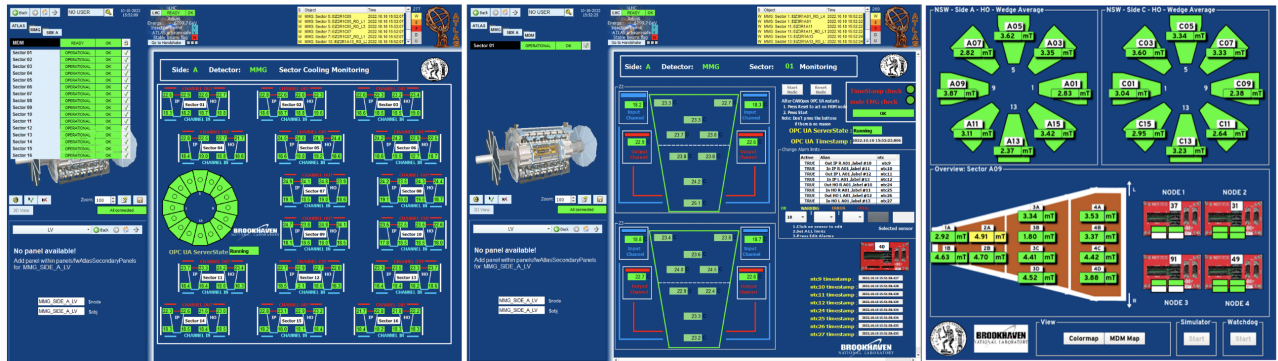


Figure 4.101: The DCS FSM and panels for the NSW MDM T-Sensor temperature and BField monitoring.

for monitoring and control purposes.

The NSW utilizes two ATCA devices for hosting the Trigger Processor[34], each dedicated to Side A/C, with blades specific to particular sectors. The NSW Trigger Processor platform adheres to the Advanced Telecommunications Computing Architecture (ATCA) standard. A Trigger Processor ”blade” comprises a carrier card, two mezzanine cards, and a Rear Transition Module (RTM). The sTGC and Micromegas share the same hardware for their trigger logic but employ different firmware. A single mezzanine card with two FPGAs, one for Micromegas and one for sTGC, handles one sector. The two FPGAs can communicate with each other via 68 fast (640 Mb/s) low-latency LVDS signals. The ATCA blade supports two such mezzanines. The backplane signal connections are currently unused.

The Carrier conforms to the ATCA standard and hosts two Xilinx Ultrascale FPGAs, one for each sector, responsible for the FELIX interface. The Xilinx Zynq System-on-Chip FPGA, running 32-bit Linux, provides board management functions, including configuring the Carrier and mezzanine FPGAs, via the Xilinx Virtual Cable (XVC) over the Ethernet network, and configuring jitter cleaners. Other board management functions are handled by the CERN IPMC card. The on-board Ethernet switch connects the Carrier’s Sector FPGAs, the Zynq processor, the Zynq FPGA fabric, and the IPMC card to the external network.

In addition to the two mentioned FPGAs, the mezzanine connects to 72 fibers via three 12-channel 10G microPOD optical receivers, three 12-channel 10G microPOD optical transmitters, and jitter cleaners for required design clocks and FPGA transceiver reference clocks. A Module Management Controller (MMC) on each mezzanine communicates with the IPMC board management card on the Carrier.

The Rear Transition Module (RTM) provides several SFP cages for serial transceivers, connecting to the on-board switch for an Ethernet transceiver, the Zynq, and the Sector FPGAs for fiber



transceivers for FELIX. RJ-45 connectors provide four LVDS lines to each of the Sector FPGAs. An LVDS trigger output signal for self-triggering of the NSW is available from one of the RJ-45 connectors. There is also an MMC on the RTM.

For communication, the ATCA OPC UA Server[71], developed by Central DCS, facilitates communication between the ATCA and the network. Subsequently, the fwAtca, also developed by Central DCS, is employed to create corresponding datapoints and establish communication between the ATCA and the individual blades. The ATCA components have been deployed under the ATL-MUONSWINF2 project on the pcatlmuo03 computer. The fwAtca JCOP component and the ATCA DCS FSM panels for the NSW are illustrated in Figure 4.102.

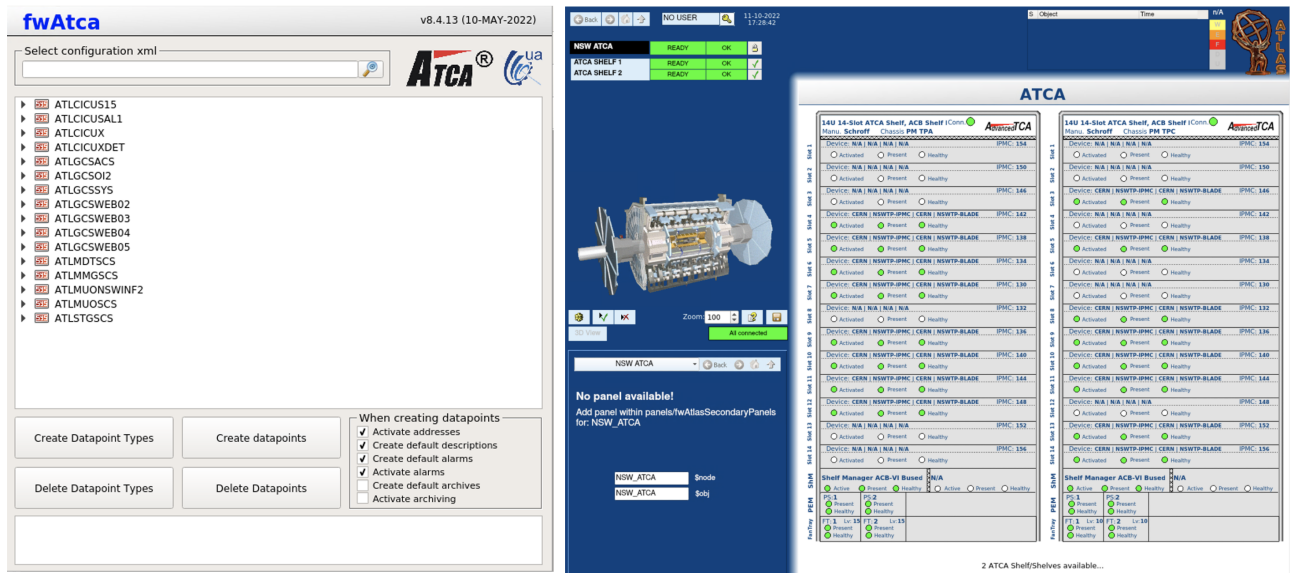


Figure 4.102: The fwAtca JCOP component and the ATCA DCS FSM panels for the NSW.

#### 4.4.10 Supervisor Control Station

As mentioned previously, all the NSW projects are encapsulated under the dedicated Supervisor Control Station (SCS). Taking the example of the MMG, the ATLMMGSCS project runs at ATLMMGSCS, and its purpose is to monitor and control all MMG-related projects.

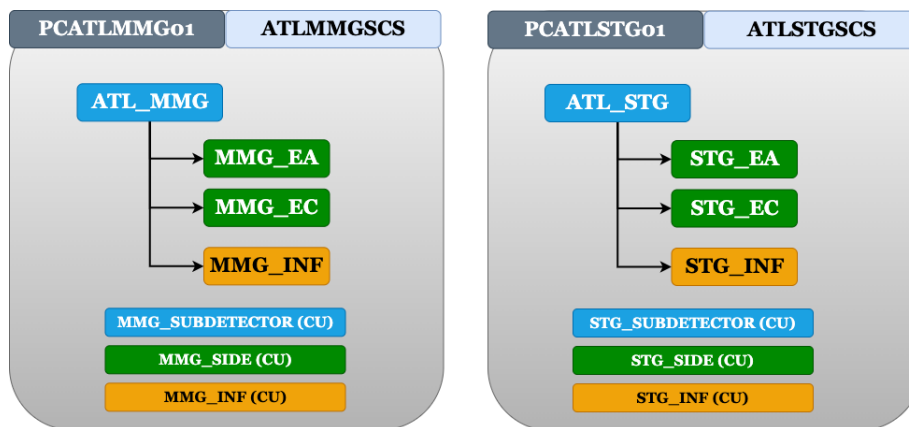


Figure 4.103: The FSM node structure of the MMG&STG following the Muon DCS schema.

For the creation of the SCS FSM, a dedicated expert panel named `mmgScs_fsm.xml` has been developed, as illustrated in Figure 4.104. This expert panel ensures that all distributed connections

are available, and if not, the user cannot perform any actions. The expert or developers have the capability to:

- Stop, Remove, Generate, and Start the SCS FSM.
- Create the Main, Side, and INF FSMs.

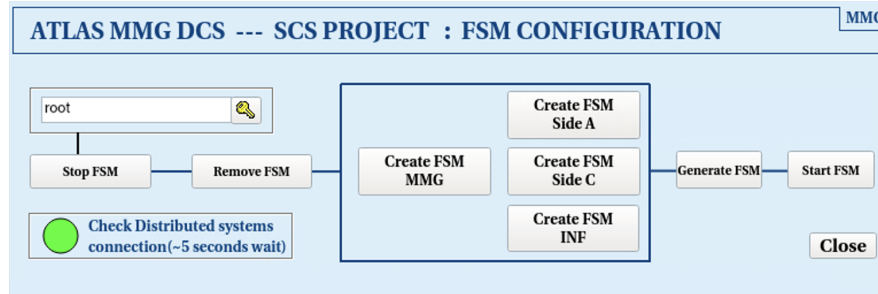


Figure 4.104: The expert panel for the generation and creation of the SCS FSM.

The SCS FSM is structured with the following FSM nodes:

- **Subdetector - CU:** This is the unique FSM node per detector.
- **Side - CU:** This node includes the HV, LV, ELTX, and MDM FSM nodes under it.
- **INF - CU:** This node encompasses all the infrastructure hardware used by the detector.

The Subdetector CU contains the following FSM states:

- **TRANSITION:** When any CUs are in TRANSITION
- **STANDBY:** When any CUs are in STANDBY
- **NOT\_READY:** When any CUs are in NOT\_READY
- **SHUTDOWN:** When all Side CUs are in SHUTDOWN
- **UNKNOWN:** When any CUs are in UNKNOWN or DEAD
- **READY:** When all Side CUs are in READY

The Subdetector CU contains the following FSM actions:

- **REFRESH:** Refreshes the FSM State & Status
- **POWER\_LV\_OFF:** Switching OFF the LV power
- **POWER\_LV\_ON:** Switching ON the LV power
- **POWER\_HV\_OFF:** Switching OFF the HV power
- **POWER\_HV\_ON:** Switching ON the HV power
- **GO\_TO\_SHUTDOWN:** Switching OFF both HV & LV

The Side CU contains the following FSM states:

- **TRANSITION:** When any HV CUs are in HV ramping mode(TRANSITION)

- **STANDBY:** When all HV CUs are in STANDBY
- **NOT\_READY:** When any CUs are in NOT\_READY
- **SHUTDOWN:** When all HV, LV, and LV Side CUs are in SHUTDOWN
- **UNKNOWN:** When any CUs are in UNKNOWN or DEAD
- **READY:** When all CUs are in READY.

The Side CU contains the following FSM actions:

- **REFRESH:** Refreshes the FSM State & Status
- **POWER\_LV\_OFF:** Switching OFF the LV power
- **POWER\_LV\_ON:** Switching ON the LV power
- **POWER\_HV\_OFF:** Switching OFF the HV power
- **POWER\_HV\_ON:** Switching ON the HV power
- **GO\_TO\_SHUTDOWN:** Switching OFF both HV & LV

The INF CU contains the following FSM states:

- **TRANSITION:** When any CU/LUs are in TRANSITION
- **STANDBY:** When any CU/LUs are in STANDBY
- **NOT\_READY:** When any CU/LUs are in NOT\_READY
- **SHUTDOWN:** When all CU/LUs are in SHUTDOWN
- **UNKNOWN:** When any CU/LUs are in UNKNOWN or DEAD
- **READY:** When all CU/LUs are in READY

The INF CU contains the following FSM actions:

- **REFRESH:** Refreshes the FSM State & Status.

In addition, overview panels for both MMG and STG detectors have been created, as illustrated in Figure 4.105. These panels empower the shifter to efficiently monitor the services and infrastructure of the NSW. The sector structure provides a comprehensive overview, allowing real-time monitoring of the HV (High Voltage), LV (Low Voltage), ELTX, and MDM (Environmental Parameters Monitoring) FSM State & Status for each sector. An essential parameter under surveillance is the OPC UA Server, enabling the monitoring of all available OPC UA Servers. Notably, the SCA OPC UA Server per sector is of particular interest, providing valuable insights into the number of offline SCAs in each sector.

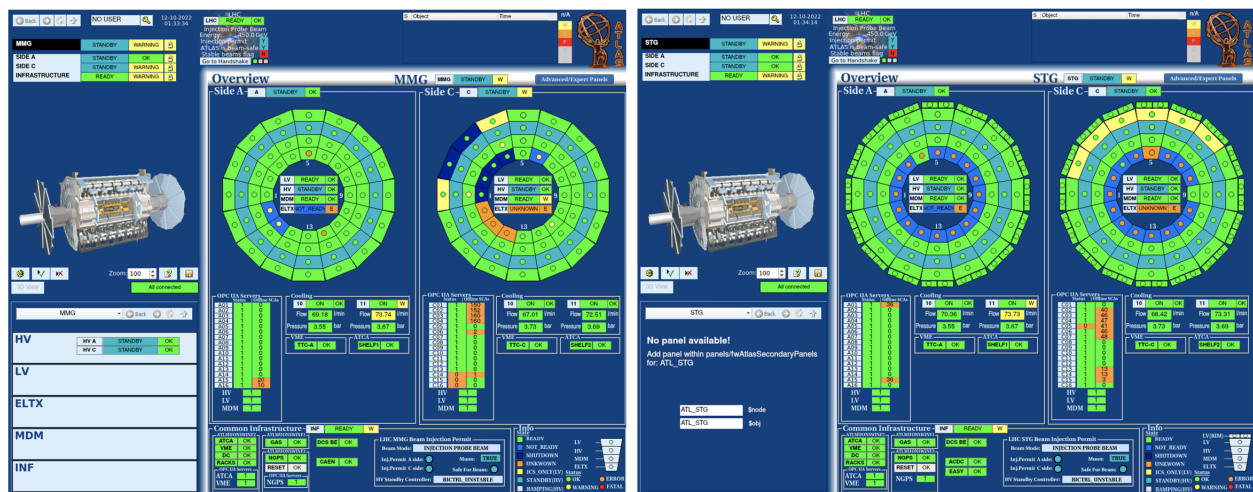


Figure 4.105: The overview panel of the detector SCS which shifter can monitor NSW services and infrastructure in a glance.

## 4.5 Contributions

For the monitoring and parameterization of all parameters of the New Small Wheel upgrade of the ATLAS detector, it is necessary to develop an automatic control system. The doctoral candidate:

- Studied and developed a prototype data acquisition and automatic control system for the gas tightness detection of Micromegas detectors.
- Studied and developed a prototype data acquisition and automatic control system for the high voltage of Micromegas detectors.
- Developed a system for monitoring environmental conditions for use in laboratories and test beam facilities.
- Implemented the automatic control system for the parameters of the NSW electronic boards, which was used during the integration and commissioning of the detectors, electronics, and services of the New Small Wheel upgrade.
- Developed a central control system for the Micromegas detector, which was exposed to cosmic rays in the BB5 building to verify its proper functioning before installation in ATLAS.
- Served as the coordinator of the team responsible for developing the central detector control system of NSW and its integration into the central detector control system of the ATLAS experiment.
- Acted as a key member of the central coordination team of the New Small Wheel upgrade.
- Studied and designed the structure and architecture of the central control system of NSW.
- Implemented the monitoring and control system for all the electronic boards of NSW.
- Developed numerous control systems for different devices and systems of NSW.

In addition, the doctoral candidate contributed to the following published papers:

- **“Methods used for Gas Tightness Test and percent Oxygen Monitoring of the NSW Micromegas Detectors of LHC-ATLAS Experiment”**  
DOI: [10.1088/1742-6596/2105/1/012022](https://doi.org/10.1088/1742-6596/2105/1/012022)

- **“The Detector Control System of the New Small Wheel for the ATLAS experiment”**  
DOI: [10.1088/1742-6596/2105/1/012025](https://doi.org/10.1088/1742-6596/2105/1/012025)
- **“The Control System of the New Small Wheel Electronics for the ATLAS experiment”**  
DOI: [10.18429/JACoW-ICALEPCS2021-FRAL04](https://doi.org/10.18429/JACoW-ICALEPCS2021-FRAL04)
- **“The Control System of the New Small Wheel Electronics for the ATLAS experiment”**  
DOI: [10.22323/1.422.0290](https://doi.org/10.22323/1.422.0290)





# Chapter 5

---

## Micromegas Detector Performance Evaluation

---

This chapter presents a comprehensive analysis of the SM2 Micromegas production module performance during the H8 testbeam at CERN, one of the first Micromegas production modules for the ATLAS NSW project. It encompasses a calibration process for over 2000 VMM channels, addresses HV instabilities through gas mixture optimizations, and explores efficiency metrics in external and self-tracking modes, alongside gas mixture variations. The chapter extends to HV performance assessments during the GIF++ testbeam at CERN's Gamma Irradiation Facility (GIF++), offering insights into Micromegas chambers and readout electronics under HL-LHC-simulated conditions. The experimental setup at GIF++ is detailed, encompassing external triggers, gamma-ray sources, muon beams, detector modules (LM2 and SM1), and BeamLine MicroMegas detectors (BL). Data acquisition and control systems are discussed, emphasizing Level 1 (L1) acceptance data. The chapter also delves into time resolution studies, crucial for accurate particle track reconstructions, particularly under inclined tracks.

## 5.1 Interaction of charged particles with matter

The way detectors in the field of High Energy Experimental Physics work is based on the way radiation and different particles interact with the detector material. The particle interaction depends primarily on the characteristics of the scattered particle and secondarily on the active material of the detector. Consequently, it is necessary to understand the mechanisms by which radiation interacts and loses its energy in matter. The interaction of charged particles with matter is governed by electromagnetic reactions. As a charged particle enters an absorbing medium, it interacts with Coulomb forces simultaneously with as many electrons as are in the particle's path. Depending on the energy of the particle and the particle-electron distance, the particle may be propelled to a higher energy layer (excitation) or completely released by the atom (ionization). During each interaction, the particle loses a small fraction of its initial energy, and after multiple scatterings the particle eventually stops. The number of ionization collisions is random, and the average free path between two ionizations  $\lambda$ , is given by

$$\lambda = \frac{1}{N\sigma_I} \quad (5.1)$$

where  $\sigma_I$  is the active cross section of the ionization for each electron and  $N$  is the electron density. The number of primary ion pairs per unit length will be equal to  $1/\lambda$  and depends on the type of charged particles, the velocity as well as the gas mixture. The probability for  $\kappa$  number of ionization interactions for a distance  $L$  follows the distribution Poisson, is given by

$$P(L/\lambda, \kappa) = \frac{(L/\lambda)^\kappa}{\kappa!} e^{-L/\lambda} \quad (5.2)$$

The linear stopping power for charged particles in an absorber is defined as the infinite energy loss to the infinite space traveled through the material according to

$$S = -\frac{dE}{dx} \quad (5.3)$$

The energy loss of the charged particle of mass  $M$ , measured in  $\text{MeV}/(\text{g}/\text{cm}^2)$  in a medium is described by the classical equation Bethe-Bloche

$$-\left\langle \frac{dE}{dx} \right\rangle = Kz^2 \frac{Z}{A} \frac{1}{\beta^2} \left[ \frac{1}{2} \ln \frac{2m_e c^2 \beta^2 \gamma^2 T_{max}}{I^2} - \beta^2 - \frac{\delta(\beta\gamma)}{2} \right] \quad (5.4)$$

where  $\beta = v/c$  the relativistic velocity of the particle,  $I$  the average excitation energy,  $K = 4\pi N_A r_e^2 m_e c^2$ ,  $\gamma = E/Mc^2$ ,  $z$  the charge of the incident particle,  $Z$  and  $A$  the atomic number and mass of the absorber, respectively,  $m_e$  is the mass of the electron,  $r_e$  is the radius of the electron,  $N_A$  is the Avogadro number,  $\delta(\beta\gamma)$  is the density effect term, and  $T_{max}$ , as shown in Eq. (5.5), is the maximum kinetic energy that can be imparted to a free electron in a collision

$$T_{max} = \frac{2m_e c^2 \beta^2 \gamma^2}{1 + 2\gamma m_e/M + (m_e/M)^2} \quad (5.5)$$

From the above Eq. (5.4), it is easy to see that the energy loss decreases drastically with the fraction  $1/\beta^2$  for small values of  $\beta\gamma$  leading to an overall minimum value. This dependence can be explained if we consider that the particle stays longer in the range of an electron if it has a low velocity and thus the energy transfer to the electron is significant. Most relativistic particles have through energy loss in this range and are commonly referred to as minimum ionization potential particles (MIPs). The ionization losses of MIPs, for all materials, range between 1 and 2  $\text{MeV}/(\text{g}/\text{cm}^2)$  slightly increasing with atomic number  $Z$ . However, when the value of the product  $\beta\gamma$  exceeds a range then the energy

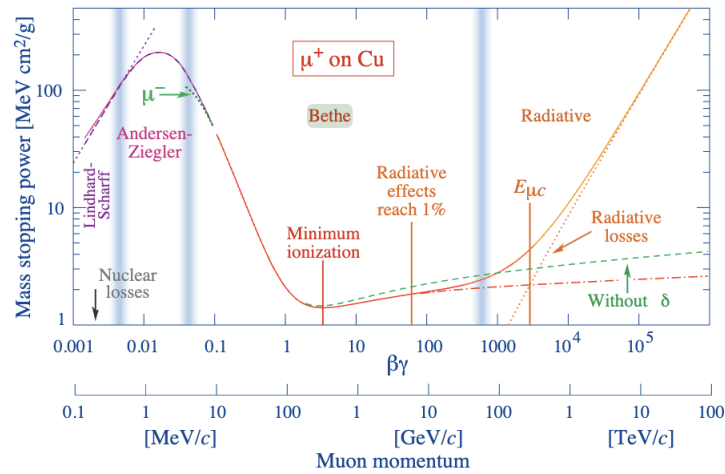


Figure 5.1: Equation Bethe-Bloch to describe the energy loss as a function of momentum of charged particles in active material. [72]

loss undergoes a relativistic increase with the slope depending on the average excitation energy  $I$ , as shown in Fig. 5.1.

Moreover, it is observed that the Bethe-Bloch equation diverges for low energies of charged particles where the charge exchange process between the particle and the absorber becomes significant. The positively charged particles will start to take electrons from the absorber, thus reducing the charge and consequently the retarding force.

The case of electrons is different, as they are compared to charged particles as unlike ionization, electrons interact mainly through radiation Bremsstrahlung. The average rate of energy loss of electrons is lower compared to charged particles as they change orbits within the detector medium due to the fact that the mass of the incident particle is equal to that of the orbital electrons it interacts with. In addition, there is the possibility that the electron will interact with the nuclei of the material it is traversing.

Photons, or otherwise gamma radiation, interact with matter but only through three interaction processes:

### Photoelectric Effect

In this phenomenon a photon, interacting with an atom, is absorbed and a photoelectron is ejected from the inner layer with kinetic energy:

$$E_{e^-} = h\nu - E_b \quad (5.6)$$

where  $E_b$  is the binding energy of the photoelectron in the crust,  $h$  is Planck constant and  $\nu$  is the frequency of the light in Hz. The ion is filled by the absorption of a free electron or by the repositioning of atomic electrons and the emission of an x-ray photon where it is most likely to be reabsorbed very close to its creation region.

### Scattering

In Compton scattering, inelastic scattering of a photon by an electron within the absorber material results in energy transfer to the electron and is related to the scattering angle of the electron. Because the scattering angle is possible for any value, the energy of the scattered electron exhibits a wide range of values. The transferred energy with the scattering angle for each interaction Coulomb can

be calculated from the conservation and energy laws and has the following form:

$$\lambda' - \lambda = \frac{h}{m_e c} (1 - \cos \theta) \quad (5.7)$$

where  $\lambda$  is the initial wavelength,  $\lambda'$  is the wavelength after scattering,  $h$  is the Planck constant,  $m_e$  is the electron rest mass,  $c$  is the speed of light and  $\theta$  is the scattering angle. It is clearly seen that for small scatterings, a small fraction of the photon energy is transferred to the electron.

### Pair Production

In the case where the incident photon energy is greater than twice the rest mass of the electron (1.02 MeV), the pair production process takes place where the photon is annihilated and replaced by an electron-positron pair. All the remaining energy is shared as kinetic energy of the two produced particles. The following Figure 5.3 shows the graph of the active cross-section of the different

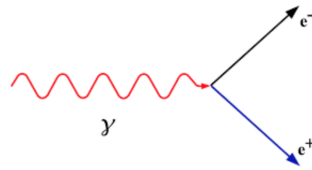


Figure 5.2: Pair Production.

gamma-ray interaction phenomena with matter. The photoelectric effect is the dominant form of

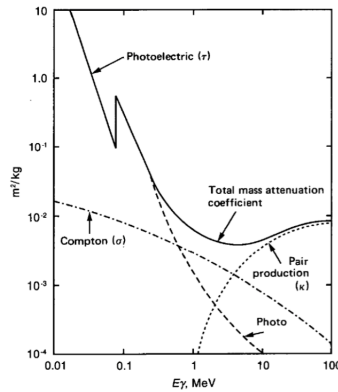


Figure 5.3: Effective cross-section of electromagnetic photon-matter interaction phenomena. [73]

interaction with gamma-ray radiation for low energy values of 1 MeV.

## 5.2 Excitation and ionization in gases

The detection of charged particles is achieved in many areas of high-energy experimental physics by the use of particle detectors and the occurrence of the phenomena of excitation and ionization as the charged particle travels through the medium of the detector.

### Excitation

In the case of excitation, an atomic electron gains energy and the atom is driven to a higher energy state. Upon the return of the atom to the steady state, a photon is emitted, and eventually there is the possibility of ionization of the gas mixture, usually consisting of a quenching gas with an ionization

energy less than the energy of the first excited state of the noble gas. The excited atoms or molecules of the noble gas can ionize the atoms of the quencher through collisions known as the Penning effect.

### Ionization

In the process of ionization, an electron-ion pair is produced when the energy of the particle crossing the gas exceeds the ionization energy of the absorber atoms. In most gasses used in detectors, the ionisation energy for the minimum electron beam is between 15 – 25 eV. The ionisation of the medium can be either primary or secondary (d-electrons). During ionization, we can estimate the approximate number of pairs,  $n_T$ , produced by knowing the total energy loss of the particle  $\Delta E$  and the average energy loss of the incoming particle per ion pair,  $W_i$ , generated by

$$n_T = \frac{\Delta E}{W_i} \quad (5.8)$$

The number of pairs is the average value of the size  $n_T$  and follows the Poisson distribution.

## 5.3 Transmission of produced ions and electrons in the gas

The principles of operation of the gas detectors to be analyzed in the next chapter are based on the formation of ions and electrons during the interaction of the particle with the gas in the detector until it reaches the readout region. The thermal motion of electrons and ions by drifting and interaction with atoms/molecules under the influence of an electric field will be analyzed below. If a strong electric field is not applied, ion-electron pairs can recombine, participate in charge transfer collisions or lose much of their energy due to the diffusion effect.

### 5.3.1 Ion Movement

Due to their large mass, compared to electrons, ions drift more slowly through a gaseous medium, losing a significant amount of energy as they interact with the atoms/molecules of the gaseous medium.

#### Drift velocity

By applying an electric field to the gaseous volume a portion of the positive ions move along the cathode field. In the case of gas detectors, the average kinetic energy of the ions is comparable to the thermal velocity of the gas atoms. When the ion of mass  $m$ , interacts with the gas molecules of mass  $M$ , the constant  $\lambda$  [74] expresses the energy loss of the ion in the laboratory system and is given by the following relation:

$$\lambda = \frac{2mM}{(m + M)^2} \quad (5.9)$$

The average drift velocity,  $v$ , of ion motion depends linearly on the drift electric field  $E$  and in the case of low electric field,  $E$ , [74] is given by the following relation

$$v = \left( \frac{1}{m + M} \right)^{3/2} \left( \frac{1}{3k_B T} \right)^{1/2} \frac{eE}{N\sigma} = \mu E \text{ (low } E) \quad (5.10)$$

while for the high electric field,  $E$ , is given by

$$v = \left[ \frac{eE}{mN\sigma} \right]^{1/2} \left[ \frac{m}{M} \left( 1 + \frac{m}{M} \right) \right]^{1/2} \text{ (high } E) \quad (5.11)$$

where  $\mu$  is the mobility of the ion in the gas,  $\sigma$  is the active cross section of the scattering of ions by gas molecules,  $k_B$  is the Boltzmann constant,  $T$  is the temperature and  $N$  is the number density. It is characteristic of the drift velocity at low fields that it is proportional to  $E$ , or that the mobility is independent of  $E$ . The value of the gas mobility is characteristic of a particular ion in a gaseous medium in the case of constant ambient conditions can be considered constant. The following table Figure 5.4 depicts the mobility of different ions for different gas mediums of the detector.

Gas	Ion	Mobility ( $\text{cm}^2\text{V}^{-1}\text{s}^{-1}$ )
Ar	$\text{Ar}^+$	1.535
Ar	$\text{CO}_2^+$	1.72
$\text{CO}_2$	$\text{CO}_2^+$	1.09
Xe	$\text{Xe}^+$	0.57
$\text{CH}_4$	$\text{CH}_4^+$	2.26
Ar	$\text{CH}_4^+$	1.87

Figure 5.4: Experimental values of ion mobility for different gas media in gas detectors. [29]

### Diffusion

In the presence of an electric field, a concentrated distribution of ions is thermally diffused symmetrically through multiple scatterings by the medium material. Their distribution in 1-D space follows a Gaussian form

$$\frac{dN}{N}(x, t) = \frac{N_0}{\sqrt{4\pi Dt}} \exp\left(-\frac{x^2}{4Dt}\right) dx \quad (5.12)$$

where  $N$  is the total number of charged particles,  $x$  (or  $y$  or  $z$ ) is the coordinate in the reference frame at the particle creation point and  $D$  is the diffusion coefficient.

The standard deviation of the above equation gives an estimate of the ion diffusion to  $\sigma_x^{ion} = \sqrt{2Dt}$ . In the presence of an electric field,  $E$ , ions move along the field lines with an average diffusion velocity of  $v_d$ . In this case, the diffusion constant  $D$ , through the temperature  $T$  is related to the mobility of the ions  $\mu$  according to the following Einstein relation [74]

$$\frac{D}{\mu} = \frac{k_B T}{e} \quad (5.13)$$

By substituting the diffusion constant from the above relation, the linear standard deviation at distance  $x$  is given by

$$\sigma_x^{ion} = \sqrt{\frac{2k_B T x}{eE}} \quad (5.14)$$

### 5.3.2 Electron Motion

In the case of electrons, the situation is very different, due to their smaller mass compared to ions, electrons transfer only a small fraction of their energy to neighboring atoms and molecules of the gas during their interaction with them.

#### Drift Velocity

In the absence of an electric field, a free electron in a gaseous medium has a thermal kinetic energy equal to  $(3/2)k_B T$ . In the case of the presence of an electric field, the electron starts to collide with



the molecules of the gaseous medium and if the average free path between two collisions is  $\Delta t$  then the drift velocity can be expressed by Townsend

$$d^e = k \frac{eE}{m} \tau \quad (5.15)$$

where  $\tau$  is the average free path between two collisions and  $k$  is a constant, with values between 0.75 and 1, depending on the energy distribution of the electrons. However, the correlation between the drift velocity and the electric field is more complicated since the  $\tau$  constant is not only affected by the electric field but also by the parameters of the gas medium of the detector.

The equation of motion for an electron with mass  $m$  as it moves inside a gas under the influence of a magnetic field  $B$  and electric field  $E$  has been optimized by Langevin [74] by adding a floating term related to the friction force. This relation takes into account the deceleration of the electrons resulting from interactions with the atoms or molecules of the gas and is as follows

$$m \frac{d\mathbf{v}_d^e}{dt} = e (\mathbf{E} + \mathbf{v}_d^e \times \mathbf{B}) - \frac{m}{\tau} \mathbf{v}_d^e \quad (5.16)$$

where  $-\frac{m}{\tau} \mathbf{v}_d^e$  is the friction force and  $\tau$ , the average time duration between two interactions. Assuming that an electron drifts under constant velocity in a uniform electric field, the drift velocity for the case of a zero magnetic field is simplified by the following equation

$$|\mathbf{v}_d^e| = \frac{eE}{m} \tau \quad (5.17)$$

Finally, Figure 5.6 below shows the dependence of the electron drift velocity for different gas mixtures and magnetic field values.

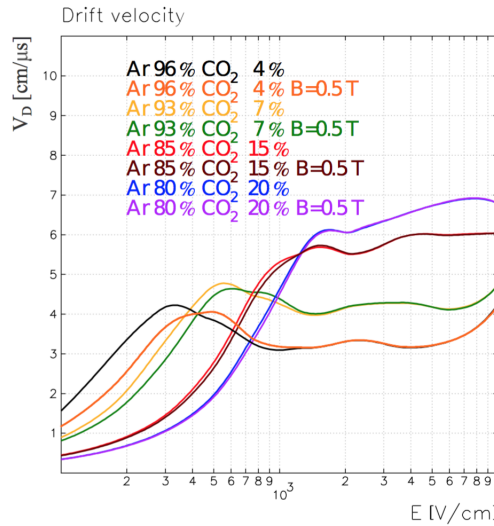


Figure 5.5: The electron drift velocity for different gas mixtures and magnetic field values. [29]

## Diffusion

Ionization electrons quickly reach thermal equilibrium[65] with gas molecules in the absence of an electric field, but because of their smaller mass, electrons diffuse with a higher diffusion constant than ions. In the presence of an electric field, the mobility of electrons differs significantly with the electric field strength as their kinetic energy can increase significantly between collisions with gas atoms/molecules and the standard deviation  $\sigma_x^e$  starts to deviate from the value  $1/\sqrt{E}$  where it has

been observed in ions. The extent of use depends on the gas as well as the electric field, where Eq. (5.18) describes this dependence where for the case of electrons we have replaced the thermal energy term with an empirical factor  $\epsilon_k$ , known as the characteristic energy.

$$\frac{D}{\mu} = \frac{\epsilon_k}{e} \quad (5.18)$$

The linear space of diffusion for the case of electrons in a high electric field will be written in the form of Eq. (5.19) where  $\epsilon_k$  depends on the gas and the electric field  $E$ . In contrast to the classical estimate, it was observed that for several gases the diffusion coefficient is not uniform in all directions of the electric field. In these cases two coefficients of variation must be taken into account, one along the direction of displacement and one along the direction transverse to it.

$$\sigma_x^e = \sqrt{\frac{2\epsilon_k x}{eE}} \quad (5.19)$$

### 5.3.3 Townsend and Signal Generation

Under the influence of a strong electric force, ionization electrons can acquire sufficient kinetic energy to further ionize neutral gas molecules, resulting in the production of secondary ionizations. Secondary electrons are also subject to the same process and higher order ionizations by the multiplication process are produced until it eventually takes the form of an avalanche, known as the Townsend effect. Due to the mass of electrons compared to ions, electrons move faster compared to ions forming a drop shape where electrons occupy the head of the drop with a slow tail of ions as depicted in Figure 5.6.

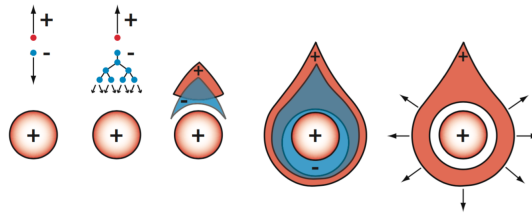


Figure 5.6: The Townsend effect and the formation of a droplet shape during the movement of ions and electrons inside the detector by the application of an electric field.

The number of secondary ion pairs produced per unit length of the drift is equivalent to a multiplicative factor, called the prime factor Townsend  $\alpha = 1/\lambda$ , where  $\lambda$  is the average free path of the ionization electron. In reality, however, the electric field is not uniform, but has the form  $\alpha = \alpha(x)$ . An initial population of electrons  $n_e$  will multiply after a distance path  $dx$  into  $dn_e$  electrons and the multiplied number of electrons for a given path  $x_1 \rightarrow x_2$  is given by Eq. (5.20), where  $n_0$  is the number of electrons at the  $x = 0$  position and  $n$  is the total number of secondary electron-ions produced along the detector volume. The multiplicative factor is then given by the ratio between the final and initial electron population,  $G = n/n_0$ .

$$dn_e = n_e \alpha dx \rightarrow n_e = n_{e,0} \exp \left( \int_{x_1}^{x_2} \alpha(x) dx \right) \quad (5.20)$$

The above expressions describe the average growth of avalanches, but in reality electron-atom interactions are dominated by statistical fluctuations and therefore the size of the avalanche must follow a probability distribution. Depending on the coefficient Townsend and the electric field, the probability of having  $n$  electrons after a path  $x$  for an avalanche starting from one electron is expressed

by the Furry law in Eq. (5.21), where the probability decreases exponentially for increasing  $n$  with a maximum at  $n = 1$ . Moreover, it has been observed experimentally that electrons, under the influence of an electric field, use a significant part of their path to reach the energy that can produce ionizations and thus the exponential, Eq. (5.21), of the equation evolves into a vertical distribution known as Polya

$$P(n, x) = \frac{\exp(-n/\bar{n})}{\bar{n}}, \quad \bar{n} = \exp(-\alpha x) \quad (5.21)$$

The motion of the avalanche products generates electrical signals at the electrodes of the detector. The electrons and positive ions move in opposite directions at different velocity and therefore cause signals with different characteristics. Depending on the configuration of the detector and the electric field, the secondary electrons reach the anode within a few nanoseconds resulting in very fast signal pulses. On the other hand, the positive ions move at a speed hundreds of times slower than the electrons and the resulting signal has a long tail with a duration of several hundred nanoseconds. Theoretically, the motion of an electron/ion causes signals to be applied to all electrode elements with signal characteristics depending on the electric field lines and the relative position of the moving charge with respect to the electrode element. In a simplified scheme with a charge particle moving along the grounded electrodes; the induced current  $I_n(t)$  at each electrode will be given by the Schockley-Ramo theorem [75]

$$I_n(t) = -\frac{q}{V_n} \mathbf{E}[\mathbf{x}(t)] \cdot \mathbf{u}(t) \quad (5.22)$$

where  $\mathbf{E}[\mathbf{x}(t)] = -\nabla\phi[\mathbf{x}(t)]$  is the field,  $\phi[\mathbf{x}(t)]$  is the potential at position  $\mathbf{x}(t)$ ,  $\mathbf{u}(t)$  is the drift velocity of the charge particle, and  $V_n$  is the conductor's potential.

In a first simplified approach, assuming a Micromegas geometry [75], with a single strip under voltage, for a charge particle  $q$ , the auxiliary current is

$$I_a = -q \frac{\mathbf{E}_A \cdot \mathbf{u}}{V_a} \quad (5.23)$$

where  $E_A$  is the electric field at the position of the charge,  $u$  is the drift velocity of the charge and  $V_a$  the potential of the strip. Taking all charges into account, as a current density term  $\mathbf{J}(\mathbf{x}, t)$  the auxiliary current takes the form

$$I_a = -\frac{1}{V_a} \int_{\Omega} \mathbf{J}(\mathbf{x}, t) \cdot \mathbf{E}(\mathbf{x}) d^3\mathbf{x} \quad (5.24)$$

The integral is over the volume where the charge is distributed. To derive the total signal formation, we need to insert the evolution of charge over time. The charge multiplication depends on the (first) Townsend coefficient  $\alpha$  which in general, among other things, is a function of the electric field. If  $n$  is the number of one type of charged particles at a certain point, then at a nearby point along the path of the moving charge the increase of the charges will be expressed as  $dn = n dr$ , where  $dr$  is the distance between the two points. In order to calculate the charge increment one has to integrate the above formula. Assuming some simplifications, the following formula [75] can be easily derived

$$I(t) = -q_0 \frac{\alpha \beta e^{\alpha \beta u_p t} u_p}{V_a} \int_0^{z_1} E_z(z) e^{\alpha \beta z} dz, \quad \beta = \frac{u_n}{u_n + u_p} \quad (5.25)$$

where  $q_0$  is the initial charge (one  $e^-$ ),  $u_p$  the velocity of the positive charges,  $u_n$  the velocity of the ions/electrons,  $E_z$  the  $z$ -component of the electric field. The derived current as a function of time is also drawn in Fig. 5.7.

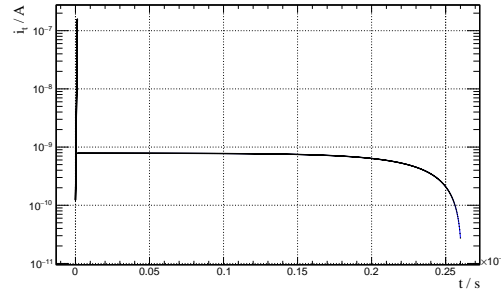


Figure 5.7: Total auxiliary current as a function of time. The peak at the origin for times less than 2 ns is due primarily to the electrons movement while after the 2 ns the distribution is due to the ion drifting towards to the mesh.[75]

## 5.4 Gas detectors

Gas detectors have been used and operated in various applications and experiments with very successful results since the last century. Despite their great complexity, they are based on the principle of ionization, where the incoming particle interacts with the gas molecules of the detector releasing electron-ion pairs where they are multiplied by the application of an electric field and finally, converted into a measurable signal. The differences between the various types of gas detectors based on the voltage applied are illustrated in Figure 5.8.

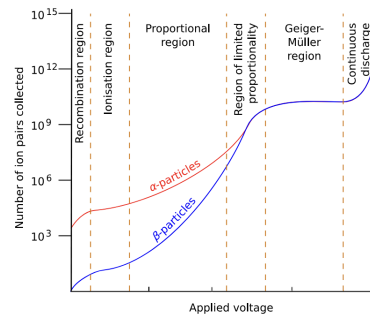


Figure 5.8: Areas of operation of gas detectors. [29]

The above Figure 5.8 shows the different voltage ranges in which the types of gas detectors could operate. At very low voltage values the field is not able to prevent recombination effects and the charge eventually collected is much smaller than the charge of primary ionization (Region I). The probability for an electron to escape recombination and capture effects increases with the voltage applied to the detector. The number of electrons increases with increasing voltage up to a limiting value reached for a voltage equal to the saturation voltage for some gasses, but the charge generated by the ionization of the gas is largely collected by the anode. With further increase of the voltage, above this saturation voltage, no increase in the collected charge is also observed. The region II in which the collected charge remains practically constant is called the ionisation region and this is where the voltage values at which the ionisation chambers operate belong. If the voltage is increased beyond the ionization region we find ourselves in the multiplication region (Region III). The electrons created by the initial ionization are in turn accelerated sufficiently, due to the high voltage  $V$ , to cause additional ionization through collisions, resulting in an increase in the number of initial carriers. In the initial part of region III, the multiplicative factor is quite dependent on the energy of the particle or on the initial number of produced ions for a given voltage  $V$ . We see that in this region the detector gives pulses of different heights for particles of different energies. This ratio between the pulse height and the initial ionization allows us to use the detector to separate particles with different energies. The region III

that involves multiplication while there is a dependence of the generated pulse (number of collected ions) is called the proportional region. In the region between III and IV, secondary ionization is particularly strong, resulting in the independence of the pulse height from the characteristics of the particle. The final charge increases with voltage and the detector in this region operates with limited proportionality. In the V region, the final charge collected is independent of the initial ionization and voltage. In this region, the dominant effect is the avalanche effect and the detector operates as a Geiger-Muller enumerator. At very high values of the voltage the ion charge distribution becomes dominant and the multiplication process will continue until the concentration causes a field that, in combination with the applied voltage, does not allow secondary ionization. Above a certain voltage value, amplification stops, due to a Raether limit. In the voltage amplification region, a continuous discharge occurs, resulting in no signal being received by the detector electronics.

## 5.5 Micromesh Gaseous Structure

The MicroMeGas detector, derived from the acronym MICROMEsh Gaseous Structure, belongs to a specific class of gas detectors, whose basic principle is the ionization of the gas medium of the detector as a particle passes through it, ionizes the gas and produces an electron/ion pair. The technology of these detectors was developed in accelerator devices and particle physics experiments. The construction and study of the specific detector was initiated at CEA-Saclay by Ioannis Giomataris [76] in the 90's. Of course, there were precursors of the Micromegas, which were built by A. Oed, G. Charpak and F. Sauli, who were involved in the first MicroStrip Gaseous Chambers. The modern model of the Micromegas detector, where we use it, owes its existence to I. Giomataris-G. Charpak (1996). The Micromegas detector is established as successful due to its stability, fast response, time resolution, good energy resolution, good spatial resolution, high efficiency, high accuracy and finally radiation resistance.

### 5.5.1 Structure and operating principle of the Micromegas detector

Typical MicroMeGas detectors consist of a flat anode electrode (drift), a gas gap a few millimeters thick that acts as a conversion and drift region (conversion gap) and a thin metallic mesh (mesh) at a typical distance of 100  $\mu\text{m}$  from the readout cathode, creating the amplification gap. A structure of cylindrical spacer columns (pillars), made of insulating material and arranged with a pitch of a few millimeters, define the height of the amplification region (amplification gap) and support the grid. The typical structure and functional parameters of a no-resistive MM are illustrated in Figure 5.9. This design, as we will see below, allows us by applying reasonable voltage values to the electrodes to obtain high values for the electric field in the amplification region ( $\sim 40 \text{ kV/cm}$ ) and relatively weak in the conversion/drift region ( $\sim 0,6 \text{ kV/cm}$ ). We thus achieve a particularly high ratio between the electric field in the amplification region and that in the conversion region, which is necessary for the ideal operation of the detector. The electric field in the drift region is characterized by a high voltage applied to the cathode and mesh while the electric field is chosen to be  $\sim 1 \text{ kV/cm}$ , and  $40 - 50 \text{ kV/cm}$  in the amplification region which achieves gain values of  $10^4$ . The anode, as mentioned above, can either be a single piece (pad) or divided into strips.

The charged particle after passing the cathode electrode (drift) is in the conversion region extending a few mm above the grid (mesh). Traversing the drift region, it interacts with the gaseous medium of the detector by depositing its energy on the gas atoms through ionization and excitation. As a result, the ionization of the gas causes the creation of electrons and ions in the conversion gap, the electrons under the influence of a weak electric field are drifting towards the mesh while the ions follow the opposite direction towards the cathode electrode. Through the micromesh, the electrons are guided to the amplification region where, due to the strong electric field prevailing in the strong-

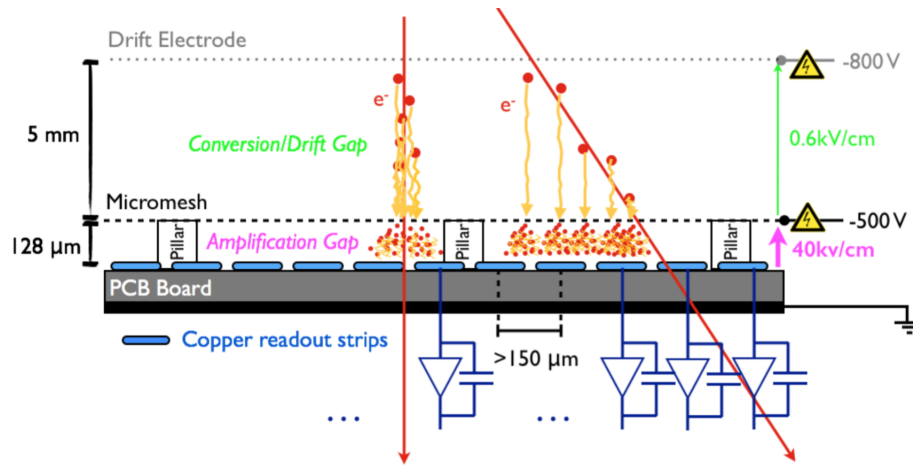


Figure 5.9: Graphical illustration of a standard cross-section of a non-resistive MicroMeGas detector showing the different parts of the internal structure of the detector and its operating principle. [65]

field amplification region. As a result, an avalanche of electrons is created which is collected by the anode strips while the secondary ions drift towards the micromesh where they are neutralized. A fraction of the ions can pass in the drift area - the so called ion backflow which at large particle fluxes may distort the drift field. Micromegas advantage is that the ion backflow is very small of the order of 5%. With an electric field in the amplification region 50 to 100 times stronger than the drift field, the micromesh is transparent to more than 95% of the electrons. Electron avalanche occurs in the thin region of the amplification in a time equal to 1 ns, producing a fast pulse in the readout strips. The ions produced in the avalanche process move towards the micromesh at velocity about 200 times slower than the electrons. The electron deformation and avalanche formation in the amplification region for vertical and angular particle trajectories are illustrated in Figure 5.9. Electrons contribution is a small fraction to the induced signal on the readout strips, with the largest contribution to the signal being due to the motion of the ions, as shown in Figure 5.9.

The electric field must be homogeneous both in the conversion region (conversion or drift gap) and in the multiplication region (amplification gap). This is achieved by using micromesh as the middle electrode. Thus the shape of the electric field is distorted near the holes of the micromesh. The knowledge of potential field lines shape near micromesh is fundamental for the operation of the detector especially for the rate of electrons passing through the micromesh, as well as for how fast the positive ions discharge in the region. Having a thin micromesh and since the electric field of the amplification gap is an order of magnitude larger than the conversion gap any potential line coming from the top of the micromesh is not returned to the bottom. The consequence of this is that most of the electrons pass through the micromesh and are completely reach the anode plane (strips).

### 5.5.2 Bulk Micromegas

The successful design of the MicroMegs detector provided a basis for further development of detectors adopting the use of micromesh to be used in various experiments with diverse requirements. A typical example of the development of MicroMegs is the invention of the bulk [77] technology. The bulk technology involves the integration of the micromesh into the printed circuit board (PCB) which is the anode from which we collect the charge and then the signal. In this way we have a compact single detector device with no individual parts. This technology now allows industrial production of the detector in large sizes and is based on printed board technology, which allows us to install the metallic mesh at a precise distance from the readout electronics (readout strips). The dominant idea of this technique, consists in confining the micromesh to a photopolymer of specific characteristic properties called Vacrel. Confinement is attained through a process of layering,



known as lamination, during the creation of the material, wherein successive layers are applied. This technique ensures the mechanical strength of the material to be manufactured. After the first piece has been manufactured, the micromesh is placed on top of it, on which a second piece of the same photopolymer is placed in the same way. This process is called encapsulation. After the closure of the micromesh in the photopolymer capsule, the capsule is exposed to radiation (exposure) in order to form the pillars which support the micromesh and finally the process is completed by the curing and polymerisation of the layers (layers of Vacrel). This process is now the basic choice for the manufacture of Micromegas detectors and the produced detectors are also characterized by smooth operation confirming all the excellent characteristics of this detector technology.

### 5.5.3 Resistive Micromegas

Despite the excellent features of the Micromegas detector technology and the promising industrial manufacturing process, the very thin amplification area together with the detailed readout structure makes the detectors particularly vulnerable to discharges (sparks). The phenomenon of discharges occurs when the number of electrons concentration exceeds the Reather limit which is  $10^8$ . In this case, the detector due to the increase in induced charge leads to a total grid discharge, where the rate of these discharges is proportional to the rate of incoming particles. This phenomenon is not catastrophic for low particle fluxes but in a high heavy particle flux beam environment it significantly affects the operation of the detector as it increases the dead time and contributes to the wear of the readout electronics. As a result, to deal with the sparks effect, it was decided to modify the detector to reduce its sensitivity to this effect.

The aforementioned drawbacks have been overcome by the development of the spark resistant Micromegas technology. In this technique, the readout strips are "guarded" with a durable high resistance insulating layer (equivalent to a  $15 - 50 \text{ M}\Omega/\text{cm}$  linear resistance) and has the same geometry as the readout strips. This non-uniformity is done to reduce the charge dissipation in many strips and reduces the intensity of the discharge current. The concept of resistive Micromegas is schematically described in Figure 5.10

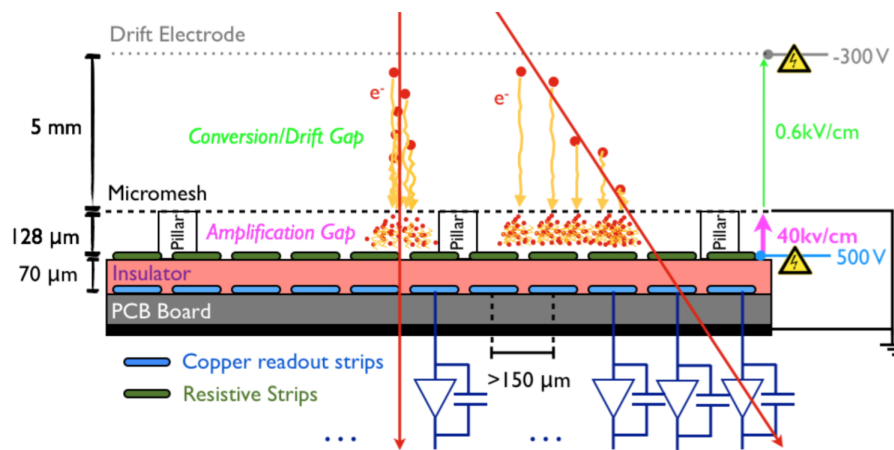


Figure 5.10: Graphic illustration of a cross-section of the resistive Micromegas detector showing the different parts of its internal structure and the principle of its operation. [65]

The charge is collected from the resistive strips, i.e. the charge is deposited on the upper side of the resistive layer, while then through the isolator it spreads and causes a charge to the readout strips by induction.

The new type of Micromegas detectors have been thoroughly studied under different conditions and using different gasses. Figure 5.11 below illustrates the comparison of the performance of the new

detectors with respect to the non-resistive detectors in a neutron environment, where the drop in the mesh voltage in the non-resistive compared to the resistive Micromegas is observed.

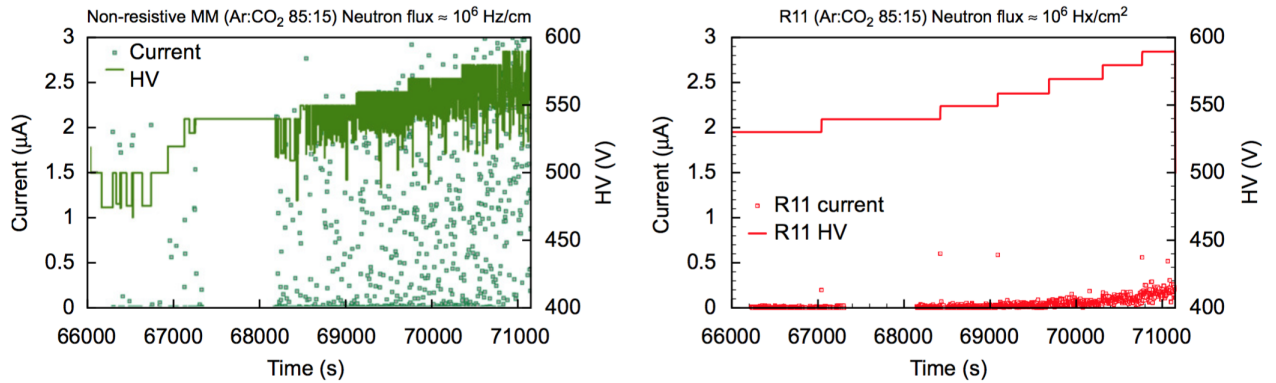


Figure 5.11: The behavior of voltage and current for a resistive and a non-resistive Micromegas in a neutron beam environment of energy 5.5 MeV total flux  $1.5 \times 10^6$  n/cm<sup>2</sup>s [78].

## 5.6 Micromegas detectors for the NSW Upgrade of ATLAS

The ATLAS experiment decided to equip the forward internal muon station and the Small Wheel with Micromegas detectors as part of the New Small Wheel upgrade. With the operation of the new arrangements, the detectors are expected to maintain their excellent characteristics while dealing with high rate particle interactions ( $\sim 25$  kHz/cm<sup>2</sup>). Several modifications to the readout and detection arrangement are also foreseen due to the large size of the detectors. The upgrade detectors differ in at least two ways from the original Micromegas design: 1) Resistive strip protection is used as described above, and 2) instead of applying negative voltages to the micromesh and keeping the resistive strips grounded, we apply positive voltage to the resistive strips and the micromesh is grounded.

The overall layout of the NSW, follows the Small Wheel model with an alternative arrangement of eight small and eight large sector detectors. The 16 sectors overlap in the azimuthal direction at their ends providing full coverage of the active area of the detector. The overall layout of the NSW is depicted in Figure 5.12 below. Each section consists of four wedges(wedges), where two

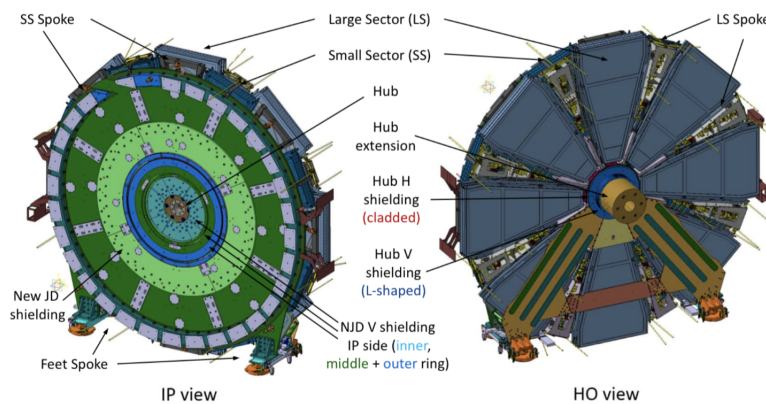


Figure 5.12: The overall layout of the New Small Wheel Upgrade.

Micromegas trajectory detectors are mounted on either side of a central 50 mm thickness gap frame and are positioned by the two sTGC detector modules, mainly used for triggering. Each wedge

consists of four layers of the same technology, with each layer being radially separated into modules. Each layer of the Micromegas detectors consists of two trapezoidal modules (M1,M2) and each module is divided radially into three and five PCB frames accordingly. The upper module (M2) consists of three PCB boards and the lower module M1 consists of five PCB boards glued exactly with an intermediate gap between them equal to  $400\text{ }\mu\text{m}$  along the radial direction. The readout layer is a  $0.5\text{ mm}$  thick PCB material equipped by photolithography with  $1024$  copper strips of height  $17\text{ }\mu\text{m}$  and pitch  $425\text{ }\mu\text{m}$  and  $450\text{ }\mu\text{m}$  for small and large type of modules, respectively. The strip orientation reveals the need for three kinds of PCB frames. One with strips moving perpendicular to the radial direction, *y-strips*, measuring the precision coordinate and the other two with strips, *stereo-strips*, inclined at a small stereo angle  $\pm 1.5^\circ$  with respect to the parallel to the radial direction, thus allowing the measurement of the second coordinate  $\phi$ . The strips are divided into two equal groups and each group is directed to opposite sides, with the first group in the upper right corner and the second group to the lower left. The arrangement of the readout boards is depicted in Figure 5.13.

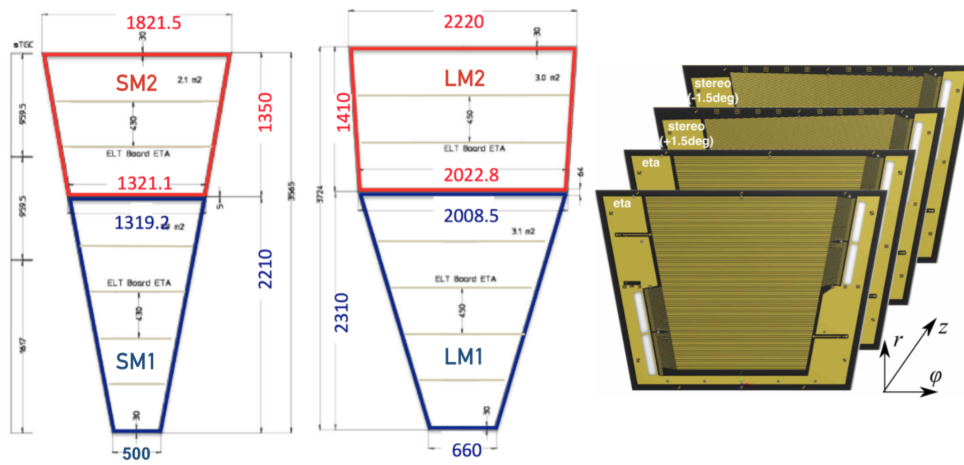


Figure 5.13: Right: Schematic representation of the four reading PCBs that would make up a MM module [79]. Left: The dimensions of the small and large NSW MM wedges. Each MM module layer consists of 8 PCBs, three for the top and five for the bottom module, respectively [29].

The New Small Wheel setup should be able to measure the overall position of the muon trajectory with an accuracy of  $80\text{ }\mu\text{m}$ . In order to meet this requirement, the relative alignment of the two reading panels must be better than  $18\text{ }\mu\text{m}$ . To achieve such a value, each plane is equipped with holes, which will guide the alignment pins during assembly, where the panels will be screwed together precisely. The cross-section of a quadruplet is illustrated in Figure 5.14. In the same figure, Figure 5.14, the outer part of the side of the quadruplet is additionally depicted. The extended space of the reading frames is to be used for routing the cables as well as cooling the electronic sensing devices. The read strips on the PCB board are contacted by the front-end board via a Zebra connector. In order to ensure a good connection of the electronic sensing devices to the PCB, a suppression bar has been placed on the outer part of the shift board.

### 5.6.1 Readout board & High Voltage Sections

In the resistive chambers implemented for the ATLAS NSW, neighbouring resistive strips are interconnected between each other every  $20\text{ mm}$  along the strips and these interconnection bridges are also shifted by  $10\text{ mm}$  from one strip to the next one. This design allows for a more homogeneous impedance between the high voltage supply line, the so-called “silver line”, and the resistive strips. Thanks to these interconnections, if a spike occurs, the huge amount of charge is evacuated through

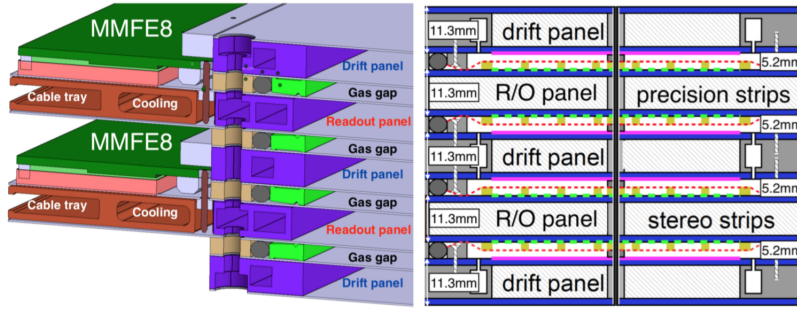


Figure 5.14: Right: The internal structure of NSW MM. Left: Transverse cross-section of the NSW MM showing the main elements of a quadropole [79].

a network of strips and not a single strip equalizing the effective resistance over the full area of the detector. Another advantage of these interconnections is that defects in the resistive pattern like e.g. broken strips become uncritical unless they are too massive. The resistive strips are interrupted in the middle of their length dividing the readout PCBs into two “HV section” and therefore the high voltage is supplied independently on both sides of the PCB. This fine segmentation, shown in Figure 5.15, prevents high voltage problems in case of local imperfections inside the amplification gap.

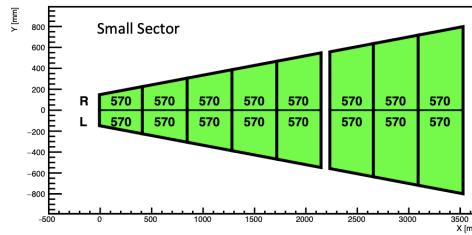


Figure 5.15: High voltage section divisions in a layer of a small sector. The same division is adopted also for the large sectors.

## 5.7 Position Reconstruction

The Micromegas should be able to provide a hit reconstruction with accuracy better than  $100\ \mu\text{m}$  per layer along the full range of muon track angles. The hit and track reconstruction techniques that have been developed for the Micromegas (MMG) chambers will be described in the following subsections. Each incoming charged particle induces a signal in a few strips per event. A simple clusterization algorithm is used to merge the adjacent strips with a signal, into a single cluster (hit). The goal of this type of detector is to reconstruct the hits of the particles that pass through it in order to determine the momentum and the charge of the particles. For this reason, the position reconstruction is an important point for the correct use of these chambers. The most used methods for position reconstruction are:

- Charge Centroid
- Micro-Time Projection Chamber ( $\mu\text{TPC}$ )
- Combination

When the particle is perpendicular to the chamber readout plane, the charge centroid method is used to provide a very accurate hit reconstruction in absence of a magnetic field. When the particle is inclined with respect to the readout plane, the  $\mu\text{TPC}$  method is used.

### 5.7.1 Charge Centroid method

The Charge Centroid method is a well established hit reconstruction mechanism for strip detectors, with the pattern of the readout strips, the material (resistivity) and the geometry of the resistive strip layer are the determinant factors of the spatial resolution. Electrons undergo scattering during their drift, and therefore their position in the amplification gap is affected by diffusion. As a result the charge induced on the strips by the primary ionization clusters is spread over several readout strips. Consequently, the amplitude of the single strip signal becomes sensitive to the cluster charge fluctuations, affected in such way the accuracy of the method, which deteriorates with the increasing track inclination angle and cannot be used for non-perpendicular tracks. Moreover, for perpendicular tracks, the timing information is not accessible and accurate since the charge of each strip is the superposition of several clusters.

Assuming a signal recorded from a strip  $i$ , with a charge,  $q_{strip,i}$ , exceeding a predefined noise threshold, proportional to the standard deviation of the measured noise signal on the strip  $i$ ,  $\sigma_{strip,i}$ . This signal can be considered as a valuable candidate for cluster building. A cluster is defined as a group of adjacent hit strips with a signal above threshold. The total charge of the cluster,  $q_{cluster}$ , can be described as the sum of the charges collected from all the strips within the cluster as

$$q_{cluster} = \sum_i q_{strip,i} \quad (5.26)$$

For tracks perpendicular to the anode plane, the cluster (hit) position is calculated by weighting the position of each strip with its signal amplitude and taking the average. The specific method, is called "centroid" and it is expressed as:

$$x_{strips} = \frac{\sum_i q_{strip,i} \times i}{\sum_i q_{strip,i}} \quad (5.27)$$

If the width of the gaussian shaped charge distribution is of the order of the strip pitch, the discrete periodic strip structure introduces a mis-reconstruction of the particles hit position. This method performs well for tracks approximately perpendicular to the chamber due to the reduced cluster dimension. In the case of inclined tracks, the primary ionization clusters are distributed along several readout strips and consequently, the single strip signal amplitude becomes sensitive to the primary cluster charge fluctuations. As a result, the accuracy of the charge centroid method deteriorates with increasing track inclination angles

### 5.7.2 $\mu$ TPC method

For perpendicular tracks, the timing information is not accurate since the charge of each strip is the superposition of several primary clusters. On the other hand, the inclined tracks provide more accurate measurements since the signal of each strip is induced by a single cluster. Additional information can be extracted for the drift time of each cluster, which if combined with the address of the strip can provide a two-dimensional reconstruction of the cluster's initial position within the chamber's drift area. For the translation of the measured time into distance the precise knowledge of the drift velocity value is presupposed. Using the ensemble of the two-dimensional points per event, the inclined or  $\mu$ TPC [65] track in the chamber can be reconstructed. This can then be used either for determining a single position in the gap, by extrapolating it to a reference point, or as a single detector segment.

### 5.7.3 Charge Centroid and $\mu$ TPC method combination

The two reconstruction methods [65] are complementary as the charge centroid method provides better spatial resolution for perpendicular tracks or for tracks with low inclination angles while the



$\mu$ TPC method is ideal for tracks with incidence angles greater than  $10^\circ$  because more strips collect charge per event. In order to improve the measurement accuracy, in particular in the small-angle region, the two algorithms can be combined by taking a weighted average of the corresponding reconstructed positions,  $x_C$  and  $x_{\mu TPC}$  using the cluster size as weight

$$x_{comb} = \frac{(n_{strips}/n_{cut})^2 x_{\mu TPC} + (n_{cut}/n_{strips})^2 x_C}{(n_{strips}/n_{cut})^2 + (n_{cut}/n_{strips})^2} \quad (5.28)$$

where  $n_{strips}$  is the cluster multiplicity (number of strip used to reconstruct the cluster) and  $n_{cut} = 4$ . In this way, the position determined with the charge centroid method is heavily weighted for small clusters. For extended clusters, as for inclined tracks, the  $\mu$ TPC result is dominant as shown in Figure 5.16. For the tracks will have incidence angles between  $7.5^\circ$  and  $30.5^\circ$  and, combining the two methods, a resolution of  $100 \mu\text{m}$  throughout the range can be obtained.

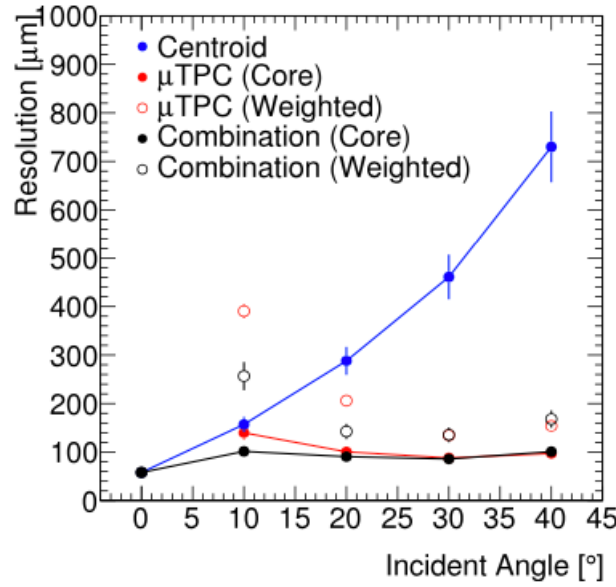


Figure 5.16: Micromegas spatial resolution as a function of the track inclination angle using charge centroid method (blue curve), the  $\mu$ TPC method (red curve) and the combination of the two (black curve). The resolutions are calculated through the fit of a double Gaussian on the difference between the reconstructed track and cluster position residuals. The final resolution is expressed in two ways: full circles are the  $\sigma$  of the core Gaussian, while empty circles are the weighted average of the Gaussian. The above results have been obtained with small Micromegas chambers using APV electronics. [80]

## 5.8 Testbeams

In this section, we delve into a comprehensive exploration of the technology through a series of meticulously conducted studies during test beams. Our objective is to provide an in-depth understanding and further characterization of this groundbreaking technology. These investigations are accompanied by a detailed exposition of the corresponding data analysis results, shedding light on the intricate facets of our findings.

Before delving into the specifics of our studies, we first provide a concise overview of the key components comprising our experimental setup. This introductory segment will serve as a foundation for comprehending the intricacies of our research, allowing readers to navigate through the subsequent detailed analyses with clarity.



Moreover, we delve into the performance assessment of the initial Micromegas modules. This rigorous evaluation aims to unearth phenomena that may either enhance or hinder the Micromegas reconstruction procedure. By scrutinizing these modules, we intend to not only identify potential improvements but also contribute to a more profound understanding of the technology's strengths and limitations.

The ensuing sections will explore these aspects in greater detail, presenting an array of experiments, observations, and data-driven insights. We invite readers to embark on this journey of discovery as we uncover the secrets, nuances, and potential breakthroughs associated with this pioneering technology.

### 5.8.1 SPS H8

#### Scope

The testbeam took place at the H8 beam line of the Super Proton Synchrotron (SPS) facility at CERN in July 2018. This significant event marked the inaugural evaluation of the first large SM2 MM module, equipped with prototype MMFE8 boards, under real beam conditions. It was conducted concurrently with the inaugural testing of the third version of the VMM front-end ASIC, which closely resembled its final production version. The overarching objectives of this testbeam encompassed a diverse range of assessments and validations:

1. **Verify the SM2 MM module's Stable Performance:** The primary goal was to ascertain the performance and functionality of the SM2 MM module under the demanding conditions of the testbeam.
2. **Validate the Electronics' Performance:** Rigorous testing was conducted to validate the electronic components and systems employed in the setup, ensuring they met the required performance standards.
3. **Test Third Version of the VMM Front-end ASIC:** The testbeam provided a unique opportunity to evaluate the third version of the VMM front-end ASIC under actual beam conditions, assessing its capabilities and limitations.
4. **Investigate the Appropriate Configuration of the VMM Parameters:** Optimization of the VMM parameters was a key objective, aiming to identify the most effective configuration for optimal data acquisition and analysis.
5. **Determination of the Optimal High Voltage Working Point:** The testbeam sought to establish the ideal high voltage working point for the system, maximizing its efficiency and sensitivity.
6. **Test Different Gas Mixtures and Specify the Detector's Impact:** Various gas mixtures were employed during the testbeam to assess their impact on the detector's performance. This investigation aimed to determine the most suitable gas mixture for future experiments.

In addition to the thorough evaluation of hardware components, the testbeam's comprehensive scope included the fine-tuning of critical parameters and configurations essential for ensuring the seamless operation of the system. This multifaceted approach aimed not only to validate the hardware but also to optimize the intricate interplay of variables that underpin the technology's functionality. The invaluable insights garnered from this rigorous endeavor are poised to serve as a cornerstone in the advancement of our comprehension of this cutting-edge technology. Moreover, these insights will play an instrumental role in charting the course for future developments, allowing us to harness the full potential of this innovation and navigate the complexities of its practical implementation with confidence and precision.

## Experimental Setup

The testbeam occurred at the H8 beamline of the Super Proton Synchrotron (SPS) at CERN, as illustrated in Figure 5.17. The H8 beamline features particles composed of 180 GeV/c pions or muons, characterized by a spot size of approximately  $\approx 1 \times 1 \text{ cm}^2$ . These beams are extracted from the SPS located in EHN1.

The H8 beamline, along with the associated H2, H4, and H6 lines, emanates from the same target source. These lines are designed to provide high-energy, high-resolution general-purpose beams that are employed for a wide array of experiments and tests.



Figure 5.17: The H8 beam line of SPS at Prevessin North area of CERN which the Micromegas testbeam experimental setup is installed.

The experimental setup for the testbeam, as depicted in Figure 5.18, comprises three one-view  $10 \times 10 \text{ cm}^2$  T'Z Micromegas chambers. These chambers are characterized as bulk resistive Micromegas with an active area of  $10 \times 10 \text{ cm}^2$  and strips measuring  $150 \mu\text{m}$  wide, with a pitch of  $250 \mu\text{m}$ . The T'Z chambers serve as references for external track reconstruction and are equipped with the MMFE8 board, which incorporates eight VMM FPGA-bearing front-ends.

The SM2 MM module on the other hand, is equipped with four MMFE8 boards. This configuration results in only half of the PCB being instrumented, with each board being placed in one detector layer, as illustrated in Figure 5.18. Additionally, two scintillators are employed as triggers for the experiment.

It's worth noting that the other chambers in the setup are comprised of different Micromegas prototypes with distinct readout systems (APV/SRS). These chambers are not utilized for track reconstruction purposes.

During the testbeam, a crucial aspect of the experimental setup involved strategically distributing the four MMFE8 boards across different PCBs. This arrangement was designed to explore and identify the most functionally advantageous positions for the chambers. By optimizing the placement of these boards, the experiment sought to enhance the overall performance and data acquisition capabilities of the setup. As showcased in Figure 5.19, the H8 experimental setup is presented from various angles, providing a holistic and multi-perspective view of the intricate apparatus. This comprehensive depiction serves as a valuable reference for understanding the spatial layout, connections, and interplay of components within the experimental environment. Figure 5.19 also includes an illustrative diagram highlighting the SM2 MM module configuration, featuring its four readout boards. This visual representation offers valuable insights into the structural organization and distribution of readout electronics within the detector, aiding in a clearer understanding of the data acquisition process.

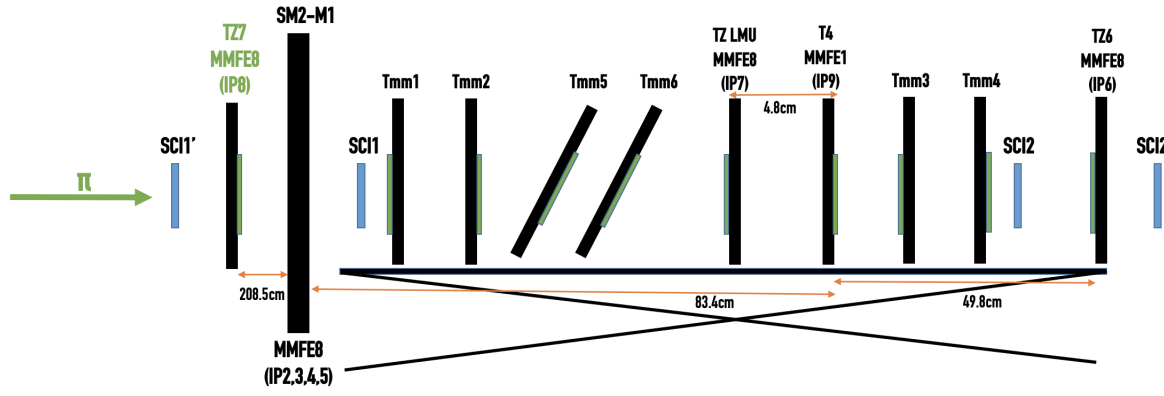


Figure 5.18: Experimental setup of the July 2018 test beam which is composed by the SM2 Micromegas chamber, three TZ Micromegas chambers which are used for the external track reconstruction and two scintillators which are used as triggers. The TZ chambers are equipped with one MMFE8 each and the SM2 with four MMFE8 boards, each board is placed on one layer of the chamber.

The planning and visualization of the testbeam setup, as exemplified by Figure 5.19, played a pivotal role in ensuring the success of the experiment. It allowed for the fine-tuning of board placement to optimize chamber functionality and provided a comprehensive overview of the H8 setup, contributing to a deeper understanding of the testbeam's objectives and outcomes.

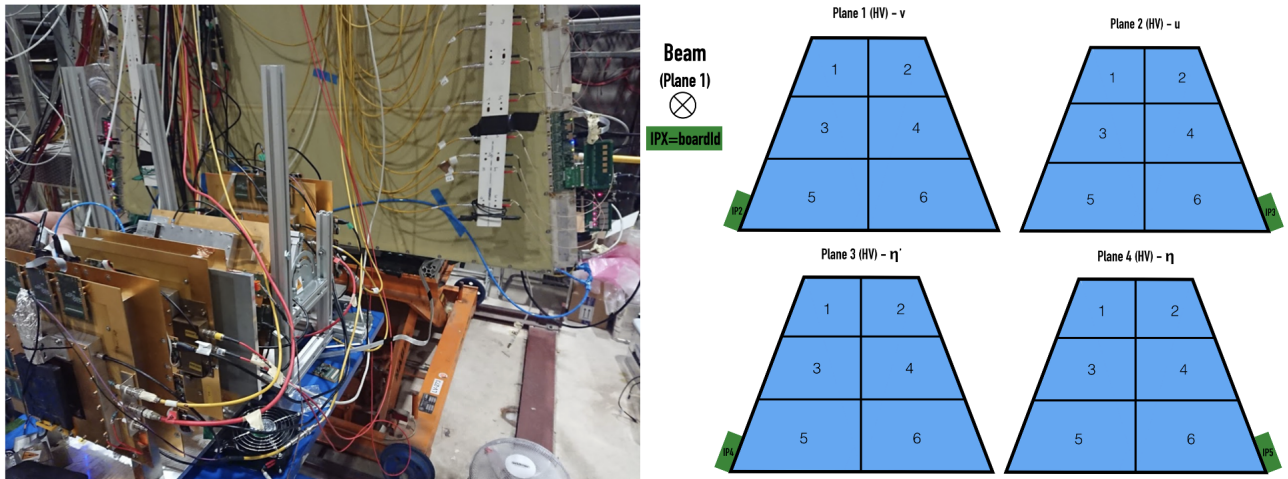


Figure 5.19: Left: The H8 setup with the SM2 MM and the TZ chamber used in the tracker with the MMFE8 readout board attached to it. Right: Diagram depicting the SM2 MM module and its four readout boards (in green rectangles).

### Readout System

The VMM Readout System (VRS)[51] Supervisory Board is an advanced FPGA-based system designed to interface seamlessly with other front-end boards equipped with VMMs and FPGAs that implement the necessary firmware. These front-end boards are commonly referred to as VRS front-end nodes.

The firmware for the VMM Readout System Supervisory Board (VSB)[81] has been implemented and successfully deployed on a Xilinx VC709 evaluation board. Connectivity is established through a custom-designed FPGA Mezzanine Board (FMC), ensuring a high degree of versatility and adaptability. This design is flexible enough to be ported onto various boards capable of connecting to

multiple VRS frontend nodes.

The overall system architecture is succinctly presented in Figure 5.20. In the VC709 implementation, the system also receives signals from the Central Trigger Formatter (CTF) module, which are then intelligently propagated to the VRS frontends as needed. The VSB board has the capability to connect with up to eight frontend nodes and one CTF module, all facilitated by nine miniSAS connectors through the FMC interface. Additionally, the board incorporates an Ethernet interface to facilitate seamless communication with the DAQ software via User Datagram Protocol (UDP). This software interface enables the forwarding of commands to the VSB logic, empowering it to dynamically control the state of the DAQ system in accordance with the user's requirements.

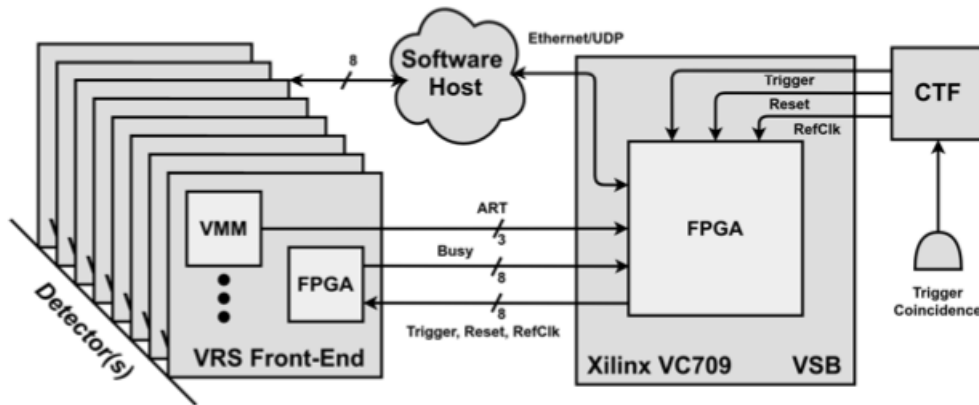


Figure 5.20: Overview of the VRS, when using the VSB in conjunction with the front ends. The VSB firmware implemented in the VC709 FPGA can support up to eight front end node connections. These connections are implemented through differential pairs over miniSAS cables, and carry the Reference Clock, SoftReset and Trigger signals. These originate from the CTF, which generates the system clock internally, receives the reset signal from a LEMO cable that is driven from a module outside of the radioactive area of the setup, and receives the trigger from a scintillator coincidence. The VSB can also receive the ART trigger primitive datastream from up to three frontends. Finally, it receives the Busy signal from all eight frontend FPGAs. All (up to nine) FPGAs of the system connect to the network via UDP over Ethernet, and the DAQ software, controls the system's overall state and receives VMM data from the frontends. [81]

The VRS serves as the central hub connecting all DAQ (Data Acquisition) nodes within the system. Its primary function is to distribute the reference clock, trigger signals, and soft-reset commands to all connected components. In this setup, scintillators play a crucial role in generating trigger signals that are subsequently sent to the coincidence module. The coincidence module, in turn, triggers the CTF, which is an integral part of the data acquisition system.

The DAQ software host interfaces with all nine FPGAs (Field-Programmable Gate Arrays) in the system via an Ethernet/UDP (User Datagram Protocol) connection. The chosen readout mode in this configuration is Level-0 Readout Mode, as it is optimized to minimize the dead-time constraints, a topic we will delve into further in the upcoming subsection.

The VMM connected to the detector processes incoming pulses without distinction, whether they originate from beam particles or other sources. The scintillator coincidence system generates a trigger-high signal that is relayed to the VSB through the CTF whenever a particle traverses the experimental setup. The VSB, upon receiving this trigger, registers it and waits for a user-configurable duration. Subsequently, the trigger is transmitted to the front-end FPGAs as an L0 (Level-0) trigger via the TTC (Trigger and Timing Control) module. The front-end FPGA promptly forwards the trigger to the VMM and enters a busy mode until the final VMM data word has been buffered in the UDP FIFO (First-In-First-Out queue).

To ensure that the L0 signal is correctly associated with the particle data, precise timing considerations are essential. The VSB's waiting time must be determined by accounting for several factors, including the VMM's L0 latency configuration, the inherent latency of the trigger system, and the VMM's integration time, which affects the temporal alignment of the shaped pulse.

This comprehensive approach guarantees the accurate synchronization of trigger signals and particle data, optimizing the data acquisition process for the system's specific requirements.

### Preliminary Studies

The success of these studies owes a great deal to the pivotal role played by the VRS DAQ (Data Acquisition) system, which facilitated data acquisition and management. Over a thousand runs were conducted under various experimental parameters, accumulating approximately 10 G of valuable data. With each channel experiencing an occupancy rate of around 5 kHz and trigger rates remaining below 100 kHz for both pion and muon beams, the readout efficiency consistently exceeded 80%.

The analysis of this extensive dataset was conducted using the ROOT Data Analysis Framework, employing C++-based routines that manipulated .ROOT ntuples. The initial phase of data analysis involved generating essential histograms, serving as validation tools to ensure the proper functioning of the chamber and associated electronics. These preliminary studies are presented in Figure 5.21, which consists of eight columns. The first four columns correspond to MMFE8 modules positioned on the SM2 MM module, while the last four columns pertain to those on the TZ chambers.

The rows within Figure 5.21 represent various histogram types, each offering unique insights into the experimental data:

- **Beam Profile:** This histogram illustrates the enabled strips when the beam traversed the chamber. The reconstruction of the beam profile relies on the spatial information obtained from 512 MMFE8 channels.
- **PDO Distribution (Peak Detector Output):** Depicting a distribution akin to a Landau distribution, this histogram showcases the particle charge on the strips. Additionally, it includes accumulations spikes originating from the VMM ADC, providing valuable insights into particle behavior.
- **TDO Distribution (Time Detector Output):** This histogram offers insights into the Time Detector Output distribution, providing critical timing information.
- **BCID Distribution (Bunch Cross ID):** Highlighting the BCID of events within 8 BC windows, this distribution becomes particularly useful during preliminary studies. It assists in configuring and optimizing VMM settings to achieve a centered and asymmetric distribution, aiding in precise data interpretation.
- **Strips per Events:** This histogram displays the number of strips that were fired per event, offering insights into the granularity and distribution of events within the chamber.

These initial histograms not only validate the proper functioning of the chamber and electronics but also serve as a foundation for subsequent, more detailed analyses. They provide crucial insights into the behavior of particles within the experimental setup, enabling further investigations and refinements in data collection and analysis techniques. In the second phase of our preliminary studies, we delve into the crucial process of data clusterization using the charge centroid method, which has been elaborated upon in preceding sections. Within our test beam setup, we strategically deploy three small, single-layer Micromegas detectors oriented perpendicular to the beam. These detectors are strategically placed both upstream and downstream of the SM2 MM module, offering invaluable external track measurements.



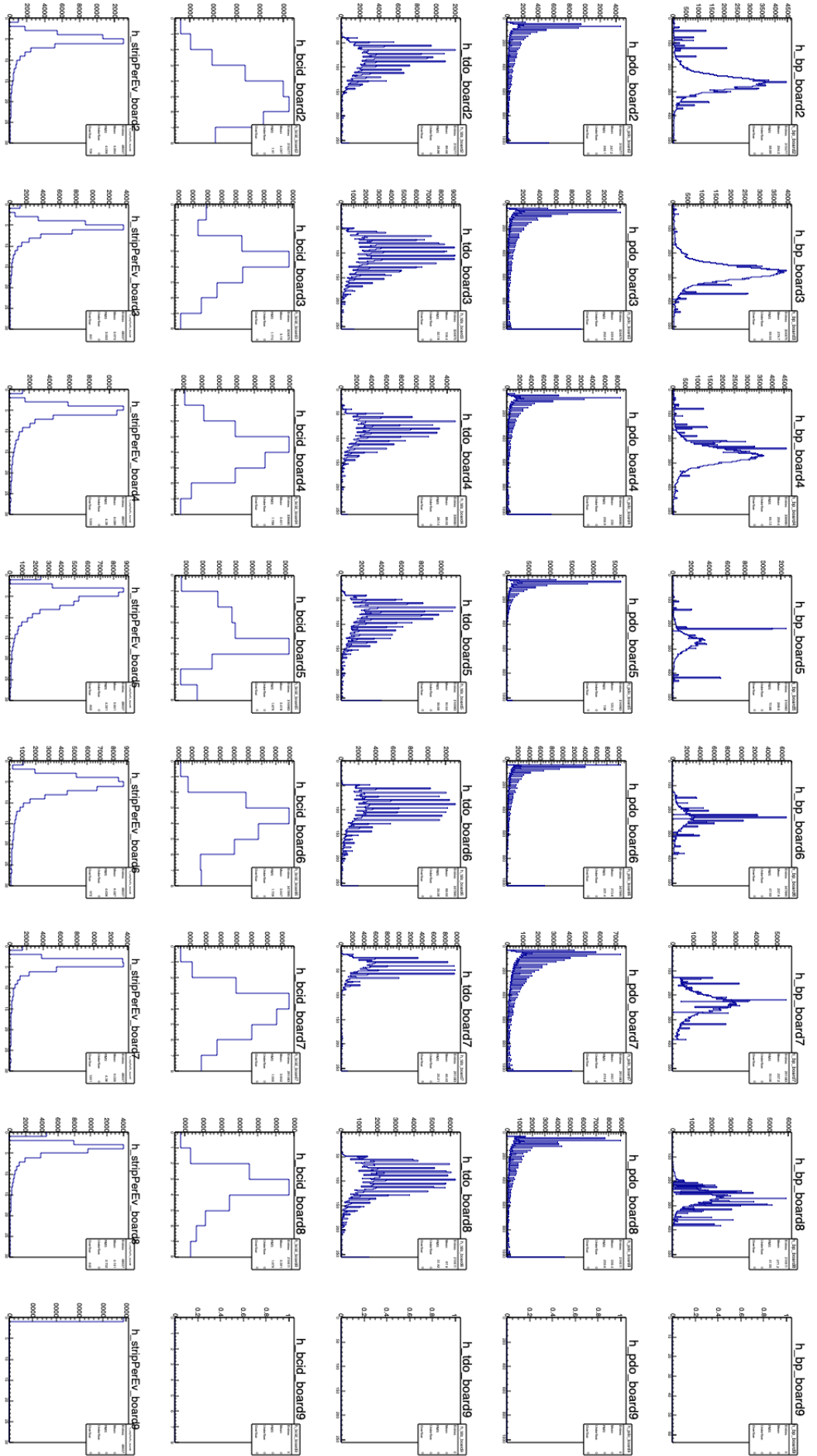


Figure 5.21: The histograms containing the preliminary studies of the testbeam data. We have eight columns, each one represents one different MMFE8 (first four are placed on the SM2 MM module and last four columns on the T<sup>1</sup>Z chambers). The rows represent the Beam profile, PDO distribution, TDO distribution, BCID distribution and Strips per Event per electronic board.



To reconstruct these tracks, we employ the centroid method by clustering strips that surpass a pre-determined threshold in each of the three detectors. This clustering process yields optimal results when it produces a single cluster per tracking detector, and when the clusters from all three detectors roughly align along a straight line. When this alignment is achieved, we fit a straight line through the cluster positions across all three detector layers, and the corresponding event is included in our comprehensive analysis.

However, to ensure the integrity of our data, events are excluded from analysis if any of the tracking detector layers meet any of the following criteria:

- Contain no clusters.
- Possess more than one cluster.
- Exhibit misalignment in cluster positions.

Our cluster reconstruction criteria stipulate that a cluster is formed if there are a minimum of two strips with a charge exceeding 30 PDO counts, thus effectively filtering out any noise. Furthermore, we impose a restriction of at most one hole within the cluster and require a charge exceeding 100 PDO counts for cluster inclusion.

Our analytical arsenal includes the following types of histograms, each playing a distinctive role in our data evaluation and interpretation:

- **Number of Clusters per Event:** This histogram provides insights into the distribution of the number of clusters per event. While the majority of events peak at one cluster, intriguingly, a subset of events exhibits zero clusters, a phenomenon attributable to inefficiencies or noise. Equally noteworthy are events featuring two or more clusters, which arise from multi-track events, often resulting from the presence of delta electron rays or noisy events.
- **Beam Profile:** This histogram visually represents the beam profile through the cluster-reconstructed positions. It offers essential information about the spatial distribution of particle tracks within our setup.
- **Cluster Charge:** This histogram serves to display the distribution of charges associated with the cluster events, shedding light on the particle characteristics and their interactions with the detectors. The distribution is fitted using Landau fit in order to get the most probable value (MPV).
- **Cluster Size for Single Cluster Events:** Focusing specifically on events characterized by the presence of a single cluster, this histogram quantifies the number of clusters generated under these conditions, providing insights into the single track behavior.
- **Cluster Size for All Cluster Events:** In this histogram, we explore the number of clusters generated across all events. For events featuring normal tracks, we observe cluster sizes typically ranging from 2 to 4, while for inclined tracks, cluster sizes tend to fall within the broader range of 5 to 8.

These comprehensive analyses enable us to gain a deeper understanding of particle behavior within our experimental setup, refine our data collection techniques, and further our quest for precision in particle physics research.

In addition to the preliminary studies mentioned earlier, we conducted additional investigations involving a HV scan of cluster charge and multiplicity. During this study, we adjusted the voltage applied to the detector strips within a range of 520 – 600 V with a step increment of 10 V.

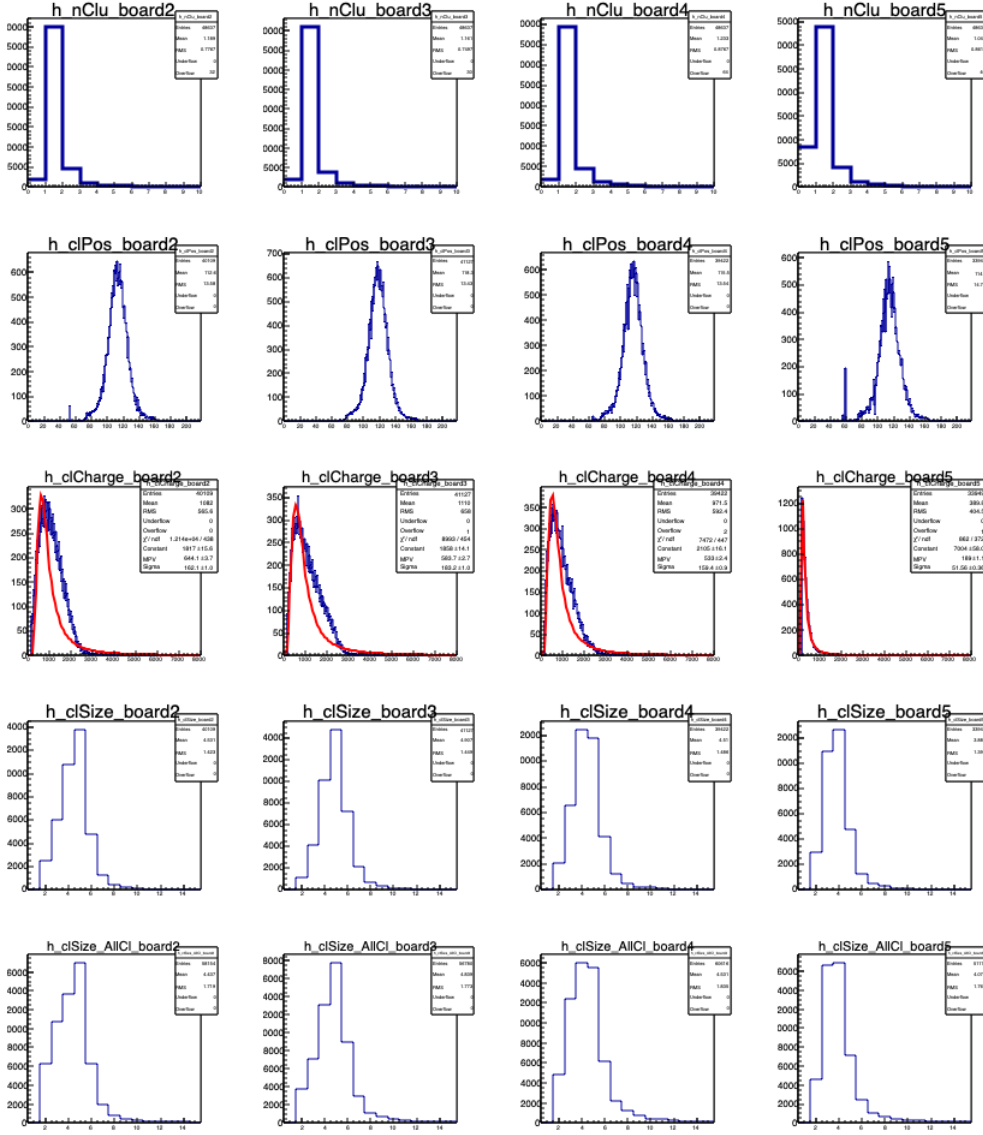


Figure 5.22: The histograms containing the preliminary clusterisation studies of the testbeam data. We have four columns, each one represents one different MMFE8 placed on the SM2 MM module. The rows represent the Number of clusters per event, Beam profile, Cluster charge, Cluster size of single cluster events, Cluster size for all cluster events per electronic board.

The first part of this study focused on the Cluster Charge Threshold Scan. For each layer of the detector, we produced plots of the mean and Most Probable Value (MPV) of the cluster charge distribution (as illustrated in the 3rd row of Figure 5.22) against the corresponding strips' voltage settings. This scan allowed us to examine how variations in voltage influenced the cluster charge characteristics. The second aspect of our investigation centered on the Cluster Multiplicity Threshold Scan. In this phase, we generated plots representing the mean cluster size distribution (depicted in the 5th row of Figure 5.22) for each detector layer, again with respect to the corresponding strips' voltage settings. This scan provided insights into how changes in voltage affected cluster multiplicity. To provide a visual representation of these HV scans, an example showcasing the Charge and Multiplicity HV scans are depicted in Figure 5.23. This figure serves as a visual aid to help comprehend the outcomes of our voltage-dependent studies.

These comprehensive studies were instrumental in gaining a deeper understanding of the impact of voltage variations on cluster charge and multiplicity, allowing us to fine-tune our detector parameters

for optimized data collection and analysis.

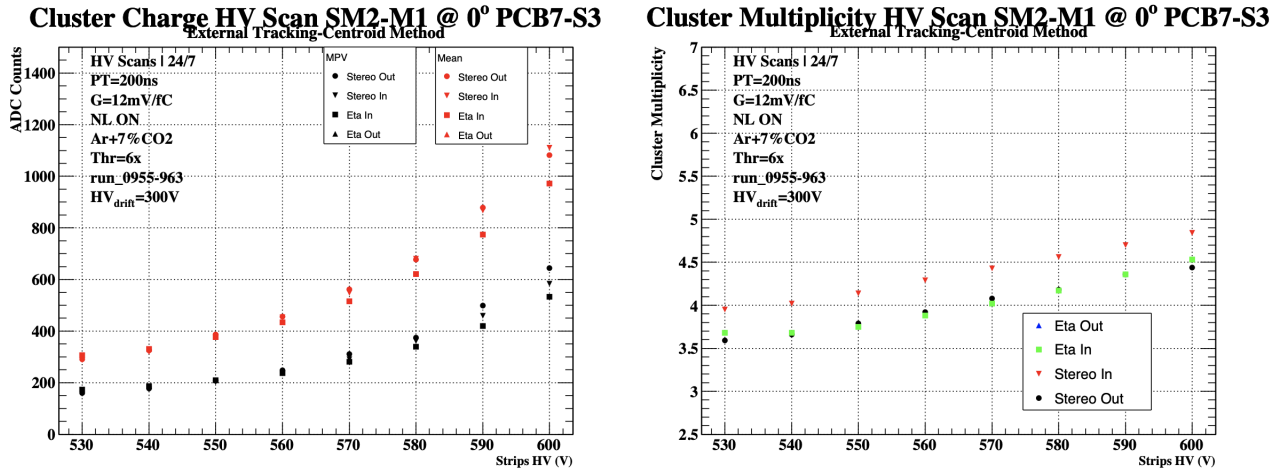


Figure 5.23: Left: Cluster charge HV scan which for each layer the mean and the mpv of the cluster charge distribution (3rd row of Figure 5.22) were produced versus the corresponding strips voltage level. Right: Cluster multiplicity hv scan which for each layer the mean the cluster size distribution (5th row of Figure 5.22) were produced versus the corresponding strips voltage level.

### Noise Levels Studies

One of the fundamental parameters governing the operation of the VMM in our setup is the charge threshold for each individual strip. This parameter is of paramount importance due to the remarkable length of the strips employed in the large Micromegas chambers, which can extend up to an astonishing 2 meters. The extensive strip length inherently translates to a substantial capacitance between adjacent strips, rendering Micromegas detectors particularly sensitive to noise.

In light of this sensitivity, it becomes imperative to quantify noise levels before commencing data collection. Equally crucial is the need to configure the VMM thresholds accordingly. To accomplish this, we employ a calibration procedure that involves sampling the analog output of the VMM, which represents the signal after passing through the shaping amplifier. This measurement yields a value referred to as the "baseline."

The determination of channel thresholds is achieved by applying a scale factor, denoted as "x," to the baseline's Root Mean Square (RMS) value. Specifically, the threshold is calculated as the median baseline value plus "x" times the RMS of the channel baseline. This approach allows us to precisely set the thresholds on the VMMs, ensuring an optimal balance between sensitivity to signals and mitigation of noise effects.

To perform this calibration effectively, we conduct dedicated runs without the presence of the particle beam. These runs serve the purpose of measuring the baseline of each channel and characterizing its fluctuations. The hardware thresholds must strike a delicate balance: they should be low enough to detect signals effectively yet high enough to maintain noise levels below the anticipated hit rate at the High-Luminosity Large Hadron Collider (HL-LHC), which is estimated at 1 kHz per strip.

It's worth noting that the noise in Micromegas detectors doesn't conform to a Gaussian distribution. Consequently, we must set thresholds at a level that prevents the selection of non-physical events while accommodating the unique characteristics of the noise profile. After careful analysis, it has been determined that the intrinsic noise in MicroMegas, driven by the high strip capacitance, is not as low as initially expected (as indicated in Figure 5.24). Consequently, to maintain the noise hit rate below the 1 kHz per strip threshold, the minimum usable threshold value is determined to be 6 times the standard deviation ( $\sigma$ ) of the baseline fluctuations. This elevated threshold level can have

implications on various standard distributions, including cluster charge, gain, and efficiency, which are critical aspects of our data analysis.

In summary, the precise calibration of VMM thresholds is a pivotal step in optimizing the performance of Micromegas detectors, especially in high-capacitance environments. Balancing sensitivity and noise mitigation is crucial for accurate data collection and analysis in our experiments. Following

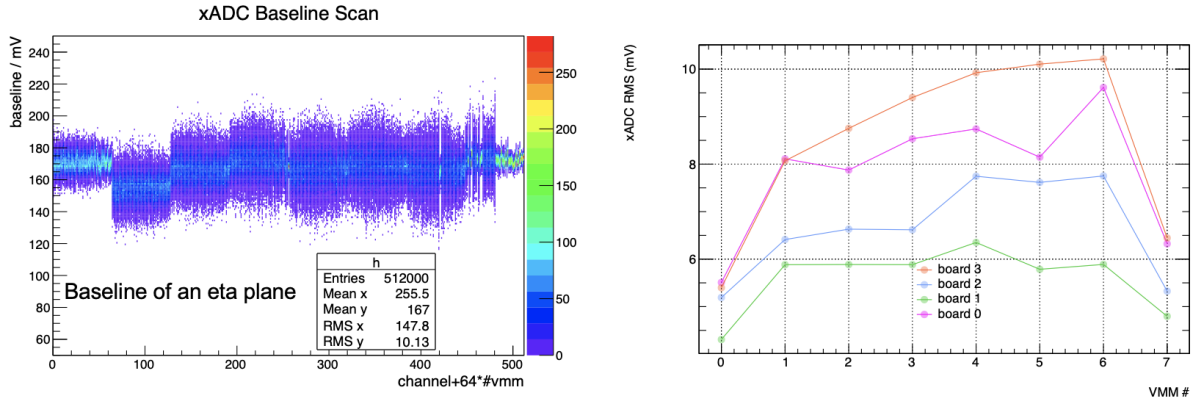


Figure 5.24: Left: Baseline of a MMFE8 which is placed on an eta layer of the SM2 MM module. Right: Noise level, in terms of xADC count per each board of each layer. The measurement was done on the PCB8 (the one with the longest strip of the small NSW sectors) with a gain of 9 mV/fC for each VMM3. This means that a threshold of  $6 \times \sigma$  is equivalent to  $\approx 6 \text{ fC} \approx 37 \text{ ke}^-$ .

the test beam experiments, significant efforts were dedicated to mitigating the noise levels within the detector, ultimately bringing them closer to the theoretical limits. These improvements primarily focused on enhancing the grounding infrastructure within the detector quadruplet and optimizing the power supply systems.

During the test beam phase, one notable challenge was imperfect grounding, which resulted in the detector's long strips unintentionally acting as antennas. This unintended consequence led to the absorption of electromagnetic distortions present in the test beam hall, an environment bustling with multiple concurrent experiments running in parallel.

To address this issue, extensive work was undertaken to refine the grounding configuration, effectively minimizing the detector's susceptibility to external electromagnetic interference. The enhancements in grounding not only reduced noise levels but also contributed to the overall stability and precision of the detector's operation.

By implementing these measures, we successfully brought the noise levels within the detector closer to the theoretical limits, paving the way for more accurate and reliable data acquisition during subsequent experiments. These improvements underscore the significance of infrastructure optimization in achieving the desired performance of advanced experimental setups.

In pursuit of comprehensive studies to optimize our experimental setup, we embarked on additional investigations by harnessing the power of varying clusterization thresholds. These studies involved an in-depth exploration of how different threshold levels ( $4 \times \sigma$ ,  $6 \times \sigma$ ,  $8 \times \sigma$ ,  $10 \times \sigma$ ,  $12 \times \sigma$ ,  $14 \times \sigma$ ) impacted our data. These threshold levels were acquired using the VRS DAQ software, affording us fine control over the sensitivity of our detectors.

With these threshold levels in hand, we proceeded to configure the VMMs with corresponding sets of configuration parameters tailored to each threshold level. This calibration process allowed us to extract valuable information from the ensuing distributions, as vividly demonstrated in Figure 5.25. For each detector layer, the following distributions were generated and analyzed:

- **Cluster Charge Threshold Scan:** In this scan, we explored the relationship between the mean and the Most Probable Value (MPV) of the cluster charge distribution (as illustrated

in the 3rd row of Figure 5.22) and the corresponding threshold level. This analysis provided insights into how varying threshold levels influenced the charge characteristics of the clusters formed within each detector layer.

- **Cluster Multiplicity Threshold Scan:** This investigation involved examining the mean cluster size distribution (as depicted in the 5th row of Figure 5.22) for each detector layer in relation to the corresponding threshold level. It allowed us to gain a deeper understanding of how changes in threshold levels impacted the multiplicity of clusters, shedding light on the behavior of particle tracks in different conditions.

These comprehensive studies enabled us to fine-tune our detector settings and gain valuable insights into the sensitivity and noise characteristics of our setup. The ability to manipulate threshold levels and observe their effects on clusterization distributions empowers us to optimize our data collection strategies and enhance the precision of our particle physics research.

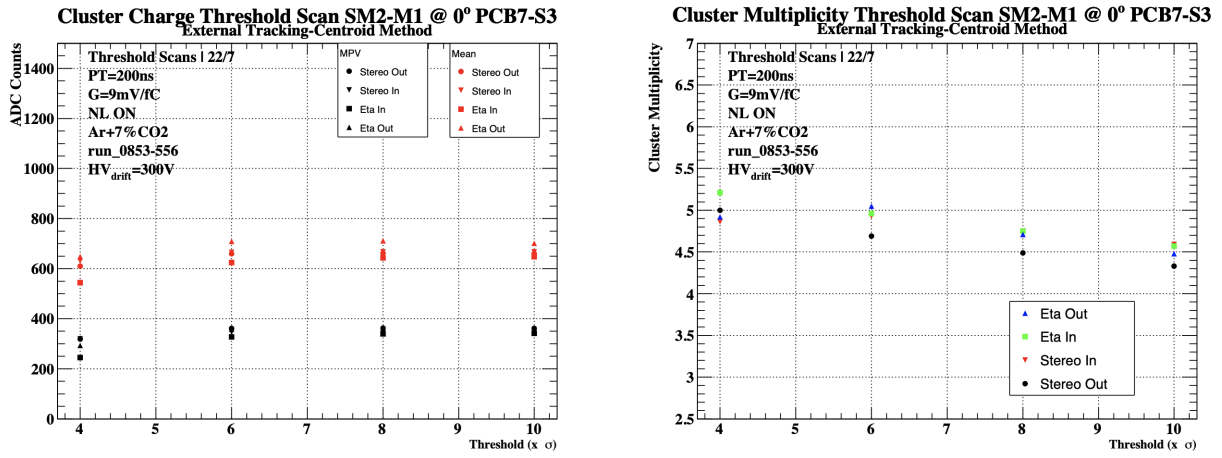


Figure 5.25: Left: Cluster charge threshold scan which for each layer the mean and the mpv of the cluster charge distribution (3rd row of Figure 5.22) were produced versus the corresponding threshold level Right: Cluster multiplicity threshold scan which for each layer the mean the cluster size distribution (5th row of Figure 5.22) were produced versus the corresponding threshold level.

### Spatial Resolution studies

During the test beam period, we conducted an extensive investigation into the spatial resolution between the layers of the SM2 MM modules. This inquiry was pivotal in assessing the precision of our detectors. To achieve this, we employed a direct comparison of the measured hits produced by the traversing particle beam on each detection layer, for instance, layers 1 and 2.

Assuming that the chamber's layers are precisely aligned perpendicular to the incident beam, with an intermediate distance of  $x$  micrometers, we denoted the hit positions on each layer as  $x_1$  and  $x_2$ , respectively. The key parameter of interest in our study was the distribution of the measured hit position difference, which we termed as  $\Delta x = x_1 - x_2$ . This distribution, known as residuals, allowed us to quantify the spatial discrepancy between the two detection layers.

The width of the residual distribution, denoted as  $\sigma_{\text{residual}}$ , encapsulates the spatial resolution of both involved detection layers. Consequently,  $\sigma_{\text{residual}}$  is influenced by the contribution of each layer to the overall spatial precision. In essence, it serves as a measure of the combined spatial resolution, offering valuable insights into the performance of our detector setup.

This study played a pivotal role in characterizing the spatial accuracy of our detector layers and ensured that our experimental setup could deliver the precision required for our particle physics

research. The ability to quantify and optimize spatial resolution is vital in accurately reconstructing particle tracks and extracting meaningful scientific insights from our experiments.

The width of the residual distribution,  $\sigma_{\text{residual}}$ , includes the spatial resolution of both involved detection layers, and thus is given by the contribution of each layer:

$$\sigma_{\text{residual}}^2 = \sigma_1^2 + \sigma_2^2 \quad (5.29)$$

If we assume that the layers are identical and operated under the same conditions, their spatial resolution is:

$$\sigma = \frac{\sigma_{\text{residual}}}{\sqrt{2}} \quad (5.30)$$

The methodology employed in our spatial resolution assessment relies on incident particle tracks that are ideally perpendicular to the detector layers. However, it's important to acknowledge that this approach, while informative, inherently sets an upper limit on the true spatial resolution. This limit arises due to potential deviations in the incident particle trajectories and the effects of multiple scattering of particles within the detector's readout structure, both of which can lead to a broadening of the residual distribution.

The residuals, representing the spatial discrepancies between various SM2 layers, are visually presented in Figure 5.26. To effectively capture the characteristics of these residual distributions, both distributions are subjected to a fitting process using a "double" Gaussian function. This modeling approach is chosen to account for the presence of tails in the distribution, which may deviate from the ideal Gaussian shape.

The "core" Gaussian component of the fitted function provides an estimate of the intrinsic detector resolution. It quantifies the detector's ability to precisely determine the position of incident particle hits, assuming ideal conditions.

Conversely, the "tail" Gaussian component represents additional uncertainty contributions introduced by factors such as the VMM chip and the time extraction procedure. These factors may introduce deviations from the ideal core Gaussian distribution, reflecting the broader complexities of the measurement process.

Of particular interest is the mean parameter extracted from these fits. It serves as an indicator of the spatial shift between the two readout planes, offering valuable insights into the quality of chamber construction and alignment between the detector layers. A well-aligned chamber would exhibit a minimal mean shift, indicating precision in layer positioning and construction.

By employing this comprehensive methodology and considering both the core and tail Gaussian components, we gain a holistic understanding of the spatial resolution of our detector setup. This approach enables us to not only quantify the intrinsic detector resolution but also identify and address additional sources of uncertainty, ultimately enhancing the precision of our experimental results and the reliability of our particle physics research.

The spatial resolution can be expressed by two ways,  $\sigma_{\text{core}}$  and  $\sigma_{\text{weighed}}$ . Where  $\sigma_{\text{core}}$  is the sigma of the Gaussian distribution and gives the spatial resolution of good events and  $\sigma_{\text{weighed}}$ :

$$\sigma_{\text{weighed}} = \frac{\sqrt{I_{\text{core}}\sigma_{\text{core}}^2 + I_{\text{tail}}\sigma_{\text{tail}}^2}}{\sqrt{I_{\text{core}} + I_{\text{tail}}}} \quad (5.31)$$

where  $I_{\text{core,tail}}$  is the integral of the single core/tail Gaussian, which takes into account also the tails due to delta rays (in small percentage) but mostly due to bad position reconstructions (hole inside the clusters, fake strip included in the clusters reconstruction).

Looking again at Figure 5.26, the achieved resolution for perpendicular tracks of all the layers is well below the 100  $\mu\text{m}$  required. The mean parameter of the fit ( $\mu$ ) is the shift between the layers and is used it order to verify the good construction and the alignment between the eta and stereo layers.

Another study, which were performed during the testbeam period, was the definition of the  $\sigma_{\text{core}}$  and



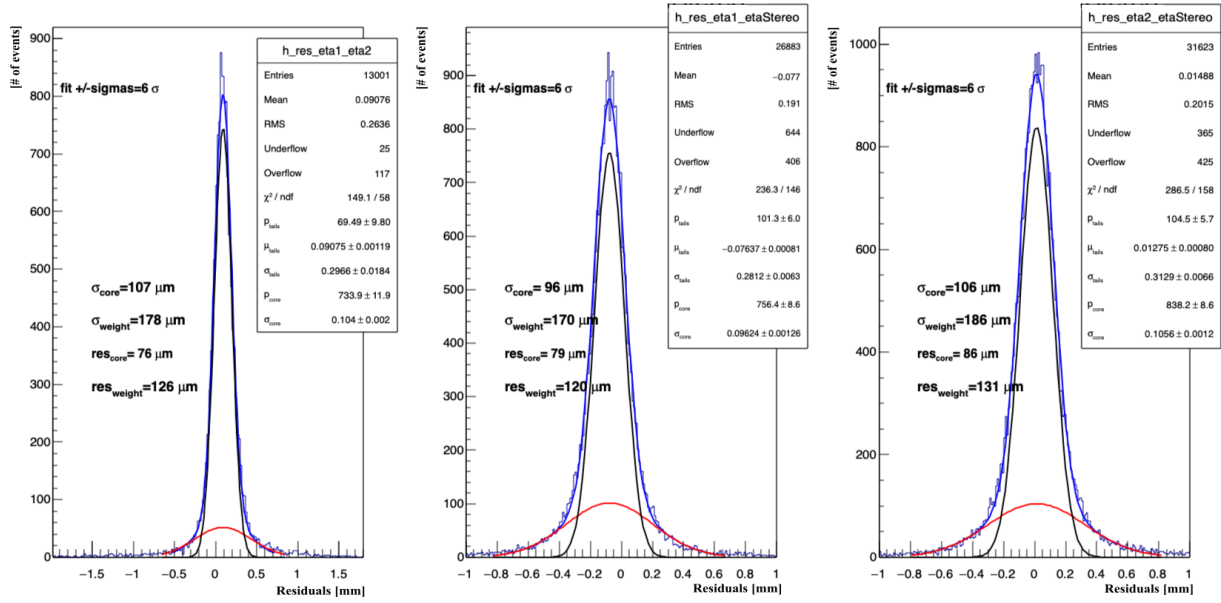


Figure 5.26: The residuals between the SM2's layers are shown. Both distributions are fitted with a "double" Gaussian function in order to take into account the tails of the distribution. The "core" Gaussian gives an estimation of the intrinsic detector resolution while the "tail" Gaussian describes the additional uncertainty contributions. The achieved resolution for perpendicular tracks of all the layers is well below the 100  $\mu\text{m}$  required.

$\sigma_{\text{weighed}}$  as a function of the strips voltage for the four layers. As shown in Figure 5.27, the strips voltage was adjusted between 520 – 600 V with a step of 10 V and the values of the resolutions are constant as a function of the amplification voltage. Most of the values are well below the required 100  $\mu\text{m}$ .

## Efficiency Studies

The detection efficiency serves as a crucial metric that quantifies a detector's capability to accurately record hits generated by the passage of charged particles through its active volume. It can be mathematically expressed as the ratio between the number of observed hits registered by the detector and the expected number of charged particles that traversed the detector during the same time interval. Throughout the course of the test beam experiments, we diligently recorded numerous runs, systematically adjusting the voltage applied to one layer at a time. This process allowed us to perform voltage scans, effectively mapping out the typical distributions and observing how efficiency fluctuated as a function of amplification voltage.

Notably, during these investigations, we adopted various definitions of efficiency to gain a comprehensive understanding of detector performance. These diverse definitions helped us explore different facets of the detector's functionality and assess its ability to accurately capture particle interactions under varying voltage conditions.

The efficiency studies conducted in this manner provided invaluable insights into the detector's sensitivity to voltage adjustments and enabled us to identify optimal operating conditions. By systematically varying the voltage and rigorously evaluating efficiency, we not only fine-tuned our detector settings but also ensured that our experimental setup could reliably and efficiently capture data, ultimately enhancing the precision of our particle physics research.

- **Hardware Efficiency:** This metric represents the fraction of events in which at least one

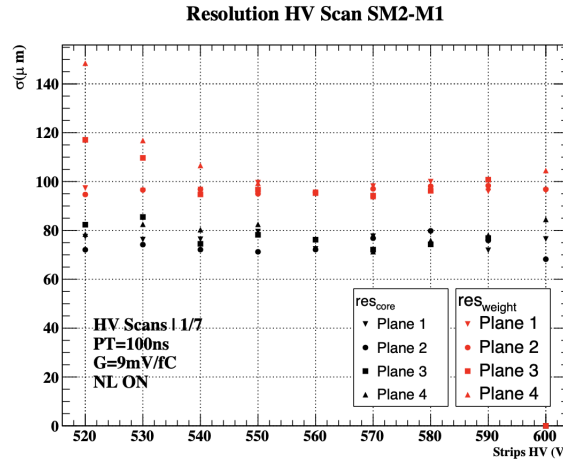


Figure 5.27: The residuals between the SM2's layers are shown. Both distributions are fitted with a "double" Gaussian function in order to take into account the tails of the distribution. The "core" Gaussian gives an estimation of the intrinsic detector resolution while the "tail" Gaussian describes the additional uncertainty contributions. The achieved resolution for perpendicular tracks of all the layers is well below the 100  $\mu\text{m}$  required.

strip within the analyzed chamber registers a signal, relative to the total number of selected events. Hardware efficiency constitutes the most fundamental analysis, offering insights into the general operational status of the chamber.

- **Cluster Efficiency:** Cluster efficiency quantifies the fraction of events in which at least one reconstructed cluster is identified within the analyzed chamber, relative to the total number of selected events. This metric extends beyond hardware efficiency and, in principle, removes noisy hits, providing a more realistic estimate of the chamber's efficiency. The efficacy of cluster reconstruction also plays a role in this efficiency calculation.
- **Software Efficiency:** This metric represents the fraction of events in which a cluster is detected within a defined window (typically  $\pm 1$  mm for perpendicular tracks) relative to the total number of selected events. Software efficiency, compared to cluster efficiency, further refines the calculation by eliminating reconstructed clusters with noisy neighboring strips.

To assess the three categories of efficiencies, we employed two distinct methods for track reconstruction: external-tracking using the telescope chambers and self-tracking utilizing information from the other three layers of the detector.

**External-Tracking:** In this approach, we reconstructed tracks using the telescope chambers as external references. This method provided a reliable benchmark for assessing hardware, cluster, and software efficiencies. It allowed us to cross-validate the performance of the chamber against an independent tracking system, ensuring the accuracy of our measurements.

**Self-Tracking:** Alternatively, we reconstructed tracks by relying solely on information from the other three layers within the detector itself. This approach demonstrated the chamber's intrinsic capability to reconstruct tracks independently, offering insights into its stand-alone performance.

Of particular interest was the intensive study of software efficiency. To comprehensively understand and optimize this aspect, we conducted various studies, including threshold and HV scans. The results of these software efficiency studies are depicted in Figure 5.28. These investigations allowed us to fine-tune the software parameters, such as thresholds and voltage settings, to maximize the efficiency of our detector. By conducting these in-depth studies, we not only optimized the performance of the chamber but also ensured the reliability of our data analysis, which is crucial for our particle physics research.

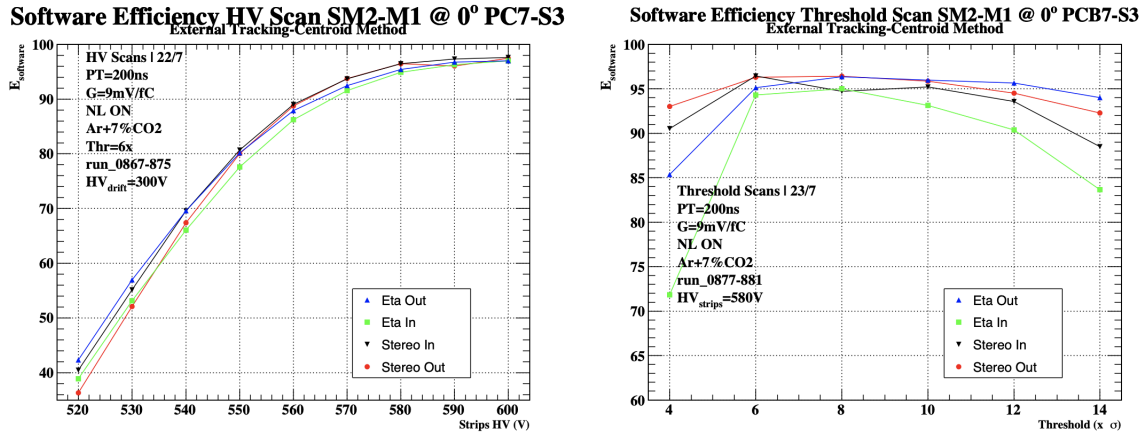


Figure 5.28: Left: The software efficiency as a function of the strips HV. Right: The software efficiency as a function of the threshold.

### Gas Studies

Another significant objective of the test beam experiments was to thoroughly investigate the effects of different gas mixtures on the cluster charge, cluster multiplicity, and software efficiency within the SM2 MM module. We conducted a comprehensive study encompassing three distinct compositions of argon and carbon dioxide during the test beam phase. The primary aim was to ascertain whether modifying the gas mixture could yield improvements in the chamber's performance:

- Ar + 7%CO<sub>2</sub> (default);
- Ar + 15%CO<sub>2</sub>;
- Ar + 30%CO<sub>2</sub>.

By systematically exploring these different gas compositions, we sought to uncover any potential enhancements in the following key parameters:

- **Cluster Charge:** We assessed how the gas mixture influenced the charge distribution of the clusters formed within the chamber. Variations in gas composition could impact the energy deposition characteristics of particles passing through the detector.
- **Cluster Multiplicity:** Our investigations also delved into the cluster multiplicity, examining how different gas mixtures affected the number of clusters formed in response to particle interactions. This parameter is vital for understanding the tracking capabilities of the detector.
- **Software Efficiency:** Additionally, we studied the software efficiency of the SM2 MM module under different gas mixture conditions. This analysis provided insights into how changes in gas composition might influence the chamber's ability to accurately reconstruct particle tracks.

By conducting these systematic studies and exploring various gas mixtures, we aimed to optimize the performance of the SM2 MM module, enhance its tracking capabilities, and fine-tune its efficiency for particle physics research. This comprehensive investigation was instrumental in identifying potential avenues for improvement in our experimental setup.

For the two new gas mixtures, a thoughtful approach was taken when selecting the drift and amplification voltages. The primary objective was to ensure that the electrons' drift velocity remained consistent, and transverse diffusion exhibited similar behavior across these different gas compositions. This voltage selection process was crucial in maintaining the detector's performance.

In Figure 5.29, we present a visual representation of the software efficiency, cluster charge, and cluster multiplicity under identical gain settings for the three distinct gas mixtures. These comparisons were conducted using a hardware threshold of  $6 \times \sigma$ , with neighbor logic activated, and two different peak time settings (100 and 200 ns). Notably, these combinations of Ar + %CO<sub>2</sub> gases yielded results that exhibited minimal variation.

It's worth noting that while these gas mixtures demonstrated similar performance in terms of software efficiency, cluster charge, and cluster multiplicity, a particular consideration was given to the fraction of the quenching gas, CO<sub>2</sub>. A higher proportion of CO<sub>2</sub> is desirable as it helps suppress sparks within the chamber, ultimately improving the stability of the amplification field. However, this does come at a cost, resulting in reduced gas gain and a lower number of primary ionizations.

A crucial finding from these experiments was the stability of spatial resolution across all gas mixtures. This stability underscores the robustness of the detector's performance and its ability to maintain consistent spatial precision across different gas compositions.

In summary, the careful selection and evaluation of gas mixtures, along with a focus on stability and performance parameters, were integral to optimizing the SM2 MM modules efficiency and reliability for particle physics research. These findings contribute to a deeper understanding of the trade-offs and considerations involved in gas mixture selection for advanced detector systems.

## HV Studies

Another crucial study conducted during the test beam period involved the evaluation of HV performance. This investigation focused on collecting and analyzing voltage and current data to assess the behavior of the detector's strips under different HV conditions. Additionally, the study aimed to understand the impact of the particle beam on the detector's HV performance.

In Figure 5.30, we present summary plots derived from multiple runs, each providing valuable insights into the HV performance of the detector. These plots allowed us to identify sections where HV behavior may have been problematic. By pinpointing these problematic HV sections, we were able to take corrective measures, adjusting the voltage settings to mitigate spike rates effectively.

The careful evaluation of HV performance is critical in ensuring the stability and reliability of the detector during particle beam experiments. Identifying and addressing issues related to HV behavior helps maintain consistent data quality and minimizes potential disruptions during data acquisition. This study played a pivotal role in optimizing the performance of the detector and enhancing its suitability for precision particle physics research.

## Conclusions

During the H8 testbeam, we conducted an extensive investigation into the performance of the SM2, one of the very first Micromegas quadruplets produced in the series. This comprehensive study encompassed multiple aspects, including the operation of the detector in the test beam, calibration of the readout electronics, and the evaluation of the detector's performance under various conditions, with a specific focus on reconstructing clusters and their positions, particularly for inclined tracks.

Prior to delving into the performance analysis, we faced the substantial task of calibrating the over 2000 VMM channels deployed within the setup. This calibration process involved refining parameters like charge thresholds and converting time and charge measurements from ADC counts to physical units. A noteworthy contribution was made to the time calibration, where we explored two distinct methodologies: a data-driven approach and one involving the injection of test pulses into the VMM channels. Ultimately, the results obtained from the data-driven calibration were used for subsequent studies on detector performance and readout system analysis.

Our studies were guided by two primary objectives. The first goal aimed to confirm the functionality of the VMM chip when used on a full-sized Micromegas quadruplet, marking its inaugural imple-

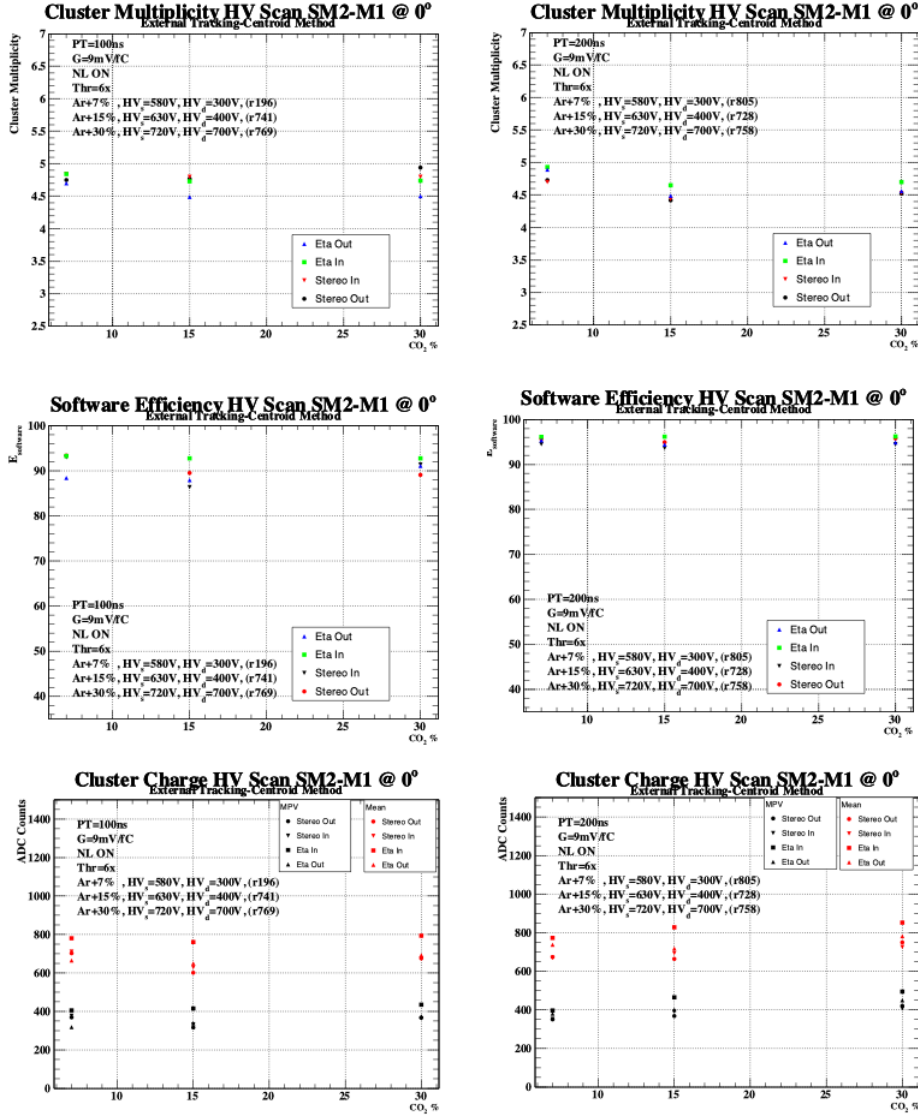


Figure 5.29: The software efficiency, cluster charge and cluster multiplicity for perpendicular tracks at the same gain for the three different gas mixtures are shown. The comparisons were made using a hardware threshold of  $6 \times \sigma$ , neighbor logic ON and two different settings of peak time (100 ns and 200 ns). There is no big difference between these three combinations of Ar + % $CO_2$ .

mentation with the final dimensions. The second objective centered on characterizing the detector's performance, specifically the resolution and reconstruction efficiency for inclined tracks, a scenario relevant to the NSW upgrade.

The studies addressing the first goal were conducted with the SM2 set perpendicular to the beam axis. As anticipated, this configuration yielded a spatial resolution of approximately 100  $\mu m$ , accompanied by a reconstruction efficiency exceeding 90%. These results validated the VMM chip's capability to successfully read out a full-sized Micromegas quadruplet. Subsequent studies with perpendicular tracks targeted the mitigation of HV instabilities within the detectors. Two approaches were pursued:

- **Gas Composition Variation:** We investigated the impact of altering the Argon and  $CO_2$  gas ratio within the operation gas. Increasing the proportion of  $CO_2$  was found to suppress sparks, rendering the detector more reliable. Importantly, both the resolution and reconstruction efficiency remained stable as a function of the  $CO_2$  fraction, affirming the viability of this approach.

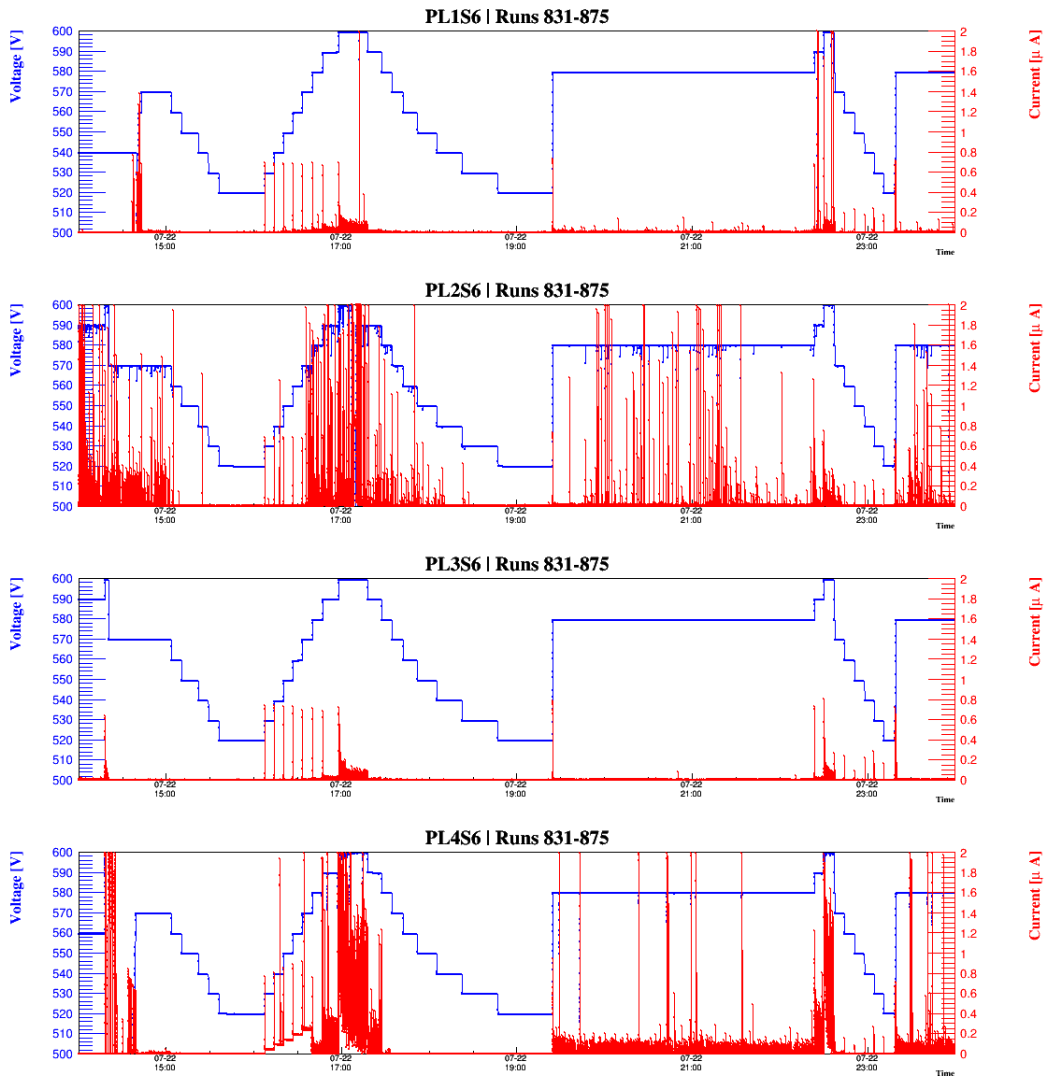


Figure 5.30: The plots show the voltage and current values as a function of the time. Several runs were taken with different voltage levels in order to identify problematic HV sections and apply the corresponding voltage value in order to decrease the spike rate.

- **Voltage Adjustment:** We explored the possibility of reducing the voltage applied to the strips from the initially planned 600 V to 570 V. Although this adjustment resulted in a significant loss of gas gain (as gain and voltage are exponentially correlated), it was established that the lowered voltage validated the reconstruction efficiency for perpendicular tracks, which consistently exceeded 90% for all layers.

In summary, our testbeam endeavors yielded valuable insights and verified the robustness of the SM2 detector, especially in addressing HV instabilities and optimizing its performance for the upcoming particle physics experiments, such as the NSW upgrade. These findings contribute to the ongoing development of advanced detector systems and their critical role in groundbreaking scientific research.



## 5.8.2 GIF++-HV Performance

### Introduction

The GIF++ facility is a dedicated bunker equipped with a  $^{137}\text{Cs}$  source, offering a gamma irradiation field with a prominent energy peak at 667 keV and a total activity of 14 TBq. This facility ensures a consistent supply of gamma irradiation throughout the year, with brief downtimes reserved for essential maintenance tasks.

Spanning an area of  $100\text{ m}^2$  and standing at a height of approximately 5 m, the GIF++ bunker is equipped with two independent irradiation zones, denoted as the upstream and downstream regions (refer to Figure 5.31 for a visual representation). This versatile setup allows for the simultaneous testing of full-size detectors, ranging up to several square meters in size, as well as a diverse range of smaller prototype detectors and electronic components.

The GIF++ irradiator, along with its complex filter systems, is illustrated in Figure 5.31. By employing a set of absorbers, the facility can precisely replicate the radiation environment encountered in the ATLAS experiment, particularly simulating the low-energy  $\gamma$  background. Figure 5.31 provides a visual representation of the GIF++ radiation field, showcasing both the downstream (right) and upstream (left) areas.

The GIF++ facility plays a pivotal role in several key research activities, including the evaluation of Micromegas chambers' behavior when exposed to prolonged radiation and the exploration of novel gas mixtures. Additionally, it serves as an invaluable resource for fundamental activities such as testing the DAQ system and the reconstruction algorithm in a realistic environment.

Furthermore, the CERN SPS H4 beamline complements the facility by delivering a low-intensity muon beam, with a variable size up to 40 cm at  $1\sigma$ . This beam traverses the GIF++ bunker, enabling the measurement of Minimum Ionizing Particles (MIP) in the presence of the  $^{137}\text{Cs}$  background. These combined capabilities make GIF++ a central hub for a wide range of research endeavors, contributing significantly to advancements in detector technology and radiation studies.

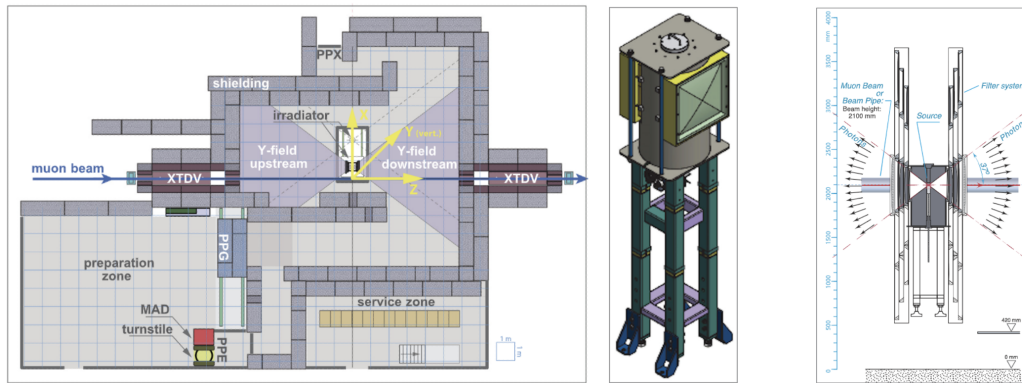


Figure 5.31: Left: Floor plan of the GIF++ facility with entrance doors MAD (material access door), PPG (personal protection gate), PPE (personal protection entrance), PPX (personal protection exit). When the facility downstream of the GIF++ requires electron beam, a beam pipe is installed along the beam line (z-axis) between the vertical mobile beam dump (XTDV). The irradiator can be displaced laterally (its center moves from  $x = 0.65\text{ m}$  to  $2.15\text{ m}$ ), to increase the distance to the beam pipe. Middle: Schematic drawing of the GIF++ irradiator with angular correction filters and independent filter systems at both sides. Right: On both sides a set of independently movable and remotely controlled attenuation filters and collimator frames permits to vary the intensity of emitted photons.

## Scope

The impressive results achieved with the ternary gas mixture, particularly in terms of HV stability under minimal particle background, prompted an extensive set of studies at the GIF++ facility. This facility offers the unique advantage of providing a gamma interaction rate higher than what is anticipated at the ATLAS experiment in the High-Luminosity Large Hadron Collider (HL-LHC). Immediately following the conclusion of the H8 testbeam, the SM2 MM module was subjected to the intense gamma photon flux within the GIF++ environment. Exposure levels reached an interaction rate of  $50 \text{ kHz/cm}^2$ , equivalent to  $2\times$  the anticipated background radiation expected in ATLAS during the HL-LHC phase. Typically, Micromegas chambers are positioned at distances ranging from 1 m to 3 m from the radiation source, where photon flux levels between  $10^6 \text{ cm}^{-2}\text{s}^{-1}$  and  $5 \times 10^7 \text{ cm}^{-2}\text{s}^{-1}$  are anticipated.

The primary objective of these studies was to measure the current generated at the amplification stage in relation to the applied high voltage and incident photon flux. Particular attention was dedicated to identifying current instabilities and spiking effects that could potentially compromise the detector's performance during extended operation within the ATLAS Detector. Our measurements, conducted at a distance of 2 m from the source, accounted for the Micromegas chamber's sensitivity to photons, resulting in an anticipated hit rate of  $40 \text{ kHz/cm}^2$ . This hit rate surpasses the expected conditions during ATLAS High-Luminosity operation by more than 2 times, especially when no filter is employed.

Comprehensive HV ramps were executed to explore the stability of the detector under high background radiation conditions. These studies encompassed the entire HV turning-on curve and extended close to the discharge point. In Figure 5.32, the positioning of the chamber in relation to the GIF++ source is visually represented. The chamber was intentionally exposed across its entire acceptance area within the irradiation cone. Notably, no additional detectors were installed between the SM2 MM module and the radiation source to ensure the uniformity of the radiation field.

This rigorous testing regimen at the GIF++ facility serves as a crucial step in evaluating the Micromegas chamber's resilience and performance under conditions that emulate the challenges expected during the HL-LHC operation in ATLAS. The insights gained from these studies are instrumental in refining and optimizing detector systems for the future of high-energy particle physics research.



Figure 5.32: The SM2 MM module in the GIF++ facility, facing the source.

## Readout System

During the course of the GIF++ testbeam at CERN, a SCADA application was developed to facilitate the precise control and monitoring of HV channels. This advanced application was designed

using the Siemens WinCC-OA software platform and was purpose-built to empower users with comprehensive control and monitoring capabilities, as depicted in Figure 5.33.

The primary objectives of this SCADA HV application were to grant users the ability to:

- **Enable or Disable HV Sections:** Users had the capability to selectively activate or deactivate various HV sections within the experimental setup, providing flexibility and control over the testing conditions.
- **Modify Channel Parameters:** The application allowed users to fine-tune channel parameters as needed, ensuring the HV system could be optimized for the specific requirements of each experiment or test scenario.
- **Data Archiving:** An essential feature of the SCADA application was its ability to archive all relevant data points generated during HV scans and tests. This archival function ensured that a comprehensive dataset was available for subsequent analysis and reference.
- **Data Export:** To further enhance the utility of the application, users could seamlessly export the archived data to files, enabling in-depth analysis and evaluation at a later stage.

Moreover, it's worth noting that an advanced iteration of the SCADA HV application was introduced and elaborated upon in Chapter 4.

This SCADA HV application played a pivotal role in streamlining and enhancing the testing procedures at the GIF++ facility. Its user-friendly interface and robust functionality empowered researchers and technicians to execute precise HV scans, gather critical data, and conduct comprehensive analyses. This level of control and monitoring was instrumental in optimizing the performance of the experimental setup and advancing our understanding of detector behavior under varying HV conditions.

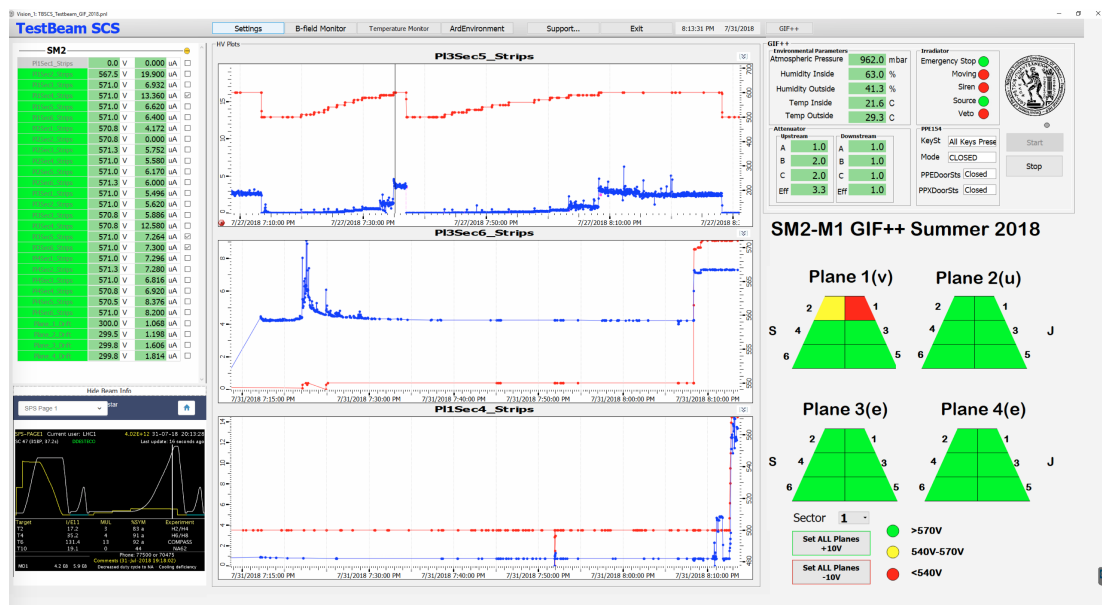


Figure 5.33: The SCADA HV application is used for the GIF++ HV source studies.

Other features of the HV control application was the ability to monitor the various GIF++ parameters and also the SPS beam status. In addition, the users were able to perform massive commands to all the HV sections via the dedicated buttons and also monitor the voltage value using colormaps of predefined limits.

## Studies

The main studies which were performed during the GIF++ testbeam was HV stability as a function of different attenuation levels which correspond to different background radiation levels. The voltage and current behavior were studied extensively by applying different HV parameters and changing the GIF++'s source accordingly in order to acquire the corresponding background radiation level. The acquired HV data were archived and exported by the SCADA HV software and a result is shown in Figure 5.34. The effect of the gamma irradiation background rate can be observed by applying the

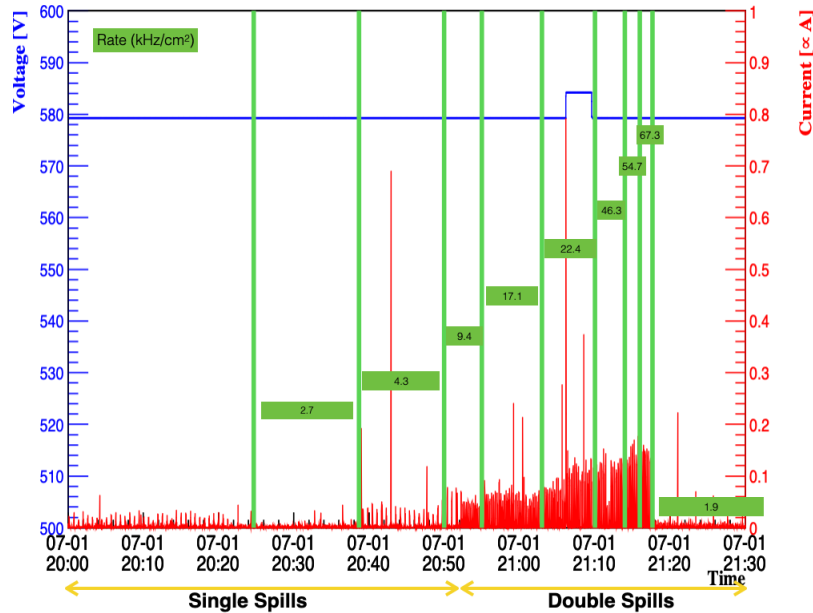


Figure 5.34: The plot contains the gamma irradiation background rate as a function of the applied voltage and the current of the corresponding HV section.

different GIF++'s source attenuation levels. Also, the effect of single/double spills of the SPS beam can be observed.

### 5.8.3 GIF++-Electronics Performance

In the pursuit of advancing our understanding of electronics performance, a carefully designed experimental setup was established. This chapter provides an exhaustive account of the key components and configurations employed in the study, aimed at investigating the response of various detector modules to gamma-ray radiation while simulating conditions relevant to the High-Luminosity Large Hadron Collider (HL-LHC) experiment. This subsection presents extensive tests carried out at the new CERN GIF++ by combining a muon beam (of 100 kHz) with a  $^{137}\text{Cs}$  radiation source of adjustable rate (up to ten times the expected rate at the HL-LHC conditions), to assess the performance of the Micromegas chambers and their readout electronics.

#### Experimental Setup

The experimental apparatus, as shown in Figure 5.35 is composed of several critical components, each serving a distinct role:

- **External Triggers:** Two scintillators were integrated into the setup, serving as external triggers. These scintillators are capable of initiating data collection when exposed to specific radiation events.

- **Gamma-Ray Source:** Central to the experiment is the utilization of a Cesium-137 ( $^{137}\text{Cs}$ ) gamma-ray source. This source emits gamma-ray radiation, essential for the investigation.
- **Muon Beam:** Use of 120 GeV muon beam of 12 kHz provided by H4 beamline.
- **Detector Modules:** Two detector modules, designated as LM2 (Large Upstream Module) and SM1 (Small Downstream Module), are central to the study. These modules, identical to those deployed in the NSW, play a pivotal role in capturing and analyzing radiation data. LM2, positioned in close proximity to the gamma-ray source, is complemented by SM1, situated approximately 1.4 m downstream from LM2. The detector under study (SM1) was mounted perpendicular to the beam direction with a possibility to tilt it up to  $29^\circ$ .
- **BeamLine MicroMegas Detectors (BL):** To facilitate precise tracking and reference measurements, four smaller BeamLine MicroMegas detectors are integrated into the setup. Operating with a ternary gas mixture consisting of  $\text{Ar} + 5\%\text{CO}_2 + 2\%\text{iC}_4\text{H}_{10}$ , these detectors boast an active area measuring  $40 \times 40 \text{ cm}^2$ .

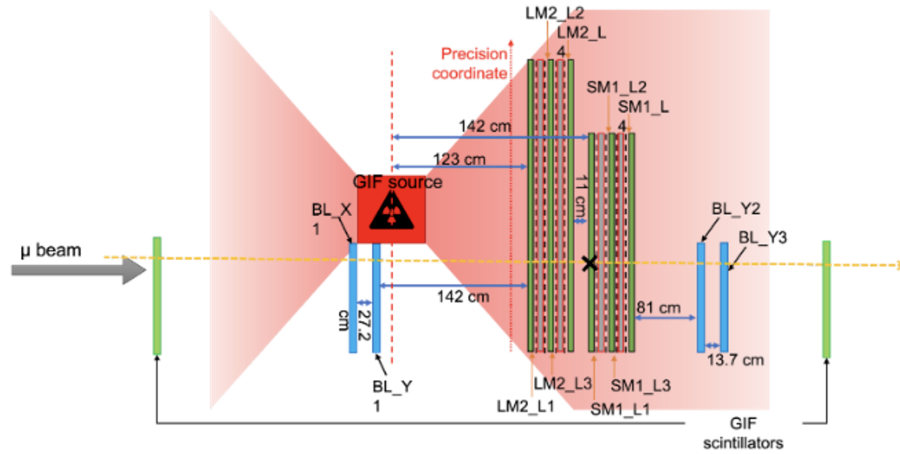


Figure 5.35: The experimental setup at GIF++.

A primary objective of this study is to emulate the conditions expected at the High-Luminosity Large Hadron Collider (HL-LHC). To achieve this, the gamma-ray irradiator at the GIF++ facility is harnessed. By situating the SM1 module approximately 1.4 m from the irradiator (corresponding to a gamma rate of  $25 \text{ kHz/cm}^2$ ), the intensity of gamma radiation can be controlled. This fine-tuning process involves the use of absorbers to align the radiation levels with those anticipated in the HL-LHC environment.

A muon beam is harnessed as a probe particle in this experiment. Its trajectory traverses the entire BL chambers and partially penetrates the SM1 and LM2 modules. Muons are preferred due to their unique penetrating properties and relevance to particle physics investigations. In summation, this designed experimental setup is poised to yield valuable insights into the response of diverse detector modules to gamma-ray radiation.

### Data Acquisition and Control

Data acquisition and event triggering represent critical aspects of this experimental endeavor. To effectively capture and manage data, 20 MMFE8 boards and four Level 1 Data-Driven Trigger Distribution Cards (L1DDCs) are strategically employed. These components facilitate the acquisition of Level 1 (L1) acceptance data. For the SM1 module, the MMFE8 boards were placed on PCBs 2 and 3.



### Time Resolution Studies

In the context of the preceding studies, the focal point of investigation predominantly centered around perpendicular tracks. These tracks have undergone comprehensive testing, particularly with the smaller chambers. Notably, the results from these studies have been corroborated using larger chambers, all while maintaining consistent levels of position reconstruction resolution. However, it is essential to acknowledge that in practical experiments, the detector will predominantly encounter the task of reconstructing particles on inclined tracks. This shift in focus towards inclined tracks introduces a new dimension of complexity. One of the paramount challenges associated with the Micromegas detector pertains to the time response of the individual eta layers. This temporal aspect of detector performance is pivotal in accurately reconstructing the trajectories and properties of particles traveling along inclined tracks. The precise handling of inclined tracks necessitates a comprehensive understanding of the detector's time response characteristics, which is a key area of interest in our research. The time resolution of the Micromegas detector was rigorously assessed in our experimental setup, focusing on runs with particles traveling at a  $30^\circ$  angle to the detector's surface. To achieve this evaluation, we employed back-to-back clusters of the SM1 eta layers, a configuration that simulated inclined particle tracks, as shown in Figure 5.36. In this assessment, particular emphasis was placed on precision, with an approach that involved selecting the closest strips within the cluster. This analysis allowed us to gain valuable insights into the detector's time response under conditions representative of practical particle trajectories, enhancing our understanding of its performance in scenarios where inclined tracks play a significant role.

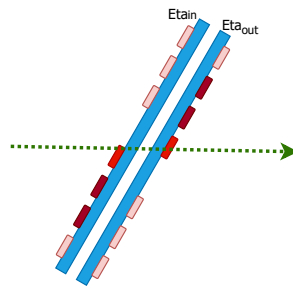


Figure 5.36: Time resolution evaluated from  $30^\circ$  runs using back-to-back clusters of the SM1 eta layers.

### Preliminary Steps

As described in the previous section 5.7, the preliminary steps is the position reconstruction using the charge centroid method.

### Calibration

In our experimental setup, the time detector plays a crucial role in measuring precise timing information. This detector utilizes a time-to-amplitude converter (TAC), which incorporates a voltage ramp that initiates either at the point of threshold-crossing or at the time-of-the-peak signal. The ramp then proceeds until the occurrence of the next BC (Bunch Crossing). This method allows us to capture accurate timing data with high fidelity.

To ensure the accuracy of our measurements, we implement TDO calibration on a channel-by-channel basis. This calibration process is essential for fine-tuning the strip time measurements specific to each channel. Additionally, a global alignment of general  $t_0$  is required across all channels. Proper calibration not only guarantees precision but is also instrumental in achieving enhanced time resolution, a vital factor for improving  $\mu$ TPC reconstruction performance.



The time calculation is based on the following formula:

$$t(\text{ns}) = \text{relBCID} \times 25\text{ns} - \frac{\text{tdo} - \text{intercept}}{\text{slope}} \quad (5.32)$$

Breakdown of the components in the equation:

- **relBCID:** This parameter represents a relative BCID (Bunch Crossing ID) value, which is multiplied by 25 ns. The BCID is crucial for timing calculations and ensures that the time measurement is synchronized with the beam's properties.
- **tdo-intercept:** The tdo-intercept is extracted from the TDO calibration process and accounts for any inherent offset or delay in the timing measurements. It is subtracted from the BCID-based time calculation.
- **slope:** The slope represents the rate of change of voltage with respect to the time. It is a critical factor for accurately translating BCID values into time measurements.

In order to calculate the *slope* and *intercept* parameters we apply a Double Fermi-Dirac fit on the distribution of the TDO for each VMM's channel. The Double Fermi-Dirac equation is:

$$f_{fd} = \left( \frac{p_0}{1 + e^{-\frac{x-p_1}{p_2}}} \right) \cdot \left( \frac{1}{1 + e^{\frac{x-p_4}{p_5}}} \right) + p_3 \quad (5.33)$$

where  $p_1 = \text{intercept}$  and  $\frac{p_4 - p_1}{25\text{ns}} = \text{slope}$ .

In summary, the calibration procedures and mathematical fits described above are integral to our experimental setup, ensuring accurate timing measurements and robust data analysis for our research endeavors. The result of the TDO channel calibration using the Double Fermi Dirac procedure can be seen on Figure 5.37.

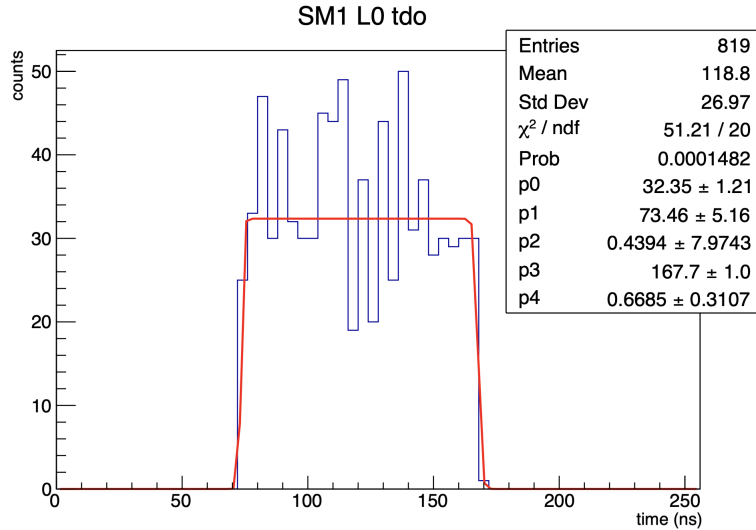


Figure 5.37: Calibration of the VMM's channels TDO using double Fermi-Dirac.

## Studies

In our experimental investigations conducted at 30° angle, we focus on extracting precise timing information from consecutive clusters within the SM1 eta layers. This approach allows us to delve deep into the temporal dynamics of our data.

Our process initiates with the selection of the calibration timing from the nearest strips within these clusters for each individual eta layer. This selection ensures that we are working with highly accurate and representative data points. To perform the timing calculations, we follow a well-defined procedure detailed in Section 5.8.3.

Subsequently, we compute the time residual, which quantifies the timing difference between the eta layers. This information serves as a fundamental aspect of our investigation, shedding light on how signals propagate within our experimental setup and providing crucial insights into the underlying physical processes.

To comprehensively characterize the timing behavior, we construct a time distribution based on these time residuals. This distribution encapsulates the full spectrum of temporal characteristics within our experiment.

To analyze this distribution effectively, we employ a bi-Gaussian fit, a robust statistical method. This fitting approach enables us to model the distribution accurately, extracting essential parameters that describes its shape, central tendencies, and any deviations from the expected behavior.

One of the vital metrics derived from this analysis is the time resolution. To quantify this resolution accurately, we normalize the sigma (standard deviation) of the time residual distribution by dividing it by the square root of 2. This normalization process ensures that our time resolution represents the accurate precision of our timing measurements.

For a visual representation of our findings and the calculated time resolution, please refer to Figure 5.38. This figure provides a visual summary of our analysis, aiding in the interpretation of our results and their significance.

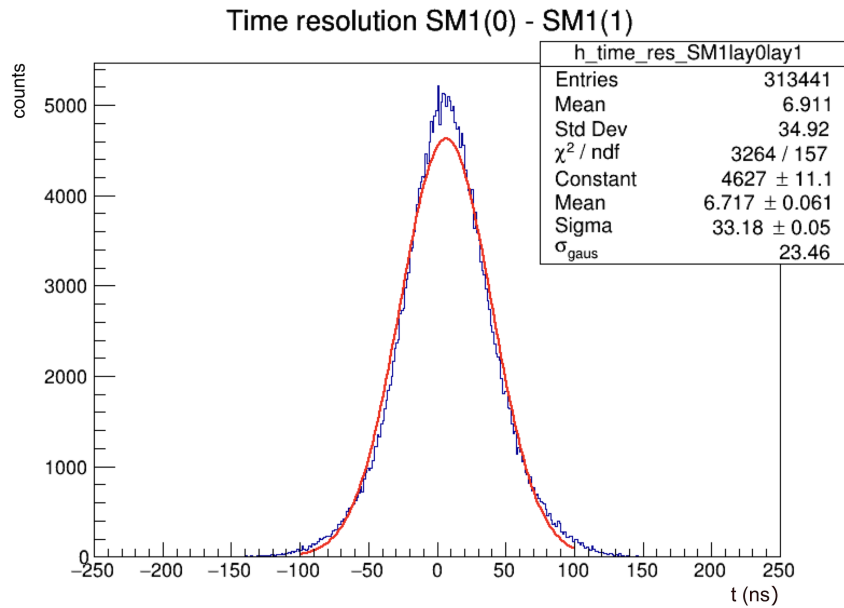


Figure 5.38: The time resolution of the SM1 detector using the back-to-back cluster of the nearest strips. The time resolution is the distribution's sigma by  $\sqrt{2}$ .

Now that we have obtained precise timing resolution, we are well-prepared to embark on a comprehensive exploration of various studies, each grounded in distinct case scenarios. These concluded studies, as well as their detailed explanations, will be presented in the upcoming sections. The full list of the studies is:

- **HV Drift**
- **Attenuation**
- **Attenuation versus Peaking Time**
- **Threshold versus Peaking Time**
- **HV Drift versus Peaking Time**
- **Threshold versus HV Strips versus Peaking Time**

### HV Drift Scan

In this particular study, we have explored the impact of varying HV values on the SM1's drift. Our observations indicate that a lower drift voltage of 250 V, in comparison to 300 V yields notably improved time resolution, as clearly demonstrated in Figure 5.39.

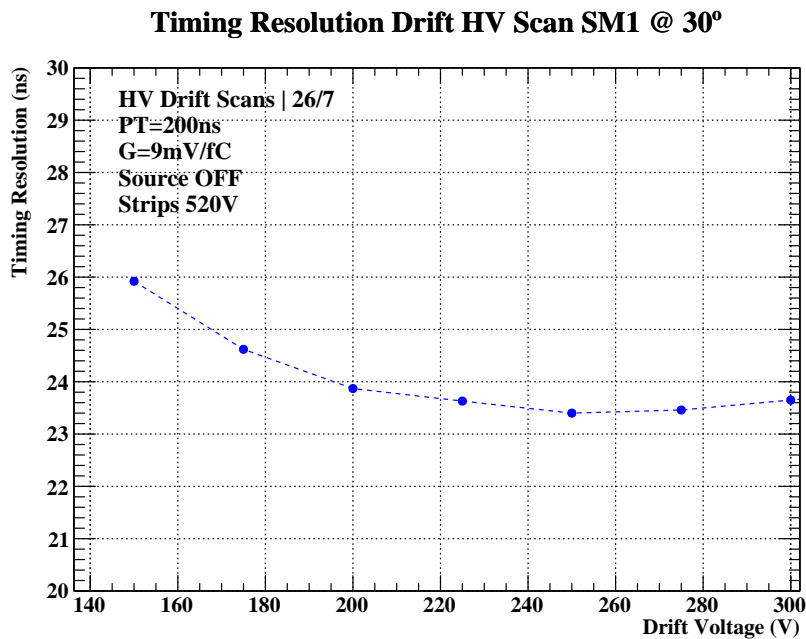


Figure 5.39: Timing resolution as a function of the Drift HV. A lower drift voltage of 250 V, in comparison to 300 V yields notably improved time resolution

### Attenuation Scan

In our next study, we investigated the influence of background radiation on timing resolution. This investigation involved the manipulation of the GIF's attenuation filter settings. Our observations revealed that the timing resolution distribution was significantly impacted, particularly for values close to the HL (High Luminosity) rate. This effect stemmed from erroneous cluster reconstruction, attributed to the heightened gamma irradiation. These findings are visually represented in Figure 5.40. For the tests, we kept the Strips HV to 530 V and Drift HV to 300 V.

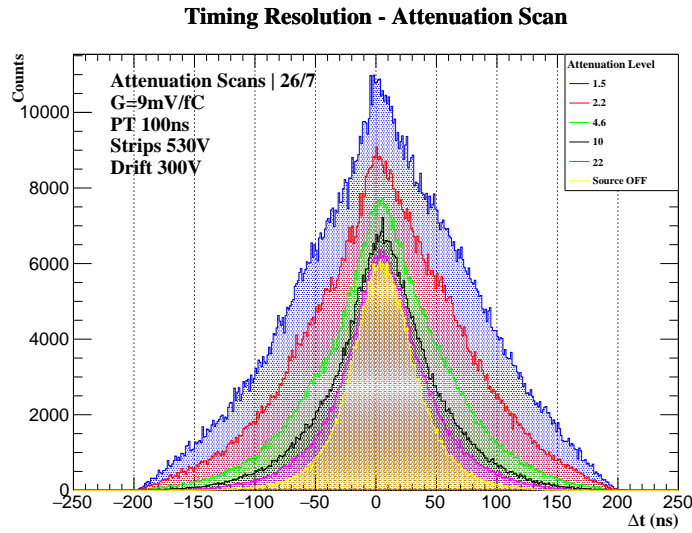


Figure 5.40: Timing resolution distribution was significantly impacted by high attenuation factors. This effect is a result from erroneous cluster reconstruction, attributed to the heightened gamma irradiation.

### Attenuation-Peaking Time Scan

Furthermore, we conducted an investigation into the influence of the VMM's Peaking Time (PT) parameters in relation to the attenuation level. Our observations revealed that a PT value of 100 ns leads to a substantial amplification in strip time measurement precision. These findings are graphically depicted in Figure 5.41. For the tests, we kept the Strips HV to 530 V, gain of 9 mV/fC and Drift HV to 300 V.

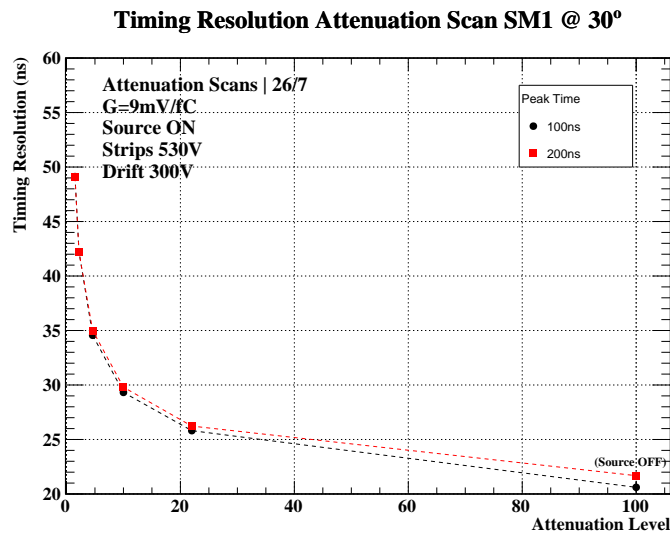


Figure 5.41: Attenuation-Peaking time scan which indicated that a PT value of 100 ns leads to a substantial amplification in timing measurement precision.

### Threshold-Peaking Time Scan

In this study, we calculated the effect of the VMM's threshold level to the timing resolution for two different values of the PT. Our observations revealed that a PT value of 100 ns leads to a substantial

amplification in strip time measurement precision. These findings are graphically depicted in Figure 5.42. For the tests, we kept the Strips HV to 530 V, gain of 9 mV/fC and Drift HV to 250 V.

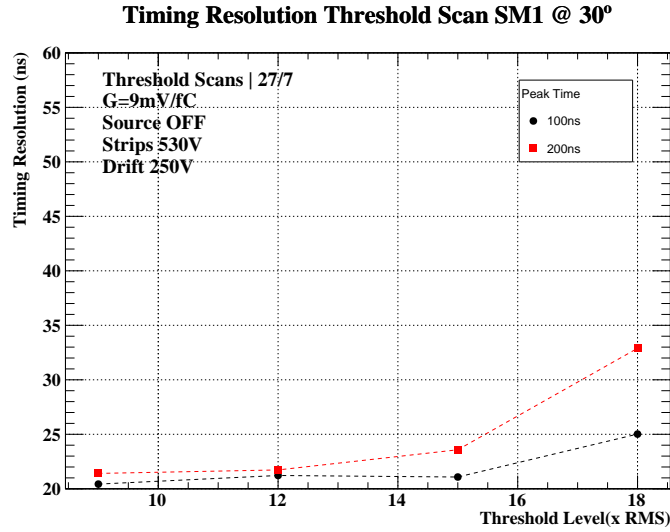


Figure 5.42: Threshold-Peaking time scan which indicated that a PT value of 100 ns leads to a substantial amplification in timing measurement precision.

### HV Drift-Peaking Time Scan

For the purpose of this study, we calculated the timing resolution while varying the Drift HV against two different values of PT. Our observations unveiled that a PT value of 100 ns substantially elevates the precision of strip time measurements. These significant findings have been visually depicted in Figure 5.43. Throughout these tests, we maintained the Strips HV at a constant of 530 V and a gain of 9 mV/fC, ensuring a consistent testing environment.

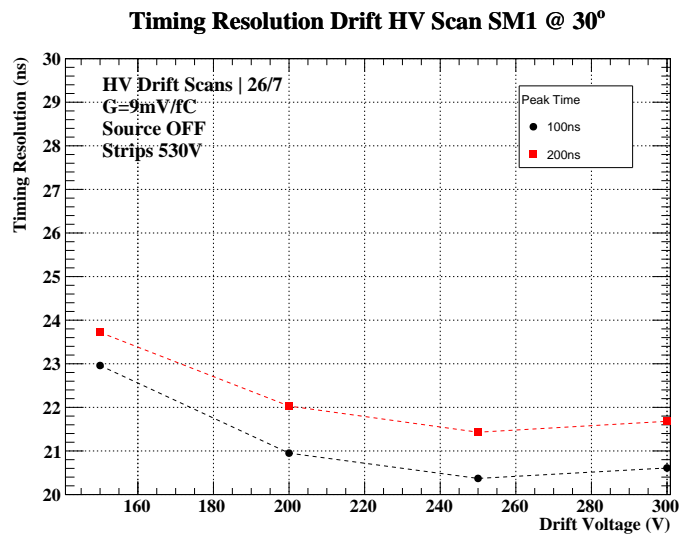


Figure 5.43: HV Drift-Peaking Time scan showing that a PT value of 100 ns substantially elevates the precision of timing measurements.

### Threshold-HV Strips-Peaking Time Scan

In our final study, we conducted an assessment of timing resolution while systematically adjusting the Strips HV across various Threshold levels, considering two different PT values. Our observations revealed a notable amplification in timing resolution with higher Strips HV settings, indicating an amplified gain within the amplification gap.

Furthermore, in a separate investigation, we arrived at a compelling conclusion that a PT value of 100 ns significantly enhances the precision of strip time measurements. These noteworthy findings have been vividly represented in Figure 5.44.

Throughout these comprehensive tests, we maintained the Drift HV at a consistent level of 250 V and ensured a constant gain of 9 mV/fC, thereby guaranteeing a reliable and standardized testing environment.

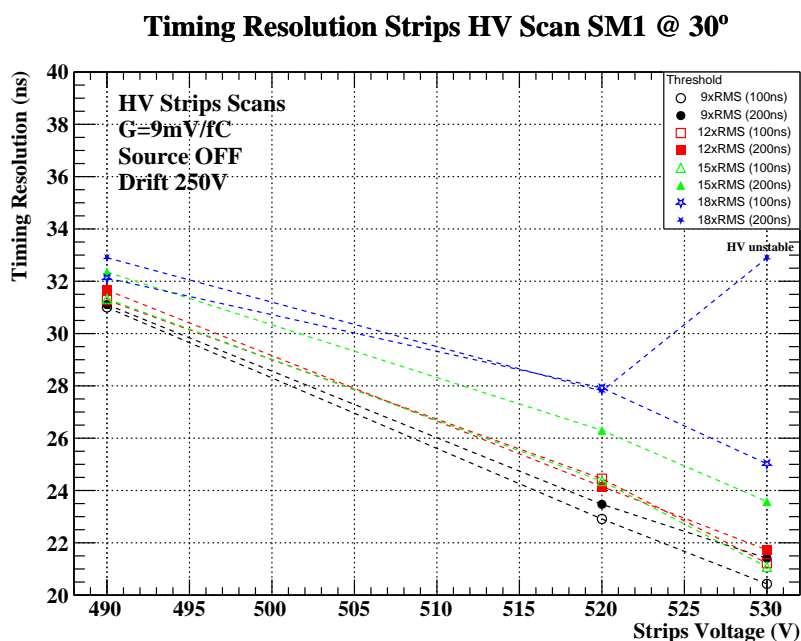


Figure 5.44: Threshold-HV Strips-Peaking Time scan which shows that higher Strips HV indicates a gain within the amplification gap and as a result a better timing resolution. In addition, a PT value of 100 ns enhances the precision of timing measurements.



## 5.9 Conclusions

The evaluation of the SM2 MM module's performance during the H8 testbeam at CERN has illuminated several critical insights and advancements. This exploration, a cornerstone of the ATLAS project's NSW upgrade, has not only demonstrated the quadruplet's capabilities but also highlighted challenges and areas for amplification. Our comprehensive analysis affirmed the robustness of the Micromegas detector technology, showcasing its suitability for high-precision tracking in the demanding environment of the ATLAS experiment. Through the rigorous calibration of over 2000 VMM channels, we achieved significant improvements in signal fidelity and detector responsiveness. Addressing HV instabilities by optimizing the gas mixtures led to a marked reduction in operational anomalies, enhancing the stability and reliability of the detector system. Moreover, the evaluation of efficiency metrics in both external and self-tracking modes, under various gas mixture conditions, provided invaluable data to refine our understanding of the detector's operational parameters and performance limits. The findings from this evaluation carry profound implications for the NSW upgrade and the broader ATLAS project. The demonstrated reliability and efficiency of the SM2 MM module underpin its potential to significantly enhance the experiment's tracking and detection capabilities. This, in turn, will contribute to the ATLAS experiment's overarching goal of delving deeper into the mysteries of the universe, from the Higgs boson's behavior to the elusive dark matter. Furthermore, the challenges and solutions identified through this process offer critical lessons for future detector development and optimization. The insights into gas mixture optimization and HV stability, in particular, provide a valuable framework for enhancing detector performance and operational stability in similar high-energy physics applications.

While this evaluation has provided substantial advancements, it beckons further exploration in several areas. Continued refinement of the calibration processes and gas mixture compositions will be essential to harnessing the full potential of the Micromegas detectors. Additionally, exploring the integration of advanced computational models and machine learning algorithms for real-time data analysis could unlock new efficiencies and capabilities. Finally, extending this evaluation framework to other detector technologies within the ATLAS experiment could foster a more holistic understanding of the system's performance and potential areas for synergy.

The evaluation of the SM2 MM module within the H8 testbeam at CERN represents a significant milestone in the quest for greater understanding through the ATLAS experiment. It embodies the relentless pursuit of precision and reliability that characterizes the field of particle physics. As we move forward, the lessons learned and the knowledge gained from this endeavor will undoubtedly contribute to shaping the future of high-energy physics research, driving us closer to unraveling the fundamental truths of our universe.

## 5.10 Contributions

During the test beam periods, which took place at CERN, prototype Micromegas detectors were exposed to muon and pion beams, which tested their proper functioning in conjunction with the VMM unit. The doctoral candidate:

- Actively participated in all test periods at CERN and developed suitable tools for real-time problem detection during data acquisition.
- Participated in data acquisition and the implementation and calibration of the detection process.

- Developed algorithms for the clusterization of vertical tracks.
- Studied and developed tools for examining the spatial resolution and performance (Software Efficiency) of the detector by analyzing vertical tracks under different conditions such as gas, high voltage, and parameters of the VMM unit.

With the completion of the integration of electronics in all the chambers of the New Small Wheel and the installation of the wheels in ATLAS, a series of tests began for the first time using muon beams and/or radioactive sources to characterize the response of the detector and its finally designed electronics in a background environment comparable to what will be imposed during the upcoming years of the accelerator's operation. The doctoral candidate:

- Actively participated in all test periods at CERN and developed suitable tools for real-time problem detection during data acquisition.
- Participated in data acquisition and the implementation and calibration of the detection process.
- Optimized and accelerated the data acquisition rate of the data acquisition system.
- Studied and developed tools for examining the timing resolution of the detector by analyzing vertical tracks under different conditions such as gas, high voltage, and parameters of the VMM unit.
- Developed algorithms for optimizing the parallel processing of multiple data and the creation of graphs with summary results.

In addition, the doctoral candidate contributed to the following paper:

- **“Long term irradiation studies and performance assessment of the ATLAS Micromegas detectors at the Gamma Irradiation Facility at CERN”**  
DOI: to be published within 2024

---

# Conclusions

---

This dissertation represents a major achievement in the journey to unravel the mysteries of the universe through experimental particle physics. My focus was on developing the Detector Control System (DCS), Data Acquisition System (DAQ) for the New Small Wheel (NSW) Upgrade in the ATLAS experiment at CERN, alongside a Performance Evaluation of the Micromegas detectors. Our team made significant progress both theoretically and practically in this area. Notably, my work was awarded on 2022 by the ATLAS experiment at CERN with the **ATLAS Outstanding Achievement Award** for outstanding contributions to the completion of the NSW integration and surface commissioning within the LS2 schedule.

In the opening chapter, I provided an overview of the Large Hadron Collider (LHC) and the ATLAS experiment, showing how these projects are revolutionizing our understanding of fundamental physics. I explored the different subsystems of the ATLAS experiment to illustrate how advanced technologies and collaboration are driving leading-edge research in particle physics. The dissertation then in Chapter 2 emphasizes into the NSW Upgrade Project, detailing the technical challenges and innovative solutions needed for high-luminosity experiments at the LHC. Through careful integration and collaboration, we tackled these challenges, pushing the boundaries of detector technology and enabling new discoveries.

In Chapter 3, I offered insights into the complex electronics of the NSW and its DAQ system. I discussed the importance of effective data flow management and system interoperability, highlighting the engineering and planning that were crucial for the project's success.

Chapter 4 focused on the critical role of the DCS in the ATLAS experiment, emphasizing its importance in maintaining detector functionality and safety. By introducing new gas-tightness stations and detailing control systems and hardware connections, I provided a comprehensive understanding of the sophisticated systems essential for particle physics experiments. Chapter 5 provided an analysis of the performance of Micromegas detectors, examining their efficiency and operational parameters under different conditions. I looked into calibration processes, high voltage stability, and efficiency optimization, demonstrating our commitment to improving detector technologies and enhancing experimental capabilities.

Looking ahead for future perspectives, this dissertation aims to serve as a guide for the Phase-2 Upgrade programs of LHC experiments, moving us towards the High-Luminosity LHC (HL-LHC). I hope that future researchers will find the knowledge and insights here useful for advancing their work in upgrading DCS and DAQ systems, developing new prototypes, and optimizing detector efficiency.

In essence, this dissertation is a significant contribution to the field of particle physics and a testament

to the power of collaborative scientific inquiry. As we continue our journey to unravel the universe's mysteries, I believe this work will serve as a cornerstone, guiding and inspiring future generations of researchers.



# Appendix A

---

## Acronyms

---

**ADC:** Analog to Digital Converter  
**ADDC:** ART Data Driver Card  
**ALICE:** A Large Ion Collider Experiment  
**ALTI:** ATLAS Local Trigger Interface  
**ART:** Address in Real Time  
**ASIC:** Application Specific Integrated Circuit  
**ATCA:** Advanced Telecommunications Computing Architecture  
**ATCN:** ATLAS Technical Network  
**BC:** Bunch Crossing  
**BCR:** Bunch Crossing Counter Reset  
**BE:** Back End  
**BCID:** Bunch Crossing Identification  
**BIS:** Beam Interlock System  
**BGA:** Ball Grid Array  
**BNL:** Brookhaven National Laboratory  
**CERN:** Conseil Européen pour la Recherche Nucleaire, or European Organization for Nuclear Research  
**CI:** Continuous Integration  
**CD:** Continuous Development  
**CU:** Control Unit  
**CDR:** Clock and Data Recovery  
**CKBC:** BunchCrossing Clock  
**CMS:** Compact Muon Solenoid  
**CPU:** Central Processing Unit  
**CMS:** Compact Muon Solenoid  
**CSC:** Cathode Strip Chamber  
**CTF:** Clock and Trigger Fanout  
**CTP:** Central Trigger Processor  
**DAC:** Digital to Analog Converter

**DAQ:** Data AcQuisition  
**DCS:** Detector Control System  
**DICE:** Dual Interlocked Cells  
**DSS:** Detector Safety System  
**DP:** DataPoint  
**DPA:** DataPoint Attribute  
**DPE:** DataPoint Element  
**DPT:** DataPoint Type  
**DU:** Device Unit  
**ECR:** Event Counter Reset  
**EF:** Event Filter  
**ELMB:** Embedded Local Monitoring Board  
**EM:** Electromagnetic Calorimeter  
**EOF:** End of Frame  
**FCS:** Frame Check Sequence  
**FEB:** Front-End Board  
**FEC:** Forward Error Correction  
**FELIX:** FrontEnd LInk eXchange  
**FID:** FELIX Identifier  
**FIFO:** FirstIn FirstOut  
**FMC:** FPGA Mezzanine Board  
**FPGA:** FieldProgrammable Gate Array  
**FRL:** Flow Rate Loss  
**FSM:** Finite State Machine  
**GBLD:** GigaBit Laser Driver  
**GBT:** GigaBit Transceiver  
**GBTIA:** GigaBit TransImpedance amplifier  
**GBT-SCA:** GigaBit Transceiver Slow Control Adapter  
**GCS:** Global Control Station  
**GEDI:** Graphic Editor  
**GPN:** General Purpose Network  
**GUI:** Graphical User Interface  
**GTS:** Gas Tightness Station  
**GUI:** Graphical User Interface  
**HDLC:** HighLevel Data Link Control  
**HDL:** Hardware Description Language  
**HLT:** HighLevel Trigger  
**HL-LHC:** High-Lumi LHC  
**HV:** High Voltage  
**I/O:** Input/Output  
**IP:** Intellectual Property / Internet Protocol /Interaction Point  
**IPv4:** Internet Protocol version 4  
**JCOP:** Joint COntrols Project  
**JTAG:** Joint Test Action Group  
**JSON:** JavaScript Object Notation  
**LAN:** Local Area Network  
**LAr:** Liquid Argon  
**LCS:** Local Control Station  
**LHC:** Large Hadron Collider



**L0(A):** Level0 (Accept)  
**L1(A):** Level1 (Accept)  
**L1DDC:** Level1 Data Driver Card  
**LS1/2/3:** Long Shutdown 1/2/3  
**LSB:** Least Significant Bit (Byte)  
**LU:** Logical Unit  
**LUT:** LookUp Table  
**LV:** Low Voltage  
**LVDS:** Low Voltage Differential Signaling  
**MAC:** Media Access Control  
**MBU:** Multi-Bit Upsets  
**miniSAS:** mini Serial Attached SCSI  
**MO:** Monitor Output  
**MDT:** Monitored Drift Tube  
**Micromegas (MM):** Micromesh Gaseous Structure  
**MMG:** Micromegas  
**MMFE:** Micromegas FrontEnd  
**MS:** Muon Spectrometer)  
**MSB:** Most Significant Bit (Byte)  
**NIM:** Nuclear Instrumentation Modules  
**NSW:** New Small Wheel  
**OCR:** Orbit Count Reset  
**OKS:** Object Kernel Support  
**OPC:** Open Platform Communications  
**PCIe:** Peripheral Component Interconnect Express  
**PDO:** Peak Detector Output  
**PDR:** Pressure Drop Rate  
**PMT:** Photo Multiplier Tube  
**PFEB:** Pad Front End Board  
**PS:** Proton Synchrotron  
**PSB:** Proton Synchrotron Booster  
**QA&QC:** Quality assurance/quality control  
**R&D:** Research and Development  
**ROD:** Read Out Driver  
**ROI:** Region Of Interest  
**RAM:** Random Access Memory  
**RMS:** Root Mean Square  
**ROC:** ReadOut Controller ROM ReadOnly Memory  
**RPC:** Resistive Plate Chamber  
**SCA:** Slow Control Adapter  
**SCAX:** Slow Control Adapter eXtension  
**SFEB:** Strips Front End Board  
**RPC:** Resistive Plate Chamber  
**SC:** Slow Control  
**SCADA:** Supervisory Control and Data Acquisition  
**SCT:** Semi Conductor Tracker  
**SEU:** Single Event Upset  
**SL:** Sector Logic  
**SM:** Small Module

**SOF:** Start of Frame  
**SPI:** Serial Peripheral Interface  
**SPS:** Super Proton Synchrotron  
**SR:** Soft Reset  
**SSH:** Secure Shell  
**STG:** smallstrip Thin Gap Chamber  
**sTGC:** smallstrip Thin Gap Chamber  
**SW:** Small Wheel  
**swROD:** Software ReadOut Driver  
**TAC:** Time to Amplitude Converter  
**TCP:** Transmission Control Protocol  
**TDAQ:** Trigger and Data Acquisition System  
**TDO:** Time Detector Output  
**TDS:** Trigger Data Serializer  
**TGC:** Thin Gap Chamber  
**ToT:** Time over Threshold  
**TMR:** Triple Modular Redundancy  
**TP:** Trigger Processor / Trigger Path / Test Pulse  
**μTPC:** micro Time Projection Chamber  
**TRT:** Transition Radiation Tracker  
**TRT:** Transition Radiation Tracker  
**TTC:** Trigger Timing and Control  
**TTL:** TransistorTransistor Logic  
**UDP:** User Datagram Protocol  
**USA15:** Underground Service Area 15  
**US15:** Underground Service 15  
**VERSO:** VMM Readout System Ethernet Readout Software  
**VHDL:** Very High Speed Integrated Circuit Hardware Description Language  
**VME:** Versa Module Europa  
**VTRx:** Versatile optical Transceiver  
**VTTx:** Versatile optical Transmitter  
**XML:** Extensible Markup Language

# Appendix B

## NSW boards SCA Connections

This appendix includes the SCA connection schematics of all the NSW electronics boards.

### MMFE8

The SCA connections of the MMFE8 board is shown on the design schematic of Figure B.1.

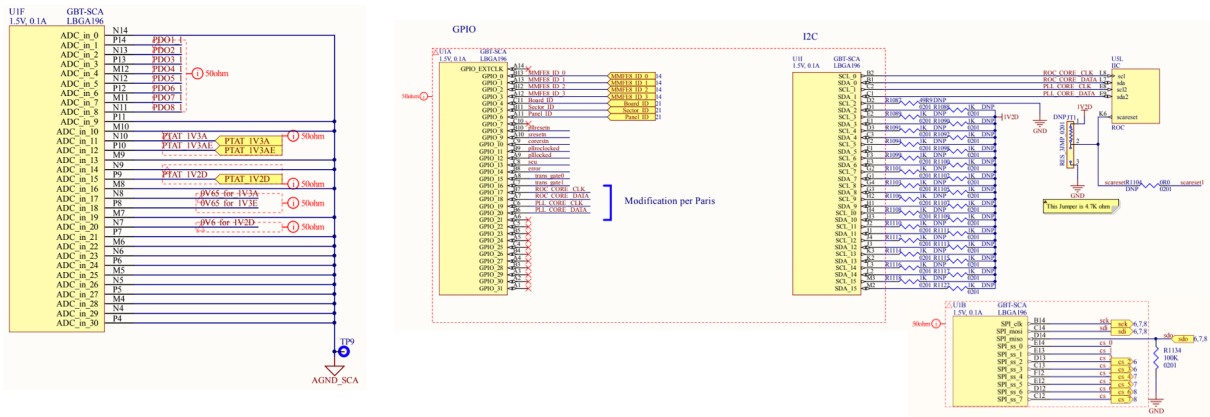


Figure B.1: SCA connections of the MMFE8 board.

### SFEB

The SCA connections of the SFEB board is shown on the design schematic of Figure B.2.

### PFEB

The SCA connections of the PFEB board is shown on the design schematic of Figure B.3.

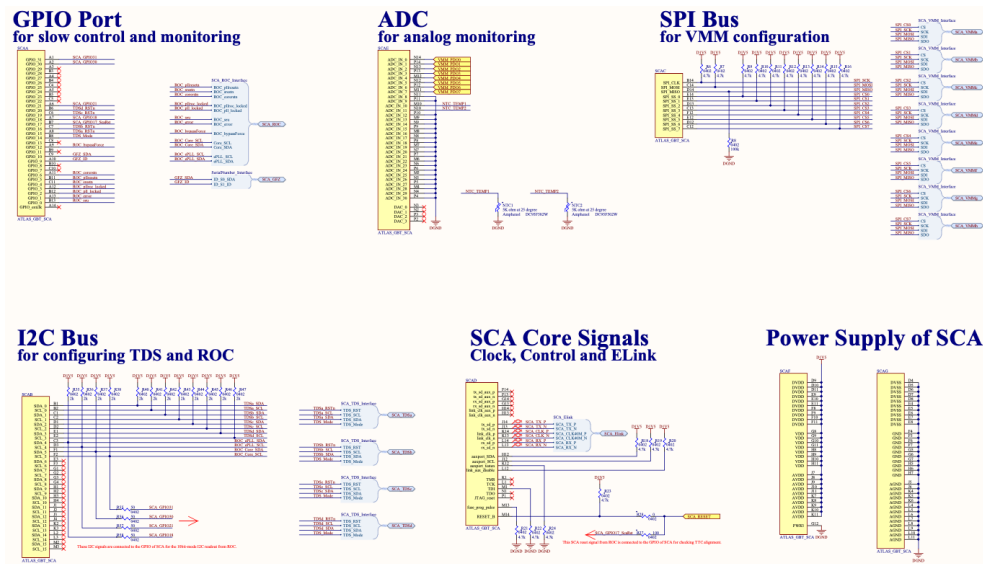


Figure B.2: SCA connections of the SFEB board.

## ADDC

The SCA connections of the ADDC board is shown on the design schematic of Figure B.4.

## L1DDC-MMG

The SCA connections of the L1DDC-MMG board is shown on the design schematic of Figure B.5.

## L1DDC-STG

The SCA connections of the L1DDC-STG board is shown on the design schematic of Figure B.6.

## Rim L1DDC

The SCA connections of the Rim L1DDC board is shown on the design schematic of Figure B.7.

## Pad Trigger

The SCA connections of the Pad Trigger board is shown on the design schematic of Figure B.8.

## Router

The SCA connections of the Router board is shown on the design schematic of Figure B.9.

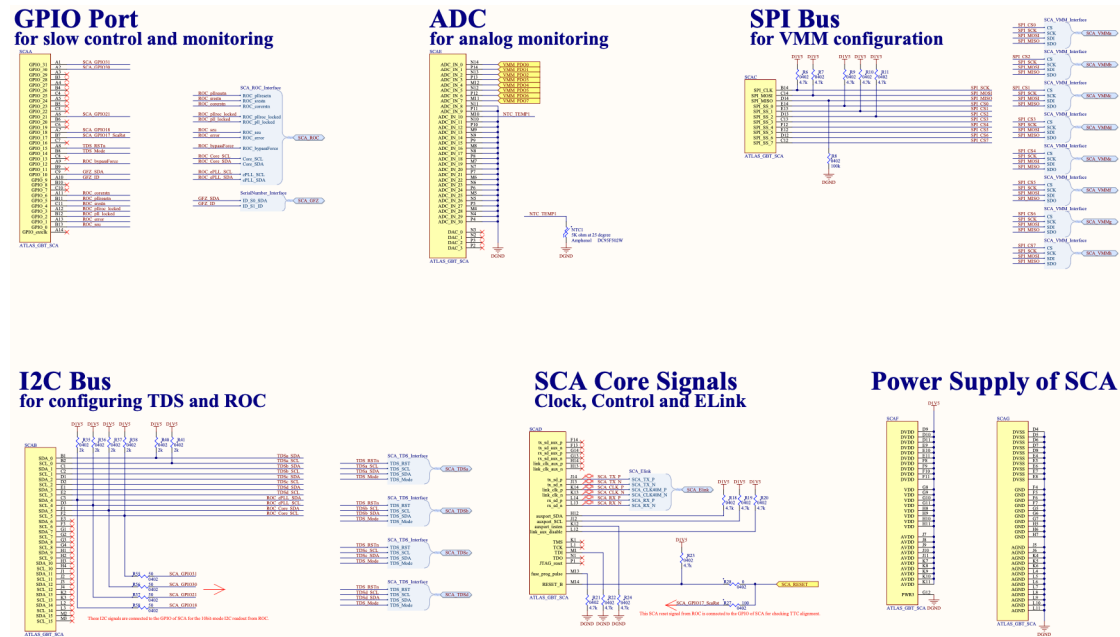


Figure B.3: SCA connections of the PFEB board.

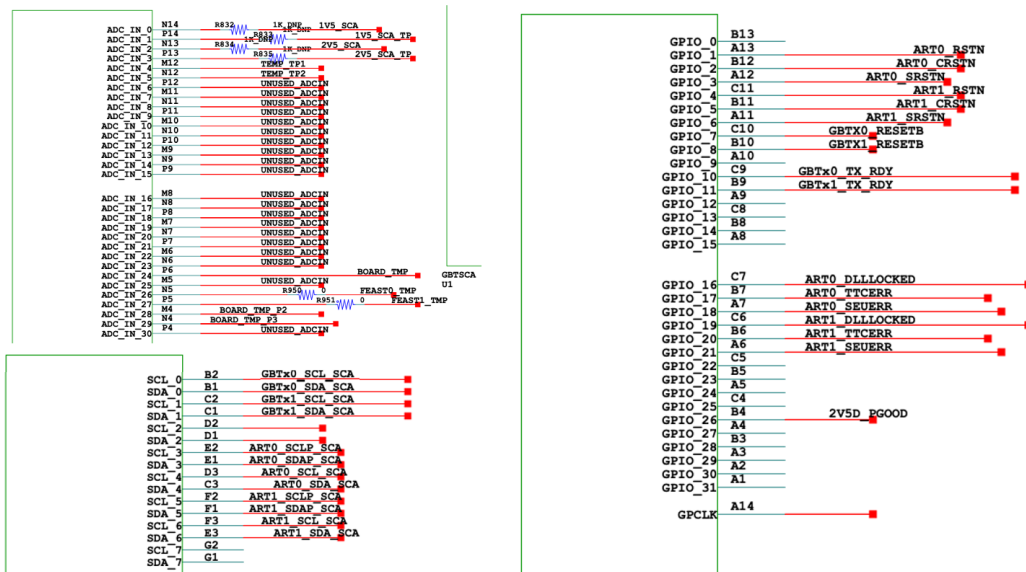


Figure B.4: SCA connections of the ADDC board.

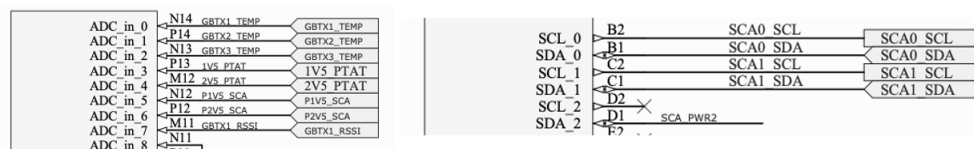


Figure B.5: SCA connections of the L1DDC-MMG board.

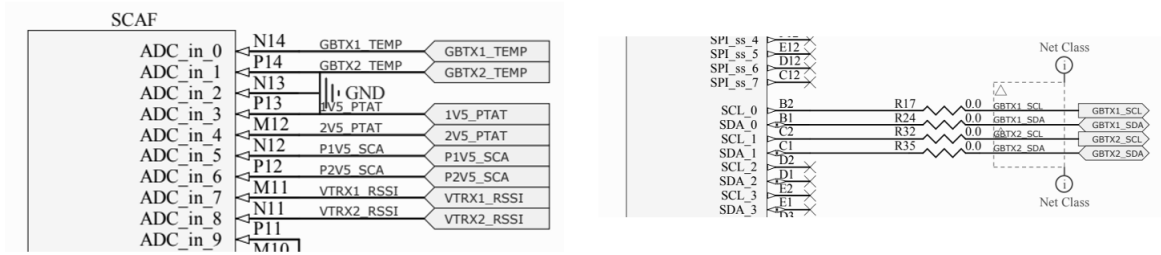


Figure B.6: SCA connections of the L1DDC-STG board.

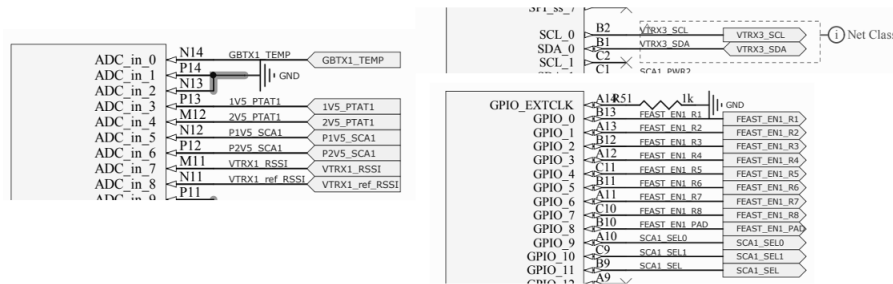


Figure B.7: SCA connections of the Rim L1DDC board.

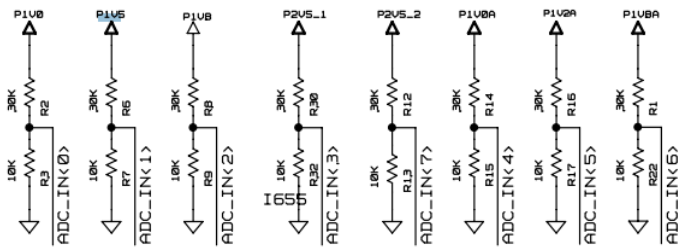


Figure B.8: SCA connections of the Pad Trigger board.

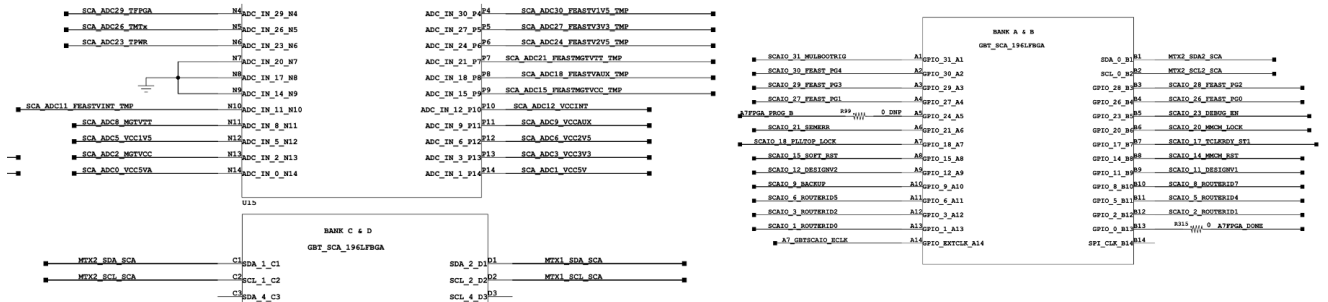


Figure B.9: SCA connections of the Router board.



# Appendix C

---

## SCA OPC UA Codes

---

### OKS example

A concrete example of an SCA object in OKS implementation for the L1DDC board is provided below:

```
<obj class="SwRodInputLink" id="ELink-sTGC-A/V0/from-SCA/L1DDC/S0/L0/P">
  <attr name="FelixId" type="u64" val="0x16d1500001bf0000"/>
  <attr name="DetectorResourceId" type="u32" val="0x6d070000"/>
  <attr name="DetectorResourceName" type="string"
    ↪ val="sTGC-A/V0/from-SCA/L1DDC/S0/L0/P"/>
</obj>
<obj class="SwRodInputLink" id="ELink-sTGC-A/V0/to-SCA/L1DDC/S0/L0/P">
  <attr name="FelixId" type="u64" val="0x16d1500001bf8000"/>
  <attr name="DetectorResourceId" type="u32" val="0x6d050000"/>
  <attr name="DetectorResourceName" type="string"
    ↪ val="sTGC-A/V0/to-SCA/L1DDC/S0/L0/P"/>
</obj>
```

### L1DDC-MMG SCA OPC UA server template

For example, the SCA OPC UA server template of the L1DDC-MMG is shown below:

```
<AnalogInputSystem generalRefreshRate="0.2" name="ai">
  <AnalogInput id="0" name="GBTX1_TEMP" enableCurrentSource="true" >
  <CalculatedVariable name="temperature"
    ↪ value="$applyGenericFormula(thermistorTemperature)" />
  </AnalogInput>
  <AnalogInput id="1" name="GBTX2_TEMP" enableCurrentSource="true" >
```

```

<CalculatedVariable name="temperature"
  ↪ value="$applyGenericFormula(thermistorTemperature)" />
</AnalogInput>
<AnalogInput id="2" name="GBTX3_TEMP" enableCurrentSource="true" >
<CalculatedVariable name="temperature"
  ↪ value="$applyGenericFormula(thermistorTemperature)" />
</AnalogInput>
<AnalogInput id="3" name="1V5_PTAT">
<CalculatedVariable name="temperature"
  ↪ value="$applyGenericFormula(feastTemperature_1V5)" />
</AnalogInput>
<AnalogInput id="4" name="2V5_PTAT">
<CalculatedVariable name="temperature"
  ↪ value="$applyGenericFormula(feastTemperature_2V5)" />
</AnalogInput>
<AnalogInput id="5" name="P1V5_SCA">
<CalculatedVariable name="power" value="$thisObjectAddress.value*3.0" />
</AnalogInput>
<AnalogInput id="6" name="P2V5_SCA">
<CalculatedVariable name="power" value="$thisObjectAddress.value*5.0" />
</AnalogInput>
<AnalogInput id="7" name="VTRX1_RSSI">
<CalculatedVariable name="power"
  ↪ value="$applyGenericFormula(rssiCurrentmA)" />
</AnalogInput>
<AnalogInput id="31" name="internalTemperature">
  <CalculatedVariable name="temperature"
    ↪ value="$applyGenericFormula(scaTemperature)" />
</AnalogInput>
</AnalogInputSystem>
<I2cMaster sclPadCmosOutput="false" name="gbtx2" masterId="0"
  ↪ busSpeed="100">
<I2cSlave numberOfBytes="3" address="2" addressingMode="7"
  ↪ name="gbtx2"></I2cSlave>
</I2cMaster>
<I2cMaster sclPadCmosOutput="false" name="gbtx3" masterId="1"
  ↪ busSpeed="100">
<I2cSlave numberOfBytes="3" address="3" addressingMode="7"
  ↪ name="gbtx3"></I2cSlave>
</I2cMaster>

```

## SCA OPC UA Server XML example

The main part of the SCA OPC UA Servers consists of the SCA objects as:

```

<SCA address="netio-next://fid/0x16d1801001808000/0x16d1801001800000"
name="sTGC-A/V0/SCA/Pad/S15/L0/R0"
idConstraint="dont_care"
recoveryActionScaStayedPowered="do_nothing"

```

```

recoveryActionScaWasRepowered="reset_and_configure"
managementFromAddressSpace="only_if_kaputt" >
&SCA_PFEb;
</SCA>

```

An example of a final SCA OPC UA Server XML file looks like:

```

<?xml version="1.0" encoding="UTF-8"?>
<!DOCTYPE configuration [

<!ENTITY SCA_formulaList SYSTEM "/det/dcs/Production/ATLAS_DCS_MUO/muoNswEltxSc
  ↳ EltxScaOpcConfigTemplates/formulaList.xml">
<!ENTITY SCA_MMFE8 SYSTEM "/det/dcs/Production/ATLAS_DCS_MUO/muoNswEltxSc
  ↳ aOpcConfigTemplates/SCA_MMFE8.xml">
<!ENTITY SCA_L1DDC SYSTEM "/det/dcs/Production/ATLAS_DCS_MUO/muoNswEltxSc
  ↳ aOpcConfigTemplates/SCA_L1DDC.xml">
<!ENTITY SCA_ADDC SYSTEM "/det/dcs/Production/ATLAS_DCS_MUO/muoNswEltxSc
  ↳ OpcConfigTemplates/SCA_ADDC.xml">
]>

<configuration xmlns="http://cern.ch/quasar/Configuration"
  ↳ xmlns:xsi="http://www.w3.org/2001/XMLSchema-instance"
  ↳ xsi:schemaLocation=
"http://cern.ch/quasar/Configuration
  ↳ /det/dcs/Production/ScaOpcUa/Configuration/Configuration.xsd ">

<StandardMetaData>
  <Log>
    <GeneralLogLevel logLevel="INF"/>
  </Log>
<SourceVariableThreadPool minThreads="0" maxThreads="100"
  ↳ maxJobs="10000"/>
</StandardMetaData>

<!-- Generated by Polyneikis using
/atlas/oks/tdaq-09-04-00/muons/segments/NSW/ELinks/NSW-ELinks-MM-A-S1.dat
  ↳ a.xml
on 05/04/2022 13:09:19 -->

&SCA_formulaList;

<AdcSampler name="adcSamplerMechanism" maxNumberThreads="2" />

<SCA address="netio-next://fid/0x16b05000003f8000/0x16b05000003f0000"
name="MM-A/V0/SCA/L1DDC/S0/L0/E"
idConstraint="dont_care"
recoveryActionScaStayedPowered="do_nothing"
recoveryActionScaWasRepowered="reset_and_configure"
managementFromAddressSpace="only_if_kaputt" >

```

```

<CalculatedVariable name="constant_1V5" value="0.0" />
<CalculatedVariable name="constant_2V5" value="0.0" />
&SCA_L1DDC;
</SCA>

<SCA address="netio-next://fid/0x16b0500000088000/0x16b0500000080000"
name="MM-A/V0/SCA/ADDC/S0/L0/E"
idConstraint="dont_care"
recoveryActionScaStayedPowered="do_nothing"
recoveryActionScaWasRepowered="reset_and_configure"
managementFromAddressSpace="only_if_kaputt" >
<CalculatedVariable name="constant_1V5" value="0.0" />
<CalculatedVariable name="constant_2V5" value="0.0" />
&SCA_ADDC;
</SCA>

...

```

## NSWConfiguration SCA Online, ID and address

The function implemented inside the src/OpcClient.cpp:

```

unsigned int nsw::OpcClient::readScaID(const std::string& node) const {
    UaoClientForOpcUaSca::SCA scanode(m_session.get(),
        ↪ UaNodeId(node.c_str(), std::uint16_t{2}));
    return scanode.readId();
}

std::string nsw::OpcClient::readScaAddress(const std::string& node) const
↪ {
    UaoClientForOpcUaSca::SCA scanode(m_session.get(),
        ↪ UaNodeId(node.c_str(), std::uint16_t{2}));
    return scanode.readAddress().toUtf8();
}

bool nsw::OpcClient::readScaOnline(const std::string& node) const {
    UaoClientForOpcUaSca::SCA scanode(m_session.get(),
        ↪ UaNodeId(node.c_str(), std::uint16_t{2}));
    return scanode.readOnline();
}

```

And the corresponding header file NSWConfiguration/OpcClient.h as:

```

// Read SCA ID
[[nodiscard]]
std::uint32_t readScaID(const std::string& node) const;

// Read SCA Address
[[nodiscard]]
std::string readScaAddress(const std::string& node) const;

```

```
// Read SCA Online Status
[[nodiscard]]
bool readScaOnline(const std::string& node) const;
```

## FreeVariable

Firstly, since the FreeVariable functions were implemented in the UaoClientForScaOpcUa, they needed to be exposed in the NSWConfiguration by creating the corresponding templated function inside "NSWConfiguration/ConfigSender.h" as follows:

```
// Read anytype SCA OPC UA's FreeVariable
template <typename T>
inline T readFreeVariable(const std::string& opcserver_ipport, const
↳ std::string& node) {
    addOpcClientIfNew(opcserver_ipport);
    return m_clients.at(opcserver_ipport)->readFreeVariable<T>(node);
}

// Write anytype SCA OPC UA's FreeVariable
template<typename T>
inline void writeFreeVariable(const std::string& opcserver_ipport,
↳ const std::string& node, T value) {
    addOpcClientIfNew(opcserver_ipport);
    m_clients[opcserver_ipport]->writeFreeVariable(node, value);
}
```

The function make available the write and read of any FreeVariable parameter and also of any type(Boolean, Byte, SByte, UInt16, Int16, UInt32, Int32, UInt64, Int64, Float, Double, String). Then, a function called "setVMMConfigurationStatusInfoDCS" was implemented inside "src/ConfigSender.cpp" as"

```
void nsw::ConfigSender::setVMMConfigurationStatusInfoDCS(const
↳ nsw::FEBConfig& feb, const nsw::VMMConfig& vmm) {

    ERS_DEBUG(1, "[" + feb.getAddress() + "," + vmm.getName() + "]"
        + " Write VMMConfigurationStatusInfo FreeVariable parameter
↳ for DCS Use");

    auto opc_ip = feb.getOpcServerIp();

    // VMM registers for temperature monitoring
    const int scmx = vmm.getGlobalRegister("scmx");
    const int sbmx = vmm.getGlobalRegister("sbmx");
    const int sbfp = vmm.getGlobalRegister("sbfp");
    const int sm = vmm.getGlobalRegister("sm");
    const int reset = vmm.getGlobalRegister("reset");

    const bool isVMMTemperatureModeEnabled = (scmx==0 && sbmx==1 &&
↳ sbfp==1 && sm==4 && reset!=3)? true:false ;
```

```
writeFreeVariable(opc_ip, feb.getAddress() + ".spi." + vmm.getName()  
    ↪ + ".configurationStatus",  
    isVMMTemperatureModeEnabled);  
}
```



---

## List of Figures

---

1	Σχηματική αναπαράσταση επιταχυντών-εγχυτήρων του LHC. Φαίνεται παραπάνω ο εγχυτήρας και οι προ-επιταχυντές που τροφοδοτούν τον 27 km δακτύλιο με δέσμες σωματιδίων. Οι δέσμες συγκρούονται σε τέσσερις πειραματικές περιοχές εισαγωγής που αντιστοιχούν στα υπόγεια πειράματα (ATLAS, CMS, ALICE, LHCb). . . . .	20
2	Γραφική αναπαράσταση του πειράματος ATLAS. Τα διαφορετικά μέρη του πειράματος σημειώνονται πάνω στο σχήμα. . . . .	20
3	Αριστερά: Το τωρινό Small Wheel στην επιφάνεια της γης πριν την εγκατάσταση του στο ATLAS. Δεξιά: Απεικόνιση της διάταξης του New Small Wheel. . . . .	22
4	Το σχήμα επισκόπησης των ηλεκτρονικών NSW για τα ηλεκτρονικά εντός και εκτός σπηλαίου του ATLAS και τη συνδεσιμότητά τους. Στους ανιχνευτές (αριστερό πλαίσιο) υπάρχουν οι πλακέτες front-end, υπεύθυνες για την ανάγνωση των 2.1 εκατομμυρίων καναλιών του NSW, καθώς και οι πλακέτες ανάγνωσης και σκανδαλισμού. Εκτός των ανιχνευτών (αριστερό πλαίσιο) υπάρχουν οι επεξεργαστές σκανδαλισμού και τα ηλεκτρονικά που θα παραδώσουν τα δεδομένα στα συστήματα σκανδαλισμού και συλλογής δεδομένων του ATLAS. . . . .	23
5	Η αρχιτεκτονική VMM (Versatile Readout ASIC for Micromegas) αποτελείται από 64 πανομοιότυπα κανάλια. Κάθε κανάλι περιλαμβάνει έναν ενισχυτή φορτίου (CA) και έναν μορφοποιητή (shaper), που επεξεργάζεται τους παλμούς εισόδου για το ύψος του παλμού και το χρονισμό. Οι αναλογικοψηφιακοί μετατροπείς (ADC) ψηφιοποιούν τις παραμέτρους που είναι αποθηκευμένες σε έναν απομονωτή FIFO (First-In-First-Out). Η λογική L0 επιλέγει δεδομένα με βάση την είσοδο σκανδαλισμού (L0) και πληροφορίες χρονοσήμανσης, που μεταδίδονται στην εξωτερική συσκευή ανάγνωσης μέσω των γραμμών D1 και D2. Οι λειτουργίες παρακολούθησης περιλαμβάνουν τις εξόδους PDO, TDO και MO. Το test-pulse strobe (CKTP) ενεργοποιεί τη δοκιμή και το chip μπορεί να επαναρυθμιστεί μέσω των ακροδεκτών ENA ή TKI. Η διαχείριση της διαμόρφωσης γίνεται μέσω των ακροδεκτών SDI, SDO, SCK και CS. Τα πρωτόκολλα σκανδαλισμού (ART, ToT, TtP, PtT, PtP, 6bADC) μεταδίδονται με ακριβή συγχρονισμό χρησιμοποιώντας τις εισόδους CKART και CK6B. Η καλά μελετημένη αρχιτεκτονική του VMM δίνει έμφαση στην ευελιξία και την αποτελεσματικότητα στην απόκτηση και ανάγνωση δεδομένων των ανιχνευτών Micromegas. . . . .	24
6	Η διάταξη της δοκιμαστικής δέσμης ακτινοβολίας νετρονίων μαζί με την πλακέτα Mini1 εξοπλισμένη με το VMM3/VMM3a. . . . .	25

7	Προεπισκόπηση της δομικής σύστασης του GBT-SCA Software. . . . .	25
8	Απλουστευμένο σχηματικό διάγραμμα της λειτουργίας SCA της NSW Electronics. . .	26
9	Το κύριο γραφικό περιβάλλον χρήστη του ATLAS DCS με όλα τα υποσυστήματα ενοποιημένα σε μία ιεραρχική δομή FSM. . . . .	27
10	Η τελική έκδοση του συστήματος ελέγχου διαρροής αερίου MM QP στο BB5. . . . .	28
11	Το ιστόγραμμα των συνολικών αποτελεσμάτων του ποσοστού διαρροής, σε σχέση με το όριο ATLAS (πράσινη οριζόντια διακεκομμένη γραμμή), από 136 Τετραπλέτων Micromegas κατά την επικύρωση της στεγανότητάς τους από τον Ιανουάριο 2019. . .	29
12	Η πειραματική διάταξη επικύρωσης υψηλής τάσης του Micromegas στο BB5. . . . .	30
13	Ο σταθμός SCA DCS για την παρακολούθηση των ηλεκτρονικών του Micromegas. . .	30
14	Ένας πραγματικός τομέας Micromegas στην εγκατάσταση Cosmics Stand στο BB5 CERN. . . . .	31
15	Η αίθουσα ελέγχου του πειράματος ATLAS. Διάφοροι μετατοπιστές οι οποίοι λειτουργούν τον ανιχνευτή ATLAS επί 24 ώρες την ημέρα και επτά ημέρες την εβδομάδα προκειμένου να τον προετοιμάσουν για την απόκτηση δεδομένων. . . . .	31
16	Ο πίνακας λειτουργίας για την προβολή επιπέδου FSM. . . . .	33
17	Γραφική απεικόνιση μίας τυποποιημένης διατομής ενός ανιχνευτή Micromegas που απεικονίζει τα διάφορα μέρη της εσωτερικής δομής του ανιχνευτή και την αρχή λειτουργίας του. . . . .	34
18	Η γραμμή δέσμης H8 του SPS στην περιοχή Preveessin North του CERN, στην οποία έχει εγκατασταθεί η πειραματική ρύθμιση δοκών δοκιμής Micromegas. . . . .	35
19	Αριστερά: Η απόδοση λογισμικού (software efficiency) είναι συνάρτηση τη υψηλής τάσης των λωρίδων ανάγνωσης (readout strips). Δεξιά: Η απόδοση λογισμικού είναι συνάρτηση του ορίου. . . . .	36
20	Εμφανίζονται η software efficiency, το cluster charge και το cluster multiplicity για κάθετες διαδρομές με το ίδιο κέρδος για τα τρία διαφορετικά μείγματα αερίων. Οι συγκρίσεις έγιναν χρησιμοποιώντας ένα κατώφλι υλικού $6 \times \sigma$ , λογική γειτονικού ON και δύο διαφορετικές ρυθμίσεις χρόνου αιχμής (100 και 200 ns). Δεν υπάρχει μεγάλη διαφορά μεταξύ αυτών των τριών συνδυασμών $Ar + CO_2$ . . . . .	38
21	Αριστερά: Κάτοψη της εγκατάστασης GIF++. Μέση: Σχηματικό σχέδιο του ακτινοβολητή GIF++ με γωνιακά διορθωτικά φίλτρα και ανεξάρτητα συστήματα φίλτρων και στις δύο πλευρές. Δεξιά: Και στις δύο πλευρές, ένα σύνολο ανεξάρτητα κινητών και τηλεχειριζόμενων φίλτρων εξασθένισης και πλαισίων ρυθμιστών επιτρέπει τη μεταβολή της έντασης των εκπεμπόμενων φωτονίων. . . . .	39
22	Η χρονική ανάλυση του ανιχνευτή SM1 χρησιμοποιώντας το σύμπλεγμα back-to-back των πλησιέστερων λωρίδων ανάγνωσης. Η ανάλυση χρόνου είναι το σίγμα της διανομής κατά $\sqrt{2}$ . . . . .	39
23	Συνδυαστικά γραφήματα μελέτης της χρονικής απόκρισης του ανιχνευτή Micromegas. . . . .	40
1.1	The LHC superconducting magnets in the 27 km LEP tunnel at CERN. . . . .	44
1.2	Schematic representation of the accelerators-injectors of LHC. Above is the injector and pre-accelerators that supply the 27 km ring with particle beams. The beams collide into four experimental input regions corresponding to the underground experiments (ATLAS, CMS, ALICE, LHCb). . . . .	45
1.3	Graphical representation of the ATLAS experiment. The different parts of the experiment are marked on the figure. . . . .	46

1.4	Photos of the three different parts of the experimental magnetic system of ATLAS. In the top left image, the cylindrical tubular magnet is inserted into the liquid argon caliper on the surface. In the Figure below, eight barrel coils inside ATLAS and to the right, one of the two end-cap toroidal magnets in their final position surrounded by barrel toroid coils. . . . .	47
1.5	Schematic representation of the magnetic system of ATLAS. The central solenoid is installed within the liquid slow calorimeter (blue), surrounded by barrel (red) and end-cap toroid coils (green). . . . .	48
1.6	Schematic representation of the different subsystems of the ATLAS internal trajectory detector. On the inside there is the Pixel Detector, then the SemiConductor Tracker and finally the Transition Radiation Tracker. . . . .	49
1.7	Left: Schematic representation of the cross section of ATLAS calorimeters. LAr and Tile are illustrated along with their segmentation in barrel and end-cap calorimeters. Right: Photograph of the barrel calorimeter mounted on the ATLAS detector. The rotating coils of the end-cap surrounding the calorimeter layout are also visible. . . .	49
1.8	Schematic representation of the ATLAS muon spectrometer. The various technologies of the probe's masonry chambers are visible. . . . .	50
1.9	Left: Schematic representation of an MDT cell of the region barrel consisting of two multilevel three-level tubes each. Right: Photograph of an MDT chamber during its construction and inspection process. . . . .	51
1.10	Left: Schematic representation of how a CSC detector operates. Right: The internal structure of a CSC. . . . .	51
1.11	Internal structure of an RPC detector. . . . .	52
1.12	Internal structure of a TGC detector. . . . .	52
1.13	Detector event display showing a Higgs decay to four electrons recorded by ATLAS in 2012. . . . .	53
1.14	The discovery of the Higgs boson during Run-1 using experiment data from ATLAS [22]. . . . .	53
1.15	The timeline of the HL-LHC. . . . .	54
2.1	The maximum average number per beam crossing over time for $p - p$ events during 2010-2012 [23]. . . . .	56
2.2	Cross-section of the ATLAS on the plane $z - y$ [26]. . . . .	56
2.3	The pseudorapidity distribution of Level-1 trigger rate in three levels [26]. . . . .	57
2.4	The efficiency of a single MDT tube and an MDT chamber, $2 \times 4$ tube levels, as a function of events from beam experiment data to luminosity $\mathcal{L} = 3 \times 10^{34} \text{ cm}^{-2}\text{s}^{-1}$ [26]. . . . .	58
2.5	Left: Illustration of the expected improvement of the muon trigger system in the end-cap region by installing the NSW. Without the NSW, the trigger candidates are only formed based on the angle of the particle tracks passing through the TGC detectors mounted on the first of the two big wheels. If the angle is compatible with a particle coming from the IP, a trigger candidate is formed. Including the Level-1 trigger information of the NSW, the track reconstruction at trigger level is improved by rejecting tracks B and C which do not come from the IP, but are induced by background particles like neutrons or particles created by the interaction with the structural elements of ATLAS or the end-cap toroid magnet. Right: The estimation of the Level-1 trigger rate for $p - p$ collisions in energy $\sqrt{s} = 14 \text{ TeV}$ with instantaneous luminosity $\mathcal{L} = 3 \times 10^{34} \text{ cm}^{-2}\text{s}^{-1}$ is plotted as a function of the threshold $p_T$ for three different configurations. . . . .	58

2.6	Left: The current Small Wheel on the surface before been installed in ATLAS. Right: Illustration of the New Small Wheel layout. . . . .	59
2.7	Left: Layout of the detectors inside a sector. Right: Illustration of a sector of the New Small Wheel. . . . .	60
2.8	The principle of operation of the sTGC detector. In the middle of a 1.4 mm wide gas gap, wires are located on where a voltage of 2.8 kV is applied. The two electrodes are segmented into different patterns. The ones uses a strip pattern to provide high spatial resolutions while the other is segmented into so-called pads, which provide a fast signal for the event selection. . . . .	61
2.9	The principle of the resistive-strip Micromegas. The stainless steel micromesh separates the gas gap of a Micromegas into two regions of different field strengths, the drift and the amplification field. In the drift region, the charged particle crossing the detector ionizes the gas molecules along its track, and due to the drift field applied between the cathode and the mesh the electrons drift towards the mesh. The amplification field between the readout electrodes and the mesh is much stronger. Therefore, the electrons entering this region undergo multiplication. Finally, the electrons created in the avalanche induce charge by the strip-like segmented readout electrodes. . . . .	62
2.10	A brief overview of the NSW hardware. . . . .	63
2.11	Left: The layout of the BB5 building which use for the Micromegas Integration. Right: The Micromegas Integration workflow, from late in production, when it was fully optimized. Each colour reflects the work of a distinct team. . . . .	64
2.12	The cosmics ray stand along with the rotation stations at BB5 during the integration of the Micromegas electronics and wedge preparation. . . . .	64
2.13	Top: 3D view of the B191 commissioning area. Bottom: High-level connectivity scheme of the commissioning procedure. . . . .	66
2.14	Left: The NSW during the transportation from the B191 commissioning site to the P1. Right: The NSW during the installation at the ATLAS cavern. . . . .	67
3.1	The NSW electronics overview scheme of on-detector and off-detector electronics and their connectivity. On the detectors (left box) there are the front-end boards, responsible for reading out the 2.1M channels of NSW, as well as the readout driver and trigger boards. Off the detectors (right box) there are the trigger processors and the aggregator electronics that will deliver the data to the ATLAS trigger and data acquisition systems. . . . .	70
3.2	Left: Photograph of the production NSW MMFE8 board. Designed in the University of Arizona, the board features eight VMMs (top row), one ROC (bottom center), and one SCA (on the righthand side of the ROC). Right: The MMFE8 block diagram showing the ESD protection, the VMM front end ASIC's, the Readout Controller ASIC, the Slow Control Adapter ASIC, the FEAST DC-to-DC converter ASIC's, and the MiniSAS twin-ax connectors for the different interfaces. [34] . . . . .	74
3.3	Left: The fully assembled production version of sTGC pFEB and sFEB. Right: The functional block diagram of the sTGC sFEB and pFEB and the connectivity on board. [47] . . . . .	75

3.4	Left: The MM-L1DDC, the sTGC-L1DDC, and the RIM-L1DDC board. MiniSAS connectors, power connector, FEAST DC-DC converters, VTRX, and VTTX are visible. GBTXs, SCA, and fan-out buffers are placed on the bottom layer of the board. Right: MM e-Link connectivity. For most FEs, additional differential pairs will be used to collect the Level-1 data. These pairs will be multiplexed in different banks and may use different e-Link speeds. Eight GBTX banks will run at 320 Mbps, one at 160 Mbps, and one at 80 Mbps, which will be used for the configuration of the VMM and ROC ASICs. . . . .	77
3.5	Left: The top side of a fully assembled ADDC production board. Right: The ADDC block diagram. Each ADDC receives 64 inputs of ART data using two ART ASIC's. Output to the Trigger Processor is via two GBTx ASIC's. [34] . . . . .	77
3.6	Left: The top side of a fully assembled Pad Trigger production board. Right: The Pad Trigger context and block diagram. [34] . . . . .	78
3.7	Left: The top side of a fully assembled Router production board. Right: Context diagram of the Router for a layer showing the four electrical inputs from each of the three Front-end boards in one layer of a sector and the four fibre outputs. [34] . . .	79
3.8	VMM3 die layout. [33] . . . . .	79
3.9	The VMM architecture consists of 64 identical channels. Each channel includes a Charge Amplifier (CA) and shaper, processing input pulses for pulse height and timing. ADCs digitize parameters stored in a First-In-First-Out (FIFO) buffer. L0 logic selects data based on trigger input (L0) and timestamp information, transmitted to the external readout device via D1 and D2 lines. Monitoring features include PDO, TDO, and MO outputs. Test-pulse strobe (CKTP) activates testing, and the chip can be reset via ENA or TKI pins. Configuration is managed through SDI, SDO, SCK, and CS pins. Trigger primitives (ART, ToT, TtP, PtT, PtP, 6bADC) are transmitted with precise synchronization using CKART and CK6B inputs. The VMM's well-conceived architecture emphasizes versatility and efficiency in Micromegas detectors' data acquisition and readout. . . . .	80
3.10	The overview of the MMFE1 board. . . . .	82
3.11	The overview of the VERSO software. [51] . . . . .	83
3.12	(a) Missing codes in the VMM's ADCs, (b) Dynamic range of trimmers illustrating the channel threshold equalization problem, (c) High baseline issue observed in some channels at higher gains. . . . .	84
3.13	The Neutron Irradiation Testbeam setup along with the Mini1 board equipped with the VMM3/VMM3a. . . . .	85
3.14	Schematic of the neutron irradiation setup used for irradiation testing. . . . .	85
3.15	The calculated mean flux for the VMM with respect to the deuteron energy . . . . .	86
3.16	An example of the neutron fluence as a function of the board/ASIC distance and also the experimental setup for one particular testbeam day. . . . .	87
3.17	An overview representation of the VMM3a Neutron Irradiation test. The total neutron flux is shown as a function of the testbeam day. In addition, the daily run's parameters (energy, current, flux, and duration) are shown. . . . .	87
3.18	Neutron fluence as a function of the board/ASIC distance and the experimental setup for one particular testbeam day. . . . .	88
3.19	Monitoring of neutron rate using a $BF_3$ neutron counter. The neutron rates are constant over time during long runs. . . . .	88

3.20	Left: The FELIX BNL712 FPGA board, which the NSW will use for its needs. It features a Xilinx® Kintex Ultrascale XCKU115 FPGA, a PCIe connector to interface with the CPU and the back-end network, and an optical coupler supporting up to 24 links. A dedicated mezzanine board receives the reference clock and the trigger information from the ATLAS TTC system. Right: FELIX and its relationship with other parts of the DAQ system. . . . .	89
3.21	Link architecture with the GBT chip set and the Versatile Link optocomponents. [53]	89
3.22	GBTX architecture and interfaces. [50] . . . . .	91
3.23	The GBT-SCA block diagram. [50] . . . . .	92
3.24	The structure of the HDLC data packet which the e-link port on the SCA ASIC implements a packet oriented full duplex transmission protocol. . . . .	93
3.25	Structure of a complete FELIX Identifier (FID), with all sub-components indicated in logical order. . . . .	94
3.26	The format of the 64-bit FID for NSW. . . . .	95
3.27	Description of the possible locations and attributes for the NSW Detector Resource Name. . . . .	96
3.28	Overview of the SCA Ecosystem. . . . .	98
3.29	The SCA Software Library stack. . . . .	98
3.30	Overview of the quasar generic server framework components. . . . .	99
3.31	The quasar design diagram of SCA OPC UA server. . . . .	101
3.32	The SCA OPC UA stack. . . . .	101
3.33	SCA connections of the Router board. . . . .	102
3.34	Block diagram of the NswXmlGenerator tool which is producing the SCA OPC UA Server XML files for the NSW . . . . .	105
3.35	Simplified schematic of the NSW Electronics SCA operation. . . . .	107
3.36	The FELIX/OPC mapping granularity of the NSW Side A. . . . .	108
3.37	Simplified illustration of the FELIX/OPC mapping. . . . .	109
3.38	SCA channel usage in the ATLAS NSW micromegas full sector slice. The setup was used to evaluate the performance of the server. . . . .	110
3.39	Left: The Micromegas PCB design schematic. Right: The MMFE8 binary code LUT.	113
3.40	The MMFE8 placed on Large Sector, PCB 2, Left side and Layer 1 (Eta). . . . .	114
3.41	The internal architecture of a VMM Capture channel showing the evolution of the main data buses that link its components. . . . .	115
3.42	Left: The schematic representation of the NSW electronics setup illustrates the pathways involved in the SCA-based calibration process. Commands are transmitted through the OPC client-server and FELIX to the on-detector electronics. The SCA ADC is then instructed to sample the analog output of the VMM. Subsequently, the acquired data is transmitted back to the custom data handler software. Right: The schematic representation illustrates the data-taking path in the calibration procedure. The partition configures the system via the OPC client-server through FELIX. The TTC system is configured to produce a sequence of test pulses along with L1A and L0A signals. The data captured during this process is then handled by the swROD. This comprehensive setup ensures effective calibration and data acquisition for the NSW system. [34] . . . . .	117

3.43	Left: A typical plot produced during the SCA-based VMM calibration procedure. Right: Baseline rms per strip for one layer of the Micromegas Small Sector C08. The layer used for the plot is of the stereo type (with the strips orthogonal to the longitudinal axis of the double wedge). The baseline rms values are indicative of the detector noise and depend on the input capacitance to each electronic channel. As expected, the rms value is increasing as a function of the strip number and the corresponding strip length. The dotted lines define the MMFE8 boards (16 in total), while bold dotted lines define the PCBs (eight in total) of the layer. The noisy channels are defined as all the channels above the red limits (1.4 times the board median), the dead channels are defined as all channels below the blue limits (0.6 times the board median), while the channels between these limits are defined as normal. Also, in each sector type, there are some standard unconnected channels that are omitted in this plot. Furthermore, the effect of the decreasing length of the strips at the beginning and at the end of the modules in the stereo layers can be observed in these areas. . . . .	119
4.1	Graphical representation of the DCS architecture of the experiment ATLAS divided into three levels: GCS, SCS and LCS. . . . .	125
4.2	State & status model of the ATLAS DCS high level objects. . . . .	126
4.3	The main user interface of ATLAS DCS with all subsystems integrated into a hierarchical structure FSM. . . . .	127
4.4	FSM operator screen components. . . . .	128
4.5	The alarm screen of the ATLAS DCS. . . . .	130
4.6	The architecture of a typical WinCC-OA system and the set of managers it consists of. . . . .	132
4.7	The PARA Database Editor of WinCC-OA and an example of a DPT's structure. . . . .	133
4.8	Graphical Editor Environment tool of WinCC-OA. . . . .	134
4.9	The system architecture and the location of JCOPFw in the core of DCS. . . . .	136
4.10	The panel to install components of the JCOPFw. . . . .	136
4.11	Modeling control system using FSM. . . . .	138
4.12	The OPC Router with its OPC UA Client Plug-in is also a client with a gateway function. . . . .	138
4.13	The experimental gauge for measuring gas leakage four Micromegas QPs in the laboratory BB5 of CERN. . . . .	142
4.14	The simplified form of the experimental gas leakage measuring device 4 MM QPs in the BB5 laboratory of CERN. . . . .	143
4.15	The measurement of the tare branch of the device sensors. . . . .	143
4.16	The leakage measurement of MM QP n of the device. . . . .	144
4.17	Filling of MM QP n with a specified pressure gas. . . . .	144
4.18	Isolation of MM QP n to measure pressure drop. . . . .	144
4.19	The final version of the MM QP gas leakage control system in BB5. The setup consists of input and output mass flow sensors, $MFS_{IN}$ and $MFS_{OUT}$ , atmospheric pressure and temperature values are recorded by sensors $DPS_{ref}$ and $TS_{ref}$ . All sensors generate analog voltage signals that are transmitted to FieldPoint where the data are digitized and are transmitted to the Gas Tightness Station for monitor and control. . . . .	145
4.20	Measurement of offset of the input and output mass flow sensors, $MFS_{IN}$ and $MFS_{OUT}$ of the experimental device. . . . .	146
4.21	Measurement of offset of the input and output mass flow sensors, $MFS_{IN}$ and $MFS_{OUT}$ of the experimental device. . . . .	146



4.22	Experimental device for mass flow sensor calibration using hypodermic medical needles. . . . .	147
4.23	Choice of method and gas to be used to measure leakage of MM QP. . . . .	147
4.24	ConFigure the settings for each node to measure gas leakage using the FRL method. . . . .	148
4.25	The control options of nodes, 1-Node Mode and 4-Node Overview Mode. . . . .	149
4.26	Check the sensors and MM QP of each node with 1-Node Mode. . . . .	149
4.27	Checking the values of the sensors and the MM QP of each node with 1-Node Mode in the FRL method. . . . .	150
4.28	Check the sensors and MM QP of each node with 1-Node Mode in the FRL method. . . . .	150
4.29	Frame for storing and extracting experimental data sensor data. . . . .	151
4.30	The structure of the export file ASCII with the sensor data and node data measured by the FRL method. . . . .	151
4.31	The exported plots using the ROOT Data Analysis Framework [69]. . . . .	152
4.32	Check the sensors and MM QP of each node with 4-Node Mode in the FRL method. . . . .	153
4.33	Use advanced analysis to determine the gas leakage of MM QP by additionally calculating the offset distribution of mass flow sensors in the FRL method. . . . .	153
4.34	The structure of the NSW QA/QC Database. . . . .	154
4.35	The structure of the NSW QA/QC Database. . . . .	154
4.36	The histogram of the overall leak rate results, with respect to the ATLAS Limit (green horizontal dashed line), of 136 MM Quads during their gas tightness validation since January 2019. [67] . . . . .	154
4.37	The CAEN mainframe SY4527 and CAEN HV boards A7038 with 32 channels which are commonly used for the Micromegas HV validation. . . . .	155
4.38	The Micromegas high voltage PCB sections mapping. . . . .	156
4.39	The Micromegas high voltage validation experimental setup at BB5. . . . .	156
4.40	The overview schematic of the Micromegas high voltage validation experimental setup at BB5. . . . .	157
4.41	The Micromegas high voltage validation experimental setup at GIF++ irradiation setup. . . . .	158
4.42	The overview schematic of the Micromegas high voltage validation experimental setup at BB5. . . . .	158
4.43	The "Setup" tab of the HV DCS where user can set the HV Mapping. . . . .	159
4.44	The panel for the HV Mapping setup via the "Settings" panel. . . . .	159
4.45	User sets the HV board and channel of the selected HV section. . . . .	160
4.46	User sets the HV board and channel of the selected HV section. . . . .	161
4.47	When user is pressing the "Save" button, the HV DCS is saving the node settings and the user enabled Nodes are appearing. . . . .	161
4.48	The main panel of HV DCS software for control and monitoring. . . . .	162
4.49	The overview panel of HV DCS software for control and monitoring all the nodes in parallel. . . . .	164
4.50	The HV control options of HV DCS software. . . . .	165
4.51	The Overview HV control options of HV DCS software. . . . .	166
4.52	The archive/export options of the HV DCS software. . . . .	166
4.53	The Run Archive DB of the HV DCS software. . . . .	167
4.54	The Alarm Limit Settings of the HV DCS software. . . . .	167
4.55	The Settings panel of the HV DCS software. . . . .	168

4.56	Left: The ArdEnvironment setup consists of the Arduino Mega 2560 and the Wiznet 5500 Ethernet Shield, Top Right: The BME280 sensor for pressure, humidity and temperature measurements, Bottom Right: The wire connection between Arduino and BME280 sensor. . . . .	168
4.57	ArdEnvironment Station main panel, user can monitor and archive/export the pressure, temperature and humidity. . . . .	170
4.58	Form of exported data and plots using ArdEnvironment Station. . . . .	170
4.59	The NSW electronics setup at the Vertical Slice laboratory. . . . .	171
4.60	The VS Arduino sensor connection schematic. The setup consists of one BME280 environmental sensor and 3 TMP36 analog sensors which are connected to the I2C and analog Arduino's interfaces accordingly. . . . .	171
4.61	Updated ArdEnvironment Station main panel. Users have now the ability to monitor the dewpoint and the VS electronics setup's cooling lines temperatures. In addition, he/she can enable/disable the automatic alarm handling notification system and can manually input the SMS/emails which he/she wants to get notification when the alarm conditions are satisfied. . . . .	172
4.62	The main SCA DCS panel for Micromegas electronics monitoring. . . . .	173
4.63	The board SCA DCS panel for Micromegas electronics monitoring. . . . .	174
4.64	A real Micromegas sector at the Cosmics Stand setup at BB5 CERN. . . . .	175
4.65	The overview schematic of the Cosmics Stand DCS Station . . . . .	176
4.66	The main panel of HV DCS software for control and monitoring. . . . .	177
4.67	The LV Station of the Cosmics Test Stand Station. . . . .	179
4.68	The SCA Station of the Cosmics Test Stand Station. . . . .	179
4.69	The MDM Station of the Cosmics Test Stand Station. . . . .	180
4.70	The Gas Station of the Cosmics Test Stand Station. . . . .	180
4.71	The Env Station of the Cosmics Test Stand Station. . . . .	181
4.72	The structure of the MUO FSM DCS. Due to the NSW Upgrade, the CSC will be removed and MMG&STG DCS will be added as new sub-detectors. . . . .	183
4.73	The FSM node structure of the MMG&STG following the Muon DCS schema. . . . .	183
4.74	The proposed MMG&STG WinCC-OA projects allocation between the sub-detector. . . . .	184
4.75	The WinCC-OA projects allocation between the various server machines. . . . .	185
4.76	Overview of the OPC UA schematic. . . . .	187
4.77	The panel "mmgEltx_fwsc_dpCreation.pnl" which creates the corresponding 16 SCA OPC UA connections and subscriptions under each project. . . . .	189
4.78	The structure of the internal mapping DPT. . . . .	191
4.79	The panel which is used for the creation of the internal mapping and the board settings. . . . .	192
4.80	The structure of the board settings DPT. . . . .	192
4.81	The panel is used for the description handling configuration for all project's datapoints. . . . .	193
4.82	The panels is used for the alarm handling configuration for all project's datapoints. . . . .	194
4.83	The panels is used for the archive handling configuration for all project's datapoints. . . . .	195
4.84	A flow chart of the logic for the status and state definition based on the VMM temperature and the configuration status. . . . .	197
4.85	The FSM Hierarchy of the ELTX projects. . . . .	198
4.86	A flow chart of the logic Board SCA DU state calculation. . . . .	198
4.87	A flow chart of the logic Board SCA DU status calculation according to the temperature and power alert limits. . . . .	199
4.88	The operation panel for the FSM Board View. . . . .	201
4.89	The operation panel for the FSM Layer View. . . . .	202
4.90	The operation panel for the FSM Sector View. . . . .	203

4.91	The operation panel for the FSM Side View. . . . .	204
4.92	The service panel of the Wiener project in order to conFigure the alert limits and the description & archive configuration. . . . .	204
4.93	The Wiener VME FSM Hierarchy. . . . .	205
4.94	The Wiener VME DU initialisation and the calculation of the various states. . . . .	205
4.95	The operation panel for the monitoring of the 3 NSW Wiener VME crates. . . . .	206
4.96	The expert panel which is used for the setup of the various DSS parts. . . . .	207
4.97	The expert panels where shifter can monitor the detector associated DSS Alarms and Actions. . . . .	208
4.98	The expert panels where shifter can monitor the detector associated DSS Alarms and Actions. . . . .	209
4.99	The DCS FSM and panels for the NSW High Voltage monitoring. . . . .	209
4.100	The DCS FSM and panels for the NSW Low Voltage monitoring. . . . .	210
4.101	The DCS FSM and panels for the NSW MDM T-Sensor temperature and BField monitoring. . . . .	210
4.102	The fwAtca JCOP component and the ATCA DCS FSM panels for the NSW. . . . .	211
4.103	The FSM node structure of the MMG&STG following the Muon DCS schema. . . . .	211
4.104	The expert panel for the generation and creation of the SCS FSM. . . . .	212
4.105	The overview panel of the detector SCS which shifter can monitor NSW services and infrastructure in a glance. . . . .	214
5.1	Equation Bethe-Bloch to describe the energy loss as a function of momentum of charged particles in active material. [72] . . . . .	219
5.2	Pair Production. . . . .	220
5.3	Effective cross-section of electromagnetic photon-matter interaction phenomena. [73] . . . . .	220
5.4	Experimental values of ion mobility for different gas media in gas detectors. [29] . . . . .	222
5.5	The electron drift velocity for different gas mixtures and magnetic field values. [29] . . . . .	223
5.6	The Townsend effect and the formation of a droplet shape during the movement of ions and electrons inside the detector by the application of an electric field. . . . .	224
5.7	Total auxiliary current as a function of time. The peak at the origin for times less than 2 ns is due primarily to the electrons movement while after the 2 ns the distribution is due to the ion drifting towards to the mesh.[75] . . . . .	226
5.8	Areas of operation of gas detectors. [29] . . . . .	226
5.9	Graphical illustration of a standard cross-section of a non-resistive MicroMeGas detector showing the different parts of the internal structure of the detector and its operating principle. [65] . . . . .	228
5.10	Graphic illustration of a cross-section of the resistive Micromegas detector showing the different parts of its internal structure and the principle of its operation. [65] . . . . .	229
5.11	The behavior of voltage and current for a resistive and a non-resistive Micromegas in a neutron beam environment of energy 5.5 MeV total flux $1.5 \times 10^6$ n/cm <sup>2</sup> s [78]. . . . .	230
5.12	The overall layout of the New Small Wheel Upgrade. . . . .	230
5.13	Right: Schematic representation of the four reading PCBs that would make up a MM module [79]. Left: The dimensions of the small and large NSW MM wedges. Each MM module layer consists of 8 PCBs, three for the top and five for the bottom module, respectively [29]. . . . .	231
5.14	Right: The internal structure of NSW MM. Left: Transverse cross-section of the NSW MM showing the main elements of a quadroplet [79]. . . . .	232
5.15	High voltage section divisions in a layer of a small sector. The same division is adopted also for the large sectors. . . . .	232

- 5.16 Micromegas spatial resolution as a function of the track inclination angle using charge centroid method (blue curve), the  $\mu$ TPC method (red curve) and the combination of the two (black curve). The resolutions are calculated through the fit of a double Gaussian on the difference between the reconstructed track and cluster position residuals. The final resolution is expressed in two ways: full circles are the  $\sigma$  of the core Gaussian, while empty circles are the weighted average of the Gaussian. The above results have been obtained with small Micromegas chambers using APV electronics. [80] . . . . . 234
- 5.17 The H8 beam line of SPS at Preessin North area of CERN which the Micromegas testbeam experimental setup is installed. . . . . 236
- 5.18 Experimental setup of the July 2018 test beam which is composed by the SM2 Micromegas chamber, three TZ Micromegas chambers which are used for the external track reconstruction and two scintillators which are used as triggers. The TZ chambers are equipped with one MMFE8 each and the SM2 with four MMFE8 boards, each board is placed on one layer of the chamber. . . . . 237
- 5.19 Left: The H8 setup with the SM2 MM and the TZ chamber used in the tracker with the MMFE8 readout board attached to it. Right: Diagram depicting the SM2 MM module and its four readout boards (in green rectangles). . . . . 237
- 5.20 Overview of the VRS, when using the VSB in conjunction with the front ends. The VSB firmware implemented in the VC709 FPGA can support up to eight front end node connections. These connections are implemented through differential pairs over miniSAS cables, and carry the Reference Clock, SoftReset and Trigger signals. These originate from the CTF, which generates the system clock internally, receives the reset signal from a LEMO cable that is driven from a module outside of the radioactive area of the setup, and receives the trigger from a scintillator coincidence. The VSB can also receive the ART trigger primitive datastream from up to three frontends. Finally, it receives the Busy signal from all eight frontend FPGAs. All (up to nine) FPGAs of the system connect to the network via UDP over Ethernet, and the DAQ software, controls the system's overall state and receives VMM data from the frontends. [81] . . . . . 238
- 5.21 The histograms containing the preliminary studies of the testbeam data. We have eight columns, each one represents one different MMFE8 (first four are placed on the SM2 MM module and last four columns on the TZ chambers). The rows represent the Beam profile, PDO distribution, TDO distribution, BCID distribution and Strips per Event per electronic board. . . . . 240
- 5.22 The histograms containing the preliminary clusterisation studies of the testbeam data. We have four columns, each one represents one different MMFE8 placed on the SM2 MM module. The rows represent the Number of clusters per event, Beam profile, Cluster charge, Cluster size of single cluster events, Cluster size for all cluster events per electronic board. . . . . 242
- 5.23 Left: Cluster charge HV scan which for each layer the mean and the mpv of the cluster charge distribution (3rd row of Figure 5.22) were produced versus the corresponding strips voltage level. Right: Cluster multiplicity hv scan which for each layer the mean the cluster size distribution (5th row of Figure 5.22) were produced versus the corresponding strips voltage level. . . . . 243

5.24	Left: Baseline of a MMFE8 which is placed on an eta layer of the SM2 MM module. Right: Noise level, in terms of xADC count per each board of each layer. The measurement was done on the PCB8 (the one with the longest strip of the small NSW sectors) with a gain of 9 mV/fC for each VMM3. This means that a threshold of $6 \times \sigma$ is equivalent to $\approx 6 \text{ fC} \approx 37 \text{ ke}^-$ . . . . .	244
5.25	Left: Cluster charge threshold scan which for each layer the mean and the mpv of the cluster charge distribution (3rd row of Figure 5.22) were produced versus the corresponding threshold level Right: Cluster multiplicity threshold scan which for each layer the mean the cluster size distribution (5th row of Figure 5.22) were produced versus the corresponding threshold level. . . . .	245
5.26	The residuals between the SM2's layers are shown. Both distributions are fitted with a "double" Gaussian function in order to take into account the tails of the distribution. The "core" Gaussian gives an estimation of the intrinsic detector resolution while the "tail" Gaussian describes the additional uncertainty contributions. The achieved resolution for perpendicular tracks of all the layers is well below the 100 $\mu\text{m}$ required. . . . .	247
5.27	The residuals between the SM2's layers are shown. Both distributions are fitted with a "double" Gaussian function in order to take into account the tails of the distribution. The "core" Gaussian gives an estimation of the intrinsic detector resolution while the "tail" Gaussian describes the additional uncertainty contributions. The achieved resolution for perpendicular tracks of all the layers is well below the 100 $\mu\text{m}$ required. . . . .	248
5.28	Left: The software efficiency as a function of the strips HV. Right: The software efficiency as a function of the threshold. . . . .	249
5.29	The software efficiency, cluster charge and cluster multiplicity for perpendicular tracks at the same gain for the three different gas mixtures are shown. The comparisons were made using a hardware threshold of $6 \times \sigma$ , neighbor logic ON and two different settings of peak time (100 ns and 200 ns). There is no big difference between these three combinations of Ar + %CO <sub>2</sub> . . . . .	251
5.30	The plots show the voltage and current values as a function of the time. Several runs were taken with different voltage levels in order to identify problematic HV sections and apply the corresponding voltage value in order to decrease the spike rate. . . . .	252
5.31	Left: Floor plan of the GIF++ facility with entrance doors MAD (material access door), PPG (personal protection gate), PPE (personal protection entrance), PPX (personal protection exit). When the facility downstream of the GIF++ requires electron beam, a beam pipe is installed along the beam line (z-axis) between the vertical mobile beam dump (XTDV). The irradiator can be displaced laterally (its center moves from $x = 0.65 \text{ m}$ to $2.15 \text{ m}$ ), to increase the distance to the beam pipe. Middle: Schematic drawing of the GIF++ irradiator with angular correction filters and independent filter systems at both sides. Right: On both sides a set of independently movable and remotely controlled attenuation filters and collimator frames permits to vary the intensity of emitted photons. . . . .	253
5.32	The SM2 MM module in the GIF++ facility, facing the source. . . . .	254
5.33	The SCADA HV application is used for the GIF++ HV source studies. . . . .	255
5.34	The plot contains the gamma irradiation background rate as a function of the applied voltage and the current of the corresponding HV section. . . . .	256
5.35	The experimental setup at GIF++. . . . .	257
5.36	Time resolution evaluated from 30° runs using back-to-back clusters of the SM1 eta layers. . . . .	258

5.37	Calibration of the VMM's channels TDO using double Fermi-Dirac. . . . .	259
5.38	The time resolution of the SM1 detector using the back-to-back cluster of the nearest strips. The time resolution is the distribution's sigma by $\sqrt{2}$ . . . . .	260
5.39	Timing resolution as a function of the Drift HV. A lower drift voltage of 250 V, in comparison to 300 V yields notably improved time resolution . . . . .	261
5.40	Timing resolution distribution was significantly impacted by high attenuation factors. This effect is a result from erroneous cluster reconstruction, attributed to the heightened gamma irradiation. . . . .	262
5.41	Attenuation-Peaking time scan which indicated that a PT value of 100 ns leads to a substantial amplification in timing measurement precision. . . . .	262
5.42	Threshold-Peaking time scan which indicated that a PT value of 100 ns leads to a substantial amplification in timing measurement precision. . . . .	263
5.43	HV Drift-Peaking Time scan showing that a PT value of 100 ns substantially elevates the precision of timing measurements. . . . .	263
5.44	Threshold-HV Strips-Peaking Time scan which shows that higher Strips HV indicates a gain within the amplification gap and as a result a better timing resolution. In addition, a PT value of 100 ns enhances the precision of timing measurements. . .	264
B.1	SCA connections of the MMFE8 board. . . . .	273
B.2	SCA connections of the SFEB board. . . . .	274
B.3	SCA connections of the PFEB board. . . . .	275
B.4	SCA connections of the ADDC board. . . . .	275
B.5	SCA connections of the L1DDC-MMG board. . . . .	275
B.6	SCA connections of the L1DDC-STG board. . . . .	276
B.7	SCA connections of the Rim L1DDC board. . . . .	276
B.8	SCA connections of the Pad Trigger board. . . . .	276
B.9	SCA connections of the Router board. . . . .	276





---

# List of Tables

---

3.1	NSW Electronics boards. . . . .	74
-----	---------------------------------	----



---

# Bibliography

---

- [1] Oliver Sim Bruning, et al. [LHC Design book](#). 2004.
- [2] Carlo Wyss. [LEP design book, v.3: LEP2](#). 1996. Vol. 1-2 publ. in 1983-84.
- [3] ATLAS Collaboration. [ATLAS detector and physics performance: Technical Design book, 1](#). 1999.
- [4] CMS Collaboration. [CMS Physics: Technical Design book Volume 2: Physics Performance](#). *J. Phys. G*, 34(CERN-LHCC-2006-021. CMS-TDR-8-2):995–1579. 669 p, 2007.
- [5] ALICE Collaboration. [ALICE: Physics Performance book. ALICE physics performance : Technical Design book](#). 32, 2005.
- [6] *LHCb : Technical Proposal*. CERN, Geneva, 1998. URL: <https://cds.cern.ch/record/622031>.
- [7] Stefan Mättig. [The Online Luminosity Calculator of ATLAS](#). *Journal of Physics: Conference Series*, 331(2):022035, 2011.
- [8] TOTEM Collaboration. [TOTEM, Total Cross Section, Elastic Scattering and Diffraction Dissociation at the LHC: Technical Proposal](#). (CERN-LHCC-99-007. LHCC-P-5), Mar 1999.
- [9] Cheuk-Yin Wong. [Introduction to high-energy heavy-ion collisions](#). 1994.
- [10] [ATLAS central solenoid: Technical Design book](#). 1997.
- [11] J P Badiou, et al. [ATLAS barrel toroid: Technical Design book](#). 1997.
- [12] [ATLAS end-cap toroids: Technical Design book](#). 1997.
- [13] S Haywood, et al. [ATLAS inner detector: Technical Design book, 2](#). 1997.
- [14] [Alignment of the ATLAS Inner Detector and its Performance in 2012](#). (ATLAS-CONF-2014-047), Jul 2014.
- [15] [ATLAS calorimeter performance: Technical Design book](#). 1996.
- [16] [ATLAS liquid-argon calorimeter: Technical Design book](#). 1996.

- [17] [ATLAS tile calorimeter: Technical Design book](#). 1996.
- [18] [ATLAS muon spectrometer: Technical Design book](#). 1997.
- [19] Peter Jenni, et al. [ATLAS high-level trigger, data-acquisition and controls: Technical Design book](#). 2003.
- [20] M Sutton, et al. [A Fast Tracking Algorithm for the ATLAS Level 2 Trigger](#). (ATL-DAQ-CONF-2006-018. ATL-COM-DAQ-2006-039), Jan 2006.
- [21] ATLAS Collaboration. [Search for exclusive Higgs and  \$Z\$  boson decays to  \$\phi\gamma\$  and  \$\rho\gamma\$  with the ATLAS detector. Search for exclusive Higgs and  \$Z\$  boson decays to  \$\phi\gamma\$  and  \$\rho\gamma\$  with the ATLAS detector](#). (CERN-EP-2017-273), Dec 2017.
- [22] Collaboration ATLAS. [Plot of invariant mass distribution of diphoton candidates after all selections of the inclusive analysis for the combined 7 TeV and 8 TeV data](#). Jul 2013.
- [23] Ariel Schwartzman. Jet energy calibration at the LHC. *Int. J. Mod. Phys. A*, 30:1546002, 2015. Article submitted to the International Journal of Modern Physics A (IJMPA) as part of the special issue on the. URL: <https://cds.cern.ch/record/2053870>, [arXiv:1509.05459](#).
- [24] Lucio Rossi et al. [The High Luminosity Large Hadron Collider: the new machine for illuminating the mysteries of Universe](#). 2015.
- [25] [Letter of Intent for the Phase-I Upgrade of the ATLAS Experiment](#). (CERN-LHCC-2011-012. LHCC-I-020), Nov 2011.
- [26] T Kawamoto, et al. New Small Wheel Technical Design Report. Technical report, 2013. ATLAS New Small Wheel Technical Design Report. URL: <https://cds.cern.ch/record/1552862>.
- [27] Collaboration ATLAS. [Letter of Intent for the Phase-II Upgrade of the ATLAS Experiment](#). (CERN-LHCC-2012-022. LHCC-I-023), Dec 2012.
- [28] A. Abusleme et al. Performance of a Full-Size Small-Strip Thin Gap Chamber Prototype for the ATLAS New Small Wheel Muon Upgrade. *Nucl. Instrum. Meth.*, A817:85–92, 2016. [arXiv:1509.06329](#), [doi:10.1016/j.nima.2016.01.087](#).
- [29] Georgios Iakovidis. Research and Development in Micromegas Detector for the ATLAS Upgrade, 2014. Presented 13 Oct 2014. URL: <https://cds.cern.ch/record/1955475>.
- [30] Luca Martinelli. Study of the MicroMegas chambers performance for the upgrade of the ATLAS experiment at LHC, Sep 2017. Presented 23 Oct 2017. URL: <https://cds.cern.ch/record/2291886>.
- [31] Theodoros Vafeiadis. Integration and commissioning of ATLAS New Small Wheel Micromegas detectors with electronics at CERN. Technical report, CERN, Geneva, 2021. URL: <https://cds.cern.ch/record/2746096>, [doi:10.22323/1.390.0791](#).
- [32] A Gabrielli, et al. [The GBT-SCA, a radiation tolerant ASIC for detector control applications in SLHC experiments](#). 2009.
- [33] Gianluigi de Geronimo, et al. The vmm3a asic. *IEEE Transactions on Nuclear Science*, 69(4):976–985, 2022. [doi:10.1109/TNS.2022.3155818](#).

- [34] G. Iakovidis, et al. The new small wheel electronics. *Journal of Instrumentation*, 18(05):P05012, may 2023. URL: <https://dx.doi.org/10.1088/1748-0221/18/05/P05012>, doi:10.1088/1748-0221/18/05/P05012.
- [35] Estel Perez Codina et al. sTGC Integration. Technical report, CERN, Geneva, 2022. URL: <https://cds.cern.ch/record/2825256>.
- [36] Aimilianos Koulouris et al. NSW 191 Commissioning. <https://gitlab.cern.ch/atlas-muon-nsw-com/NSW-COMMISSIONING-INT1>, 2022.
- [37] Maximilien Brice et al. New Small Wheel (NSW) descent into ATLAS' "side A" of the experimental cavern. 2021. General Photo. URL: <https://cds.cern.ch/record/2775525>.
- [38] Polyneikis Tzanis. Development of the Configuration, Calibration and Monitoring System of the New Small Wheel Electronics for the ATLAS experiment. Technical report, CERN, Geneva, 2021. URL: <https://cds.cern.ch/record/2781336>.
- [39] Kevin Thomas Bauer. *FELIX: the new detector readout system for the ATLAS experiment*. (ATL-DAQ-PROC-2017-042), Nov 2017.
- [40] H J Burckhart, et al. *The Common Infrastructure Control of the ATLAS experiment*. 2008.
- [41] Radu Mihai Coliban, et al. *The Read Out Controller for the ATLAS New Small Wheel*. Jan 2016.
- [42] Panagiotis Gkoutoumis. *Level-1 Data Driver Card of the ATLAS New Small Wheel Upgrade Compatible with the Phase II 1 MHz Readout Scheme*. (ATL-MUON-PROC-2016-010), Nov 2016.
- [43] L Yao, et al. *The address in real time data driver card for the MicroMegas detector of the ATLAS muon upgrade*, volume 12. 2017.
- [44] Jinhong Wang, et al. Design of a trigger data serializer asic for the upgrade of the atlas forward muon spectrometer. *IEEE Transactions on Nuclear Science*, 64(12):2958–2965, December 2017. URL: <http://dx.doi.org/10.1109/TNS.2017.2771266>, doi:10.1109/tns.2017.2771266.
- [45] Xueye Hu, et al. A signal packet router for the upgrade of the muon spectrometer at the atlas experiment. *Nuclear Instruments and Methods in Physics Research Section A: Accelerators, Spectrometers, Detectors and Associated Equipment*, 1044:167504, 2022. URL: <https://www.sciencedirect.com/science/article/pii/S0168900222007963>, doi:10.1016/j.nima.2022.167504.
- [46] Serguei Kolos, et al. New software-based readout driver for the atlas experiment. *IEEE Transactions on Nuclear Science*, 68(8):1811–1817, 2021. doi:10.1109/TNS.2021.3083987.
- [47] P. Miao, et al. The development of the front-end boards for the small-strip thin gap chambers detector system of the atlas muon new small wheel upgrade. *Journal of Instrumentation*, 15:P11024–P11024, 11 2020. doi:10.1088/1748-0221/15/11/P11024.
- [48] Georgios Iakovidis, et al. *VMM - An ASIC for Micropattern Detectors*. (ATL-MUON-PROC-2015-015), Nov 2015.
- [49] Christos Bakalis. Guide learning of vhdl language and application in the firmware development for the mmfe8 boards for the upgrade of atlas experiment at cern. 2017.

- [50] Panagiotis Gkoutoumis. Design and development of the Level-1 Data Driver Card (L1DDC) for the New Small Wheel upgrade of the ATLAS experiment at CERN, May 2019. Presented 08 Apr 2019. URL: <https://cds.cern.ch/record/2674048>.
- [51] T. Alexopoulos, et al. The vmm readout system. *Nuclear Instruments and Methods in Physics Research Section A: Accelerators, Spectrometers, Detectors and Associated Equipment*, 955:163306, 2020. URL: <https://www.sciencedirect.com/science/article/pii/S0168900219315529>, doi:10.1016/j.nima.2019.163306.
- [52] R. Vlastou, et al. Characterization of the neutron flux distribution at the athens tandem accelerator ncsr “demokritos”. *Nuclear Instruments and Methods in Physics Research Section B: Beam Interactions with Materials and Atoms*, 269(24):3266–3270, 2011. Proceedings of the 10th European Conference on Accelerators in Applied Research and Technology (ECAART10). URL: <https://www.sciencedirect.com/science/article/pii/S0168583X11003661>, doi:10.1016/j.nimb.2011.04.015.
- [53] Lidia Amaral, et al. A 5 gb/s radiation tolerant laser driver in cmos 0.13  $\mu\text{m}$  technology. pages 321–325, 01 2009.
- [54] Lorne Levinson. New Small Wheel Electronics, 2022.
- [55] R. Jones, et al. The oks persistent in-memory object manager. *Nuclear Science, IEEE Transactions on*, 45:1958 – 1964, 09 1998. doi:10.1109/23.710971.
- [56] Paraschos Moschovakos, et al. A Software Suite For The Radiation Tolerant Giga-Bit Transceiver - Slow Control Adapter. Technical report, CERN, Geneva, 2019. 31/10/2019. URL: <https://cds.cern.ch/record/2694316>.
- [57] ATLAS Central DCS Team. SCA Software, 2022.
- [58] ATLAS Central DCS Team. SCA OPC UA Server, 2022.
- [59] ATLAS Central DCS Team. SCA OPC UA Client, 2022.
- [60] ATLAS Central DCS Team. fwSca, 2022.
- [61] P.P. Nikiel, et al. quasar : The Full-Stack Solution for Creation of OPC-UA Middleware. In *Proc. ICALEPCS’19*, number 17 in International Conference on Accelerator and Large Experimental Physics Control Systems, pages 453–457. JACoW Publishing, Geneva, Switzerland, 08 2020. <https://doi.org/10.18429/JACoW-ICALEPCS2019-MOPHA100>. URL: <https://jacow.org/icalepcs2019/papers/mopha100.pdf>, doi:10.18429/JACoW-ICALEPCS2019-MOPHA100.
- [62] Polyneikis Tzanis. NSW XML Generator. <https://gitlab.cern.ch/ptzanis/nswxmlgenerator>, 2022.
- [63] A Barriuso Poy, et al. The detector control system of the ATLAS experiment. *JINST*, 3:P05006, 2008.
- [64] Siemens. WinCC-OA. <http://w3.siemens.com/mcms/human-machine-interface/en/visualization-software/scada/pages/default.aspx>.

- [65] Konstantinos Ntekas. Performance characterization of the Micromegas detector for the New Small Wheel upgrade and Development and improvement of the Muon Spectrometer Detector Control System in the ATLAS experiment, 2016. Presented 2016. URL: <https://cds.cern.ch/record/2143887>.
- [66] P P Nikiel, et al. [OPC Unified Architecture within the Control System of the ATLAS Experiment](#). Mar 2014.
- [67] T. Alexopoulos, et al. Methods used for gas tightness test and percent oxygen monitoring of the NSW micromegas detectors of LHC-ATLAS experiment. *Journal of Physics: Conference Series*, 2105(1):012022, nov 2021. doi:10.1088/1742-6596/2105/1/012022.
- [68] Theodoros Alexopoulos, et al. [Investigation of Gas Leak Test Methods for the NSW Micromegas Multiplet's Mass Production](#). (ATL-COM-MUON-2015-054), Oct 2015.
- [69] CERN. Root data analysis framework. <https://root.cern.ch/>, 2017.
- [70] O Beltramello, et al. The Detector Safety System of the ATLAS experiment. *JINST*, 4:P09012, 2009. URL: <https://cds.cern.ch/record/1229189>, doi:10.1088/1748-0221/4/09/P09012.
- [71] ATLAS Central DCS Team. ATCA OPC UA Server. <https://gitlab.cern.ch/atlas-dcs-opcua-servers/AtcaOpcUa>, 2022.
- [72] Particle Data Group. Review of Particle Physics. *Progress of Theoretical and Experimental Physics*, 2022(8):083C01, 08 2022. arXiv:<https://academic.oup.com/ptep/article-pdf/2022/8/083C01/49175539/ptac097.pdf>, doi:10.1093/ptep/ptac097.
- [73] Hiroyuki Toda. *Fundamentals of X-Ray Imaging*, pages 17–49. Springer Singapore, Singapore, 2021. doi:10.1007/978-981-16-0590-1\_2.
- [74] Walter Blum, et al. *Particle detection with drift chambers*. Particle Acceleration and Detection. 2008. doi:10.1007/978-3-540-76684-1.
- [75] Manolis Dris et al. Signal formation in various detectors, 2017. arXiv:1406.3217.
- [76] Y. Giomataris, et al. Micromegas: a high-granularity position-sensitive gaseous detector for high particle-flux environments. *Nuclear Instruments and Methods in Physics Research Section A: Accelerators, Spectrometers, Detectors and Associated Equipment*, 376(1):29–35, 1996. URL: <https://www.sciencedirect.com/science/article/pii/0168900296001751>, doi:10.1016/0168-9002(96)00175-1.
- [77] I. Giomataris, et al. [Micromegas in a bulk](#). *Nuclear Instruments and Methods in Physics Research Section A: Accelerators, Spectrometers, Detectors and Associated Equipment*, 560(2):405 – 408, 2006. doi:10.1016/j.nima.2005.12.222.
- [78] T Alexopoulos, et al. [Study of resistive micromegas detectors in a mixed neutron and photon radiation environment](#). *Journal of Instrumentation*, 2012.
- [79] M Byszewski et al. [Resistive-strips micromegas detectors with two-dimensional readout](#). *Journal of Instrumentation*, page C02060, 2012.



- [80] T. Alexopoulos, et al. Performance studies of resistive-strip bulk micromegas detectors in view of the atlas new small wheel upgrade. *Nuclear Instruments and Methods in Physics Research Section A: Accelerators, Spectrometers, Detectors and Associated Equipment*, 937:125–140, 2019. URL: <https://www.sciencedirect.com/science/article/pii/S0168900219305194>, doi:10.1016/j.nima.2019.04.050.
- [81] Christos Bakalis. Research and Development of the Electronics and Data Acquisition System for the New Small Wheel Upgrade of the ATLAS Detector at CERN and Performance Evaluation of the Micromegas Chamber. Έρευνα και Ανάπτυξη των Ηλεκτρονικών και του Συστήματος Απόσπασης Δεδομένων της Αναβάθμισης New Small Wheel του Ανιχνευτή ATLAS στο CERN, και Χαρακτηρισμός της Απόδοσης του Θαλάμου Micromegas, 2021. Presented 16 Jul 2021. URL: <https://cds.cern.ch/record/2778078>.